

**CONSEQUENCES OF GIANT LANDSLIDES ON OCEAN ISLAND MAGMATISM:  
VOLCANIC AND GEOCHEMICAL EVOLUTION OF THE TENO MASSIF, TENERIFE,  
AND EL HIERRO ISLAND (CANARY ARCHIPELAGO)**

PhD Thesis

University of Dublin, Trinity College

2009

MARC-ANTOINE LONGPRÉ

I hereby declare that this thesis has not been submitted as an exercise for a degree at this or any other University. The work submitted is entirely my own except where otherwise stated. I agree that the Library may lend or copy this thesis upon request.

---

Marc-Antoine Longpré



## SUMMARY

Large-scale, catastrophic mass-wasting is a major process contributing to the dismantling of oceanic intra-plate volcanoes. Recent studies, however, have highlighted possible feedback relationships between lateral collapse events, or incipient flank instability, and subsequent episodes of structural re-arrangement and/or renewed volcano growth. A direct connection between the occurrence of giant landslides and changes in the geochemical regime of ocean island volcanoes has also been postulated, but lacked focussed in-depth testing at natural examples.

Utilising detailed field observations and petrological and geochemical techniques, this work evaluates possible links between large-scale landslides and subsequent volcanism/magmatism at two carefully selected type-localities, both situated in the Canary Archipelago: the Teno massif, on the island of Tenerife, and El Hierro Island, for which refined details of the volcanic and geochemical evolution are provided.

The Teno massif, discussed in Chapter 3, is a deeply eroded Miocene shield-volcano that was built in four major eruptive phases punctuated by at least two lateral collapses, each removing  $>20\text{-}25\text{ km}^3$  of the volcano's north flank. Inspection of angular unconformities, defining concentric palaeo-landslide embayments and fundamental stratigraphic boundaries, reveals the presence of abundant juvenile pyroclastic deposits, otherwise subdued in the region, indicating that extensive explosive eruptions occurred in close association with giant lateral collapse of the Teno volcano. Logging of post-collapse stratigraphic sequences, coupled with geochemical data and magma density calculations, indicates that, while relatively evolved magmas were produced just before flank collapses, dense and poorly-differentiated ankaramitic magmas, carrying large and abundant olivine and clinopyroxene crystals, were more frequently erupted after. Petrographic textures, mineral chemistry and clinopyroxene-melt thermobarometry reveal that the post-collapse Teno volcano was probably fed by system of interconnected sills and dykes, located at 20 to 45 km depth ( $P=350\text{-}1440\text{ MPa}$ ) in the upper mantle, from which ascending magma batches were able to rapidly propagate to the surface. The zirconium/niobium ratio and rare earth element (REE) concentrations of the lavas that were erupted in the short time-interval between the two landslides suggest peak degrees of partial melting in the mantle at this point of Teno's sub-aerial evolution.

Chapter 4 addresses the case of El Hierro, Canary Archipelago's youngest, smallest and westernmost island, where two of the most recent large-scale flank collapses on Atlantic volcanoes have taken place. The destructive Las Playas debris avalanche ( $\sim 25\text{-}50\text{ km}^3$ , dated between 176-145 ka) and El Golfo debris avalanche ( $150\text{-}180\text{ km}^3$ , bracketed between 134-21 ka) produced great coastal embayments bounded by vertiginous cliffs frequently in excess of a thousand meters. Since the large El Golfo landslide, the majority of pre-historic eruptions have taken place within the collapse embayment, reproducing a pattern commonly seen at volcanoes that have suffered a recent flank collapse. The ca. 6-4 ka ankaramitic Tanganasoga volcano, the largest volcanic

construction within the El Golfo embayment, may represent the future focal point of volcanism on the island. Logging of well-exposed stratigraphic profiles reveals that, after the eruptions of highly differentiated products at the mature El Golfo volcano, a return to more mafic and denser magmas (largely ankaramites), coinciding in time with the 'recent' giant landslides, has characterised the on-going Rift Volcanism phase. Petrography, mineral chemistry and thermobarometry indicate that Rift magmas have stagnated and crystallised olivine and clinopyroxene at upper mantle depth, between about 15 and 45 km below present sea level ( $P=340\text{--}1360$  MPa). Trace element concentrations (e.g. Zr/Nb and REE) of recent lavas, most of which post-date the Las Playas landslide and some of which also post-date the El Golfo landslide, are compatible with an increase in mean mantle melt fractions in the Rift Volcanism phase relative to the late El Golfo Volcano phase.

In Chapter 5, numerical models are used to quantify the perturbations that a large landslide may cause to the volcanic system. The decompression due to unloading decreases with depth, but retains significant magnitudes down to depths of magma storage under the Teno volcano and El Hierro Island. At these depths, stress changes obtained are comparable, although generally of larger magnitudes, than those that have been shown to externally trigger seismic and volcanic activity. However, stress changes may be insignificant at depths relevant to mantle melting beneath ocean island volcanoes.

Further implications of thermobarometric calculations are outlined in Chapter 6. It is argued that the main depths of magma storage at Teno and El Hierro may have been controlled by flexural stresses that are brought about by the load of the volcanic edifice itself. In addition, the role of flank collapse in causing the disruption of shallow magma reservoirs is discussed and proposed as a significant factor playing part in the magma feeding system evolution of oceanic volcanoes.

Observed changes in the eruptive regimes at the type-localities, such as an increase in pyroclastic activity and the renewed eruptions of dense mafic magmas at the expense of differentiated magma types of lower density, indicate that volcanic edifice mass-wasting can drastically alter magmatic feeding system processes, such as storage, accumulation, transport, mixing, degassing and differentiation of magmas. Landslide-induced disturbances in the state of stress of the volcanic and magmatic system can reach the upper mantle, retaining relatively large magnitudes down to depths of magma storage beneath oceanic hot-spot volcanoes. However, despite geochemical data compatible with this possibility, giant landslides appear unlikely to affect mantle melting beneath ocean island volcanoes, as the resulting decompression probably does not propagate to relevant depths in significant amplitudes. Nevertheless, the case-studies of the Miocene Teno volcano, on Tenerife, and of El Hierro Island suggest that destructive (and constructive) processes play a role thus far underestimated in regulating the geochemical regimes of many ocean island volcanoes.

## **ACKNOWLEDGEMENTS**

My first thanks have to go to my supervisor, Valentin Troll, for his infallible support throughout this project. His backing, on scientific, academic, organisational, financial and personal matters, has been very valuable. Valentin taught me a lot, directly and indirectly, and prepared me for my future professional endeavours.

I also owe a lot to Thor Hansteen, who has been a dedicated advisor all along this research. His constructive criticism on my work pushed me to considerably improve my understanding of petrology. Thor's logistical support during my stays at IFM-GEOMAR was also greatly appreciated. I am also grateful to Thomas Walter, for discussions and input, and for having contributed to a successful and pleasant stay at GFZ Potsdam. I benefitted from instructive scientific discussions (verbal or written) with many other people, including Andrea Manconi, Rodrigo del Potro, Andreas Klügel, John MacLennan, Steve Jones, Keith Putirka, Thomas Sisson and Raphaël Paris. Thanks also to John Graham for giving me my first opportunity to discover the science of teaching.

For logistical and technical support they provided, I am thankful to Juan Carlos Carracedo, Mario Thöner, Gerhard Brey, Neil Kearney, Declan Burke, Francis Hendron and Maura Morgan.

Of course, I have to thank all my fellow Pearse St. office mates and VAMP friends (wherever they are now) for a wide range of reasons, from company on Canarian volcanoes, to enthusiastic scientific talks in the Long Stone, to daily supply of entertainment and delicious veggie food. Millions of thanks, especially to Jane, Graeme, Fiona, Eoghan, Brian, Eleanor, Sebastian, Paul, Audray, Frances, Karina, Orla and Hilary.

To the other main actors in my Dublin life, past and present housemates and friends, especially Laura, Sergio, Boris, Alexandra and Margherita, thanks for the countless distractions and lively chats around the "dinner" and pub table.

Clin d'œil à mes vieilles branches québécoises qui, malgré l'éloignement prolongé, sont restées présentes aux moments opportuns...entre autres, Marie-Evelyne, Simon, Marie-Pierre, Matthieu, Raphaël, Claire et Nathalie. Un petit mot pour ma famille, mes frérots Louis-Philippe et Félix-Arthur, mon spère Marc et Julie, et particulièrement ma maman Danielle et papa François pour leur amour, leur écoute, leur soutien inconditionnel et leurs encouragements. Merci!

Finally, I wish to acknowledge the Natural Science and Engineering Research Council of Canada and Trinity College Dublin for their financial support, which allowed me to undertake this Irish postgraduate adventure.

## TABLE OF CONTENTS

<b>CHAPTER 1: INTRODUCTION .....</b>	<b>1</b>
<b>1.1 Prelude: The Rise of Volcano Flank Collapses .....</b>	<b>1</b>
<b>1.2 Underlying Hypothesis, Aims and Structure of Thesis .....</b>	<b>1</b>
1.2.1 <i>Scientific Problem</i> .....	1
1.2.2 <i>Thesis Objectives</i> .....	2
1.2.3 <i>Thesis Structure</i> .....	3
<b>1.3 Evolution of Hawaiian and Canarian Volcanoes: a Comparison .....</b>	<b>4</b>
1.3.1 <i>Tectonic Setting</i> .....	4
1.3.2 <i>Volcano Growth</i> .....	5
1.3.2.a <i>The Pre-Shield Stage</i> .....	6
1.3.2.b <i>The Shield Stage</i> .....	6
1.3.2.c <i>The Post-Shield Stage</i> .....	7
1.3.2.d <i>The Rejuvenated Stage</i> .....	8
1.3.2.e <i>Rift zones</i> .....	8
1.3.3 <i>Volcano Decay</i> .....	9
1.3.3.a <i>Erosion</i> .....	9
1.3.3.b <i>Subsidence</i> .....	9
1.3.3.c <i>Giant Mass-Wasting Events</i> .....	10
<b>Figures .....</b>	<b>12</b>
<b>Tables.....</b>	<b>14</b>
<b>CHAPTER 2 – METHODOLOGY .....</b>	<b>15</b>
<b>2.1 Field Work.....</b>	<b>15</b>
2.1.1 <i>Nomenclature</i> .....	15
2.1.2 <i>Mapping and Logging</i> .....	15
2.1.3 <i>Sampling</i> .....	16
<b>2.2 Sample Preparation .....</b>	<b>16</b>
<b>2.3 Analytical Techniques .....</b>	<b>17</b>
2.3.1 <i>X-Ray Fluorescence (XRF)</i> .....	17
2.3.2 <i>Inductively Coupled Plasma Mass Spectrometry (ICP-MS)</i> .....	17
2.3.3 <i>Electron Microprobe (EMP)</i> .....	18
<b>2.4 Geochemical Data Filtering .....</b>	<b>18</b>
<b>2.5 Thermobarometry .....</b>	<b>19</b>
2.5.1 <i>Theoretical Background and Uncertainties</i> .....	19
2.5.2 <i>Equilibrium Tests</i> .....	19
2.5.3 <i>Pressure to Depth Conversion</i> .....	21
<b>2.6 Numerical Modelling.....</b>	<b>21</b>
<b>Tables.....</b>	<b>22</b>
<b>CHAPTER 3 – THE TENO MASSIF .....</b>	<b>24</b>
<b>3.1 Introduction and Geological Background .....</b>	<b>24</b>
<b>3.2 Stratigraphy of the Teno Massif .....</b>	<b>25</b>
3.2.1 <i>Previous Work</i> .....	25
3.2.2 <i>New Stratigraphic Constraints</i> .....	26

<b>3.3 Description of Stratigraphic Units .....</b>	<b>27</b>
3.3.1 Masca Formation.....	27
3.3.2 Masca Unconformity.....	27
3.3.3 Carrizales Formation .....	28
3.3.3.a Barranco del Carrizal log.....	28
3.3.3.b Masca-Cruz de Gilda log.....	29
3.3.4 Carrizales Unconformity .....	29
3.3.4.a Cherfe Outcrop.....	30
3.3.5 El Palmar Formation.....	30
3.3.5.a Alto Carrizal Outcrop.....	31
3.3.5.b Alto Carrizal-La Tabaiba log.....	32
3.3.6 Los Gigantes Formation .....	32
<b>3.4 Petrology and Geochemistry .....</b>	<b>33</b>
3.4.1 Petrography .....	33
3.4.1.a Lava Samples .....	33
3.4.1.b Pyroclastic Samples.....	34
3.4.2 Rock Major and Trace Element Chemistry.....	35
3.4.2.a Total-Alkali-Silica Classification.....	35
3.4.2.b Major and Trace Element Variations Versus MgO .....	35
3.4.2.c Incompatible Trace and Rare Earth Elements.....	36
3.4.2.d Major and Trace Element Variations Versus Stratigraphic Level .....	36
3.4.2.d.I Entire Teno Sequence .....	36
3.4.2.d.II Detailed Masca-La Tabaiba Sequence.....	38
3.4.3 Mineral Chemistry.....	39
3.4.4 Thermobarometry.....	40
3.4.5 Magma Density Calculations .....	42
<b>3.5 Discussion.....</b>	<b>42</b>
3.5.1 Implications of Breccia and Pyroclastic Deposits.....	43
3.5.2 Implications of Stratigraphic Logs and Magma Density Calculations .....	45
3.5.3 Implications of Petrological and Geochemical Results .....	45
3.5.3.a Magma Ascent Conditions .....	45
3.5.3.b Thermobarometry, Magma Storage and Fractional Crystallisation .....	47
3.5.3.c Partial Melting and Magmatic Cycles .....	52
3.5.3.c.I Blobs of Upwelling Plume Material .....	54
3.5.3.c.II Destruction of the Volcanic Edifice.....	55
3.5.3.c.III Transition Between Shield and Post-Shield Volcanism.....	56
3.5.4 An Evolutionary Model for the Teno Volcano .....	57
<b>3.6 Conclusions .....</b>	<b>59</b>
<b>Figures .....</b>	<b>61</b>
<b>Tables.....</b>	<b>77</b>
 <b>CHAPTER 4 – EL HIERRO ISLAND .....</b>	 <b>85</b>
<b>4.1 Introduction .....</b>	<b>85</b>
<b>4.2 Background and Previous Work .....</b>	<b>86</b>
4.2.1 Edifice Morphology: Rift Zones and Giant Collapse Structures .....	86
4.2.1.a Rift Zones.....	86
4.2.1.b The Tiñor Collapse.....	87
4.2.1.c The El Julán Landslide .....	87
4.2.1.d The Las Playas/San Andrés Landslide(s) .....	88
4.2.1.e The El Golfo Landslide.....	88
4.2.2 Stratigraphy of El Hierro Island .....	89
4.2.2.a Early Work .....	89
4.2.2.b The Tiñor Volcano Formation.....	90
4.2.2.c The El Golfo Volcano Formation .....	91
4.2.2.d The Rift Volcanism Formation.....	91
4.2.3 Petrology .....	91

<b>4.3 Field Work</b>	<b>92</b>
4.3.1 <i>Pre-El Golfo Landslide Volcanics</i>	93
4.3.1.a Peña Log	93
4.3.1.b Jinama Log	94
4.3.1.c Sabinosa Log	94
4.3.2 <i>Post-El Golfo Landslide Volcanics</i>	95
4.3.2.a The Tanganasoga Volcano	96
4.3.3 <i>Rift Volcanism With Uncertain Timing Relative to the El Golfo Landslide</i>	96
<b>4.4 Petrology and Geochemistry</b>	<b>97</b>
4.4.1 <i>Petrography</i>	97
4.4.2 <i>Rock Major and Trace Element Chemistry</i>	98
4.4.2.a Total-Alkali-Silica Classification	98
4.4.2.b Major and Trace Element Variations Versus MgO	99
4.4.2.c Incompatible Trace and Rare Earth Elements	99
4.4.2.d Major and Trace Element Variations Versus Stratigraphic Level	100
4.4.3 <i>Mineral Chemistry</i>	101
4.4.4 <i>Thermobarometry</i>	102
4.4.5 <i>Magma Density Calculations</i>	103
<b>4.5 Discussion</b>	<b>104</b>
4.5.1 <i>Implications of Breccias and the Distribution of Post-Collapse Vents</i>	104
4.5.2 <i>Implications of Logs, the Distribution of Ankaramites and Magma Density</i>	106
4.5.3 <i>Implications of Petrological and Geochemical Results</i>	107
4.5.3.a Magma Ascent Conditions	107
4.5.3.b Fractional Crystallisation and Magma Storage Conditions	108
4.5.3.c Partial Melting and Magmatic Cycles	112
<b>4.6 Conclusions</b>	<b>113</b>
<b>Figures</b>	<b>115</b>
<b>Tables</b>	<b>130</b>
 <b>CHAPTER 5 – NUMERICAL MODELLING</b>	 <b>138</b>
5.1 <b>Introduction</b>	138
5.1.1 <i>Note on Collaborative Research</i>	138
5.2 <b>Methods</b>	138
5.2.1 <i>Model Setup and Physical Parameters</i>	138
5.2.2 <i>Calculation Procedures</i>	139
5.3 <b>Results</b>	139
5.4 <b>Discussion</b>	140
5.4.1 <i>Comparison With Other Studies</i>	140
5.4.2 <i>Possible Effects of Plumbing System Dynamics</i>	141
5.4.3 <i>Possible Effects on Melt Generation</i>	141
5.4.4 <i>Limitations of Models</i>	143
5.5 <b>Conclusions</b>	143
<b>Figures</b>	144
 <b>CHAPTER 6 –MAGMA PLUMBING AT OCEANIC VOLCANOES</b>	 <b>146</b>
6.1 <b>Introduction</b>	146
6.2 <b>Controls on Magma Storage and Transport</b>	146
6.3 <b>Plumbing System Evolution at Ocean Island Volcanoes</b>	149
<b>Figures</b>	152

<b>CHAPTER 7 – CONCLUSIONS AND OUTLOOK.....</b>	<b>154</b>
7.1 Chapter 1: Introduction .....	154
7.2 Chapter 3: The Teno Massif.....	155
7.3 Chapter 4: El Hierro Island.....	156
7.4 Chapter 5: Numerical Modelling.....	157
7.5 Chapter 6: Magma Plumbing at Oceanic Volcanoes: More Implications.....	158
7.6 General Conclusions .....	158
7.7 Possible Avenues for Further Research .....	159
<b>REFERENCES .....</b>	<b>161</b>

## **APPENDIX A:**

Longpré, M.-A., R. del Potro, V. R. Troll, and G. R. Nicoll (2008), Engineering geology and future stability of the El Risco landslide, NW-Gran Canaria, Spain, Bulletin of Engineering Geology and the Environment, 67(2), 165-172.

## **APPENDIX B: ADDITIONAL STRATIGRAPHIC CONSTRAINTS (CHAPTER 3)**

## **APPENDIX C: MINERAL CHEMISTRY PLOTS (TENOMASSIF)**

## **APPENDIX D: MINERAL CHEMISTRY PLOTS (EL HIERRO)**

## **APPENDIX E: MINERAL CHEMISTRY TABLES (TENOMASSIF)**

Microsoft Excel files on annexed CD

## **APPENDIX F: MINERAL CHEMISTRY TABLES (EL HIERRO)**

Microsoft Excel files on annexed CD

## CHAPTER 1 – INTRODUCTION

### 1.1 Prelude: The Rise of Volcano Flank Collapses

Modern volcanology took a giant leap on May 18<sup>th</sup>, 1980, as Mount St. Helens, in Washington State, USA, was the site of one of the most important geologic event of the 20<sup>th</sup> Century [*Glicken*, 1996 and references therein]. Indeed, the climactic eruption of the volcano provided an unprecedented window into the processes that may occur during a major volcanic eruption. One of these processes, the lateral collapse of the volcano, was dramatically displayed during the first moments of this event, producing the largest mass-movement in recorded history [*Glicken*, 1996]. Triggered by a magnitude 5.1 earthquake, the sliding of the first of three rockslide-debris avalanche blocks unroofed and decompressed a shallow magma intrusion (cryptodome) and its surrounding hydrothermal system, resulting in the initial explosions of a lateral blast that devastated 600 km<sup>2</sup> of mature forest [*Glicken*, 1996 and references therein]. Mount St. Helens, once a youthful, conical volcano, was left deeply incised by a horseshoe-shaped depression, losing 400 m in height during the event. Since May 18<sup>th</sup>, 1980, evidence of edifice failure, in the shape of amphitheatre-like reentrants carved into volcanic edifices or the associated large debris avalanches deposits, has been identified at several hundred volcanoes [see *McGuire*, 1996 and references therein]. With a worldwide recurrence time for lateral collapse of strato-volcanoes of once every 25 years over the past ~500 years, volcano instability poses a significant hazard that requires a sustained high-level of research on the causes and effects of volcano flank collapses [*Siebert*, 1992; *McGuire*, 1996].

### 1.2 Underlying Hypothesis, Aims and Structure of Thesis

#### 1.2.1 Scientific Problem

The Mount St. Helens example highlights how flank collapse, or incipient instability, can dramatically affect the behaviour of an andesitic strato-volcano. As it will be discussed in this chapter, intra-plate oceanic volcanoes too, like continental arc strato-volcanoes, are frequently subjected to lateral collapse during their lifetime; only, the volumes involved in these landslides may be up to three orders of magnitude larger than in the case of Mount St. Helens (~2.5 km<sup>3</sup> for Mount St. Helens [*Glicken*, 1996 and references therein] compared to 5,000 km<sup>3</sup> for Hawaii [*Moore et al.*, 1994]). In this context, it should be expected that the volcanic activity of ocean island volcanoes may also be disturbed and



altered by such large-scale landsliding; however, the dissimilarities in tectonic setting and in the volcanic systems of andesitic strato-volcanoes relative to basaltic shield-volcanoes are likely to result in a significantly different set of phenomena, on different size- and time-scales.

Feedback processes between flank instability and magma plumbing have been documented at both extinct and active oceanic volcanoes and may result in the reconfiguration of existing rift zones and ultimately promote the formation of new rift zones [Lipman *et al.*, 1991; Day *et al.*, 1999a; 1999b; Walter and Schmincke, 2002; Walter and Troll, 2003; Tibaldi, 2004; Walter *et al.*, 2005a; 2005b]. In addition, Amelung and Day [2002] proposed that giant lateral collapses may lead to the removal or extinction of pre-existing shallow magma reservoirs. Yet, further studies suggest that large-scale landsliding may also affect the geochemical regime of ocean island volcanoes. Apparent increases in the degree of partial melting in the mantle have been attributed to collapse-induced decompression [Presley *et al.*, 1997; Hildenbrand *et al.*, 2004]. A direct link between the reduction of significant overburden during mass-wasting and apparent subsequent adjustments of the magmatic system has therefore been repeatedly inferred in the literature, but lacks focussed in-depth testing at natural examples.

### 1.2.2 Thesis Objectives

The broad aim of this thesis is therefore to improve our knowledge on the consequences that large-scale landslide events may have on the volcanic regime of ocean island volcanoes. To achieve this, two exemplary natural laboratories were selected: the Teno massif, on the island of Tenerife, and El Hierro Island, both situated in the Canary Archipelago. The two study areas are complementary. Firstly, the Teno massif, which represents the eroded remnant of a Miocene volcano that suffered two giant landslides ca. 6 Ma ago, is ideal to study temporal variations in the volcanic regime with respect to ancient, successive collapse events. There, the well-exposed volcanic stratigraphy is clearly divided by angular unconformities, which are the relics of the palaeo-landslide scars, and pre- and post-collapse lava formations can be observed and sampled. On the other hand, El Hierro offers a geologically more recent analogue of a similar setting. Indeed, this young volcanic island has been the site of the most recent giant landslides in the Canary Islands as well as that of numerous eruptions in the Holocene and Upper Pleistocene. This offers the unique opportunity to study the early stages of volcanic reconstruction after giant lateral collapse. The pre-collapse volcanic stratigraphy is

superbly exposed in a >1000-m-high landslide headwall and post-collapse products are also widely accessible within the collapse embayment.

More specifically, the thesis objectives are to:

- a) Utilise systematic field observations of the stratigraphic sequence at the two type-localities to identify potential variations in their volcanic regimes through time.
- b) Employ petrological and geochemical techniques in conjunction to study the temporal evolution of the magmatic system beneath the two study areas.
- c) Use thermobarometry (based on clinopyroxene-melt equilibria) to determine the depths of long-term magma stagnation at the type-localities.
- d) Explore, through a set of numerical models, the physical effects of surface unloading on the magma plumbing system of a volcanic edifice analogous to the type-localities.
- e) Integrate the results obtained in a) to d) in order to formulate a general scheme that illustrates the role of giant landslide events in the magmatic evolution of ocean island volcanoes.

### 1.2.3 Thesis Structure

In the present chapter, current concepts of ocean island volcano evolution are reviewed and discussed, providing a base for subsequent discussion throughout the thesis. In Chapter 2, the details of analytical procedures and uncertainties that are common to the study of both type-localities are provided. Chapter 3 and Chapter 4 are the core sections of the thesis; they present the results of field, petrological and geochemical studies of the Teno massif and El Hierro Island, respectively. Chapter 5 is a brief account of numerical modelling results on the physical effects that giant landslides generate in the deep subsurface beneath ocean island volcanoes. In Chapter 6, we elaborate further on the implications of the results of Chapter 3 and Chapter 4, especially regarding the thermobarometric data. Finally, Chapter 7 brings together the main conclusions of the thesis, while an outlook to future work is presented.

Appendix A presents a case-study, published by *Longpré et al.* [2008a], on the structure and stability of a small-scale landslide in NW-Gran Canaria. This work was performed during the period of registration of the author on the higher degree register at

the University of Dublin. Appendix B contains additional details on new stratigraphic constraints presented in Chapter 3 for the Teno massif. Appendices C and D provide a graphical account of mineral chemistry data for Chapter 3 and Chapter 4, respectively. Appendices E and F are Microsoft Excel files containing all mineral chemistry data obtained from electron microprobe analysis. They are included on a CD attached to this thesis.

### 1.3 Evolution of Hawaiian and Canarian Volcanoes: a Comparison

#### 1.3.1 Tectonic Setting

The Hawaiian volcanoes (Figure 1.1a, b), located in the middle of the Pacific plate on a 73- to 106-Ma-old sea floor, are the archetypal ‘hot-spot’ volcanoes; that is to say that their existence is due to the presence of a near-stationary mantle plume, where thermally anomalous material originating from deep in the Earth, perhaps the core-mantle interface, rises and eventually melts to generate magma [Wilson, 1963]. The rapid motion of the Pacific plate relative to the vigorous Hawaiian hot-spot (buoyancy flux of 8.7 Mg/s [Sleep, 1990]) resulted in the formation of a 5,800-km-long chain of volcanoes in the course of the last ~75-80 Ma, for an average volcanic propagation rate of ~8.6 cm/year [Clague and Dalrymple, 1987].

There is now general acceptance that the Canary Islands (Figure 1.1c) also, like Hawaii, owe their origin to a mantle hot-spot, although substantial debate on the matter has taken place until relatively recently [Anguita and Hernán, 1975; Araña and Ortiz, 1991; Holik *et al.*, 1991; Hoernle and Schmincke, 1993a; Carracedo *et al.*, 1998; Anguita and Hernán, 2000]. The Selvagen Islands and neighbouring seamounts to the NNE of the archipelago also appear to have been produced by the early activity of the Canary hot-spot [see Geldmacher *et al.*, 2001]. Unlike Hawaii, the Canary Islands are located close to a continental margin, with the easternmost islands of Lanzarote and Fuerteventura only ~100 km from the continental shelf off the Moroccan coast. The archipelago lies on one of the oldest sea floors on Earth (Jurassic age of 175 Ma east of Lanzarote and 156 Ma west of El Hierro [e.g. Roest *et al.*, 1992]), implying a maximum oceanic lithosphere thickness. In drastic contrast to the Pacific plate, the African plate is near-stationary [e.g. Morgan, 1983]; as a result, since the onset of magmatism at >60 Ma to Upper Cretaceous times [e.g. Holik *et al.*, 1991; Collier and Watts, 2001], the relatively weak Canary hot-spot (buoyancy flux of <1 Mg/s [Sleep, 1990]) only produced a ~800-km-long and ~450-km-

wide belt of seamounts and islands, from Lars Seamount in northeast to El Hierro Island in the southwest [Geldmacher *et al.*, 2001]. Using the oldest K-Ar ages available for the main Canary Islands (~20 Ma for Fuerteventura [Coello *et al.*, 1992; Ancochea *et al.*, 1996]), Carracedo *et al.* [1998] calculated a volcanic propagation rate of 1.9 cm/year.

Most, if not all, of the peculiarities of Canarian volcanoes (with respect to Hawaiian volcanoes) outlined below may be explained by the greater lithospheric thickness, lower plume flux and, especially, slower plate motion [see Carracedo *et al.*, 1998]. However, some apparent features of Canarian volcanism, such as multiple magmatic cycles on a single island and the historic eruption of tholeiitic basalt on one of the oldest, easternmost islands (Lanzarote), remain difficult to reconcile with a simple, continuously active mantle plume. This led Hoernle and Schmincke [1993a] to propose that the Canary hot-spot is characterised, from 100-200 km depth, by a broad region of upwelling (>600 km long and > 200 km wide), where solitary waves, or “blobs”, of plume material rise beneath the islands. In this model, the decompression melting of a single blob produces a discrete magmatic cycle, in which the saturation of magmas in SiO<sub>2</sub> initially increases and then decreases. Whilst this “blob model” seemingly provides a sensible explanation for the evolution of Gran Canaria, on which it is largely based [Hoernle and Schmincke, 1993b; a], detailed geochemical evolution of more individual volcanoes have to be integrated to determine if this model is viable, essential or unnecessary to explain the characteristics of Canarian volcanism across the entire archipelago.

### 1.3.2 Volcano Growth

Along the Hawaiian Ridge, each seamount or island has been built by successively overlapping volcanoes; e.g. the ‘Big Island’ of Hawaii is constructed of 5 volcanic centres: Kilauea, Mauna Loa, Mauna Kea, Hualalai and Kohala (Figure 1.1a). Each Hawaiian volcano typically grows through four stages, these are the pre-shield, shield, post-shield and rejuvenated (or post-erosional) stages (Figure 1.1b), although a volcano may become extinct before this sequence is complete [Clague and Dalrymple, 1987].

As in Hawaii, each island of the Canary Archipelago represents the product of coalescing volcanoes (Figure 1.1c). For example, Tenerife is the amalgamation of the Central shield, Teno, Anaga, Las Cañadas and Teide-Pico Viejo volcanoes [e.g. Guillou *et al.*, 2004]. This fact, however, has generally been overlooked when comparing the well-defined four-stage evolution of Hawaiian volcanoes to that of Canarian volcanoes; instead,

most authors have referred to islands, as opposed to individual volcanoes, to be, say, in the ‘shield stage’ [cf. *Carracedo et al.*, 1998; *Geldmacher et al.*, 2001; *Paris et al.*, 2005b]. Although a two-step evolution (the shield stage and rejuvenated stage) is most readily identifiable [*Carracedo et al.*, 1998], equivalents of the four Hawaiian stages have nonetheless been proposed to occur in the Canaries (Figure 1.1) [*Carracedo et al.*, 1998; *Paris et al.*, 2005b].

In the case of Hawaii, magma supply rates, storage system configuration and erupted lava types (and entrained xenoliths) differ considerably for each stage of the eruptive sequence (Figure 1.1a, b)[e.g. *Clague*, 1987]; such systematics are, however, only very poorly constrained for Canarian volcanoes.

### 1.3.2.a The Pre-Shield Stage

The seamount, pre-shield stage, lasting for some 0.2-0.3 Ma, is typified by Loihi seamount, the youngest Hawaiian volcano (Figure 1.1b). This stage is apparently characterised by low magma supply rates and by the sub-marine eruptions of alkali basalts. A “deep magma reservoir”, perhaps near the crust-mantle interface, begins to form, which allows appreciable differentiation of the alkalic magmas [*Clague and Dixon*, 2000].

Remnants of the seamount volcano, in drastic contrast to Hawaii, are thought to be exposed above sea level on the Canary Islands of Fuerteventura, La Gomera and La Palma (Figure 1.1c) [e.g. *Cendrero*, 1970; *Stillman et al.*, 1975; *Staudigel and Schmincke*, 1984; *Carracedo et al.*, 1998]. Similar rock formations, characterised by variably deformed and uplifted sequences of sub-marine sediments, pillow basalts and dyke and sill complexes also occur above sea level in the Cape Verde and Madeira archipelagos [e.g. *Stillman et al.*, 1982; *Geldmacher et al.*, 2000]. The duration of the pre-shield stage for Canarian volcanoes is unknown, although it is most likely substantially longer than in Hawaii [cf. *Paris et al.*, 2005b].

### 1.3.2.b The Shield Stage

In the lapse of 0.7-1 Ma, Hawaiian volcanoes in their main shield stage rapidly build up 95-98% of their mass through frequent and voluminous eruptions of tholeiitic basalt (Figure 1.1b). This sustained magma supply also results in the formation of shallow magma chambers as the temperature of the crust is sufficiently high to prevent magma solidification [*Clague and Dixon*, 2000]. Mauna Loa and Kilauea are the classic examples of volcanoes in the shield stage of growth.

Peak magma supply rates also characterise the sub-aerial shield stage of Canarian volcanoes, resulting in rapid volcano growth for a period of 1-2 Ma [e.g. *McDougall and Schmincke*, 1976; *Carracedo et al.*, 2001; *Guillou et al.*, 2004]. In contrast to the predominance of tholeiitic basalts in the Hawaiian shield stage, however, a much wider spectrum of magma compositions is involved in the Canary Islands, with a generally higher degree of alkalinity. Indeed, even though the bulk of the shield volcanics are basaltic in nature, tholeiitic basalt is rather rare (mostly found on Gran Canaria [*Hoernle and Schmincke*, 1993b]) and alkali basalt and basanite, with associated differentiated lavas, are much more abundant [*Ancochea et al.*, 1996; *Thirlwall et al.*, 2000; *Carracedo et al.*, 2001]. Volcanoes in their shield stage are located on the islands of La Palma and El Hierro (Figure 1.1c) [cf. *Carracedo et al.*, 1998; *Paris et al.*, 2005b].

### 1.3.2.c The Post-Shield Stage

Most, but not all, Hawaiian volcanoes go through the post-shield stage, whereby a thin cap of alkalic lavas covers the main tholeiitic shield (Figure 1.1b). This eruptive phase lasts for 0.2-0.9 Ma and accounts for ~1% of the volcano volume [e.g. *Clague and Dixon*, 2000; *Tagami et al.*, 2003]. Magma supply rates greatly diminish early in this stage, causing magma reservoirs and conduits in the edifice and upper crust to freeze. Only the “deep magma reservoir” persists until late in this evolutionary phase. The post-shield stage of growth is particularly well-documented at Mauna Kea volcano, where fractionation of clinopyroxene-rich assemblages in the uppermost mantle (~800 MPa) is inferred to have yielded the late eruptions of hawaiitic magmas [*Frey et al.*, 1990].

Probably due to the wider compositional range of the Canarian shield stage volcanics, the distinction between the shield and the post-shield stage has rarely been made and is generally ignored [e.g. *Carracedo et al.*, 1998]. However, marked compositional variations or structural discontinuity without discernable temporal gap in volcanic activity may be used to discern the shield and post-shield stages of development [*Paris et al.*, 2005b]. Notably, the eruptions on Gran Canaria of highly differentiated products (~40 rhyolitic, trachytic and phonolitic ignimbrites) shortly followed the formation of a basaltic shield and may represent a long-lasting post-shield stage [cf. *McDougall and Schmincke*, 1976; *Schmincke*, 1976; Figure 8 of *Paris et al.*, 2005b]. *Paris et al.* [2005b], who identified a post-shield phase on the island of La Gomera, proposed that this eruptive stage may last for up to 5 Ma at Canarian volcanoes and that Taburiente volcano on La Palma may currently be at this phase of development (Figure 1.1c).

#### 1.3.2.d The Rejuvenated Stage

In Hawaii, the final, rejuvenated eruptive stage (Figure 1.1b) is preceded by 0.25-2.5 Ma of volcanic hiatus during which the volcano is incised by erosion [*Clague and Dalrymple, 1988*]. Accounting for much less than 1% of the volcano mass, this stage is characterised by the sporadic supply of strongly alkaline lavas that erupt from short-lived vents randomly scattered on the flanks of the volcano. These magmas appear to transit directly from upper mantle depths to the surface, implying the lack of significant magma storage system [e.g. *Clague, 1987*]. The rejuvenated eruptive stage, which is absent on several Hawaiian volcanoes, may last for up to 3.2 Ma [*Clague and Dalrymple, 1988; Clague and Dixon, 2000*].

In the Canaries, the onset of rejuvenated volcanism appears to occur after a much longer period of volcanic quiescence of 4-5 Ma during which the shields are deeply eroded [*Carracedo et al., 1998; Paris et al., 2005b*]. In contrast to Hawaii, the volumes involved in this phase are far from trivial, although they are still greatly inferior to those of the shield stage. The Las Cañadas and Teide-Pico Viejo strato-volcanoes on Tenerife and the Roque Nublo strato-volcano on Gran Canaria are fine examples of voluminous episodes of rejuvenated volcanism [*Pérez Torrado et al., 1995; Carracedo et al., 2007*]. The products of rejuvenated volcanism vary widely in composition, from the tholeiitic basalts (although this may have been a contaminated basanitic magma [*Aparicio et al., 2006*]) erupted during the 1730-1736 eruption of Lanzarote to the phonolitic, sub-plinian deposits of Montaña Blanca in Tenerife [*Carracedo et al., 1992; Ablay et al., 1995*]. There is, however, a clear tendency for a higher proportion of highly differentiated products compared to the shield stage volcanics. In the Canaries, the duration of the rejuvenated stage largely exceeds 3 Ma, but a clearer picture awaits better constraints on the duration of volcanic stages in the eastern islands of Fuerteventura and Lanzarote [cf. *Coello et al., 1992; Ancochea et al., 1996; Paris et al., 2005b*]. The islands of Lanzarote, Fuerteventura, Gran Canaria and Tenerife have all been the sites of rejuvenated volcanism in the Holocene, whilst La Gomera is thought to be in the volcanic hiatus between the post-shield and rejuvenated stages (Figure 1.1c) [*Carracedo et al., 1998; Paris et al., 2005b*].

#### 1.3.2.e Rift zones

Rift zones are striking constructional features of both Hawaiian and Canarian volcanoes; at youthful volcanoes, they are expressed in the form of narrow topographic ridges often characterised by a high density of aligned eruptive vents; at eroded centres, they are

expressed as swarms of parallel dykes, with increasingly dense packing with depth [*Fiske and Jackson*, 1972; *Lipman*, 1980; *Dieterich*, 1988; *Walker*, 1992; *Carracedo*, 1994; *Carracedo*, 1999; *Walker*, 1999]. Whilst all 14 centres that make up the Hawaiian Islands show two or more identifiable rift zones, single- or triple-rift systems are present on all Canary Islands, except perhaps La Gomera and Gran Canaria (Figure 1.1a, c) [*Fiske and Jackson*, 1972; *Carracedo*, 1994; *Walter and Troll*, 2003; *Paris et al.*, 2005b]. Hawaiian rift zones have been shown to extend to some 6-10 km depth and their location are thought to be mainly controlled by gravitational stresses within an edifice, but also by the buttressing influence of pre-existing shields [e.g. *Fiske and Jackson*, 1972; *Ryan*, 1988]. *Carracedo* [1994] proposed that Canarian rift zones, unlike their Hawaiian counterparts, develop as a result of magma-induced upward doming of the crust, causing regular,  $\sim 120^\circ$ -spaced fracture patterns that obey a “least-effort” principle; however, there is growing evidence that these features are largely controlled by gravitational stresses within the volcanic edifice itself [*Walter*, 2003; *Walter and Troll*, 2003; *Walter et al.*, 2005b; *Münn et al.*, 2006].

### 1.3.3 Volcano Decay

#### 1.3.3.a Erosion

Higher rainfall probably results in higher erosion rates in Hawaii compared to the dryer Canaries [*Carracedo*, 1999]. However, extended periods of volcanic hiatus whilst the volcano remains above sea level permit extensive incision of the dormant/extinct Canarian volcanoes; this typically results in the formation of deep radial canyons, locally called ‘barrancos’, in alternation with adjacent ridges [e.g. *Paris et al.*, 2005b]. Nevertheless, the contribution of long-term erosion to volcano decay is thought to be minimal, largely surpassed by the action of subsidence (Hawaii) and episodic mass-wasting (Hawaii and Canaries) [e.g. *Moore*, 1987; *Moore et al.*, 1994; *Carracedo*, 1999; *Gee et al.*, 2001b].

#### 1.3.4 Subsidence

Hawaiian volcanoes have a relatively short sub-aerial history (the oldest emerged island is less than 6 Ma old [*MacDonald et al.*, 1983]); within a few million years after emergence, they subside below sea level. Indeed, as plate motion carries Hawaiian volcanoes away from the hot-spot, the heated lithosphere starts to cool again and, in doing so, thickens and subsides; this results in increasing sea floor depth away from the hot-spot and progressive submergence of volcanoes below sea level [e.g. *Moore*, 1987]. Whilst subsidence is a



major process driving the disappearance of Hawaiian volcanoes below sea level, it does not contribute significantly to the decay of Canarian volcanoes. In fact, Canarian volcanoes show little or no evidence of subsidence or uplift since emergence and their sub-aerial history may extend for more than 20 Ma (Figure 1.1c) [Carracedo, 1999 and references therein]. The slow motion of the African plate as well as the age of the lithosphere may explain such long-term stability of the Canary Islands, as well as the Cape Verde Islands, with respect to sea level [Stillman *et al.*, 1982; Carracedo *et al.*, 1998].

#### 1.3.4.a Giant Mass-Wasting Events

After decades of debate on their existence [e.g. Moore, 1964; MacDonald, 1965; Ridley, 1971; Hausen, 1972; Moore *et al.*, 1989; Holcomb and Searle, 1991], giant landslides, some of the largest on Earth with volumes exceeding 1,000 km<sup>3</sup>, are now viewed as normal occurrences within the lifespan of virtually all oceanic shield-volcanoes [McGuire, 1996 and references therein]. The results of sub-marine surveys are unequivocal: on the Hawaiian Ridge, at least 68 major landslides with more than 20-km-long deposits were identified [Moore *et al.*, 1994], on La Réunion Island alone, Oehler *et al.* [2008] compiled 37 individual events while 20-30 have been documented in the Canary Archipelago (Figure 1.2, Table 1.1).

Moore *et al.* [1994] outlined a number of diagnostic features of the great Hawaiian landslides that are likely applicable to all marine volcanoes, although, size-wise, Hawaiian landslides tend to be larger. These authors categorised the landslides into two end-member types, slumps and debris avalanches, but reported several cases of intermediate forms. Slumps are generally both wide (up to 100 km) and thick (up to 10 km) and are typically characterised by slow and progressive movement, although sporadic co-seismic slip may result in rapid displacement of several meters at once [Lipman *et al.*, 1985b]. The structure of a slump's mobile mass is relatively coherent and undisturbed and part of it remains rooted in the source region (for an example of a small-scale analogous structure, see Appendix A). Debris avalanches, in contrast, are usually characterised by well-defined amphitheatres in their source regions and hummocky terrain in their distal parts, with megablocks up to 2 km across. Their morphology implies a more complete disaggregation of the moving mass compared to slumps. Debris avalanches are long (up to 230 km) and thin (0.5-2 km) features and evidence for up-hill movement indicates high emplacement velocities (>100 km/h, [Lipman *et al.*, 1988]). Nevertheless, the two emplacement mechanisms are not reciprocally exclusive, with some debris avalanches forming from the

disintegration of slumps or parts of slumps [e.g. *Moore et al.*, 1994]. Note that, in this thesis, the term ‘landslide’ is used in its broadest meaning, which encompasses all types of slope movement, including submarine features [cf. *Moore et al.*, 1989].

Although landslides occur throughout the lifetime of ocean island volcanoes, they are largest and recur at a higher frequency when the volcanic edifices are most active, i.e. at the peak of their growth. Large-scale edifice destabilisation therefore plays in key role in the morphological and structural evolution of marine volcanoes: there is an inherent conflict between constructive (magma intrusions and extrusions) and destructive processes (mass-wasting and other erosion mechanisms) at the paroxysm of ocean island volcano evolution [*McGuire*, 1996 and references therein]. For the Canary Islands, *Paris* [2002] and *Paris et al.* [2005b] have estimated the erosion rates (mass-wasting and long-term erosion combined) to be on the order of 200-900 m, 60-160 m, 200-800 m per million years during the shield stage, volcanic hiatus and rejuvenated stage, respectively.

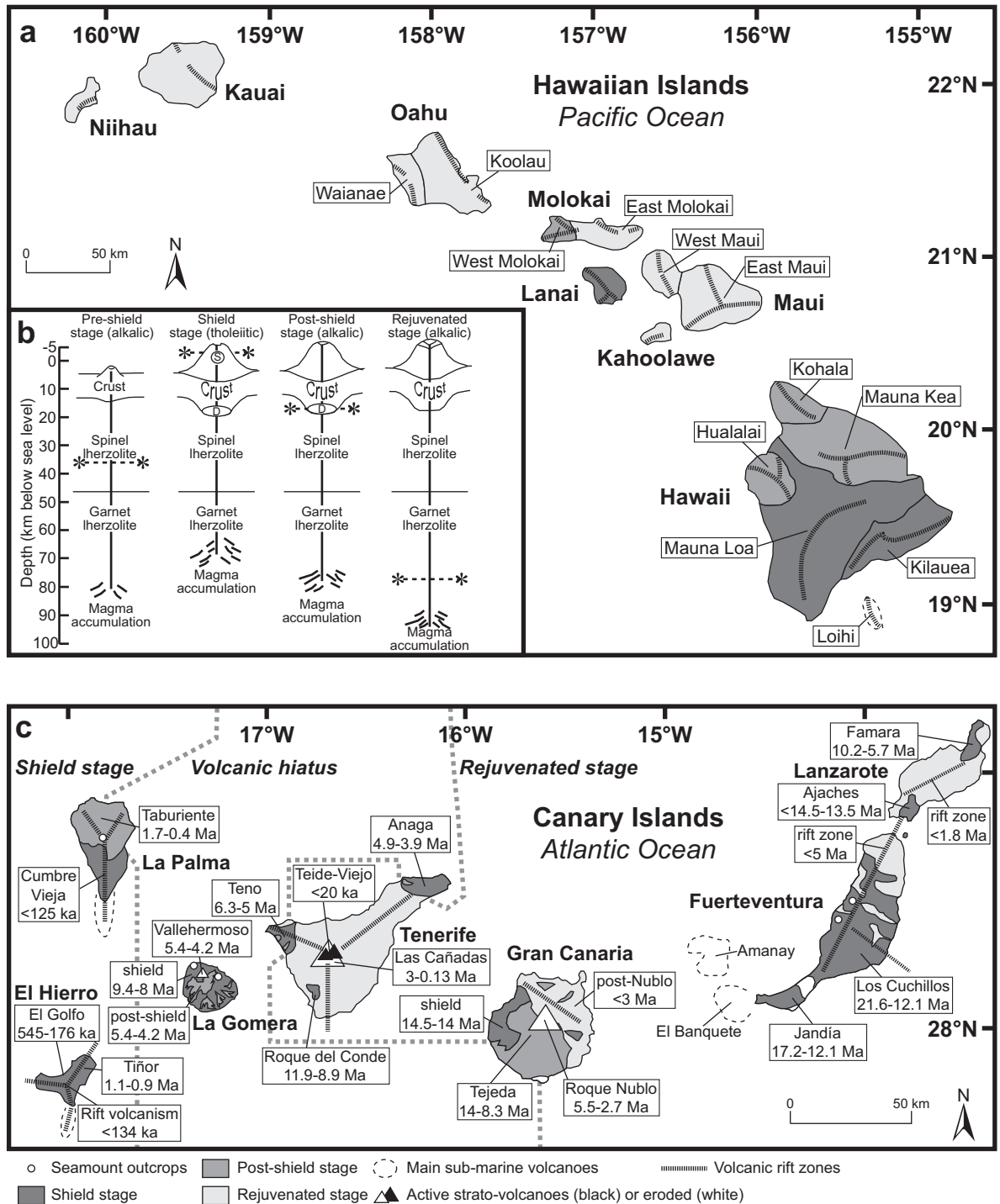


**Figure 1.1** **a** Map of the Hawaiian Islands, their volcanoes and associated rift zones. Shades of grey represent the last eruptive stage exposed at a particular volcano, after *Langenheim and Clague* [1987]. **b** Schematic diagram depicting the systematic evolution of Hawaiian volcanoes; for each of the four stages, magma supply rates, storage system configuration and erupted lava types (and entrained xenoliths) differ considerably, after *Clague* [1987]. Lines denoted \*---\* indicate maximum depth from which xenoliths are brought to the surface. A "deep" magma storage zone may start to form at the base of the flexed oceanic crust in the pre-shield stage, but is fully developed (labelled D) during the shield stage and persists until late in the post-shield stage. A shallow magma storage zone (labelled S) appears to exist only during the shield stage. **c** Map of the Canary Islands, their main volcanoes and associated rift zones, adapted from *Paris et al.* [2005b]. Volcanics from the different stages of evolution are approximately mapped.

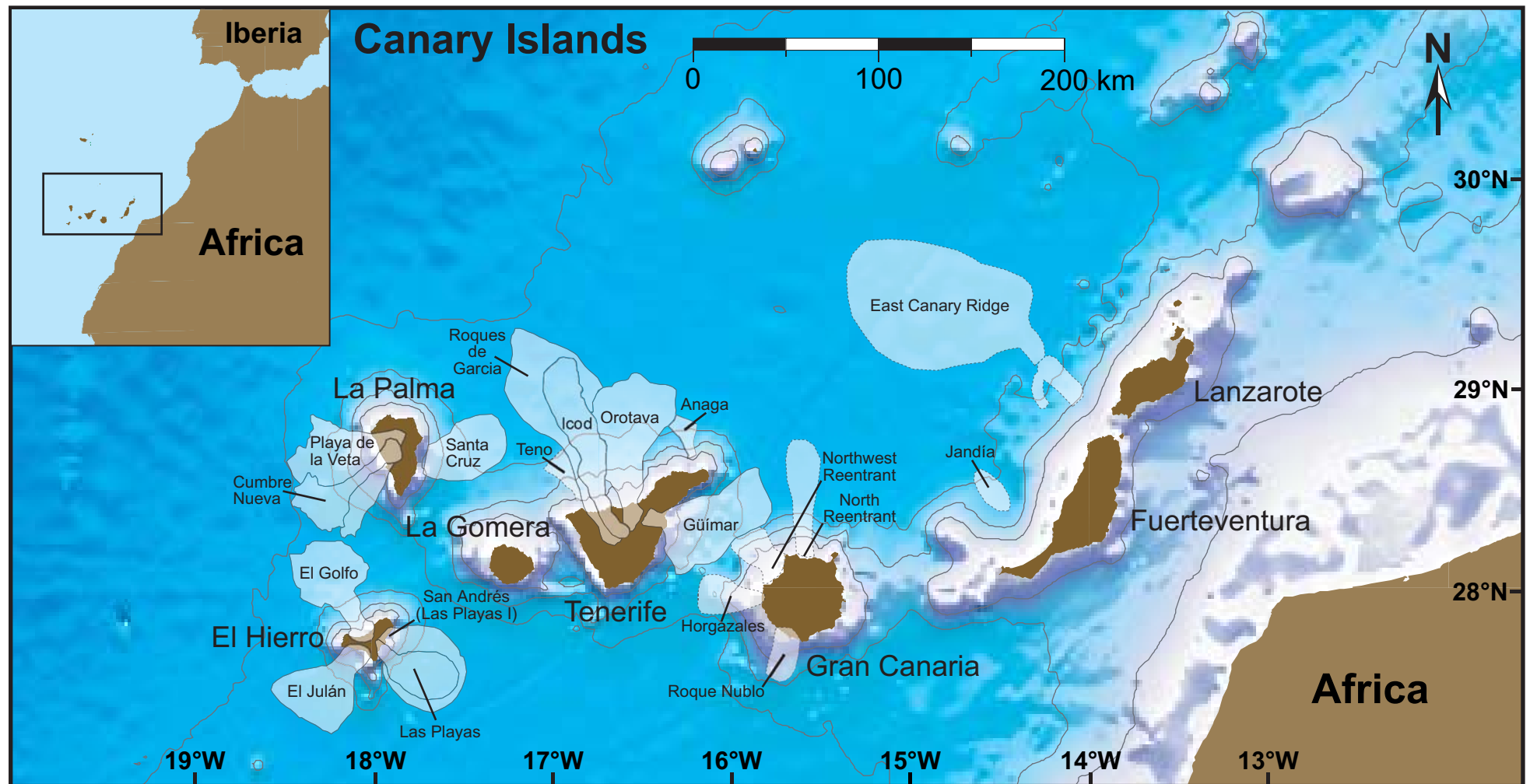


**Figure 1.2** Distribution of large-scale landslide deposits in the Canary Archipelago, with data from *Masson et al.* [2002] and references therein for El Hierro, La Palma and Tenerife and from *Krastel et al.* [2001] and references therein for Gran Canaria, Fuerteventura and Lanzarote. Additional landslide deposits may exist, especially associated with the eastern islands, some of which have been documented by *Carracedo et al.* [1999b], *Stillman* [1999] and *Acosta et al.* [2003]. Further landslides evidenced by on-land studies [e.g. *Walter and Schmincke*, 2002; *Paris et al.*, 2005b] are not indicated on this map. Details are listed in Table 1.1.

**Table 1.1** Documented large-scale landslides in the Canary Archipelago. h/l and A/V<sup>2/3</sup> are the ratios of the height vs. length and the area vs. volume to the power of 2/3 of the landslide deposits, respectively.

Edifice volume (km <sup>3</sup> )	Volcano volume (km <sup>3</sup> )	Landslide	Area (km <sup>2</sup> )	Volume (km <sup>3</sup> )	Height (km)	Runout (km)	h/l	A/V <sup>2/3</sup>	Age (ka)	Type
El Hierro: sub-aerial 140 <sup>a</sup> , total 5500 <sup>b</sup> , 13000 <sup>c</sup>	<i>Rift</i>	–	–	–	–	–	–	–	–	–
	<i>El Golfo: 2000<sup>d</sup></i>	El Golfo	1500 <sup>e,f,g</sup> , 2600 <sup>i</sup>	150–180 <sup>e,f,g</sup>	5 <sup>e,f,g</sup>	65 <sup>e,f,g</sup>	0.072-0.076 <sup>e,f,g</sup>	47-53 <sup>e,f,g</sup>	13-17 <sup>e</sup> , 21-134 <sup>a</sup>	Debris avalanche <sup>e,f,g</sup>
		Las Playas (II)	700 <sup>h</sup> , 950 <sup>j,g</sup>	25-35 <sup>h</sup> , <50 <sup>g</sup>	4.5 <sup>f,g</sup>	50 <sup>j,g</sup>	0.086-0.09 <sup>f,g</sup>	70 <sup>g</sup> , >98 <sup>i</sup>	145–176 <sup>f,j</sup>	Debris avalanche <sup>f,g</sup>
		San Andrés/Las Playas I	1700 <sup>f,g</sup>	? <sup>g</sup>	4-4.5 <sup>f,g</sup>	50 <sup>j,g</sup>	0.088 <sup>i</sup>	–	145–545 <sup>f,g,j</sup>	Slump <sup>c,f,g,j</sup>
		El Julán	>1600 <sup>h</sup> , 1800 <sup>g</sup>	60-120 <sup>h</sup> , 130 <sup>g</sup>	4.6 <sup>g</sup>	60 <sup>g</sup>	0.077 <sup>f,g</sup>	70 <sup>i</sup>	15-190 <sup>h</sup> , >160 <sup>g</sup> , >200 <sup>i</sup>	Slump or debris
	<i>Tiñor: 2000<sup>d</sup></i>	Tiñor	–	–	–	–	–	–	545-882 <sup>a,i,j</sup>	–
	<i>Southern Ridge</i>	–	–	–	–	–	–	–	–	–
–	Canary	40000 <sup>o,g</sup>	400 <sup>o,g</sup>	1.45 <sup>o,g</sup>	600 <sup>o,g</sup>	0.0024 <sup>o,g</sup>	740 <sup>o,g</sup>	13–17 <sup>o,g</sup>	Debris flow <sup>o,g</sup>	
–	Saharan	48000 <sup>g</sup>	1100 <sup>g</sup>	3.2 <sup>g</sup>	700 <sup>g</sup>	0.0036 <sup>g</sup>	450 <sup>g</sup>	60 <sup>g</sup>	Debris flow <sup>g</sup>	
La Palma: total 6500 <sup>k</sup>	<i>Cumbre Vieja: sub-aerial 125<sup>l</sup></i>	–	–	–	–	–	–	–	–	–
	<i>Cumbre Nueva</i>	Cumbre Nueva	780 <sup>k</sup>	95 <sup>k</sup>	6 <sup>g,h,k</sup>	80 <sup>g,h,k</sup>	0.075 <sup>g,h,k</sup>	37 <sup>g,h,k</sup>	125–536 <sup>k</sup>	Debris avalanche <sup>k</sup>
		Playa de la Veta	1200 <sup>n</sup> , 2000 <sup>k</sup>	650 <sup>k</sup>	6 <sup>g,h,k</sup>	80 <sup>g,h,k</sup>	0.075 <sup>g,h,k</sup>	27 <sup>g,h,k</sup>	800–1000 <sup>k</sup>	Debris avalanche complex <sup>k</sup>
	Santa Cruz	1000 <sup>g</sup>	? <sup>g</sup>	3.5 <sup>g</sup>	50 <sup>g</sup>	0.077 <sup>g</sup>	–	>900 <sup>g</sup>	Debris avalanche <sup>g</sup>	
La Gomera	–	Garajonay	89 <sup>m</sup>	40-45 <sup>m</sup>	–	–	–	–	8000 <sup>m</sup>	–
Tenerife: sub-aerial 2000 <sup>n</sup> , total 15000 <sup>n</sup> , 23600 <sup>n</sup> , 100000-150000 <sup>o</sup>	<i>Las Cañadas I, II and III: 1000-1200<sup>p</sup>, sub-aerial, total 3000-3600<sup>p</sup></i>	Icod	1500 <sup>q</sup> , 1700 <sup>q</sup>	150 <sup>q</sup> , 1000 <sup>h</sup>	6.8 <sup>q</sup>	95 <sup>q</sup> , 105 <sup>q</sup>	0.065 <sup>q</sup>	60 <sup>q</sup>	150–170 <sup>n,p,i</sup>	Debris avalanche/flow <sup>q</sup>
		Orotava	2100 <sup>q</sup> , 2200 <sup>q</sup>	500 <sup>q</sup> , 1000 <sup>h</sup>	6.6 <sup>q</sup>	75 <sup>q</sup> , 90 <sup>q</sup>	0.073 <sup>q</sup>	33 <sup>q</sup>	540–690 <sup>q</sup>	Debris avalanche <sup>q</sup>
		Roques de García	2200 <sup>q</sup> , 4500 <sup>g</sup>	500 <sup>q</sup> , 1000 <sup>h</sup>	7 <sup>q</sup>	95 <sup>q</sup> , 130 <sup>q</sup>	0.054 <sup>q</sup>	71 <sup>q</sup>	600-1400 <sup>q</sup>	Debris avalanche <sup>g</sup>
		Güímar	1600 <sup>h</sup> , 2600 <sup>q</sup>	>120 <sup>h</sup> , 300 <sup>q</sup>	>4 <sup>q</sup>	>50 <sup>q</sup> , 85 <sup>q</sup>	? <sup>q</sup>	66 <sup>q</sup>	780–840 <sup>h</sup>	Debris avalanche <sup>q</sup>
	<i>Anaga: 333-666<sup>n</sup></i>	Anaga	>400 <sup>q</sup> , 500 <sup>q</sup>	? <sup>q</sup>	>3.5 <sup>q</sup>	33 <sup>q</sup>	? <sup>q</sup>	–	>>1000 <sup>l</sup> , >3000 <sup>m</sup>	Debris avalanche <sup>g</sup>
	<i>Teno: 333-666<sup>n</sup></i>	Carrizales	>33 <sup>m</sup> , 50 <sup>l</sup> , 400 <sup>q</sup>	>20-25 <sup>m</sup>	–	35 <sup>q</sup>	–	–	>5500, <6100 <sup>q</sup>	Debris avalanche <sup>p,f</sup>
		Masca	>33 <sup>m</sup> , 50 <sup>l</sup> , 400 <sup>q</sup>	>20-25 <sup>m</sup>	–	35 <sup>q</sup>	–	–	ca. 6100 <sup>q</sup>	Debris avalanche <sup>p,f</sup>
	<i>Roque del Conde: 333-666<sup>n</sup></i>	–	–	–	–	–	–	–	–	–
Gran Canaria: sub-aerial 824 <sup>v</sup> , total 30600 <sup>v</sup>	?	Galdar <sup>q</sup>	300 <sup>q</sup>	–	–	30 <sup>q</sup>	–	–	3500-4000 <sup>q</sup>	Debris avalanche <sup>q</sup>
	?	South West <sup>q</sup>	250 <sup>q</sup>	–	–	30 <sup>q</sup>	–	–	3500-4000 <sup>q</sup>	Debris avalanche <sup>q</sup>
	?	Roque Nublo	150 <sup>q</sup> , 330 <sup>h,v</sup>	34 <sup>h,v</sup>	–	12 <sup>q</sup>	–	–	3500-4000 <sup>h,q,v</sup>	Debris avalanche <sup>h,q,v</sup>
	?	Las Palmas <sup>q</sup>	1100 <sup>q</sup>	–	–	45 <sup>q</sup>	–	–	3500-4000, 9000 <sup>q</sup>	Debris avalanche <sup>q</sup>
	?	Fataga	? <sup>h</sup>	? <sup>h</sup>	–	–	–	–	9000-11500 <sup>h</sup>	Debris avalanches <sup>h</sup>
	?	Agáete <sup>q</sup>	200 <sup>q</sup>	–	–	30 <sup>q</sup>	–	–	12000-14000 <sup>q</sup>	Debris avalanche <sup>q</sup>
	?	Horgazales	>1000 <sup>h,v</sup>	>80 <sup>h,v</sup>	–	–	–	–	14000-15000 <sup>h,v</sup>	–
	?	Northwest reentrant	400 <sup>q</sup> , >500 <sup>h,v</sup>	>50 <sup>h,v</sup>	–	50 <sup>q,v</sup>	–	–	14000-15000 <sup>h,v</sup>	Slump? <sup>h,v</sup>
	?	North reentrant	>700 <sup>h,v</sup>	>60 <sup>h,v</sup>	–	–	–	–	12000-15000 <sup>h,v</sup>	–
Fuerteventura & Lanzarote	?	East Canary Ridge <sup>h</sup>	>400/>2000 <sup>h</sup>	>35/>20 <sup>h</sup>	–	–	–	–	<100 <sup>h</sup>	Slump/debris flow? <sup>h</sup>
	?	Jandía <sup>h</sup>	250 <sup>h</sup>	25 <sup>h</sup>	–	–	–	–	<2000 <sup>h</sup>	Debris avalanche <sup>h</sup>
	?	Lanzarote <sup>q</sup>	>800 <sup>q</sup>	–	–	>40 <sup>q</sup>	–	–	16000-18000 <sup>q</sup>	Slump? <sup>q</sup>
	?	Pto. Rosario <sup>q</sup>	3500 <sup>q</sup>	–	–	70 <sup>q</sup>	–	–	>17500 <sup>q</sup>	Debris avalanche? <sup>q</sup>
	?	S Pto. Rosario <sup>q</sup>	1200 <sup>q</sup>	–	–	35 <sup>q</sup>	–	–	>17500 <sup>q</sup>	Debris avalanche? <sup>q</sup>

<sup>a</sup> Carracedo et al. [1999b]; <sup>b</sup> Schmincke [1994]; <sup>c</sup> Day et al. [1997]; <sup>d</sup> Based on conical edifice diameter=35 km and height=6 km [Münn et al., 2006]; <sup>e</sup> Masson [1996]; <sup>f</sup> Gee et al. [2001b]; <sup>g</sup> Masson et al. [2002]; <sup>h</sup> Krastel et al. [2001]; <sup>i</sup> Guillou et al. [1996]; <sup>j</sup> Carracedo et al. [2001]; <sup>k</sup> Urgeles et al. [1999]; <sup>l</sup> Carracedo et al. [1999a]; <sup>m</sup> Paris et al. [2005a]; <sup>n</sup> Ancochea et al. [1990]; <sup>o</sup> Watts et al. [1997]; <sup>p</sup> Cantagrel et al. [1999]; <sup>q</sup> Acosta et al. [2003]; <sup>r</sup> Walter and Schmincke [2002]; <sup>s</sup> Palomo et al. [1997]; <sup>t</sup> Watts and Masson [1995]; <sup>u</sup> Chapter 3 of this work; <sup>v</sup> Funck and Schmincke [1998]

## CHAPTER 2 – METHODOLOGY

### 2.1 Field Work

#### 2.1.1 Nomenclature

Throughout the evaluation of field work results of this thesis, modal mineralogy is used as the best discriminator for Teno and El Hierro lava types. However, in the absence of quartz, alkali feldspar and feldspathoid phenocrysts, the QAPF classification of the IUGS [Le Maitre *et al.*, 1989] is impractical. Four main modal mineralogy types are observed and defined here: 1) aphyric to sub-aphyric (<5 vol. % phenocrysts of olivine/clinopyroxene/plagioclase, called ***aphyric basalt***); 2) plagioclase-phyric (5-40 vol. %, called ***plagioclase basalt***, which is sometimes referred to as “trachyte” in the literature); 3) moderately olivine- and/or clinopyroxene-phyric (5-20 vol. %, called ***basalt***) and highly olivine-clinopyroxene-phyric (>20 vol. %, called ***ankaramite***). Note that these names are used here as field terms that do not imply a particular position in the total-alkali-silica chemical classification diagram [e.g. Le Bas *et al.*, 1986]. The descriptions of primary volcanoclastic rocks adhere to the revised classification of White and Houghton [2006].

#### 2.1.2 Mapping and Logging

Positions of key localities were determined using a handheld GPS device and have a precision of  $\pm 10$  m [Garmin Ltd, 2007]. UTM coordinates (datum WGS84) are given in the format [Easting (m) 3xxxx0, Northing (m) 31yyyy0] for Teno and [Easting (m) xxxxx0, Northing (m) 30yyyy0] for El Hierro. Because the divide between UTM longitude zones 27R and 28R passes straight through the island of El Hierro, GPS coordinates of points falling inside zone 27R were converted, using GEOTRANS freeware (available from the U.S. National Geospatial-Intelligence Agency website), as if zone 28R encompassed the whole island. Uncertainties associated with this conversion are negligible. The use of the recent REGCAN95 reference system, specifically designed for Canary Island geodesy, would also have resolved this issue, but, unfortunately, this datum is not yet available for most handheld GPS.

Logging of stratigraphic sections was undertaken on the principle that the thickness of near-horizontal lava flows (or group of flows) can be estimated with altitude readings. Approximate altitudes of notable boundaries in the stratigraphic sequence were measured

using a barometric altimeter built-in into the GPS. Calibration to sea level was frequently performed and, although the accuracy of the reading has a significant error ( $\pm 3$  m), precision is good ( $\pm 0.3$  m) [Garmin Ltd, 2007]. Although logging was carried out along oblique profiles, the sequences obtained are considered to yield representative cross-sections through the volcanic edifice. Absolute vertical position of lava piles may have been affected by post-emplacement deformation at Teno (along deformation zones associated with the unconformities [see *Walter and Schmincke*, 2002]), but relative stratigraphic level is thought to be preserved.

### 2.1.3 Sampling

After reconnaissance of the most suitable outcrop localities, representative and mostly alteration-free rock samples ( $1\text{--}1.5\text{ dm}^3$ ) were obtained using a rock hammer. If any, weathered surfaces of lava samples were mostly chipped off directly at the sampling sites, except for pyroclastic samples of Teno, which showed pervasive moderate alteration. Positions and altitudes of sampling sites were recorded by GPS and will be provided together with the sample lists in Chapter 3 and 4.

## 2.2 Sample Preparation

Upon return from the field, rock samples were sawed into smaller blocks,  $\sim 10\text{--}200\text{ cm}^3$  in size, and any remaining weathered surfaces were removed at this point. For all samples, selected blocks were mounted on glass plates and thin sections were prepared by Neil Kearney, Declan Burke, Francis Hendron and Maura Morgan, who are members of the technical staff in the Department of Geology at Trinity College. Other blocks of samples selected for geochemical analysis were reduced to rock chips using a jaw crusher. Chips were washed and sieved to eliminate rock powder. For a few samples, the chips included isolated weathered fragments, which were removed by hand-picking. About 15–20 g of clean rock chips were subsequently ground to powder using a Tema mill.

For ankaramitic samples,  $\sim 5$  g of rocks chips free of phenocrysts, i.e made of groundmass material, were extracted by hand-picking under a stereomicroscope. These microcrystalline groundmass separates were powdered to the nm-scale using an agate mill and an agate mortar and pestle. Then, the fine powders were fused on an Ir-filament and quenched to glass under air at the Institute of Mineralogy at the University of Frankfurt [see also *Galipp et al.*, 2006].

Prior to analysis by electron microprobe (see below), glass shards were mounted into small discs (0.5 cm high, 2 cm in diameter), using epoxy. Also, representative phenocrysts of olivine, clinopyroxene and plagioclase were identified during reconnaissance thin section observations and were targeted for analysis. The positions of suitable core-to-rim profiles were logged using a computer program linked to the microscope to facilitate their location during microprobe work.

## 2.3 Analytical Techniques

### 2.3.1 X-Ray Fluorescence (XRF)

Major and trace element compositions of all whole-rock samples were determined by X-Ray Fluorescence (XRF), using a Philips PW1480 automatic X-ray spectrometer at IFM-GEOMAR, Kiel, Germany. International geological reference samples were used for calibration of the instrument [see also *Abratis et al.*, 2002]. Glass beads made from the sample powders fused with lithium tetraborate were obtained following the methods of *Norrish and Hutton* [1969], with modifications after *Harvey et al.* [1973] and *Schroeder et al.* [1980]. All analyses were carried out with a Rh tube. Loss on ignition values (LOI) were determined by infra-red photometry (Rosemount CSA 5003) after heating the rock powder to 960 °C.

### 2.3.2 Inductively Coupled Plasma Mass Spectrometry (ICP-MS)

Selected powdered samples (7 from Teno, 9 from El Hierro) were sent to Acme Analytical Laboratories Ltd., Vancouver, Canada, for determination of rare earth element (REE) concentrations by ICP-MS. Acme Labs follow a standard procedure for analysis of REE. A 0.2 g sample fraction is weighed into a graphite crucible and mixed with 1.5 g of lithium metaborate/tetraborate flux. The flux/sample charge is heated at 980°C for 30 minutes in a muffle furnace. The sample is subsequently cooled and the bead obtained is dissolved in 100 mL of 5% HNO<sub>3</sub> (ACS grade nitric acid in de-mineralised water). An aliquot of the solution is poured into a polypropylene test tube. Sample solutions are then aspirated into an ICP mass spectrometer (Perkin-Elmer Elan 6000 or 9000).

To monitor analytical precision and accuracy for each sample batch, Acme Labs incorporates a sample blank, a sample duplicate (in this case sample TN28) and a standard reference material (Standard SO-18). Quality control results are listed in Table 2.1 and indicate the high precision and accuracy of the REE data.



---

### 2.3.3 *Electron Microprobe (EMP)*

The major element chemistry of minerals and glass shards (obtained from fused groundmass separates) was analysed with a CAMEBAX SX-50 electron microprobe at IFM-GEOMAR. Analyses were carried with a peak counting time of 20 s under a scanned beam and an acceleration voltage of 15 kV. Beam size and beam current varied according to the material being analysed:

- 1) for glass samples, a defocused beam ( $3 \times 4 \mu\text{m}$ ) with a current of 10 nA was used to minimise alkali loss;
- 2) olivine crystals were analysed with a focused beam ( $1 \mu\text{m}$ ) of 50 nA;
- 3) clinopyroxene and plagioclase crystals were also analysed with a focused beam ( $1 \mu\text{m}$ ) but with a current of 20 nA.

The glass shards were analysed in 10 different points, whilst phenocrysts were analysed in core-to-rim profiles of 5-15 points (olivine), 10-50 points (clinopyroxene) and 5 to 10 points (plagioclase) with 2 to 5 additional rim analyses per crystal.

Regular analyses of reference samples for glass, olivine, clinopyroxene and plagioclase were used for calibration of the EMP. The mean error (average difference between the measured and suggested working values) and standard error (standard deviation of the mean error) are listed in Table 2.2 as percentages of the expected oxide values. Major constituents ( $>1$  wt%, e.g.  $\text{SiO}_2$ ) of glass/minerals have small errors, typically  $<2\%$ , although measurement of minor oxides involves larger uncertainties.

## 2.4 Geochemical Data Filtering

Loss on ignition values (LOIs are listed together with whole-rock data in Chapter 3 and Chapter 4) were low for most samples, consistent with their unaltered appearance. Glass analyses were verified to yield sums of  $100\% \pm 2\%$  and to be homogeneous for each sample. A sample average composition (listed with standard deviation for each oxide in Chapter 3 and Chapter 4) was used for plotting. Alkali loss was checked to be negligible by verifying that the fused groundmass compositions fall on the liquid line of descent for their respective magma suites. Note that whole-rock and fused groundmass major element compositions, as well as all data from the scientific literature used for comparison, were recalculated on a volatile-free basis with all iron as  $\text{FeO}_t$  prior to plotting.

Olivine and plagioclase analyses were considered of satisfactory quality if their oxide totals summed to  $100\% \pm 2\%$ . Clinopyroxene analyses were more thoroughly quality controlled by selecting only those yielding sums approaching 100%, 0 wt %  $K_2O$  and four cations per six oxygens.

## 2.5 Thermobarometry

### 2.5.1 Theoretical Background and Uncertainties

*Putirka et al.* [1996] developed expressions based on the jadeite-diopside/hedenbergite-liquid and jadeite-liquid exchange equilibria (Equations 2.1 and 2.2) that can respectively be used as thermometers and thermobarometers of clinopyroxene-melt equilibration.

Equation 2.1

$$\frac{10^4}{T} = 6.73 - 0.26 * \ln \left[ \frac{Jd^{cpx} * Ca^{liq} * Fm^{liq}}{DiHd^{cpx} * Na^{liq} * Al^{liq}} \right] - 0.86 * \ln \left[ \frac{Mg^{liq}}{Mg^{liq} + Fe^{liq}} \right] + 0.52 * \ln [Ca^{liq}]$$

Equation 2.2

$$P = -54.3 + 299 * \frac{T}{10^4} + 36.4 * \frac{T}{10^4} \ln \left[ \frac{Jd^{cpx}}{[Si^{liq}]^2 * Na^{liq} * Al^{liq}} \right] + 367 * [Na^{liq} * Al^{liq}]$$

In these formulations, pressure is in kbar and temperature is in Kelvin, but, in this work, the results will be presented in MPa and °C. Quantities such as  $Na^{liq}$  refer to the cation fraction of the given oxide (e.g.  $NaO_{1/2}$ ) in the liquid or in clinopyroxene and  $Fm = (Mg^{liq} + Fe_{total}^{liq})$ . Equations 2.1 and 2.2 estimate temperature and pressure with uncertainties of  $\pm 27$  °C and  $\pm 140$  MPa, respectively.

### 2.5.2 Equilibrium Tests

Validity of equilibrium conditions between clinopyroxenes and host melt (fused groundmass or whole-rock compositions, details in Chapter 3 and Chapter 4) was assessed by comparing the observed clinopyroxene  $Mg\# = \text{molar } Mg / (Mg + Fe^{total}) \times 100$  to the clinopyroxene  $Mg\#$  predicted by the formulations of *Duke* [1976] (Equation 2.3) and *Putirka* [1999] (Equation 2.4).

Equation 2.3

$$\log \frac{(X_{Fe}^{cpx})}{(X_{Mg}^{cpx})} = -0.564 + 0.755 \log \frac{(X_{Fe}^L)}{(X_{Mg}^L)}$$

Rewritten as:

$$Mg\#_{predicted} = \frac{100}{1 + 10^{(-0.564 + 0.755 \log(\frac{X_{Fe}^L}{X_{Mg}^L}))}}$$

Where e.g.  $X_{Mg}^L$  is the mole fraction of MgO in the liquid.

Equation 2.4

$$\ln \left[ \frac{Fe^{cpx} Mg^{liq}}{Mg^{cpx} Fe^{liq}} \right] = 31.8 - 36.8[Si^{liq}] - 4.76[Na^{liq}] + 17 \ln[Si^{liq}] - \frac{3879}{T} - 0.014 \frac{P}{T}$$

Rewritten as:

$$Mg\#_{predicted} = \frac{100}{1 + (\frac{Fe^{liq}}{Mg^{liq}}) e^{(31.8 - 36.8[Si^{liq}] - 4.76[Na^{liq}] + 17 \ln[Si^{liq}] - \frac{3879}{T} - 0.014 \frac{P}{T})}}$$

If the ratio  $Mg\#_{observed}/Mg\#_{predicted} = 1 \pm 0.05$  the compositions of the clinopyroxene and the melt were considered to be in chemical equilibrium [cf. *Klügel et al.*, 2000; *MacLennan et al.*, 2001; *Schwarz et al.*, 2004; *Klügel et al.*, 2005]. If this ratio did not satisfy the above criterion, the P-T estimate was discarded. A possible source of uncertainty here resides in the potential effect of the presence of ferric iron in both clinopyroxene and host melt. Although of doubtful accuracy [see *McGuire et al.*, 1989], the methods of *Lindsley* [1983] and *Droop* [1987] indicate that significant amounts of  $Fe^{3+}$  are required for clinopyroxene charge balance. Based on previous redox state investigations of Canary Island magmas [e.g. *Gurenko et al.*, 1996; *Klügel et al.*, 2000], we assumed  $f_{O_2} = QFM+1$  and calculated (using the model of *Kress and Carmichael* [1988]) that Teno and El Hierro magmas may have had  $Fe_2O_3/FeO_{total}$  wt % ratios between 0.10 and 0.12. However, since the effect of redox conditions were not explored by *Duke* [1976] and *Putirka* [1999], all iron was treated as divalent in the clinopyroxene equilibrium tests [cf. *Schwarz et al.*, 2004], the results of which will be presented in Chapter 3 and Chapter 4.

As most samples contained olivine, the consistency of the data was further tested by comparing calculated crystallisation temperatures of olivine [*Beattie*, 1993; *Putirka*, 1997] to those of clinopyroxene [*Putirka et al.*, 1996]. For this purpose, we selected olivine analyses yielding  $Mg\#_{observed}/Mg\#_{predicted} = 1 \pm 0.05$ , using the method of *Ford et al.* [1983] to determine predicted cation fractions of Mg and  $Fe^{2+}$  in olivine. The thermometers of

*Beattie* [1993] and *Putirka* [1997] estimate crystallisation temperature of olivine with uncertainties of  $\pm 10$  and  $\pm 31$  °C, respectively.

Note that the thermobarometers are expected to be applicable to a wide range of  $f_{O_2}$ , encompassing that inferred for Teno and El Hierro magmas [cf. *Putirka et al.*, 2003]. Moreover, *MacLennan et al.* [2001] found that the presence of  $Fe^{3+}$  in clinopyroxene was unlikely to yield overestimated pressure results [cf. *Neumann et al.*, 1999]. Also, *Klügel et al.* [2005] and *Mordick and Glazner* [2006] showed that, if the analytical error is low, the thermobarometric calculations using the formulations of *Putirka et al.* [1996] can be considered precise and accurate.

### 2.5.3 Pressure to Depth Conversion

Pressure is converted to depth by assuming a volcanic edifice height of 5.5 km (consistent with both Teno and El Hierro) with an average density of  $2600 \text{ kg/m}^3$  [*Collier and Watts*, 2001], a thick pre-volcanic sediment cover and igneous oceanic crust with a total thickness of 11 km at Teno and 9 km at El Hierro with an average density of  $2700 \text{ kg/m}^3$  [cf. *Ranero et al.*, 1995; *Watts et al.*, 1997] and an average upper mantle density of  $3240 \text{ kg/m}^3$  [*Ranero et al.*, 1995]. Atmospheric pressure thus corresponds to the volcano summit  $\sim 1.5$  km above present sea level, with the Moho situated at 15 km for Teno and 13 km for El Hierro [*Banda et al.*, 1981; *Ranero et al.*, 1995; *Watts et al.*, 1997].

## 2.6 Numerical Modelling

For coherency, the procedures, setup and results of our numerical models will be outlined together in Chapter 5.

**Table 2.1** Quality control report of rare earth element data obtained from Acme Labs. All values in ppm.

<u>Analyte</u>	<u>Detection limit</u>	<u>TN28</u>	<u>TN28 replicate</u>	<u>Standard SO-18</u>	<u>Standard SO-18</u>	<u>Standard SO-18</u> <u>expected</u>	<u>Blank</u>
La	0.1	28.3	28.3	12.5	12.6	12.3	<0.1
Ce	0.1	62.4	62.4	27.5	27.6	27.1	<0.1
Pr	0.02	8.04	8.06	3.45	3.47	3.45	<0.02
Nd	0.3	32.3	32.8	14.1	13.8	14	<0.3
Sm	0.05	7.2	7.08	2.9	2.94	3	<0.05
Eu	0.02	2.34	2.38	0.9	0.89	0.89	<0.02
Gd	0.05	6.6	6.87	2.93	2.95	2.93	<0.05
Tb	0.01	1.04	1.03	0.52	0.53	0.53	<0.01
Dy	0.05	5.18	5.22	3	3.07	3	<0.05
Ho	0.02	1.02	0.94	0.63	0.64	0.62	<0.02
Er	0.03	2.35	2.31	1.83	1.84	1.84	<0.03
Tm	0.01	0.32	0.33	0.29	0.3	0.29	<0.01
Yb	0.05	1.8	1.87	1.8	1.81	1.79	<0.05
Lu	0.01	0.26	0.26	0.28	0.28	0.27	<0.01

**Table 2.2** Evaluation of EMP analytical uncertainties based on repeated analysis of standards. Expected composition of standards (Exp.) used at IFM-GEOMAR, mean error (ME) and standard error (SE) on the expected oxide values are listed.

	<b>Glass (JDF)</b>			<b>Olivine (SC)</b>			<b>Cpx (K.Augite)</b>			<b>Plagioclase</b>		
	<u>Exp. (wt%)</u>	<u>ME (%)</u>	<u>SE (%)</u>	<u>Exp. (wt%)</u>	<u>ME (%)</u>	<u>SE (%)</u>	<u>Exp. (wt%)</u>	<u>ME (%)</u>	<u>SE (%)</u>	<u>Exp. (wt%)</u>	<u>ME (%)</u>	<u>SE (%)</u>
SiO <sub>2</sub>	50.80	1.3	0.7	40.81	0.5	0.5	50.73	0.5	0.3	51.25	0.3	0.2
TiO <sub>2</sub>	1.93	6.6	4.6	–	–	–	0.74	5.5	3.5	0.05	14.0	13.2
Al <sub>2</sub> O <sub>3</sub>	13.80	1.1	0.7	0.03	–	–	8.73	0.9	0.6	30.91	0.5	0.3
FeO	12.17	1.5	1.2	9.55	1.1	0.6	6.34	1.3	1.0	0.46	6.9	5.4
MnO	0.22	15.8	11.6	0.14	10.0	8.4	0.13	16.2	13.1	0.01	–	–
MgO	6.83	1.6	1.1	49.42	0.6	0.5	16.65	0.7	0.5	0.14	8.1	6.5
CaO	10.80	1.0	1.0	0.09	24.6	20.8	15.82	0.8	0.4	13.64	0.5	0.5
Na <sub>2</sub> O	2.77	1.1	0.9	–	–	–	1.27	1.5	1.1	3.45	1.2	1.2
K <sub>2</sub> O	0.22	12.1	7.4	–	–	–	0.00	–	–	0.18	16.1	14.6
P <sub>2</sub> O <sub>5</sub>	0.23	24.6	16.4	–	–	–	–	–	–	–	–	–
Cr <sub>2</sub> O <sub>3</sub>	–	–	–	0.01	131.9	77.6	–	–	–	–	–	–
NiO	–	–	–	0.37	8.3	4.7	–	–	–	–	–	–
Total	99.77			100.43			100.41			100.09		

## CHAPTER 3 – THE TENO MASSIF

### 3.1 Introduction and Geological Background

The Teno massif is a mountainous region and a protected natural park of northwestern Tenerife, the largest and highest of the Canary Islands. The massif's distinct morphology and geological features are the relics of an ancient, independent volcanic edifice. Indeed, Tenerife was largely built up between 11.9 and 3.9 Ma by the coalescence of at least three independent shield-volcanoes, with discrete magmatic sources [see Figure 13 of *Thirlwall et al.*, 2000]. The remnants of these volcanoes crop out in the Roque del Conde (South), Teno (NW) and Anaga (NE) massifs (Figure 3.1) [*Ancochea et al.*, 1990; *Thirlwall et al.*, 2000; *Guillou et al.*, 2004]. The Roque del Conde massif, with radiometric dates between 11.9 and 8.9 Ma, represents the earliest stages of sub-aerial volcanism on the island and is thought to be the only exposed part of the much larger Central shield [*Guillou et al.*, 2004]. The later Teno (between ~6.3 and ~5.0 Ma) and Anaga (between 4.9 and 3.9 Ma) shields emerged in the northwest and northeast parts of the island, respectively [*Guillou et al.*, 2004; *Leonhardt and Soffel*, 2006]. Emissions from the Roque del Conde (Central shield), Teno and Anaga volcanoes are largely basaltic, with abundant alkali basalts and picrobasalts (often ankaramites), common basanites and less frequent, more evolved hawaiites, mugearites and benmoreites [*Thirlwall et al.*, 2000].

Some 2 Ma of volcanic hiatus and erosion followed the last eruptions at Anaga before rejuvenated volcanism formed the voluminous Las Cañadas edifice in central Tenerife essentially between 1.9 and 0.2 Ma and the later twin strato-volcano complex, Teide-Pico Viejo [*Ancochea et al.*, 1990]. This rejuvenated volcanism, although varied in composition, is significantly more alkalic and presents much higher proportions of felsic products (phonolites) than the older basaltic shields [e.g. *Ablay et al.*, 1998]. The most recent eruption on Tenerife took place on the Northwest Rift zone of the central edifices in 1909 [*Carracedo et al.*, 2007].

Several episodes of mass-wasting events appear to have removed a cumulative volume of more than 1000 km<sup>3</sup> from the upper slopes of Tenerife [*Masson et al.*, 2002]. These giant landslides occurred as early as 6 Ma and as late as 150 ka and have affected most of Tenerife's main volcanoes, including that of Teno [*Masson et al.*, 2002; *Carracedo et al.*, 2007 and references therein].

In this chapter, we use the late Miocene Teno volcano as a type-example, where it can be shown that volcanism was markedly affected by the occurrence of two successive giant landslides. Firstly, available information on the stratigraphy of the eroded volcano will be outlined and revised in the light of new observations. Secondly, the main stratigraphic units will be described in detail in the new stratigraphic framework. Results of field work, petrography, whole-rock and mineral chemistry, thermobarometry as well as magma density calculations will be presented. In the discussion, these results will be put together to improve our knowledge on Teno's volcanic evolution and it will be argued that large flank collapses influenced (1) the eruptive regime and (2) the deep magma plumbing system of the volcanic edifice.

## 3.2 Stratigraphy of the Teno Massif

### 3.2.1 Previous Work

The Teno massif reaches a maximum elevation in excess of 1,300 m above sea level at Cumbre Bolicos (Figure 3.2). Ridges, bounded by > 200 m high cliffs, and eroded canyons ("barrancos"), ~500 m deep, expose most of the stratigraphic sequence. Work by *Ancochea et al.* [1990] defined a lower sequence (seaward dipping) and an upper sequence (near-horizontal), separated by a prominent angular unconformity. *Cantagrel et al.* [1999] proposed that the breccia marking this discordance represents the remains of a ~6-Ma-old debris avalanche with deposits extending off-shore to the north [*Watts and Masson*, 1995]. *Walter and Schmincke* [2002] showed that volcanism at Teno was dominated by two rift zones (oriented NW and S) and perhaps third one (NW) that would define an eruptive focus situated about 2 km north-northeast of Masca village. These authors also mapped two major angular unconformities in the massif, which they interpreted to represent the relics of two distinct palaeo-landslide scars. The evolution of Teno was thus divided into three stratigraphic formations separated by the unconformities: 1) Los Gigantes Formation (LGF); 2) Carrizales Formation (CF); and 3) El Palmar Formation (EPF) [*Walter and Schmincke*, 2002]. However, *Guillou et al.* [2004] pointed out that the outermost part of the Los Gigantes Formation must be equivalent to or younger than the El Palmar Formation based on K/Ar dating and magnetostratigraphy. *Leonhardt and Soffel* [2006] reconciled these previous observations whilst providing further palaeomagnetic data. These authors defined the oldest series of lavas, exposed in the Barranco de Masca and underlying the first unconformity, as the Masca Formation (MF), which they infer to have been extruded during the reverse polarity chron C3An.1r, from 6.27 to 6.14 Ma ago [see *Cande and Kent*,



1995]. Subsequently, a series of events are thought to have taken place during the normal polarity chron C3An.1n, lasting ~250 ka from 6.14 to 5.89 Ma ago. To begin with, a first giant landslide, the Masca Collapse, was followed by the infill of the collapse embayment by the Carrizales Formation lavas. Then, a second landslide occurred, the Carrizales Collapse, this time followed by the extrusion of most of the El Palmar Formation. After a possible hiatus in volcanic activity during the next reverse polarity chron, the youngest Miocene lavas in Teno were extruded during the normal polarity interval C3n.4n, from 5.23 to 4.98 Ma ago. These volcanics that overlie the Masca Formation without apparent unconformity and form the cliffs of Los Gigantes retain the name Los Gigantes Formation (Figures 3.1, 3.2, 3.3). A ~4 Ma gap in volcanic activity separates Los Gigantes eruptions from the Pleistocene volcanics that have been dated between 706 and 153 ka and interpreted as distal products of the Northwest Rift of the recent and active central edifices [Carracedo *et al.*, 2007].

### 3.2.2 *New Stratigraphic Constraints*

The apparent rapid growth of Teno and limitations of current dating techniques imply that the published data can only provide a coarse portrait of the detailed volcanic evolution. The establishment of a stratigraphic framework based on such data is highly dependent on a correct understanding of the volcano's structural development. Our analysis is based on the rationale that the major angular unconformities exposed in the Teno massif represent fundamental stratigraphic boundaries. Indeed, over a ~7-km-wide region extending from Roques del Carrizal ridge in the west to near Santiago del Teide in the east, Teno's stratigraphic sequences are clearly divided by two steep angular unconformities (Figures 3.1, 3.2, 3.3). Following from *Walter and Schmincke* [2002], these unconformities, herein referred to as the Masca and Carrizales unconformities, were largely re-mapped in the course of this study; details of their location are outlined in Appendix B. We integrated outcrop and oblique photograph data, as well as sample localities for published radiometric dates and palaeomagnetic measurements, into Google Earth freeware; this allowed a precise assessment of sample localities with respect to the location of stratigraphic boundaries. Because rocks that directly underlie an unconformity are necessarily older than rocks that overly this same unconformity, we carefully checked that previously published observations and data conform to this principle. In this process, we encountered some conflicting data and irregularities that call for re-adjustment of previous work. Nevertheless, we essentially adopt a stratigraphic framework that only differs in detail

from that proposed by *Leonhardt and Soffel* [2006]. The main results of our analysis are mapped in Figures 3.1 and 3.2 and summarised in Table 3.1. Further details of the discrepancies encountered and our potential solutions are outlined and discussed in the Appendix B.

### 3.3 Description of Stratigraphic Units

In this section, we describe Teno's stratigraphic formations with emphasis to temporal variations in the typology and mineralogy of volcanic products, using key outcrop localities and stratigraphic sections (Figures 3.4, 3.5). Although scarce, published field observations of Teno volcanics are summarised. Structural observations and data on dyke swarms, faults and shear zones have been provided by *Walter and Schmincke* [2002] and *Marinoni and Gudmundsson* [2000] and will only be briefly mentioned here.

#### 3.3.1 Masca Formation

The Masca Formation consists predominantly of <1-m-thick basaltic lava flows that are frequently clastic with minor scoria deposits, commonly intruded by numerous dykes [see also *Ancochea et al.*, 1990; *Walter and Schmincke*, 2002]. These volcanics dip steeply seaward (up to 40°) at the base of the sequence exposed in deep barrancos, although this inclination gradually becomes less pronounced with increasing stratigraphic level. In addition to common basalts, aphyric basalts and plagioclase basalts, ankaramites are also found, such as the 10-20-cm-thick flows showing evidence of crystal settling at the main Masca village car park. Moreover, *Walter and Schmincke* [2002] noted the occurrence of an "80-m-thick glassy phonolitic agglutinate with discontinuous spatter lenses" near the top of the Masca Formation. This conspicuous pyroclastic unit, a thick vitric tuff with common lithics [cf. *Schmid*, 1981; *White and Houghton*, 2006], is best exposed at [320080, 3132280] and about 730 m of altitude, some 500 m east of Masca village along the road to Santiago del Teide, just below the Carrizales Unconformity (Figures 3.2, 3.4a, sample TN36). Masca volcanics are generally more altered than the remainder of Teno rocks; this is particularly true in the proximity of the Masca Unconformity, where local faults and shear zones have deformed the lava pile [see *Walter and Schmincke*, 2002].

#### 3.3.2 Masca Unconformity

The Masca Unconformity is the oldest and southwesternmost of the two angular unconformities exposed in the Teno massif (Figures 3.1, 3.2, 3.3) and is generally marked

by the occurrence of a 10-15-m-thick polymict breccia [see also *Barrera et al.*, 1989; *Ancochea et al.*, 1990; *Walter and Schmincke*, 2002]. As noted by *Walter and Schmincke* [2002], the breccia, with modal decimetric basaltic, plagioclase-phyric and ankaramitic blocks, is commonly found interbedded and sometimes mixed with lithified scoriaceous-lapilli deposits (coarse-to-medium lapilli-tuffs [cf. *White and Houghton*, 2006]). This can be observed at outcrops near [318250, 3133400], whilst larger blocks reaching ~2 m are found at the base of the breccia at [319280, 3132600]. As seen in Figure 3.4b, the lapilli-tuffs are occasionally observed resting directly on older Masca lavas, with the breccia found a few meters higher up. The unconformity and the associated breccia and lapilli-tuffs dip steeply, from 30 to 60° N depending on locality.

### 3.3.3 Carrizales Formation

The Carrizales Formation, consisting mainly of near-horizontal lava flows, differs markedly from the older, steeply dipping Masca Formation (Figure 3.3). In comparison, it is intruded by fewer dykes and is characterised by the virtual absence of pyroclastic rocks [see also *Ancochea et al.*, 1990; *Walter and Schmincke*, 2002; *Guillou et al.*, 2004]. In a thin zone parallel to and just underlying the Carrizales Unconformity, the Carrizales rocks are heavily deformed by abundant small-scale fracture sets and shear zones in a well-exposed deformation band [see *Walter and Schmincke*, 2002]. Two main sections, where Carrizales rocks were found in contact with the Masca Unconformity, were investigated in more detail: (1) in the Barranco del Carrizal; and (2) along road TF-436 between Masca village and the view point at Cruz de Gilda (Figure 3.2).

#### 3.3.3.a Barranco del Carrizal log

This section starts northwest of Carrizales Bajo, near [316840, 3134470] at an altitude of 460 m and continues up stratigraphy towards [316900, 3134540] at about 560 m above sea level (Figures 3.2, 3.5a). At the base of the section, the altered, purplish-blue clastic lavas of the Masca Formation are crosscut by the polymict breccia that marks the Masca Unconformity. In nearby outcrops, the breccia shows variable thickness, from 4-5 m to <1 m. A 30-40-cm-thick ash-rich layer, containing clinopyroxene phenocrysts, tops the steeply dipping (~60° N) breccia. This very coarse tuff is overlain by ankaramitic lavas of the Carrizales Formation. These clastic, phenocryst-rich lavas dip up to 25° N and are dominant up to an altitude of ~500 m, after which aphyric to sub-aphyric basalts are found until the top of the investigated profile. A change in the dip direction of the lavas from

NNW to NE is observed near 540 m of altitude. The abundance of ankaramitic lava flows rich in large (some up to 3 cm across) olivine and clinopyroxene crystals at the base of the Carrizales sequence was also noticed by *Walter and Schmincke* [2002].

### 3.3.3.b Masca-Cruz de Gilda log

The geometry of the Masca Unconformity near Masca village (Figures 3.2, 3.3c, see also Appendix B) implies that the first Carrizales lavas along the Masca-Cruz de Gilda log (Figure 3.5b) are encountered some 200 m north along the road at [319550, 3132600] and ~630 m of altitude, where reddish scoriaceous lapilli-tuffs are overlain by an aphyric lava flow. This corresponds to the locality for samples TE5-6 of *Thirlwall et al.* [2000] [M. Thirlwall, personal communication 2007] as well as sample TN-6 of *Guillou et al.* [2004]. These groups of workers obtained virtually identical ages of  $6.02 \pm 0.18$  and  $5.99 \pm 0.09$  Ma, respectively, at this locality. According to geographical coordinates given in their paper, *Leonhardt and Soffel* [2006] obtained a normal polarity reading near this site, in contrast to the reverse polarity determined for TN-6 of *Guillou et al.* [2004] (Figure 3.2). Following outcrops along the road, the sequence consists of lava flows with varying contents of clinopyroxene and olivine phenocrysts, including several ankaramitic flows. At altitudes around 720 m, however, plagioclase-phyric lavas become dominant until the top of the profile that is progressing up stratigraphy until near Cruz de Gilda (Figures 3.4c, 3.5b). These flows are thin, generally <50-cm-thick, and characterised by abundant elongated plagioclase phenocrysts up to 5 mm in length. Samples TN27 to TN30 were collected near the top of this sequence. Near Cruz de Gilda, a few isolated ankaramitic flows (samples TN31 and TN32) top the sequence and outcrops of polymict breccia marking the Carrizales Unconformity can be seen only a few meters above the road, indicating that this profile spans almost the entire Carrizales Formation exposed in this part of Teno. The combination of the Barranco del Carrizal and Masca-Cruz de Gilda logs implies a minimum thickness of ~200-300 m for the Carrizales lava pile (Figure 3.5a, b), although *Walter and Schmincke* [2002] calculated that it may have been as thick as 700 m before it was truncated by the Carrizales Collapse.

### 3.3.4 Carrizales Unconformity

The thickness of the Carrizales Unconformity breccia overall substantially exceeds that of the Masca Unconformity breccia (10-15 m). Indeed, *Walter and Schmincke* [2002] estimated its thickness to be approximately 35 m, above Masca village, where it dips 35° to

the northeast. Further to the west, we recorded a maximum thickness of ~42 m near [318320, 3133850], where an extensive outcrop of the Carrizales Unconformity breccia is found (Figure 3.2). At this locality, the breccia appears to comprise several discrete beds inclined 40-45° to the NNE, each a few meters in thickness. The breccia consists of moderately-to-poorly sorted clasts (2-200 cm), which commonly span the full spectrum of modal mineralogy of Teno lavas within a single outcrop [see also *Walter and Schmincke, 2002*].

#### 3.3.4.a Cherfe Outcrop

In eastern Teno, towards Santiago del Teide, the polymict breccia that corresponds to the Carrizales Unconformity is exposed near [321170, 3131910] at ~1090 m of altitude, where it dips ~30-40° NW (Figures 3.2, 3.3a, 3.4d, e, f). Overall, this locality, herein called the Cherfe outcrop, can be described from base to top to grade from breccia, to lapilli-tuff, to tuff-breccia and back to breccia, following the classification of *White and Houghton [2006]*. At the base of the outcrop, the breccia has a purplish colour, is poorly sorted and includes lapilli and scoriaceous-lapilli as well as up to meter-sized blocks. Plagioclase-phyric lava blocks are very common and are generally smaller than other block types. The matrix is ash-rich, with dispersed clinopyroxene crystals and altered olivines. Up-section within the breccia, the colour of the matrix takes a yellow-orangey tone, due to the gradually increasing content of lapilli and ash. This is accompanied by an increase in the concentration of clinopyroxene crystals. Eventually, a fine-to-medium lapilli-tuff horizon dominated by orangey lapilli and ash with scattered lava blocks (1-100 cm in size) is reached (Figure 3.4e). This deposit also contains clinopyroxene and olivine crystals (up to 20 vol. %) and small lithics (<5 cm) of plagioclase-phyric lava. Dark scoria with fluidal shapes are also present, containing 15-20 vol. % of clinopyroxene and olivine phenocrysts (Figure 3.4f). These predominantly orangey pyroclastic materials can be seen many meters up the steep, ~30-m-high outcrop, but decrease in abundance upwards as lava blocks become dominant again. Although their concentration varies along the thickness of the outcrop, the orangey pyroclastic materials are very similar in appearance throughout.

#### 3.3.5 El Palmar Formation

The El Palmar Formation is composed of a thick pile of near-horizontal (dip <5° N) lavas that directly overlies the Carrizales Unconformity (Figures 3.1, 3.2, 3.3). Where in contact with the unconformity, these lavas are found at their lowest stratigraphic level near 690 m

of altitude. These lavas, however, are found at lower elevations in the El Palmar valley (Figure 3.1), although this may not correspond to lower stratigraphic level. Cumbre Bolicos, the highest point of the Teno massif, marks the top of this formation, giving it an approximate thickness in excess of 600-700 m (Figure 3.2) [cf. *Walter and Schmincke, 2002*].

### 3.3.5.a Alto Carrizal Outcrop

Near [318140, 3134040], at the junction of road TF-436 and the secondary road descending towards Los Carrizales village, a complicated sequence of rock types is encountered within a few tens of meters, exposing the details of the transition between the deformed rocks of the Carrizales Formation, the pyroclastic rocks and the breccia of the Carrizales Unconformity and the overlying El Palmar Formation lavas (Figures 3.2, 3.4g, h).

The southeasternmost part of the outcrop (at the lowest stratigraphic position) consists of highly deformed and altered Carrizales Formation ankaramitic rocks, intruded by several dykes. A sill-like feature shows boudinage-like deformation, near the sharp contact (dip  $\sim 45^\circ$  NNW) with a 50-to-100-cm-thick yellowish lapilli-tuff bed. The tuff contains dark, fluidal, fiamme-like features and sparse clinopyroxene and olivine phenocrysts in an ash-rich matrix. Near the top of this layer, lithic clasts and small blocks of lava become common, and eventually dominate to form the overlying polymict breccia with blocks up to 1 m across. The breccia matrix includes fine grained yellowish lapilli and ash, as well as common large clinopyroxene phenocrysts and small clasts of different compositions. The initially polymict breccia grades into a near-monomict breccia, showing dominantly ankaramitic blocks, before regaining its polymict character. Then, over a  $\sim 2$  m thickness, the breccia mainly consists of aphyric to sub-aphyric lava blocks. In this part of the outcrop, the breccia has a purplish-red matrix, containing small clasts and scoriaceous-lapilli (purplish-pink) as well as a small portion ( $<1-2$  vol. %) of clinopyroxene phenocrysts. Gradually, over a  $\sim 1.5$  m thickness, the polymict breccia matrix becomes dominated by yellowish lapilli and ash, and is marked by an increase in crystal content ( $\sim 20$  vol. % of large clinopyroxene crystals reaching 2 cm in size). A sharp contact marks the top of the breccia, which is overlain by a layer (still NNW-dipping) of fine yellowish tuff (10-30 cm thick), with  $\sim 15-20$  vol. % of clinopyroxene ( $<1$  cm) and olivine ( $<0.5$  cm) crystals in an ashy matrix. Over a 50 cm thickness, the colour changes to purple although some yellowish material is dispersed throughout. Scoria with clinopyroxene and olivine

phenocrysts are dominant, whilst the matrix also includes large clinopyroxene crystals. This scoriaceous lapilli-tuff is overlain by a sequence of N-dipping ankaramitic lava flows, which represent the lowest lavas of the El Palmar Formation along this road cut.

#### 3.3.5.b Alto Carrizal-La Tabaiba log

Figure 3.5c shows the stratigraphic sequence logged from the Alto Carrizal outcrop to La Tabaiba (Figure 3.2), following the main road up to ~825 m elevation and spanning ~135 m of stratigraphic thickness. The lowest El Palmar lavas are 5 ankaramitic flows, each 5-6 m in thickness (their steep N-dip result in lower apparent thickness shown in Figure 3.5c), with abundant scoria near their top, are followed by a sequence of near-horizontal, columnar ankaramitic lavas (Figure 3.4g). At an altitude of 715 m near [318011, 3134201], lithified lapilli, scoria and bombs are encountered, dipping south to southeast. These are intruded by several dykes a few tens of meters along the road and their dip direction eventually shifts west, defining the conical geometry of a fossil vent (Figure 3.5c). Going further up along the road, the pyroclastics rocks are overlain by additional ankaramitic lavas up to ~765 m of altitude, where the first aphyric or sub-aphyric lava flow of the El Palmar Formation is encountered along this profile. Aphyric to sub-aphyric and near-horizontal lava flows dominate the stratigraphy up to the highest elevation along this profile at La Tabaiba, with the exception of ankaramitic lavas near 800 m of altitude.

#### 3.3.6 *Los Gigantes Formation*

Although this formation may largely be equivalent to the upper El Palmar Formation [cf. *Guillou et al.*, 2004], it occurs outside the palaeo-landslide embayment defined by the Carrizales Unconformity; it forms the outermost portions of the massif with the Los Gigantes cliffs as the type locality (Figures 3.1, 3.2, 3.3). The formation consists mainly of gently seaward dipping (10-25° S to SW) lavas of varying composition (plagioclase basalt to ankaramite) and some reddish scoriaceous lapilli-tuffs [cf. *Walter and Schmincke*, 2002]. Los Gigantes lavas are apparently broadly concordant on top of the significantly older Masca Formation; this resulted in confusion about the stratigraphic sequence in southern and western Teno [*Walter and Schmincke*, 2002; *Guillou et al.*, 2004; *Leonhardt and Soffel*, 2006]. Though thus far unidentified, a paraconformity or a disconformity is probably present between these two inclined lava piles (Figure 3.3a, b, see also Appendix B).

### 3.4 Petrology and Geochemistry

Unaltered lava samples were systematically collected from the main profile extending from Masca village to La Tabaiba (Figures 3.2, 3.5b, c), as well as from some other key localities, spanning a total stratigraphic height of ca. 650 m. All lava samples and their respective stratigraphic position used in the petrological and geochemical analysis of this chapter are listed Table 3.2. Pyroclastic rocks were also sampled for petrographic analysis, but, with the exception of the unaltered TN36, were not used for geochemical analyses due to their advanced state of hydration and thus are not listed in Table 3.2. Most samples can be confidently assigned to a particular formation based on locality relative to the observed angular unconformities. Note that, within a particular formation, we sorted samples according to altitude. This obviously is an approximation of stratigraphic position and in some cases, especially when samples from the same formation were taken in distant areas, true stratigraphy may not always be reflected. Particularly, samples from the northwest of Teno (TE23, TE51-54 of *Thirlwall et al.* [2000] and TF88 of *Neumann et al.* [1999]), which we assign to the Masca Formation (Figure 3.1), are difficult to sort with respect to samples from the Barranco de Masca. Also, samples in the northeast (TE26-27 and TE30-36 of *Thirlwall et al.* [2000]), which we consider to belong to the El Palmar Formation (Figure 3.1), were collected at relatively low altitudes, but it is unclear whether these are stratigraphically above or below samples from, e.g. the Alto Carrizal-La Tabaiba sequence. Care has therefore to be taken when interpreting potential stratigraphy-geochemistry trends involving these particular samples. Although no precise locality or altitude was given for samples of *Neumann et al.* [1999], the sample locations described by the authors allow their classification within the Masca Formation (TF88) and the El Palmar Formation (TF93 and TF94).

#### 3.4.1 Petrography

##### 3.4.1.a Lava Samples

Modal phenocryst abundances of our samples as well as those of *Thirlwall et al.* [2000] are listed in Table 3.2, while more detailed petrographic observations are presented in Table 3.3. Overall, clinopyroxene and olivine are the most common phenocryst phases in Teno lavas. They occur either as euhedral or subhedral crystals and anhedral crystals are rare. Many subhedral crystals have embayed rims and some show partly resorbed cores. Clinopyroxene generally displays concentric zoning patterns, although sector zoning and



optically unzoned crystals also occur. A ubiquitous feature in virtually all clinopyroxene phenocrysts from most lava samples is the occurrence of conspicuous outer rims, characterised by a slightly darker color. Often, these rims host microcrysts of acicular apatite and prismatic magnetite. At high-magnification, these rims are commonly observed interlocking with laths of matrix plagioclase and sometimes forming dendritic protrusions (Figure 3.6). Olivine phenocrysts are optically homogeneous, except for a slight change in birefringence commonly observed at their outer rims. Despite the high crystallinity of ankaramitic samples, the scarcity of crystal aggregates (glomerocrysts) of olivine and clinopyroxene is remarkable. When observed, the glomerocrysts usually consist of many, much smaller crystals than the regular phenocrysts. Although most samples lack plagioclase phenocrysts, a few have abundant plagioclase crystals. Once present, plagioclase commonly occurs as glomerocrysts, consisting of acicular crystals arranged in star-like patterns. Small amounts of Ti-magnetite phenocrysts are present in many samples. In most cases, these are euhedral to subhedral, but anhedral crystals are also observed in several samples. The microcrystalline matrix of lava samples contains varying proportions of plagioclase laths, Fe-Ti oxides, clinopyroxene microphenocrysts and cryptocrystalline material. Some rare olivine microphenocrysts are present in the matrix of a few samples only, whilst accessory apatite is common. Basalts, aphyric basalts and plagioclase basalts commonly show a vesicular texture, whereas most ankaramites lack vesicles.

When combining our petrographic observations with those of *Thirlwall et al.* [2000], we note the virtual disappearance of plagioclase as a phenocryst phase for the El Palmar lavas (Table 3.3). In fact, plagioclase phenocrysts only occur in lavas at lowest and highest elevations/stratigraphic levels in this formation. Although as yet not identified in our sample set, *Thirlwall et al.* [2000] noted the appearance of kaersutite in low-MgO lavas of the upper part of the El Palmar Formation and in the Los Gigantes Formation exclusively.

#### 3.4.1.b Pyroclastic Samples

Sample TN36 (Figures 3.2, 3.4a, Table 3.3) is particularly noteworthy: its groundmass is entirely composed of volcanic glass (~78 vol. %) and it contains phenocrysts of plagioclase (~5 vol. %), unzoned greenish clinopyroxene (~2 vol. %), and Fe-Ti oxide (<0.1 vol. %), as well as common lithic clasts (~15 vol. %). In the other pyroclastic samples (TN2, TN4, TN14, TN20-26, see Figure 3.2 for sample localities), clinopyroxene is typically the most common phenocryst phase. Olivine is present in lesser amounts and is generally highly

altered to iddingsite, whereas phenocrysts of plagioclase and Fe-Ti oxide are found in minor amounts or are simply absent. The matrix of these samples is mostly made-up of altered cryptocrystalline material and devitrified glass, although many also contain patches of petrographically pristine volcanic glass. All pyroclastic samples show common vesicles, but lack sedimentary structures in thin section.

### 3.4.2 Rock Major and Trace Element Chemistry

#### 3.4.2.a Total-Alkali-Silica Classification

The chemical composition of our whole-rock and fused groundmass samples is provided in Table 3.4. The major and trace element chemistry and its implications for magma petrogenesis at the basaltic shields of Tenerife are widely discussed by *Thirlwall et al.* [2000]. We follow on these authors' detailed work regarding the chemical classification of Teno rock types. Using the Total-Alkali-Silica classification (Figure 3.7), most rocks fall in the fields of picrobasalt, basanite and alkali basalt whilst a few samples plot in the hawaiite, mugearite, benmoreite and trachyte fields. For consistency with the analysis of *Thirlwall et al.* [2000], we take the extrapolation of the tephrite/basanite-hawaiite field boundary to distinguish basanites from alkali basalts. By applying this divide, only some samples from the El Palmar Formation and the Los Gigantes Formation are classified as basanites (Figure 3.7, Table 3.2). Ankaramites fall in the picrobasalt and alkali basalt fields (some ankaramites are picrites according to the classification of *Le Bas* [2000], see Table 3.2), whereas their respective groundmass compositions plot in the alkali basalt field, with the exception of sample TN7, which has lower crystal content and a basanitic groundmass composition. Note that the highest SiO<sub>2</sub> contents are found in the Masca vitric tuff TN36 and sample TE53, respectively classified as trachyte and mugearite, and Los Gigantes samples TE42, TE44 and TE46 that are benmoreites (Figure 3.7, Table 3.2). In turn, samples from the El Palmar (in this case at generally restrained SiO<sub>2</sub>) and Los Gigantes lavas display the highest concentrations of alkali elements.

#### 3.4.2.b Major and Trace Element Variations Versus MgO

Figure 3.8 complements the information provided by *Thirlwall et al.* [2000], presenting MgO variation plots as a tool to identify mineral phases that might have fractionated during magmatic differentiation. At MgO values >6 wt%, all plots show somewhat diffuse trends, but pronounced inflections are observed at ~6 wt% MgO, especially for SiO<sub>2</sub>, TiO<sub>2</sub>, FeO<sub>t</sub>, CaO and V. The Masca trachytic tuff (TN36) has low Sr, whilst Los Gigantes

benmoreites (TE42, TE44 and TE46) show a slight inflection at high Sr values. These low-MgO samples all have low  $P_2O_5$  contents. Notably, Carrizales rocks show slightly higher  $FeO_t$  than the other formations and, for the low-MgO plagioclase basalts (TN27-30), are characterised by rather low  $Na_2O/Al_2O_3$ . Groundmass separate compositions fall on the liquid line of descent for all major element oxides except  $P_2O_5$ .

#### 3.4.2.c Incompatible Trace and Rare Earth Elements

The concentrations of trace elements that are incompatible in crystalline phases are known to increase in the residual melt as fractional crystallisation proceeds. In contrast, the ratios of such incompatible elements are mostly insensitive to differentiation processes but vary according to the extent of melting of a source, assuming homogeneous source composition. In Figure 3.9, Zr/Nb is plotted against Nb concentration to monitor both crystal fractionation and partial melting processes [cf. *Thirlwall et al.*, 2000]. Highest Nb values are found for the Masca trachytic tuff TN36 and Los Gigantes benmoreites, although some El Palmar samples show similarly high Nb concentrations. While, overall, Carrizales lavas display the lowest Nb abundances, they are characterised by the highest Zr/Nb ratios, only matched by that of TN36.

In mafic melts, rare earth elements (REE) are all incompatible (to a decreasing extent from La to Lu) and, although it also increases during fractional crystallisation, their concentration in the melt is particularly sensitive to partial melting processes. Assuming a source with homogeneous REE contents, low melt fractions are expected to yield higher concentrations of, especially, the light REE, whereas higher degrees of partial melting result in relatively depleted values. Figure 3.10 and Table 3.5 present REE data for Teno lava samples that were specifically analysed for REE concentrations by high precision methods (see Chapter 2 for analytical procedures, and cf. *Neumann et al.* [1999] and *Thirlwall et al.* [2000]). To get an overall picture, means for each of the stratigraphic formations were calculated and plotted together with the corresponding data range. Despite significant overlap, the mean and highest concentrations of REE for a particular formation increase from the oldest (Masca) to the youngest (Los Gigantes) lavas, with the notable exception of the Carrizales Formation which appears relatively depleted in light REE.

#### 3.4.2.d Major and Trace Element Variations Versus Stratigraphic Level

##### 3.4.2.d.1 Entire Teno Sequence

To further investigate temporal variation in the geochemical character of Teno volcanic rocks, we constructed plots of oxide abundances, oxide ratios, normative minerals, trace element concentrations and ratios as a function of the stratigraphic level, using the sequence of samples established in Table 3.2. Note that upper Carrizales ankaramites were excluded from these plots to prevent a sample bias: these ankaramites represent only 5-10% of the rock volume at this stratigraphic level compared to 90-95% for plagioclase basalts (samples TN27-30, see Figure 3.4c, 3.5b). Six of the most instructive examples of these plots are presented in Figure 3.11. Firstly, the SiO<sub>2</sub> content of igneous rocks is widely used as an indicator of magmatic differentiation. For mafic magmas, however, it may also correlate with, especially, the depth, but also the extent of partial melting of the mantle [e.g. *Hirose and Kushiro*, 1993; *Hoernle and Schmincke*, 1993a; *Francis*, 1995 and references therein]. The SiO<sub>2</sub> contents of Teno lavas are mostly confined within ~43 and 50 wt% (with the notable exceptions of samples TN36, TE53, TE42, TE44, and TE46, see also Figure 3.7 and Tables 3.2, 3.4) and no systematic trends with respect to stratigraphic level are evident within this range (Figure 3.11a).

The magnesium number ( $Mg\# = \text{molar Mg}/(\text{Mg} + \text{Fe}^{\text{total}}) \cdot 100$ ) is a particularly useful index of magmatic differentiation in basaltic to intermediate magmas; it decreases rapidly as mafic minerals fractionate. Teno lavas have highly variable Mg#, but samples showing the lowest values also show highest SiO<sub>2</sub> and lowest CaO (Figure 3.11b, d). Several post-collapse El Palmar samples show high Mg# values between 60 and 70.

Given a homogeneous mantle source, the P<sub>2</sub>O<sub>5</sub>/Al<sub>2</sub>O<sub>3</sub> ratio may also be used as a proxy for the degree of partial melting [e.g. *Hoernle and Schmincke*, 1993a]. Indeed, the P<sub>2</sub>O<sub>5</sub>/Al<sub>2</sub>O<sub>3</sub> ratio should increase systematically with decreasing degrees of partial melting and will be preserved in the rocks if clinopyroxene fractionation, which would remove substantial amounts of Al<sub>2</sub>O<sub>3</sub> from the melt, is minor. However, variations in the P<sub>2</sub>O<sub>5</sub>/Al<sub>2</sub>O<sub>3</sub> ratio in the old basaltic shields of Tenerife have been partly assigned to source heterogeneity [*Thirlwall et al.*, 2000]. In any case, this parameter does not correlate well with stratigraphic level at Teno and the range of values is limited, mostly from 0.01 to 0.06 with the exception of anomalously high ratios (~0.1) in two upper El Palmar samples (Figure 3.11c).

Another approach to compare mafic lavas in terms of the degrees of mantle partial melting from which they originated may be to use normative mineralogy. A number of experimental studies [e.g. *Falloon et al.*, 1997 and references therein] have shown that low-degree partial melts of fertile lherzolite are olivine and nepheline normative (silica-

undersaturated), whereas, at higher degrees of melting, the melts gradually become silica-saturated with normative olivine and hypersthene. CIPW norms were calculated for all Teno samples using the model of *Kress and Carmichael* [1988] to determine  $\text{Fe}^{3+}/\text{Fe}^{2+}$ , assuming an oxygen fugacity of one log unit above the Quartz-Fayalite-Magnetite buffer [cf. *Gurenko et al.*, 1996; *Klügel et al.*, 2000]. Most Teno rocks are silica-undersaturated, with only 13 out of 70 samples lacking normative nepheline (Figure 3.11f). Samples from the Masca Formation in the northwest, inferred to be at the lowest stratigraphic level, show relatively high normative nepheline. Higher up in the Barranco de Masca sequence, the degree of silica undersaturation decreases while all Carrizales Formation samples have low or nil normative nepheline. Samples from the northeast, probably at a low stratigraphic level within the El Palmar Formation, also have relatively low normative nepheline. From Alto Carrizal up to an elevation of about 900 m, there is a tendency for increasing normative nepheline. This trend appears to be reversed in the uppermost El Palmar, with the samples at highest altitudes in the region of Cumbre Bolicos showing low degrees of silica undersaturation. Los Gigantes lavas at low elevations show similarly low normative nepheline, whereas samples at high altitudes display a large range of values (Figure 3.11f).

To elaborate on the approach used in Figure 3.9, the ratio of incompatible trace elements Zr/Nb is plotted with respect to stratigraphic level in Figure 3.11e. The resulting data spread reveals patterns somewhat similar, however mirrored, to the trends described for normative nepheline variations; i.e. the highest Zr/Nb ratios are found for the upper Masca and Carrizales formations, with relatively high ratios also observed for the upper El Palmar and lower Los Gigantes rocks.

#### **3.4.2.d.II Detailed Masca-La Tabaiba Sequence**

Zooming in to the stratigraphically well-constrained sampling profile that spans the Masca, Carrizales and El Palmar formations (starting from Barranco de Masca and following the road towards La Tabaiba across both angular unconformities (Figure 3.2)) reveals cyclic patterns in the  $\text{SiO}_2$  and Mg# contents of Teno volcanics (Figure 3.12). Whilst within each formation there is a tendency for increasing  $\text{SiO}_2$  and decreasing Mg# with increasing stratigraphic level, there is a clear shift to lower  $\text{SiO}_2$  and higher Mg# at the transitions between the formations. Indeed, the vitric trachytic tuff (TN36) from the upper part of the Masca Formation contains 64.6 wt%  $\text{SiO}_2$  and 1.3 wt% MgO (Mg# = 31) compared to an average of 45.5 wt%  $\text{SiO}_2$  and 5.7 wt% MgO (Mg# = 44) for the lowermost Carrizales lavas (TE5-6) along this section. In turn, plagioclase basalts dominant in the upper Carrizales Formation (Figures 3.4c, 3.5b, samples TN27-30) are characterised by relatively

high SiO<sub>2</sub> and low MgO (average 47.3 and 4.3 wt%, respectively, Mg# = 39). In contrast, the lowermost lavas of the El Palmar Formation overlying the Carrizales Unconformity, have significantly lower SiO<sub>2</sub> and much higher MgO (average 43.9 and 11.5 wt%, respectively, Mg# = 60).

### 3.4.3 Mineral Chemistry

The chemical composition of olivine, clinopyroxene and plagioclase phenocrysts was analysed for several El Palmar lavas, one Los Gigantes sample (TN16) as well as for some pyroclastics samples. We concentrated our analysis on euhedral and unresorbed crystals, but some subhedral crystals were also targeted. In addition, we investigated a few sector-zoned crystals, by probing two different hourglass-shaped crystal faces. These data were obtained with the main purpose of carrying out the thermobarometric study presented in section 3.4.4. However, mineral chemistry can be used directly to evaluate the role of a number of processes, such as magma transport and degassing, crystal fractionation and magma mixing. In this chapter, the main chemical characteristics of the analysed phenocrysts will be concisely described; for further details, appendices C and E contain chemical plots for the whole dataset and for individual samples, as well as full data tables. Figure 3.13a, b shows the overall composition of clinopyroxene and plagioclase phenocrysts compiled in ternary diagrams. Examples of core-to-rim chemical profiles in clinopyroxene and olivine crystals are also shown. Note that the range of values displayed on the Y-axes in Figure 3.13c and d span the variation from the full Teno dataset.

As a whole, olivine analyses (14 samples, 58 crystals, 560 EMP analyses) result in the compositional range Fo<sub>69-85</sub>. However, olivine crystals with forsterite content >82 were identified in only four thin sections (TN1, TN5, TN20 and TN24) and, with the exception of TN19, only rim analyses returned Fo<77. Clinopyroxene crystals are all diopsidic augites, with an overall variation in clinopyroxene components limited to the range Wo<sub>43-50</sub>En<sub>35-43</sub>Fs<sub>8-15</sub> (for 18 samples, 106 crystals, 1355 EMP analyses, see Figure 3.13a). The clinopyroxene magnesium number (Mg# = molar Mg/(Mg+Fe<sup>total</sup>)) spans the range 69 to 87; however, 80% of analyses in the interiors of clinopyroxene yield Mg# = 75-82. While some Fe-rich profiles of sector-zoned crystals give Mg# < 75, most data points at these low values correspond to outer rim analyses (e.g. Figure 3.13c, see also Appendix C). Although a limited number of plagioclase crystals were studied (3 samples, 7 crystals, 72 EMP analyses), the range in composition retrieved is substantial and extends from bytownite to labradorite (An<sub>64-87</sub>Ab<sub>12-34</sub>Or<sub>0-6</sub>, Figure 3.13b) [cf. *Klein and Hurlbut Jr.*, 1993].

Chemical profiles of clinopyroxene phenocryst interiors indicate generally constant, but locally slightly fluctuating major element compositions (Figure 3.13c, Appendix C). Marked core-to-rim zoning is rather rare, but is observed in a few instances; see e.g. gradual reverse zoning and step-like normal zoning in clinopyroxenes of samples TN1 and TN7, respectively (Appendix C). In addition, a few samples (e.g. TN1) show evidence for at least two different crystal populations. Overall, the composition of olivine interiors is remarkably homogeneous at both the crystal and sample scales. However, in 14 out of 18 samples both clinopyroxene and olivine show steep normal Fe-Mg zonations, typically 20-40  $\mu\text{m}$  wide, at their outer rims. This occurs together with zoning in Si, Ti, Al, Ca, Na (clinopyroxene) and Si, Mn, Ca, Ni (olivine) over the same widths (Figure 3.13c, d, Appendix C). Na-salite (green-core clinopyroxenes rich in  $\text{Na}^+$  and  $\text{Fe}^{3+}$ ), characterised by relatively low Mg# cores and steep reverse zoning at their rims (Al-salite) as reported by *Neumann et al.* [1999], were not observed in our sample set.

#### 3.4.4 Thermobarometry

For certain mineral phases, such as clinopyroxene and olivine, chemical exchange between the magma and growing phenocrysts at equilibrium is dependent on the pressure and temperature of crystallisation [e.g. *Roeder and Emslie*, 1970; *Ford et al.*, 1983; *Beattie*, 1993; *Putirka et al.*, 1996; *Putirka*, 1997]. Consequently, the composition of crystals and ‘melt’ that appear to have equilibrated can thus be used to estimate the pressure and temperature of crystallisation. These physical quantities are in turn commonly used to constrain magma storage conditions [e.g. *Putirka*, 1997; *Klügel et al.*, 2005; *Klügel and Klein*, 2006; *Mordick and Glazner*, 2006]. Here, we use chemical thermobarometry, based on clinopyroxene-melt and olivine-melt equilibria [*Beattie*, 1993; *Putirka et al.*, 1996; *Putirka*, 1997] to constrain the pressure and temperature conditions within the magma plumbing system of the Teno volcano at the time of emplacement of the El Palmar Formation, i.e. the lavas erupted after the Carrizales Collapse.

Before performing thermobarometric calculations, we have carried out a series of equilibrium tests, the procedure of which was outlined in Chapter 2. The results of these tests are presented in Figure 3.14 (clinopyroxene) and Figure 3.15 (olivine). For clinopyroxene the results indicate that: 1) crystal interiors are in relatively good chemical equilibrium with the ‘melt’ composition (in most cases, the chemistry of fused groundmass, Figure 3.14a to d); 2) many outer rims of crystals (up to 77% of analyses) are comparatively in disequilibrium with the melt chemistry (Figure 3.14a to d); and 3) most

crystals in ankaramitic samples show better equilibrium with the fused groundmass composition than with the whole-rock composition (Figure 3.14e, f).

Similar observations are made in Figure 3.15. Indeed, like for clinopyroxene, olivine crystal interiors are in good agreement with the fused groundmass chemistry, whereas crystal rims generally appear in disequilibrium. Also, crystals from ankaramites are more compatible with the fused groundmass than with the whole-rock (Figure 3.15c, d). We will elaborate further on the implications of the equilibrium tests in the discussion section.

Following from several previous workers [e.g. *Schwarz et al.*, 2004; *Klügel et al.*, 2005; *Mordick and Glazner*, 2006], our approach isolates each clinopyroxene crystal and corresponding host melt as a system from which P-T conditions may be estimated. Complete P-T results are shown in Table 3.6. Thermobarometric calculations, using the outermost phenocryst composition in equilibrium with the corresponding melt, indicate that the last equilibrium crystallisation of the selected 84 clinopyroxene crystals occurred at pressures and temperatures ranging from 300-1410 MPa (mean=960 MPa; standard deviation ( $\sigma$ )=213 MPa) and 1150-1290 °C (Figure 3.16). Although an almost complete overlap in calculated pressures exists between the basaltic and ankaramitic samples, the latter appear to have crystallised at slightly higher temperatures. Crystallisation temperatures calculated for olivine are similar to, but generally slightly higher than, those of clinopyroxene with ranges of 1180-1330 °C and 1200-1300 °C, using the thermometers of *Beattie* [1993] and *Putirka* [1997], respectively (Figure 3.16e, Table 3.6).

As the analysis of *Putirka et al.* [2003] suggests, the average calculated pressure for all analyses that yield equilibrium within a crystal may serve as a representative value of the bulk crystal growth history. This is hereafter referred to as ‘bulk crystallisation’. Calculations of bulk crystallisation conditions of the phenocrysts show similar results to that of the last equilibrium crystallisation with P-T ranges of 350-1440 MPa (mean=980 MPa;  $\sigma$ =202 MPa; Figure 3.16) and 1150-1290 °C.

Alternatively, a more macroscopic method may be adopted, which considers the magma as a whole; in this case, all equilibrium P-T values for all clinopyroxenes in a rock/lava sample may be taken as equally valid. Sample means of equilibrium pressures and temperature and associated standard deviations may also be plotted in a graph such as



Figure 3.16c. In comparison with the P-T of bulk crystallisation, this approach is found to yield essentially equivalent results and sample averages were left out for legibility.

### 3.4.5 Magma Density Calculations

Magma density may be an important factor controlling the preferential tapping of certain magma types/compositions [e.g. *Stolper and Walker*, 1980; *Pinel and Jaupart*, 2004]. Indeed, the ‘eruptibility’ of magmas may depend on a critical density that is a function of edifice load; as a volcano grows in size, ascent of dense (likely mafic and volatile-poor) magmas may be discouraged and the eruption of more evolved magmas, often enriched in volatiles may be promoted [*Pinel and Jaupart*, 2000; 2003]. We estimated the density of Teno magmas using the PETROLOG computer program [*Danyushevsky*, 2001]. Calculations were performed on an anhydrous basis, assuming  $f_{O_2}$ =QFM+1,  $P$ =900 MPa and melts at their liquidus temperature (calculated with PETROLOG). The presence of phenocrysts in magma was also taken into account. For samples with <10 vol. % olivine + clinopyroxene, the density of the melt is taken as a reasonable approximation of the magma density. For samples with >10 vol. % olivine + clinopyroxene, the magma density is calculated using a melt density of 2.72 g/cm<sup>3</sup> (average from fused groundmass samples) and the phenocryst proportions of Table 3.2 ( $\rho_{\text{olivine}}$ =3.4 g/cm<sup>3</sup> (~Fo<sub>80</sub>) and  $\rho_{\text{clinopyroxene}}$ =3.2 g/cm<sup>3</sup>). Plagioclase (due to its density nearly equal to melt density) as well as Fe-Ti oxide and amphibole (due to their small abundances) are considered negligible in these calculations. Results indicate that ankaramitic magmas ( $\rho$ =2.98±0.08 g/cm<sup>3</sup>) were substantially denser than magmas that were erupted as aphyric ( $\rho$ =2.69±0.09 g/cm<sup>3</sup>), plagioclase-phyric ( $\rho$ =2.67±0.11 g/cm<sup>3</sup>) and basaltic ( $\rho$ =2.76±0.05 g/cm<sup>3</sup>) lavas. The lowest magma density was obtained from sample TN36 ( $\rho$ =2.42 g/cm<sup>3</sup>) of trachytic composition.

## 3.5 Discussion

The main results of this study may be summarised as: (1) relatively extensive outcrops of pyroclastic rocks are associated with the two angular unconformities at several localities in the Teno massif; (2) ankaramitic magmas, considerably denser than other Teno magma types, were predominantly erupted in both the lower post-collapse sequences of the Carrizales and El Palmar formations; (3) certain geochemical parameters, such as normative nepheline, Zr/Nb and, at higher stratigraphic resolution, SiO<sub>2</sub> and Mg#, correlate with the unconformity-bounded stratigraphic framework; (4) with a few exceptions of

zoned crystals, phenocrysts of clinopyroxene and olivine generally show little chemical variability in their interiors, whereas steep normal zoning commonly occurs only at their outer rims; and (5) crystallisation of clinopyroxene took place at a range of relatively high pressures, with a maximum frequency distribution between 800 and 900 MPa.

### 3.5.1 *Implications of Breccia and Pyroclastic Deposits*

*Barrera et al.* [1989] and *Ancochea et al.* [1990] suggested that the Teno breccia (at the Masca Unconformity) formed through explosive eruptions and lahars. In contrast, *Cantagrel et al.* [1999] proposed that it represents the on-land remains of a debris avalanche with associated deposits extending off-shore [see *Watts and Masson*, 1995]. The more detailed study of *Walter and Schmincke* [2002] revealed the occurrence of two major and geometrically largely similar unconformities, interpreted to define ancient landslide embayments. These authors inferred that the breccias represented debris flow deposits emplaced wet in several episodes, in line with the works of *Barrera et al.* [1989] and *Ancochea et al.* [1990].

Indeed, although the blocks (< 2 m across) making up the bulk of Teno breccias are moderately-to-poorly sorted on the cm-to-m scale, true debris avalanche deposits are typically *very* poorly sorted in that they commonly include ‘mega-blocks’ of tens or even hundreds of meters across [e.g. *Siebert*, 1984; *Glicken*, 1996; *Branney et al.*, 2008]. Such mega-blocks were not found at Teno. In addition, the especially thick breccia pile along the road to the east of the Alto Carrizal outcrop clearly consists of several beds in its upper part, hinting towards a more progressive deposition mechanism, at least at this locality. In this context, primary debris avalanche deposits (syn-giant landslide) may not be preserved at Teno, and the breccias may have largely formed through erosion of the unstable landslide headwall over the course of years to millennia following the successive lateral collapses of the volcano. Similar breccias, also found at the base of a palaeo-landslide scar on the island of La Gomera, were interpreted likewise [*Paris et al.*, 2005b] and modern analogues may be gradually forming in more recent giant landslide amphitheatres, such as the El Golfo embayment on El Hierro (see Chapter 4) [cf. *Carracedo et al.*, 1999b].

Nevertheless, parts of the breccias must have been emplaced rapidly, as suggested by the close association of pyroclastic rocks. At key localities such as the Alto Carrizal and Cherfe outcrops (Figures 3.2, 3.4d, e, f, h), the presence of scoria with fluidal shapes and fiamme-like features strongly suggests that the pyroclasts are juvenile and were deposited

hot during explosive eruptions. Petrographic observations, confirming the uniformity of the matrix of pyroclastic rocks as well as the lack of fine-scale sedimentary structures, also favour a juvenile (as opposed to a remobilised) origin for all pyroclastic rocks sampled. Although such pyroclastic eruptions may have occurred sometime after the major landslide phase, the position of the lapilli-tuffs, dominantly sandwiched between the palaeo-embayment surface and the breccia pile, advocates for a close temporal association with giant landsliding. In turn, the presence of the ashy matrix consolidating the breccias over significant thicknesses suggests the virtually simultaneous deposition of the blocks and the pyroclastic materials. Considering the uniform appearance of the pyroclastic materials at individual localities, in their constitution and especially in their weathering pattern, we argue for single explosive eruptions, at least locally. Blocks and pyroclasts adding up to significant thicknesses (e.g. at least 20 m at the Cherfe outcrop) were thus probably deposited in the time span of an eruption, which may have lasted for up to a few years if we consider the 1730-1736 Lanzarote eruption as a long-duration end-member for Canarian volcanoes [cf. *Carracedo et al.*, 1992]. In such a scenario, parts of the breccias would represent secondary landslides that accompanied pyroclastic eruptions from vents at the base of, or on, the landslide headwall.

Over the course of Teno's evolution, such explosive activity must have been unusual: apart from some pyroclastic deposits in the Masca Formation and perhaps areas of the Los Gigantes Formation, pyroclastic rocks are largely restricted to the unconformities and are overall extremely rare in the Teno massif. This suggests a rather drastic effect of both landslides on the upper levels of the volcano's magma plumbing system, with repercussions over a wide region of the failed edifice. Each of the lateral collapses of Teno probably displaced at least 20-25 km<sup>3</sup> of volcanic material, but the area enclosed by the unconformities (33-50 km<sup>2</sup>), which is greater than that of more recent landslide embayments such as Las Playas on El Hierro (8 km<sup>2</sup>), could indicate individual volumes in excess of 50 km<sup>3</sup> [cf. *Masson et al.*, 2002; *Walter and Schmincke*, 2002; *Paris et al.*, 2005a]. The giant landslides at the Teno shield may thus have been large enough to rearrange the shallow volcano-tectonic stress field at the nucleus of the rift system [cf. *Walter and Schmincke*, 2002], resulting in widespread explosive activity that would have drained existing shallow magma reservoirs. Similar claims were made by *Lipman et al.* [1991], who suggested that lateral collapse associated with the formation of the southwest Hawaii slide complex on Mauna Loa may have resulted in sudden, large phreatomagmatic

eruptions from the landslide headwall, in an event to some extent analogous to the 18 May 1980 eruption of Mount St. Helens.

### 3.5.2 *Implications of Stratigraphic Logs and Magma Density Calculations*

Logging of well-exposed profiles directly overlying both angular unconformities reveals comparable patterns in the sequence of eruptive products following each of the lateral collapses. In fact, above both collapse unconformities, lavas found at the lowest stratigraphic levels are dominantly ankaramites that are very rich in clinopyroxene and olivine megacrysts up to 3 cm across (Figures 3.4g, 3.5). Although such lavas are found in all formations and all areas of the massif, it is striking that their relative abundance markedly increases directly above the angular unconformities. Above the Masca Unconformity, the lower Carrizales ankaramites gradually give way up-section to plagioclase-phyric lavas, which are dominant in the upper Carrizales Formation. Most remarkably, however, these plagioclase basalts completely disappear above the Carrizales Unconformity and, again, numerous ankaramitic lava flows return to the overlying, post-collapse sequence of the lower El Palmar Formation. In this case, ankaramitic lavas eventually grade in to aphyric to sub-aphyric lavas, in the mid El Palmar Formation (Figure 3.5).

Intuitively and in agreement with our magma density calculations, ankaramitic magmas that were charged with abundant ferromagnesian phenocrysts, such as those erupted in the early post-collapse lavas at Teno ( $\rho=2.98\pm0.08$  g/cm<sup>3</sup>), were likely denser than aphyric ( $\rho=2.69\pm0.09$  g/cm<sup>3</sup>), plagioclase-phyric ( $\rho=2.67\pm0.11$  g/cm<sup>3</sup>) and moderately-clinopyroxene-olivine-phyric magmas ( $\rho=2.76\pm0.05$  g/cm<sup>3</sup>). In addition, if we consider that the ankaramites were probably volatile-poor with respect to other Teno magma types (consistent with their lack of vesicles), these density contrasts would likely be enhanced. We therefore postulate that both the Masca and Carrizales collapses, through the rapid unloading of several tens of km<sup>3</sup> of near-surface rocks, may have facilitated the tapping of denser magmas, previously restrained to crystallise at depth. This is in agreement with findings of *Pinel and Jaupart* [2000; 2005], whose numerical and physical arguments predict that edifice destruction should promote the renewed eruptions of denser, likely more primitive magmas.

### 3.5.3 Implications of Petrological and Geochemical Results

#### 3.5.3.a Magma Ascent Conditions

Petrographic observations show that clinopyroxenes in El Palmar lavas display overgrowth rims that appear to have crystallised rapidly. Indeed, the occurrence of widespread acicular apatite inclusions within and some dendritic protrusions on phenocryst and microphenocryst rims points towards accelerated growth rates (Figure 3.6, Table 3.3) [Wyllie *et al.*, 1962; Lofgren, 1974; Wass, 1979; Humphreys *et al.*, 2006]. In addition, the clustering of Fe-Ti oxide microcrysts within the outer rims of the clinopyroxenes suggests a change to a multiply saturated system; perhaps due to a variation in pressure, temperature and/or oxygen fugacity [cf. Perugini *et al.*, 2003]. Moreover, the passive enrichment of Ti and Fe<sup>3+</sup> in the melt during prolonged olivine and clinopyroxene crystallisation may have favoured last-stage Ti-magnetite precipitation and is probably responsible for the high-Ti content and the distinctive colouration of the clinopyroxene outer rims [e.g. Wass, 1979].

The steep normal Fe-Mg zoning associated with the darker tinged rims is, compared with the chemistry of clinopyroxene interiors, out of equilibrium with the melt (Figures 3.6, 3.13, 3.14, see also Appendix C). The even steeper zonations at the rims of olivines have similar widths (on the order of 20-40 µm) to those observed on clinopyroxenes. This suggests that the zonations are related to growth rather than diffusion, as volume diffusion rates under these conditions would be about two orders of magnitude higher in olivine than in clinopyroxene [Freer, 1981]. The comparable zonation widths for Fe-Mg, Ca, Ni and Ti (Figure 3.13, Appendix C), despite distinct diffusion coefficients for these elements [e.g. Freer, 1981], further support this interpretation. Klügel *et al.* [2000], based on such diffusion kinetics arguments, quantified the time-scales involved in the formation of essentially identical zonations in olivines from Cumbre Vieja volcano on the island of La Palma. These authors suggested that the zonations most probably formed during accelerated crystal growth over the course of a few days at most; such time-scales thus appear likely for the growth of Teno's El Palmar phenocryst rims.

Exsolution of volatiles upon magma decompression is a well-documented cause of rapid crystallisation of plagioclase in hydrous, dacitic magma [e.g. Blundy and Cashman, 2005]. However, the phase relations of Rutherford *et al.* [1985] imply that precipitation of other anhydrous phases, such as pyroxenes and Fe-Ti oxides, should also be favoured and/or accelerated by magma ascent and degassing. Moreover, observations by Sparks and

*Pinkerton* [1978] and *Lipman et al.* [1985a] suggest that this mechanism also applies to basaltic magmas, and may result in the precipitation of clinopyroxene and olivine, in addition to plagioclase.

Although H<sub>2</sub>O (and SO<sub>2</sub>) may degas mostly at shallow levels just before or upon eruption [*Gurenko and Schmincke*, 2000], Canarian mafic alkalic melts with ~1% dissolved CO<sub>2</sub> probably begin to exsolve a CO<sub>2</sub>-H<sub>2</sub>O fluid phase (containing some ~90% CO<sub>2</sub>, ~10% H<sub>2</sub>O [cf. *Sachs and Hansteen*, 2000]) at pressures in excess of 1000 MPa [cf. *Dixon*, 1997; *Hansteen et al.*, 1998 and references therein]. Degassing thus starts at upper mantle levels, but is enhanced and becomes progressively enriched in H<sub>2</sub>O during magma ascent [cf. *Dixon*, 1997], resulting in substantial magma undercooling. We therefore propose that out-of-equilibrium, decompressional crystallisation, associated with degassing and large degrees of undercooling, resulted in the rapid growth of clinopyroxene and olivine rims [cf. *Klügel et al.*, 2000]. This mechanism may also have played a role in saturation of Fe-Ti oxides and plagioclase.

### 3.5.3.b Thermobarometry, Magma Storage and Fractional Crystallisation

The aim of our thermobarometry analysis has been mainly to constrain the depth of magma reservoirs and/or conduits of Teno's Miocene plumbing system. As outlined in Chapter 2, the thermobarometers of *Putirka et al.* [1996] require the input of suitable melt and clinopyroxene compositions. *Putirka* [1997] notes: "the limiting condition for extracting P-T information is that magma and coexisting crystals have approximated a closed equilibrium system which has recorded a period of magma storage and pyroxene growth". To date, the calculations have been applied to different melt compositions such as basalt, basanite and tephrite [e.g. *Putirka*, 1997; *Klügel et al.*, 2000]. Major element compositions of whole-rock (sometimes corrected for the presence of phenocryst phases other than clinopyroxene), natural glass or fused groundmass samples may be used as input melt [e.g. *Putirka*, 1997; *Schwarz et al.*, 2004; *Mordick and Glazner*, 2006]. Pressures have been quoted for phenocryst rims, cores, grain averages and sample averages.

In this study, we used whole-rock and fused groundmass compositions to approximate the melt compositions for basaltic and ankaramitic samples, respectively. By analysing the groundmass separates for the ankaramites, we ensured that the melt composition is not controlled by the presence of abundant phenocrysts that appear to have accumulated in suspension in the magma chamber [cf. *Thirlwall et al.*, 2000]. Our

equilibrium tests and mineral chemistry data show that the fused groundmass composition is an accurate representation of the liquid that was in equilibrium with the clinopyroxenes and validates our approximation (Figures 3.13, 3.14).

The last episode of equilibrium crystal growth may be recorded in the outer rims of phenocrysts, providing information on the P-T conditions prevailing just prior to final magma ascent and eruption. As commonly encountered in our data set, however, it is possible that the phenocrysts rims show signs of disequilibrium with the melt, texturally and/or chemically, whilst the remainder of the crystal profile may indicate equilibrium (Figures 3.6, 3.13; 3.14). Thermobarometric calculations using the composition of such rims may lead to potentially meaningless P-T estimates as the required conditions for the use of the thermobarometer are not satisfied. To overcome this problem, we have selected the outermost composition(s) (for each clinopyroxene phenocryst) yielding equilibrium  $Mg^{\#}_{\text{observed}}/Mg^{\#}_{\text{predicted}}$  ratio(s) to obtain the P-T value(s) of the ‘last equilibrium crystallisation’. If multiple analyses satisfy the criterion, the mean of the corresponding calculated pressures and temperatures is used. If rim analyses do not satisfy the criterion, the analysis that indicates equilibrium closest to the rim is selected. This usually represents the analysis directly preceding the outer rim analyses, some tens of microns away.

Our equilibrium tests show that, in most phenocrysts analysed, several spots along a core-to-rim profile indicate equilibrium with the melt [cf. *Mordick and Glazner, 2006*]. This is illustrated in the mineral chemistry data (Figure 3.13, Appendix C); indeed, the concentric optical zoning observed in most clinopyroxene phenocryst interiors translates, in most case, into very limited compositional fluctuations. As noted by *Thirlwall et al. [2000]*, we emphasise the overall compositional similarity of clinopyroxene interiors. Under these inferred conditions, the homogeneity of olivine interiors may be expected from its simpler crystal structure (relative to clinopyroxene). We note, however, that this homogeneity may also partly reflect olivine’s aptitude for rapid internal diffusion at high magmatic temperatures [e.g. *Freer, 1981*].

We thus propose that the clinopyroxenes coexisted for the bulk of their growth history with a liquid of chemical composition closely approaching the final (erupted) melt composition (in our case that of the fused groundmass or the whole-rock). Teno’s mafic magmas may therefore have been crystallising in fairly stagnant reservoirs, but characterised by frequent influx and mixing of fresh mafic melt normalising the system’s composition [cf. *O’Hara, 1977; Neumann et al., 1999*]. Such plumbing system dynamics

may explain the presence of slightly resorbed subhedral clinopyroxene crystals. However, mixing of strongly dissimilar magmas evidenced in some samples bearing  $\geq 2$  chemically distinct crystal populations (e.g. TN1, Appendix C) appears to have been a subordinate process overall. Then, the inferred rapid ascent of magmas may have disabled volumetrically significant phenocryst crystallisation *en route* to eruption (only the outer rims) and hence preserved the main features of pre-ascent melt chemistry. In this context, P-T histories extracted from clinopyroxene phenocrysts may be valid not only for the outermost composition of a crystal. The similarity of the ‘bulk crystallisation’ and ‘last equilibrium crystallisation’ histograms (Figure 3.16) would thus indicate that very few crystals have crystallised at successively lower pressures.

Equilibrium crystallisation pressures determined for phenocrysts from Teno lavas, mostly of the El Palmar Formation, indicate that long-term magma storage beneath Teno occurred virtually exclusively at depths of 20 to 45 km below sea level. Such uppermost mantle magma storage is in agreement with the occurrence of mantle xenoliths on several of the Canary Islands. Indeed, these rocks, which commonly show pervasive overprinting from basaltic melts, have been interpreted as wall-rocks of upper mantle magma reservoirs at depths down to about 35 km [Neumann, 1991; Hansteen *et al.*, 1998], providing strong indirect support for the ranges of storage depths reported here for the Teno edifice. Teno’s upper mantle magma plumbing system may have consisted of a plexus of discrete sill-like and dyke-like magma-filled fractures, some of which were most probably interconnected. Similar models sharing some similarities with a magma mush column [Marsh, 1996] have been proposed for the island of La Palma and for the Madeira Archipelago, where upper mantle magma storage depths were also evidenced [Schwarz *et al.*, 2004; Klügel *et al.*, 2005]. Mantle-level clinopyroxene crystallisation/fractionation is also thought to be an important process at Hawaii (e.g. Mauna Kea volcano, [Frey *et al.*, 1990]) and Iceland (e.g. Krafla and Theistareykir volcanic systems, [MacLennan *et al.*, 2001]). Although we envisage the plumbing system of the Teno volcano to be similar to that of Cumbre Vieja volcano on the island of La Palma [cf. Klügel *et al.*, 2005], we note the following distinctive characteristics: 1) the main level of magma storage/crystallisation is located at slightly greater depths at Teno; 2) the relatively homogeneous character of the El Palmar Formation phenocrysts may indicate comparatively large and homogeneous individual reservoirs; 3) the lack of low-Mg#, greenish clinopyroxene (i.e. green-core or Na-salite) may assign a minimal role to mixing between significantly more evolved magmas and



Teno's mafic El Palmar magmas, contrasting with observations at several other Canarian volcanoes [cf. *Neumann et al.*, 1999; *Klügel et al.*, 2000; *Troll and Schmincke*, 2002].

Our data partly contrast with initial results reported by *Neumann et al.* [1999] for Teno and other localities on Tenerife. These authors concluded, on the basis of the statistical approach of *Soesoo* [1997] and calculations using the MELTS models [*Ghiorso and Sack*, 1995], that crystallisation most likely took place at pressures between 200 and 500 MPa, corresponding to depths within the volcanic edifice to the base of the oceanic crust. However, by comparing the *Soesoo* [1997] results with experimental data of *Thompson* [1974] for alkalic melts, *Greenwood* [2001] suggested that the *Soesoo* [1997] method might underestimate pressure by ~400 MPa. Moreover, *Putirka et al.* [2003] showed that the use of the MELTS models to calculate crystallisation conditions cannot be recommended. On the other hand, the *Putirka et al.* [1996] approach appears to provide the most precise and accurate clinopyroxene thermobarometers available for mafic compositions [*MacLennan et al.*, 2001; *Putirka et al.*, 2003; *Klügel et al.*, 2005; *Mordick and Glazner*, 2006]. When using the *Putirka et al.* [1996] formulations, *Neumann et al.* [1999] obtained pressure ranges for Teno lavas nearly identical to the results presented in this study. *Neumann et al.* [1999] moreover supported their low pressure estimates using fluid inclusion microthermometry on gabbroic and nepheline syenite xenoliths, but were not able to perform this technique on magmatic phenocrysts. As the xenoliths may have been entrained at a late stage by ascending magmas and considering that fluid inclusions have the ability to rapidly re-equilibrate to lower pressures [see e.g. *Hansteen et al.*, 1998], the microthermometry data obtained by *Neumann et al.* [1999] do not exclude main storage at deeper levels for the host magmas. Although shallow storage has probably been an important process for the younger Las Cañadas and Pico Viejo-Teide edifices [e.g. *Martí et al.*, 1994; *Ablay et al.*, 1998; *Carracedo et al.*, 2007], we do not consider the evidence presented by *Neumann et al.* [1999] conclusive for the Teno volcano.

The only robust evidence for extensive long-term magma storage within the volcanic edifice or the oceanic crust during the evolution of Teno consists in the eruption of felsic pyroclastic material, such as the thick trachytic tuff (TN36, with 64.6 wt% SiO<sub>2</sub>) of the upper Masca Formation. The formation and eruption of such magma batches probably require the existence of a fairly shallow magma chamber system 'just before' the Masca Collapse at ~6.1 Ma. It is unclear whether the abundant plagioclase phenocrysts in

the upper Carrizales lavas would also indicate crustal-level magma storage and differentiation [cf. *Hoernle and Schmincke*, 1993b; *Thirlwall et al.*, 2000].

Coupled with the evidence for rapid magma ascent preserved in the clinopyroxene and olivine outer rims, our thermobarometric data imply that Teno magmas must have ascended from mantle depths within days. Short term, shallow (within volcanic edifice and upper crust) stagnation of magmas before eruptions may have occurred on time scales on the order of hours to days at most [cf. *Klügel et al.*, 2000]. However, our data do not exclude magmatic intrusions becoming arrested at crustal levels without leading to eruptions, as previous studies have suggested it might be the case for most dykes [e.g. *Gudmundsson et al.*, 1999]. During the time of emplacement of the El Palmar Formation, however, it appears that the intrusions that fed eruptions were able to rapidly propagate from upper mantle depths to the surface. Such a rapid magma transport from great depths has also been proposed for e.g. the 1950 eruption of Mauna Loa volcano [*Thornber and Trusdell*, 2008].

Overall, substantial crystal fractionation must have taken place in fairly deep magma reservoirs and upon magma ascent within the plumbing system. The high SiO<sub>2</sub> and alkali (Figure 3.7), low MgO (Figure 3.8) and high Nb (Figure 3.9) of some Masca and Los Gigantes samples (especially TN36, TE42, TE44, TE46 and TE53) all suggest that the peak degrees of magmatic differentiation were reached both early and late in the sub-aerial evolution of Teno. Although some El Palmar samples (especially 3 hawaiites, Figure 3.7, Table 3.2) probably experienced significant degrees of fractional crystallisation, most appear moderately to poorly differentiated, whereas Carrizales lavas were seemingly the least affected by differentiation processes overall (Figures 3.7, 3.8, 3.9).

As discussed by *Thirlwall et al.* [2000], the trends seen at MgO > 6 wt% (in Figure 3.8) are probably controlled by clinopyroxene and olivine fractionation/accumulation, while the pronounced inflections at ~6 wt% MgO seem to indicate the onset of significant magnetite fractionation. Notably, Carrizales low-MgO basalts lack a steep decrease in V concentration, suggesting that these rocks have not suffered significant magnetite removal. Plots for Sr and P<sub>2</sub>O<sub>5</sub> suggest that the Masca trachytic tuff as well as the Los Gigantes benmoreites probably fractionated plagioclase and apatite [cf. *Thirlwall et al.*, 2000], whilst the Carrizales low-MgO basalts (with somewhat low Na<sub>2</sub>O/Al<sub>2</sub>O<sub>3</sub>) may indicate that plagioclase removal generally does not start until MgO < 3-4 wt%. The low P<sub>2</sub>O<sub>5</sub> content of groundmass separates is probably artificial, reflecting the mechanical removal during

sample preparation of apatite microcrystals hosted in the rims of clinopyroxene phenocrysts [cf. *Longpré et al.*, 2008b].

Perhaps unsurprisingly, the return of ankaramitic lavas in both of the lower post-collapse sequences, i.e. in the Carrizales and El Palmar formations (Figure 3.5), translates into cyclic variations in whole-rock  $\text{SiO}_2$  contents and Mg# of the lavas along the Barranco de Masca-La Tabaiba sampling profile (Figures 3.2, 3.12). Although Mg# of up to 70 (MgO = 17.0 wt%) reflect the abundance of accumulated ferromagnesian clinopyroxene and olivine phenocrysts [see *Thirlwall et al.*, 2000], lower El Palmar groundmass compositions still have Mg# of 52 on average, a significant increase compared to upper Carrizales plagioclase basalts (Mg# = 39). It thus appears from Figure 3.12 that magma differentiation processes, such as those that produced the pre-Masca Collapse trachytic magma (TN36) and the pre-Carrizales Collapse low-MgO plagioclase basalts (TN27-30) were efficient just prior to landsliding, but were temporarily shut down or at least diminished after each collapse, only gradually returning to take substantial effect in the mid-to-late post-collapse lava sequences. At least in the case of the Masca Collapse, this was probably coupled with the removal of shallow magma reservoirs, as will be further discussed in Chapter 6. The argumentation presented here thus advocates further for considerable disturbance of the magma plumbing system directly caused by the lateral collapses of the volcano; again, in line with the works of *Pinel and Jaupart* [2000; 2005].

### 3.5.3.c Mantle Source, Partial Melting and Magmatic Cycles

*Thirlwall et al.* [2000] showed that each of the Roque del Conde, Teno and Anaga massifs must have had a different mantle source. Indeed, the K/Nb and K/Ba ratios are distinct for each of the basaltic shields even though their lavas have similar Zr/Nb ratios and degrees of alkalinity. Isotopic data reported by *Simonsen et al.* [2000] also support mantle source differences between the massifs, with Teno displaying a more radiogenic Pd and Nd isotope signature, indicative of a young HIMU-like source perhaps representing subducted oceanic crust with a ~1 Ga residence time in the mantle. Isotopic composition, however, appears relatively homogeneous through time at each of the geographic areas of Tenerife [*Simonsen et al.*, 2000]. At Teno, the distinct trend of K/Nb vs. Zr/Nb (see Figure 13 of *Thirlwall et al.* [2000]) and the similar  $\text{SiO}_2$  contents of mafic lavas probably also reflect a comparable mantle source and similar depths of melting throughout this volcano's evolution. The melting column under Teno, as well as under Roque del Conde and Anaga,

is inferred to have extended from depths corresponding to pressures in excess of 3 GPa to shallower than the garnet-spinel facies transition.

Overlapping Zr/Nb ratios, coupled with distinct K/Nb, K/Ba and isotopic ratios, imply that Zr/Nb does not vary strongly in the mantle source (s) of Tenerife. On the other hand, Zr/Nb is sensitive to partial melting behaviour in the mantle, as shown by simple quantitative geochemical modelling using the batch melting equation:

$$C_L/C_O = 1/[D_{RS} + F(1 - D_{RS})]$$

where  $C_L$  and  $C_O$  are the concentration of Zr or Nb in the melt and the unmelted source, respectively,  $D_{RS}$  is the bulk distribution coefficient of the residual solid and  $F$  is the weight fraction of melt produced by partial melting. Considering a garnet peridotite source (59.8% olivine, 21.1% orthopyroxene, 7.6% clinopyroxene and 11.5% garnet), mineral/melt partition coefficients compiled by *Rollinson* [1993] and primitive mantle Zr and Nb source abundances [*Wood et al.*, 1979], we obtain Zr/Nb ratios of  $\sim 7.7$  for  $F < 0.05\%$  and of up to 11.3 for  $F = 5\%$ . Zr/Nb ratios at Teno are lower (between  $\sim 3.3$  and 5.8) than those obtained by these first order calculations. As ratios remain nearly constant at  $F < 0.05\%$ , these lower values cannot be explained by lower melt fractions than modelled here, but rather reflect (1) poorly defined partition coefficients of Zr and Nb [*Thirlwall et al.*, 2000], (2) a different mineralogy of the source rock, with a possible component of spinel peridotite, and/or (3) different initial concentrations ( $C_O$ ) of Zr and Nb in the source rock. Using a different set of parameter values, *Thirlwall et al.* [2000] performed more elaborate modelling of trace element behaviour during partial melting and argued that mean melt fractions were probably low. These authors' modelling show that the range of Zr/Nb ratios at Teno could be produced by 0.1% to  $\sim 2\%$  melting of a MORB-source, with melts derived from both the garnet and spinel stability fields.

Thus using Zr/Nb as a proxy for partial melting, *Thirlwall et al.* [2000] noted that the geochemistry of Teno lavas was consistent with a progressively waning melt fraction through time (see their Figure 12). However, additional sampling and the recognition of unconformity-bounded stratigraphic units reveals a slightly more complicated picture. In fact, the comparatively high Zr/Nb (Figures 3.9, 3.11e), low REE (Figure 3.10) and low normative nepheline (Figure 3.11f) of Carrizales lavas with respect to other Teno formations strongly suggest peak degrees of partial melting 'just after' the Masca Collapse, more than 0.2 Ma after Teno's first sub-aerial emissions. Earlier, pre-collapse Masca samples (mainly represented by TE1-4 from Barranco de Masca) generally have slightly lower Zr/Nb, except for TN36, although, for this low-MgO sample (1.3 wt%), fractional

crystallisation of titanite might have occurred and increased the Zr/Nb ratio [cf. *Ablay et al.*, 1998; *Thirlwall et al.*, 2000]. On the other hand, after this temporal increase in melt fraction during the extrusion of Carrizales lavas, later lower-to-mid El Palmar lavas are indeed consistent with a decreasing extent of partial melting with time (e.g. high normative nepheline, low Zr/Nb, Figure 3.11e, f), as suggested by *Thirlwall et al.* [2000]. Intriguingly, however, further fluctuations in normative nepheline and Zr/Nb for the lower Los Gigantes lavas, and perhaps the uppermost El Palmar rocks, may once more indicate temporally increased melt fractions with respect to e.g. mid El Palmar lavas. Three possible scenarios that may account for these observations are discussed below: (1) the geochemical evolution of Teno was controlled by the melting of successive mantle blobs [cf. *Hoernle and Schmincke*, 1993a], (2) repeated partial edifice destruction through lateral collapses, during a single magmatic cycle, gave rise to partial melting fluctuations, and (3) the chemical signatures correspond to a transition from the shield stage (Masca and Carrizales lavas) to the post-shield stage (El Palmar and Los Gigantes lavas) of volcanic growth, similar to that seen at typical Hawaiian volcanoes.

#### **3.5.3.c.i Blobs of Upwelling Plume Material**

Zr/Nb and normative nepheline variations seen in Figure 3.11e and f may be attributed to two successive blob-induced melting cycles. Beginning near the time of emergence of Teno above sea level, the melting of a main blob may have produced the Masca, Carrizales and the better part of El Palmar magmas. In this context, the Carrizales Formation would originate from melts formed in the hotter centre of this blob, where highest degrees of partial melting result in the least silica-undersaturated magmas. A second, much smaller blob-cycle may be held responsible for the uppermost El Palmar lavas and the Los Gigantes Formation. Such interpretations, however, rely partly on the assumption that the samples from the northwest (TE23 and TE51-54 of *Thirlwall et al.* [2000]) and northeast (TE26-27 and TE30-36 of *Thirlwall et al.* [2000]) represent the *lower* portion of the Masca and El Palmar formations, respectively. As mentioned earlier, the sorting of these samples with respect to others of the same formation involves inherent uncertainties (Table 3.2, Figure 3.11a). Nevertheless, if we accept that the sub-aerial portion of the Teno edifice (being perhaps 10% of total volcano volume) was produced by the melting of two successive blobs of upwelling plume material, it follows that the complete, mostly submarine edifice must result from the melting of many more of such blobs (assuming blobs of semi-comparable sizes). Whether it is reasonable or not to consider that perhaps

10-20 (or more) mantle blobs produced the Teno edifice remains unaddressed by the present work.

In turn, a blob-governed evolution for the Teno volcano would be expected to yield distinctive trends in temporal variations of  $\text{SiO}_2$  and  $\text{P}_2\text{O}_5/\text{Al}_2\text{O}_3$ , the characteristic proxies used by *Hoernle and Schmincke* [1993a] to develop their model (see their Figure 8). Such trends are not observed at Teno (Figure 3.11a, c). Whilst the “blob model” seemingly provides a sensible explanation for the evolution of Gran Canaria, on which it is largely based [*Hoernle and Schmincke*, 1993a; b], the distinguishing features of blob-induced magmatic cycles are not necessarily reproduced at other Canarian volcanoes, such as Teno.

### **3.5.3.c.II Destruction of the Volcanic Edifice**

Because mantle melting under Canarian volcanoes is thought to be due to decompression of upwelling plume material [*Hoernle and Schmincke*, 1993a; b], variations in pressure due to the addition or subtraction of a surface load (volcanic construction/destruction) may result in feedback-related changes in the rate and degree of mantle melting, if the effect of such loading/unloading ‘propagates’ down to the melting region. A useful analogy may be that of ice sheet loading/unloading during glaciation/deglaciation periods in Iceland that has drastically affected volcanism [*Hardarson and Fitton*, 1991; *Sigvaldason et al.*, 1992; *Jull and McKenzie*, 1996; *Slater et al.*, 1998; *MacLennan et al.*, 2002]. Indeed, after reduced melt generation during glaciation, ice unloading at the end of the last ice age resulted in a prodigious increase of melt generation and eruption rates by a factor of 30. Post-glacial lavas were found to show greater range of and generally higher MgO and to have significantly lower light REE concentrations [*Slater et al.*, 1998; *MacLennan et al.*, 2002]. However, as it will be further discussed in Chapter 5, the drastic differences in the geodynamic settings of Iceland (characterised by the presence of both a spreading ridge and a mantle plume) and intra-plate oceanic volcanoes imply significant dissimilarities in the effect of unloading on melt generation.

Although it has not yet been the focus of any study whether or not unloading of a surface rock mass during large-scale landsliding can lead to similar disturbance in rates of mantle melting, *Presley et al.* [1997], who studied the post-shield activity of Waianae volcano, on Oahu, Hawaii, suggested that it may be feasible. These authors argued, through simple melting calculations, that the decompression associated with the Waianae slump is more than sufficient to have caused the apparent ~1% increase in the degree of melting to explain the differences between the pre-slump (Palehua Member) and post-

slump (Kolekole) lavas. Similar claims were made by *Hildenbrand et al.* [2004] for Tahiti-Nui Island (French Polynesia). The latter authors attributed an increase in eruptive rate as well as variation in certain trace elements, apparently caused by increased mantle melting, to be the result of a decompression-response to lateral collapse of the volcanic edifice.

At Teno, the short time interval (probably within ~250 ka [*Leonhardt and Soffel*, 2006]) between the last deposits of the Masca Formation, the successive giant landslides and subsequent extrusion of scar-infilling Carrizales and El Palmar lavas (combined thickness >1000 m), coupled with the associated changes in chemical composition of the lavas (Figures 3.9, 3.10, 3.11), is compatible with the hypothesis that the collapses of the volcano may also have produced an increased rate of melt generation in the mantle. Whilst the geochemical features of Carrizales lavas would thus be a result of the Masca Collapse, El Palmar lavas do not bear a similar signature of increased partial melting that, in this context, may be expected after the Carrizales Collapse. However, the effect of this second lateral collapse may have been insufficient to overcome the competing tendency of gradually waning magma supply from the mantle.

### **3.5.3.c.III Transition Between Shield and Post-Shield Volcanism**

Alternatively, the chemical patterns seen at Teno may be due to a transition between the shield stage and post-shield stage of growth at this volcano. In this third scenario, the Masca and Carrizales formations would represent the peak of the shield stage, with moderately high magma supply brought about by maximum melt production. The gradually more alkalic El Palmar lavas, indicating declining melt fractions, may mark a transition to the post-shield stage of volcanism, similar to what is observed in Hawaii as a volcano (e.g. Mauna Kea) migrates away from the hot-spot [e.g. *Frey et al.*, 1990; 1991]. In this context, Los Gigantes lavas would also correspond to post-shield stage volcanics (Figure 3.11). Nevertheless, the large volume of the rapidly extruded El Palmar lavas, despite waning melt production at this point, is paradoxical and would have to be explained by the increased tapping of previously pooled magma triggered by landslide-related unloading [cf. *Sigvaldason et al.*, 1992].

Although the possibility that Teno's geochemical evolution may have been controlled by multiple mantle blobs cannot be fully ruled out at this stage, we favour a model in which a somewhat typical hot-spot volcano evolution (keeping in mind the extreme tectonic setting of the Canary Islands (Chapter 1) [e.g. *Hoernle and Schmincke*, 1993a; b; *Carracedo et al.*, 1998]), influenced by large-scale mass-wasting events, best

explains the nature and the chemical cyclicity of Teno volcanics. The landslide-induced changes at Teno appear to have extended all the way from the surface (increase in pyroclastic activity) through the deep magma plumbing system (sudden increase in eruptions of less evolved, denser magmas stored at uppermost mantle levels). Apparent higher degrees of partial melting during the extrusion of Carrizales Formation following the Masca Collapse are compatible with a potential influence of landsliding on mantle partial melting; however, it remains unclear if such interactions are physically realistic (further details in Chapter 5).

#### 3.5.4 *An Evolutionary Model for the Teno Volcano*

On the basis of the data presented, we now propose a sequence of events that mark the evolution of the Teno volcano. A schematic representation of this model is presented in Figure 3.17.

From about 6.3 to 6.1 Ma ago, alternation of phreatomagmatic and effusive basaltic eruptions constructed the initially steep, sub-aerial Teno edifice (Figure 3.17a). At this stage, melt generation rates in the upper mantle were moderately high, resulting in sustained magma supply. This, coupled with the effect of volcano load, may have permitted the formation of shallow magma reservoirs, presumably within the volcanic edifice, where some of Teno's most evolved (trachytic) magmas were produced. These highly differentiated, low-density magmas were erupted once Teno had reached a significant size and its northern slopes became unstable.

Eventually, after a phase of gradual flank creep, the northern flank of Teno failed ~6.1 Ma ago (Figure 3.17b), producing a U-shaped embayment some 5-10 km across. This resulted in the depressurisation of the shallow magma reservoir(s), leading to widespread explosive eruptions from vents at the base of, or on, the landslide headwall. These pyroclastic eruptions occurred contemporaneously with secondary landslides, probably associated with rapid erosion of the landslide headwall that closely followed the main landslide phase. Shallow magma reservoirs may have been largely drained at that point.

The decompression effect of this giant landslide also affected the volcano's deep plumbing system, in facilitating the tapping of dense magmas that had previously accumulated at uppermost mantle levels (Figure 3.17c). The volcano being at the peak of its sub-aerial shield stage, melt generation (presumably within the spinel stability field) was high at this point. This resulted in the rapid filling of the Masca Collapse embayment



by the less evolved, near-horizontal Carrizales lavas that were initially mostly ankaramites, but eventually became dominated by plagioclase basalts, all of which were characterised by low degrees of silica-undersaturation and high Zr/Nb. It is unclear whether the low-MgO plagioclase basalts evolved in crustal magma reservoirs. This Carrizales sequence is at least 200-300 m thick, but plausibly reached as much as 700 m in thickness [cf. *Walter and Schmincke, 2002*].

This rapid volcano-regrowth led to renewed flank instability in the north. After periods of flank creep, the Carrizales lava pile collapsed seaward, forming a second giant landslide embayment (Figure 3.17d). As in the case of the first collapse, widespread pyroclastic eruptions were closely associated with landsliding; lapilli-tuffs and polymict breccias were deposited on the walls of the landslide amphitheatre.

The deep plumbing system was once more disturbed by surface unloading; plagioclase phenocrysts, abundant in the upper pre-Carrizales Collapse sequence, virtually disappeared in the post-collapse El Palmar sequence (Figure 3.17e). Again, dense ankaramitic magmas were preferentially tapped in the early post-collapse eruptive episode, but this time, they were eventually superseded by crystal-poor basanitic lavas. The mean melt fractions started to decrease shortly after the second (Carrizales) collapse, and this may have been due to the overall declining influence of the hot-spot as the volcano entered the more alkalic post-shield stage of development. During this phase (and probably during most of the earlier Carrizales and following Los Gigantes phases), magma storage took place in the upper mantle, and there is no evidence for prolonged storage of magmas at shallow depths. Both giant landslides and subsequent embayment infilling took place in a short time span, probably within ~250 ka, from ~6.1 to 5.9 Ma ago.

The uppermost part of the El Palmar Formation (largely eroded today) may have been emplaced nearly contemporaneously to Teno's youngest Miocene lavas (5.2-5.0 Ma), the Los Gigantes Formation, that overflowed the filled collapse embayment (Figure 3.17f), although a hiatus in activity is suggested by magnetostratigraphy [*Leonhardt and Soffel, 2006*]. Instability in the melting region may have resulted in temporally restricted fluctuations in melt fractions late in the post-shield stage of this volcano. Some Los Gigantes lavas were the product of substantial degrees of magmatic differentiation, not encountered since the pre-collapse, upper Masca Formation. Magma supply eventually became too low and Miocene magma conduits shut off. The Teno volcano was subject to substantial erosion, gradually forming the landscape we see today. Scattered Pleistocene

eruptions occurred in Teno's eroded lowlands and may represent rejuvenated volcanism from its own plumbing system after a ~4 Ma hiatus or may be the distal products of the Northwest Rift of the Las Cañadas and Teide-Pico Viejo edifices.

### 3.6 Conclusions

The main conclusions of this chapter are:

- (1) Major angular unconformities, representing palaeo-landslide embayments, are fundamental stratigraphic boundaries at Teno and have to be closely adhered to for the establishment of a consistent stratigraphic framework at this and other similar volcanoes.
- (2) Extensive explosive volcanism was closely associated with the large-scale lateral collapses of the Teno volcano in the late Miocene.
- (3) Some of Teno's most evolved magmas were produced just prior to giant landslide events. Less differentiated, denser magmas frequently charged with comparatively large olivine and clinopyroxene phenocrysts, were erupted 'immediately' following the large-scale collapses. While the late pre-collapse volcano appears to have had a shallow magma reservoir system, the younger post-collapse Teno volcano was likely fed directly from the upper mantle, where magmas accumulated, partially crystallised and differentiated at depths ranging from 20 to 45 km. Magma ascent from these depths to the surface was a rapid process, probably taking place over the course of days.
- (4) The lavas erupted after the first collapse, the Carrizales Formation, appear to originate from higher mean mantle melt fractions than the other stratigraphic formations of Teno.
- (5) We propose a scenario in which the successive collapses of the Teno volcano played a key role in regulating the eruptive regime and the density (indirectly, the composition) of magmas that could be tapped. The giant lateral collapses of the Teno shield-volcano appear to have re-arranged the shallow volcano-tectonic stress field, resulting in widespread pyroclastic activity that may have drained pre-existing shallow magma reservoirs. The removal of tens of km<sup>3</sup> of near-surface rocks may have been sufficient in transmitting a substantial pressure decrease at depth, which in turn may have facilitated the extrusion of denser magmas stored at

upper mantle levels. Although neither the influence of successive melting of multiple mantle blobs, nor that of collapse-induced decompression can be discarded at this stage, we propose that variations in melt production indicate that Teno underwent a transition from its peak shield-building stage (Carrizales Formation) to its post-shield stage, early during the extrusion of the El Palmar Formation.

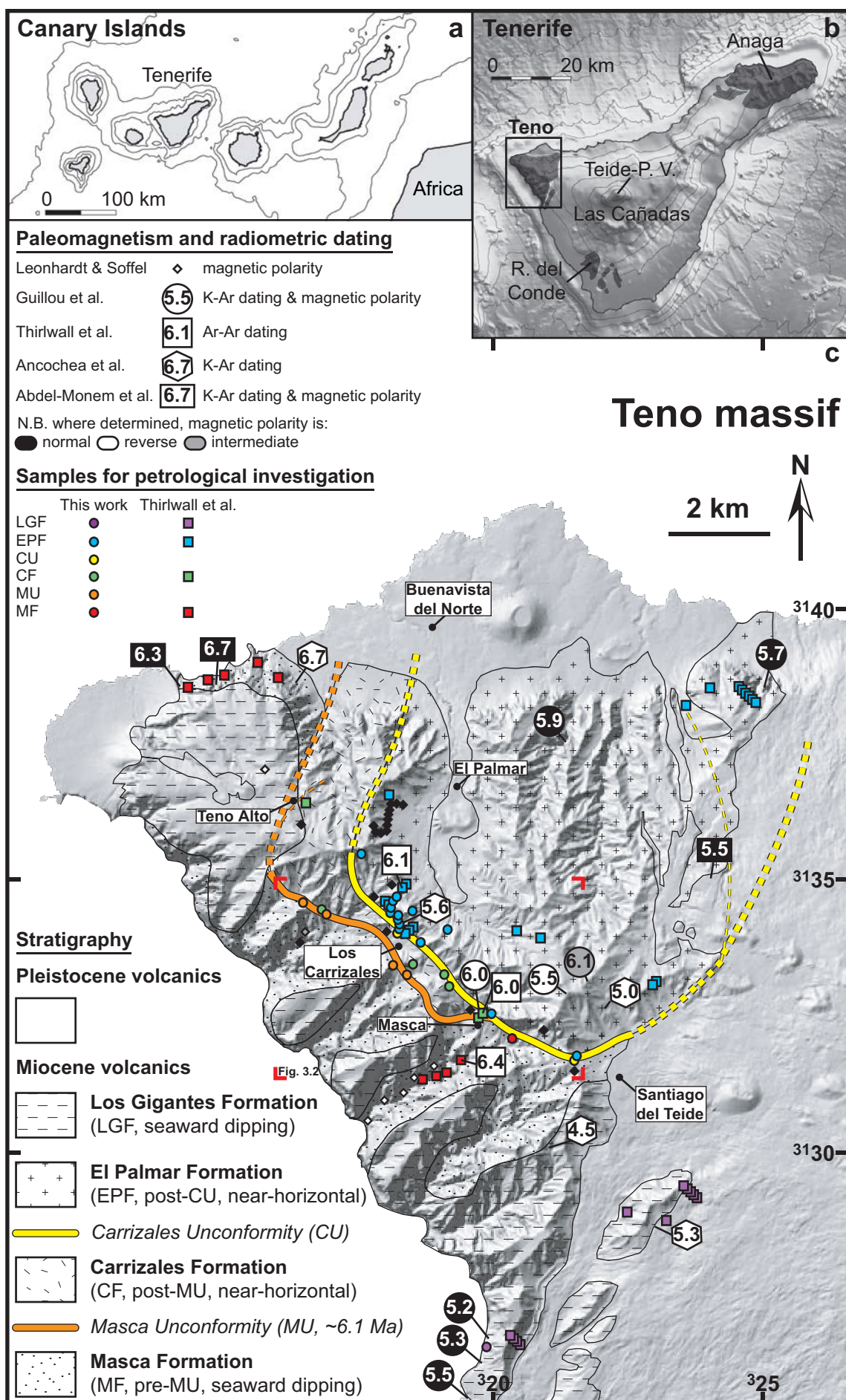


**Figure 3.1** See full figure caption on page of Figure 3.3.

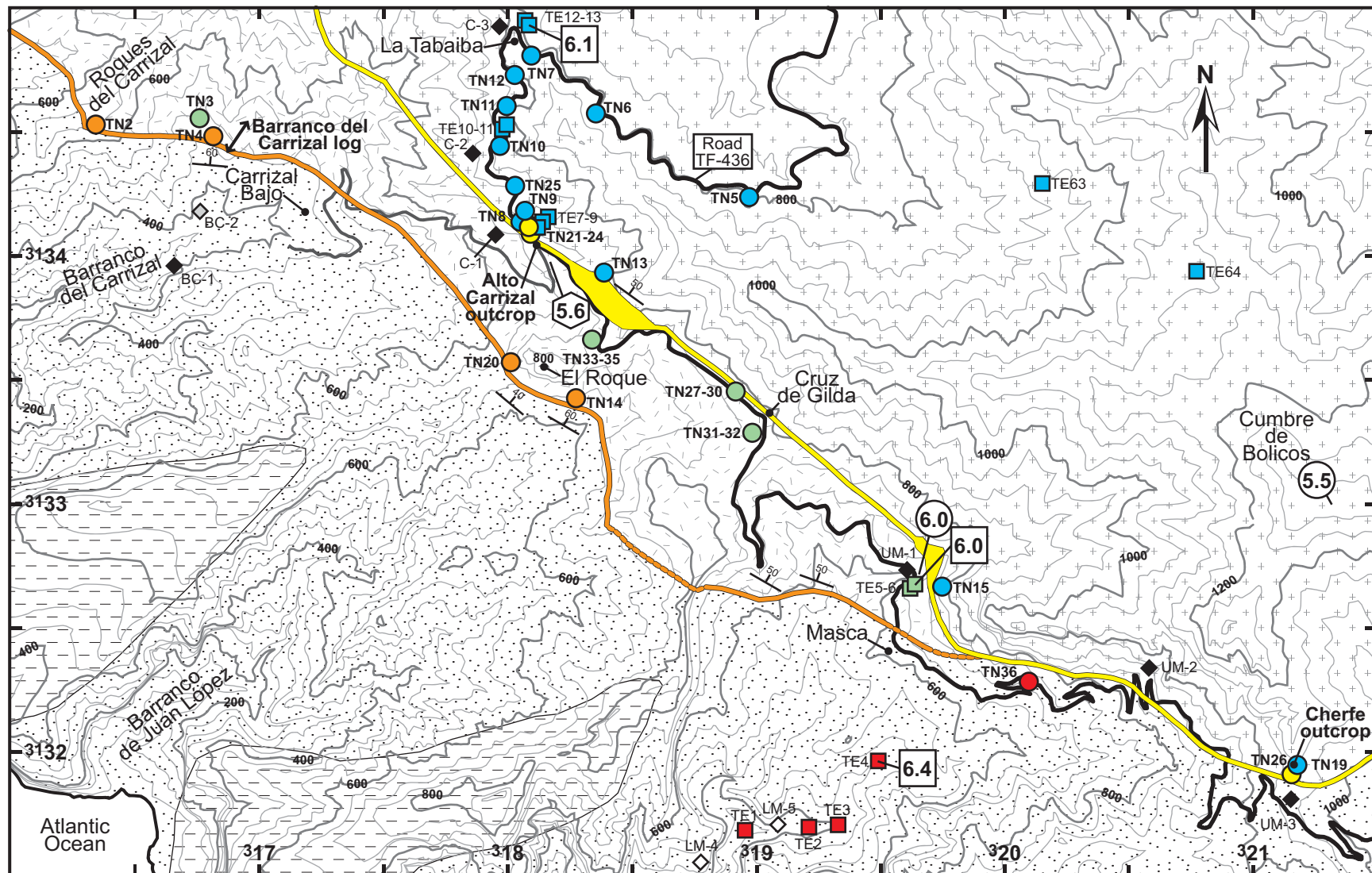
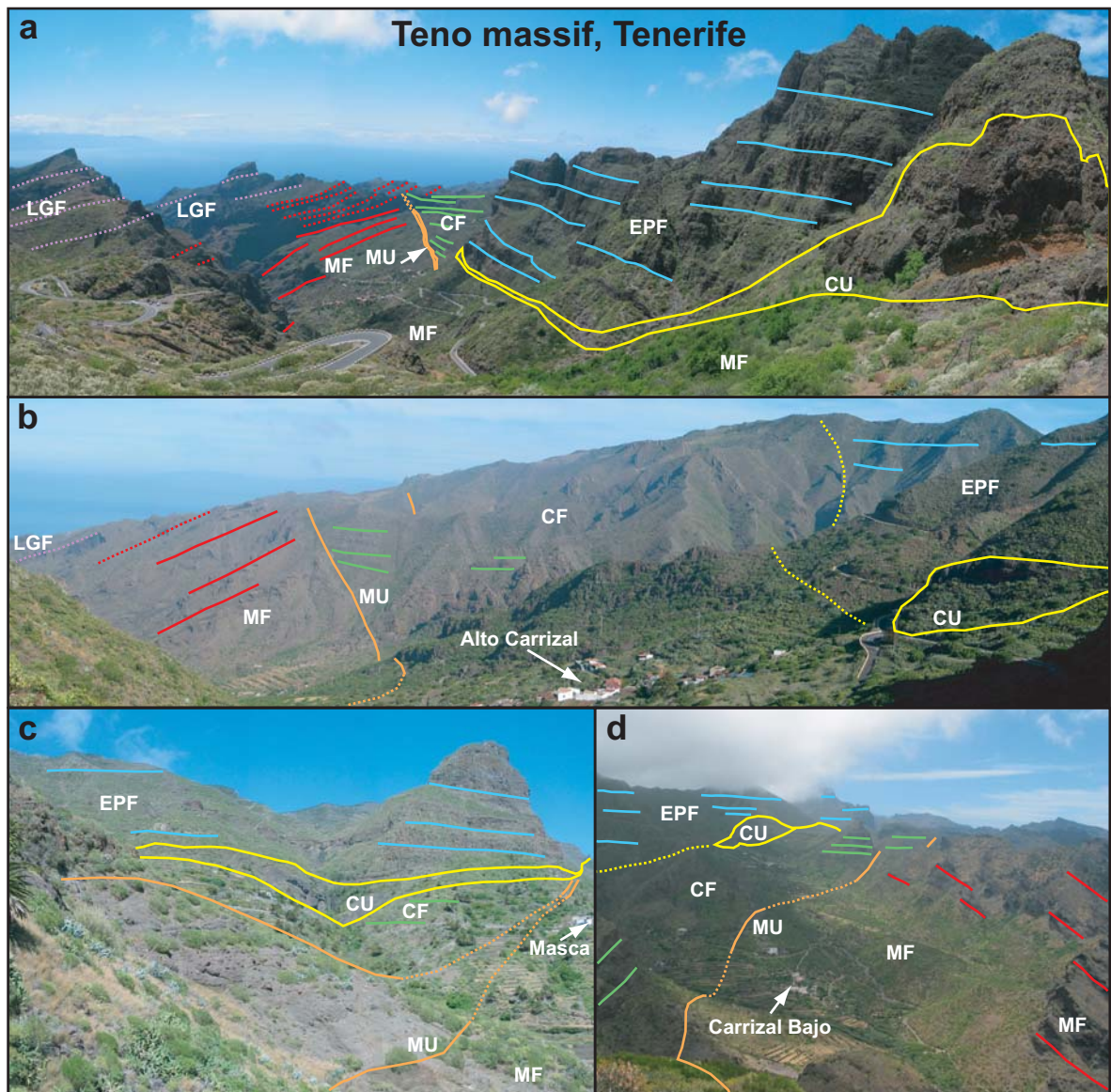


Figure 3.2 See full figure caption on page of Figure 3.3.





**Figure 3.3** The unconformity-bounded stratigraphic formations of the Teno massif: MF: Masca Formation (red); MU: Masca Unconformity (orange); CF: Carrizales Formation (green); CU: Carrizales Unconformity (yellow); EPF: El Palmar Formation (blue); and LGF: Los Gigantes Formation (purple). **a** Photo (looking west) taken from near Cherfe outcrop in eastern Teno, before the descent of TF-436 toward Santiago del Teide. The exact position of the transition between the Masca and Los Gigantes formations is uncertain. **b** Photo (looking northwest) taken from near El Roque (Figure 3.2). The Masca Unconformity is particularly well observed from this point. **c** Photo (looking east) taken from the barranco just west of Masca village. The angular unconformities converge just above the village. **d** Photo (looking east-southeast) taken near TN2 sample locality (Figure 3.2). The steeply dipping volcanics of the Masca Formation are clearly seen on the right hand side (south).

**Caption of Figure 3.1 a** The Canary Islands and the central position of Tenerife within the archipelago. **b** Map of Tenerife, showing the location of the Teno massif in the northwest of the island. **c** Geological map of the Teno massif, including data from *Walter and Schmincke* [2002], *Guillou et al.* [2004] and *Carracedo et al.* [2007]. Radiometric and palaeomagnetic study sites are plotted. Sample locations for this work (circles) and *Thirlwall et al.* [2000] (squares) are colour-coded according to the stratigraphic formation to which they are assigned. UTM coordinate grid is shown, tick marks are spaced by 5 km. The area framed by red corners is enlarged in Figure 3.2.

**Caption of Figure 3.2** Topographic map (50 m contours) of the area enclosing road TF-436 between the Cherfe outcrop and La Tabaiba. All symbols as in Figure 3.1. Sample names are indicated (see also Table 3.4), as well as key outcrop/stratigraphic profile localities discussed in the text. Strike and dip symbols represent measured attitudes of the unconformities. UTM coordinate grid is shown, tick marks are spaced by 500 m.



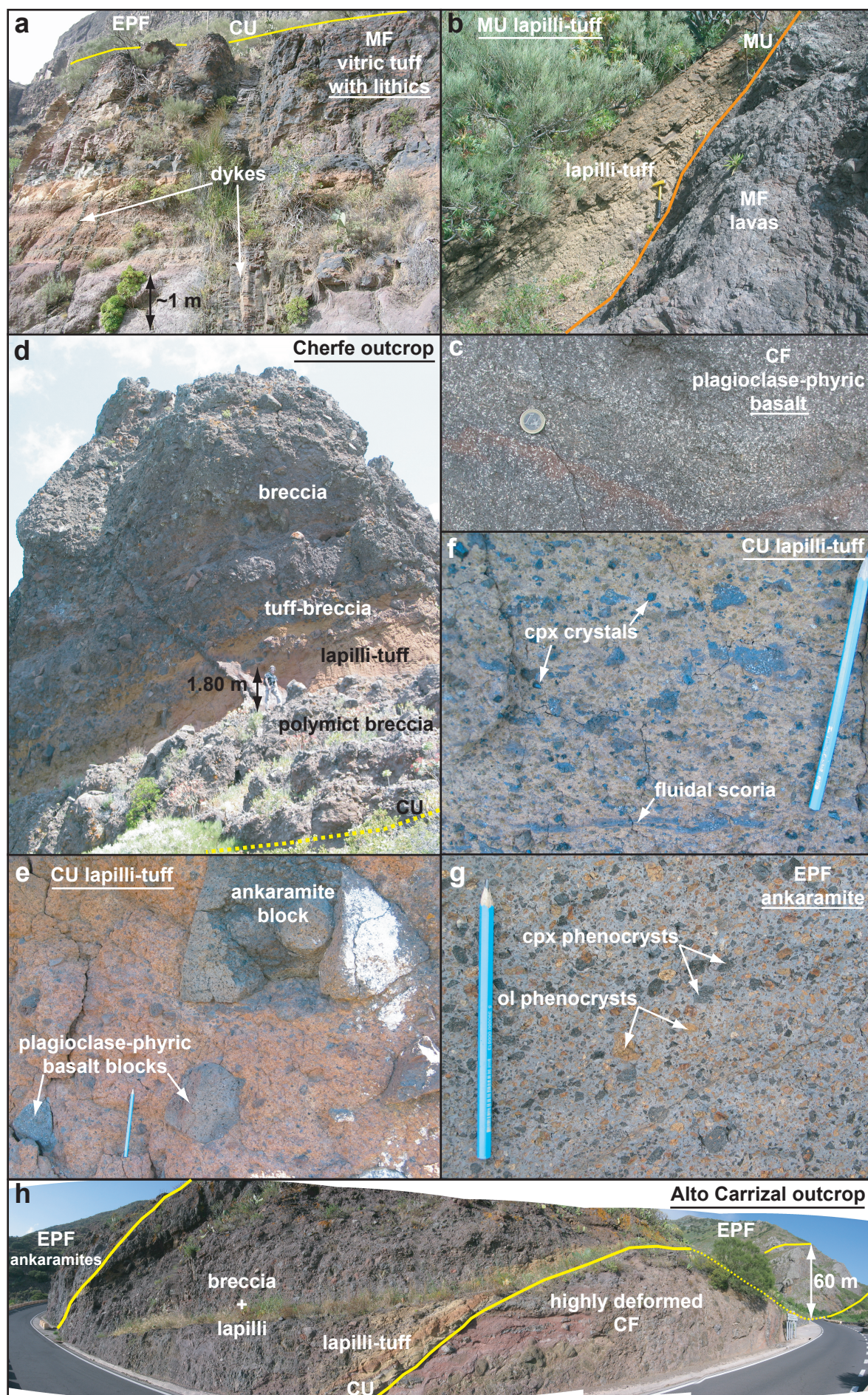


**Figure 3.4** See full figure caption on page of Figure 3.7.



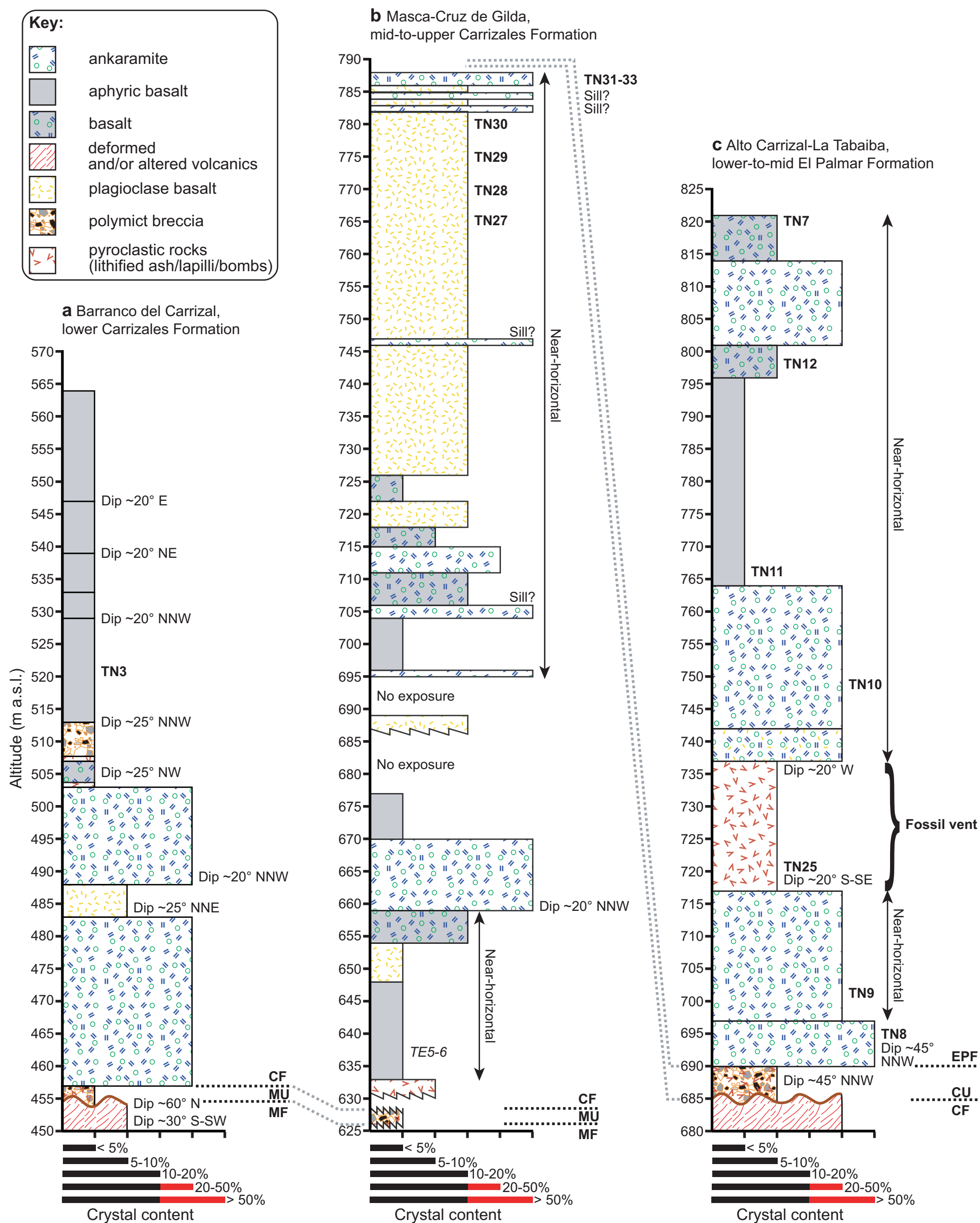


**Figure 3.5** Logs of key stratigraphic sequences at Teno, with the crystal content of volcanic rocks and altitude as the X- and Y-axis, respectively. Acronyms of formation names are the same as in Figures 3.1 and 3.3. Descriptions of stratigraphic sequence are provided in the text. Note that lavas at the base of the post-collapse sequences typically dip ~N, but that, overall, post-collapse formations consist of near-horizontal lavas. Sample localities for this work, as well as for TE5-6 of *Thirlwall et al.* [2000] [M. Thirlwall, personal communication 2007], are indicated. **a** Section on the western slopes of Barranco del Carrizal, lower Carrizales Formation. **b** Section starting just north of Masca village and ending near Cruz de Gilda, mid-to-upper Carrizales Formation. **c** Section from the Alto Carrizal outcrop following road TF-436 towards La Tabaiba, lower-to-mid El Palmar Formation.



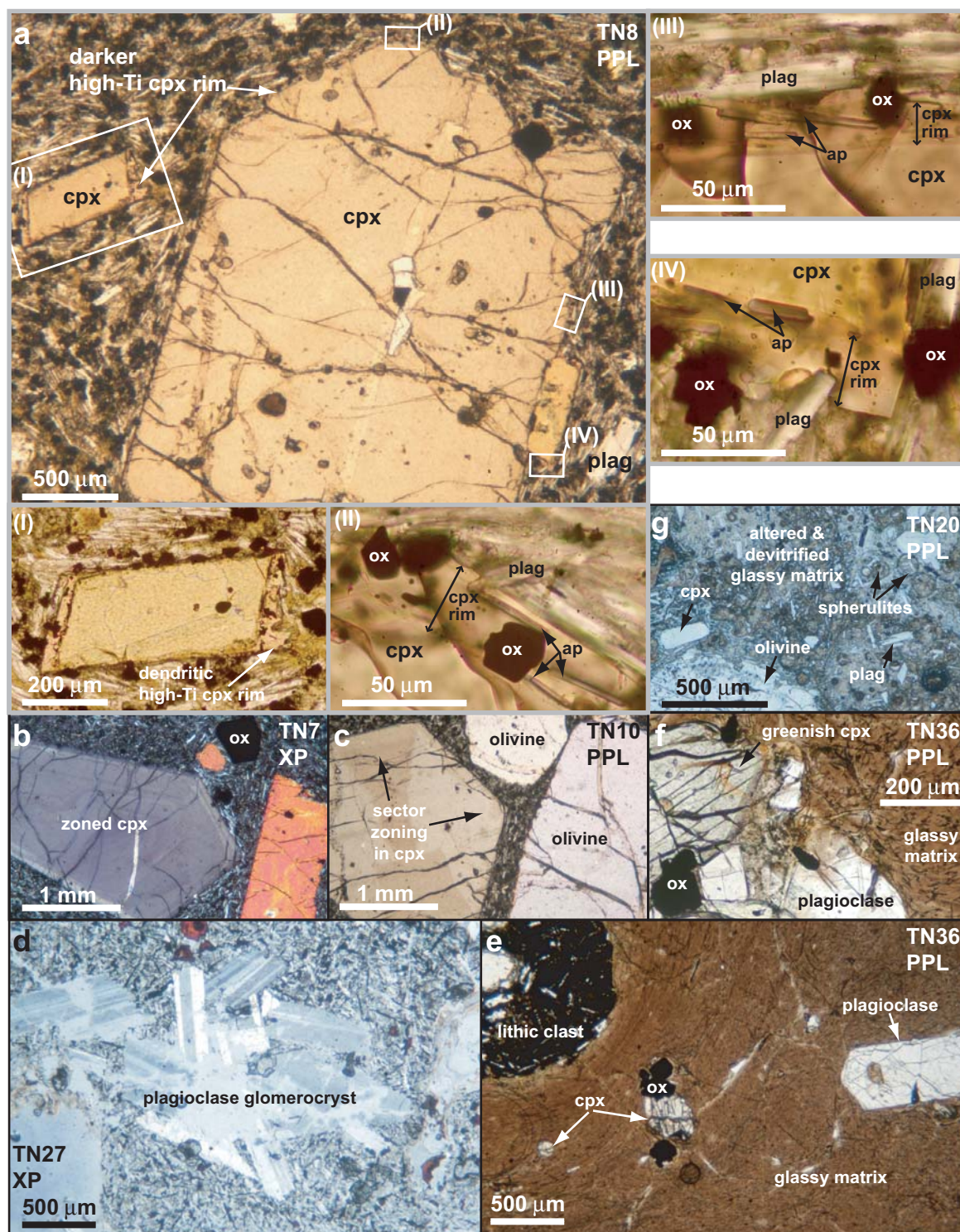


**Figure 3.6** Thin section photomicrographs of Teno samples. **a** Outer rims of clinopyroxenes show a darker colouration, commonly bear acicular apatite and Fe-Ti oxide inclusions and sometimes form dendritic protrusions. **b** Concentric zoning in clinopyroxene. **c** Olivine crystals and an example of sector zoning in clinopyroxene. **d** Plagioclase glomerocryst in upper Carrizales plagioclase basalts. **e** The glassy matrix of TN36. **f** Greenish clinopyroxene, plagioclase and Fe-Ti oxide phenocrysts in TN36. **g** An example of textures seen in the pyroclastic samples collected at the angular unconformities.

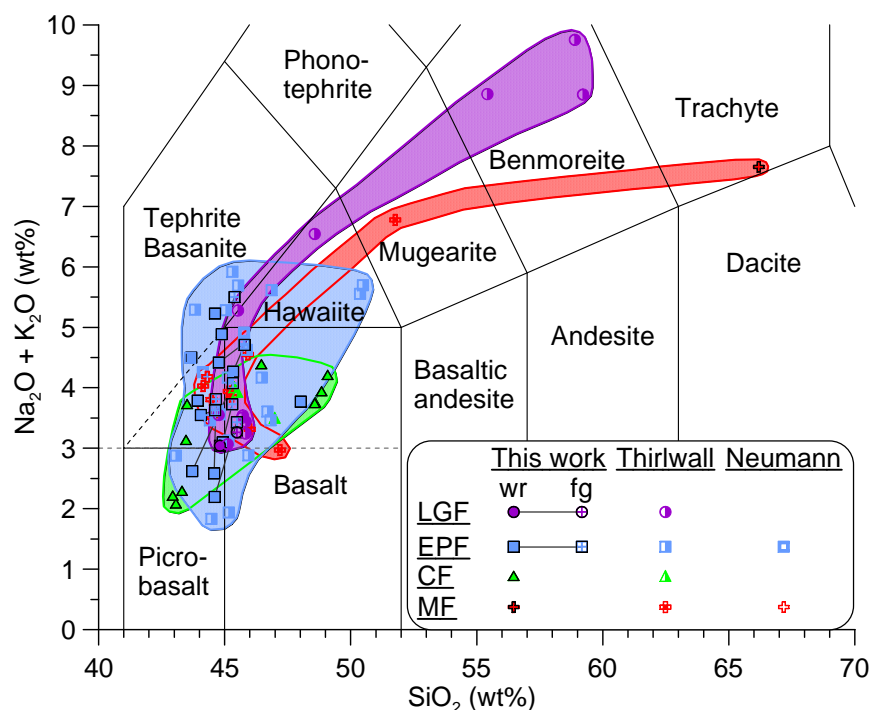


**Figure 3.7** Total-alkali-silica chemical classification of Teno rock samples. Data are from *Thirlwall et al.* [2000], *Neumann et al.* [1999] and this work. Colour-shaded fields group samples from individual stratigraphic formations (MF: red; CF: green; EPF: blue; and LGF: purple). In this and following plots, fused groundmass (fg) compositions are linked to their respective whole-rock (wr) chemistry using tie-lines. Alkali basalt and basanitic suites are divided by extrapolation of the Tephrite Basanite-Hawaiiite field boundary (oblique dash-line) [after *Thirlwall et al.*, 2000]. Rocks falling in the picrobasalt and basalt fields having <3 wt% alkalis (horizontal dash-line) and >12 wt% MgO are picrites (see Table 4) [*Le Bas*, 2000].

**Caption of Figure 3.4** **a** The thick, felsic pyroclastic deposits near the top of the Masca Formation. Sample location of TN36. **b** Juvenile pyroclastic deposit resting at the Masca Unconformity near El Roque. **c** Typical appearance of the plagioclase-phyric lavas of the upper Carrizales Formation. **d** The Cherfe outcrop showing steeply dipping polymict breccias mixed and interbedded with lapilli-tuffs, marking the Carrizales Unconformity in eastern Teno. **e** At Cherfe outcrop; large lava blocks incorporated in pyroclastic deposits. **f** Close up of Cherfe pyroclastics, showing clinopyroxene phenocrysts and fluidal scoria. **g** Representative example of lower El Palmar ankaramitic lavas. **h** The Alto Carrizal outcrop, showing a complex sequence of highly deformed Carrizales rocks overlain by pyroclastic rocks and breccias of the Carrizales Unconformity, in turn overlain by El Palmar ankaramites.

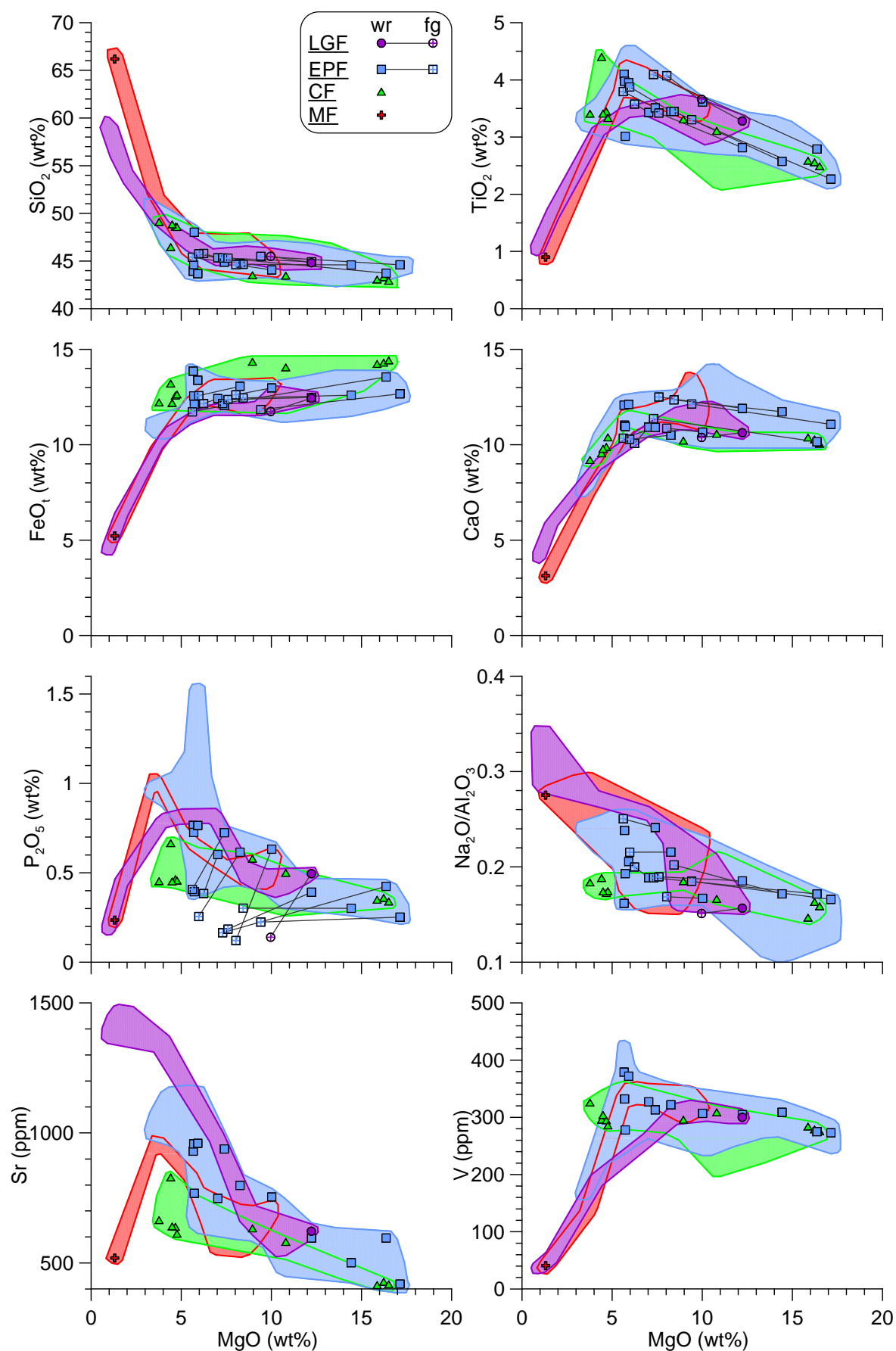


**Figure 3.8** Variation of selected major and trace elements as a function of MgO content. Fields are as in Figure 3.7 and include all published Teno data, but only our samples appear in this plot for legibility. See text for details.



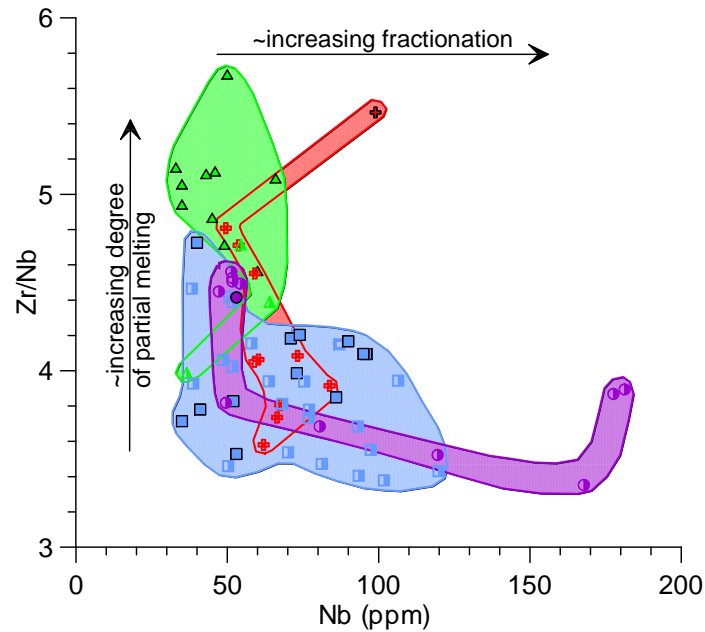


**Figure 3.9** Zr/Nb vs. Nb for Teno lavas, symbols as in Figure 3.7. The gross effects of fractional crystallisation and mantle partial melting are shown: fractionation generally increases the concentration of Nb in the melt with little effect on the Zr/Nb ratio; on the other hand, increasing degrees of melting translate into a marked increase in Zr/Nb with comparatively little effect on Nb. The highest degrees of crystal fractionation have been experienced by some Masca and Los Gigantes samples, whilst El Palmar lavas appear comparatively moderately to poorly fractionated. Carrizales lavas were seemingly the least affected by fractional crystallisation. In turn, it appears that Carrizales lavas were produced by the highest degrees of partial melting in the mantle.

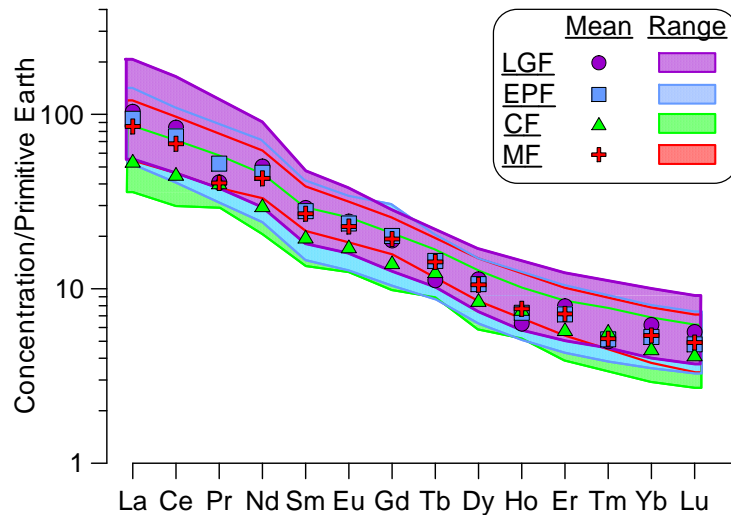


**Figure 3.10** Spider diagram showing normalised (to the Primitive Earth source of [McKenzie and O'Nions [1991]] abundances of rare earth elements (REE) in Teno lavas. Only high precision measurements determined by Isotope Dilution [Thirlwall *et al.*, 2000] and ICP mass spectrometry [Neumann *et al.*, 1999; this work] are included. Means and data ranges are presented for each of the stratigraphic formations (MF: 5 samples; CF: 4 samples; EPF: 10 samples; LGF: 4 samples). Whilst an overall temporal increase in REE concentrations can be discerned from the oldest Masca Formation, to the youngest El Palmar and Los Gigantes formations, Carrizales lavas (extruded after the first giant landslide) appear relatively depleted, especially in the light REE, possibly indicating higher mean melt fractions.

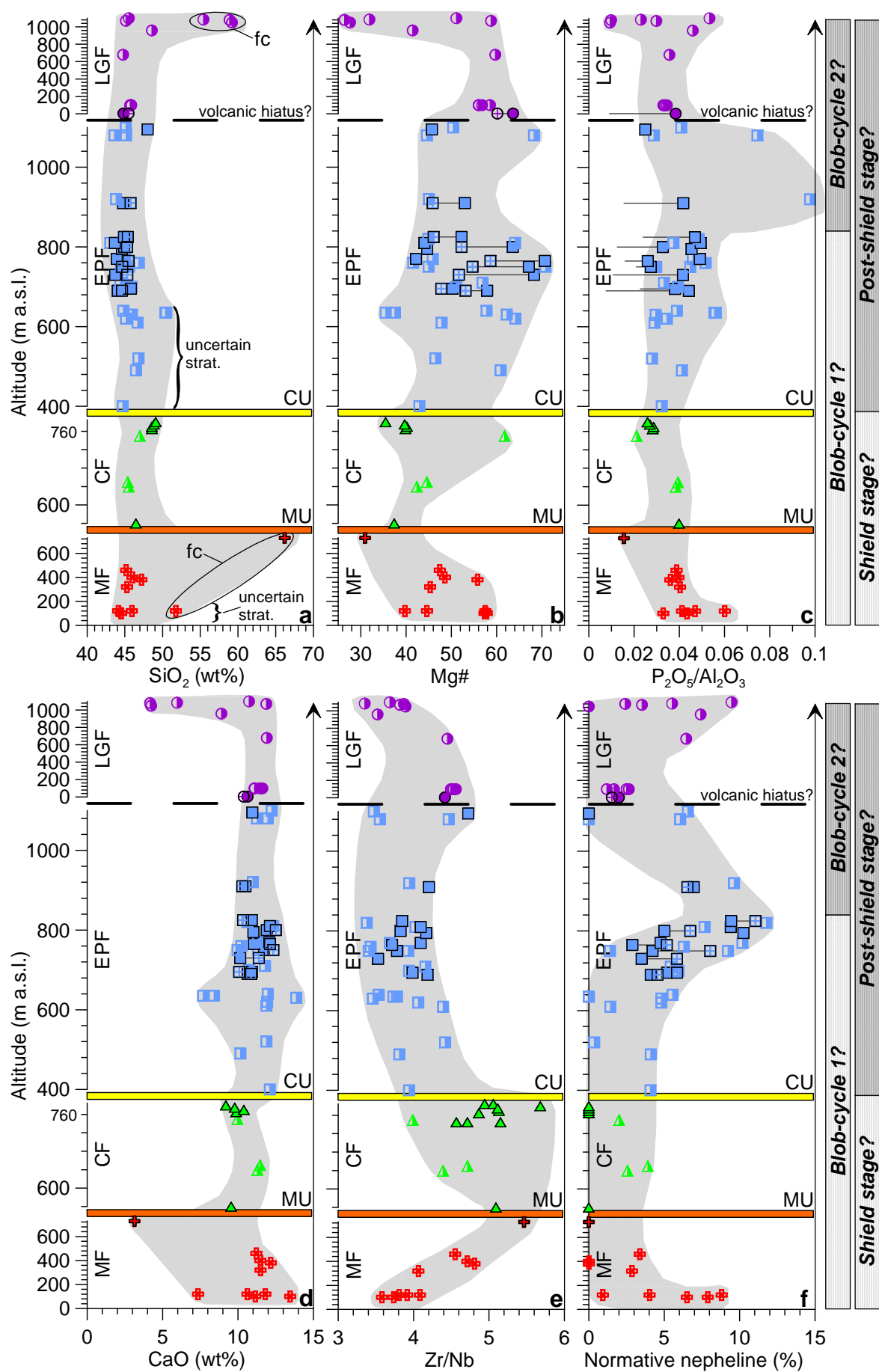


**Figure 3.11** See full figure caption on page of Figure 3.12.

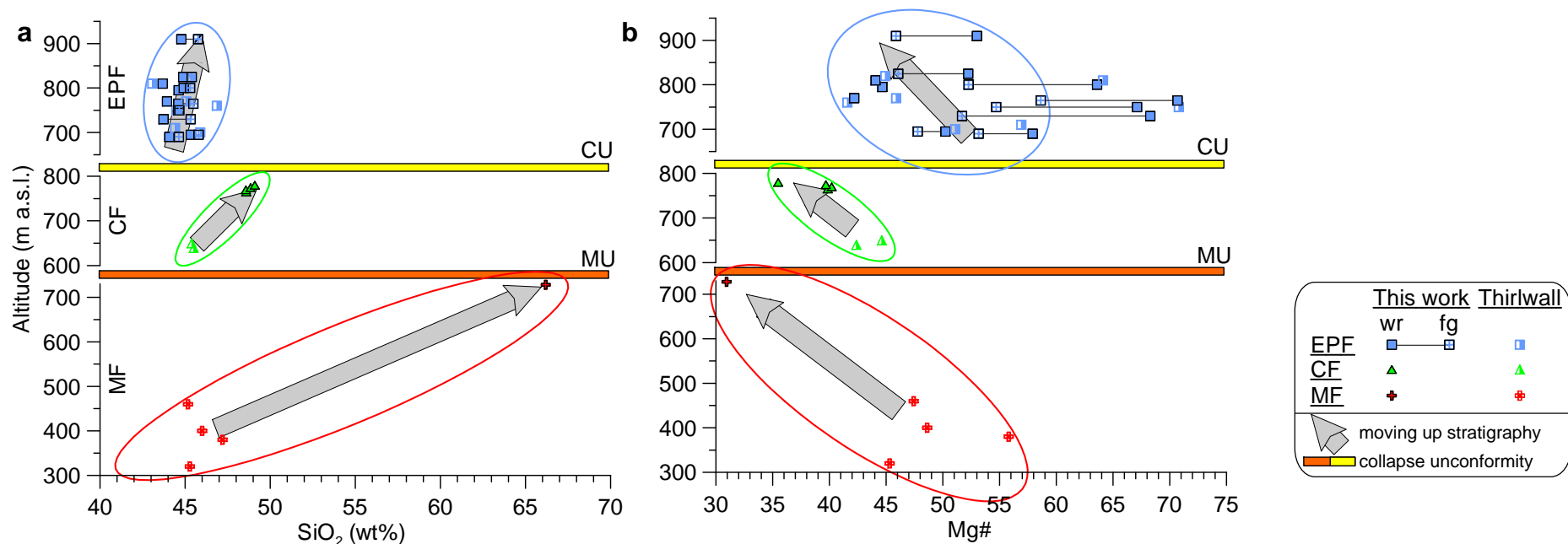


**Figure 3.12** Altitude vs. content of **a** SiO<sub>2</sub> and **b** Mg# along the stratigraphically well-constrained profile from Barranco de Masca to La Tabaiba. Stacked Y-axes (as in Figure 3.11) are used for each of the formations. The presence of the angular unconformities is also indicated, marking the timing of the Teno volcano's giant flank collapses. A pronounced decrease in SiO<sub>2</sub> coupled with an increase in Mg# is observed across each unconformity, suggesting that both the Masca and Carrizales collapses provoked a return to the eruptions of more mafic (i.e. less differentiated) magma types.

**Caption of Figure 3.11** Stratigraphic level (indicated by altitude) vs. proxy geochemical parameters; **a** SiO<sub>2</sub>, **b** P<sub>2</sub>O<sub>5</sub>/Al<sub>2</sub>O<sub>3</sub>, **c** normative nepheline and **d** Zr/Nb. Symbols are as in Figure 3.7. Each formation has its own Y-axis, the length of which is scaled to the number of samples available for a particular formation. Major (200 m) and minor (40 m) tick marks have constant values in all Y-axes. The stratigraphic boundaries (Masca and Carrizales unconformities) are shown, as well as the possible occurrence of a volcanic hiatus between the extrusion of the El Palmar and Los Gigantes formations. The effect of extensive fractional crystallisation (fc) is indicated. Artificially P<sub>2</sub>O<sub>5</sub>-poor fused groundmass samples were omitted in **b**. Trends shown as shaded bands are further explained in the text. The extent of possible blob-induced magmatic cycles or, alternatively, the shield and post-shield stages of evolution is indicated by bars in the central part of the diagram.

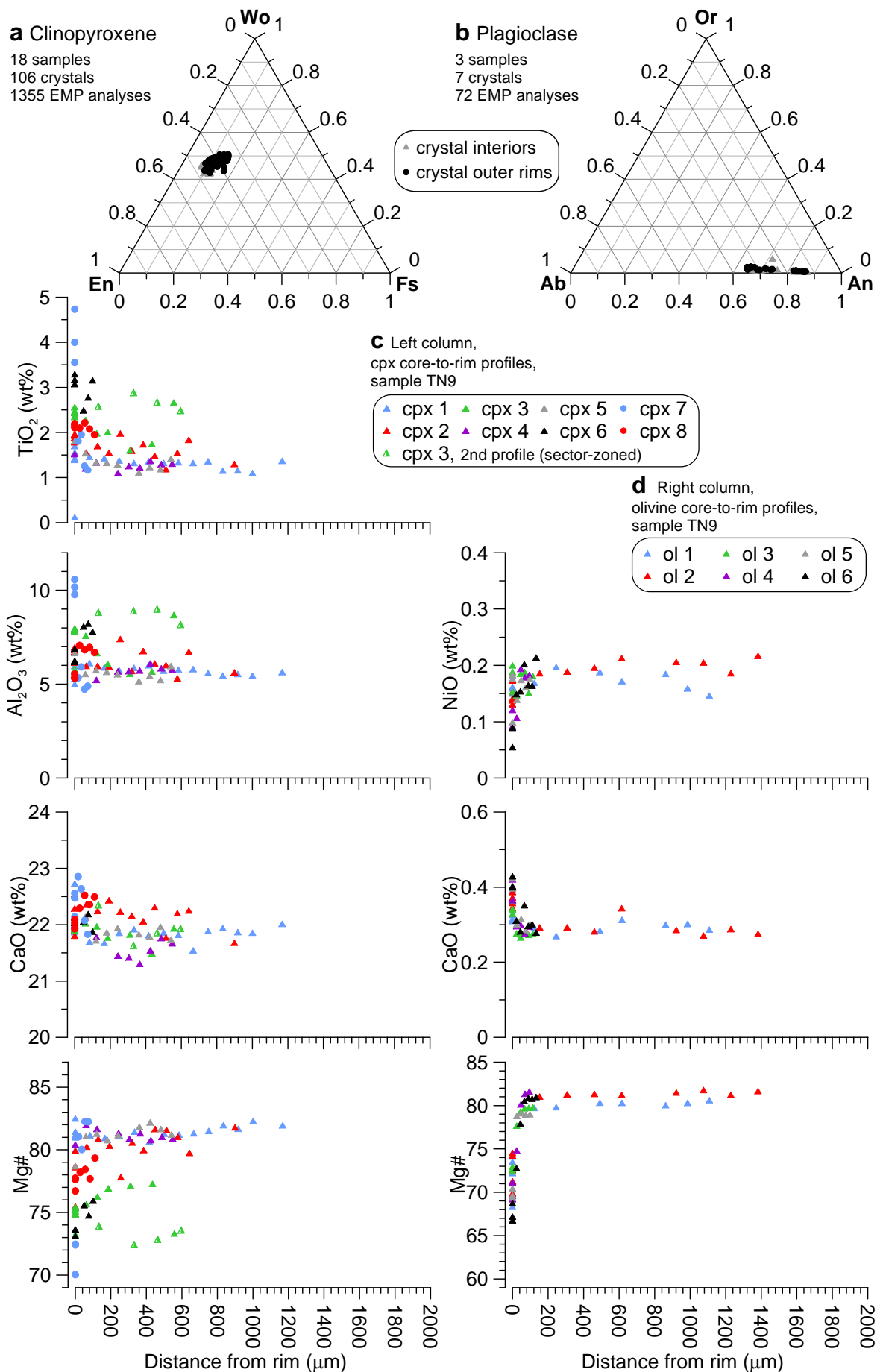


**Figure 3.13** Mineral chemistry of Teno samples. **a** Ternary diagram of cpx composition. **b** Ternary diagram of plagioclase composition. **c** Core-to-rim chemical profiles of cpx from representative sample TN9. **d** As **c**, but for olivine crystals. See text for details.

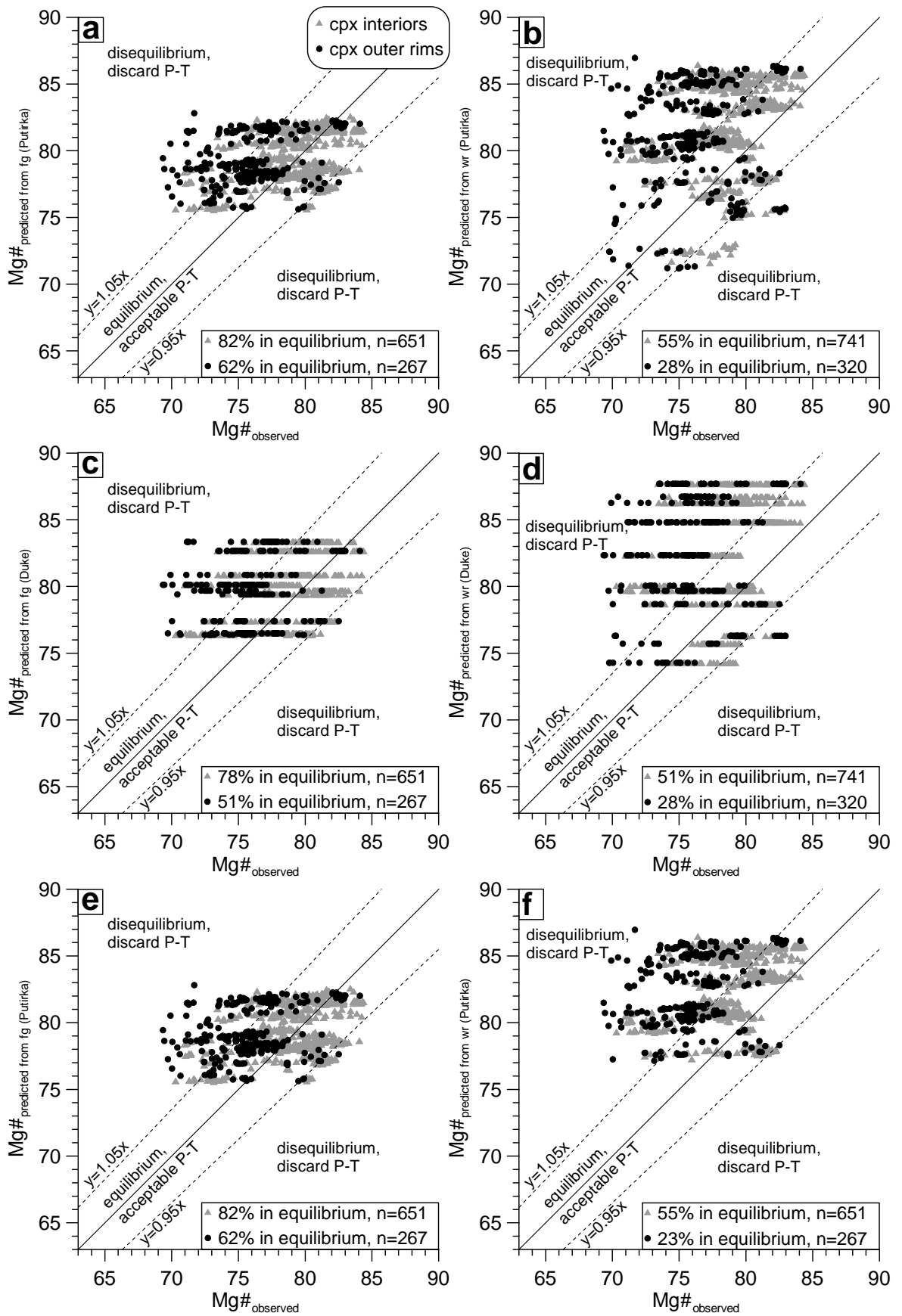


**Figure 3.14** Equilibrium tests for cpx-melt pairs from Teno samples. **a** Using Putirka [1999]'s formulation, for all samples for which a fused groundmass (fg) composition was obtained. **b** Putirka [1999], for all samples for which a whole-rock (wr) composition was obtained. **c** Using Duke [1976]'s formulation, all samples for which a fg composition was obtained. **d** Duke [1976], all samples for which a wr composition was obtained. **e** Putirka [1999], fg composition of ankaramites for which both fg and wr compositions were obtained. **f** Putirka [1999], wr composition of ankaramites for which both fg and wr compositions were obtained.



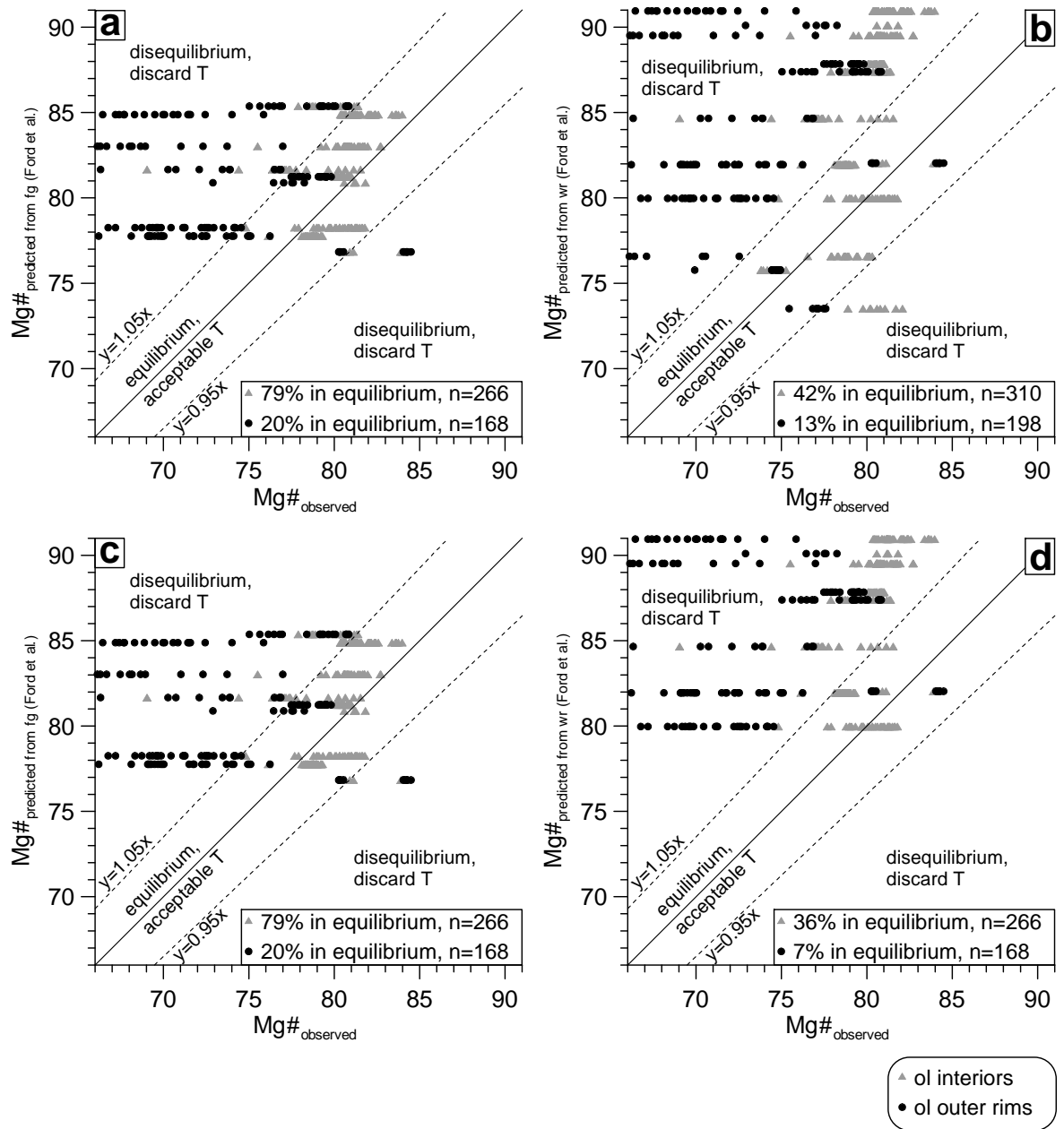


**Figure 3.15** Equilibrium tests, using *Ford et al.* [1983]'s formulations, for olivine-melt pairs from Teno samples. **a** For all samples for which a fused groundmass (fg) composition was obtained. **b** For all samples for which a whole-rock (wr) composition was obtained. **c** Using the fg composition of ankaramites for which both fg and wr compositions were obtained. **d** Using the wr composition of ankaramites for which both fg and wr compositions were obtained.

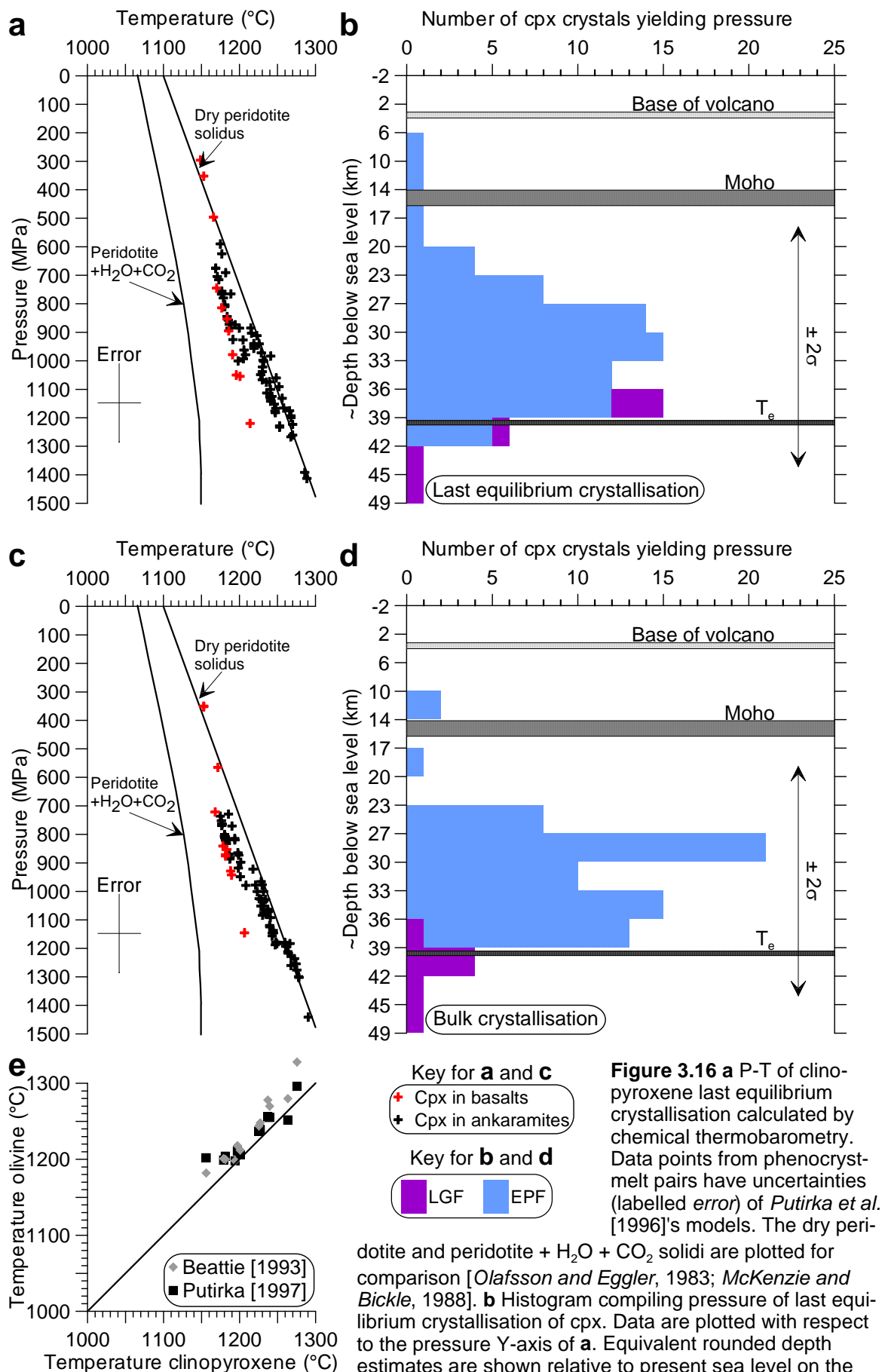


**Figure 3.16** a P-T of clinopyroxene last equilibrium crystallisation calculated by chemical thermobarometry. Data points from phenocryst-melt pairs have uncertainties (labelled error) of Putirka *et al.* [1996]'s models. The dry peridotite and peridotite + H<sub>2</sub>O + CO<sub>2</sub> solidi are plotted for comparison [Olafsson and Eggler, 1983; McKenzie and Bickle, 1988]. **b** Histogram compiling pressure of last equilibrium crystallisation of cpx. Data are plotted with respect to the pressure Y-axis of **a**. Equivalent rounded depth estimates are shown relative to present sea level on the Y-axis. Bars of different colours, indicating stratigraphic divisions, are stacked, e.g. read that 12 crystals of the EPF and 3 crystals of the LGF yielded last equilibrium crystallisation pressure between 1100 and 1200 MPa (between ~36 km and 39 km b.s.l.). **c** As in **a**, for bulk crystallisation. **d** As in **b**, for bulk crystallisation. **e** T of olivine crystallisation (sample mean) vs. that of cpx.

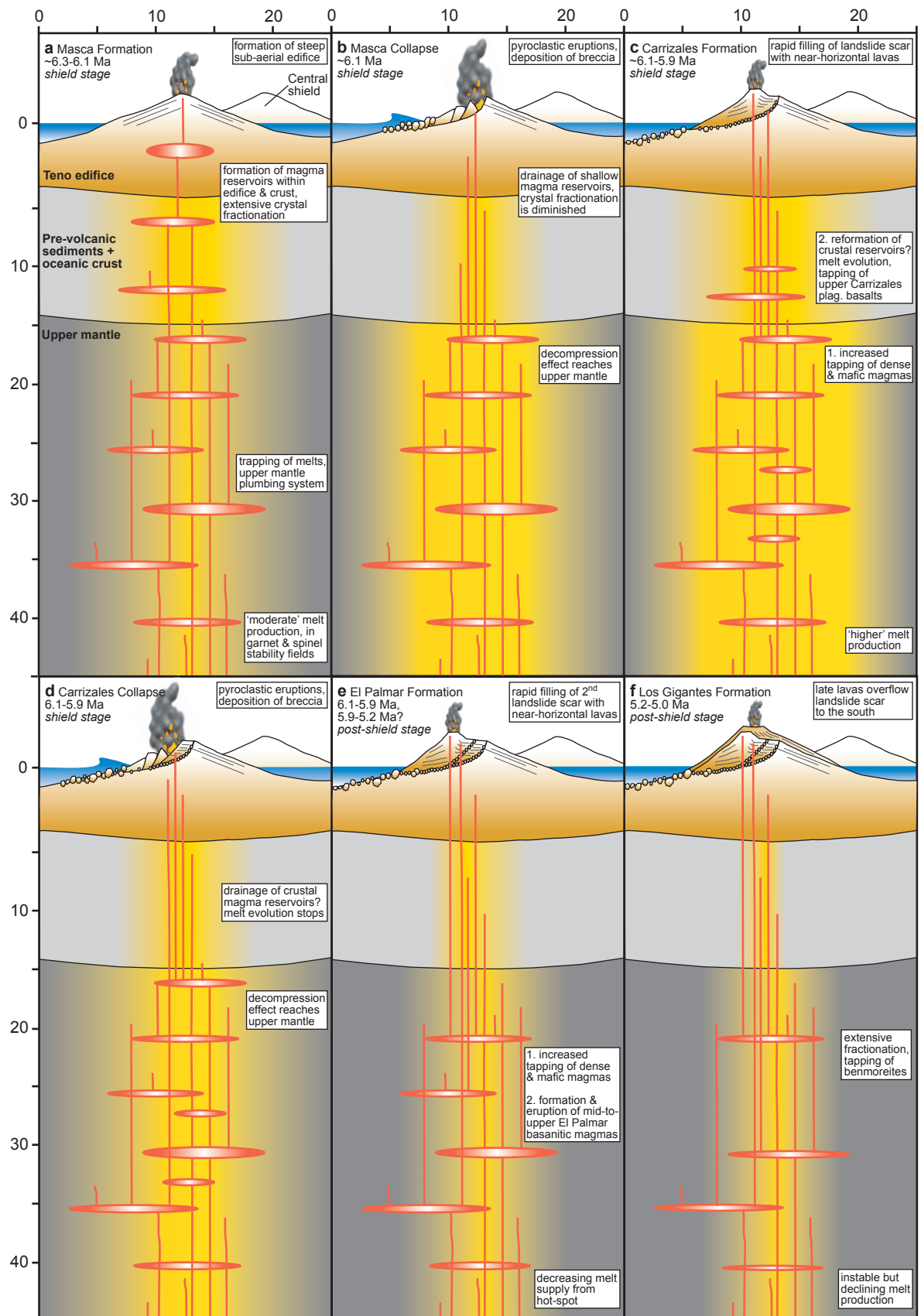


**Figure 3.17** Conceptual model of the evolution of the Teno volcano. Depth and horizontal distance values are in kilometres. The height of the volcanic edifice is exaggerated. Magma storage depth range is caricatured from thermobarometric data [see also Longpré *et al.*, 2008b]. See main text for model descriptions.

**Table 3.1** Revised stratigraphy of the Teno massif. K-Ar, Ar-Ar and magnetostratigraphy sites of <sup>a</sup>*Abdel-Monem et al.* [1972], <sup>b</sup>*Ancochea et al.* [1990], <sup>c</sup>*Thirlwall et al.* [2000], <sup>d</sup>*Guillou et al.* [2004], and <sup>e</sup>*Leonhardt and Soffel* [2006] were plotted on Google Earth, allowing their correct correlation with the corresponding stratigraphic formations.

Formation	Type locality	K-Ar and Ar-Ar ages (Ma)	Polarity readings	Inferred polarity chron	Corresponding age (Ma)
Los Gigantes	Los Gigantes cliffs upper northwest Teno	4.5 <sup>b</sup> , 5.2 <sup>d</sup> , 5.3 <sup>b</sup> , 5.3 <sup>d</sup> , 5.5 <sup>d</sup>	N <sup>d</sup> , N <sup>d</sup> , N <sup>d</sup> R <sup>e</sup>	C3n.4n C3n.4r ?	4.980-5.230 5.230-5.894 ?
El Palmar	Upper Cumbre Bolicos	5.0 <sup>b</sup> , 5.5 <sup>d</sup> , 6.1 <sup>d</sup>	I <sup>d</sup> , R <sup>d</sup>	C3n.4r	5.230-5.894
	Mid between Alto Carrizal and La Tabaiba	5.5 <sup>a</sup> , 5.6 <sup>b</sup> , 5.7 <sup>d</sup> , 5.9 <sup>d</sup> , 6.1 <sup>c</sup>	N <sup>a</sup> , N <sup>d</sup> , N <sup>d</sup> , I <sup>e</sup> , 13 × N <sup>e</sup>	C3An.1n	5.894-6.137
	Lower				
Carrizales	Upper from Masca village to Cruz de Gilda		N <sup>e</sup> , N <sup>e</sup>	beginning of C3An.1n	5.894-6.137
	Mid Barranco del Carrizal log and ~200 m north of Masca	6.0 <sup>c</sup> , 6.0 <sup>d</sup>	R <sup>d</sup> , N <sup>e</sup>	end of C3An.1r /beginning of C3An.1n	6.137-6.269
	Lower				
Masca	Upper locality for sample TN36 and on road near Cherfe outcrop		N <sup>e</sup>	beginning of C3An.1n	5.894-6.137
	Mid Barranco de Masca	6.4 <sup>c</sup>	5 × R <sup>e</sup>	C3An.1r	6.137-6.269
	Lower lower northwest Teno, Barranco del Carrizal	6.3 <sup>a</sup> , 6.7 <sup>a</sup> , 6.7 <sup>b</sup>	N <sup>a</sup> , N <sup>a</sup> , N <sup>e</sup> , I <sup>e</sup>	end of C3An.2n	6.269-6.567

**Table 3.2** Classification of samples used in the geochemical analysis of this chapter. Sample names in normal, italic and bold type fonts refer to samples from *Thirlwall et al.* [2000], *Neumann et al.* [1999] and this work, respectively. UTM coordinates of our samples are given. Geographic areas are also indicated for samples of *Thirlwall et al.* [2000]: LM = Lower Masca, MM = Middle Masca, UM = Upper Masca and Teno Alto, NW = NW Teno, E = Erjos, NE = NE Teno, A = Arguayo and LG = Los Gigantes. Field names, extrapolated from modal mineralogy in the case of samples of *Thirlwall et al.* [2000], and chemical names based on a modified version of the total-alkali-silica diagram (Figure 3.7) of the IUGS are compared [cf. *Thirlwall et al.*, 2000]. Alkali basalts and basalts were distinguished based on the presence of nepheline in the CIPW norm. Modal mineralogy is given for the sample sets of this study and that of *Thirlwall et al.* [2000].

Formation	Sample	Locality (Thirlwall et al.)	UTM coordinates		Altitude (m a.s.l.)	Rock types		Mineral modes (%)				
			Easting	Northing		Field name	Chemical name	OI	Cpx	Plag	Fe-Ti oxide	Amph.
Los Gigantes	TE45	A	—	—	1100	basalt	basanite	7	13	0.5	0.5	0.1
	TE44	A	—	—	1085	aphyric basalt	benmoreite	—	0.2	3	0.3	0.1
	TE42	A	—	—	1080	aphyric basalt	benmoreite	—	—	1	0.3	0.4
	TE43	A	—	—	1070	ankaramite	alkali basalt	20	20	—	0.2	0.1
	TE46	A	—	—	1050	trachyte	benmoreite	—	0.3	40	1	0.2
	TE41	A	—	—	960	basalt	hawaiite	—	6	—	2	7
	TE15	A	—	—	680	ankaramite	alkali basalt	15	25	—	0.5	—
	TE37	LG	—	—	100	aphyric basalt	alkali basalt	4	0.1	—	—	—
	TE38	LG	—	—	100	basalt	alkali basalt	5	5	—	—	—
	TE39	LG	—	—	100	basalt	alkali basalt	4	6	—	—	—
	TE40	LG	—	—	100	basalt	alkali basalt	5	2	—	—	—
El Palmar	<b>TN16</b>		319620	3126370	4	ankaramite	alkali basalt	15	21	3	1	—
	TE24	E	—	—	1100	aphyric basalt	alkali basalt	0.5	1	—	—	—
	<b>TN19</b>		321180	3131970	1095	trachyte	basalt	7	3	20	—	—
	TE25	E	—	—	1080	ankaramite	picrite	40	30	—	—	—
	TE64	UM	—	—	1080	aphyric basalt	basanite	—	—	—	—	—
	TE63	UM	—	—	920	basalt	basanite	—	4	—	1.5	4
	<b>TN1</b>		317460	3135620	910	ankaramite	alkali basalt	10	18	—	2	—
	<i>TF93</i>	?	—	—	?	?	alkali basalt	—	—	—	—	—
	<i>TF94</i>	?	—	—	?	?	alkali basalt	—	—	—	—	—
	<b>TN7</b>		318070	3134840	825	ankaramite	alkali basalt	10	13	—	2	—
	TE12	UM	—	—	820	aphyric basalt	basanite	0.5	2	—	1	—
	<b>TN6</b>		318360	3134580	810	aphyric basalt	basanite	0.5	0.5	—	<0.5	—
	TE13	UM	—	—	810	ankaramite	picrite	30	30	—	3	—
	<b>TN13</b>		318390	3133930	800	ankaramite	alkali basalt	20	20	—	—	—
	<b>TN12</b>		318020	3134750	795	aphyric basalt	basanite	2	2.9	—	0.1	—
	<b>TN11</b>		317960	3134580	770	aphyric basalt	alkali basalt	0.2	0.2	—	0.1	—
	TE11	UM	—	—	770	basalt	basanite	3	3	—	0.5	—
	<b>TN5</b>		318970	3134250	765	ankaramite	picrite	30	25	—	—	—
	TE10	UM	—	—	760	aphyric basalt	hawaiite	0.2	0.2	—	—	—
	<b>TN10</b>		317960	3134450	750	ankaramite	picrite	23	30	—	2	—
	TE62	UM	—	—	750	aphyric basalt	basanite	—	—	—	0.1	—
	TE9	MM	—	—	750	ankaramite	picrite	35	35	—	—	—
	<b>TN15</b>		319720	3132630	730	ankaramite	picrite	27	27	—	1	—
	TE8	MM	—	—	710	ankaramite	alkali basalt	10	50	10	5	—
	TE7	MM	—	—	700	ankaramite	alkali basalt	5	25	5	3	—
	<b>TN9</b>		318060	3134160	695	ankaramite	alkali basalt	28	25	—	2	—
	<b>TN8</b>		318090	3134110	690	ankaramite	alkali basalt	6	16	4	4	—
	TE34	NE	—	—	640	ankaramite	alkali basalt	12	25	0.5	1	—
	TE33	NE	—	—	635	aphyric basalt	hawaiite	—	—	2	0.5	—
	TE35	NE	—	—	635	aphyric basalt	hawaiite	0	0.1	4	0.5	—
	TE32	NE	—	—	630	ankaramite	alkali basalt	20	30	—	4	—
	TE36	NE	—	—	620	ankaramite	alkali basalt	35	25	—	—	—
	TE31	NE	—	—	610	aphyric basalt	alkali basalt	1	1	—	—	—
	TE27	NE	—	—	520	aphyric basalt	alkali basalt	2	1	—	—	—
	TE26	NE	—	—	490	ankaramite	alkali basalt	20	20	25	5	—
	TE30	NE	—	—	400	aphyric basalt	alkali basalt	—	—	—	—	—
Carrizales	<b>TN32</b>		318990	3133270	785	ankaramite	picrite	23	18	4	<1	—
	<b>TN31</b>		318990	3133270	785	ankaramite	picrite	24	21	5	<1	—
	<b>TN30</b>		318920	3133450	780	trachyte	basalt	<1	5	15	—	—
	<b>TN29</b>		318920	3133450	775	trachyte	basalt	<1	4	16	—	—
	<b>TN28</b>		318920	3133450	770	trachyte	basalt	<1	2	23	—	—
	<b>TN27</b>		318920	3133450	765	trachyte	basalt	1	2	32	—	—
	TE61	UM	—	—	750	basalt	alkali basalt	10	0.5	—	—	—
	<b>TN33</b>		318370	3133620	745	ankaramite	alkali basalt	12	18	5	—	—
	<b>TN34</b>		318370	3133620	745	ankaramite	picrite	20	20	5	<1	—
	<b>TN35</b>		318370	3133620	745	ankaramite	alkali basalt	15	20	5	—	—
	TE6	LM	—	—	650	basalt	alkali basalt	3	3	—	—	—
	TE5	LM	—	—	640	aphyric basalt	alkali basalt	0	0.5	3	—	—
Masca	<b>TN3</b>		316700	3134580	560	aphyric basalt	basalt	0.3	<0.5	1.5	0.2	—
	<b>TN36</b>		320080	3132280	730	vitric tuff	trachyte	—	2	5	<0.1	—
	TE4	LM	—	—	460	trachyte	alkali basalt	4	0.5	25	—	—
	TE3	LM	—	—	400	trachyte	basalt	3	4	10	—	—
	TE2	LM	—	—	380	ankaramite	basalt	25	25	—	—	—
	TE1	LM	—	—	320	aphyric basalt	alkali basalt	—	—	—	—	—
	TE52	NW	—	—	120	aphyric basalt	alkali basalt	0.2	0.4	3	0.5	—
	TE53	NW	—	—	120	trachyte	mugearite	0.5	—	8	0.5	—
	TE54	NW	—	—	120	basalt	alkali basalt	8	0.2	—	—	—
	TE51	NW	—	—	100	basalt	alkali basalt	4	10	—	—	—
	TE23	NW	—	—	100	basalt	alkali basalt	7	3	—	0.5	—
	<i>TF88</i>	NW	—	—	?	?	alkali basalt	—	—	—	—	—

**Table 3.3** Summary of petrographic observations for Teno samples. All figures are modal estimates in vol. %.

Sample:		TN1	TN2	TN3	TN4	TN5	TN6	TN7	TN8	TN9	TN10	TN11	TN12	TN13	TN14	TN15	TN16	TN19	TN20	TN21	TN22	TN23	TN24	TN25	TN26	TN27	TN28	TN29	TN30	TN31	TN32	TN33	TN34	TN35	TN36
Phenocrysts	Olivine mode euhedral subhedral anhedral zoned iddingsitised	10		0	10	30	1	9	6	28	23	0	2	20	1	27	15	7	3		1	2	9		5	1	<1	<1	<1	24	23	12	20	15	
	Cpx mode euhedral subhedral anhedral concentrically zoned sectorially zoned unzoned	18	1	<0.5	10	25	1	14	16	25	30	0	3	20	6	27	21	3	2		7	10	20	2	8	2	2	4	5	21	18	18	20	20	2
	Plag mode euhedral subhedral anhedral acicular		1	2	10				4								3	20								32	23	16	15	5	4	5	5	5	5
	Fe-Ti oxide mode euhedral subhedral anhedral	2		0		<0.5	2	4	2	2	0	0				1	1		<1				1		<1					<1	<1		<1		<0.1
Groundmass	Olivine	4		<1		<1	1		<1				<1			16	18			<1					<1	5	25	29			16	18	20	17	20
	Cpx	11		5		16	30	13	14	15	16	15	21		20	24	28	10	5			3	5	3	18	25	26	5	7	20	23	30	30	25	
	Plag	32	15	49		20	50	30	32	15	18	20	38	27	9	20	24	21	<1						2	15	18	5		14	14	15	8	15	
	Fe-Ti oxide	25	3	25		9	18	23	19	15	11	30	24	12		9	18	21	<1						2	<1	<1			<1	<1	<1	<1	<1	
	Apatite	<1	<1		<1	<1	<1	<1	<1	<1	<1	<1	<1	<1	<1	<1			<1			<1		2	<1	<1			<1	<1	<1	<1	<1		
	Cryptocrystalline material/devitrified glass		5	19					10	5		50	18		?		21	58	10	35	39	55	40	55	30	25	2	70	73						
	Glass	35																		15	45	28	30		40		5								78
Ash/lapilli/oxidised/hydrated					33										84									40											
Lithic clasts			40		37														12	5	25		5												15
Total phenocrysts		30	2	2	30	55	1	25	30	55	55	1	5	40	7	55	40	30	5	0	8	12	30	2	13	35	25	20	20	50	45	35	45	40	7
Total groundmass		70	58	98	33	45	99	76	70	45	45	100	95	60	93	45	60	70	83	95	67	88	65	98	87	65	75	80	80	50	55	65	55	60	78
Textures and notes	High birefringence at olivine rims																																		
	Dark overgrowth rim on cpx																																		
	Apatite in cpx rims	a/e				a	a/e	a/e	a	a/e	a/e		a	e/a		e/a	e/a	a/e	a											e/a	e/a	e	e	e/a	
	Fe-Ti oxide in cpx rims																																		
	Aligned groundmass plagioclase	yes	yes			no	yes	yes	yes	no	no	yes	yes	no		no	no	no	no	yes				yes						no	no	no	no	no	no
Glomerocrysts																																			
Vesicles																																			

Key:  abundant, for mode >50%  
 common, for mode >20%, <50%  
 some, for mode >5%, <20%  
 rare, for mode <5%  
 blank: not observed  
a=acicular apatite crystals  
e=equant apatite crystals  
s=glomerocrysts formed of crystals smaller than modal phenocryst sizes

**Table 3.4** Major and trace element composition of whole-rock (wr, determined by XRF) and fused groundmass (fg, determined by EMP) samples. Major and trace elements are given in weight percent and ppm values, respectively. Fused groundmass compositions represent the average, with standard deviation ( $\sigma$ ), of 10 microprobe analyses on different points of the glass shards. Total includes major elements, with all Fe as FeO. Loss on ignition (LOI) values are also listed.

Sample	TN1			TN3	TN5			TN6	TN7			TN8			TN9			TN10			TN11
	wr	fg	$\sigma$		wr	fg	$\sigma$		wr	fg	$\sigma$	wr	fg	$\sigma$	wr	fg	$\sigma$	wr	fg	$\sigma$	
SiO <sub>2</sub>	44.38	45.50	0.57	45.38	44.30	45.63	0.38	42.23	43.98	44.98	1.05	43.18	44.18	0.57	44.40	45.54	0.63	44.32	44.64	0.68	42.44
TiO <sub>2</sub>	3.42	3.85	0.19	4.30	2.25	3.32	0.13	3.82	3.44	3.76	0.17	3.54	4.03	0.16	3.36	3.56	0.23	2.56	3.45	0.11	3.96
Al <sub>2</sub> O <sub>3</sub>	14.61	16.26	0.29	16.31	9.59	14.03	0.12	14.98	15.14	16.87	0.36	14.02	15.68	0.20	15.48	16.80	0.22	10.95	14.36	0.19	15.09
FeO <sub>t</sub>	12.95	12.50	0.28	12.90	12.58	11.88	0.21	12.94	11.81	11.62	0.16	12.72	12.49	0.30	12.17	12.09	0.17	12.53	12.45	0.41	13.39
MnO	0.18	0.18	0.02	0.19	0.17	0.18	0.03	0.18	0.17	0.19	0.03	0.17	0.19	0.06	0.17	0.21	0.05	0.17	0.18	0.04	0.18
MgO	8.19	5.94	0.11	4.32	17.02	9.45	0.11	5.72	7.25	5.57	0.10	9.82	7.95	0.08	6.89	6.21	0.09	14.34	8.44	0.13	5.48
CaO	10.41	10.23	0.09	9.33	10.99	12.17	0.11	11.72	10.69	10.25	0.13	10.44	10.76	0.10	10.70	10.02	0.09	11.66	12.35	0.12	11.67
Na <sub>2</sub> O	3.15	3.50	0.19	3.07	1.59	2.59	0.11	3.08	3.65	4.23	0.16	2.34	2.64	0.08	2.92	3.36	0.04	1.88	2.90	0.05	2.44
K <sub>2</sub> O	1.23	1.20	0.10	1.22	0.59	0.85	0.04	1.27	1.14	1.22	0.10	1.14	0.95	0.06	1.26	1.33	0.03	0.69	0.91	0.05	1.22
P <sub>2</sub> O <sub>5</sub>	0.61	0.25	0.14	0.65	0.25	0.22	0.06	0.74	0.71	0.40	0.24	0.62	0.12	0.03	0.59	0.38	0.12	0.30	0.30	0.10	0.74
Total	99.13	99.42		97.67	99.33	100.33		96.68	97.98	99.08		97.99	99.00		97.94	99.49		99.40	99.97		96.61
LOI	0.79			1.28	0.44			1.75	2.08			1.89			1.86			0.50			1.53
Co	67			44	90			50	51			59			51			74			54
Cr	382			<18	1064			36	212			528			177			896			<18
Ni	145			<2	496			53	98			219			94			372			58
V	322			296	273			372	313			327			307			309			379
Zn	121			127	92			129	118			112			117			96			131
Ce	93			92	56			88	86			82			88			56			112
La	32			32	32			35	213			42			39			25			198
Nb	74			66	35			95	86			73			71			41			96
Ga	21			19	13			22	22			18			21			17			24
Pb	4			<4	4			<4	10			<4			<4			<4			<4
Pr	7			13	<4			16	52			7			10			<4			57
Rb	28			24	17			28	44			26			30			18			27
Ba	323			326	143			414	417			349			314			203			404
Sr	798			829	419			960	938			748			754			501			930
Th	<4			<4	<4			<4	<4			9			<4			<4			5
Y	28			35	17			32	28			30			29			20			30
Zr	311			336	130			389	331			291			297			155			393

**Table 3.4:** continued.

Sample	TN12	TN13			TN15			TN16			TN19	TN27	TN28	TN29	TN30	TN31	TN32	TN33	TN34	TN35	TN36
	wr	wr	fg	σ	wr	fg	σ	wr	fg	σ	wr	wr	wr	wr	wr	wr	wr	wr	wr	wr	wr
SiO <sub>2</sub>	44.23	44.68	45.00	0.56	43.23	44.72	0.57	43.44	45.08	0.78	47.49	47.65	47.54	46.79	47.06	42.94	43.31	43.51	43.07	43.47	64.6
TiO <sub>2</sub>	3.94	2.80	3.40	0.20	2.76	4.04	0.18	3.18	3.63	0.26	2.98	3.31	3.32	3.21	3.34	2.49	2.56	3.31	2.59	3.11	0.88
Al <sub>2</sub> O <sub>3</sub>	15.86	11.93	14.59	0.32	10.09	15.09	0.15	12.51	15.05	0.31	15.66	16.99	16.28	15.35	15.93	9.39	9.68	13.45	9.67	12.74	14.83
FeO <sub>t</sub>	12.45	12.41	12.29	0.35	13.40	12.00	0.57	12.06	11.64	0.32	11.99	11.86	11.87	12.17	12.18	12.98	12.88	12.91	12.81	12.65	5.09
MnO	0.17	0.18	0.21	0.03	0.17	0.20	0.05	0.17	0.19	0.05	0.16	0.13	0.13	0.15	0.14	0.20	0.20	0.18	0.19	0.18	0.15
MgO	5.64	12.16	7.54	0.08	16.18	7.20	0.07	11.84	9.87	0.11	5.66	3.66	4.38	4.59	4.53	16.52	16.23	8.95	15.87	10.80	1.28
CaO	10.93	11.84	12.43	0.14	10.04	11.22	0.15	10.31	10.29	0.11	10.83	8.93	9.53	10.01	9.57	10.05	10.28	10.22	10.38	10.58	3.06
Na <sub>2</sub> O	3.78	2.21	2.77	0.15	1.73	2.85	0.14	1.96	2.27	0.06	3.02	3.12	2.84	2.68	2.75	1.49	1.58	2.49	1.42	2.12	4.08
K <sub>2</sub> O	1.40	0.87	0.94	0.07	0.86	1.18	0.09	0.99	0.96	0.04	0.71	0.97	1.00	0.93	0.89	0.73	0.72	1.24	0.67	1.02	3.39
P <sub>2</sub> O <sub>5</sub>	0.72	0.39	0.18	0.10	0.42	0.16	0.07	0.48	0.14	0.08	0.39	0.44	0.44	0.44	0.45	0.34	0.36	0.58	0.35	0.50	0.23
Total	99.12	99.47	99.33		98.88	98.67		96.94	99.11		98.89	97.06	97.33	96.32	96.84	97.13	97.80	96.84	97.02	97.17	97.59
LOI	0.82	0.63			0.78			2.73			0.75	1.80	1.74	2.65	2.15	1.29	1.22	1.67	1.66	1.90	2.99
Co	43	67			79			60			49	36	40	46	40	75	71	56	74	55	184
Cr	81	779			1043			657			45	143	98	95	94	1113	1063	355	1087	536	<12
Ni	44	278			495			233			73	72	79	84	88	471	456	194	456	255	-
V	332	305			275			300			278	326	304	286	295	276	279	296	284	309	41
Zn	126	101			106			101			104	94	110	105	107	92	96	106	92	101	106
Ce	90	82			51			86			49	62	60	48	52	40	38	69	46	58	160
La	31	54			43			34			27	15	<14	25	<14	<14	<14	<14	<14	<14	48
Nb	90	52			53			53			40	50	43	46	45	35	35	60	33	49	99
Ga	19	16			14			18			21	23	19	20	22	13	16	20	16	21	20
Pb	7	<4			<4			<4			5	<4	<4	<4	<4	6	6	<4	<4	9	<1
Pr	24	4			<4			13			6	<4	<4	<4	4	<4	<4	7	<4	8	9
Rb	32	18			21			19			15	19	18	13	13	16	14	28	16	21	87
Ba	402	221			251			231			188	246	217	238	258	191	225	322	202	228	621
Sr	958	596			596			622			768	665	641	613	639	418	428	633	415	581	519
Th	<4	<4			<4			<4			<4	<4	<4	<4	<4	<4	<4	<4	<4	<4	16
Y	29	27			20			27			23	30	28	32	30	20	21	29	20	26	42
Zr	375	199			187			234			189	284	220	236	219	177	173	274	170	231	541



**Table 3.5** ICP-MS rare earth element data in ppm.

Sample	TN3	TN7	TN8	TN10	TN16	TN28	TN32
La	44.7	56.3	49.7	30.8	34.9	28.3	25.3
Ce	93.9	112.9	100.7	61.5	74.0	62.4	54.1
Pr	12.0	13.5	12.3	7.4	9.0	8.0	6.9
Nd	46.9	50.8	46.2	28.2	34.3	32.3	27.3
Sm	9.7	9.6	9.0	5.5	6.9	7.2	5.9
Eu	3.1	3.0	2.8	1.8	2.3	2.3	1.9
Gd	9.0	8.2	7.9	5.2	6.3	6.6	5.4
Tb	1.3	1.2	1.1	0.8	0.9	1.0	0.8
Dy	6.8	5.6	5.5	3.9	4.6	5.2	4.1
Ho	1.2	1.0	1.0	0.7	0.8	1.0	0.7
Er	3.0	2.2	2.3	1.7	2.0	2.4	1.8
Tm	0.4	0.3	0.3	0.2	0.3	0.3	0.3
Yb	2.4	1.6	1.7	1.4	1.6	1.8	1.4
Lu	0.3	0.2	0.2	0.2	0.2	0.3	0.2

**Table 3.6** Thermobarometry results for Teno samples.

Sample crystal	Pressure (P, MPa), calculated depth (z, km b.s.l.) and temperature (T, °C) of clinopyroxene crystallisation						Sample crystal	Temperature (T, °C) of olivine crystallisation	
	Bulk P	~z	Last Eq. P	~z	Bulk T	Last Eq. T		T (Beattie)	T (Putirka)
TN1_cpx1	918	30.3	993	32.7	1198	1205	TN1_ol1	Diseq.	Diseq.
TN1_cpx2	948	31.3	874	28.9	1201	1195	TN1_ol2	1212	1206
TN1_cpx3	980	32.2	802	26.7	1204	1204	—	—	—
<b>TN1 mean</b>	<b>944</b>	<b>31.1</b>	<b>890</b>	<b>29.4</b>	<b>1201</b>	<b>1201</b>	<b>TN1 mean</b>	<b>1212</b>	<b>1206</b>
TN5_cpx2	1192	38.9	1060	34.8	1261	1248	TN5_ol1	1307	1281
TN5_cpx3	1217	39.7	1132	37.0	1264	1256	TN5_ol2	1307	1281
TN5_cpx6	1228	40.0	1090	35.7	1268	1252	TN5_ol3	1307	1283
TN5b_cpx1	1212	39.5	1261	41.1	1264	1270	TN5b_ol1	1307	1279
TN5b_cpx2	1183	38.6	983	32.4	1260	1241	TN5b_ol2	1307	1276
TN5b_cpx3	1179	38.5	1166	38.1	1260	1258	TN5b_ol3	1307	1281
TN5b_cpx4	1260	41.1	1267	41.3	1268	1268	—	1307	1280
<b>TN5 mean</b>	<b>1210</b>	<b>39.5</b>	<b>1137</b>	<b>37.2</b>	<b>1263</b>	<b>1256</b>	<b>TN5 mean</b>	<b>1280</b>	<b>1252</b>
TN7_cpx1	769	25.6	765	25.5	1177	1176	TN7_ol2	1200	1204
TN7_cpx2	886	29.3	871	28.8	1187	1187	TN7_ol3	1200	1204
TN7_cpx3	869	28.8	1001	32.9	1186	1198	TN7_ol4	1200	1204
TN7_cpx4	807	26.8	857	28.4	1180	1185	TN7_ol5	1200	1210
TN7_cpx5	813	27.0	810	26.9	1181	1181	TN7_ol6	1200	1204
TN7_cpx6	881	29.1	867	28.7	1188	1187	TN7_ol7	1200	1206
TN7_cpx7	822	27.3	925	30.5	1182	1191	TN7b_ol1	1200	1203
TN7_cpx8	870	28.8	885	29.3	1186	1188	TN7b_ol2	1200	1203
TN7b_cpx1	832	27.6	804	26.7	1183	1181	—	—	—
TN7b_cpx2	808	26.8	780	25.9	1181	1179	—	—	—
TN7b_cpx3	819	27.2	676	22.7	1182	1169	—	—	—
TN7b_cpx4	801	26.6	845	28.0	1180	1184	—	—	—
TN7b_cpx5	752	25.1	756	25.2	1176	1177	—	—	—
TN7b_cpx6	811	26.9	767	25.5	1182	1177	—	—	—
TN7b_cpx7	736	24.6	675	22.6	1175	1169	—	—	—
TN7b_cpx8	763	25.4	705	23.6	1177	1171	—	—	—
TN7b_cpx9	764	25.5	716	23.9	1177	1173	—	—	—
<b>TN7 mean</b>	<b>812</b>	<b>27.0</b>	<b>806</b>	<b>26.8</b>	<b>1181</b>	<b>1181</b>	<b>TN7 mean</b>	<b>1200</b>	<b>1204</b>
TN8_cpx1	1187	38.8	1177	38.4	1247	1247	TN8_ol1	Diseq.	Diseq.
TN8_cpx2	1125	36.8	1126	36.9	1240	1240	TN8_ol2	1270	1255
TN8_cpx3	1035	34.0	1075	35.2	1232	1235	TN8_ol3	Diseq.	Diseq.
TN8_cpx4	1079	35.4	1142	37.3	1235	1241	TN8_ol4	Diseq.	Diseq.
TN8_cpx5	1156	37.8	1132	37.0	1243	1240	TN8_ol5	Diseq.	Diseq.
TN8_cpx6	1074	35.2	1021	33.6	1236	1231	—	—	—
TN8_cpx7	1146	37.5	1182	38.6	1243	1247	—	—	—
TN8_cpx8	1120	36.6	1074	35.2	1240	1240	—	—	—
<b>TN8 mean</b>	<b>1115</b>	<b>36.5</b>	<b>1116</b>	<b>36.5</b>	<b>1239</b>	<b>1240</b>	<b>TN8 mean</b>	<b>1270</b>	<b>1255</b>
TN9_cpx1	819	27.2	625	21.1	1194	1177	TN9_ol1	1218	1210
TN9_cpx2	814	27.0	886	29.3	1194	1200	TN9_ol2	1218	1209
TN9_cpx3	898	29.7	927	30.6	1202	1205	TN9_ol3	1218	1213
TN9_cpx4	873	28.9	765	25.5	1199	1189	TN9_ol4	1218	1213
TN9_cpx5	864	28.6	979	32.2	1198	1208	TN9_ol5	1218	1213
TN9_cpx6	979	32.2	963	31.7	1209	1206	TN9_ol6	1218	1211
TN9_cpx7	729	24.4	691	23.2	1185	1182	—	—	—
TN9_cpx8	771	25.7	590	20.0	1190	1175	—	—	—
<b>TN9 mean</b>	<b>852</b>	<b>28.2</b>	<b>803</b>	<b>26.7</b>	<b>1197</b>	<b>1193</b>	<b>TN9 mean</b>	<b>1218</b>	<b>1211</b>

Table 3.6 Continued.

Sample crystal	Pressure (P, MPa), calculated depth (z, km b.s.l.) and temperature (T, °C) of clinopyroxene crystallisation						Sample crystal	Temperature (T, °C) of olivine crystallisation	
	Bulk P	~z	Last Eq. P	~z	Bulk T	Last Eq. T		T (Beattie)	T (Putirka)
TN10_cpx1	1029	33.8	972	32.0	1234	1229	TN10_ol1	1278	1255
TN10_cpx2	976	32.1	1002	33.0	1230	1232	TN10_ol2	1278	1256
TN10_cpx3	966	31.8	998	32.8	1229	1231	TN10_ol3	1278	1257
TN10_cpx4	1000	32.9	912	30.1	1232	1223	TN10_ol4	1278	1258
TN10_cpx5	1071	35.1	1100	36.0	1238	1241	TN10_ol5	1278	1256
TN10_cpx6	1062	34.8	1152	37.7	1237	1246	TN10_ol6	1278	1252
TN10_cpx8	1092	35.8	1167	38.1	1241	1248	TN10_ol7	1278	1256
TN10_cpx9	1183	38.6	1228	40.1	1249	1253	TN10_ol8	1278	1256
TN10_cpx11	1137	37.2	1125	36.8	1244	1243	—	—	—
TN10_cpx12	1146	37.5	940	31.0	1245	1226	—	—	—
TN10_cpx13	1177	38.5	1233	40.2	1248	1253	—	—	—
<b>TN10 mean</b>	<b>1059</b>	<b>34.7</b>	<b>1075</b>	<b>35.3</b>	<b>1237</b>	<b>1238</b>	<b>TN10 mean</b>	<b>1278</b>	<b>1256</b>
TN11_cpx1	1145	37.5	1219	39.8	1207	1214	TN11_ol1	1198	1197
TN11_cpx2	928	30.6	895	29.6	1188	1186	TN11_ol2	1198	1199
TN11_cpx3	942	31.1	1055	34.6	1190	1201	—	—	—
TN11_cpx4	853	28.3	853	28.3	1183	1184	—	—	—
<b>TN11 mean</b>	<b>995</b>	<b>32.7</b>	<b>1006</b>	<b>33.1</b>	<b>1194</b>	<b>1196</b>	<b>TN11 mean</b>	<b>1198</b>	<b>1198</b>
TN12_cpx1	872	28.8	1050	34.5	1182	1196	TN12_ol1	1204	1198
TN12_cpx2	876	29.0	814	27.0	1182	1177	TN12_ol2	1204	1197
TN12_cpx3	721	24.1	745	24.9	1168	1170	TN12_ol3	1204	1200
TN12_cpx4	841	27.9	979	32.2	1178	1191	TN12_ol4	1204	1200
<b>TN12 mean</b>	<b>845</b>	<b>28.0</b>	<b>897</b>	<b>29.6</b>	<b>1179</b>	<b>1183</b>	<b>TN12 mean</b>	<b>1201</b>	<b>1199</b>
TN13_cpx1	1051	34.5	885	29.3	1230	1215	TN13_ol1	1248	1240
TN13_cpx2	1028	33.8	1039	34.1	1228	1230	TN13_ol2	1248	1238
TN13_cpx3	1074	35.2	1113	36.4	1232	1236	TN13_ol3	1248	1238
TN13_cpx4	922	30.4	903	29.8	1218	1216	—	—	—
<b>TN13 mean</b>	<b>1019</b>	<b>33.5</b>	<b>985</b>	<b>32.4</b>	<b>1227</b>	<b>1224</b>	<b>TN13 mean</b>	<b>1248</b>	<b>1239</b>
TN15_cpx1	978	32.2	947	31.2	1221	1219	TN15_ol1	1244	1237
TN15_cpx2	1084	35.5	956	31.5	1231	1219	—	—	—
TN15_cpx3	1052	34.5	1067	35.0	1228	1230	—	—	—
TN15_cpx4	1001	32.9	1049	34.4	1223	1228	—	—	—
TN15_cpx5	1025	33.7	940	31.0	1226	1219	—	—	—
<b>TN15 mean</b>	<b>1022</b>	<b>33.6</b>	<b>992</b>	<b>32.6</b>	<b>1225</b>	<b>1223</b>	<b>TN15 mean</b>	<b>1244</b>	<b>1237</b>
TN16_cpx1	1254	40.9	1175	38.4	1274	1266	TN16_ol1	1328	1296
TN16_cpx2	1302	42.4	1199	39.2	1278	1268	TN16_ol2	Diseq.	Diseq.
TN16_cpx3	1276	41.6	1413	45.9	1275	1289	TN16_ol3	Diseq.	Diseq.
TN16_cpx4	1299	42.3	1223	39.9	1278	1270	TN16_ol4	Diseq.	Diseq.
TN16_cpx5	1183	38.6	1392	45.2	1266	1286	TN16_ol5	Diseq.	Diseq.
TN16_cpx6	1441	46.8	—	—	1291	—	—	—	—
TN16_cpx7	1236	40.3	1193	39.0	1272	1268	—	—	—
<b>TN16 mean</b>	<b>1273</b>	<b>41.5</b>	<b>1266</b>	<b>41.2</b>	<b>1275</b>	<b>1274</b>	<b>TN16 mean</b>	<b>1328</b>	<b>1296</b>
TN19_cpx1	350	11.9	296	9.9	1153	1149	TN19_ol1	1182	1202
TN19_cpx2	352	12.0	352	12.0	1153	1153	TN19_ol3	1182	1202
TN19_cpx3	Diseq.	Diseq.	Diseq.	Diseq.	Diseq.	Diseq.	TN19_ol4	1182	1204
TN19_cpx4	Diseq.	Diseq.	Diseq.	Diseq.	Diseq.	Diseq.	—	—	—
TN19_cpx5	Diseq.	Diseq.	Diseq.	Diseq.	Diseq.	Diseq.	—	—	—
TN19_cpx6	565	19.2	496	17.0	1172	1166	—	—	—
<b>TN19 mean</b>	<b>382</b>	<b>13.1</b>	<b>381</b>	<b>13.1</b>	<b>1156</b>	<b>1156</b>	<b>TN19 mean</b>	<b>1182</b>	<b>1202</b>

## CHAPTER 4 – EL HIERRO ISLAND

### 4.1 Introduction

The island of El Hierro, which was declared a UNESCO Biosphere Reserve in the year 2000, is a small, remote island situated at the westernmost end of the Canary Archipelago. It is characterised by a peculiar ‘boomerang’ or ‘stellate’ shape (Figure 4.1). In geological terms, the island is merely the small sub-aerial fraction ( $280 \text{ km}^2$ ,  $140 \text{ km}^3$ ) of a truncated volcanic edifice of much larger size (some  $5,500 \text{ km}^3$  [Schmincke, 1994]) that is rising from a  $\sim 4,000\text{-m}$ -deep sea floor to a maximum elevation of  $1,501 \text{ m}$  above sea level. The great embayments of El Golfo and Las Playas, with cliff heights frequently in excess of a thousand meters, are vestiges of destructive events that affected this volcanic edifice, now exposed in vertiginous panoramic cross-sections. Despite the abundance of well-preserved constructive volcanic landmarks (El Hierro has the densest distribution of eruptive vents in the Canary Islands) and the island’s position believed to currently overlie the Canary hot-spot [e.g. Holik *et al.*, 1991], no eruptions have been witnessed in historical times. However, a possible eruption at Lomo Negro volcano may have occurred in 1793, although records are dubious [Hernández Pacheco, 1982]. This lack of recent volcanic activity, coupled with the island’s comparatively remote location, may have contributed to divert geological attention to the other islands of the archipelago; indeed, surprisingly little work had been done on El Hierro before the pioneering investigations of Guillou *et al.* [1996] and Carracedo *et al.* [2001].

This chapter exploits the unique setting of this young volcanic island. The combination of well-exposed pre-collapse stratigraphic sequences and abundant post-collapse volcanism provides a rare opportunity to study ‘recent’ potential interactions between large-scale volcano flank collapses and volcanism/magmatism. First, background information and a summary of previous works will be presented. Then, the results of field work, petrography, whole-rock major and trace element chemistry, mineral chemistry, thermobarometry and magma density calculations, will be outlined. In a discussion section, these results will be integrated and interpreted and their main implications towards our initial hypothesis will be argued. Finally, a summary of the chief conclusions will be provided.

## 4.2 Background and Previous Work

### 4.2.1 Edifice Morphology: Rift Zones and Giant Collapse Structures

#### 4.2.1.a Rift Zones

The conspicuous ‘stellate’ geometry of the island is matched by the concentration of sub-aerial eruptive vents along three main ridges with azimuths separated by approximately 120° (Figures 4.1, 4.2). These ridges, oriented NW, NE and S, are thought to be the topographic expression of rift zones, where dyke emplacement is favoured according to a geometry of least stress fracture [e.g. *Carracedo*, 1994; *Carracedo et al.*, 2001 and references therein]. The alignment of dyke swarms is in general agreement with the existence of such rift zones (Figure 4.2). On the sub-marine slopes of the edifice, however, pinnacles (interpreted as emission vents) at the extension of the NW- and NE-ridges become increasingly dispersed with depth, indicating a lesser influence of the associated rift zones away from the apical region (Figure 4.1b) [*Gee et al.*, 2001a]. The S-ridge, however, is drastically different; it is much longer, narrower and has steeper flanks compared to the NW- and NE-ridges. This sub-marine topographic feature is moreover characterised by a prominent saddle near 27°30' N, 17°58' W, south of which the ridge flanks are heavily incised by gullies [*Gee et al.*, 2001a], in contrast with the smoother, more subdued morphology to the north. This led *Gee et al.* [2001a] to propose that the S-ridge partly represents the remnants of a stable, older edifice, not ‘connected’ to El Hierro’s southward propagating rift zone (Figure 4.1b).

The diffuse character of at least the NW- and NE- rift zones away from the edifice summit may indicate that their development is largely controlled by gravitational stresses in the upper part of the volcanic edifice [e.g. *Münn et al.*, 2006]. In turn, preferential intrusion of magma along El Hierro’s rift zones may have regulated the gravitational stability of the volcanic edifice [e.g. *Elsworth and Voight*, 1996]. Indeed, four and possibly five separate lateral collapses, or partial collapses, seem to have affected the El Hierro edifice in the last 1.12 Ma [*Carracedo et al.*, 2001 and references therein], all of which have occurred between two of the three rift zone arms. Before reviewing the island’s stratigraphy in section 4.2.2, evidence for each of the large-scale volcano flank failures is presented below. As seen in the Chapter 3 for the Teno volcano, such major tectonic events largely influence the structural development of a volcano; a fact that the geologist wishing to reconstruct of the volcanic history has to consider.

#### 4.2.1.b The Tiñor Collapse

*Hausen* [1972] was the first to suggest that the El Golfo and Las Playas natural amphitheatres formed through catastrophic gravitational mass-wasting. Since then, bathymetric and on-shore data have confirmed this hypothesis and have allowed the recognition of further collapse structures, the oldest of which is the Tiñor collapse [*Carracedo et al.*, 1999b; 2001]. In contrast to the younger giant landslides of El Hierro, the Tiñor collapse left no clear trace at the surface and evidence for its occurrence resides in the differences of the K-Ar ages and magnetic polarities of the lavas found on either sides of the NE-ridge. On the west side of the ridge, lavas exposed in a horizontal tunnel (*galería*) excavated in the El Golfo scarp towards the south all have normal magnetic polarity (Brunhes epoch) and a sample taken at the end of the tunnel was dated at 543 ka [*Guillou et al.*, 1996]. However, lavas at similar elevations but observed at the surface and in *galerías* in the eastern part of the island show reverse magnetic polarity (Matuyama pre-Jaramillo sub-chron) and are significantly older ( $>1.04$  Ma) (Figure 4.1, 4.2). This apparent discordance between the lavas was interpreted to originate from the presence of a concealed, NW-facing collapse embayment [e.g. *Carracedo et al.*, 1999b]. Interestingly, the Tiñor landslide has not been recognised off-shore [*Gee et al.*, 2001b; *Masson et al.*, 2002] and the discrepancies observed by *Guillou et al.* [1996] could potentially also be explained by a NW-directed migration of the NE-rift activity with time, although a buried collapse embayment remains the geometrically simplest solution. A topographic anomaly between the Ventejís vent group and the smoother grounds to the east may mark the location of the buried collapse scarp (Figures 4.1, 4.2).

#### 4.2.1.c The El Julán Landslide

*Holcomb and Searle* [1991] mapped chaotic deposits on the seafloor southwest of El Hierro, which they interpreted as the deposits of a large landslide ( $>100$  km<sup>3</sup>), the El Julán landslide. On-shore, a ~16-km-wide embayment, fully draped with young, seaward-dipping lavas, probably hides the buried landslide scarp. The age of this flank collapse is poorly constrained but probably exceeds 60 ka and may be older than 200 ka [*Gee et al.*, 2001b; *Krastel et al.*, 2001; *Masson et al.*, 2002]. The scarcity of blocks, together with the presence of faults within the off-shore deposit, suggests that the El Julán landslide may be a slump or slump/debris avalanche complex. In this scenario, limited displacement in the slump headwall would provide an explanation as to why later volcanism has been able to

completely cover the collapse scarp, an unusual situation for landslides of comparable age in the western Canaries [Masson *et al.*, 2002].

#### 4.2.1.d The Las Playas/San Andrés Landslide(s)

The SE-flank of El Hierro is the site of the Las Playas embayment and the San Andrés fault system (Figures 4.1, 4.2, 4.3). Off-shore studies have identified a 25-50 km<sup>3</sup> debris avalanche deposit covering an area of 700-950 km<sup>2</sup> immediately down-slope of the Las Playas embayment [Krastel *et al.*, 2001; Masson *et al.*, 2002]. This debris avalanche deposit was found to overlie a broader area of deformed strata located off-shore of the San Andrés fault system [Masson *et al.*, 2002]. Just northeast of the Las Playas embayment on-shore, a topographic scarp draped with recent lava flows is collinear with a ~10-km-long normal fault segment parallel to the coastline, with downthrow of the hangingwall of up to 300 m. Further to the northeast, the fault splits into at least two E-W trending segments, one of which is a strike-slip fault whilst the other is dominantly dip-slip [Day *et al.*, 1997]. Combining both on-shore and off-shore evidence, the SE-flank geometry appears to relate to a giant slump/debris avalanche complex, similar to some features observed on the Hawaiian Islands [Moore *et al.*, 1994; Masson *et al.*, 2002]. Catastrophic failure giving rise to the Las Playas embayment took place between 176 and 145 ka [cf. Guillou *et al.*, 1996]; it is unclear, however, whether the formation of the San Andrés fault system, which apparently involved only one major episode of fault movement [Day *et al.*, 1997], significantly pre-dates or was contemporaneous with this event.

#### 4.2.1.e The El Golfo Landslide

The spectacular El Golfo embayment, some 15 km across with cliffs up to 1.4 km in height, is the sub-aerial part of the scar left by a 150-180 km<sup>3</sup> debris avalanche that travelled as far as 65 km from El Hierro's shore (Figures 4.1, 4.2, 4.3). The El Golfo landslide is the most recent large-scale flank collapse to have taken place in the Canary Archipelago; however, the exact age of the El Golfo landslide is matter of debate. Whilst radiometric dating by Guillou *et al.* [1996] and Szérméta *et al.* [1999] bracket the event between 134±4 ka and 21±3, off-shore evidence points towards a younger age of ~15 ka [Masson, 1996; Masson *et al.*, 2002]. Carracedo *et al.* [1999b] argued that the El Golfo embayment is probably as old as the youngest dated lavas affected by the collapse (~100-130 ka) based on the presence of an underground marine abrasion platform, identified through several boreholes at the bottom of the landslide scarp. Such a feature would require a significant period of post-collapse erosion before post-collapse lava flows partly

filled the embayment, for which a maximum age of 21 ka has been obtained. To reconcile the conflicting on- and off-shore evidence, *Carracedo et al.* [1999b] postulated the occurrence of two events; 1) a sub-aerial collapse at ~130 ka, and 2) a largely sub-marine collapse between 17 and 9 ka. There is, however, no off-shore evidence for more than one collapse on the northwest flank of El Hierro [*Masson et al.*, 2002]. Notably, pre-collapse lavas dated at 134 ka by *Sz  r  m  ta et al.* [1999] were sampled low on the flank of the volcanic edifice at an altitude of 740 m, whilst pre-collapse lavas may be found at much higher altitudes (up to 1501 m). Although technically at the same stratigraphic level, the lavas at higher altitudes were erupted closer to the pre-collapse edifice summit and may be significantly younger than 134 ka. Until further radiometric dating of these lavas is performed, we consider the available evidence to merely indicate that the El Golfo landslide occurred sometime between  $134 \pm 4$  ka and  $21 \pm 3$ .

## 4.2.2 Stratigraphy of El Hierro Island

### 4.2.2.a Early Work

*Hausen* [1972], who gave a general description of the island's geology, referred to two major stratigraphic series: 1) the Tableland Series, "built of flat-lying volcanic strata of basaltic nature", and 2) the Adventive Volcanic Formation, formed of recent cinder cones, lavas and pyroclastic deposits. *Abdel-Monem et al.* [1972] performed the first reconnaissance radiometric dating campaign of El Hierro lithologies (K-Ar of 4 whole-rock samples), coupled with palaeomagnetic determinations. Although they obtained an age of 3.05 Ma at the base of the Tableland Series, these authors argued that the entire island was younger and built within the Brunhes epoch (younger than 0.78 Ma [e.g. *Cande and Kent*, 1995]); an age of 3.05 Ma could not be reconciled with the younger dates obtained ( $<0.2$  Ma) and the lack of evidence for a  $>2$  Ma volcanic hiatus. *Pellicer* [1977] offered the first thorough analysis of El Hierro's volcanism and produced a comprehensive geological map. This worker divided the volcanic products into three cycles: 1) the Old Series, largely exposed in the El Golfo cliffs, and characterised by "trachytic" emissions near the top of its ~1400-m-thick sequence, 2) the Intermediate Series, covering most of the island's surface with mostly well-preserved vents and associated lavas and pyroclastics, and 3) the Recent Series, consisting of fresh-looking 'a'a and pahoehoe lava flows emitted at the island's extremities. Notably, *Pellicer* [1977] provided a schematic map of the Tanganasoga volcano, which will be discussed later in this chapter, and two  $C^{14}$  ages near this site. The carbonised material retrieved from ash- and lapilli-rich beds yielded ages of



6.7 and 4.2 ka, interpreted to mark the time of transition from the Intermediate to the Recent Series. Following from *Abdel-Monem et al.* [1972], *Fuster et al.* [1993] undertook a slightly more ambitious project to reconstruct the geochronology of the island, using conventional whole-rock K-Ar dating on 12 lava samples. These authors pointed out that part of the volcanics in the northeast were likely relatively old (some 0.8 Ma) whilst they could not further resolve the young age (probably <50 ka) of most of the Intermediate and Recent Series.

A clearer spatial and temporal portrait of El Hierro's volcanism awaited the more rigorous approach of *Guillou et al.* [1996] and *Sz  r  m  ta et al.* [1999], who combined an unspiked K-Ar dating technique suitable for young rocks with detailed magnetic polarity stratigraphy. Based on these new data coupled with extensive field mapping, *Carracedo et al.* [2001] proposed a revised, considerably more detailed volcanic and structural model of island evolution. According to the latter authors, the sub-aerial rocks of El Hierro can be divided into three main mappable units that replace previously defined stratigraphic divisions and that relate to successive volcanic edifices/phases: 1) the Ti  or Volcano Formation, 2) the El Golfo Volcano Formation, and 3) the Rift Volcanism Formation, each separated by major tectonic events (giant landslides).

#### 4.2.2.b The Ti  or Volcano Formation

The Ti  or Volcano Formation (TVF), with outcrops limited to the northeast of the island and within the Las Playas embayment (Figure 4.2), represents the earliest stage of sub-aerial volcanism on El Hierro. In contrast to the neighbouring island of La Palma, exposures of the seamount volcano have not been found on El Hierro [*Carracedo et al.*, 2001]. *Guillou et al.* [1996] showed that the Ti  or edifice grew rapidly in the upper part of the Matuyama reverse polarity epoch from the steeply seaward dipping coastal lavas near Puerto de La Estaca emitted some 1.12 Ma ago to the late emissions of the Ventej  s vents dated at ~882 ka and situated between the towns of Valverde and San Andr  s (Figure 4.1, 4.2). Notably, the Ventej  s eruptions, with the largest (up to ~1 km across) crater morphology preserved on the island and characteristically xenolith-rich lavas flows, may represent a terminal explosive stage of the Ti  or volcano that occurred before the edifice suffered the NW-directed Ti  or landslide [*Carracedo et al.*, 2001].

#### 4.2.2.c The El Golfo Volcano Formation

A new volcanic edifice, the El Golfo volcano, appears to have grown within the Tiñor collapse embayment, eventually filling it completely and spilling lava flows to the east to partially cover the older, truncated volcano [Carracedo *et al.*, 2001]. One of the stratigraphically lowest lavas inferred to have infilled the Tiñor collapse amphitheatre yielded an age of 545 ka, leaving room for speculation about a possible ~340 ka hiatus after the late emissions of the Tiñor volcano around 882 ka ago (Figures 4.1, 4.2) [cf. Carracedo *et al.*, 2001]. It appears that the El Golfo Volcano Formation (EGVF) was fully extruded during the Brunhes period, corroborating the unreliability of the old radiometric age of 3.05 Ma [cf. Abdel-Monem *et al.*, 1972; Guillou *et al.*, 1996]. Carracedo *et al.* [2001] noted that the El Golfo Volcano Formation may be sub-divided into two units: 1) a lower part, mostly consisting of strombolian and surtseyan pyroclastics with only minor lava flows, and 2) an upper part, dominantly composed of lava flows. Differentiated lava and block and ash flows, with an age of 176 ka [Guillou *et al.*, 1996], are found near the top of this second unit and are thought to represent the last phase of activity of the El Golfo volcano (Figures 4.1, 4.2, 4.3, 4.4). This volcanic edifice may therefore have been active for a period of ~360-380 ka, mostly between 545 and 176 ka, before a new cycle of activity, the Rift volcanism, commenced.

#### 4.2.2.d The Rift Volcanism Formation

Radiometric ages (between 158 and 2.5 ka [Pellicer, 1977; Guillou *et al.*, 1996; Szérméta *et al.*, 1999]) obtained for the emissions of the so-called Rift volcanism (herein Rift Volcanism Formation (RVF)) show no evidence of a gap in activity following the final eruptions of the El Golfo volcano. Despite local unconformities especially within the Las Playas and El Golfo embayments and near the coastline, Rift lavas rest generally conformable on the earlier El Golfo edifice [Carracedo *et al.*, 2001]. According to Guillou *et al.* [1996], a change in dip direction of the lavas from northeast (El Golfo Volcano Formation) to southwest (Rift Volcanism Formation) allows the distinction between the formations, at least in the northeast part of the El Golfo scarp.

#### 4.2.3 Petrology

In addition to general petrographic descriptions, Hausen [1972] provided the first chemical data on 12 whole-rock samples, showing that El Hierro rocks were typical alkali basalts of the “Atlantic region”. Subsequently, Pellicer [1977; 1979] published further petrographic

data and whole-rock major element compositions of 91 samples from lava flows and dykes. This large sample set returned a relatively wide range of compositions, but with a “Bunsen-Daly gap” between the mafic and felsic end-members. In addition, *Pellicer* [1979] noted a trend of increasing alkalinity in the products of the Intermediate and Recent Series with respect to the Old Series, which he attributed to a gradually decreasing degree of partial melting in the mantle. Despite a significantly smaller set of 13 samples (representative of the three recently established eruptive cycles), *Carracedo et al.* [2001] presented a relatively comprehensive overview of the main petrological features of El Hierro rocks. These workers argued for a relatively simple geochemical evolution of El Hierro, with the Tiñor Volcano Formation characterised by the most primitive lavas, the subsequent El Golfo Volcano Formation showing more evolved products (most notably the late “trachytic” products) and, finally, the Rift lavas that display a wide, although mafic compositional range (i.e. “trachytes” are not present). The three eruptive cycles were interpreted to relate to the same stationary magmatic source; the chemical variations in major and trace element composition were chiefly attributed to fractional crystallisation of olivine, clinopyroxene and Fe-Ti oxides. Based on the Rare Earth Element (REE) concentration of the most primitive Tiñor samples, *Carracedo et al.* [2001] proposed that El Hierro’s alkalic magmas originate from low degrees of melting of a depleted mantle source at 80-108 km depth, in the garnet stability field, with increasing melt fraction (up to 1.16-2.2%) in the garnet-spinel transition zone at 81-93 km.

### 4.3 Field Work

Here we summarise the results of two field campaigns conducted during the summers of 2005 and 2006. As in Chapter 3, focus is given to variations in the typology and mineralogy of volcanics as a function of stratigraphic position, but the occurrence and characteristics of intrusive rocks (which are all dykes) will be briefly noted. Our approach herein will concentrate on the younger volcanics of El Hierro, the El Golfo Volcano and Rift Volcanism formations, and the El Golfo landslide event will serve as a reference point in time. Volcanic rocks cut by and exposed in the El Golfo cliffs necessarily pre-date the landslide and are referred to as “pre-collapse volcanics” (abbreviated pre-EGL in figures). This includes all of the El Golfo Volcano Formation and part of the Rift Volcanism Formation. In contrast, lava flows and pyroclastic deposits that drape the floor and the steep surface of the landslide scar must be younger than the El Golfo landslide. These are called “post-collapse volcanics” (post-EGL) and all of these belong to the Rift Volcanism

Formation. However, volcanic rocks found on the NW, NE and S ridges, above and far from the El Golfo embayment, cannot confidently be assigned to any of these two categories based on field relations alone. Therefore, the relative age of such volcanics (also all part of the Rift Volcanism Formation) with respect to the El Golfo landslide event is uncertain (labelled ?-EGL in figures).

For our field evaluation, comparatively little attention is given to the temporal relationship of volcanics relative to the Las Playas landslide. This is simply because field relations do not allow a close comparison of pre- and post-Las Playas landslide volcanics; the two hiking paths that give access to the Las Playas collapse embayment follow slopes that are draped by isolated post-collapse lavas with very little exposure of pre-collapse stratigraphy. In figures and plots, however, the relative age of samples with respect to the Las Playas landslide is indicated to be older (pre-LPL), younger (post-LPL) or uncertain (?-LPL).

#### 4.3.1 Pre-El Golfo Landslide Volcanics

##### 4.3.1.a Peña Log

Following a hiking trail, Camino de la Peña, starting near Las Puntas at [205460, 3077370] and an altitude of 160 m above sea level (a.s.l.) and ending at [206390, 3078610] and an altitude of 760 m, we logged the exceptionally well-exposed stratigraphic sequence that offers a cross-section through the eastern part of the pre-collapse volcano (Figures 4.1, 4.2, 4.5a). This sequence is well-dated by the works of *Guillou et al.* [1996] and *Széréméta et al.* [1999], from 545 ka at the foot to 134 ka at the top of the cliff (Figures 4.1, 4.5a). In the first ~150 m of the section, pyroclastic rocks composed of lithified lapilli and minor bombs, which may be classified as “lapilli-tuffs” [cf. *White and Houghton*, 2006], are predominant, with only minor occurrences of aphyric, basaltic and ankaramitic lavas flows (Figure 4.5a). The pyroclastics have variable dips, are intruded by numerous NE-trending dykes and define several overlapping fossil vents exposed in cross-section. From altitudes of ~330 to 470 m, aphyric to moderately-olivine-clinopyroxene-phyric basaltic flows are most frequently encountered. Relatively suddenly, however, pale-coloured volcanics with plagioclase as the main phenocryst phase become common near 480 m and extend up to ~600 m of altitude. These intermediate-to-felsic volcanics appear to be present over a large portion of the island at a similar stratigraphic position (Figures 4.2, 4.3b, 4.4a). Along Camino de la Peña, they include several lava flows, a pumiceous unit bearing some basaltic clasts (sample EH21, Figure 4.4c) and a monomict breccia unit at [206260,

3078440] composed of blocks up to 0.5 m across in a fine grained matrix (sample CIHI02 of *Guillou et al.* [1996] and *Carracedo et al.* [2001]). Above these deposits, in the top 140 m of the Peña profile, there is a shift to lava flows that are more mafic, including several basalts and ankaramites (e.g. samples EH4-5). Notably, no dykes are observed to cut into the upper 300 m of this sequence.

#### 4.3.1.b Jinama Log

Camino de Jinama starts about 1 km east of the town of Frontera, where a church has been built on a young, post-collapse cinder cone at [204160, 3073690] and 355 m of altitude. The path climbs the El Golfo cliffs through some largely vegetated areas towards Mirador de Jinama at [206180, 3074470] and an altitude of ~1230 m, providing a cross-section closely corresponding to the centre of the pre-collapse volcano (Figure 4.1, 4.2, 4.5b) [cf. *Carracedo et al.*, 2001]. From the foot of the cliff to an altitude of ~770 m, however, only minor outcrops of pre-collapse lapilli-tuffs and basaltic lava flows are observed, with the exposure being chiefly limited to post-collapse volcanics that drape the steep slopes (Figure 4.5 b). This part of the log will thus be described in the Post-El Golfo Landslide Volcanics section below. Between ~770 and ~980 m of altitude, exposure mainly consists of pre-collapse lapilli-tuffs and aphyric to moderately-olivine-clinopyroxene-phyric basaltic flows, as well as some ankaramites. Several dykes are also seen and mostly strike E-W (Figure 4.5 b). Higher up along the profile, from ~1000 to ~1100 m of altitude, exposure is poor, but common dykes with NE and SE trends are observed, many of which are plagioclase-phyric. According to the geological map of *Carracedo et al.* [2001] (Figure 4.2), this would correspond to the level of exposure of the intermediate-to-felsic products of the upper El Golfo volcano, which may be hidden by the vegetation cover here. The uppermost 100 m of the sequence consists of fossil cinder cones marked by abundant lapilli-tuffs with variable dips and the occurrence of further dykes (Figure 4.5b).

#### 4.3.1.c Sabinosa Log

A third hiking trail, Camino de Sabinosa, allows to inspect the pre-collapse volcano in the western parts of the El Golfo cliffs. From the town of Sabinosa, near [194490, 3072940] and 330 m of altitude, the path progresses up the stratigraphic sequence of the NW-rift until the top of the cliff is reached at [193200, 3072760] and 880 m (Figure 4.1, 4.2, 4.5c). In this case, however, exposure is largely restrained by the vegetation cover. Pre-collapse rocks crop out scarcely along the path, from 430 to 780 m of altitude, where ankaramitic volcanics as well as dykes (frequently E-W-trending) appear most common. Aphyric to

moderately-olivine-clinopyroxene-phyric basaltic lapilli-tuffs and flows also occur, but in lesser amounts. In the upper 80 m of the sequence, dark, fresh and crystal-poor lapilli deposits are widespread and well-exposed, together with minor basaltic to ankaramitic lava flows (Figure 4.5c). These deposits are broadly conformable on lower (and older) lavas and may correspond to the Rift Volcanism Formation defined by Carracedo *et al.* [2001].

#### 4.3.2 Post-El Golfo Landslide Volcanics

Inside the El Golfo embayment, post-collapse eruptions originated from vents located at the base of, or directly resting on, the landslide headwall (Figures 4.1, 4.2). These eruptions produced platform-forming lava flows and, thus, probably post-date the last glacial maximum (i.e. they are likely younger than ~20 ka, in agreement with a borehole sample dated at 21 ka) [Carracedo *et al.*, 1999b; 2001]. Although no stratigraphic sequences as detailed as those described for pre-collapse volcanics are available here, the products of post-collapse volcanism were investigated at the base of the Jinama log, near Sabinosa and at several other localities spatially distributed over a large portion of the embayment.

At the bottom of the Jinama log, thin, moderately-olivine-clinopyroxene-phyric basaltic lava flows and pyroclastic deposits, with steep NW dips towards the inside of the El Golfo embayment, are commonly exposed from ~560 to ~770 m of altitude (Figure 4.5b). Notably, near [204770, 3073500] at an altitude of about 500 m, polymict breccias are observed in outcrop as well as in the walls of a barranco, where they are sandwiched between steeply-dipping post-collapse pyroclastic deposits and lava flows (Figure 4.4a).

Similar field relations are seen at the base of the Sabinosa log. Indeed, looking west from [194290, 3072710] at ~510 m of altitude, polymict breccias are also seen overlain by post-collapse lapilli deposits and lavas. In marked resemblance to field observations in the Teno massif (Chapter 3), such breccias were also observed in the Las Playas embayment, where they are overlain by post-collapse lavas (Figure 4.4e).

Although post-collapse basaltic lavas are observed at the bottom of the Jinama log, it appears that a large portion of post-collapse volcanics in and around the El Golfo embayment are ankaramites (Figure 4.6a). Indeed, out of the 62 post-collapse localities investigated, 55% were ankaramites as opposed to 45% of basaltic products. This is in marked contrast with pre-collapse volcanics that showed basaltic mineralogy at 72% of localities investigated, with only 28% of ankaramites (Figure 4.6b). Noteworthy examples

include the Lomo Negro cinder cone, which may have formed during a possible historic eruption in 1793, and associated lava platforms in the northwest corner of the island (samples EH11A, EH12, Figures 4.1, 4.2). In addition, vents and lavas in the eastern part of the embayment are also commonly ankaramitic (e.g. sample EH20, Figures 4.1, 4.2). Most strikingly, however, extensive ankaramitic eruptions must have originated from the most prominent volcanic construction within the El Golfo embayment, the Tanganasoga volcano.

#### 4.3.2.a The Tanganasoga Volcano

At least ten post-collapse eruptive vents have produced the Tanganasoga volcano, which form a large bulge in the centre-west part of the embayment (Figure 4.1, 4.2, 4.4b). The vent complex is accessible from a hiking path heading west from Malpaso, the highest point on El Hierro at [200230, 3070900] and 1501 m above sea level. The path runs along the edge of the cliffs, where some of the stratigraphically highest pre-collapse lavas are found (e.g. samples EH16-18). At [198930, 3070460], a smaller trail descends the lapilli-covered collapse scarp, where limited pre-collapse products are observed. At the base of the steep slope at an altitude of ~1300 m near [198550, 3070690], an angular unconformity marks the transition between the pre- and post-collapse volcanics (Figure 4.4b). A first cinder cone is encountered near [198490, 3070840], where most of the lava bombs are aphyric to moderately-olivine-clinopyroxene-phyric basalts. This cone, whose shape is poorly preserved, also appears to have produced the relatively extensive basaltic lava flows just east of the vent complex (sample EH15, Figures 4.2, 4.4b). Walking north from the first cone to [198290, 3071420] and 1360 m altitude, five craters up to ~200 m in diameter are observed. Bombs up to ~1 m across and lapilli are widespread and, strikingly, these show extremely high contents of clinopyroxene and olivine crystals up to 50 vol. %. Within loose lapilli deposits found on the slopes of the cones, large, often intact clinopyroxene crystals are ubiquitous and frequently reach 1.5-2 cm, with the largest found being 3 cm across (Figure 4.4b). These vents were thus the source of extensive and voluminous ankaramitic volcanism. Indeed, down slope from Tanganasoga, most lava flows observed on road cuts are ankaramites (e.g. EH13-14, Figure 4.6a).

#### 4.3.3 *Rift Volcanism With Uncertain Timing Relative to the El Golfo Landslide*

The spatial relationship (relative to the El Golfo embayment) of numerous young cinder cones, lava flows and pyroclastic deposits that are exposed as part of the NW-, NE- and S-ridges of El Hierro does not allow their classification as pre- or post-collapse volcanics

(Figure 4.2). Nevertheless, we have investigated numerous localities, especially on the NW- and S-ridges and found that, apart from a few ankaramitic platform-forming flows, most cinder cones and lavas flows on the S-ridges are aphyric to moderately-olivine-clinopyroxene-phyric (e.g. sample EH19, Figure 4.1, 4.2, 4.6). On the steep slopes dipping towards the El Julán embayment, however, ankaramites are frequent, but also accompanied by common basaltic volcanics. Out of 71 localities investigated, 70% were basaltic and 30% were ankaramitic (Figure 4.6b).

#### 4.4 Petrology and Geochemistry

Table 4.1 lists all samples used for the petrological and geochemical analysis in this chapter. Relative stratigraphic position was established based on available radiometric ages, combined with constraints from sample localities (Figures 4.1, 4.2). Chemical analyses of *Hausen* [1972], *Pellicer* [1979] and *Abratis et al.* [2002] were investigated, but not included in this evaluation because their corresponding sample localities (when provided) do not allow their classification within the stratigraphic framework. Most of our and *Carracedo et al.* [2001]’s samples, on the other hand, can be confidently assigned to one of the three main stratigraphic formations; however, further sub-divisions serve to situate the samples in time with respect to (mostly) the Las Playas and El Golfo landslides. Where relative stratigraphic position of samples could not be evaluated by other means, altitude was used as a sorting criterion. As discussed in Chapter 3, this may be a reasonable approximation of stratigraphic position (here especially for the TVF and EGVF), but, in certain cases, it results in unavoidable uncertainties. For example, samples from lava flows filling the El Golfo embayment are difficult to sort with respect to each other as they do not occur in clear stratigraphic sequences. This could introduce noise in potential stratigraphy-geochemistry trends *within* each of the Rift Volcanism Formation sub-divisions. On the other hand, there is good stratigraphic control *between* the different formations and sub-divisions (TVF, EGVF, RVF1, RVF2, RVF3, RVF4).

##### 4.4.1 Petrography

A summary of petrographic observations, including modal phenocryst abundances, groundmass constituents and notable textures, is presented in Table 4.2. Like at Teno, clinopyroxene and olivine phenocrysts are dominant in El Hierro lavas. Only two samples (EH5 and EH18) do not contain clinopyroxene; in these samples, olivine is the only phenocryst phase and occurs as small euhedral to subhedral crystals (<2 mm). In other



samples, olivine and clinopyroxene phenocrysts are either euhedral and unresorbed or subhedral and commonly showing embayed rims and/or partly resorbed cores. Anhedra crystals are rare. Clinopyroxene commonly shows concentric zoning, especially in outer parts of crystals. Scattered examples of sector zoning are observed, whilst optically homogeneous crystals are not uncommon. An overgrowth rim in clinopyroxene, similar to that described for Teno samples, is observed in about half of the thin sections, but it is comparatively thinner and only rarely hosts Fe-Ti oxide inclusions. Apatite microcrystals are present in some of these rims, but this texture is not commonplace here and apatite displays more equant habits than in Teno samples. Although scarce in most samples, glomerocrysts are more common than in Teno lavas and frequently occur as aggregates of numerous small crystals. Plagioclase phenocrysts are absent from the majority of samples; however, EH16-17, EH21 and some samples from the Tanganasoga volcano are plagioclase-phyric (Table 4.2). Fe-Ti oxide is a minor phenocryst phase in most samples, but can constitute up to ~8 % of the rock volume in certain cases. These crystals show variable habits in thin section and euhedral, subhedral and anhedra shapes are regularly found in the same sample. Rare amphiboles (kaersutite) are present in four samples and are characterised by anhedra shapes and halos of Fe-Ti oxide microcrystals around their rims. The matrix of El Hierro lava samples is mostly microcrystalline, containing varying proportions of plagioclase laths, Fe-Ti oxides, clinopyroxene microphenocrysts and accessory apatite. Cryptocrystalline material, however, is also present in many samples, notably in the lava bomb samples of the Tanganasoga volcano. Rare olivine microcrystals are present in the matrix of a few samples only. Most samples, except a few ankaramites, show common vesicles.

#### 4.4.2 *Rock Major and Trace Element Chemistry*

##### 4.4.2.a Total-Alkali-Silica Classification

The chemical composition of our El Hierro samples is given in Table 4.3. Most El Hierro rocks fall in the field of tephrite/basanite of the Total-Alkali-Silica classification (Figure 4.8), but some samples plot in the picobasalt, hawaiiite, benmoreite and trachyte fields. Using the same criterion as in Chapter 3 (i.e. the extrapolation of the tephrite/basanite-hawaiiite field boundary), we note that only occasional samples are alkali basalts, whilst basanites are more common (Figure 4.8, Table 4.1), underlining a more alkaline character of El Hierro volcanics compared to those of e.g. Teno on Tenerife. Tephrites are distinct from basanites by having <10% olivine in their CIPW norm. Most ankaramites are

basanites here, but some are classified as alkali basalts and picrites (see Table 4.1) [cf. *Le Bas*, 2000], whereas their corresponding fused groundmass separates have basanite, hawaiite, tephrite and even foidite compositions. Note that the highest SiO<sub>2</sub> contents are found in the intermediate-to-felsic upper El Golfo Volcano samples CIHI02 and EH21, which are respectively classified as benmoreite and trachyte (Figure 4.8, Table 4.1). In turn, many Rift Volcanism Formation samples have low SiO<sub>2</sub> and, at a given silica content, have higher concentrations of alkali elements than Tiñor Volcano and El Golfo Volcano samples.

#### 4.4.2.b Major and Trace Element Variations Versus MgO

Figure 4.9 presents MgO variation plots that significantly expand the data available, enabling a more complete description of the role of fractionating mineral phases [cf. *Carracedo et al.*, 2001]. At MgO values 5-6 wt%, there is a break in slope in the trends of SiO<sub>2</sub>, TiO<sub>2</sub>, FeO<sub>t</sub>, CaO and V, although, for the Rift Volcanism Formation, this may occur at higher MgO values around 9 wt% (see e.g. TiO<sub>2</sub> and V). The Rift Volcanism samples are also characterised by higher TiO<sub>2</sub>, FeO<sub>t</sub>, and V at a given MgO content. Only the two intermediate-to-felsic samples of the El Golfo Volcano produce a positive trend in the P<sub>2</sub>O<sub>5</sub> plot. Three low-MgO samples of the Rift Volcanism Formation have comparatively low Na<sub>2</sub>O/Al<sub>2</sub>O<sub>3</sub>. Fused groundmass compositions generally fall on the liquid line of descent for all major element oxides except P<sub>2</sub>O<sub>5</sub> and, at MgO between 6 and 9 wt%, for TiO<sub>2</sub> and FeO<sub>t</sub>.

#### 4.4.2.c Incompatible Trace and Rare Earth Elements

Plots of the Zr/Nb ratio against Nb concentration (Figure 4.10) may be useful to assess the roles of both crystal fractionation and partial melting in controlling the chemistry of Canarian volcanics [cf. *Thirlwall et al.*, 2000]. In El Hierro's case, the highest Nb values are found in the upper El Golfo Formation, followed by some Rift Volcanism samples that have Nb concentrations of up to ~120 ppm. Tiñor Volcano samples appear to be characterised by both lower Nb and higher Zr/Nb than the El Golfo Volcano Formation. Although part of the range in Zr/Nb values for the Rift Volcanism samples overlaps with that of the El Golfo Volcano Formation, many have Zr/Nb ratios as high as those of the Tiñor volcanic rocks.

To obtain additional constraints on the mantle source and the relative extent of partial melting during the extrusion of each stratigraphic formation, high precision REE

data for El Hierro volcanics are presented in Figure 4.11 and Table 4.4. Mean concentrations were calculated for the Tiñor Volcano Formation, the El Golfo Formation and for each of the sub-divisions of the Rift Volcanism Formation. The yellow field, however, encompasses all Rift Volcanism samples. Data ranges show some overlap for all formations; however, the older Tiñor Volcano Formation overall displays the lowest mean concentrations, while its successor, the El Golfo Volcano Formation, is characterised by the highest REE concentrations. The youngest El Hierro volcanics, the Rift Volcanism Formation, show intermediate values, being depleted in REE relative to the El Golfo Volcano Formation.

#### 4.4.2.d Major and Trace Element Variations Versus Stratigraphic Level

Here again, we use a similar approach to that developed earlier (in Chapter 3, i.e. Figure 3.11), whereby we evaluate temporal geochemical variations in El Hierro volcanic products with multiple plots of proxy parameters versus stratigraphic level. For El Hierro, however, approximate age is a more appropriate Y-axis variable than altitude to denote stratigraphic level. Using the sample sequence given in Table 4.1, virtual proportional ages were determined for undated samples based on brackets provided by available radiometric dates. For consistency with our analysis in Chapter 3,  $\text{SiO}_2$ , Mg#,  $\text{P}_2\text{O}_5/\text{Al}_2\text{O}_3$ , CaO, Zr/Nb and normative nepheline are once more the parameters selected in Figure 4.12.

Most El Hierro lavas have  $\text{SiO}_2$  contents in the range of ~40 to 50 wt%, except for the two samples of the upper El Golfo Volcano Formation. These more silica-rich samples are in drastic contrast with many of the younger Rift Volcanism samples that have particularly low  $\text{SiO}_2$ , even compared to the lower El Golfo Volcano and Tiñor formations (Figure 4.12a).

The magnesium number varies largely between 40 and 70 at El Hierro (Figure 4.12b). In the upper El Golfo Volcano Formation, Mg# reaches lower values (down to 27), also associated with low CaO (Figure 4.12d). In general, post-collapse Rift Volcanism lavas have significantly higher Mg# than pre-collapse El Golfo Volcano rocks.

The ratio  $\text{P}_2\text{O}_5/\text{Al}_2\text{O}_3$  in El Hierro samples is largely confined within 0.04 and 0.08 with the exception of two low ratios (0.01-0.02), again for the upper El Golfo Volcano samples (Figure 4.12c). Excluding these two outliers, Tiñor Volcano rocks appear to show generally lower values than El Golfo Volcano and Rift Volcanism volcanics, although this distinction may be rather subtle.

Figure 4.12e shows the variation of the Zr/Nb ratio with stratigraphy. In this case, there appears to be an overall systematic decrease in this incompatible element ratio from

the oldest Tiñor Volcano samples to the upper El Golfo Volcano sequence, with the exception of the benmoreite and trachyte samples that are shifted to higher values. Rift Volcanism samples that post-date the Las Playas landslide show relatively high Zr/Nb ratios similar to those of the upper Tiñor Volcano and lower El Golfo Volcano samples.

The normative mineralogy (CIPW norm) of all El Hierro samples was obtained, as in Chapter 3, with the  $\text{Fe}^{3+}/\text{Fe}^{2+}$  ratio determined using the approach of *Kress and Carmichael* [1988] assuming an oxygen fugacity of QFM+1 [cf. *Gurenko et al.*, 1996; *Klügel et al.*, 2000]. All El Hierro rocks are moderately to strongly silica-undersaturated, with normative nepheline values between 0.71 and 15.23 wt% (Figure 4.12f). There is no apparent systematic variation in normative nepheline throughout the Tiñor Volcano and El Golfo Volcano sequences, with a large range of values uncorrelated with stratigraphic position. However, the youngest Rift Volcanism samples mark a sudden decrease in normative nepheline, followed by a progressive increase with stratigraphic level.

#### 4.4.3 Mineral Chemistry

The composition of largely euhedral and unresorbed phenocrysts of olivine, clinopyroxene and plagioclase were determined for several Rift Volcanism samples and one Tiñor Volcano sample (EH3). As outlined in Chapter 3, such data are required to perform thermobarometric calculations and can directly provide insights into magma ascent and storage processes. Figure 4.13 presents ternary diagrams of clinopyroxene and plagioclase components as well as examples of core-to-rim chemical profiles in clinopyroxene and olivine crystals from representative sample EH7. The range of values spanned by the Y-axes in Figure 4.13c and d were chosen as to encompass the variation from the full El Hierro dataset. Here, we briefly outline the main chemical features of the analysed phenocrysts; graphs for the whole dataset, graphs for individual samples and full data tables are documented in the appendices D and F.

The overall compositional range of olivine (22 samples, 95 crystals, 886 EMP analyses) is  $\text{Fo}_{66-91}$ , although most samples contain  $\text{Fo}_{78-81}$  olivine. Except for six samples (EH13, EH15-17, EH26 and EH29) that host  $\text{Fo}_{72-77}$  olivines, low forsterite contents were generally restrained to outer rim analyses; e.g. only rims show compositions  $<\text{Fo}_{72}$ . Magnesium-rich olivine ( $\text{Fo}_{85-91}$ ) was found in samples EH5 and EH18, in which it is the only phenocryst phase and occurs as numerous small crystals ( $<2$  mm). All clinopyroxene phenocrysts analysed (22 samples, 127 crystals, 1871 EMP analyses) are diopsidic augites, with a limited compositional range of  $\text{Wo}_{44-52}\text{En}_{30-45}\text{Fs}_{9-17}$  (Figure 4.13a). The magnesium

number ( $Mg\# = \text{molar } Mg/(Mg+Fe^{\text{total}})$ ) of clinopyroxene varies from 63 to 83 overall; however, the range 75-80 encompasses most of the data and lower values largely correspond to outer rim analyses (e.g. Figure 4.13c, see also Appendix D). Even though relatively few plagioclase crystals were investigated (5 samples, 9 crystals, 81 EMP analyses), the compositional range obtained is larger than for clinopyroxene and spans the fields of labradorite and bytownite ( $An_{54-75}Ab_{24-43}Or_{1-8}$ , Figure 4.13b) [cf. *Klein and Hurlbut Jr.*, 1993].

Very few clinopyroxene crystals selected for analysis display pronounced core-to-rim chemical zoning, resulting in generally flat chemical profiles. The same is true for olivine crystals that have mostly compositionally homogeneous interiors (e.g. Figure 4.13c, d, see also Appendix D). There are, however, several exceptions to this general rule; in e.g. samples EH19 and EH29, at least two populations of clinopyroxene and olivine crystals are present, one of which shows reverse zoning. In sample EH13, clinopyroxene crystals indicate at least one normal and one reverse zoning event, while  $Fo_{76}$  olivine only shows weak normal zoning (see Appendix D). Remarkably, however, most samples (17 out of 22) show steep normal Fe-Mg zoning in both clinopyroxene and olivine, which is also accompanied by zoning in Si, Ti, Al, Ca, Na (clinopyroxene) and Si, Mn, Ca, Ni (olivine), in the outermost 20-40  $\mu m$  of the crystals only (e.g. Figure 4.13c, d, see also Appendix D).

#### 4.4.4 Thermobarometry

Whole-rock, fused groundmass and mineral chemistry data, coupled with the thermobarometric formulations of *Putirka et al.* [1996], may be used again in this chapter, this time, to investigate the pressure and temperature conditions of magma storage during the latest phase of volcanism of El Hierro, the Rift volcanism.

Equilibrium tests are useful and necessary to verify the suitability of the clinopyroxene-melt and olivine-melt pairs before performing thermobarometric calculations (Chapter 3). For El Hierro samples, the clinopyroxene-melt equilibrium tests indicate that: 1) interiors of clinopyroxenes appear in equilibrium with the ‘melt’ composition (i.e. the chemistry of the whole-rock and/or fused groundmass, Figure 4.14a to f); 2) a significant proportion (up to 66%) of outer rim analyses returned compositions incompatible (in disequilibrium) with the melt chemistry (Figure 4.14a to f); and 3) for most ankaramites, the fused groundmass composition seems to be more appropriate than

the whole-rock composition to represent the liquid that was in equilibrium with the clinopyroxenes (Figure 4.14e, f).

In turn, Figure 4.15 shows that olivine interiors, too, appear in satisfactory equilibrium with the melt, although less so than for clinopyroxene. Again, crystal rims yield a comparatively poorer fit with the predicted magnesium number than olivine interiors, although the contrast is not pronounced here. Moreover, fused groundmass is once more revealed as the melt's most suitable equivalent for ankaramitic samples (Figure 4.15c, d).

The results of our thermobarometry analysis are listed in Table 4.5. Thermobarometric calculations, using the outermost phenocryst composition in equilibrium with the corresponding melt, indicate that the 91 clinopyroxene-melt pairs fit for interpretation last equilibrated at pressures and temperatures ranging from 0-1390 MPa (mean=850 MPa; standard deviation ( $\sigma$ )=260 MPa) and 1100-1260 °C (Figure 4.16a, b). There is a complete overlap in calculated pressures and temperatures between the basaltic and ankaramitic samples, although pressure estimates >1000 MPa were all obtained from the latter.

Pressure and temperature estimates of the 'bulk crystallisation', obtained by averaging results from all analyses that yield equilibrium within a crystal, return slightly narrower P-T ranges than those of the last equilibrium crystallisation. Most notably, some crystals from samples EH4 and EH9, which appear to have last equilibrated at low pressures, show higher bulk crystallisation pressures; i.e. in this case, no pressure estimates approach 0 MPa. Indeed, bulk crystallisation P-T ranges are 340-1360 MPa (mean=930 MPa;  $\sigma$ =200 MPa) and 1110-1250 °C (Figure 4.16c, d, Table 4.5).

In general, crystallisation temperatures calculated for olivine are comparable to those of clinopyroxene, though overall slightly higher (Figure 4.16e). However, olivines richer in Mg from samples EH5, EH18 and EH19 return significantly higher temperatures for overall ranges of 1110-1420 °C and 1140-1310 °C, using the thermometers of *Beattie* [1993] and *Putirka* [1997], respectively (see also Table 4.5).

#### 4.4.5 Magma Density Calculations

Using the same procedure as for Teno magmas, we used the PETROLOG computer program [*Danyushevsky*, 2001] to estimate the density of El Hierro magmas. Densities

were calculated on an anhydrous basis, with  $f_{O_2}=QFM+1$ ,  $P=900$  MPa and  $T=\text{liquidus}$  temperature (calculated with PETROLOG). For samples with  $<10$  vol. % olivine + clinopyroxene, the density of the melt (with composition=whole rock) is considered a fair approximation of the magma density. For samples with  $>10$  vol. % olivine + clinopyroxene, the magma density is calculated using a melt density extrapolated from the sample's fused groundmass composition, if available, and the phenocryst proportions of Table 4.2 ( $\rho_{\text{olivine}}=3.4$  g/cm<sup>3</sup> ( $\sim\text{Fo}_{80}$ ) and  $\rho_{\text{cpx}}=3.2$  g/cm<sup>3</sup>). Where groundmass compositions were not obtained for a particular sample, a melt density of 2.75 g/cm<sup>3</sup> (average from all fused groundmass samples) was used. Plagioclase (due to its density nearly equal to melt density), Fe-Ti oxide and amphibole (due to their small abundances) are considered negligible in these calculations.

Like at Teno, results indicate that El Hierro ankaramitic magmas ( $\rho=2.93\pm0.07$  g/cm<sup>3</sup>) are substantially more dense than magmas that are aphyric ( $\rho=2.66\pm0.03$  g/cm<sup>3</sup>) or basaltic ( $\rho=2.79\pm0.08$  g/cm<sup>3</sup>). The lowest magma densities were obtained from the intermediate-to-felsic samples EH21 and CIHI02 ( $\rho=2.45\pm0.03$  g/cm<sup>3</sup>).

## 4.5 Discussion

The key results of our El Hierro study may be recapitulated as follows: (1) several eruptive vents as well as breccia and pyroclastic deposits, younger but in appearance similar to those seen at the Teno volcano, occur at the base of, and directly resting on, the El Golfo landslide scarp; (2) after the eruption of low-density, intermediate-to-felsic pre-collapse products, an anomalously high proportion of post-El Golfo landslide eruptions seems to have involved dense ankaramitic magmas, most notably at the prominent Tanganasoga volcano; (3) a number of geochemical parameters, particularly the Zr/Nb ratio, appear to vary as a function of stratigraphic level; (4) although examples of gradual normal and reverse zoning are observed, most clinopyroxene and olivine crystals have relatively chemically homogeneous interiors, with steep normal zoning only occurring at their outermost rims; and (5) clinopyroxene-melt equilibration has taken place at a considerable range of pressures, with a maximum frequency distribution between 800 and 900 MPa.

### 4.5.1 Implications of Breccias and the Distribution of Post-Collapse Vents

Polymict breccia deposits occur at the base of both the Las Playas and El Golfo landslide scarps and, in the case of the latter, were found interbedded with fresh juvenile pyroclastics. Even though emphasis was not given to these deposits during our El Hierro

field work, their striking resemblance to the breccias and pyroclastic rocks observed at Teno's major angular unconformities is noteworthy and suggests equivalent emplacement processes. We note, however, that, in contrast to Teno, El Hierro breccias were not observed in thick sequences and were not seen directly in contact with the landslide scarp/unconformity. Nevertheless, the occurrence and apparent on-going formation of such deposits in the giant landslide amphitheatres of El Hierro support the view that they largely form through the erosion of the landslide headwall, up to tens of millennia after the flank collapse event. As argued for Teno, breccia deposition may be rapid in episodes and be associated with eruptive activity; however, the combined evidence from La Gomera [Paris *et al.*, 2005b], Teno [Walter and Schmincke, 2002; Chapter 3], Anaga [Walter *et al.*, 2005b] and El Hierro (this chapter) indicates that polymict breccia deposits may largely form through more progressive processes and such debris flow deposits may be a general feature of both modern and palaeo-landslide scars. Although such deposits are intimately linked with landsliding, confusion with true debris avalanche deposits should be avoided. To our knowledge, on-land examples of debris avalanche deposits that are demonstrably syn-collapse and can be linked to off-shore deposits are scarce in the Canary Islands and may rarely be preserved in the marine environment of island volcanoes in general. A spectacular exception to this is the recently discovered 731 ka debris avalanche in southern Tenerife [Branney *et al.*, 2008].

Within the El Golfo embayment, the steeply-dipping pyroclastic deposits, largely lapilli-tuffs, seem to be derived from nearby, well-preserved vents that are found highly concentrated at the base of, and on, the landslide scarp (Figures 4.1, 4.2) [cf. Carracedo *et al.*, 2001]. After the El Golfo landslide incised into parts of the NE- and NW-rift zones, later eruptions would have been much less likely to occur on the remnants of the ridges because of available fissures at lower altitudes for ascending magma [cf. Lipman *et al.*, 1991]. As a matter of fact, the majority of platform-forming eruptions, most of which (if not all) post-date the landslide, occurred within the El Golfo embayment [cf. Carracedo *et al.*, 2001]. Dyke intrusions propagating through the former rift zone structure would most likely break out at the base of the landslide headwall, resulting in a concentration of post-collapse volcanism within the collapse embayment. The configuration of volcanoes around the world that have been affected by large-scale gravitational collapse is in general agreement with this principle. Indeed, several authors have reported rapid constructional phases following collapse that are generally concentrated in the landslide-source regions; e.g. on the islands of Hawaii (Mauna Loa volcano) [Lipman *et al.*, 1991], Tenerife (Teno



and Teide-Pico Viejo volcanoes) [Walter and Schmincke, 2002; Carracedo *et al.*, 2007; Chapter 3], La Palma (Bejenado volcano) [Carracedo *et al.*, 1999a], Fogo (Pico do Fogo volcano) [Day *et al.*, 1999b], Tahiti-Nui (northern depression) [Hildenbrand *et al.*, 2004], La Gomera (Garajonay embayment) [Paris *et al.*, 2005b] and La Réunion (Piton de la Fournaise volcano) [Oehler *et al.*, 2008].

Historical records of volcanic activity on El Hierro are questionable; however, there is little doubt that an eruption will occur in the foreseeable future. Although an eruption could occur virtually anywhere on the island, the current architecture of the edifice makes the El Golfo embayment the most probable site of such an event, with potential hazards for settlements of Sabinosa and Frontera. The Tanganasoga volcano, certainly the most outstanding example of post-El Golfo landslide eruptions, may be the embryonic expression of the future focus of volcanism on El Hierro.

#### 4.5.2 *Implications of Logs, the Distribution of Ankaramites and Magma Density*

Logging of the El Golfo cliffs, especially at Camino de la Peña, reveals extremely detailed information on the eruptive regime of the pre-El Golfo landslide volcanic edifice. The base of the Peña section indicates that this part of the young El Golfo volcano was characterised by pyroclastic eruptions. Because this volcanic activity took place at low altitudes, interactions between magma and sea water may have increased the explosivity of eruptions. However, the presence of equivalent deposits at much higher altitude in the upper Jinama profile, where a major influence of water would have been unlikely, may instead imply that such abundant fossil cinder cones are a clue for proximity to the main palaeo-rift zone axis.

Carracedo *et al.* [2001] noted the absence of dykes in the upper part of the Peña profile (see also Figure 4.5a) and proposed that this contrast with the lower part of the sequence marked a change towards the centralisation of the activity near the El Golfo volcano summit. However, abundant dykes are exposed in the upper part of both the Jinama and Sabinosa sections and it thus seems that the mature El Golfo volcano was still largely influenced by rift zone eruptions. The lack of dykes in the upper Camino de la Peña may be a function of the locality and orientation of the profile; while the core of the partly destroyed rift may be exposed at the bottom of the cliff, the upper portion of the section may display areas representative of the volcano flank, farther from the rift locus.

One of the most conspicuous features of the pre-collapse volcano is the occurrence of the pale-coloured, intermediate-to-felsic products that can be observed at outcrops along Camino de la Peña and at a distance in the cliffs of El Golfo and Las Playas [see also *Pellicer*, 1977; *Carracedo et al.*, 2001]. The disappearance of such pale-coloured volcanics is marked by the return of more mafic products, at least at the Peña profile. This change in the volcanic regime must have taken place between 176 and 134 ka, which coincides with the timing of the Las Playas landslide bracketed between 176 and 145 ka.

At the island scale, ankaramitic lavas are a non-negligible, yet relatively minor, component of El Hierro volcanics [see also *Pellicer*, 1977]. Indeed, crystal-poor lava types dominate the large-volume pre-collapse volcano and ankaramites are proportionally subdued, except perhaps in the NW, although exposure along Camino de Sabinosa is not conclusive (Figures 4.5, 4.6). In marked contrast, our statistical approach, although not infallible, strongly suggests that post-collapse volcanism has been dominated by eruptions of ankaramitic magmas. Therefore, like at Teno, growth and collapse of the volcano (first the Las Playas landslide, then the El Golfo landslide) appear to have had important repercussions in the plumbing system. The load of the mature El Golfo volcano may have impeded ascent of dense magmas to the surface and thus promoted the formation of shallow magma chambers, where magmas were forced to differentiate. Only the low-density melts produced were able to reach the surface at this point. Then, the rapid displacement of up to a total of some 230 km<sup>3</sup> (volumes of both landslides added) of rock overburden may have permitted numerous eruptions of ankaramitic magmas that had been restrained to crystallise at depth as they were too dense to ascend beneath the volcano. The increased tapping of denser magmas observed at both our case-studies is a physically predicted consequence of volcano destruction [*Pinel and Jaupart*, 2000; 2004; 2005] and we would expect volcanoes around the world to react similarly after a flank collapse event.

### 4.5.3 Implications of Petrological and Geochemical Results

#### 4.5.3.a Magma Ascent Conditions

Thin section observations of El Hierro's Rift Volcanism samples point towards magma ascent conditions slightly different to those proposed for the Teno volcano. Indeed, the comparatively poorly developed clinopyroxene overgrowth rims, coupled with the rarity of acicular apatite (apatite microcrysts frequently show equant habits) and Fe-Ti oxide inclusions within these outer rims, suggest slower final stage growth rates and perhaps less drastic change in pressure, temperature and  $f_{O_2}$  conditions (compare Figures 3.6 and 4.7

and Tables 3.2 and 4.2) [Wyllie *et al.*, 1962; Wass, 1979; Perugini *et al.*, 2003; Humphreys *et al.*, 2006]. This may have been brought about by more progressive magma ascent from the storage zone to the surface. Clinopyroxene outer rims, although here commonly inconspicuous, probably owe their characteristic colour to a higher content in Ti and, perhaps, Fe<sup>3+</sup>, that may have been forced through the passive enrichment of these elements in the melt during extensive olivine and clinopyroxene crystallisation at an earlier stage [cf. Wass, 1979].

Despite inferred slower ascent rates than at Teno, final stage crystallisation of olivine and clinopyroxene phenocrysts in El Hierro lavas was still largely achieved under disequilibrium conditions (Figures 4.14, 4.15). For reasons identical to those advanced in Chapter 3, the outer rims of phenocrysts cannot have formed through diffusion processes and must be crystal growth features (Figure 4.13c, d) [cf. Freer, 1981]. We suggest that this growth may have been once more driven by magma ascent, decompression and associated exsolution of volatiles. The presence of euhedral sector-zoned augites in several samples, especially from the Tanganasoga volcano (Table 4.2), is in agreement with such ascent conditions [Brophy *et al.*, 1999]. The more alkaline nature of El Hierro magmas (compared to Teno) would have been likely to decrease preferential partitioning of CO<sub>2</sub> in the vapour in favour of H<sub>2</sub>O and, hence, for an equivalent pressure drop, increase the effect of decompressional crystallisation and related rim growth [Dixon, 1997].

Timescales of magma transfers and ascent at El Hierro were thus slower than at Teno and may have been comparable to those inferred for historic eruptions of La Palma. Although most of the magma involved in the 1949 eruption of Cumbre Vieja volcano is thought to have ascended rapidly from the mantle, Klügel *et al.* [2000] proposed that early magma intrusions were emplaced within the crust up to 13 years before the event. In the case of the 1971 eruption, final stage magma ascent appears to have begun weeks to months prior to eruption [Klügel *et al.*, 1997]. Warning of an eminent eruption at El Hierro in the form of seismic or other precursors may thus come anytime from years to only hours prior to fissure break out at the surface.

#### 4.5.3.b Fractional Crystallisation and Magma Storage Conditions

Consistent with field observations of intermediate-to-felsic volcanics in the upper El Golfo Volcano Formation, the high SiO<sub>2</sub> and alkali (Figure 4.8), low MgO (Figure 4.9) and high Nb (Figure 4.10) of samples EH21 and CIHI02 indicate that the maximal extent of magmatic differentiation were reached between 261 and 176 ka, while the El Golfo

volcano seem to have been at the apex of its development [see also *Carracedo et al.*, 2001]. Older Tiñor Volcano rocks show the most subtle chemical signatures of crystal fractionation. Although several Rift Volcanism samples, including tephrites and hawaiites, must have experienced non-negligible fractional crystallisation, these young volcanics also appear poorly differentiated compared to upper El Golfo Volcano samples (Figures 4.8, 4.9, 4.10).

Figure 4.9 shows that ferromagnesian minerals play a major role in the differentiation process at El Hierro, as observed by *Carracedo et al.* [2001]. If Teno can be taken as a model, the trends at  $\text{MgO} > 5\text{-}6\text{ wt\%}$  probably mostly relate to olivine and clinopyroxene fractionation/accumulation. The bend at ca.  $5\text{-}6\text{ wt\%}$  MgO could then correlate with the commencement of significant Ti-magnetite fractionation. However, several samples with  $\text{MgO} > 5\text{-}6\text{ wt\%}$  already bear Fe-Ti oxide crystals and a decrease in V (which strongly partitions in magnetite [e.g. *Toplis and Corgne*, 2002]) starting at  $\text{MgO} \sim 9\text{ wt\%}$  suggests that this mineral phase begins to fractionate relatively early, at least in Rift Volcanism magmas. The inflections seen at  $\text{MgO} > 5\text{-}6\text{ wt\%}$  may thus indicate an increase the amount of olivine, clinopyroxene and Fe-Ti oxides removed by fractional crystallisation at this point. Fractionation of plagioclase is hard to identify in El Hierro lavas and probably only took place for low-MgO samples ( $< 3\text{-}4\text{ wt\%}$ ), as suggested by the still low  $\text{Na}_2\text{O}/\text{Al}_2\text{O}_3$  of samples EH1, EH8 and EH16, which are aphyric or plagioclase-phyric. However, plagioclase segregation has most certainly taken place for the upper El Golfo Volcano samples EH21 and CIHI02, which also clearly experienced apatite removal.

Despite scarce thin section evidence for the presence of abundant apatite inclusions in clinopyroxene, fused groundmass separates of El Hierro samples, like those of Teno, are anomalously low in  $\text{P}_2\text{O}_5$ , probably indicating the still important coupling of clinopyroxene and apatite removal during sample preparation. The data points that fall off the liquid line of descent, especially in the  $\text{TiO}_2$  plot, may also reflect limitations of the hand-picking technique in reproducing true  $\text{TiO}_2$  contents of El Hierro liquids. This may have resulted from the small size of Fe-Ti oxide phenocrysts that could not be extracted manually under the stereomicroscope. Note that both the anomalous  $\text{P}_2\text{O}_5$  and  $\text{TiO}_2$  of the fused groundmass samples have very little implications for this work, as these elements do not take part in the thermobarometric calculations (see Chapter 2).

The major and trace element composition of El Hierro samples is thus to a large extent controlled by fractional crystallisation, which, again, probably occurs in magma

reservoirs beneath or within the volcanic edifice. Our equilibrium tests appear to indicate that most clinopyroxene and olivine crystals analysed crystallised at near-equilibrium conditions (at least in terms of Fe-Mg exchange) throughout most of their growth history from host melts that closely correspond to the whole-rocks (for basaltic samples) or groundmass separates (for ankaramitic samples) (Figures 4.13c, 4.14). It thus appears that most of these euhedral crystals are true phenocrysts that formed in the magma in which they were erupted. However, the presence of common subhedral crystals with embayed rims, together with examples of gradual normal, but especially reverse chemical zoning, points towards a significant role of crystal exchange and mixing between magmas of different compositions. It thus seems likely that some of the chemical variability (or even similarity) of El Hierro magmas is inherited from magma mixing processes, in addition to crystal fractionation. The equilibrium tests have the potential to isolate xenocrysts that do not belong in their host magma; for example, samples EH16 and EH19 contain clinopyroxene crystals that crystallised from magmas respectively more mafic and more evolved that were unrelated to the whole-rock or groundmass composition. However, the tests cannot rule out the presence of “antecrysts” (crystals that are cognate to the magma system, but that are not true phenocrysts because they essentially grew in earlier magma (s) rather than the liquid in which they were finally contained) if these formed in a magma compositionally similar to the whole-rock or fused groundmass.

The above argumentation has implications for the origin of the ankaramites: because most crystals are in chemical equilibrium with the fused groundmass, it seems most likely that the ankaramites represent liquid-dominated (framework) accumulates, where crystals are in suspension in a melt (e.g. perhaps in the lower part of a sill-like magma reservoir). Alternatively, ankaramitic magmas may be filtered residua from which a crystal-poor magma has escaped. A third possibility is that ankaramites are mixed magmas, which aggregated several crystal populations from originally chemically similar magma batches. In any case, it appears implausible that these magmas are solid-dominated cumulates that would have been disrupted by unrelated ascending magma batches. If this would be true, glomerocrysts may be expected to be plentiful and show cumulate textures, which is the neither case for El Hierro nor for Teno. Moreover, in such a context, widespread apparent equilibrium between melt and crystals would be too fortuitous and highly unlikely.

In this perspective, the thermobarometric results indicate that El Hierro's mafic alkalic Rift Volcanism magmas crystallised (and probably also fractionated) clinopyroxene, but probably also olivine and Fe-Ti oxides as well, at upper mantle depths, mostly between 15 and 45 km below sea level, as implied by the considerable pressure range retrieved. As the apparently fourth liquidus phase for most El Hierro magmas, it is unclear at which point/depth plagioclase crystallisation starts [cf. *Hoernle and Schmincke, 1993b; Thirlwall et al., 2000*], but petrographic textures suggest it may mostly occur in late-stage magma ascent or temporal shallow storage. Again, we imagine a magma plumbing architecture made of a plexus of largely interconnected sills and dykes, similar to that proposed for Cumbre Vieja volcano on La Palma. In contrast to Teno, the histograms of the last equilibrium crystallisation and the bulk crystallisation show significant differences. Indeed, although the main level of magma storage is in both cases between 800 and 900 MPa, many crystals in El Hierro lavas last crystallised under equilibrium at lower pressures, including two near-zero pressure estimates. We propose that this feature adds weight to the petrographic evidence for comparatively slower ascent at El Hierro relative to Teno, at least for some magma batches.

Contrasting with the apparent lack of a well-developed system of shallow magma reservoirs in the Rift Volcanism phase, it appears highly likely that the mature El Golfo volcano was fed by a shallow plumbing system, at least between 261 and 176 ka. Then, intermediate-to-felsic volcanics were erupted, including a possible block and ash flow unit. Considering the timing of the Las Playas debris avalanche and that of the El Golfo landslide (although not well-constrained for the latter), the disappearance of shallow magma reservoirs, coupled with a sharp decrease in the extent of magmatic differentiation between the El Golfo Volcano and Rift Volcanism formations, is once more coincident with large-scale lateral collapse of the volcano. Therefore, giant mass-wasting events are the most plausible cause of the disruption of crustal magma storage systems and, thereby, of environments favourable to magma evolution at El Hierro and other volcanoes such as Teno, but also e.g. Waianae volcano, Hawaii (see also Chapter 6) [*Presley et al., 1997; Amelung and Day, 2002*]. This provides a second mechanism, other than density filtering (see section 4.5.2), for the renewal of eruptions of more mafic magmas after volcano lateral collapses.

### 4.5.3.c Partial Melting and Magmatic Cycles

Low-degree partial melting of upwelling mantle under El Hierro probably begins at pressures  $>3$  GPa, in the garnet stability field, and extends to the garnet-spinel transition zone, between 81 and 93 km depth, where maximum melt fractions may reach  $\sim 2.2$  % [Carracedo *et al.*, 2001]. Although limitations are brought about the lack of isotopic data for El Hierro and by the small sample set for the older phases of volcanism (Tiñor Volcano and El Golfo Volcano), available evidence supports a comparable mantle source for all of the island's volcanic formations. Indeed, Carracedo *et al.* [2001] argued for a relatively simple geochemical evolution of El Hierro, in which the successive eruptive phases relate to the same stationary mantle source. This is in agreement with Figure 4.12, which shows no evidence for more than one magmatic cycle that may have been due to partial melting of successive mantle blobs [cf. Hoernle and Schmincke, 1993a]. However, the somewhat low  $\text{SiO}_2$  and high  $\text{FeO}_t$  of the Rift Volcanism Formation could potentially reflect deeper melting [e.g. Hirose and Kushiro, 1993]. It is thus unlikely that the higher Zr/Nb of some Rift Volcanism lavas with respect to the El Golfo Volcano Formation is inherited from shallower melting [cf. Thirlwall *et al.*, 2000]. Here again, Zr/Nb ratio is thought to vary mostly according to the degree of partial melting and, as discussed in Chapter 3, we may expect the range of values displayed in Figure 4.12e to be produced by low-degree partial melting, from  $\sim 0.1$  to  $\sim 2\%$ .

In this respect, the comparatively high Zr/Nb (Figures 4.10, 4.12e), low REE (Figure 4.11) and low normative nepheline (Figure 4.12f) of the oldest Rift Volcanism samples (which just post-date the Las Playas landslide) are consistent with an increase in melt fractions early in this phase of activity, shortly after catastrophic dismantling of the mature El Golfo volcano. Samples of the upper El Golfo Volcano Formation are probably too felsic to yield faithful Zr/Nb (i.e. representative of melt ratio at time of melting); Ablay *et al.* [1998] and Thirlwall *et al.* [2000] have shown that this incompatible trace element ratio may increase significantly in Tenerife magmas with  $\text{MgO} < 3$  wt% due to fractional crystallisation of titanite [see also Troll *et al.*, 2003]. We thus expect similar effects of elemental fractionation of the Zr/Nb ratio at El Hierro and, although it cannot be shown, unaltered Zr/Nb ratios of EH21 and CIHI02 should probably be close to the value of underlying sample CIHI03 ( $\text{Zr/Nb} \approx 4$ , Figure 4.12e). The Zr/Nb ratio remains high throughout the Rift Volcanism Formation with respect to the El Golfo Volcano Formation; however, normative nepheline appears to rapidly increase again after the Las Playas

landslide. The data are thus compatible with the possibility that a temporal increase in degrees of partial melting, accompanied by a short-lived decrease in silica-undersaturation of the Rift magmas, may be a direct consequence of the large-scale landsliding. However, to fully resolve this puzzling problem at El Hierro, further data (additional 50-100 rock samples) may be required to increase stratigraphic resolution and statistical significance. Moreover, because of the uncertain timing of the El Golfo landslide, it is difficult to determine which of the Las Playas and El Golfo landslides may have had larger effect or if the effects of both events were simply complementary. Considering the much larger size of the El Golfo landslide, we expect more pronounced consequences of this recent collapse.

## 4.6 Conclusions

In summary, we conclude that:

- (1) Several recent pre-historic eruptions (platform-forming), producing cinder cones, lava flows and lapilli-tuff beds, have occurred preferentially at the base of the El Golfo landslide scarp, following a pattern commonly seen at volcanoes that have suffered a lateral flank collapse. Future volcanic activity at El Hierro is most likely to concentrate within the El Golfo embayment, perhaps with the ankaramitic Tanganasoga volcano as a focal point.
- (2) After the eruptions of highly differentiated products at the mature El Golfo volcano, a return to more mafic and denser magmas (largely ankaramites), coinciding in time with the ‘recent’ giant landslides, has characterised the Rift Volcanism phase. While the late El Golfo volcano appears to have had well-developed shallow magma reservoirs, post-collapse Rift magmas have stagnated and crystallised olivine and clinopyroxene (and Fe-Ti oxide?) at upper mantle depth, between about 15 and 45 km below present sea level. Magma ascending from such depth may take as little as a few hours to as much as several years to reach the surface, if it ever does.
- (3) Lavas of the Rift Volcanism Formation, most of which post-date the Las Playas landslide and some of which also post-date the El Golfo landslide, are likely to have been produced by higher mean degree of partial melting of the mantle than the older, pre-collapse El Golfo Volcano Formation lavas.



- 
- (4) We advance that the latest large-scale flank collapses of the El Hierro edifice markedly influenced its ‘recent’ volcanic and magmatic history in controlling the locality and style of post-collapse eruptions, allowing the ascent of very dense magmas rich in olivine and clinopyroxene megacrysts and perhaps even altering melt generation processes in the mantle. As the pre-collapse El Golfo volcano grew to its maximum size, magma differentiation was favoured and the eruption of low-density melts promoted. However, in isolation or put together, the Las Playas and El Golfo landslides appear to have disturbed the shallow volcano-tectonic stress field, causing the disappearance of shallow magma reservoirs and favouring venting at the base of large El Golfo landslide scarp. The subtraction of about 230 km<sup>3</sup>, a surface load superior to the island’s current sub-aerial volume, is likely to have caused a significant depressurisation at depth, which in turn may have permitted the eruptions of ankaramitic magmas through the mobilisation of stagnant melt parcels. Although statistical verification awaits further work on the island, our data are compatible with the possibility that the unloading-related decompression may have induced a temporal increase in partial melting of upper mantle rocks in the early Rift Volcanism phase.



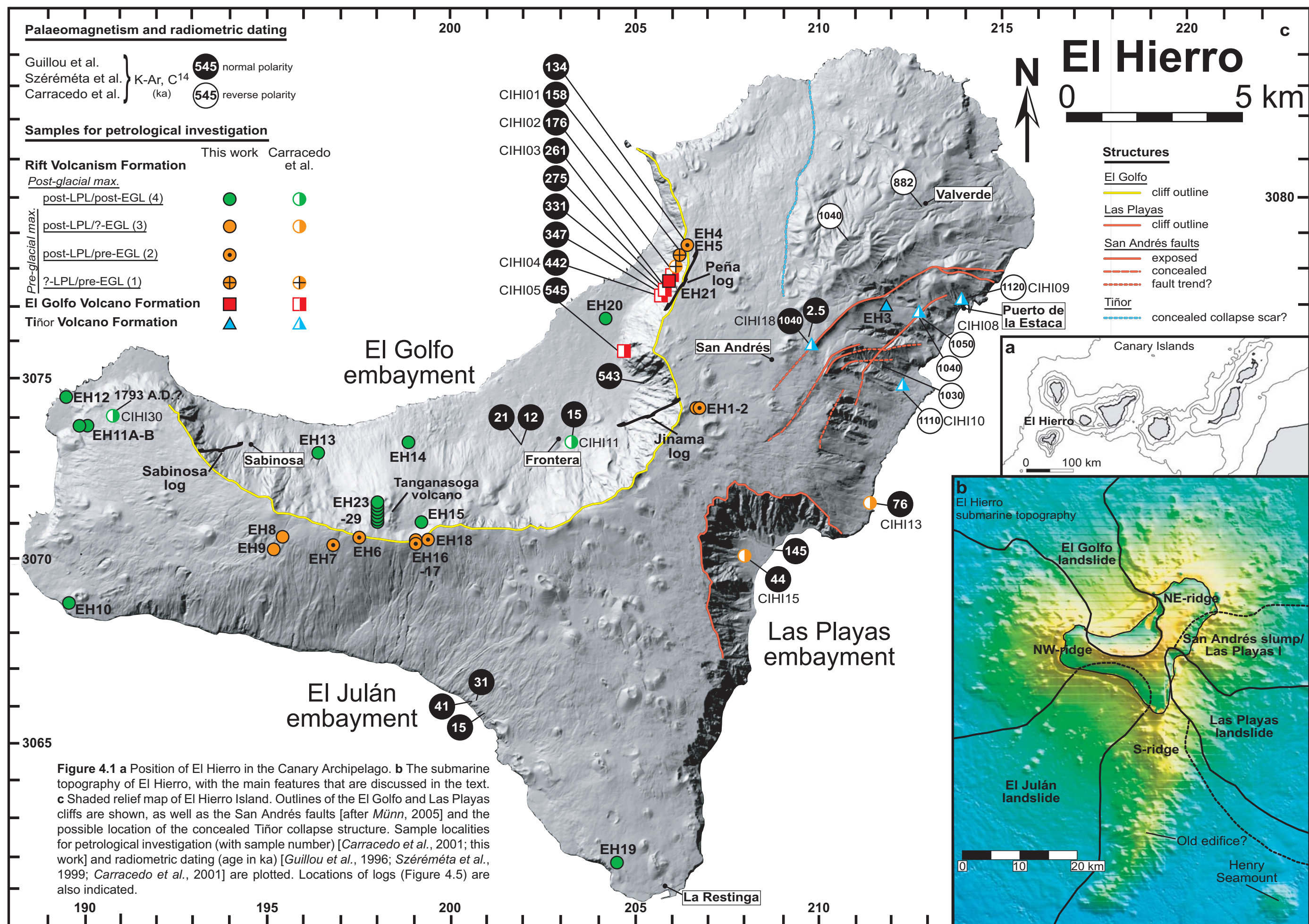




Figure 4.2

# **Geology of El Hierro Island,** after Carracedo *et al.* [2001].

0 SCALE 5 km  
Contour interval 25 m  
(Topography GRAFCAN)  
UTM WGS 84, REGCAN 95

## **SEDIMENTARY FORMATIONS**

	Alluvial fill
	Recent piedmont (4th generation)
	3rd generation
	2nd generation
	1st generation

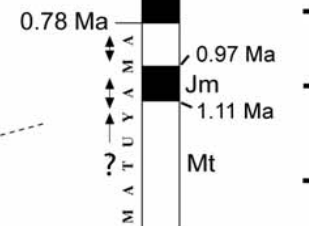
Pre-platform-forming eruptions

## **VOLCANIC FORMATIONS**

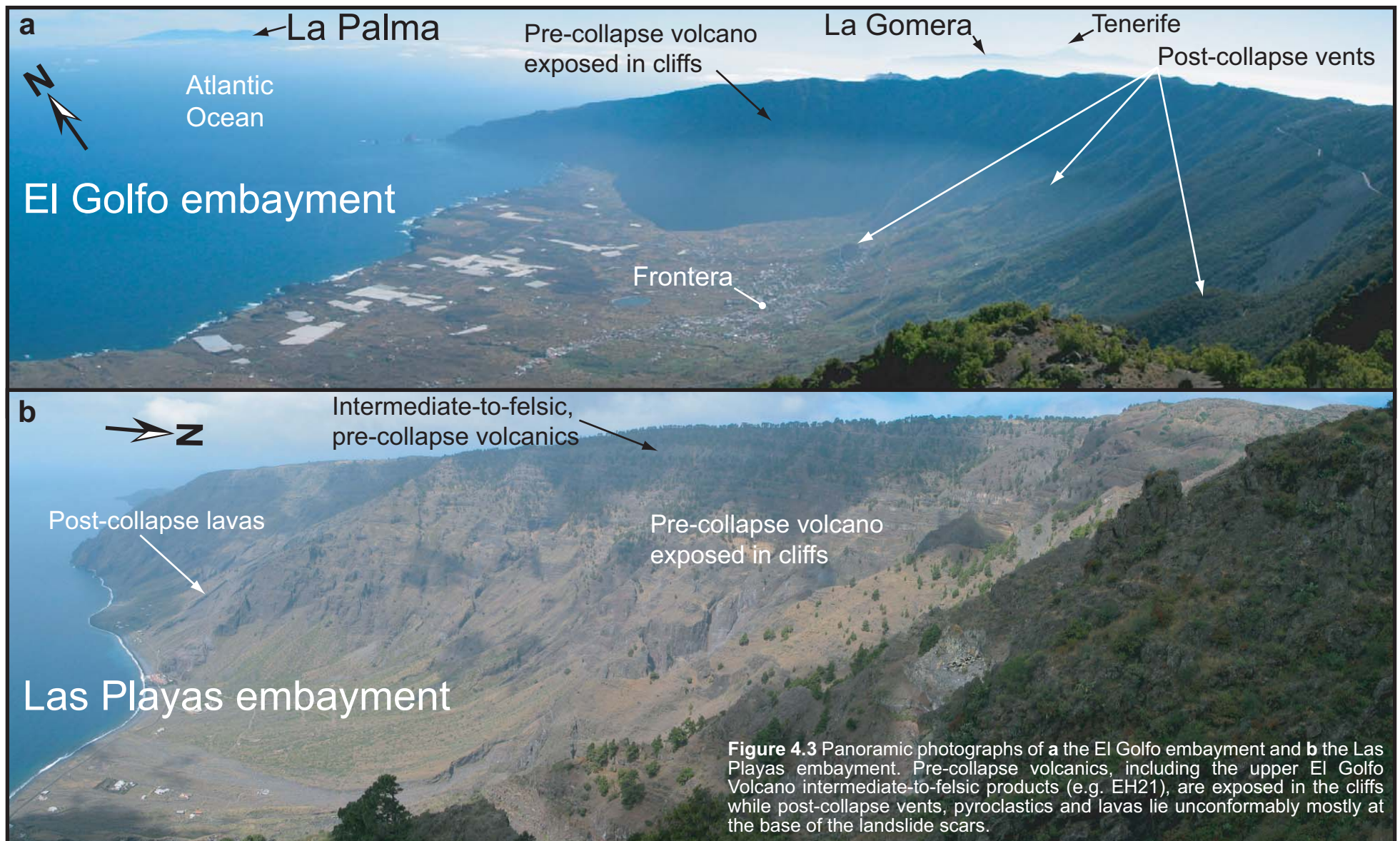
<b>RIFT VOLCANISM</b>	Post-date maximum glacial	Pyroclasts	Platform-forming eruptions
		Lavas	
	Pre-date maximum glacial	Pyroclasts	Cliff-forming eruptions
		Phreatomag. Lavas	
<b>EL GOLFO VOLCANO</b>		Differentiated lavas (trachybasalts, trachytes)	
		Basaltic volcanics	
<b>TIÑOR VOLCANO</b>		Ventejís lavas	
		Pyroclasts	
		Horizontal lavas	
		Dipping lavas	

**SYMBOLS**

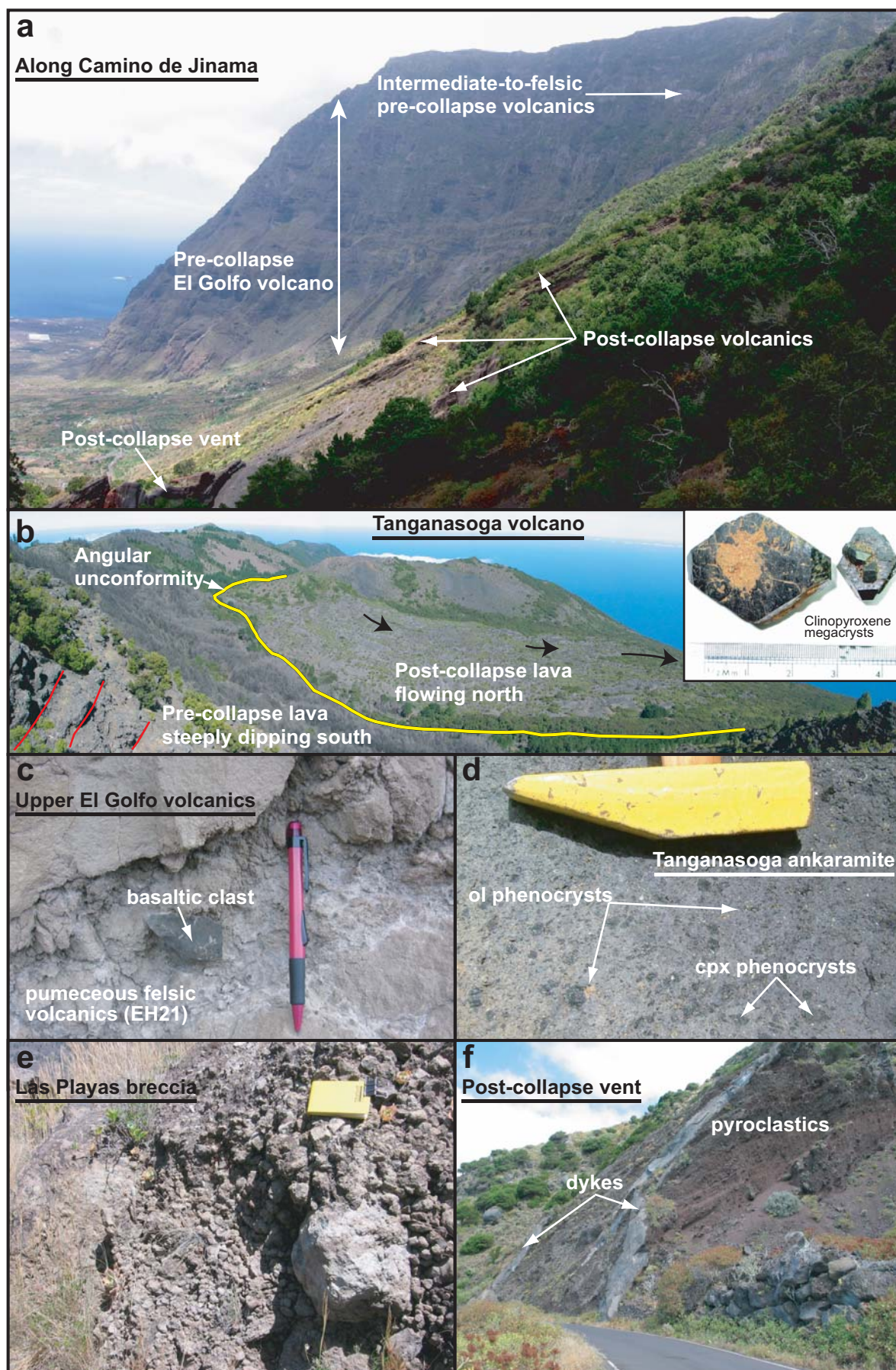
	Levees		outcropping	Fault
	Front of lava flows		buried	
	Direction of flows		Tensional fractures	
	Crater		Basaltic dykes	





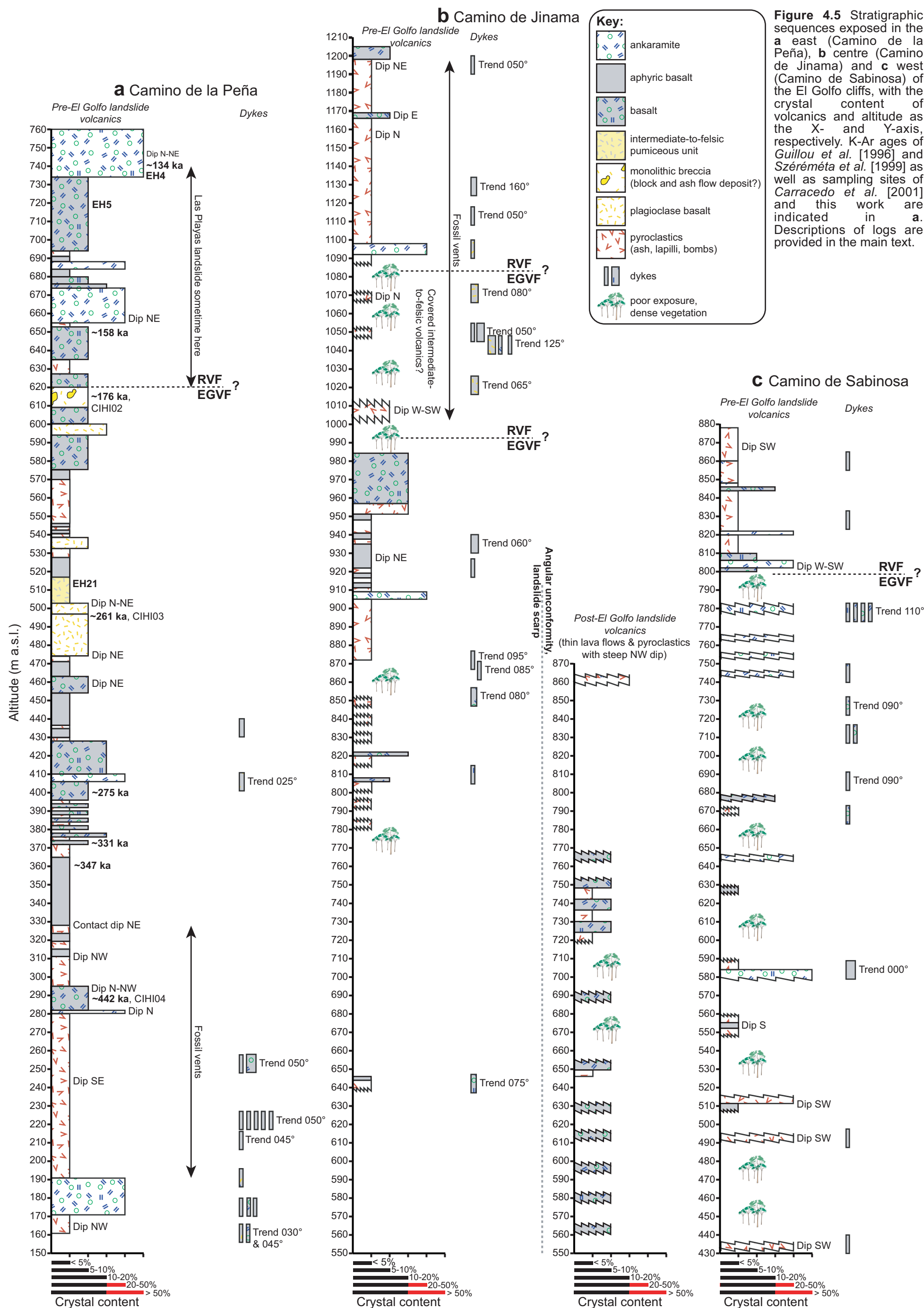






**Figure 4.4** Photographs of field relations. **a** Pre- and post-El Golfo landslide volcanics along Camino de Jinama. **b** The Tanganasoga volcano, which spitted abundant clinopyroxene megacrysts, is the most prominent volcanic construction within the El Golfo embayment. **c** Upper El Golfo Volcano felsic volcanics along Camino de la Peña. **d** Typical example of post-collapse ankaramitic lava. **e** Post-Las Playas landslide breccias. **f** Post-El Golfo landslide vent.





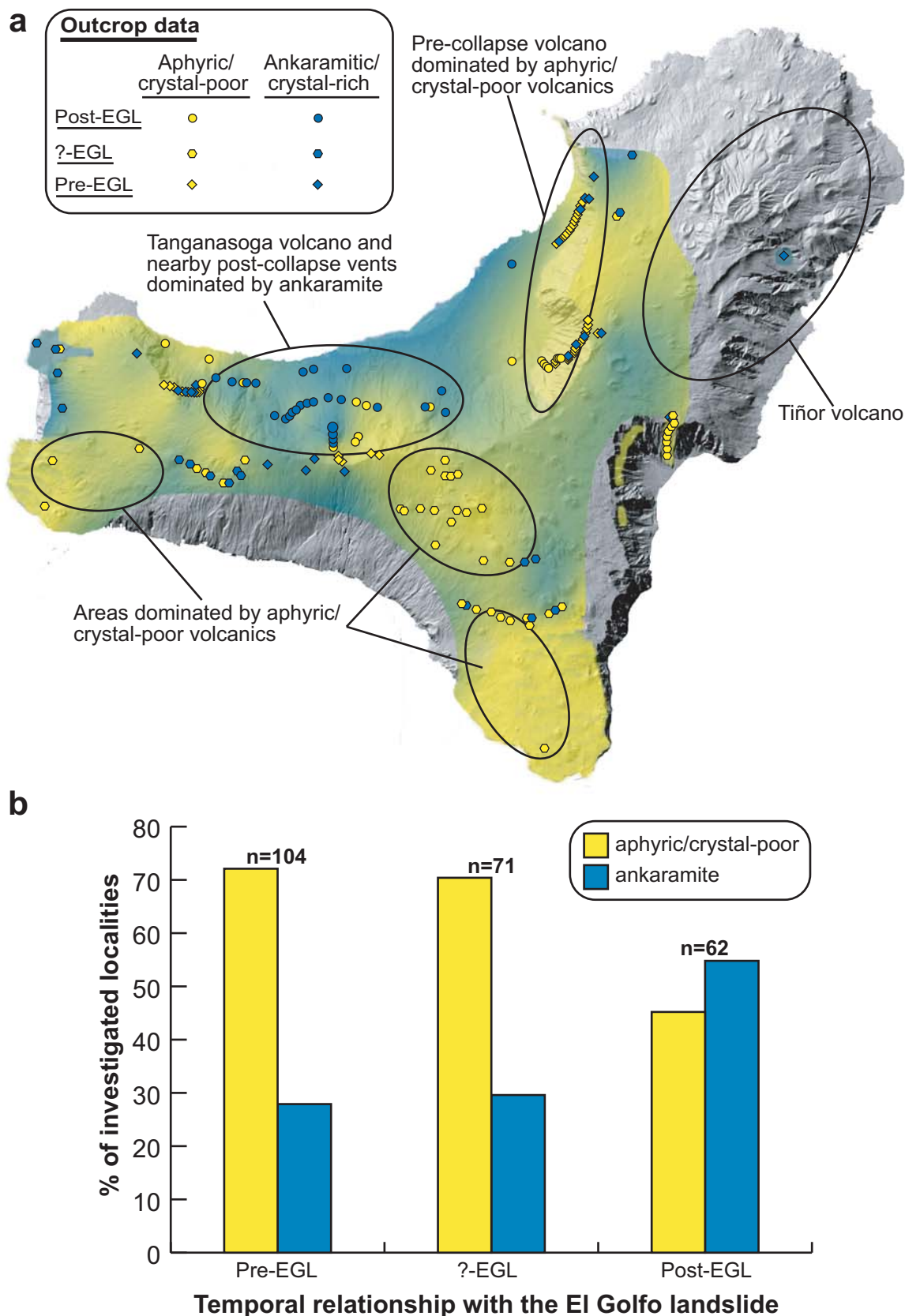


**Figure 4.6 a** Map of El Hierro with the typology of volcanics observed at outcrops [here simplified as either aphyric-to-nearly-aphyric (yellow) or ankaramitic—crystal-rich (blue)] shown as a function of temporal relationship with the El Golfo giant landslide [post-El Golfo landslide (post-EGL, circles), uncertain (?-EGL, hexagons), pre-El Golfo landslide (pre-EGL, diamonds)]. Shades of yellow and blue are based on interpolation of outcrop data points and mapping. **b** Histogram of the distribution of aphyric/crystal-poor and ankaramitic volcanics as a function of timing with respect to the El Golfo landslide. Post-landslide volcanics clearly show a higher proportion of ankaramitic products.



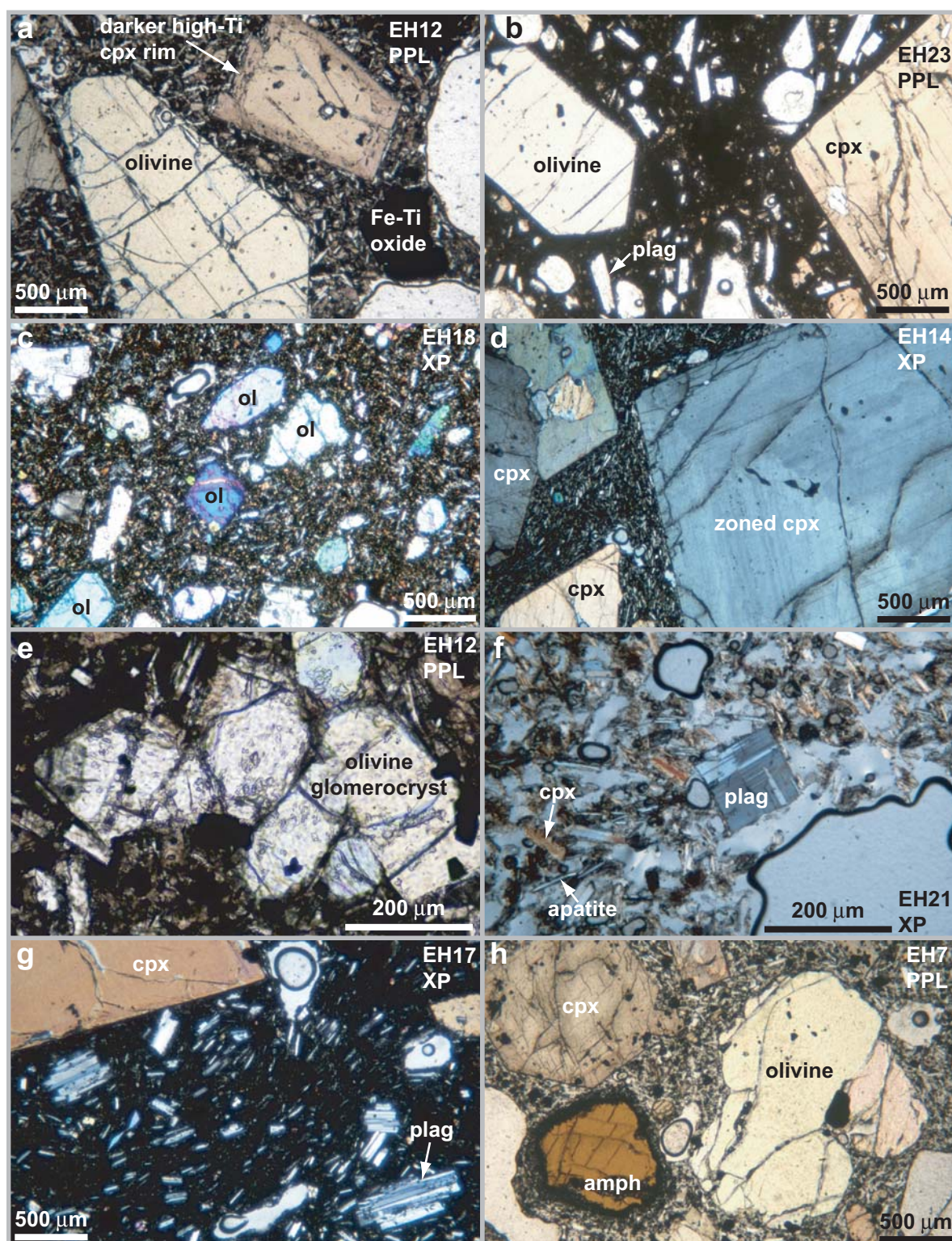
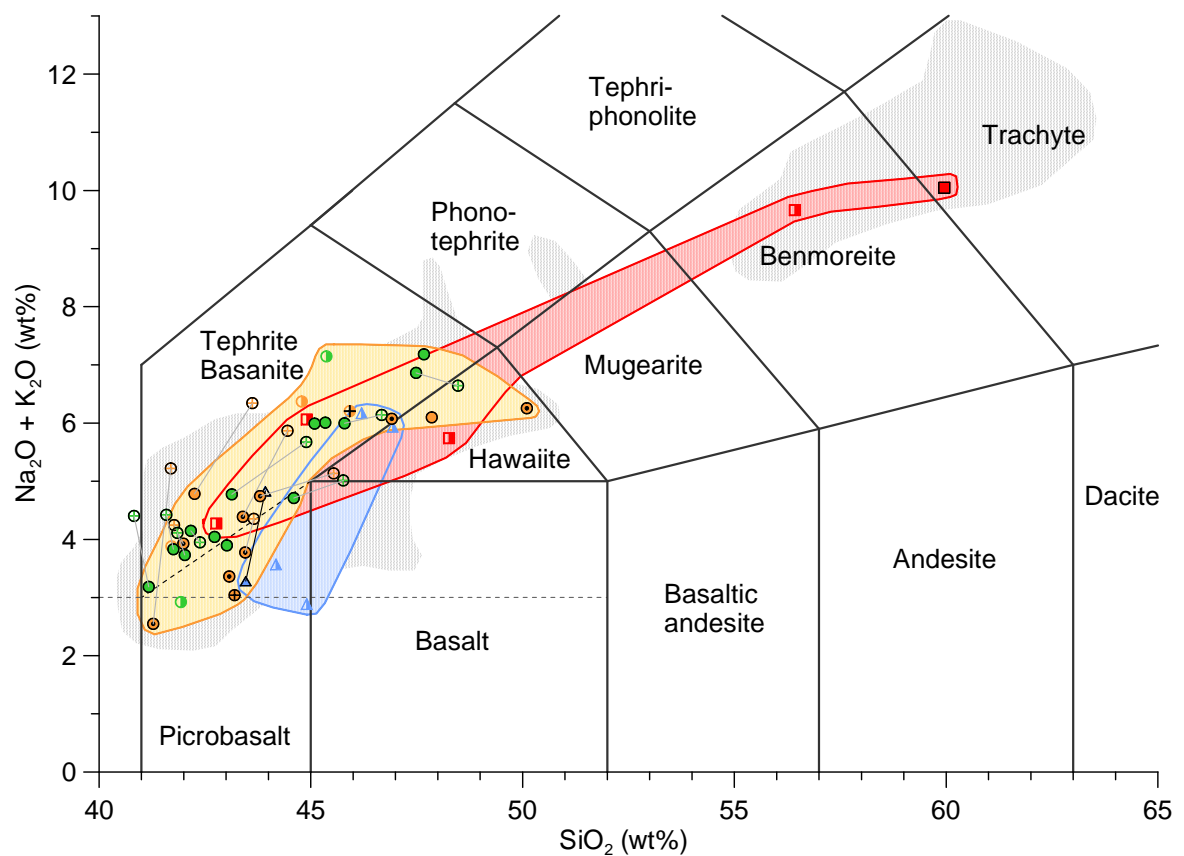


**Figure 4.7** Thin section photomicrographs of El Hierro samples, PPL=plain polarised light, XP=under crossed polars. **a** An example of a clinopyroxene showing a darker colouration at its outer rim. **b** Further examples of euhedral olivine and clinopyroxene crystals; this sample from Tanganasoga volcano also bears plagioclase. **c** Olivine-phyric sample EH18 does not bear cpx. **d** Concentric optical zoning in cpx phenocrysts. **e** Olivine glomerocryst, made of small crystals. **f** Plagioclase-dominated sample EH21 from the upper El Golfo Volcano Formation. **g** Aligned plagioclase crystals and microlites in cryptocrystalline groundmass. **h** EH7 is an example of amphibole-bearing sample. Kaersutite shows characteristic cleavage, dark colour and break-down reaction rim.





	This work		Carracedo
	wr	fg	
<b>RVF</b>			
<u>Post-glacial max</u>			
<u>Pre-glacial max</u>	post-LPL/post-EGL (4)	●	⊕
	post-LPL/?-EGL (3)	●	⊕
	post-LPL/pre-EGL (2)	●	⊕
	?-LPL/pre-EGL (1)	●	⊕
<b>EGVF</b>			
<b>TVF</b>			

**Figure 4.8** Total-Alkali-Silica classification of El Hierro samples. Data from this work and that of Carracedo *et al.* [2001] are plotted: RVF: Rift Volcanism Formation (yellow field) with subdivisions 1, 2, 3, 4 indicated by orange and green circles; EGVF: El Golfo Volcano Formation (red field, red squares); TVF: Tiñor Volcano Formation (blue field, blue triangles). Fused groundmass (fg) compositions are linked to their respective whole-rock (wr) equivalent with a tie-line. Grey fields encompass the data of Hausen [1972] and Pellicer [1979]. The extrapolation of the hawaiiite-basanite division is used to discriminate alkali basalts from basanite [Thirlwall *et al.*, 2000].

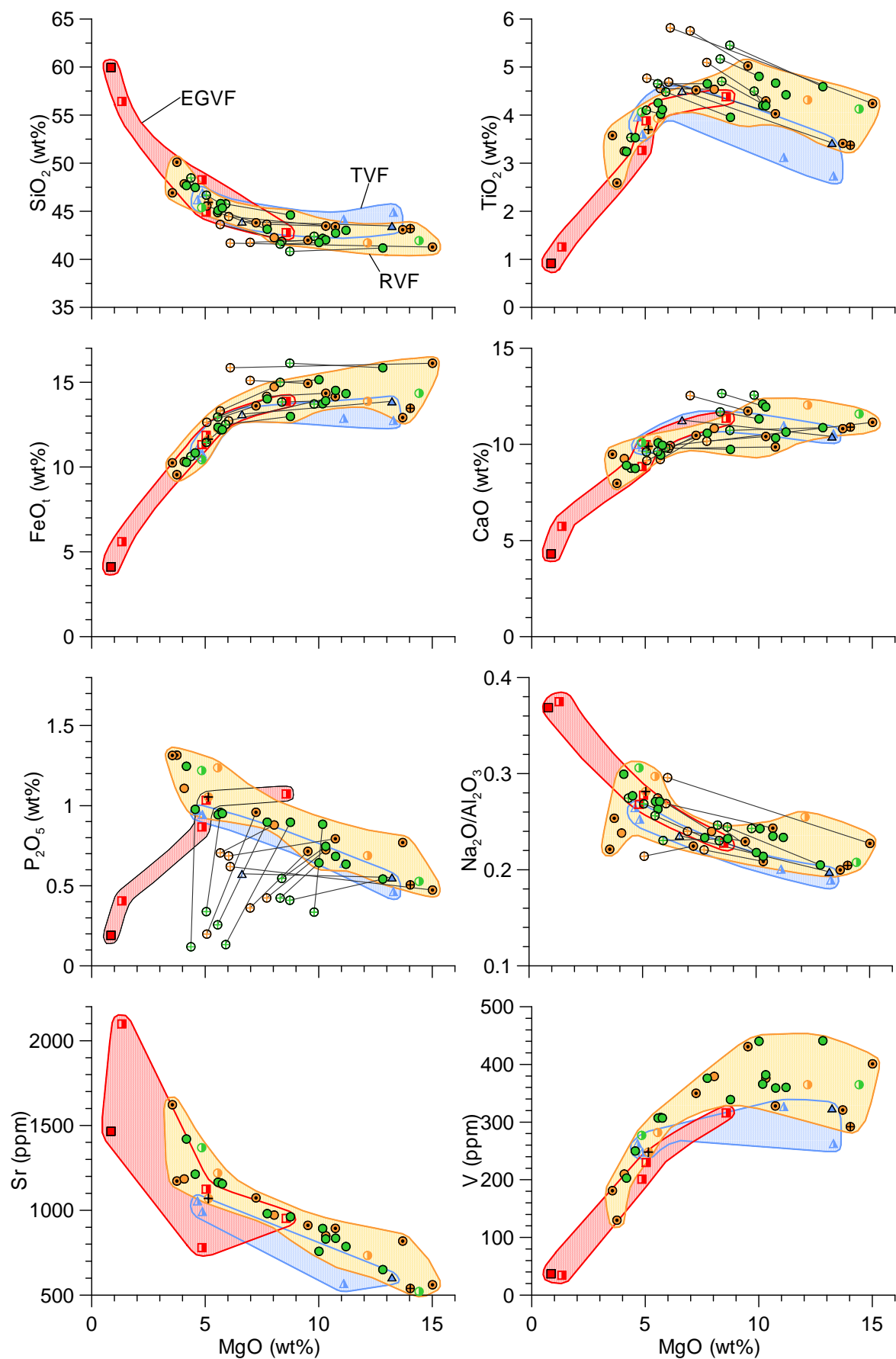


**Figure 4.9** Variation of selected major and trace elements as a function of MgO content for El Hierro samples. Fields, symbols and tie-lines are as in Figure 4.8 (TAS classification). However, data from *Hausen* [1972] and *Pellicer* [1979] were omitted for clarity. See text for details.

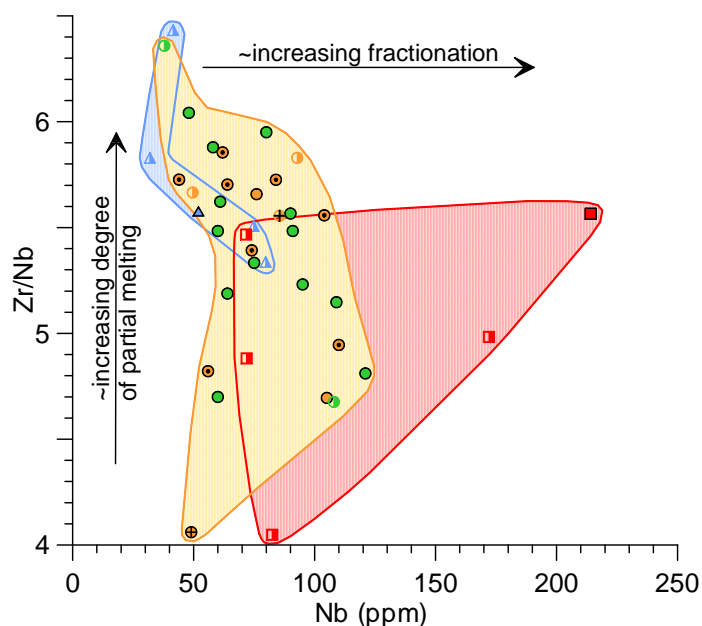


**Figure 4.10** Zr/Nb vs. Nb for El Hierro lavas, symbols as in Figure 4.8. The gross effects of fractional crystallisation and mantle partial melting are shown. The highest degrees of fractionation have been experienced by upper El Golfo Volcano samples, whereas Tiñor Volcano and Rift Volcanism samples seem relatively moderately-to-poorly differentiated. Tiñor Volcano and some Rift Volcanism samples appear to have been produced by comparatively high degrees of partial melting in the mantle.

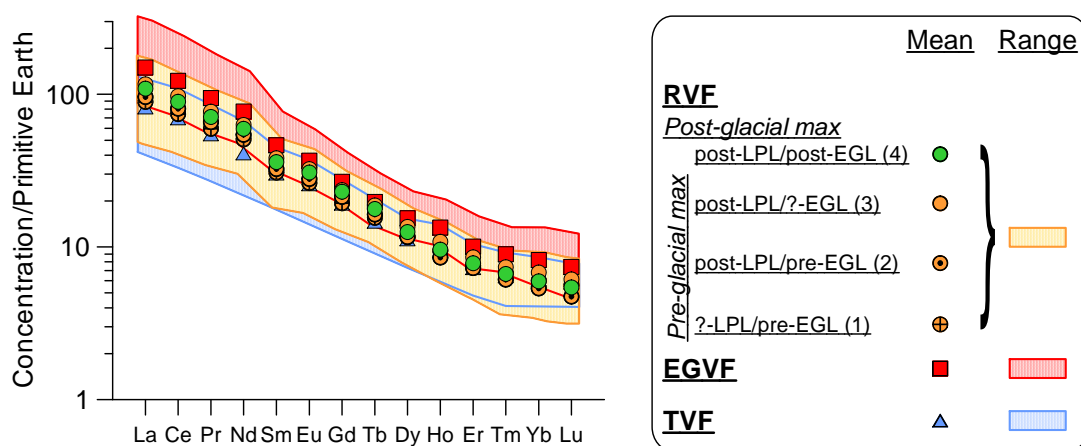


**Figure 4.11** Spider diagram showing normalised (to the Primitive Earth source of *McKenzie and O'Nions* [1991]) abundances of rare earth elements (REE) in El Hierro lavas. Only high precision measurements determined by ICP mass spectrometry [*Carracedo et al.*, 2001; this work] are included. Means are presented for each of the stratigraphic divisions, whereas data ranges are shown as fields for: the TVF: 4 samples; EGVE: 4 samples; RVF: 14 samples. The oldest Tiñor Volcano Formation is most depleted in light REE, followed by the young Rift Volcanism Formation. The El Golfo Volcano Formation show the highest mean concentrations of REE.

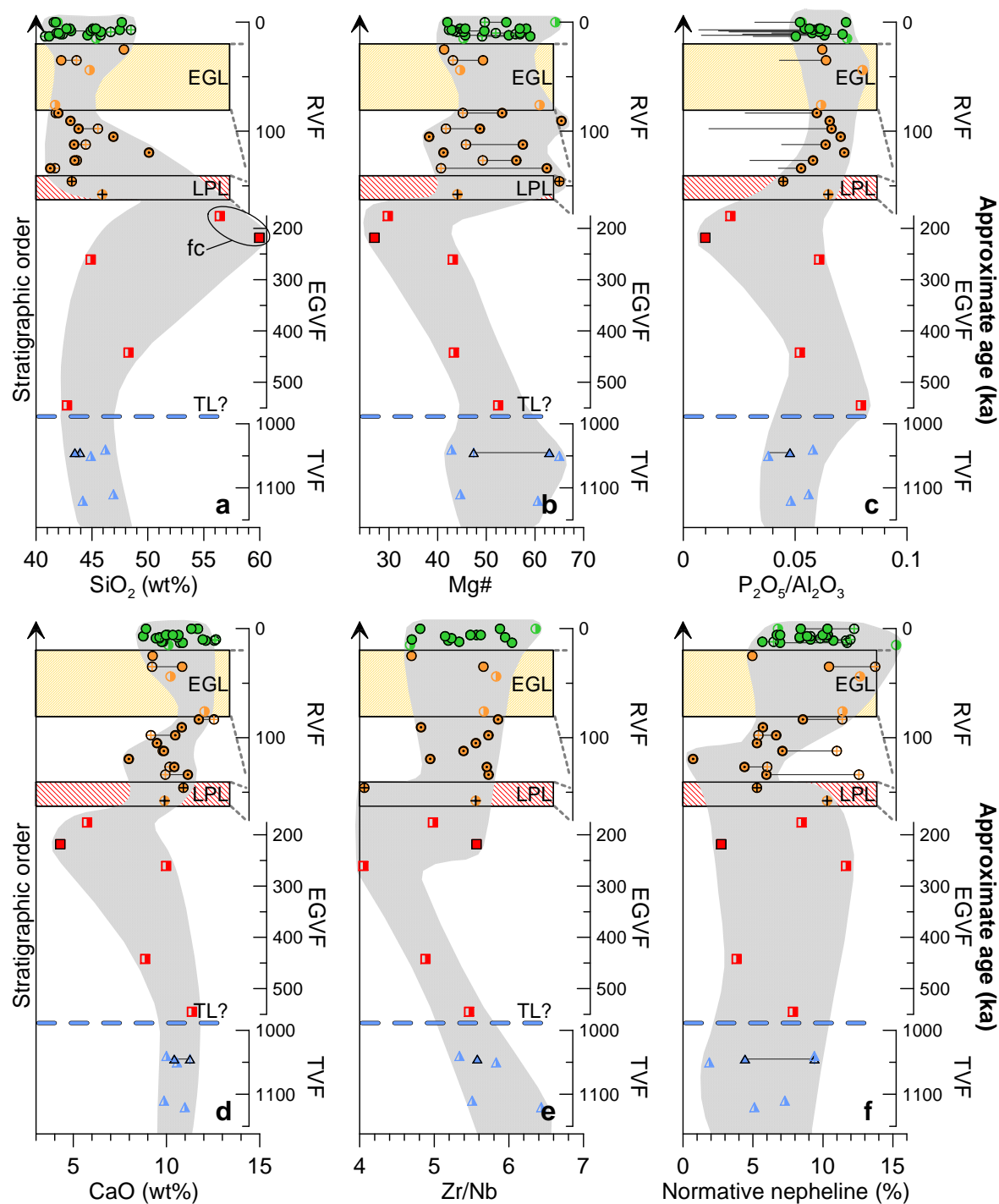


**Figure 4.12** Stratigraphic level (indicated by approximate age) vs. proxy geochemical parameters; **a**  $\text{SiO}_2$ , **b** Mg#, **c**  $\text{P}_2\text{O}_5/\text{Al}_2\text{O}_3$ , **d** CaO **e** Zr/Nb and **f** normative nepheline. Symbols are as in Figure 4.8. Each formation has its own Y-axis. A virtual proportional age was given to samples that were not dated by radiometric techniques based on brackets provided by available ages as well as on stratigraphic constraints. Major (100 ka) and minor (50 ka) tick marks have constant values in all Y-axes. The timing of the Las Playas and El Golfo giant landslides is indicated by rectangle. The effect of extensive fractional crystallisation (fc) is indicated. Artificially  $\text{P}_2\text{O}_5$ -poor fused groundmass samples were omitted in **c**. Trends shown as shaded bands are further explained in the text.

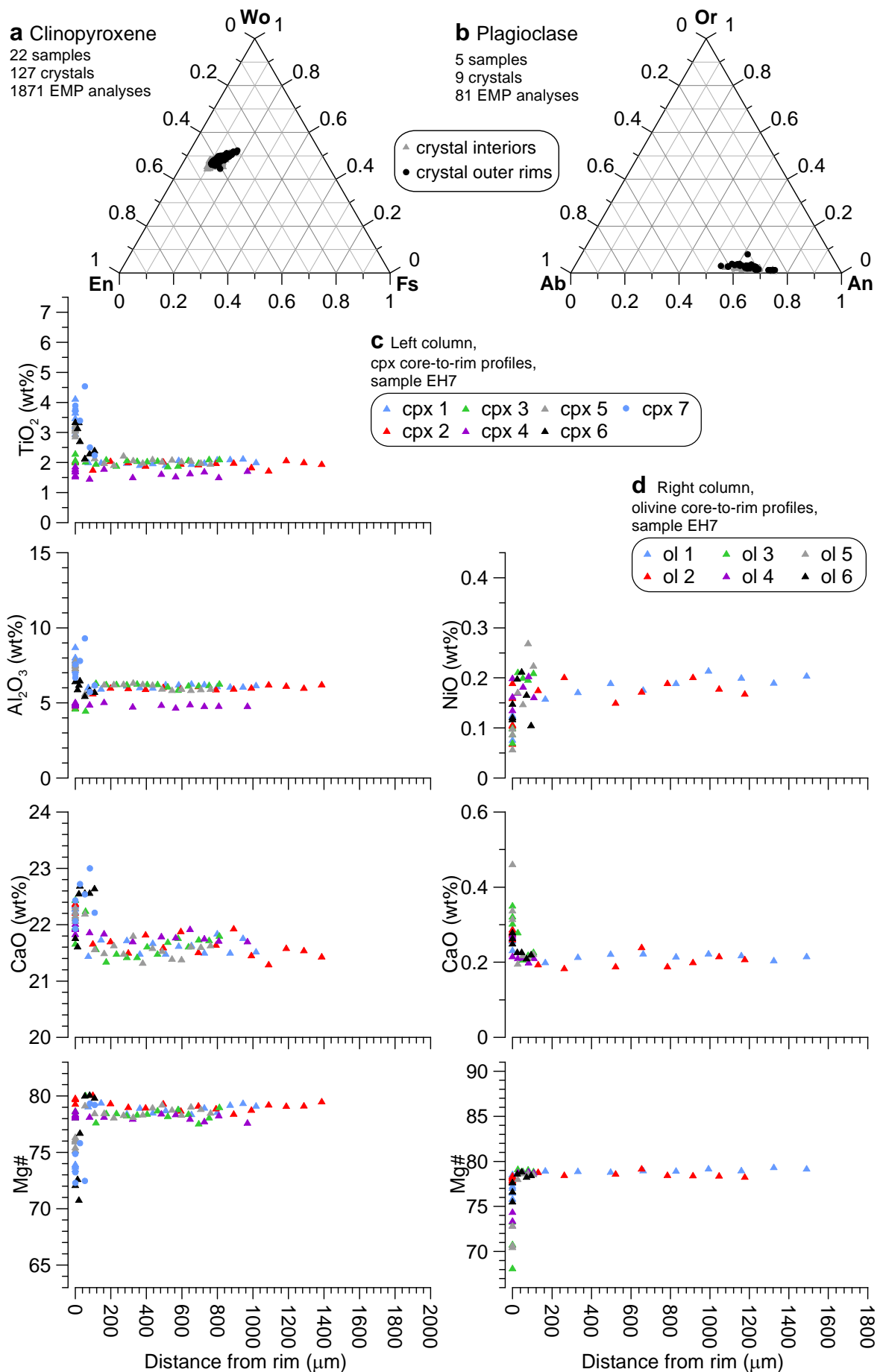


**Figure 4.13** Mineral chemistry of El Hierro samples. **a** Ternary diagram of cpx composition. **b** Ternary diagram of plagioclase composition. **c** Core-to-rim chemical profiles of cpx from representative sample EH7. **d** As **c**, but for olivine crystals. See text for details.

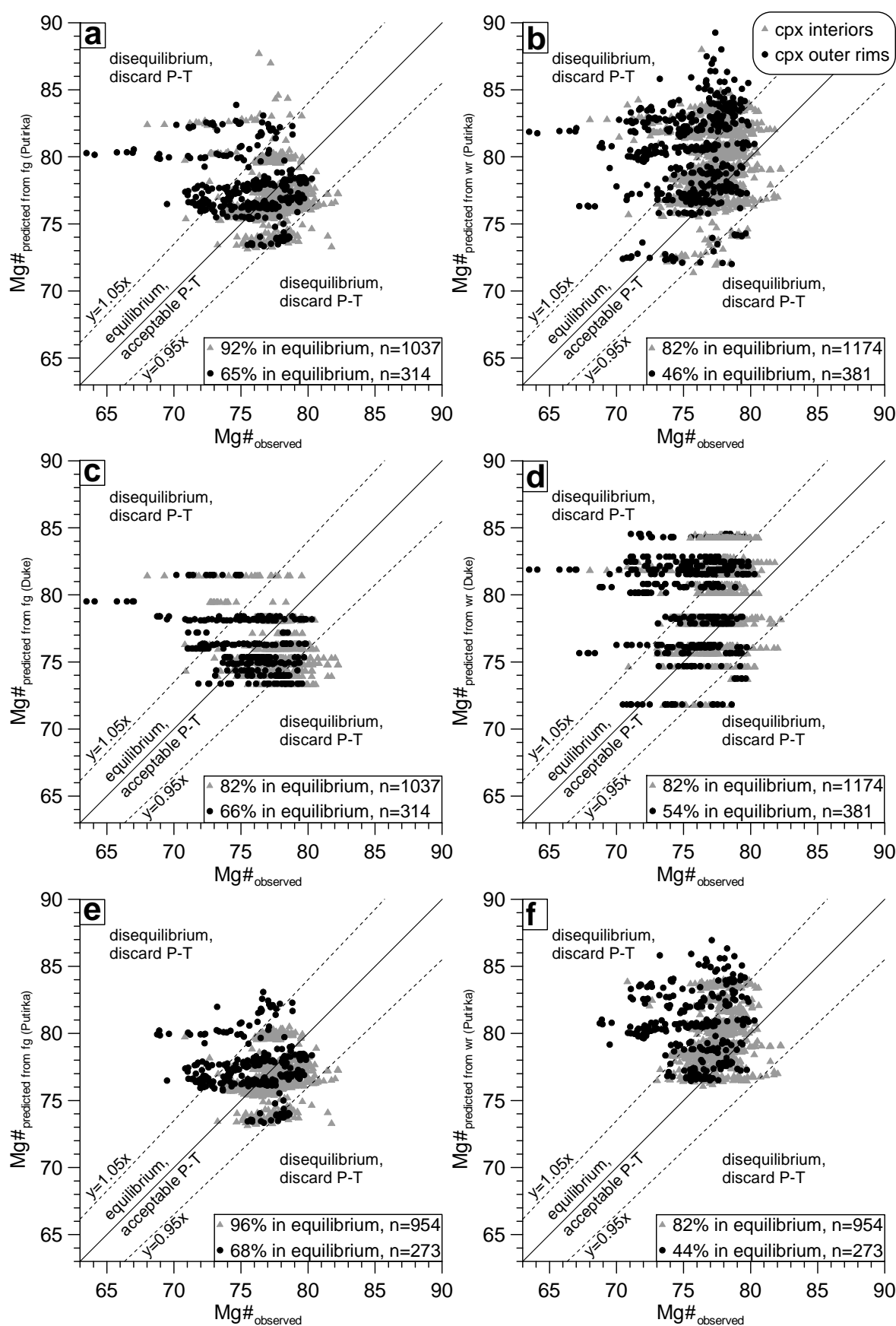


**Figure 4.14** Equilibrium tests for cpx-melt pairs from El Hierro samples. **a** Using *Putirka* [1999]'s formulation, for all samples for which a fused groundmass (fg) composition was obtained. **b** *Putirka* [1999], for all samples for which a whole-rock (wr) composition was obtained. **c** Using *Duke* [1976]'s formulation, all samples for which a fg composition was obtained. **d** *Duke* [1976], all samples for which a wr composition was obtained. **e** *Putirka* [1999], fg composition of ankaramites for which both fg and wr compositions were obtained. **f** *Putirka* [1999], wr composition of ankaramites for which both fg and wr compositions were obtained.

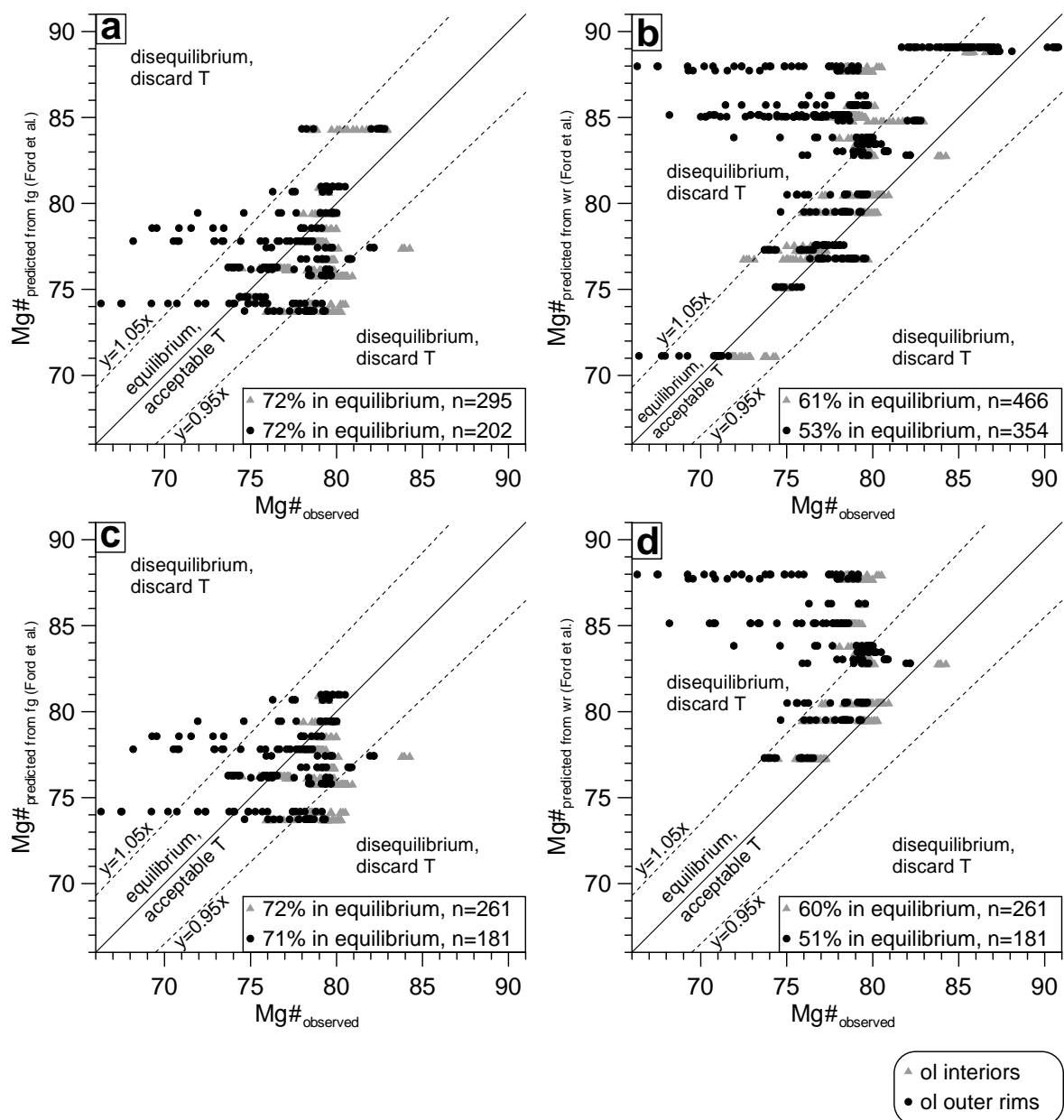


**Figure 4.15** Equilibrium tests, using *Ford et al.* [1983]'s formulations, for olivine-melt pairs from El Hierro samples. **a** For all samples for which a fused groundmass (fg) composition was obtained. **b** For all samples for which a whole-rock (wr) composition was obtained. **c** Using the fg composition of ankaramites for which both fg and wr compositions were obtained. **d** Using the wr composition of ankaramites for which both fg and wr compositions were obtained.

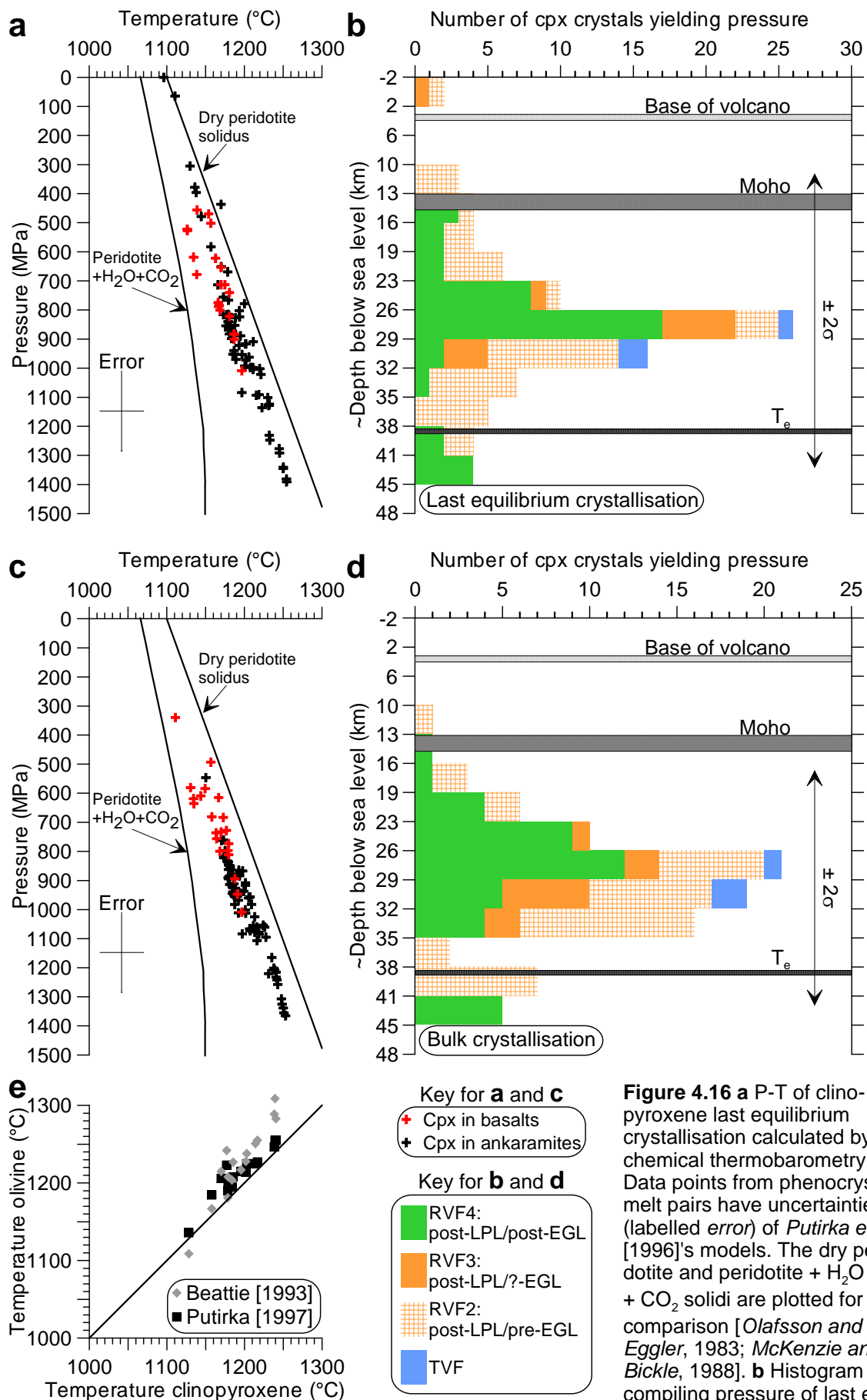


**Figure 4.16** a P-T of clinopyroxene last equilibrium crystallisation calculated by chemical thermobarometry. Data points from phenocryst-melt pairs have uncertainties (labelled error) of Putirka *et al.* [1996]'s models. The dry peridotite and peridotite + H<sub>2</sub>O + CO<sub>2</sub> solidi are plotted for comparison [Olafsson and Eggler, 1983; McKenzie and Bickle, 1988]. b Histogram compiling pressure of last equilibrium crystallisation of cpx. Data are plotted with respect to the pressure Y-axis of a. Equivalent rounded depth estimates are shown relative to present sea level on the Y-axis. Bars of different colours, indicating stratigraphic divisions, are stacked. c As in a, for bulk crystallisation. d As in b, for bulk crystallisation. e T of olivine crystallisation (sample mean) vs. that of cpx.








**Table 4.1:** Stratigraphic formations, sub-divisions and associated samples for El Hierro volcanics. Locality, rock type nomenclature and modal mineralogy are given where known. \*Inferred from descriptions of Carracedo *et al.* [2001].

Formation	Sub-divisions	Sample	Age (ka)	UTM		Altitude (m a.s.l.)	Rock types	
				Easting	Northing		Field name	Chemical name
Rift Volcanism	Post-glacial maximum					250	ankaramite*	picrite
						250	ankaramite	basanite
						250	aphyric basalt	tephrite
						1370	ankaramite	basanite
						1370	basalt	alkali basalt
						1355	basalt	basanite
						1325	basalt	tephrite
						1260	basalt	tephrite
						275	ankaramite	basanite
						240	ankaramite	basanite
						125	basalt	basanite
						115	basalt	basanite
						45	ankaramite	alkali basalt
						35	ankaramite	basanite
						190	aphyric basalt*	tephrite
El Golfo Volcano	Pre-glacial maximum					1105	aphyric basalt	hawaiite
						1025	ankaramite	basanite
						205	–	tephrite
						80	–	basanite
						1415	ankaramite	basanite
						1405	basalt	alkali basalt
						1390	ankaramite	basanite
						1390	plag. Basalt	tephrite
						1270	ankaramite	basanite
						1250	aphyric basalt	hawaiite
						1245	ankaramite	alkali basalt
						735	ankaramite	picrite
						720	basalt	alkali basalt
						650	–	tephrite
Tiñor Volcano	Pre-Tiñor landslide?					600	intermed.-felsic*	benmoreite
						520	intermed.-felsic	trachyte
						500	aphyric basalt*	basanite
						290	aphyric basalt*	hawaiite
						100	–	basanite
						980	aphyric basalt*	tephrite
						450	ankaramite	alkali basalt
						400	–	picrite
						160	aphyric basalt*	hawaiite
						110	–	alkali basalt

**Table 4.2:** Petrography of El Hierro samples. All figures are modal estimates in vol.%.

Sample:			EH1	EH2	EH3	EH4	EH5	EH6	EH7	EH8	EH9	EH10	EH11A	EH11B	EH12	EH13	EH14	EH15	EH16	EH17	EH18	EH19	EH20	EH21	EH23	EH26	EH27	EH28	EH29	
Phenocrysts	Olivine	mode		20	21	20	15	11	17	<1	7	6	15		25	9	5	1	<1	3	15	10	13		17	1	13	8	0.5	
		euhedral																												
		subhedral																												
		anhedral																												
	zoned																													
	Cpx	mode		23	18	25		9	18	<1	28	4	20	<1	20	13	30	5	3	20		2	12		20	6	16	10	6	
euhedral																														
subhedral																														
anhedral																														
concentrically zoned																														
sector-zoned																														
unzoned																														
Plag	mode																<1	1	40	5				5	10	<1	4	<1		
	euhedral																													
	subhedral																													
	anhedral																													
acicular																														
Fe-Ti oxide	mode		2	1	5		<1	3	<1	8		5		5	3	5	3	2	7			2		3	1	2	2	1.5		
	euhedral																													
	subhedral																													
	anhedral																													
Amphibole	mode							2	<1	2		<1																		
Groundmass	Olivine			<1	<1	<1		<1				<1		<1		2	3	5	11	1	<1		<1			1	2	1		
	Cpx	10	16	15	13	43	36	15	20	14	45	21		25	2	3	5	11	3	43	35	15	19	5		5	6	2		
	Plag	55	22	27	25	26	20	30	45	14	23	18		20	38	15	18	22	10	17	9	37	57	10	9	10	8	9		
	Fe-Ti oxide	20	17	18	13	17	28	15	20	14	14	9		5	15	12	14	11	10	26	18	15	5							
	Apatite	5	<1	<1	<1	<1	<1	<1	<1	<1	<1	<1		<1	2	<1	<1	3	<1		<1		5							
	Cryptocrystalline material/devitrified glass	10							15	14	9	12	100		19	30	54	8	41			26	7	10	35	83	49	62	80	
Total phenocrysts			0	45	40	50	15	20	40	1	45	10	40	0	50	25	40	10	45	35	15	12	27	5	50	8	35	20	8	
Total groundmass			100	55	60	50	85	84	60	99	55	90	60	100	50	75	60	90	55	65	85	88	73	95	50	92	65	80	92	
Textures and notes	High birefringence at olivine rims																no	no	no	no		no								
	Overgrowth rim on cpx																no	no	no	no		no								
	Apatite in cpx rims		e/a				e/a	a/e		a/e	e/a	a/e		e								e/a		a		no				
	Fe-Ti oxide in cpx rims																													
	Aligned groundmass plag/vesicles	yes	yes	no	no	no	no	no	yes	no	no	no	yes	no	yes	yes	yes	no	yes	no	no	no	yes	yes	no	no	no	no	yes	
	Glomerocrysts		s	l		l	s	l		l	s (ol)	l		l (ol)	s	l	l/s	l/s	l/s	s	s	l		s/l	l/s	s/l	l/s	s/l		
Replacement textures			plag>o x?	plag>o x?	ox> ol?	cpx> ox	ox> amph	ox> amph	ox> amph								cpx> ox			pl> cpx?						cpx> ox?	plag> ox			
Vesicles																														

**Key:**  abundant, for mode >50%  
 common, for mode >20%, <50%  
 some, for mode >5%, <20%  
 rare, for mode <5%  
 blank: not observed

a=acicular apatite crystals  
e=equant apatite crystals  
r=crystal rims  
c=crystal cores  
l=glomerocrysts formed of crystals of modal phenocryst sizes  
s=glomerocrysts formed of crystals smaller than modal phenocryst sizes

**Table 4.3** Major and trace element chemistry of whole-rock (wr) and fused groundmass (fg) for El Hierro samples. Fused groundmass compositions are mean of ~10 analyses with standard deviation ( $\sigma$ ).

Sample	EH1	EH2			EH3			EH4			EH5	EH6			EH7			EH8	EH9		
	wr	wr	fg	$\sigma$	wr	fg	$\sigma$	wr	fg	$\sigma$	wr	wr	fg	$\sigma$	wr	fg	$\sigma$	wr	wr	fg	$\sigma$
SiO <sub>2</sub>	49.52	43.17	43.43	0.39	43.31	43.45	0.301	40.97	41.35	0.23	42.76	41.70	41.00	0.33	43.21	44.04	0.55	47.08	41.80	43.28	0.96
TiO <sub>2</sub>	2.56	4.27	5.07	0.19	3.41	4.458	0.223	4.21	5.77	0.18	3.34	4.99	5.65	0.34	4.01	4.65	0.12	3.20	4.49	4.52	0.21
Al <sub>2</sub> O <sub>3</sub>	18.06	12.41	14.16	0.14	11.53	14.78	0.142	8.93	14.45	0.17	11.20	11.90	12.79	0.12	12.42	15.42	0.31	17.55	13.63	16.25	0.41
FeO <sub>t</sub>	9.44	14.25	14.08	0.26	13.82	12.97	0.119	16.00	15.72	0.34	13.33	14.82	14.83	0.72	14.08	12.60	0.20	10.15	14.56	13.20	0.42
MnO	0.19	0.18	0.21	0.04	0.19	0.21	0.048	0.18	0.19	0.05	0.17	0.18	0.22	0.06	0.18	0.19	0.04	0.19	0.18	0.21	0.05
MgO	3.71	10.25	7.67	0.14	13.18	6.551	0.053	14.90	6.05	0.13	13.89	9.46	6.86	0.16	10.69	5.98	0.10	4.01	7.95	5.62	0.15
CaO	7.88	10.35	10.11	0.14	10.38	11.14	0.131	11.06	9.85	0.11	10.79	11.65	12.31	0.23	9.82	9.71	0.18	9.11	10.72	9.15	0.14
Na <sub>2</sub> O	4.58	2.59	3.13	0.05	2.28	3.483	0.024	2.03	4.27	0.13	2.29	2.73	3.07	0.19	3.02	4.14	0.13	4.18	3.27	4.46	0.17
K <sub>2</sub> O	1.60	1.16	1.20	0.05	0.99	1.293	0.043	0.50	0.90	0.02	0.72	1.17	1.10	0.08	1.35	1.67	0.08	1.82	1.46	1.83	0.06
P <sub>2</sub> O <sub>5</sub>	1.30	0.72	0.42	0.10	0.55	0.569	0.04	0.47	0.61	0.08	0.50	0.71	0.35	0.15	0.79	0.68	0.11	1.09	0.87	0.70	0.12
Total	98.84	99.35			99.64	98.91		99.25	99.17		98.99	99.31	98.17		99.57	99.08		98.38	98.93	99.21	
LOI	0.54	0.30			0.14			0.19			0.18	0.38			0.22			0.70	0.29		
Co	26	61			67			79			73	61			61			32	55		
Cr	<18	598			776			792			624	422			436			<18	208		
Ni	<2	271			335			411			438	226			265			3	126		
V	130	376			324			401			292	431			328			210	379		
Zn	138	127			110			124			97	126			129			129	136		
Ce	133	107			65			69			60	76			75			150	116		
La	76	19			35			28			32	25			34			53	29		
Nb	110	64			52			44			49	62			74			105	76		
Ga	22	20			18			20			18	23			22			26	23		
Pb	<4	<4			<4			<4			<4	<4			<4			5	<4		
Pr	23	10			12			<4			<4	27			6			20	25		
Rb	27	27			25			14			16	26			33			41	34		
Ba	589	332			226			276			249	372			383			537	453		
Sr	1173	850			605			561			540	912			894			1185	972		
Th	<4	<4			8			5			<4	<4			<4			7	<4		
Y	37	33			26			24			22	32			33			42	37		
Zr	544	365			290			252			199	363			399			493	430		

**Table 4.3** Continued.

Sample	EH10			EH11A			EH11B	EH12			EH13			EH14			EH15			EH16
	wr	fg	$\sigma$	wr	fg	$\sigma$	wr	wr	fg	$\sigma$	wr	fg	$\sigma$	wr	fg	$\sigma$	wr	fg	$\sigma$	wr
SiO <sub>2</sub>	41.66	41.70	0.42	41.54	40.87	0.52	47.07	40.99	40.53	0.62	45.43	45.79	0.57	42.83	44.38	0.75	46.65	48.06	0.97	46.43
TiO <sub>2</sub>	4.16	4.68	0.18	4.78	5.08	0.21	3.20	4.57	5.41	0.23	3.99	4.02	0.17	4.62	4.60	0.26	3.47	3.51	0.22	3.54
Al <sub>2</sub> O <sub>3</sub>	12.85	13.71	0.09	12.25	13.01	0.18	16.90	10.73	13.01	0.18	15.63	16.13	0.19	13.93	15.99	0.26	16.54	17.14	0.31	18.48
FeO <sub>t</sub>	13.79	13.78	0.22	15.06	14.73	0.52	10.14	15.78	16.00	0.68	12.09	11.24	0.15	13.91	12.80	0.71	10.64	10.53	0.72	10.14
MnO	0.18	0.19	0.09	0.17	0.19	0.05	0.20	0.18	0.22	0.05	0.17	0.18	0.07	0.18	0.23	0.04	0.17	0.20	0.05	0.16
MgO	10.22	8.34	0.10	9.96	8.16	0.22	4.12	12.77	8.66	0.25	5.63	4.96	0.11	7.68	5.49	0.08	4.48	4.34	0.10	3.52
CaO	11.84	12.60	0.19	11.27	11.49	0.13	8.79	10.82	10.65	0.18	9.36	9.43	0.09	10.51	9.51	0.15	8.59	8.69	0.13	9.39
Na <sub>2</sub> O	2.75	3.16	0.12	2.67	3.21	0.10	5.06	2.20	3.18	0.12	4.11	4.33	0.12	3.25	4.10	0.18	4.58	4.70	0.19	4.09
K <sub>2</sub> O	0.95	0.94	0.05	1.14	1.14	0.09	2.03	0.97	1.19	0.04	1.84	1.69	0.10	1.49	1.51	0.09	2.16	1.89	0.05	1.92
P <sub>2</sub> O <sub>5</sub>	0.74	0.54	0.11	0.64	0.42	0.15	1.23	0.54	0.41	0.07	0.95	0.33	0.20	0.89	0.25	0.12	0.96	0.12	0.05	1.30
Total	99.14	99.64		99.48	98.28		98.74	99.55	99.27		99.20	98.11		99.29	98.86		98.24	99.16		98.97
LOI	0.15			0.14			0.13	0.15			0.14			0.19			0.28			0.79
Co	58			60			31	72			39			52			33			32
Cr	416			506			<18	692			93			170			42			27
Ni	237			238			2	358			64			143			34			27
V	382			440			203	441			308			376			250			181
Zn	110			123			140	125			127			134			128			116
Ce	75			83			164	83			133			115			177			149
La	27			70			69	29			56			29			59			46
Nb	60			58			121	48			95			80			109			104
Ga	19			18			27	17			26			21			22			21
Pb	<4			<4			<4	7			5			6			5			<4
Pr	8			37			41	11			11			11			25			35
Rb	19			22			49	21			44			32			51			43
Ba	333			292			639	280			528			394			584			611
Sr	831			758			1420	650			1162			981			1213			1622
Th	<4			<4			9	<4			8			<4			6			4
Y	30			34			43	30			39			37			43			41
Zr	282			341			582	290			497			476			561			578

**Table 4.3** Continued.

Sample	<u>EH17</u>			<u>EH18</u>	<u>EH19</u>			<u>EH20</u>			<u>EH21</u>	<u>EH23</u>	<u>EH26</u>	<u>EH28</u>	<u>EH29</u>
	wr	fg	$\sigma$	wr	wr	fg	$\sigma$	wr	fg	$\sigma$	wr	wr	wr	wr	wr
SiO <sub>2</sub>	43.39	45.17	0.53	42.53	41.98	42.20	0.23	44.31	45.45	0.86	59.67	42.49	44.84	42.71	44.93
TiO <sub>2</sub>	4.48	4.73	0.23	3.37	4.18	4.48	0.22	3.93	4.45	0.16	0.91	4.64	4.07	4.39	4.24
Al <sub>2</sub> O <sub>3</sub>	14.33	17.12	0.16	11.61	12.36	12.56	0.10	14.11	16.06	0.19	19.29	12.05	15.31	11.60	15.50
FeO <sub>t</sub>	13.48	12.53	0.25	12.75	13.67	13.65	0.32	12.89	12.42	0.50	4.09	14.43	12.07	14.23	12.30
MnO	0.18	0.25	0.04	0.18	0.18	0.18	0.04	0.17	0.21	0.04	0.24	0.18	0.18	0.17	0.18
MgO	7.17	5.03	0.09	13.53	10.13	9.76	0.19	8.70	5.86	0.08	0.85	10.68	5.69	11.12	5.55
CaO	10.37	9.08	0.10	10.68	12.04	12.51	0.13	9.67	9.75	0.09	4.28	10.28	9.85	10.57	10.04
Na <sub>2</sub> O	3.22	3.66	0.23	2.32	3.00	3.05	0.08	3.28	3.70	0.20	7.11	2.83	4.15	2.71	4.20
K <sub>2</sub> O	1.48	1.43	0.10	1.00	1.13	0.88	0.07	1.40	1.28	0.06	2.89	1.19	1.79	1.16	1.77
P <sub>2</sub> O <sub>5</sub>	0.95	0.20	0.10	0.76	0.88	0.33	0.08	0.89	0.13	0.08	0.19	0.68	0.94	0.63	0.94
Total	99.05	99.20		98.73	99.55	99.60		99.35	99.31		99.52	99.45	98.89	99.29	99.65
LOI	0.55			0.56	0.14			0.27			0.88	0.25	0.21	0.33	0.34
Co	51			69	57			51			37	99	80	98	79
Cr	207			661	432			362			<9	322	49	439	28
Ni	112			417	213			192			–	245	40	264	26
V	350			321	366			339			37	359	307	360	307
Zn	137			106	116			125			149	127	132	126	129
Ce	129			93	113			126			302	83	102	78	101
La	37			113	81			35			149	36	218	103	40
Nb	84			56	64			75			214	61	91	60	90
Ga	21			17	23			23			28	20	24	22	25
Pb	<4			5	<4			6			<4	<4	<1	5	–
Pr	24			21	34			15			30	7	36	18	11
Rb	33			23	23			29			93	25	40	28	40
Ba	445			346	361			397			868	279	479	311	491
Sr	1073			819	893			962			1465	835	1156	787	1166
Th	<4			5	8			<4			23	7	12	5	<4
Y	40			27	31			35			53	31	40	28	39
Zr	481			270	332			400			1191	343	499	329	501

**Table 4.3** ICP-MS rare earth element data in ppm.

Sample	<u>EH2</u>	<u>EH4</u>	<u>EH5</u>	<u>EH8</u>	<u>EH14</u>	<u>EH16</u>	<u>EH18</u>	<u>EH19</u>	<u>EH26</u>
La	48.4	34.2	28.9	76.3	58.4	82.4	46.6	54.5	71.9
Ce	105.1	75.3	63.5	157.5	123.7	173.1	97.1	113.7	152.6
Pr	13.6	10.0	8.3	19.2	16.0	21.8	12.5	14.3	18.8
Nd	54.7	40.9	34.9	73.9	66.8	87.2	51.9	57.4	73.6
Sm	11.0	8.7	7.0	13.5	13.2	15.9	9.8	11.0	13.9
Eu	3.5	2.7	2.3	4.4	4.2	5.2	3.2	3.5	4.5
Gd	9.4	7.6	6.4	11.8	11.3	13.3	8.6	9.7	11.7
Tb	1.4	1.0	1.0	1.7	1.6	1.9	1.2	1.4	1.7
Dy	6.6	5.1	4.8	8.2	7.4	9.0	5.9	6.4	8.0
Ho	1.1	0.9	0.8	1.5	1.3	1.5	1.0	1.1	1.3
Er	2.7	2.1	2.1	3.6	3.2	3.7	2.4	2.5	3.3
Tm	0.4	0.3	0.3	0.5	0.4	0.5	0.3	0.3	0.4
Yb	2.0	1.5	1.6	2.8	2.4	2.7	1.8	1.9	2.5
Lu	0.3	0.2	0.2	0.4	0.3	0.4	0.2	0.3	0.4

Table 4.5 Thermobarometry results for El Hierro samples.

Sample_ crystal	Pressure (P, MPa), calculated depth (z, km b.s.l.) and temperature (T, °C) of clinopyroxene crystallisation						Sample_ crystal	Temperature (T, °C) of olivine crystallisation	
	Bulk P	~z	Last Eq. P	~z	Bulk T	Last Eq. T		T (Beattie)	T (Putirka)
EH2_cpx1	1207	39.1	1126	36.5	1239	1231	EH2_ol1	1283	1255
EH2_cpx2	1257	40.6	909	29.7	1243	1211	EH2_ol2	1283	1254
EH2_cpx3	1242	40.2	1021	33.2	1242	1221	EH2_ol3	1283	1258
EH2_cpx4	1232	39.9	1128	36.6	1241	1232	EH2_ol4	1283	1257
EH2_cpx5	1201	38.9	1002	32.6	1238	1220	—	—	—
EH2_cpx6	1215	39.3	1102	35.7	1241	1230	—	—	—
EH2_cpx7	1165	37.7	1124	36.4	1235	1232	—	—	—
<b>EH2 mean</b>	<b>1224</b>	<b>39.6</b>	<b>1059</b>	<b>34.4</b>	<b>1240</b>	<b>1225</b>	<b>EH2 mean</b>	<b>1283</b>	<b>1255</b>
EH3_cpx1	961	31.3	962	31.4	1206	1206	EH3_ol1	1238	1224
EH3_cpx2	908	29.6	917	29.9	1201	1202	EH3_ol2	1238	1226
EH3_cpx3	867	28.4	823	27.0	1198	1194	EH3_ol3	1238	1223
—	—	—	—	—	—	—	EH3_ol4	1238	1225
<b>EH3 mean</b>	<b>927</b>	<b>30.3</b>	<b>901</b>	<b>29.4</b>	<b>1203</b>	<b>1201</b>	<b>EH3 mean</b>	<b>1238</b>	<b>1225</b>
EH4_cpx1	890	29.1	396	13.5	1179	1138	EH4_ol1	1242	1219
EH4_cpx2	816	26.8	305	10.2	1174	1130	EH4_ol2	1242	1221
EH4_cpx3	914	29.8	854	28.0	1181	1176	EH4_ol3	1242	1228
EH4_cpx4	894	29.2	65	0.5	1180	1111	EH4_ol4	1242	1233
EH4_cpx5	822	26.9	478	16.1	1173	1144	EH4_ol5	Diseq.	Diseq.
EH4_cpx6	945	30.8	952	31.0	1184	1185	EH4_ol6	1242	1225
EH4_cpx7	982	32.0	1084	35.2	1188	1197	—	—	—
EH4_cpx8	546	18.3	378	13.0	1150	1136	—	—	—
<b>EH4 mean</b>	<b>860</b>	<b>28.1</b>	<b>564</b>	<b>18.8</b>	<b>1177</b>	<b>1152</b>	<b>EH4 mean</b>	<b>1242</b>	<b>1223</b>
—	—	—	—	—	—	—	EH5_ol1	1416	1311
—	—	—	—	—	—	—	EH5_ol2	1416	1310
—	—	—	—	—	—	—	<b>EH5 mean</b>	<b>1416</b>	<b>1311</b>
EH6_cpx1	1077	35.0	669	22.1	1213	1179	EH6_ol1	1251	1224
EH6_cpx2	1107	35.9	998	32.5	1216	1208	EH6_ol2	Diseq.	Diseq.
EH6_cpx3	917	29.9	917	29.9	1201	1201	EH6_ol3	1251	1227
EH6_cpx4	1055	34.3	1093	35.5	1212	1215	—	—	—
<b>EH6 mean</b>	<b>1082</b>	<b>35.1</b>	<b>919</b>	<b>30.0</b>	<b>1214</b>	<b>1201</b>	<b>EH6 mean</b>	<b>1251</b>	<b>1225</b>
EH7_cpx1	1073	34.8	993	32.3	1208	1201	EH7_ol1	1228	1214
EH7_cpx2	1013	32.9	766	25.2	1202	1179	EH7_ol2	1228	1213
EH7_cpx3	1001	32.6	650	21.6	1201	1170	EH7_ol3	1228	1212
EH7_cpx4	944	30.8	922	30.1	1195	1193	EH7_ol4	1228	1215
EH7_cpx5	1066	34.6	996	32.4	1207	1201	EH7_ol5	1228	1212
EH7_cpx6	882	28.8	853	27.9	1190	1188	EH7_ol6	1228	1214
EH7_cpx7	878	28.7	953	31.1	1190	1197	—	—	—
<b>EH7 mean</b>	<b>1011</b>	<b>32.9</b>	<b>876</b>	<b>28.7</b>	<b>1202</b>	<b>1190</b>	<b>EH7 mean</b>	<b>1228</b>	<b>1214</b>
EH9_cpx1	1083	35.2	816	26.8	1197	1173	EH9_ol2	1227	1207
EH9_cpx2	949	30.9	882	28.8	1187	1181	EH9_ol3	1227	1210
EH9_cpx3	955	31.1	860	28.1	1187	1180	EH9_ol4	1227	1209
EH9_cpx4	939	30.6	970	31.6	1185	1189	EH9_ol5	1227	1208
EH9_cpx5	862	28.2	952	31.0	1179	1187	EH9_ol6	1227	1205
EH9_cpx6	921	30.1	713	23.5	1184	1166	—	—	—
EH9_cpx7	885	28.9	869	28.4	1181	1180	—	—	—
EH9_cpx8	1011	32.9	940	30.6	1192	1187	—	—	—
EH9_cpx9	762	25.1	0	-2.0	1170	1096	—	—	—
EH9_cpx10	953	31.1	898	29.3	1187	1183	—	—	—
<b>EH9 mean</b>	<b>936</b>	<b>30.5</b>	<b>790</b>	<b>25.9</b>	<b>1185</b>	<b>1172</b>	<b>EH9 mean</b>	<b>1227</b>	<b>1208</b>
EH11_cpx1	1054	34.2	437	14.8	1224	1170	EH11_ol1	1289	1246
EH11_cpx2	1325	42.8	1345	43.4	1249	1250	EH11_ol2	1289	1248
EH11_cpx3	1095	35.5	1292	41.7	1228	1245	—	—	—
EH11_cpx4	1355	43.7	1277	41.3	1251	1245	—	—	—
EH11_cpx5	1339	43.2	1391	44.8	1250	1255	—	—	—
<b>EH11 mean</b>	<b>1211</b>	<b>39.2</b>	<b>1148</b>	<b>37.2</b>	<b>1238</b>	<b>1233</b>	<b>EH11 mean</b>	<b>1289</b>	<b>1247</b>
EH12_cpx1	1365	44.0	1341	43.3	1253	1250	EH12_ol1	1309	1255
EH12_cpx2	1061	34.5	778	25.6	1226	1200	—	—	—
EH12_cpx3	1307	42.2	1381	44.5	1248	1254	—	—	—
<b>EH12 mean</b>	<b>1209</b>	<b>39.1</b>	<b>1167</b>	<b>37.8</b>	<b>1239</b>	<b>1235</b>	<b>EH12 mean</b>	<b>1309</b>	<b>1255</b>

Table 4.5 Continued.

Sample_ crystal	Pressure (P, MPa), calculated depth (z, km b.s.l.) and temperature (T, °C) of clinopyroxene crystallisation						Sample_ crystal	Temperature (T, °C) of olivine crystallisation	
	Bulk P	~z	Last Eq. P	~z	Bulk T	Last Eq. T		T (Beattie)	T (Putirka)
EH13_cpx1	837	27.4	817	26.8	1179	1177	EH13_ol1	1181	1191
EH13_cpx2	848	27.8	840	27.5	1180	1179	EH13_ol2	1181	1189
EH13_cpx3	798	26.2	582	19.4	1175	1157	EH13_ol3	1181	1189
EH13_cpx4	833	27.3	841	27.5	1178	1179	EH13_ol4	1181	1189
EH13_cpx5	834	27.3	867	28.4	1178	1181	EH13_ol5	1181	1191
<b>EH13 mean</b>	<b>831</b>	<b>27.2</b>	<b>789</b>	<b>25.9</b>	<b>1178</b>	<b>1175</b>	<b>EH13 mean</b>	<b>1181</b>	<b>1190</b>
EH14_cpx1	760	25.0	756	24.9	1173	1173	EH14_ol1	Diseq.	Diseq.
EH14_cpx2	859	28.1	853	27.9	1182	1182	EH14_ol2	Diseq.	Diseq.
EH14_cpx4	968	31.5	878	28.7	1192	1184	EH14_ol3	1204	1197
EH14_cpx5	883	28.9	815	26.7	1184	1179	EH14_ol4	1204	1195
EH14_cpx7	912	29.8	874	28.6	1187	1185	EH14_ol5	1204	1197
EH14_cpx8	927	30.2	818	26.8	1189	1180	EH14_ol6	1204	1195
EH14_cpx9	849	27.8	826	27.1	1182	1180	—	—	—
EH14_cpx10	879	28.7	872	28.5	1184	1184	—	—	—
<b>EH14 mean</b>	<b>880</b>	<b>28.8</b>	<b>837</b>	<b>27.4</b>	<b>1184</b>	<b>1180</b>	<b>EH14 mean</b>	<b>1204</b>	<b>1195</b>
EH15_cpx1	584	19.5	456	15.4	1149	1139	EH15_ol1	1167	1185
EH15_cpx2	681	22.5	800	26.3	1158	1169	EH15_ol2	1167	1185
EH15_cpx3	736	24.2	784	25.8	1163	1168	EH15_ol3	1167	1184
EH15_cpx4	799	26.2	774	25.5	1168	1166	—	—	—
EH15_cpx5	756	24.9	788	25.9	1164	1167	—	—	—
<b>EH15 mean</b>	<b>678</b>	<b>22.4</b>	<b>721</b>	<b>23.8</b>	<b>1158</b>	<b>1162</b>	<b>EH15 mean</b>	<b>1167</b>	<b>1185</b>
EH16_cpx1	Diseq.	Diseq.	Diseq.	Diseq.	Diseq.	Diseq.	EH16_ol1	1109	1135
EH16_cpx2	636	21.1	678	22.4	1135	1138	EH16_ol2	1109	1135
EH16_cpx3	581	19.4	527	17.7	1131	1126	EH16_ol3	1109	1136
EH16_cpx4	340	11.5	522	17.5	1111	1126	EH16_ol4	1109	1139
EH16_cpx5	619	20.6	619	20.6	1134	1134	—	—	—
<b>EH16 mean</b>	<b>550</b>	<b>18.4</b>	<b>587</b>	<b>19.5</b>	<b>1128</b>	<b>1131</b>	<b>EH16 mean</b>	<b>1109</b>	<b>1136</b>
EH17_cpx1	1025	33.3	1004	32.7	1213	1211	EH17_ol1	1255	1226
EH17_cpx2	1085	35.2	1136	36.8	1219	1223	EH17_ol2	1255	1231
EH17_cpx3	1060	34.4	998	32.5	1216	1211	EH17_ol3	1255	1225
EH17_cpx4	1077	35.0	1248	40.3	1218	1233	EH17_ol4	1255	1226
EH17_cpx5	1220	39.5	1231	39.8	1231	1232	EH17_ol5	1255	1224
EH17_cpx6	956	31.2	802	26.3	1207	1194	—	—	—
EH17_cpx7	983	32.0	1091	35.4	1209	1219	—	—	—
<b>EH17 mean</b>	<b>1063</b>	<b>34.5</b>	<b>1073</b>	<b>34.8</b>	<b>1217</b>	<b>1217</b>	<b>EH17 mean</b>	<b>1255</b>	<b>1227</b>
—	—	—	—	—	—	—	EH18_ol1	1412	1302
—	—	—	—	—	—	—	EH18_ol2	1412	1308
—	—	—	—	—	—	—	EH18_ol3	1412	1309
—	—	—	—	—	—	—	EH18_ol4	1412	1307
—	—	—	—	—	—	—	EH18_ol5	1412	1307
—	—	—	—	—	—	—	EH18_ol6	1412	1307
—	—	—	—	—	—	—	EH18_ol7	1412	1306
—	—	—	—	—	—	—	<b>EH18 mean</b>	<b>1412</b>	<b>1306</b>
EH19_cpx1	Diseq.	Diseq.	Diseq.	Diseq.	Diseq.	Diseq.	EH19_ol1	1340	1291
EH19_cpx2	Diseq.	Diseq.	Diseq.	Diseq.	Diseq.	Diseq.	EH19_ol2	1340	1292
EH19_cpx3	Diseq.	Diseq.	Diseq.	Diseq.	Diseq.	Diseq.	EH19_ol3	1340	1294
EH19_cpx4	Diseq.	Diseq.	Diseq.	Diseq.	Diseq.	Diseq.	EH19_ol4	1340	1291
<b>EH19 mean</b>	—	—	—	—	—	—	<b>EH19 mean</b>	<b>1340</b>	<b>1292</b>
EH20_cpx1	884	28.9	827	27.1	1194	1189	EH20_ol1	1217	1214
EH20_cpx2	865	28.3	889	29.1	1193	1195	EH20_ol2	1217	1215
EH20_cpx3	938	30.6	973	31.7	1199	1202	—	—	—
<b>EH20 mean</b>	<b>898</b>	<b>29.3</b>	<b>896</b>	<b>29.3</b>	<b>1195</b>	<b>1195</b>	<b>EH20 mean</b>	<b>1217</b>	<b>1215</b>
EH26_cpx1	773	25.4	653	21.6	1180	1170	EH26_ol1	1215	1207
EH26_cpx2	615	20.4	502	16.9	1167	1157	EH26_ol2	1215	1208
EH26_cpx3	493	16.6	713	23.5	1157	1175	EH26_ol3	1215	1205
EH26_cpx4	609	20.2	470	15.9	1144	1154	—	—	—
EH26_cpx5	683	22.6	740	24.4	1173	1181	—	—	—
<b>EH26 mean</b>	<b>670</b>	<b>22.2</b>	<b>616</b>	<b>20.5</b>	<b>1170</b>	<b>1167</b>	<b>EH26 mean</b>	<b>1215</b>	<b>1206</b>
EH29_cpx1	797	26.2	884	28.9	1179	1187	EH29_ol1	1208	1200
EH29_cpx2	894	29.2	822	26.9	1188	1181	EH29_ol2	1208	1202
EH29_cpx3	733	24.1	622	20.7	1170	1163	EH29_ol3	1208	1198
EH29_cpx4	811	26.6	883	28.9	1180	1187	EH29_ol4	1208	1196
EH29_cpx5	1009	32.8	1009	32.8	1197	1197	EH29_ol5	1208	1196
EH29_cpx6	728	24.0	713	23.5	1177	1170	EH29_ol6	1208	1196
EH29_cpx7	947	30.9	901	29.4	1191	1187	—	—	—
<b>EH29 mean</b>	<b>807</b>	<b>26.5</b>	<b>833</b>	<b>27.3</b>	<b>1179</b>	<b>1182</b>	<b>EH29 mean</b>	<b>1208</b>	<b>1199</b>



## CHAPTER 5 – NUMERICAL MODELLING

### 5.1 Introduction

Numerical models can be used to simulate a range of natural and geological phenomena, including e.g. the load of a volcanic edifice on the lithosphere [e.g. *Watts, 2001*]. In Chapter 3 and Chapter 4, we showed that giant landslides have had observable consequences on subsequent volcanism and magmatism at both the Teno volcano and El Hierro Island. In this chapter, we present the results of numerical models that aim to verify the physical feasibility of such feedback processes between volcanic destruction and construction and to quantify the perturbations that a large-scale landslide, similar in size to the El Golfo landslide, may cause to the deep volcanic plumbing system.

#### *5.1.1 Note on Collaborative Research*

The results presented in this chapter are the outcome of collaborative research. The present author's contribution to this topic largely took place during a three-week stay in March 2007 at GeoForschungsZentrum (GFZ) Potsdam, Germany, where he was a visiting student hosted by Dr Thomas R. Walter. Most of the work was carried out in close collaboration with Andrea Manconi, a PhD student supervised by Dr Walter. The author provided input that helped constructing the models, i.e. in terms of the physical parameters to be used, and dimensions of the model setup. However, all technical aspects of the numerical models, including programming and running of the simulations, are the work of the GFZ researchers and the present author could not reproduce the numerical models on his own.

### 5.2 Methods

#### *5.2.1 Model Setup and Physical Parameters*

The numerical models were constructed using Abaqus, a commercial code based on finite element method (FEM). The model setup is shown in Figure 5.1 and was determined on the basis of the morphology and geological and tectonic setting of the El Hierro edifice (Chapter 4). We used an axisymmetric geometry, 90 km long in the radial, x, direction and 36 km deep in the vertical, z, downward direction. The model was divided in ~80,000 square elements, with a finer mesh (maximum resolution of 0.2 km) in the regions of interest within the whole domain. As boundary conditions, we imposed a set of infinite

elements to the left and the bottom of the model, in order to avoid interference due to boundary effects [Zienkiewicz, 1989].

The loading conditions were modelled as distributed pressure by means of the distributed load user subroutine [DLOAD in *Abaqus Manual*, 2005]. The amplitude of the distributed load of the volcanic edifice was obtained from:

$$q_x = \rho_v g h_v \left(1 - \frac{x}{L}\right)$$

where  $\rho_v$  is the bulk density of the volcanic edifice,  $g$  is the gravitational acceleration,  $h_v$  is the maximum elevation of the edifice above the seafloor,  $x$  is the radial coordinate and  $L$  is the radius of the edifice. Using  $\rho_v=2700 \text{ kg/m}^3$ ,  $g=9.81 \text{ m/s}^2$ ,  $h_v=6 \text{ km}$  and  $L=30 \text{ km}$ , we simulate the load (applied force) of a conical volcanic edifice of about  $5,500 \text{ km}^3$ , comparable with estimates for the El Hierro edifice volume (see Table 1.1) [cf. *Schmincke*, 1994]. The axisymmetric model represents a mechanically homogeneous elastic material, assuming a Poisson's ratio ( $\nu$ ) of 0.25 and a Young's modulus ( $E$ ) of 30 GPa [cf. *Pinel and Jaupart*, 2005]. The topographic volcanic edifice (and the stress changes within it) and load of sea water on the lithosphere were ignored [cf. *Watts*, 2001].

### 5.2.2 Calculation Procedures

The analysis was performed in two steps: 1) application of the volcanic edifice load; and 2) unloading of 3% of the initial volcanic load, according to estimates of El Golfo landslide volume ( $150\text{-}180 \text{ km}^3$ ) (see Table 1.1) [e.g. *Masson et al.*, 2002]. After surface unloading, variation in mean stress (hereinafter referred to as pressure (in undrained conditions)) in the lithosphere in a profile directly beneath the volcanic edifice is then analysed in a X-Y plot. These pressure variations may be used to infer the potential migration direction of fluids at depth. Variation in principal stress components, such as stress invariants like maximum/minimum tensile/compressive stresses, can also be calculated at any point of the model. Here, we are particularly interested in the variation in maximum tensile stress ( $\Delta S_3$ , also called opening stress), which gives an indication of the possibility of fracture formation and/propagation.

## 5.3 Results

Although not measured in these models, the surface mass unloading must cause a large decompression, i.e. a decrease in pressure, within the volcanic edifice, with amplitudes

approaching pressure values formally exerted by the removed load towards the surface. Within the simulated lithosphere, the decompression amplitudes decay exponentially, but remain substantial down to significant depths (Figure 5.2a). At depths equivalent to the Moho (13-15 km below sea level), the change in pressure is about -1.5 MPa (-15 bars); this decreases to about -0.6 MPa (-6 bars) at a depths between 26-30 km, corresponding to the main level of magma storage identified under Teno and El Hierro (Figure 5.2a). Looking at  $\Delta S_3$ , maximum amplitudes in tensile stress variation are on the order of 3.5 MPa at the Moho depths and about 1 MPa at 26-30 km below sea level.

## 5.4 Discussion

The results of the numerical models confirm that surface mass unloading analogous to e.g. the El Golfo landslide must produce perturbations in the state of stress within the volcanic edifice and in the lithosphere beneath. To evaluate the significance of these stress variations, we can compare our results with those of recent studies that have looked into the effects of static stress changes on the occurrence of externally triggered seismic and volcanic activity [e.g. *Stein*, 1999; *Hill et al.*, 2002].

### 5.4.1 Comparison With Other Studies

The Coulomb failure stress (CFS) criterion is commonly used to study static stress changes and has been applied to investigate earthquake occurrence [*Stein*, 1999], relationships between remote/local seismicity and active volcanoes [e.g. *Nostro et al.*, 1998; *Walter and Amelung*, 2006] and interactions of intrusions and eruptions with volcano flank movements [*Walter et al.*, 2005a]. Typically, values of  $\Delta CFS > 0.1$  MPa (>1 bar) are thought to be capable of triggering tectonic and volcanic events. However, stress triggering may occur even below 0.01 MPa; for example, *Tanaka et al.* [2004] reported tidal triggering of earthquakes, with related  $\Delta CFS$  on the order of 0.001 MPa. Volcanic systems that have already evolved to a critical state may also be susceptible to such small perturbations [see *Hill et al.*, 2002; *Walter and Amelung*, 2006].

As previously mentioned, the variation in maximum tensile stress ( $\Delta S_3$ ), when compared with intrinsic values of rock tensile strength, gives an estimate of the possibility of a fracture initiation in opening mode and/or fracture propagation. This stress invariant assumes amplitudes similar to those  $\Delta CFS$  values; hence, variations in tensile stress and Coulomb failure stress criterion may be compared [see *Walter and Amelung*, 2006]. Values of tensile stress changes obtained in this work (from ~5 to ~1 MPa between 13 and 30 km

below sea level) are within the same range, though actually generally larger, than perturbations that appear to have triggered earthquakes, volcanic eruptions and volcano-earthquake interactions at e.g. Mount Etna (Italy), Mauna Loa volcano (Hawaii) and Mount Vesuvius (Italy) (Figure 5.2b, c) [*Nostro et al.*, 1998; *Walter and Amelung*, 2004; *Walter et al.*, 2005a; *Walter and Amelung*, 2006].

#### 5.4.2 Possible Effects on Plumbing System Dynamics

Multiple consequences of such stress changes on the magmatic system of ocean island volcanoes may be considered. First, we know that Canarian mafic magmas are volatile-saturated at high pressure ( $>1000$  MPa) and exsolve a  $\text{CO}_2$ -dominated vapour phase (Chapters 3, 4) [cf. *Dixon*, 1997; *Hansteen et al.*, 1998]. Thus, a depressurisation of the magma storage environment on the order of a few megapascals may be sufficient to enhance bubble formation and  $\text{CO}_2$  degassing [cf. *Pinel and Jaupart*, 2005; *Walter and Amelung*, 2006]. This may result in a gas exsolution/magma density feedback, allowing the rapid ascent of dense magmas previously trapped at great depth. This decompression can also affect dyke initiation or dyke propagation at magma chamber walls [cf. *Pinel and Jaupart*, 2005]. Stress changes at depth of magma storage are capable to induce pressure gradients within magma reservoirs and conduits, potentially leading to magma migration, convection and mixing within a chamber [*Manconi et al.*, manuscript in preparation 2008]. Increased rate of magma chamber replenishment may be expected if reservoir and source had remained connected or renewed replenishment may be triggered if the connection had closed [*Pinel and Jaupart*, 2005]. Effects of surface unloading, including commonly proposed eruption triggers, thus have the potential to substantially alter plumbing system dynamics at volcanic systems such as El Hierro. Changes in the eruptive regime observed at Teno (Chapter 3) and El Hierro (Chapter 4), such as an increase in pyroclastic activity and enhanced tapping of dense magmas, are amongst expected repercussions of large-scale volcano flank collapses.

#### 5.4.3 Possible Effects on Melt Generation

The numerical models of *Jull and McKenzie* [1996] have shown that ice unloading during deglaciation can cause increased melt production in Iceland's spreading ridge system. In the presence of both a mantle plume and a spreading ridge, the young Icelandic crust and lithosphere are warmer and more ductile than old oceanic or continental upper mantle. The resulting melting interval is thus thick (about 100 km), from the base of the crust at 20 km

depth to the solidus at about 115 km depth. *Jull and McKenzie* [1996] found that, despite largest decompression amplitudes ( $\Delta P = -20$  MPa) just below the ice sheet, the maximum effect on mantle melting was actually much deeper, at a depth of about 80 km.

The Icelandic case differs considerably from hot-spot settings without spreading ridge, such as Hawaii or the Canary Islands, where the older and colder oceanic lithosphere results in a significant mechanical boundary layer [*Watson and McKenzie*, 1991; *Hoernle and Schmincke*, 1993b]. Under these conditions, the melting zone is thinner and restrained at much greater depth, i.e. in the spinel and garnet (mostly) stability fields between about ~70-140 km depth [e.g. *Watson and McKenzie*, 1991; *Hoernle and Schmincke*, 1993b; *Carracedo et al.*, 2001].

As already mentioned in Chapter 3, *Presley et al.* [1997] proposed that an increase in the degrees of mantle melting of about 1% may have occurred as a consequence of the Waianae slump on the island of Oahu, Hawaii. However, these authors oversimplified their calculations in transposing the pressure decrease values at the surface (at the base of the removed volcano flank) to the melting region at depth. At Waianae, estimates of decompression at the surface, based on landslide volume and landslide source area, lead  $\Delta P = -100$  to  $-200$  MPa [*Presley et al.*, 1997]. Using a similar approximation for mean decompression within the El Golfo embayment (only sub-aerial part), we obtain  $\Delta P = -20$  MPa, assuming a density of  $2,700 \text{ kg/m}^3$  and average thickness of 800 m ( $h = \text{embayment volume/area} = 40 \text{ km}^3/55 \text{ km}^2$ , [*Paris et al.*, 2005a]) for the landslide mass. As indicated by our numerical models, however, surface decompression amplitudes of e.g. 20 MPa (similar to El Hierro and Iceland) or 100-200 MPa (Hawaii) decrease exponentially with depth (Figure 5.2a). Despite available geochemical data in agreement with potential increased melt fractions after landsliding at Hawaii [*Presley et al.*, 1997], Tahiti-Nui [*Hildenbrand et al.*, 2004], Teno (Chapter 3) and perhaps also El Hierro (Chapter 4), decompression values at depths relevant to mantle melting in these regions are probably too low ( $\ll 0.5$  MPa, see Figure 5.2a) to result in increased melt production. A more focused numerical analysis, based on that of *Jull and McKenzie* [1996], will be required to fully assess this question. Such an analysis is beyond the scope of this study, but is a promising avenue for future work.

#### 5.4.4 Limitations of Models

To simplify our models, we have used a mechanically homogeneous medium to simulate the lithosphere beneath the volcanic edifice and have ignored the load of sea water. This is obviously an unrealistic situation and a layered lithosphere made of a crust and upper mantle with distinct material properties may be more appropriate. However, mechanical heterogeneities have the overall effect of amplifying the stress changes at depth [Manconi *et al.*, 2007; Manconi *et al.*, manuscript in preparation 2008], implying that their omission in the present models does not alter our conclusions. The effect of sea water load was tested and was found to result in a negligible decrease in the retrieved pressure changes. Note that, on the other hand, the removal of 3% of the volcanic edifice is a conservative estimate. The volume of the volcanic system affected by mass-wasting (the El Golfo volcano,  $\sim 2,000 \text{ km}^3$ , see Table 1.1) is substantially smaller than the whole El Hierro edifice ( $\sim 5,500 \text{ km}^3$ ), meaning that the El Golfo landslide may in fact represent an unloading of up to 9%. In addition, an important component of the system, magma, is ignored in these models. Preliminary results show that, again, the introduction of this weak material amplifies the stress changes up to 30%, especially at the interface between magma chambers and strong lithospheric materials [Manconi *et al.*, manuscript in preparation 2008].

### 5.5 Conclusions

In summary, the results of finite element models presented here show that perturbations caused by surface mass unloading during large-scale landslides are relatively large compared to other documented triggering events. The decompression due to unloading decreases with depth, but retains significant magnitudes down to depths of magma storage under the Teno volcano and El Hierro Island. Observed changes in the eruptive regimes of our type-localities, such as an increase in pyroclastic activity and the renewed eruptions of dense mafic magmas, are probably due to these perturbations in the state of stress of the lithosphere. However, it is still unsure whether decompression due to large-scale landslides can result in increased degrees of partial melting of the mantle under oceanic hot-spot volcanoes, but our results suggest that this process may be physically unrealistic.

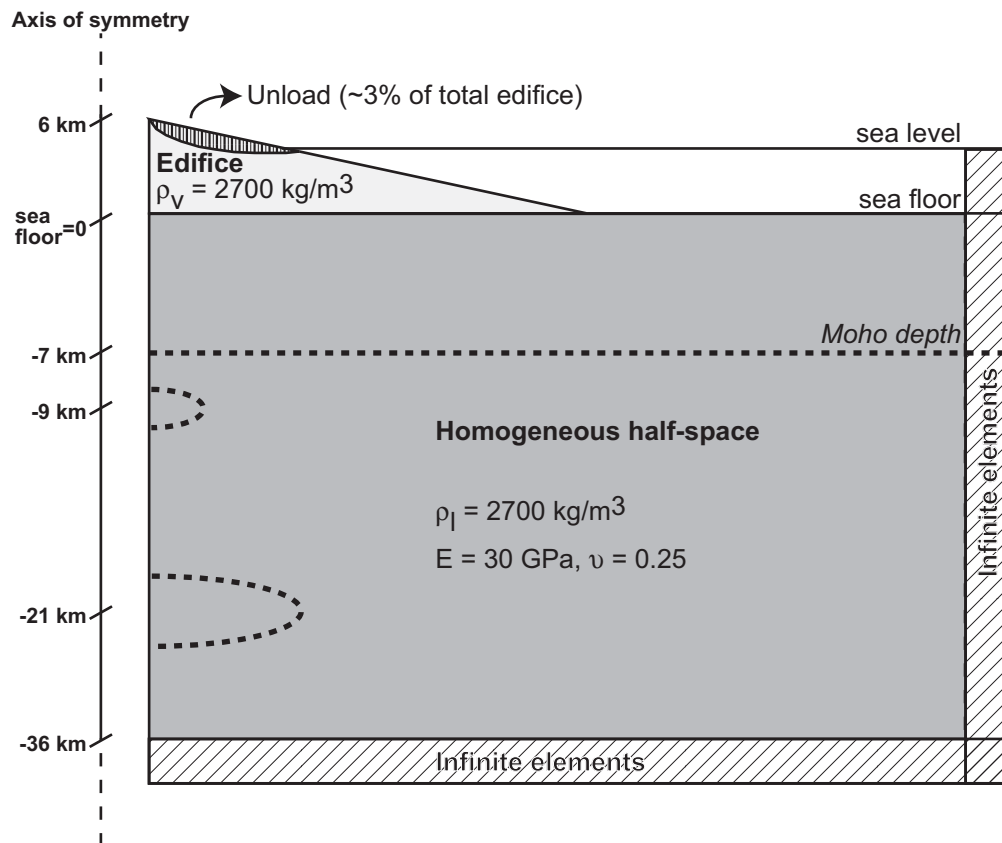


**Figure 5.1** Setup of numerical models built with the Abaqus code, using homogeneous half-space as analogue lithosphere.  $\rho$  = density,  $E$  = Young's modulus and  $\nu$  = Poisson's ratio.

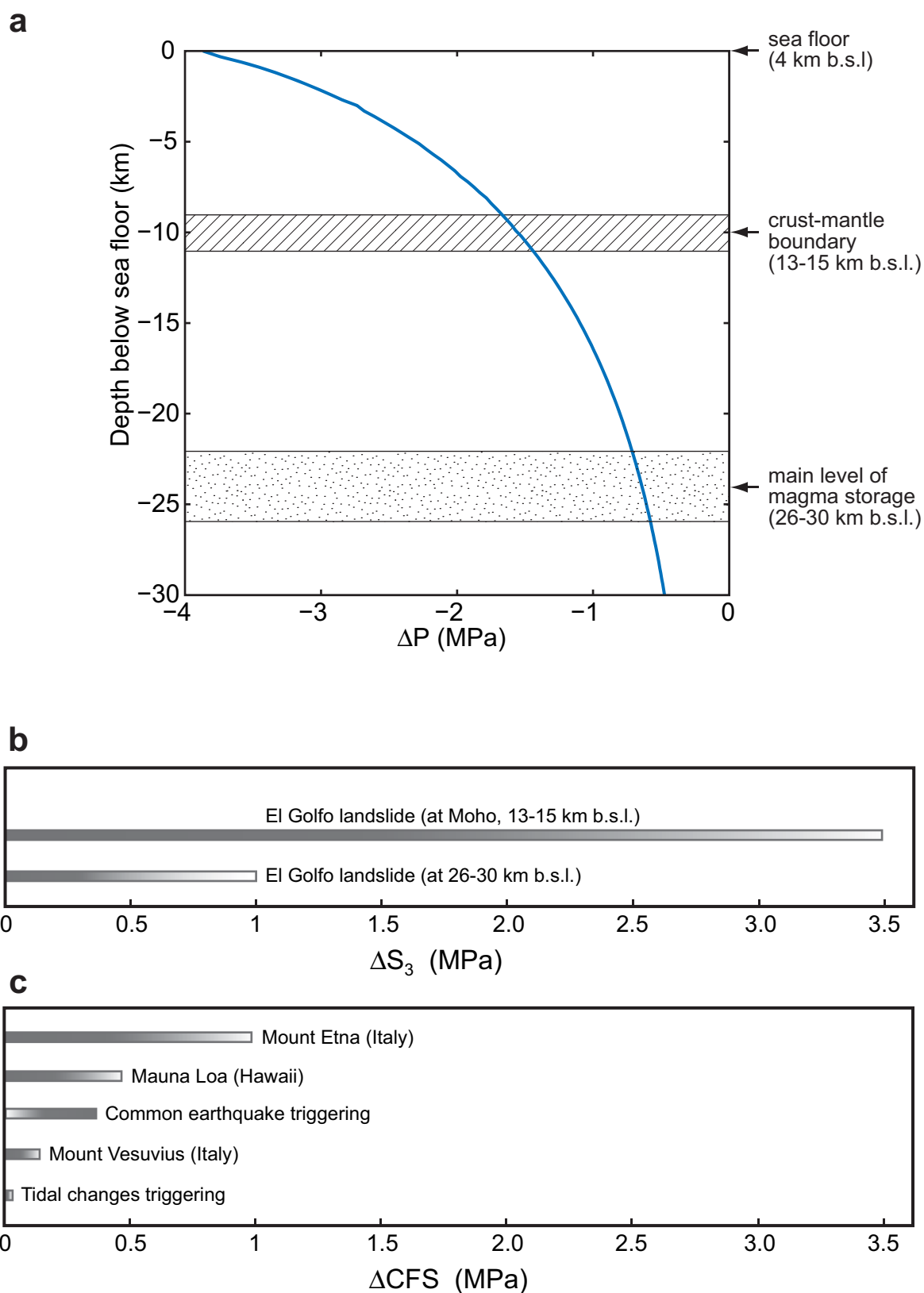


**Figure 5.2** **a** Variation in pressure in the lithosphere directly beneath the volcanic edifice after simulation of unloading due to the El Golfo landslide. **b** Order of magnitude of maximum tensile stress ( $S_3$ ) change after unloading at the Moho and at the depth of main magma storage under El Hierro. **c** Comparison with variations in Coulomb Failure Stress thought to trigger earthquakes and volcano-earthquake interactions. See text for details and references.



**CHAPTER 6 –MAGMA PLUMBING AT OCEANIC VOLCANOES: MORE IMPLICATIONS****6.1 Introduction**

The nature and dynamics of magma plumbing systems are key variables required to understand the behaviour of overlying volcanic edifices. With the exception of a few intensely studied localities [e.g. *Pallister et al.*, 1992; *Tilling and Dvorak*, 1993], these variables are typically unconstrained at individual volcanoes worldwide. Where attempted, studies of magma storage and transport have revealed complex plumbing geometries in a range of geological settings [e.g. *Marsh*, 1996; *Andronico et al.*, 2005], indicating that assumptions of shallow, spherical-elliptical magma chambers may be generally oversimplified. A variety of techniques, ranging from remote geophysical monitoring of eruptions to studies of fluid inclusions trapped in minerals, can provide information on magma storage and transport and the rates at which these processes might occur [e.g. *Hansteen et al.*, 1998; *Amelung and Day*, 2002]. At highly active, basaltic shield-volcanoes, geophysical monitoring is an effective tool to investigate plumbing system geometries [e.g. *Peltier et al.*, 2007]. In the Canary Islands, however, the low eruption frequency results in poor deformation and volcano-seismic data sets and, hence, volcanologists have to rely on alternative methods to study the magma plumbing system of Canarian volcanoes.

In Chapter 3 and Chapter 4, we have used chemical thermobarometry to obtain a wealth of information of the magma plumbing systems of the Teno volcano and the El Hierro edifice. Here, these data are evaluated in a wider context. The structure and properties of the volcanic edifice, oceanic crust and upper mantle, as well as the state of stress within the oceanic lithosphere, are integrated with P-T estimates to investigate possible controls on magma storage and transport at Canarian and other oceanic volcanoes. Then, the evolution of the plumbing systems at our type-localities, which may be typical of Canarian volcanoes, is compared to the general pattern of evolution at Hawaiian volcanoes reviewed in Chapter 1.

**6.2 Controls on Magma Storage and Transport**

Magma transport is thought to be controlled by contrasts in the densities and/or thermomechanical properties of the host rocks [see *Clague and Dixon*, 2000; *Klügel et al.*, 2005 and references therein].

The crust-mantle boundary marks an important density contrast in the lithosphere. On the margins of Tenerife and El Hierro, the Moho is located at depths between 13 and 15 km below sea level (Figure 6.1) [*Banda et al.*, 1981; *Ranero et al.*, 1995; *Watts et al.*, 1997]. Seismically, however, the crust-mantle boundary may be a thick transition zone rather than a thin discontinuity under some parts of the Canary Islands, as demonstrated for Gran Canaria and, to a lesser extent, Tenerife [*Ye et al.*, 1999; *Dañobeitia and Canales*, 2000]. In any case and even though their buoyancy may significantly decrease in the lower crust [e.g. *Takada*, 1989], ascending magmas are not necessarily expected to stagnate at the Moho due to the apparent lack of a level of neutral buoyancy at this interface [e.g. *Hansteen et al.*, 1998]. However, once established for one reason or another, magma reservoirs at near-Moho depths may damp the ascent of subsequent magma batches [e.g. *Clague*, 1987].

The long-term elastic thickness of the lithosphere ( $T_e$ ) may be related to a significant thermomechanical boundary [cf. *Bodine et al.*, 1981; *Putirka*, 1997]. At Loihi and Mauna Kea volcanoes, Hawaii, *Putirka* [1997] noticed that the shallowest magma storage depth estimates extracted from thermobarometric data coincide with estimates of  $T_e$ . This author proposed that a change in the mechanical behaviour of the lithosphere below  $T_e$  inhibits fracture transport of magma. In the Canary Islands, estimates of  $T_e$  have been matter of substantial debate [see *Collier and Watts*, 2001]. Early estimates of the lithosphere's effective elastic thickness ranged from 20 km [*Watts*, 1994] to 48 km [*Filmer and McNutt*, 1989]. However, *Dañobeitia et al.* [1994] subsequently proposed a best-fit  $T_e$  of 35 km. *Collier and Watts* [2001] also argued that a  $T_e$  of 35 km is most likely, in agreement with values predicted by the cooling plate models [see e.g. *Watts and Zhong*, 2000 and references therein]. This implies that the thermal effects associated with the Canary hot-spot have not significantly weakened the lithosphere under the Canary Islands [see also *Canales and Dañobeitia*, 1998]. Therefore for the purpose of this discussion, we place the postulated thermomechanical contrast at a depth of ~39 km below sea level (depth =  $T_e$  + approximated water depth (4 km), Figure 6.1). This depth estimate compares well with hypocentres [*Instituto Geográfico Nacional*, 1975-2007], which cluster above a depth of ~40 km below sea level for 91% of calculated events and may indeed indicate a change in the thermomechanical behaviour of the lithosphere at this level (Figure 6.1c). Taking into account the depth range yielded by our thermobarometric calculations ( $\pm 2$  standard deviations imply 20-45 km for Teno and 15-45 km for El Hierro), it seems that magma storage beneath our type-localities was largely confined from a few kilometres

below the Moho to the base of the long-term elastic lithosphere in the upper mantle (Figure 6.1). This therefore differs from the findings of *Putirka* [1997], who proposed that  $T_e$  may provide an upper as opposed to a lower bound to magma storage. If a thermomechanical contrast controls the upper limit of magma stagnation, its association with  $T_e$  is thus not universal and may merely be accidental at Loihi and Mauna Kea.

An attractive alternative explanation for magma storage depth control at Teno, El Hierro and other oceanic volcanoes may be found in the flexural model of *ten Brink and Brocher* [1987]. Flexural stresses deviating from lithostatic pressure (deviatoric stresses) are produced by the load of the volcanic edifice; the upper and lower parts of the lithosphere are in deviatoric compression and tension, respectively (Figure 6.1) [*ten Brink and Brocher*, 1987; see also *McGovern*, 2007]. As deviatoric compressive stresses overcome magma pressure in ascending dyke tips, magma stagnation (and sill formation) may be promoted. In turn, the deviatoric tensional stresses inferred to exist in the lower part of the elastic lithosphere may favour the formation of cracks, assuming equal magma and lithostatic pressure at this level [*Weertman*, 1971]. This may help channel magma into the lower elastic lithosphere. Combined together, these mechanisms may create an efficient magma trap in the lower long-term elastic lithosphere. We therefore propose that the upper limit of magma storage found at Teno and El Hierro and potentially at many other ocean island volcanoes with relatively low magma fluxes may be governed by compressive flexural stresses in the upper part of the elastic lithosphere. In addition, the occurrence of deviatoric tensional stresses in the lower part of the elastic lithosphere may explain the bottom limit given by our thermobarometric data. In this scenario, vertical intrusions (and potential subsequent eruptions) occur as magma pressure increases sufficiently due to degassing and/or crystallisation to overcome the horizontal compressive stresses due to edifice load [*ten Brink and Brocher*, 1987].

Available geophysical evidence for magmatic underplating in the Canary Archipelago is ambiguous [see *Watts et al.*, 1997; *Ye et al.*, 1999; *Dañobeitia and Canales*, 2000], as opposed to other intra-plate ocean islands (e.g. Hawaii, Marquesas, La Réunion) [*Watts et al.*, 1985; *Caress et al.*, 1995; *Charvis et al.*, 1999]. However, our thermobarometric data corroborate evidence from other petrological studies [*Hansteen et al.*, 1998; *Klügel et al.*, 2005], suggesting that sub-Moho mafic magmatic intrusions must contribute considerably to crustal thickening (underplating) under Canarian volcanoes. Flexural stresses successfully account for the occurrence of plutonic complexes near the

crust-mantle boundary under Hawaiian Islands; a situation that can probably be extrapolated to the Canary Archipelago [*ten Brink and Brocher*, 1987; *Dañobeitia and Canales*, 2000; *McGovern*, 2007].

The fact that hypocentres beneath the Canary Islands appear to extend significantly deeper than the long-term elastic thickness of the plate (Figure 6.1c) and beyond the probable 600°C isotherm (extent of mantle earthquakes, see *McKenzie et al.* [2005], Figure 7) may imply that CO<sub>2</sub>-rich fluids liberated by ascending magmas enable brittle failure through elevated pore fluid pressures [*Wilshire and Kirby*, 1989; *Wright and Klein*, 2006]. Such mechanism may provide independent evidence for magma storage and transport at upper mantle depths beneath the Canary Islands.

### 6.3 Plumbing System Evolution at Ocean Island Volcanoes

As discussed in Chapter 1, Hawaiian volcanoes, and their magmatic feeding system, evolve throughout their lifespan, in a more or less generalised manner (see Figure 1.1b). Other ocean island volcanoes may also follow similar evolutionary cycles; so far, however, the smaller datasets available, sometimes coupled with different tectonic complications, have not allowed recognition of such patterns to the extent achieved for Hawaiian volcanoes. The information we gathered on the Teno and El Hierro volcanic edifices, especially in regards to their magma plumbing system, allows further comparison with other intra-plate volcanoes. It will be seen that magma supply rate, though playing an important role, may not be the only major control on plumbing system development.

According to the Hawaiian model, oceanic volcanoes in their shield stage are characterised by high magma supply rates, and thus can develop shallow magma reservoirs [e.g. *Clague*, 1987]. Volcanoes such as Kilauea, Mauna Loa and, to a lesser extent, Piton de la Fournaise, conform well to this category [e.g. *Dvorak and Dzurisin*, 1997; *Peltier et al.*, 2007]. Yet, other intra-plate volcanoes apparently in their shield stage of growth, such as those of the Atlantic islands of La Palma, El Hierro, Fogo and Madeira, have low magma fluxes [*Carracedo*, 1999; *Amelung and Day*, 2002; *Schwarz et al.*, 2004]. Accordingly to this low magma supply rate, these volcanoes tend to lack a shallow plumbing system [*Amelung and Day*, 2002; *Schwarz et al.*, 2004; *Klügel et al.*, 2005; Chapter 4]. The magma plumbing system geometries at these Atlantic localities appear comparable, suggesting a role of underlying similarities in volcanic and tectonic settings. The plume flux (weak for most Atlantic hot-spots [*Sleep*, 1990]), the age and thickness of

the lithosphere (old and thick for the Madeira, Canary and Cape Verde hot-spots) and the velocity of the moving oceanic plate probably play a major role in defining singularities at intra-plate volcano chains [e.g. *Hoernle and Schmincke*, 1993b; *Carracedo et al.*, 1998; *Klügel and Klein*, 2006].

It appears, however, that a wider spectrum of factors, other than magma supply rate and tectonic setting, is required to explain discrepancies at individual volcanoes. *Amelung and Day* [2002] noted further departures from the general Hawaiian pattern at the Galapagos volcanoes, which, in spite of their relatively low magma supply rates, maintain shallow magma reservoirs. These authors proposed that the occurrence of ‘recent’ giant mass-wasting events may explain the lack of shallow reservoirs at volcanoes with high magma fluxes. Conversely, the absence of such giant landslides in the recent geologic past of volcanoes with relatively low magma supply rates may allow the formation of a shallow plumbing system.

Teno’s apparent lack of extensive shallow magma chambers at the time of emplacement of the El Palmar Formation (Chapter 3) is consistent with the situation of many Atlantic volcanoes in their shield-building stage. However, it also strongly resembles the post-shield stage of Mauna Kea volcano (see Figure 1.1b) [*Frey et al.*, 1990]. The oldest sub-aerial volcanics at Teno, the Masca Formation, are found stratigraphically below the two angular unconformities that represent the giant landslide scarps. This sequence includes a thick vitric tuff of trachytic composition (64.6 wt % SiO<sub>2</sub>) near its top, suggesting the temporary presence of an evolved shallow magma plumbing system earlier in the volcano’s evolution. Overall Miocene magma supply rates at Teno were on the order of  $\sim 1 \text{ km}^3/\text{kyr}$  [*Leonhardt and Soffel*, 2006], comparable to values for the Galapagos volcanoes [*Naumann and Geist*, 2000 and references therein]. The large volumes of the post-collapse Carrizales and El Palmar formations are inconsistent with a reduced magma supply after the emplacement of the Masca Formation, excluding low magma fluxes as a cause for shallow reservoir solidification.

El Hierro appears to have been characterised by low magma supply throughout its sub-aerial history, which, according to the Hawaiian model should not allow the formation of shallow magma reservoirs. If we take into account the present-day sub-aerial volume of the edifice ( $\sim 140 \text{ km}^3$ ) and add the sub-aerial embayment volumes to account for mass-wasting (El Golfo:  $40 \text{ km}^3$ ; Las Playas:  $5 \text{ km}^3$ ; and El Julán:  $20 \text{ km}^3$ ), we obtain a modest growth rate of  $\sim 0.2 \text{ km}^3/\text{ka}$  over the last 1.12 Ma [cf. *Carracedo*, 1999]. In agreement with

this low magma supply, El Hierro's most recent, largely post-landslide Rift Volcanism phase has been fed virtually exclusively by upper mantle magma reservoirs (Chapter 4). However, before the Las Playas and El Golfo giant landslides, the fully grown El Golfo volcano appear to have been linked to a shallow system of reservoirs despite still low supply rates. These reservoirs produced El Hierro's most differentiated magmas (up to 60 wt% SiO<sub>2</sub>), some of which were extruded between 261 and 176 ka, including a possibly explosive block and ash flow eruption.

The close temporal relationship between giant landslide events and the disappearance of shallow magma reservoirs (coupled with a sharp decrease in the extent of magmatic differentiation) at both Teno and El Hierro supports the causal effect suggested by *Amelung and Day* [2002]. We propose that the lack of a shallow plumbing system at the time of emplacement of the El Palmar Formation may be linked to the successive occurrence of the Masca and Carrizales collapses at the Teno volcano. Similarly, the absence of well-developed magma storage system within El Hierro's edifice in the recent Rift Volcanism phase may be due to the destructive effects of the Las Playas landslide and, especially, the El Golfo collapse. The rapid unloading of several tens of km<sup>3</sup> of near-surface rocks may have provoked the opening of new magma pathways upon re-arrangement of the local volcano-tectonic stress field, in agreement with our numerical modelling results (in Chapter 5). We suggest that eruptions that may have been closely associated with collapse drained shallow magma chambers. It thus appears that a model of the evolution of magma feeding system at Canarian volcanoes, but also at other oceanic volcanoes, should include the role of large-scale flank collapses in disrupting shallow magma plumbing systems (Figure 6.2).

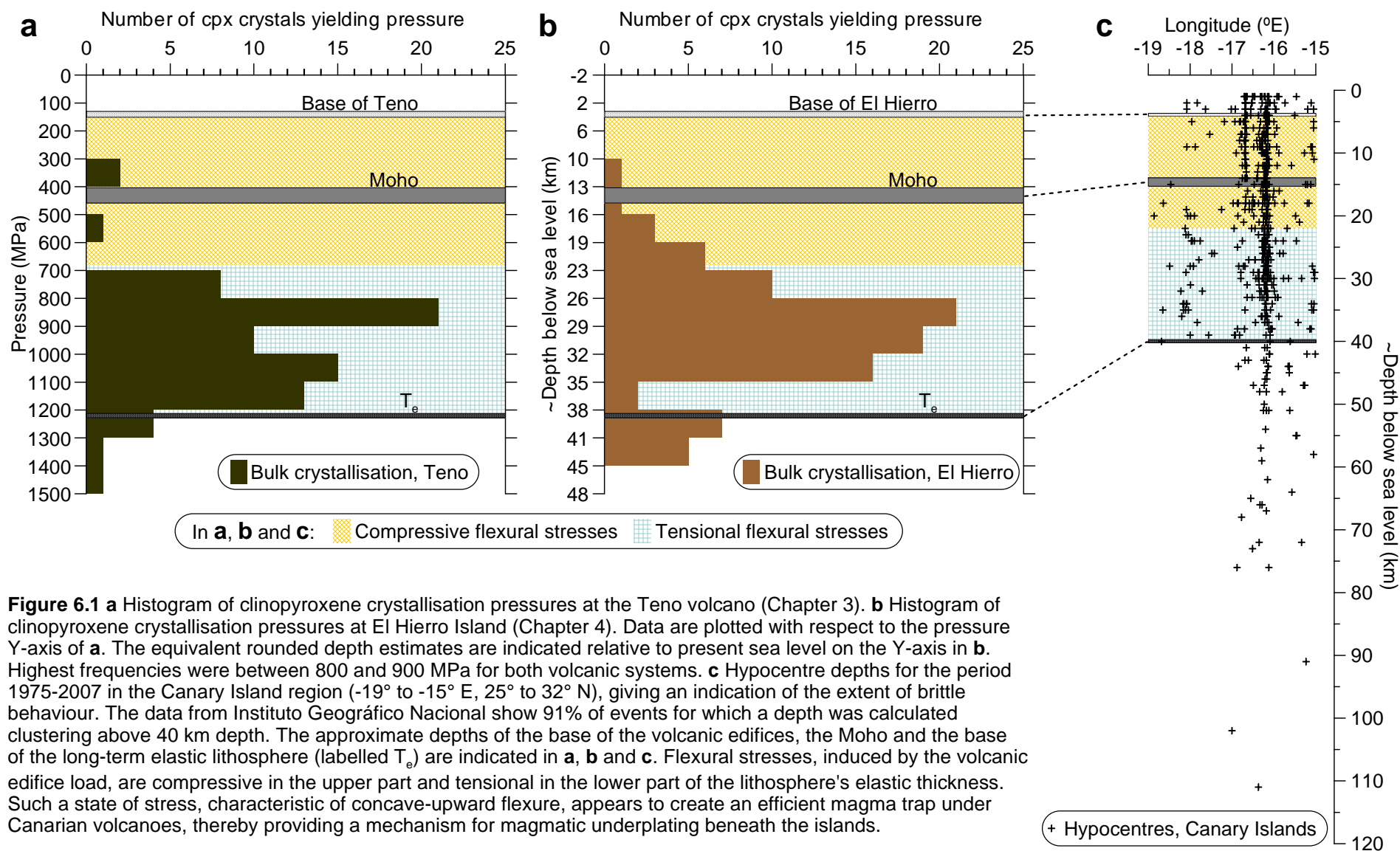


**Figure 6.1** **a** Histogram of clinopyroxene crystallisation pressures at the Teno volcano (Chapter 3). **b** Histogram of clinopyroxene crystallisation pressures at El Hierro Island (Chapter 4). Data are plotted with respect to the pressure Y-axis of **a**. The equivalent rounded depth estimates are indicated relative to present sea level on the Y-axis in **b**. Highest frequencies were between 800 and 900 MPa for both volcanic systems. **c** Hypocentre depths for the period 1975-2007 in the Canary Island region (-19° to -15° E, 25° to 32° N), giving an indication of the extent of brittle behaviour. The data from Instituto Geográfico Nacional show 91% of events for which a depth was calculated clustering above 40 km depth. The approximate depths of the base of the volcanic edifices, the Moho and the base of the long-term elastic lithosphere (labelled  $T_e$ ) are indicated in **a**, **b** and **c**. Flexural stresses, induced by the volcanic edifice load, are compressive in the upper part and tensional in the lower part of the lithosphere's elastic thickness. Such a state of stress, characteristic of concave-upward flexure, appears to create an efficient magma trap under Canarian volcanoes, thereby providing a mechanism for magmatic underplating beneath the islands.

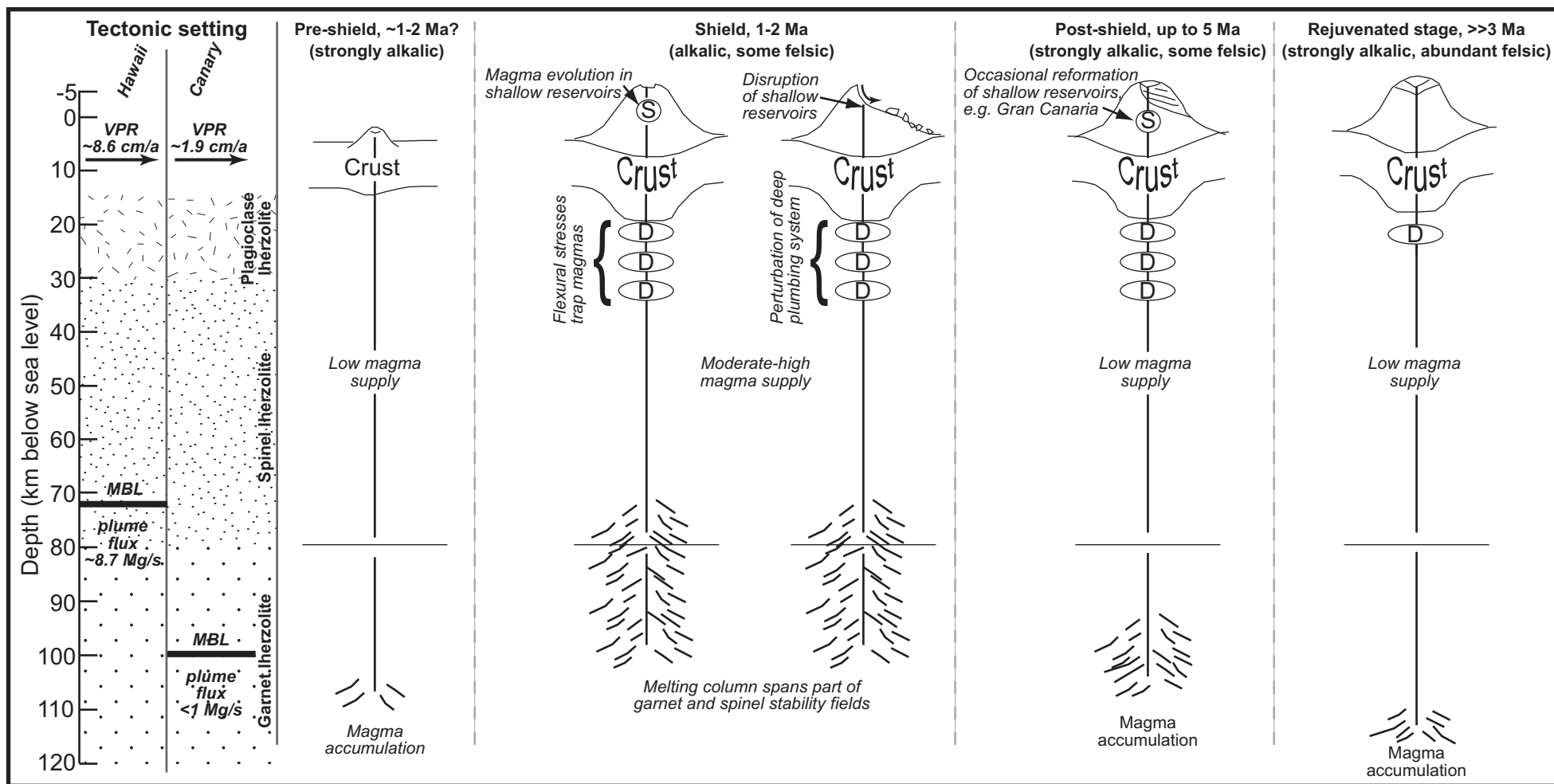


**Figure 6.2** Schematic diagram of the evolution of Canarian volcanoes and their magmatic feeding system. Stages of evolution resemble those proposed for Hawaiian volcanoes (see Figure 1.1b) [e.g. *Clague*, 1987], but a lower plume flux, an older and thicker oceanic lithosphere and a slower plate velocity result in: 1) overall lower magma supply; 2) longer duration of volcanic stages; 3) a higher alkalinity and much wider compositional variability of volcanic products in the Canary Islands compared to Hawaii. Apart from being largely controlled by magma supply, the formation, location and persistence of magma storage systems are also influenced by flexural stresses induced by the growing volcanic edifice, as well as by the occurrence of giant mass-wasting events. Lateral collapse of an oceanic volcano perturbs the stress field in the edifice and underlying lithosphere and may cause the disruption of shallow magma chambers. Although most frequently occurring during the shield stage (as depicted here), large-scale landslides can affect Canarian volcanoes at any stage of evolution. VPR=volcanic propagation rate, after *Clague and Dalrymple* [1987] and *Carracedo et al.* [1998]; MBL=mechanical boundary layer, after *Watson and McKenzie* [1991] and *Hoernle and Schmincke* [1993b]; S=shallow magma reservoirs; D=deep magma reservoirs.



## CHAPTER 7 – CONCLUSIONS AND OUTLOOK

Since giant landslide deposits were first documented in the 1960's [e.g. *Moore*, 1964], and through the Mount St. Helens scientific awakening, the volcanological community has come to more duly appreciate the role of large-scale landsliding in the dismantling of effectively all marine hot-spot volcanoes and, hence, its role in ocean island evolution. More recently, independent studies have raised convincing evidence for feedback mechanisms between volcanic destruction and structural reorganisation of subsequent volcanic growth [e.g. *Lipman et al.*, 1991; *Day et al.*, 1999b; *Walter et al.*, 2005b]. And the possibility that volcano flank collapse might even affect the geochemical regime of a volcano has been proposed [*Presley et al.*, 1997; *Hildenbrand et al.*, 2004; *Pinel and Jaupart*, 2005]. The main purpose of this thesis was to further investigate this last hypothesis and to gain knowledge on the potential repercussions of large-scale landslides on the volcanic and magmatic evolution of oceanic volcanoes. In order to reach this goal, we carefully selected suitable type-localities in the Canary Archipelago: the Teno massif, a Miocene shield-volcano on the island of Tenerife, and El Hierro, a youthful volcanic island. Detailed field studies were carried out and sampling of volcanic lithologies allowed subsequent petrological and geochemical analysis. Numerical models helped to further test our hypothesis. Let us now summarise the key findings of this study.

### 7.1 Chapter 1: Introduction

In a review of scientific literature, a number of current concepts were laid out that are fundamental to our study. Most importantly, we have seen that the volcanoes of the Canary Islands, like those of Hawaii, owe their existence to the presence of a mantle plume originating in the deep mantle [e.g. *Wilson*, 1963; *Hoernle and Schmincke*, 1993a]. Volcanism in Hawaii and in the Canaries displays, however, substantial dissimilarities. Distinct geodynamic settings, i.e. a much lower plume flux, an older and thicker lithosphere, and a much slower (near-stationary) plate velocity for the Canary Islands compared to Hawaii, can account for most, if not all, of these differences [e.g. *Hoernle and Schmincke*, 1993b; *Carracedo*, 1999]. The lesser amount of data available for Canarian volcanoes and their longer and more diversified volcanic activity may have thus far masked clear cycles of evolution, which are better defined for Hawaiian volcanoes [*Clague and Dalrymple*, 1987; *Carracedo et al.*, 1998; *Paris et al.*, 2005b]. Nonetheless, Hawaiian

and Canarian volcanoes share many points in common, one of which is the occurrence of recurrent giant flank collapses during their lifespan.

## 7.2 Chapter 3: The Teno Massif

After outlining methods and procedures in Chapter 2, the results and conclusions of our study of the Teno massif were presented in Chapter 3. These may be recapitulated as follows:

- (1) Ancient landslide scars may be recognised at eroded volcanoes. In the case of Teno, these are marked by steep angular unconformities, defining concentric palaeo-embayments and fundamental stratigraphic boundaries. Studies that aim to reconstruct the evolution of volcanoes similar to Teno, through e.g. radiometric dating and magnetostratigraphy, have to meticulously consider such structures, if present.
- (2) Inspection of the collapse unconformities reveals the presence of abundant juvenile pyroclastic deposits, otherwise subdued in the Teno massif, indicating that extensive explosive eruptions occurred in close association with giant lateral collapse of the Teno volcano in the late Miocene.
- (3) The examination of post-collapse stratigraphic sequences, coupled with geochemical analysis, indicates that dense and poorly-differentiated ankaramitic magmas, carrying large and abundant olivine and clinopyroxene crystals, were more frequently erupted following landslide events. Prior to each collapse, crustal reservoirs may have been well-established and produced highly evolved magma that erupted explosively in at least one occasion. Thermobarometry reveals that, in contrast, the younger post-collapse Teno volcano lacked a shallow plumbing system and was fed directly from 20 to 45 km depth. A complex system of interconnected sills and dykes is likely to have served as a magma storage environment in the upper mantle, where magmas of similar composition mixed, accumulated, partially crystallised and differentiated. Petrographic textures, coupled with mineral chemistry, advocate for rapid magma transfers from storage depths to the site of eruption, on time-scales of days.
- (4) Trace element chemistry of the Carrizales lavas, which were erupted in the short time-interval between the two landslides, suggests peak degrees of partial melting in the mantle at this point of Teno's sub-aerial evolution.

- 
- (5) In a non-unique, conceptual model of volcanic evolution, it is proposed that both Teno's eruptive regime at the surface and dynamics of magma plumbing at depth were highly influenced by the volcano load and lateral collapse events. Landslide-related perturbations in the stress field within the volcanic edifice and oceanic crust beneath are thought to have opened new magma pathways, resulting in extensive pyroclastic activity shortly following collapse. While this may have drained pre-established crustal magma pockets, the unloading effect appears to have propagated down to deeper levels, where ankaramitic magmas were stored. This decompression may have shifted these dense magmas into the 'eruptible density window' [cf. *Pinel and Jaupart, 2004*], thus explaining the abundance of ankaramites in the post-collapse lava sequences. Even though geochemical variations with stratigraphy may be consistent with either a blob-governed evolution, or collapse-induced fluctuations in the degrees of mantle partial melting, patterns seen at Teno may be best explained by a transition between Hawaiian-like stages of development (shield stage to post-shield stage), soon after the second collapse of the volcano.

### 7.3 Chapter 4: El Hierro Island

Our second case-study was presented in Chapter 4 and focussed on the volcanic and geochemical evolution of El Hierro Island. Key results and conclusions are here reviewed:

- (1) Since the large El Golfo landslide dated between 134 and 21 ka, the majority of pre-historic eruptions (post-dating the last glacial maximum) have taken place at the base of, and on, the collapse headwall, producing well-preserved vents, lava flows and lapilli-tuff beds. Such structural influence on post-collapse focus of volcanism is a general feature of volcanoes that have been the site of a recent flank collapse. The ca. 6-4 ka ankaramitic Tanganasoga volcano, the largest volcanic construction within the El Golfo embayment, may be the embryonic manifestation of the future centre of volcanism on the island.
- (2) Logging of well-exposed stratigraphic profiles reveals that, between 261 and 176 ka, the pre-collapse El Golfo volcano erupted highly evolved magmas that were probably produced by crustal-level magmatic differentiation. Coinciding with the occurrence of the Las Playas landslide and continuing after the El Golfo landslide, a renewal of more mafic eruptions, often involving dense ankaramitic magmas, has

characterised the on-going Rift Volcanism phase. In contrast to the intermediate-to-felsic deposits of the late El Golfo volcano, post-collapse Rift magmas have been tapped from depths. Thermobarometric calculations indicate that olivine and clinopyroxene crystallisation occurs in the uppermost mantle, between about 15 and 45 km below present sea level. On the basis of historic patterns observed at the neighbouring La Palma Island, characterised by a similar plumbing system [cf. *Klügel et al.*, 1997; *Klügel et al.*, 2000; *Klügel et al.*, 2005], precursors of an impending eruption at El Hierro may be manifested as little as a few hours to as much as several years before fracture break out at the surface.

- (3) Trace element concentrations of recent Rift Volcanism lavas, most of which post-date the Las Playas landslide and some of which also post-date the El Golfo landslide, are compatible with an increase in mean mantle melt fractions relative to pre-collapse El Golfo Volcano Formation lavas.
- (4) The Upper Pleistocene and Holocene volcanic and magmatic evolution of El Hierro Island seems to have been strongly affected by the edifice's two most recent flank collapses. Indeed, we suggest that the combined effects of the Las Playas and El Golfo giant landslides may have controlled the locality and style of post-collapse eruptions, by providing new least-effort magma pathways. The collapses may also have contributed to the disappearance of shallow reservoirs established during the late El Golfo Volcano phase, when the volcano load imposed a filter that impeded the ascent of dense magmas. Unloading of a lava pile some 230 km<sup>3</sup> in total volume, on the other hand, is proposed to have permitted the mobilisation of very dense ankaramitic magmas that otherwise might have been trapped at depth. While available data are in agreement with a potential increase in mantle melt generation caused by landsliding in the early Rift Volcanism phase, statistical verification may require additional sampling of 50-100 lava flows.

## 7.4 Chapter 5: Numerical Modelling

In Chapter 5, numerical models were used to quantify the stress changes at depth caused by a surface unloading analogue to the El Golfo landslide; this allowed testing for a physical explanation for the results of the two previous chapters. The stress perturbations obtained are comparable, although generally of larger magnitudes, than those that have been shown to externally trigger seismic and volcanic activity. Depressurisation occurs in the

lithosphere (and must also occur within the volcanic edifice), but the effect of unloading decreases exponentially with depth. However, substantial amplitudes are maintained down to depths of magma storage at both our type-localities, thus accounting for our field and geochemical observations. On the other hand, stress changes may be insignificant at depths relevant to mantle melting beneath ocean island volcanoes, such as Teno, El Hierro or those of Hawaii, but numerical models dedicated to this topic may be required for full assessment.

## 7.5 Chapter 6: Magma Plumbing at Oceanic Volcanoes: More Implications

Apart from providing a means to describe the magma feeding system at Teno and El Hierro, the thermobarometric data collected in this thesis have wider implications. In fact, these data strongly support other petrological studies [*Hansteen et al.*, 1998; *Klügel et al.*, 2005], suggesting that magmatic underplating is an important process in the Canary Islands, despite the lack of consensus of geophysical studies in the region. In addition, barometric data obtained in this study are in agreement with an important influence of flexural stresses (induced by the volcanic edifice load) in controlling depths of magma stagnation in the lithosphere. This model, first put forward by *ten Brink and Brocher* [1987], may effectively explain the formation of plutonic complexes detected at sub-Moho depths beneath many oceanic volcanoes [e.g. *ten Brink and Brocher*, 1987; *Caress et al.*, 1995; *Charvis et al.*, 1999; *Dañobeitia and Canales*, 2000; *McGovern*, 2007].

As a final remark for Chapter 6, our studies of Teno and El Hierro point towards another major control on magma storage system configuration/depth, in addition to magma supply rate and the influence of flexural stresses. That is, the role that large-scale flank collapses may play in destroying shallow magmatic systems, and thus retrograding magma storage at greater depths until crustal reservoirs can be re-established. This possibility should be included in a scheme of magma feeding system evolution at Canarian, and other similar volcanoes.

## 7.6 General Conclusions

The case-studies of the Miocene Teno volcano, on Tenerife, and of El Hierro Island suggest that destructive (and constructive) processes play a role thus far underestimated in regulating the geochemical regimes of many ocean island volcanoes. The results presented here considerably expand an already growing body of evidence [e.g. *Presley et al.*, 1997; *Hildenbrand et al.*, 2004; *Pinel and Jaupart*, 2005], indicating that volcanic edifice mass-

wasting can drastically alter magmatic feeding system processes, such as storage, accumulation, transport, mixing, degassing and differentiation of magmas. Landslide-induced disturbances in the state of stress of the volcanic and magmatic system can reach the upper mantle, retaining relatively large magnitudes down to depths of magma storage beneath oceanic hot-spot volcanoes. However, despite geochemical data compatible with this possibility [Presley *et al.*, 1997; Hildenbrand *et al.*, 2004; this work], giant landslides appear unlikely to affect mantle melting beneath ocean island volcanoes, as the resulting decompression probably does not propagate to relevant depths in significant amplitudes.

## 7.7 Possible Avenues for Further Research

In addition to the conclusions discussed above, sizeable potential for future research ensues from this study, with follow-on projects already being taken up or planned in some cases.

Despite representing a key piece of the puzzle for a better understanding of Canarian volcanism, the geology of El Hierro Island has thus far been under-studied. The works of Guillou *et al.* [1996] and Carracedo *et al.* [2001] provided a well-constrained stratigraphic framework for the island. And with the results of this thesis, additional information on the magma plumbing system and the general geochemical evolution of the island is available. However, a more extensive sample set is required to go in further details, especially to detect temporal effects of the action and the characteristics of the Canary mantle plume. An ambitious sampling campaign (50-100, more if possible, samples) could be undertaken. This would allow a more robust evaluation of progressive and/or drastic changes in the major, trace and rare earth element chemistry of El Hierro's volcanics through time and would provide a solid framework for comparison with Hawaiian and other Canarian volcanoes, as well as other hot-spot volcanoes situated on slow moving plates. This project may be part of the author's post-doctoral research.

In Chapter 4, we mentioned the particular interest of the Tanganasoga volcano, on El Hierro, for the place and volume it occupies within the El Golfo embayment, as well as for the composition of its products. Although not analysed for this work, about 50 loose and intact clinopyroxene megacrysts, from 1.5 to 3 cm in longest dimension, were collected at Tanganasoga. The peculiarity of these volcanic ejecta found on the slope of recent Holocene cinder cones is striking. A systematic study of these interesting crystals may provide further details on the magma storage system of El Hierro and the processes at

---

play within it. This study could be undertaken in the very near future as samples are already available.

More detailed numerical modelling is currently being performed to complement the results of Chapter 5. This research, led by GFZ Potsdam researchers, integrates further complexity to the models, including the effect of a stratified lithosphere. A manuscript, to which the present author contributes, is being prepared for publication. In addition, a new set of numerical models, based on the approach of *Jull and McKenzie* [1996], could be used to assess more directly the physical feasibility of increased partial melting due to landslide-induced decompression.

Finally, clinopyroxene-melt thermobarometry, combined with mineral chemistry and other techniques, is a promising tool to gain knowledge on the plumbing system of basaltic volcanoes in general. Additional case-studies, similar to those presented in this thesis, at other localities (e.g. Cape Verde, Hawaii, Réunion) would allow a more complete comparison of the deep magmatic feeding system of other oceanic volcanoes. This may help determining if the hypothesis in which the depths of magma stagnation in the upper mantle are largely controlled by the flexural stresses induced by the volcanic edifice itself is globally viable or not.

## REFERENCES

- Abaqus/Standard users manual*, (2005), Pawtucket, Rhode Island.
- Abdel-Monem, A., N. D. Watkins, and P. W. Gast (1972), Potassium-argon ages, volcanic stratigraphy, and geomagnetic polarity history of the Canary Islands; Tenerife, La Palma and Hierro, *American Journal of Science*, 272(9), 805-825.
- Ablay, G. J., G. G. J. Ernst, J. Martí, and R. S. J. Sparks (1995), The ~2 ka subplinian eruption of Montaña Blanca, Tenerife, *Bulletin of Volcanology*, 57(5), 337-355.
- Ablay, G. J., M. R. Carroll, M. R. Palmer, J. Martí, and R. S. J. Sparks (1998), Basanite-phonolite lineages of the Teide-Pico Viejo volcanic complex, Tenerife, Canary Islands, *Journal of Petrology*, 39(5), 905-936.
- Abratis, M., H.-U. Schmincke, and T. H. Hansteen (2002), Composition and evolution of submarine volcanic rocks from the central and western Canary Islands, *International Journal of Earth Sciences*, 91(4), 562-582.
- Acosta, J., E. Uchupi, A. Muñoz, P. Herranz, C. Palomo, and M. Ballesteros (2003), Geologic evolution of the Canarian Islands of Lanzarote, Fuerteventura, Gran Canaria and La Gomera and comparison of landslides at these islands with those at Tenerife, La Palma and El Hierro, *Marine Geophysical Researches*, 24(1), 1-40.
- Amelung, F., and S. J. Day (2002), InSAR observations of the 1995 Fogo, Cape Verde, eruption – Implications for the effects of collapse events upon island volcanoes, *Geophysical Research Letters*, 29(12), 47-41.
- Ancochea, E., J. M. Fuster, E. Ibarrola, A. Cendrero, J. Coello, F. Hernan, J. M. Cantagrel, and C. Jamond (1990), Volcanic evolution of the island of Tenerife (Canary Islands) in the light of new K-Ar data, *Journal of Volcanology and Geothermal Research*, 44(3-4), 231-249.
- Ancochea, E., J. L. Brändle, C. R. Cubas, F. Hernán, and M. J. Huertas (1996), Volcanic complexes in the eastern ridge of the Canary Islands: the Miocene activity of the island of Fuerteventura, *Journal of Volcanology and Geothermal Research*, 70(3-4), 183-204.
- Andronico, D., S. Branca, S. Calvari, M. Burton, T. Caltabiano, R. A. Corsaro, P. Del Carlo, G. Garfi, L. Lodato, and L. Miraglia (2005), A multi-disciplinary study of the 2002–03 Etna eruption: insights into a complex plumbing system, *Bulletin of Volcanology*, 67(4), 314-330.
- Anguita, F., and F. Hernán (1975), A propagating fracture model versus a hot-spot origin for the Canary islands, *Earth and Planetary Science Letters*, 27(1), 11-19.
- Anguita, F., and F. Hernán (2000), The Canary Islands origin: a unifying model, *Journal of Volcanology and Geothermal Research*, 103(1-4), 1-26.
- Aparicio, A., M. A. Bustillo, R. Garcia, and V. Araña (2006), Metasedimentary xenoliths in the lavas of the Timanfaya eruption (1730–1736, Lanzarote, Canary Islands): metamorphism and contamination processes, *Geological Magazine*, 143(02), 181-193.
- Araña, V., and R. Ortiz (1991), The Canary Islands: Tectonics, magmatism and geodynamic framework, in *Magmatism in Extensional Structural Settings – the Phanerozoic African Plate*, edited by A. B. Kampunzu and R. T. Lubala, pp. 209-249, Springer, New York.
- Banda, E., J. J. Dañobeitia, E. Surinach, and J. Ansorge (1981), Features of crustal structure under the Canary Islands, *Earth and Planetary Science Letters*, 55(1), 11-24.
- Barrera, J. L., J. A. Gomez, and F. Bellido (1989), Mapa geológico de España, E. 1: 25,000, IGME, Madrid.
- Beattie, P. (1993), Olivine-melt and orthopyroxene-melt equilibria, *Contributions to Mineralogy and Petrology*, 115(1), 103-111.
- Blundy, J., and K. Cashman (2005), Rapid decompression-driven crystallization recorded by melt inclusions from Mount St. Helens volcano, *Geology*, 33(10), 793-796.
- Bodine, J. H., M. S. Steckler, and A. B. Watts (1981), Observations of flexure and the rheology of the oceanic lithosphere, *Journal of Geophysical Research*, 86(B5), 3695-3707.
- Branney, M., P. Dávila-Harris, M. Storey, C. Mac Niocaill, and C. Kirkham-Smith (2008), Eruption-triggered giant landslide at an ocean-island volcano: evidence from a newly discovered onshore debris-



- 
- avalanche deposit, Tenerife, paper presented at IAVCEI General Assembly, Reykjavík, Iceland, 17-22 August
- Brophy, J. G., C. S. Whittington, and Y. R. Park (1999), Sector-zoned augite megacrysts in Aleutian high alumina basalts: implications for the conditions of basalt crystallization and the generation of calc-alkaline series magmas, *Contributions to Mineralogy and Petrology*, 135(2), 277-290.
- Canales, J. P., and J. J. Dañobeitia (1998), The Canary Islands swell: a coherence analysis of bathymetry and gravity, *Geophysical Journal International*, 132(3), 479-488.
- Cande, S. C., and D. V. Kent (1995), Revised calibration of the geomagnetic polarity timescale for the Late Cretaceous and Cenozoic, *Journal of Geophysical Research*, 100(B4), 6093-6095.
- Cantagrel, J. M., N. O. Arnaud, E. Ancochea, J. M. Fuster, and M. J. Huertas (1999), Repeated debris avalanches on Tenerife and genesis of Las Cañadas caldera wall (Canary Islands), *Geology*, 27(8), 739-742.
- Caress, D. W., M. K. McNutt, R. S. Detrick, and J. C. Mutter (1995), Seismic imaging of hotspot-related crustal underplating beneath the Marquesas Islands, *Nature*, 373(6515), 600-603.
- Carracedo, J. C., E. Rodríguez Badiola, and V. Soler (1992), The 1730-1736 eruption of Lanzarote, Canary Islands: a long, high-magnitude basaltic fissure eruption, *Journal of Volcanology and Geothermal Research*, 53(1-4), 239-250.
- Carracedo, J. C. (1994), The Canary Islands: an example of structural control on the growth of large oceanic-island volcanoes, *Journal of Volcanology and Geothermal Research*, 60, 225-241.
- Carracedo, J. C., S. J. Day, H. Guillou, E. Rodríguez Badiola, J. A. Canas, and F. J. Pérez Torrado (1998), Hotspot volcanism close to a passive continental margin: the Canary Islands, *Geological Magazine*, 135(05), 591-604.
- Carracedo, J. C. (1999), Growth, structure, instability and collapse of Canarian volcanoes and comparisons with Hawaiian volcanoes, *Journal of Volcanology and Geothermal Research*, 94(1-4), 1-19.
- Carracedo, J. C., S. J. Day, H. Guillou, and P. Gravestock (1999a), Later stages of volcanic evolution of La Palma, Canary Islands; rift evolution, giant landslides, and the genesis of the Caldera de Taburiente, *Geological Society of America Bulletin*, 111(5), 755-768.
- Carracedo, J. C., S. J. Day, H. Guillou, and F. J. Pérez Torrado (1999b), Giant Quaternary landslides in the evolution of La Palma and El Hierro, Canary Islands, *Journal of Volcanology and Geothermal Research*, 94(1-4), 169-190.
- Carracedo, J. C., E. Rodríguez Badiola, H. Guillou, J. de la Nuez, and F. J. Pérez Torrado (2001), Geology and volcanology of La Palma and El Hierro, Western Canaries, *Estudios Geológicos*, 57, 175-273.
- Carracedo, J. C., E. Rodríguez Badiola, H. Guillou, M. Paterne, S. Scaillet, F. J. Pérez Torrado, R. Paris, U. Fra-Paleo, and A. Hansen (2007), Eruptive and structural history of Teide Volcano and rift zones of Tenerife, Canary Islands, *Geological Society of America Bulletin*, 119(9-10), 1027-1051.
- Cendrero, A. (1970), The volcano-plutonic complex of La Gomera (Canary Islands), *Bulletin of Volcanology*, 34(2), 537-561.
- Charvis, P., A. Laesanpura, J. Gallart, A. Hirn, J. C. Lépine, B. de Voogd, T. A. Minshall, Y. Hello, and B. Pontoise (1999), Spatial distribution of hotspot material added to the lithosphere under La Réunion, from wide-angle seismic data, *Journal of Geophysical Research*, 104(B2), 2875-2894.
- Clague, D. A. (1987), Hawaiian xenolith populations, magma supply rates, and development of magma chambers, *Bulletin of Volcanology*, 49(4), 577-587.
- Clague, D. A., and G. B. Dalrymple (1987), The Hawaiian-Emperor volcanic chain. Part I. Geologic evolution, in *Volcanism in Hawaii*, edited by R. W. Decker, T. L. Wright and P. H. Stauffer, pp. 5-54, US Geological Survey Professional Paper 1350.
- Clague, D. A., and G. B. Dalrymple (1988), Age and petrology of alkalic postshield and rejuvenated-stage lava from Kauai, Hawaii, *Contributions to Mineralogy and Petrology*, 99(2), 202-218.
- Clague, D. A., and J. E. Dixon (2000), Extrinsic controls on the evolution of Hawaiian ocean island volcanoes, *Geochemistry Geophysics Geosystems*, 1, 12.
- Coello, J., J. M. Cantagrel, F. Hernan, J. M. Fuster, E. Ibarrola, E. Ancochea, C. Casquet, C. Jamond, J. R. Diaz De Teran, and A. Cendrero (1992), Evolution of the eastern volcanic ridge of the Canary Islands based on new K-Ar data, *Journal of Volcanology and Geothermal Research*, 53(1-4), 251-274.

- 
- Collier, J. S., and A. B. Watts (2001), Lithospheric response to volcanic loading by the Canary Islands: constraints from seismic reflection data in their flexural moat, *Geophysical Journal International*, 147(3), 660-676.
- Dañobeitia, J. J., J. P. Canales, and G. A. Dehghani (1994), An estimation of the elastic thickness of the lithosphere in the Canary Archipelago using admittance function, *Geophysical Research Letters*, 21(24), 2649-2652.
- Dañobeitia, J. J., and J. P. Canales (2000), Magmatic underplating in the Canary Archipelago, *Journal of Volcanology and Geothermal Research*, 103(1-4), 27-41.
- Danyushevsky, L. V. (2001), The effect of small amounts of H<sub>2</sub>O on crystallisation of mid-ocean ridge and backarc basin magmas, *Journal of Volcanology and Geothermal Research*, 110(3-4), 265-280.
- Day, S. J., J. C. Carracedo, and H. Guillou (1997), Age and geometry of an aborted rift flank collapse: the San Andres fault system, El Hierro, Canary Islands, *Geological Magazine*, 134(04), 523-537.
- Day, S. J., J. C. Carracedo, H. Guillou, and P. Gravestock (1999a), Recent structural evolution of the Cumbre Vieja volcano, La Palma, Canary Islands: volcanic rift zone reconfiguration as a precursor to volcano flank instability?, *Journal of Volcanology and Geothermal Research*, 94(1-4).
- Day, S. J., S. I. N. Heleno da Silva, and J. F. B. D. Fonseca (1999b), A past giant lateral collapse and present-day flank instability of Fogo, Cape Verde Islands, *Journal of Volcanology and Geothermal Research*, 94(1-4), 191-218.
- Dieterich, J. H. (1988), Growth and persistence of Hawaiian volcanic rift zones, *Journal of Geophysical Research*, 93(B5), 4258-4270.
- Dixon, J. E. (1997), Degassing of alkalic basalts, *American Mineralogist*, 82(3-4), 368-378.
- Droop, G. T. R. (1987), A general equation for estimating Fe<sup>3+</sup> concentrations in ferromagnesian silicates and oxides from microprobe analyses, using stoichiometric criteria, *Mineralogical Magazine*, 51(361), 431-435.
- Duke, J. M. (1976), Distribution of the period four transition elements among olivine, calcic clinopyroxene and mafic silicate liquid: experimental results, *Journal of Petrology*, 17(4), 499-521.
- Dvorak, J. J., and D. Dzurisin (1997), Volcano geodesy: The search for magma reservoirs and the formation of eruptive vents, *Reviews of Geophysics*, 35(3), 343-384.
- Elsworth, D., and B. Voight (1996), Evaluation of volcano flank instability triggered by dyke intrusion, in *Volcano Instability on the Earth and Other Planets*, edited by W. J. McGuire, A. P. Jones and J. Neuberg, pp. 45-53, Geological Society of London Special Publication No. 110.
- Falloon, T. J., D. H. Green, H. S. C. O'Neill, and W. O. Hibberson (1997), Experimental tests of low degree peridotite partial melt compositions: implications for the nature of anhydrous near-solidus peridotite melts at 1 GPa, *Earth and Planetary Science Letters*, 152(1-4), 149-162.
- Filmer, P. E., and M. K. McNutt (1989), Geoid anomalies over the Canary Islands Group, *Marine Geophysical Researches*, 11(2), 77-87.
- Fiske, R. S., and E. D. Jackson (1972), Orientation and growth of Hawaiian volcanic rifts: the effect of regional structure and gravitational stresses, *Proceedings of the Royal Society of London. Series A, Mathematical and Physical Sciences (1934-1990)*, 329(1578), 299-326.
- Ford, C. E., D. G. Russell, J. A. Craven, and M. R. Fisk (1983), Olivine-liquid equilibria: temperature, pressure, and composition dependence of the crystal/liquid cation partition coefficients for Mg, Fe<sup>2+</sup>, Ca, and Mn, *Journal of Petrology*, 24(3), 256-265.
- Francis, D. (1995), The implications of picritic lavas for the mantle sources of terrestrial volcanism, *Lithos*, 34(1), 89-105.
- Freer, R. (1981), Diffusion in silicate minerals and glasses: A data digest and guide to the literature, *Contributions to Mineralogy and Petrology*, 76(4), 440-454.
- Frey, F. A., W. S. Wise, M. O. Garcia, H. West, S. T. Kwon, and A. Kennedy (1990), Evolution of Mauna Kea volcano, Hawaii: Petrologic and geochemical constraints on postshield volcanism, *Journal of Geophysical Research*, 95(B2), 1271-1300.
- Frey, F. A., M. O. Garcia, W. S. Wise, A. Kennedy, P. Gurriet, and F. Albarède (1991), The evolution of Mauna Kea volcano, Hawaii: Petrogenesis of tholeiitic and alkalic basalts, *Journal of Geophysical Research*, 96(B9), 14347-14375.

- Funck, T., and H.-U. Schmincke (1998), Growth and destruction of Gran Canaria deduced from seismic reflection and bathymetric data, *Journal of Geophysical Research*, 103(B7), 15393-15408.
- Fuster, J. M., F. Hernán, A. Cendrero, J. Coello, J. M. Cantagrel, E. Ancochea, and E. Ibarrola (1993), Geocronología de la Isla de El Hierro (Islas Canarias), *Boletín de la Real Sociedad Española de Historia Natural. Sección Geológica*, 88(1-4), 85-97.
- Galipp, K., A. Klügel, and T. H. Hansteen (2006), Changing depths of magma fractionation and stagnation during the evolution of an oceanic island volcano: La Palma (Canary Islands), *Journal of Volcanology and Geothermal Research*, 155(3-4), 285-306.
- Garmin Ltd (2007), *GPSMAP 76CSx mapping GPS owner's manual*.
- Gee, M. J. R., D. G. Masson, A. B. Watts, and N. C. Mitchell (2001a), Offshore continuation of volcanic rift zones, El Hierro, Canary Islands, *Journal of Volcanology and Geothermal Research*, 105(1-2), 107-119.
- Gee, M. J. R., A. B. Watts, D. G. Masson, and N. C. Mitchell (2001b), Landslides and the evolution of El Hierro in the Canary Islands, *Marine Geology*, 177(3-4), 271-293.
- Geldmacher, J., P. van den Bogaard, K. Hoernle, and H.-U. Schmincke (2000), The  $^{40}\text{Ar}/^{39}\text{Ar}$  age dating of the Madeira Archipelago and hotspot track (eastern North Atlantic), *Geochemistry, Geophysics, Geosystems*, 1, 1999GC000018.
- Geldmacher, J., K. Hoernle, P. van den Bogaard, G. Zankl, and D. Garbe-Schönberg (2001), Earlier history of the  $\geq 70$ -Ma-old Canary hotspot based on the temporal and geochemical evolution of the Selvagen Archipelago and neighboring seamounts in the eastern North Atlantic, *Journal of Volcanology and Geothermal Research*, 111(1-4), 55-87.
- Ghiorso, M. S., and R. O. Sack (1995), Chemical transfer in magmatic processes IV. A revised and internally consistent thermodynamic model for the interpolation and extrapolation of liquid-solid equilibria in magmatic systems at elevated temperatures and pressures, *Contributions to Mineralogy and Petrology*, 119, 197-212.
- Glicken, H. (1996), *Rockslide-debris avalanche of May 18, 1980, Mount St. Helens volcano, Washington*, 90 pp., US Geological Survey, Open File Report 96-677.
- Greenwood, J. C. (2001), The secular geochemical evolution of the Trindade mantle plume, PhD thesis, 292 pp, University of Cambridge.
- Gudmundsson, A., L. B. Marinoni, and J. Marti (1999), Injection and arrest of dykes: implications for volcanic hazards, *Journal of Volcanology and Geothermal Research*, 88(1), 1-13.
- Guillou, H., J. C. Carracedo, F. J. Pérez Torrado, and E. Rodríguez Badiola (1996), K-Ar ages and magnetic stratigraphy of a hotspot-induced, fast grown oceanic island: El Hierro, Canary Islands, *Journal of Volcanology and Geothermal Research*, 73(1-2), 141-155.
- Guillou, H., J. C. Carracedo, R. Paris, and F. J. Pérez Torrado (2004), Implications for the early shield-stage evolution of Tenerife from K/Ar ages and magnetic stratigraphy, *Earth and Planetary Science Letters*, 222(2), 599-614.
- Gurenko, A. A., T. H. Hansteen, and H.-U. Schmincke (1996), Evolution of parental magmas of Miocene shield basalts of Gran Canaria (Canary Islands): constraints from crystal, melt and fluid inclusions in minerals, *Contributions to Mineralogy and Petrology*, 124(3), 422-435.
- Gurenko, A. A., and H.-U. Schmincke (2000), S concentrations and its speciation in Miocene basaltic magmas north and south of Gran Canaria (Canary Islands): constraints from glass inclusions in olivine and clinopyroxene, *Geochimica et Cosmochimica Acta*, 64(13), 2321-2337.
- Hansteen, T. H., A. Klügel, and H.-U. Schmincke (1998), Multi-stage magma ascent beneath the Canary Islands: evidence from fluid inclusions, *Contributions to Mineralogy and Petrology*, 132(1), 48-64.
- Hardarson, B. S., and J. G. Fitton (1991), Increased mantle melting beneath Snæfellsjökull volcano during Late Pleistocene deglaciation, *Nature*, 353(6339), 62-64.
- Harvey, P. K., D. M. Taylor, R. D. Hendry, and F. Bancroft (1973), An accurate fusion method for the analysis of rocks and chemically related materials by X-ray fluorescence spectrometry, *X-ray Spectrometry*, 2, 33-34.
- Hausen, H. (1972), Outlines of the geology of El Hierro, *Commentationes Physico-Mathematicae*, 43, 65-167.
- Hernández Pacheco, A. (1982), Sobre una posible erupción en 1793 en la isla de El Hierro (Canarias), *Estudios Geológicos*, 38, 15-25.

- Hildenbrand, A., P. Y. Gillot, and I. Le Roy (2004), Volcano-tectonic and geochemical evolution of an oceanic intra-plate volcano: Tahiti-Nui (French Polynesia), *Earth and Planetary Science Letters*, 217(3-4), 349-365.
- Hill, D. P., F. Pollitz, and C. Newhall (2002), Earthquake-volcano interactions, *Physics Today*, 55(11), 41-47.
- Hirose, K., and I. Kushiro (1993), Partial melting of dry peridotites at high pressures: Determination of compositions of melts segregated from peridotite using aggregates of diamond, *Earth and Planetary Science Letters*, 114(4), 477-489.
- Hoernle, K., and H.-U. Schmincke (1993a), The role of partial melting in the 15-Ma geochemical evolution of Gran Canaria: a blob model for the Canary Hotspot, *Journal of Petrology*, 34(3), 599-626.
- Hoernle, K., and H.-U. Schmincke (1993b), The petrology of the tholeiites through melilite nephelinites on Gran Canaria, Canary Islands: crystal fractionation, accumulation, and depths of melting, *Journal of Petrology*, 34(3), 573-597.
- Holcomb, R. T., and R. C. Searle (1991), Large landslides from oceanic volcanoes, *Marine Geotechnology*, 10(1-2), 19-32.
- Holik, J. S., P. D. Rabinowitz, and J. A. Austin (1991), Effects of Canary hotspot volcanism on structure of oceanic crust off Morocco, *Journal of Geophysical Research*, 96(B7), 12039-12067.
- Humphreys, M. C. S., J. D. Blundy, and R. S. J. Sparks (2006), Magma evolution and open-system processes at Shiveluch volcano: insights from phenocryst zoning, *Journal of Petrology*, 47(12), 2303-2334.
- Instituto Geográfico Nacional (1975-2007), Catálogo y boletines sísmicos, edited, Ministerio de Fomento, Servicio de información sísmica.
- Jull, M., and D. McKenzie (1996), The effect of deglaciation on mantle melting beneath Iceland, *Journal of Geophysical Research*, 101(B10), 21815-21828.
- Klein, C., and C. S. Hurlbut Jr. (1993), *Manual of Mineralogy*, 21<sup>st</sup>/after J. D. Dana ed., John Wiley & Sons, Inc., New York.
- Klügel, A., T. H. Hansteen, and H.-U. Schmincke (1997), Rates of magma ascent and depths of magma reservoirs beneath La Palma (Canary Islands), *Terra Nova*, 9(3), 117-121.
- Klügel, A., K. A. Hoernle, H.-U. Schmincke, and J. D. L. White (2000), The chemically zoned 1949 eruption on La Palma (Canary Islands): Petrologic evolution and magma supply dynamics of a rift zone eruption, *Journal of Geophysical Research*, 105(B3), 5997-6016.
- Klügel, A., T. H. Hansteen, and K. Galipp (2005), Magma storage and underplating beneath Cumbre Vieja volcano, La Palma (Canary Islands), *Earth and Planetary Science Letters*, 236, 211-226.
- Klügel, A., and F. Klein (2006), Complex magma storage and ascent at embryonic submarine volcanoes from the Madeira Archipelago, *Geology*, 34(5), 337-340.
- Krastel, S., H.-U. Schmincke, C. L. Jacobs, R. Rihm, T. P. Le Bas, and B. Alibés (2001), Submarine landslides around the Canary Islands, *Journal of Geophysical Research*, 106(B3), 3977-3998.
- Kress, V. C., and I. S. E. Carmichael (1988), Stoichiometry of the iron oxidation reaction in silicate melts, *American Mineralogist*, 73(11-12), 1267-1274.
- Le Bas, M. J., R. W. Le Maitre, A. Streckeisen, and B. Zanettin (1986), A chemical classification of volcanic rocks based on the total alkali-silica diagram, *Journal of Petrology*, 27(3), 745-750.
- Le Bas, M. J. (2000), IUGS reclassification of the high-Mg and picritic volcanic rocks, *Journal of Petrology*, 41(10), 1467-1470.
- Le Maitre, R. W., P. Bateman, A. Dudek, J. Keller, L. Lameyre, P. Sabine, R. Schmidt, H. Sorensen, W. A. R. Streckeisen, and B. Zanettin (1989), *A Classification of Igneous rocks and Glossary of Terms: Recommendations of the International Union of Geological Sciences Subcommittee on the Systematics of Igneous Rocks*, 193 pp., Blackwell Scientific Publications, Oxford.
- Leonhardt, R., and H. C. Soffel (2006), The growth, collapse and quiescence of Teno volcano, Tenerife: new constraints from paleomagnetic data, *International Journal of Earth Sciences*, 95(6), 1053-1064.
- Lindsley, D. H. (1983), Pyroxene thermometry, *American Mineralogist*, 68(5-6), 477-493.
- Lipman, P. W. (1980), The southwest rift zone of Mauna Loa: Implications for structural evolution of Hawaiian volcanoes, *American Journal of Science*, 280, 752-776.

- Lipman, P. W., N. G. Banks, and J. M. Rhodes (1985a), Degassing-induced crystallization of basaltic magma and effects on lava rheology, *Nature*, 317(6038), 604-607.
- Lipman, P. W., J. P. Lockwood, R. T. Okamura, D. A. Swanson, and K. M. Yamashita (1985b), Ground deformation associated with the 1975 magnitude-7.2 earthquake and resulting changes in activity of Kilauea volcano, Hawaii, *US Geological Survey Professional Paper*, 1276.
- Lipman, P. W., W. R. Normark, J. G. Moore, J. B. Wilson, and C. E. Gutmacher (1988), The giant submarine Alike debris slide, Mauna Loa, Hawaii, *Journal of Geophysical Research*, 93(B5), 4279-4299.
- Lipman, P. W., J. M. Rhodes, and G. B. Dalrymple (1991), The Ninole Basalt—Implications for the structural evolution of Mauna Loa volcano, Hawaii, *Bulletin of Volcanology*, 53(1), 1-19.
- Lofgren, G. (1974), An experimental study of plagioclase crystal morphology: isothermal crystallization, *American Journal of Science*, 274, 243-273.
- Longpré, M.-A., R. del Potro, V. R. Troll, and G. R. Nicoll (2008a), Engineering geology and future stability of the El Risco landslide, NW-Gran Canaria, Spain, *Bulletin of Engineering Geology and the Environment*, 67(2), 165-172.
- Longpré, M.-A., V. R. Troll, and T. H. Hansteen (2008b), Upper mantle magma storage and transport under a Canarian shield-volcano, Teno, Tenerife (Spain), *Journal of Geophysical Research*, 113, B08203, DOI: 10.1029/2007JB005422.
- MacDonald, G. A. (1965), Hawaiian calderas, *Pacific Science*, 19, 320-334.
- MacDonald, G. A., A. T. Abbott, and F. L. Peterson (1983), *Volcanoes in the Sea: The Geology of Hawaii*, 2<sup>nd</sup> ed., University of Hawaii Press, Honolulu.
- MacLennan, J., D. McKenzie, K. Gronvold, and L. Slater (2001), Crustal accretion under northern Iceland, *Earth and Planetary Science Letters*, 191(3-4), 295-310.
- MacLennan, J., M. Jull, D. McKenzie, L. Slater, and K. Grönvold (2002), The link between volcanism and deglaciation in Iceland, *Geochemistry Geophysics Geosystems*, 3(11), 1062.
- Manconi, A., T. R. Walter, and F. Amelung (2007), Effects of mechanical layering on volcano deformation, *Geophysical Journal International*, 170, 952-958.
- Marinoni, L. B., and A. Gudmundsson (2000), Dykes, faults and palaeostresses in the Teno and Anaga massifs of Tenerife (Canary Islands), *Journal of Volcanology and Geothermal Research*, 103(1-4), 83-103.
- Marsh, B. D. (1996), Solidification fronts and magmatic evolution, *Mineralogical Magazine*, 60(1), 5-40.
- Martí, J., J. Mitjavila, and V. Araña (1994), Stratigraphy, structure and geochronology of the Las Cañadas caldera (Tenerife, Canary Islands), *Geological Magazine*, 131, 715-727.
- Masson, D. G. (1996), Catastrophic collapse of the volcanic island of Hierro 15 ka ago and the history of landslides in the Canary Islands, *Geology*, 24(3), 231-234.
- Masson, D. G., A. B. Watts, M. J. R. Gee, R. Urgeles, N. C. Mitchell, T. P. Le Bas, and M. Canals (2002), Slope failures on the flanks of the western Canary Islands, *Earth-Science Reviews*, 57(1-2), 1-35.
- McDougall, I., and H.-U. Schmincke (1976), Geochronology of Gran Canaria, Canary Islands: Age of shield building volcanism and other magmatic phases, *Bulletin of Volcanology*, 40(1), 57-77.
- McGovern, P. J. (2007), Flexural stresses beneath Hawaii: Implications for the October 15, 2006, earthquakes and magma ascent, *Geophysical Research Letters*, 34, L23305, DOI: 10.1029/2007GL031305.
- McGuire, A. V., M. D. Dyar, and K. A. Ward (1989), Neglected  $\text{Fe}^{3+}/\text{Fe}^{2+}$  ratios—A study of  $\text{Fe}^{3+}$  content of megacrysts from alkali basalts, *Geology*, 17(8), 687-690.
- McGuire, W. J. (1996), Volcano instability: a review of contemporary themes, in *Volcano Instability on the Earth and Other Planets*, edited by W. J. McGuire, A. P. Jones and J. Neuberg, pp. 1-23, Geological Society London Special Publication No. 110.
- McKenzie, D., and M. J. Bickle (1988), The volume and composition of melt generated by extension of the lithosphere, *Journal of Petrology*, 29(3), 625-679.
- McKenzie, D., and R. K. O'Nions (1991), Partial melt distributions from inversion of rare earth element concentrations, *Journal of Petrology*, 32(5), 1021-1091.
- McKenzie, D., J. Jackson, and K. Priestley (2005), Thermal structure of oceanic and continental lithosphere, *Earth and Planetary Science Letters*, 233(3-4), 337-349.

- Moore, J. G. (1964), Giant submarine landslides on the Hawaiian Ridge, *US Geological Survey Special Paper*, 501-D, 95-98.
- Moore, J. G. (1987), Subsidence in the Hawaiian Ridge, in *Volcanism in Hawaii*, edited by R. W. Decker, T. L. Wright and P. H. Stauffer, pp. 85-100, US Geological Survey Professional Paper 1350.
- Moore, J. G., D. A. Clague, R. T. Holcomb, P. W. Lipman, W. R. Normark, and M. E. Torresan (1989), Prodigious submarine landslides on the Hawaiian Ridge, *Journal of Geophysical Research*, 94(B12), 17465-17484.
- Moore, J. G., W. R. Normark, and R. T. Holcomb (1994), Giant Hawaiian landslides, *Annual Review of Earth and Planetary Sciences*, 22(1), 119-144.
- Mordick, B. E., and A. F. Glazner (2006), Clinopyroxene thermobarometry of basalts from the Coso and Big Pine volcanic fields, California, *Contributions to Mineralogy and Petrology*, 152(1), 111-124.
- Morgan, W. J. (1983), Hotspot tracks and the early rifting of the Atlantic, *Tectonophysics*, 94, 123-139.
- Münn, S. (2005), Structural analysis of gravity driven deformations of El Hierro, Diploma thesis, 135 pp, University of Kiel, Germany.
- Münn, S., T. R. Walter, and A. Klügel (2006), Gravitational spreading controls rift zones and flank instability on El Hierro, Canary Islands, *Geological Magazine*, 143(03), 257-268.
- Naumann, T., and D. Geist (2000), Physical volcanology and structural development of Cerro Azul Volcano, Isabela Island, Galápagos: implications for the development of Galápagos-type shield volcanoes, *Bulletin of Volcanology*, 61(8), 497-514.
- Neumann, E.-R. (1991), Ultramafic and mafic xenoliths from Hierro, Canary Islands: evidence for melt infiltration in the upper mantle, *Contributions to Mineralogy and Petrology*, 106(2), 236-252.
- Neumann, E.-R., E. Wulff-Pedersen, S. L. Simonsen, N. J. Pearson, J. Martí, and J. Mitjavila (1999), Evidence for fractional crystallization of periodically refilled magma chambers in Tenerife, Canary Islands, *Journal of Petrology*, 40(7), 1089-1123.
- Norrish, K., and J. T. Hutton (1969), An accurate X-ray spectrographic method for the analysis of a wide range of geological samples, *Geochimica et Cosmochimica Acta*, 33(4), 431-453.
- Nostro, C., R. S. Stein, M. Cocco, M. E. Belardinelli, and W. Marzocchi (1998), Two-way coupling between Vesuvius eruptions and southern Apennine earthquakes, Italy, by elastic stress transfer, *Journal of Geophysical Research*, 103(B10), 24487-24504.
- O'Hara, M. J. (1977), Geochemical evolution during fractional crystallisation of a periodically refilled magma chamber, *Nature*, 266(5602), 503-507.
- Oehler, J. F., J. F. Lénat, and P. Labazuy (2008), Growth and collapse of the Reunion Island volcanoes, *Bulletin of Volcanology*, 70(6), 717-742.
- Olafsson, M., and D. H. Eggler (1983), Phase relations of amphibole, amphibole-carbonate, and phlogopite-carbonate peridotite: petrologic constraints on the asthenosphere, *Earth and Planetary Science Letters*, 64(2), 305-315.
- Pallister, J. S., R. P. Hoblitt, D. R. Crandell, and D. R. Mullineaux (1992), Mount St. Helens a decade after the 1980 eruptions: magmatic models, chemical cycles, and a revised hazards assessment, *Bulletin of Volcanology*, 54(2), 126-146.
- Palomo, C., J. Acosta, J. L. Sanz, P. Herranz, A. Muñoz, E. Uchupi, and J. Escartin (1997), Morphometric interpretation of the northwest and southeast slopes of Tenerife, Canary Islands, *Journal of Geophysical Research*, 102(B9), 20325-20342.
- Paris, R. (2002), Rythmes de construction et de destruction des édifices volcaniques de point chaud: l'exemple des Iles Canaries (Espagne), Ph.D. thesis, Université Paris 1 Panthéon – Sorbonne.
- Paris, R., J. C. Carracedo, and F. J. Pérez Torrado (2005a), Massive flank failures and tsunamis in the Canary Islands: past, present, future, *Zeitschrift für Geomorphologie, Supplementbände*, 140, 37-54.
- Paris, R., H. Guillou, J. C. Carracedo, and F. J. Pérez Torrado (2005b), Volcanic and morphological evolution of La Gomera (Canary Islands), based on new K-Ar ages and magnetic stratigraphy: implications for oceanic island evolution, *Journal of the Geological Society, London*, 162(3), 501-512.
- Pellicer, J. M. (1977), Estudio volcánológico de la Isla de El Hierro (Islas Canarias), *Estudios Geológicos*, 33, 181-197.

- Pellicer, J. M. (1979), Estudio geoquímico del vulcanismo de la isla de Hierro Archipiélago Canario, *Estudios Geológicos*, 35, 15-29.
- Peltier, A., T. Staudacher, and P. Bachèlery (2007), Constraints on magma transfers and structures involved in the 2003 activity at Piton de la Fournaise from displacement data, *Journal of Geophysical Research*, 112(B03207), DOI: 10.1029/2006JB004379.
- Pérez Torrado, F. J., J. C. Carracedo, and J. Mangas (1995), Geochronology and stratigraphy of the Roque Nublo Cycle, Gran Canaria, Canary Islands, *Journal of the Geological Society, London*, 152(5), 807-818.
- Perugini, D., T. Busa, G. Poli, and S. Nazzareni (2003), The role of chaotic dynamics and flow fields in the development of disequilibrium textures in volcanic rocks, *Journal of Petrology*, 44(4), 733-756.
- Pinel, V., and C. Jaupart (2000), The effect of edifice load on magma ascent beneath a volcano, *Philosophical Transactions of the Royal Society: Mathematical, Physical and Engineering Sciences*, 358(1770), 1515-1532.
- Pinel, V., and C. Jaupart (2003), Magma chamber behavior beneath a volcanic edifice, *Journal of Geophysical Research*, 108(B2), 2072.
- Pinel, V., and C. Jaupart (2004), Likelihood of basaltic eruptions as a function of volatile content and volcanic edifice size, *Journal of Volcanology and Geothermal Research*, 137(1-3), 201-217.
- Pinel, V., and C. Jaupart (2005), Some consequences of volcanic edifice destruction for eruption conditions, *Journal of Volcanology and Geothermal Research*, 145(1-2), 68-80.
- Presley, T. K., J. M. Sinton, and M. Pringle (1997), Postshield volcanism and catastrophic mass wasting of the Waianae Volcano, Oahu, Hawaii, *Bulletin of Volcanology*, 58(8), 597-616.
- Putirka, K., M. Johnson, R. Kinzler, J. Longhi, and D. Walker (1996), Thermobarometry of mafic igneous rocks based on clinopyroxene-liquid equilibria, 0-30 kbar, *Contributions to Mineralogy and Petrology*, 123(1), 92-108.
- Putirka, K. (1997), Magma transport at Hawaii; inferences based on igneous thermobarometry, *Geology*, 25(1), 69.
- Putirka, K. (1999), Clinopyroxene+liquid equilibria to 100 kbar and 2450 K, *Contributions to Mineralogy and Petrology*, 135(2), 151-163.
- Putirka, K., H. Mikaelian, F. Ryerson, and H. Shaw (2003), New clinopyroxene-liquid thermobarometers for mafic, evolved, and volatile-bearing lava compositions, with applications to lavas from Tibet and the Snake River Plain, Idaho, *American Mineralogist*, 88(10), 1542-1554.
- Ranero, C. R., M. Torne, and E. Banda (1995), Gravity and multichannel seismic reflection constraints on the lithospheric structure of the Canary Swell, *Marine Geophysical Researches*, 17(6), 519-534.
- Ridley, W. I. (1971), The origin of some collapse structures in the Canary Islands, *Geological Magazine*, 108(6), 477-484.
- Roeder, P. L., and R. F. Emslie (1970), Olivine-liquid equilibrium, *Contributions to Mineralogy and Petrology*, 29(4), 275-289.
- Roest, W. R., J. J. Dañobeitia, J. Verhoef, and B. J. Collette (1992), Magnetic anomalies in the Canary Basin and the Mesozoic evolution of the Central North Atlantic, *Marine Geophysical Researches*, 14(1), 1-24.
- Rollinson, H. R. (1993), *Using Geochemical Data: Evaluation, Presentation, Interpretation*, 352 pp., Pearson Prentice Hall, Essex, UK.
- Rutherford, M. J., H. Sigurdsson, S. Carey, and A. Davis (1985), The May 18, 1980, eruption of Mount St. Helens. I-Melt composition and experimental phase equilibria, *Journal of Geophysical Research*, 90, 2929-2947.
- Ryan, M. P. (1988), The mechanics and three-dimensional internal structure of active magmatic systems: Kilauea Volcano, Hawaii, *Journal of Geophysical Research*, 93(B5), 4213-4248.
- Sachs, P. M., and T. H. Hansteen (2000), Pleistocene underplating and metasomatism of the lower continental crust: a xenolith study, *Journal of Petrology*, 41(3), 331-356.
- Schmid, R. (1981), Descriptive nomenclature and classification of pyroclastic deposits and fragments: Recommendations of the IUGS Subcommittee on the Systematics of Igneous Rocks, *Geology*, 9(1), 41-43.

- Schmincke, H.-U. (1976), The geology of the Canary Islands, in *Biogeography and Ecology in the Canary Islands*, edited by G. Kunkel, pp. 67-184, W. Junk, The Hague.
- Schmincke, H.-U. (1994), *Geological field guide of Gran Canaria*, 7<sup>th</sup> ed., 179 pp., Pluto Press, Kiel, Germany.
- Schroeder, B., G. Thompson, M. Sulanowska, and J. N. Ludden (1980), Analysis of geologic materials using an automated X-ray fluorescence system, *X-ray Spectrometry*, 9, 198-205.
- Schwarz, S., A. Klügel, and C. Wohlgemuth-Ueberwasser (2004), Melt extraction pathways and stagnation depths beneath the Madeira and Desertas rift zones (NE Atlantic) inferred from barometric studies, *Contributions to Mineralogy and Petrology*, 147(2), 228-240.
- Siebert, L. (1984), Large volcanic debris avalanches: characteristics of source areas, deposits, and associated eruptions, *Journal of Volcanology and Geothermal Research*, 22(3-4), 163-197.
- Siebert, L. (1992), Threats from debris avalanches, *Nature*, 356(6371), 658-659.
- Sigvaldason, G. E., K. Annertz, and M. Nilsson (1992), Effect of glacier loading/deloading on volcanism: postglacial volcanic production rate of the Dyngjufjöll area, central Iceland, *Bulletin of Volcanology*, 54(5), 385-392.
- Simonsen, S. L., E. R. Neumann, and K. Seim (2000), Sr-Nd-Pb isotope and trace-element geochemistry evidence for a young HIMU source and assimilation at Tenerife (Canary Island), *Journal of Volcanology and Geothermal Research*, 103(1-4), 299-312.
- Slater, L., M. Jull, D. McKenzie, and K. Gronvöld (1998), Deglaciation effects on mantle melting under Iceland: results from the northern volcanic zone, *Earth and Planetary Science Letters*, 164(1-2), 151-164.
- Sleep, N. H. (1990), Hotspots and mantle plumes: Some phenomenology, *Journal of Geophysical Research*, 95(5), 6715-6736.
- Soesoo, A. (1997), A multivariate statistical analysis of clinopyroxene composition: empirical coordinates for the crystallisation PT-estimations, *GFF*, 46, 55-60.
- Sparks, R. S. J., and H. Pinkerton (1978), Effect of degassing on rheology of basaltic lava, *Nature*, 276(5686), 385-386.
- Staudigel, H., and H.-U. Schmincke (1984), The Pliocene Seamount Series of La Palma/Canary Islands, *Journal of Geophysical Research*, 89(B13), 11195-11215.
- Stein, R. S. (1999), The role of stress transfer in earthquake occurrence, *Nature*, 402(6762), 605-609.
- Stillman, C. J., M. J. Bennell-Baker, J. D. Smewing, J. M. Fuster, M. Munoz, and J. Sagredo (1975), Basal complex of Fuerteventura (Canary Islands) is an oceanic intrusive complex with rift-system affinities, *Nature*, 257(5526), 469-471.
- Stillman, C. J., H. Furnes, M. J. Le Bas, A. H. F. Robertson, and J. Zielonka (1982), The geological history of Maio, Cape Verde Islands, *Journal of the Geological Society, London*, 139(3), 347-361.
- Stolper, E., and D. Walker (1980), Melt density and the average composition of basalt, *Contributions to Mineralogy and Petrology*, 74(1), 7-12.
- Székéméty, N., C. Laj, H. Guillou, C. Kissel, A. Mazaud, and J. C. Carracedo (1999), Geomagnetic paleosecular variation in the Brunhes period, from the island of El Hierro (Canary Islands), *Earth and Planetary Science Letters*, 165(3-4), 241-253.
- Tagami, T., Y. Nishimitsu, and D. R. Sherrod (2003), Rejuvenated-stage volcanism after 0.6-m.y. quiescence at West Maui volcano, Hawaii: new evidence from K-Ar ages and chemistry of Lahaina Volcanics, *Journal of Volcanology and Geothermal Research*, 120(3-4), 207-214.
- Takada, A. (1989), Magma transport and reservoir formation by a system of propagating cracks, *Bulletin of Volcanology*, 52(2), 118-126.
- Tanaka, S., M. Ohtake, and H. Sato (2004), Tidal triggering of earthquakes in Japan related to the regional tectonic stress, *Earth Planets Space*, 56(5), 511-515.
- ten Brink, U. S., and T. M. Brocher (1987), Multichannel seismic evidence for a subcrustal intrusive complex under Oahu and a model for Hawaiian volcanism, *Journal of Geophysical Research*, 92(B13), 13687-13707.



- Thirlwall, M. F., B. S. Singer, and G. F. Marriner (2000),  $^{39}\text{Ar}$ - $^{40}\text{Ar}$  ages and geochemistry of the basaltic shield stage of Tenerife, Canary Islands, Spain, *Journal of Volcanology and Geothermal Research*, 103(1), 247-297.
- Thompson, R. N. (1974), Some high-pressure pyroxenes, *Mineralogical Magazine*, 39, 768-787.
- Thornber, C., and F. Trusdell (2008), Field, petrologic and experimental evidence for rapid transport of large magma volumes from great depths during the 1950 eruption of Mauna Loa, paper presented at IAVCEI General Assembly, Reykjavík, Iceland, 17-22 August
- Tibaldi, A. (2004), Major changes in volcano behaviour after a sector collapse: insights from Stromboli, Italy, *Terra Nova*, 16(1), 2-8.
- Tilling, R. I., and J. J. Dvorak (1993), Anatomy of a basaltic volcano, *Nature*, 363(6425), 125-133.
- Toplis, M., and A. Corgne (2002), An experimental study of element partitioning between magnetite, clinopyroxene and iron-bearing silicate liquids with particular emphasis on vanadium, *Contributions to Mineralogy and Petrology*, 144(1), 22-37.
- Troll, V. R., and H.-U. Schmincke (2002), Magma mixing and crustal recycling recorded in ternary feldspar from compositionally zoned peralkaline Ignimbrite 'A', Gran Canaria, Canary Islands, *Journal of Petrology*, 43(2), 243-270.
- Troll, V. R., P. M. Sachs, H.-U. Schmincke, and M. Sumita (2003), The REE-Ti mineral chevkinite in comenditic magmas from Gran Canaria, Spain: a SYXRF-probe study, *Contributions to Mineralogy and Petrology*, 145(6), 730-741.
- Urgeles, R., D. G. Masson, M. Canals, A. B. Watts, and T. Le Bas (1999), Recurrent large-scale landsliding on the west flank of La Palma, Canary Islands, *Journal of Geophysical Research*, 104(B11), 25,331.
- Walker, G. P. L. (1992), "Coherent intrusion complexes" in large basaltic volcanoes — a new structural model, *Journal of Volcanology and Geothermal Research*, 50(1-2), 41-54.
- Walker, G. P. L. (1999), Volcanic rift zones and their intrusion swarms, *Journal of Volcanology and Geothermal Research*, 94(1-4), 21-34.
- Walter, T. R., and H.-U. Schmincke (2002), Rifting, recurrent landsliding and Miocene structural reorganization on NW-Tenerife (Canary Islands), *International Journal of Earth Sciences*, 91(4), 615-628.
- Walter, T. R. (2003), Buttrressing and fractional spreading of Tenerife, an experimental approach on the formation of rift zones, *Geophysical Research Letters*, 30(6), 1296.
- Walter, T. R., and V. R. Troll (2003), Experiments on rift zone evolution in unstable volcanic edifices, *Journal of Volcanology and Geothermal Research*, 127(1-2), 107-120.
- Walter, T. R., and F. Amelung (2004), Influence of volcanic activity at Mauna Loa, Hawaii, on earthquake occurrence in the Kaoiki Seismic Zone, *Geophysical Research Letters*, 31, L07622, DOI: 10.1029/2003GL019131.
- Walter, T. R., V. Acocella, M. Neri, and F. Amelung (2005a), Feedback processes between magmatic events and flank movement at Mount Etna (Italy) during the 2002-2003 eruption, *Journal of Geophysical Research*, 110, B10205.
- Walter, T. R., V. R. Troll, B. Cailleau, A. Belousov, H.-U. Schmincke, F. Amelung, and P. van den Bogaard (2005b), Rift zone reorganization through flank instability in ocean island volcanoes: an example from Tenerife, Canary Islands, *Bulletin of Volcanology*, 67(4), 281-291.
- Walter, T. R., and F. Amelung (2006), Volcano-earthquake interaction at Mauna Loa volcano, Hawaii, *Journal of Geophysical Research*, 111(B5), B05204, DOI: 10.1029/2005JB003861.
- Wass, S. Y. (1979), Multiple origins of clinopyroxenes in alkali basaltic rocks, *Lithos*, 12, 115-132.
- Watson, S., and D. McKenzie (1991), Melt generation by plumes: a study of Hawaiian volcanism, *Journal of Petrology*, 32(3), 501-537.
- Watts, A. B., U. S. ten Brink, P. Buhl, and T. M. Brocher (1985), A multichannel seismic study of lithospheric flexure across the Hawaiian-Emperor seamount chain, *Nature*, 315(6015), 105-111.
- Watts, A. B. (1994), Crustal structure, gravity anomalies and flexure of the in the vicinity of the Canary Islands, *Geophysical Journal International*, 119, 648-666.

- 
- Watts, A. B., and D. G. Masson (1995), A giant landslide on the north flank of Tenerife, Canary Islands, *Journal of Geophysical Research*, 100(B12), 24487-24498.
- Watts, A. B., C. Peirce, J. Collier, R. Dalwood, J. P. Canales, and T. J. Henstock (1997), A seismic study of lithospheric flexure in the vicinity of Tenerife, Canary Islands, *Earth and Planetary Science Letters*, 146(3-4), 431-447.
- Watts, A. B., and S. Zhong (2000), Observations of flexure and the rheology of oceanic lithosphere, *Geophysical Journal International*, 142(3), 855-875.
- Watts, A. B. (2001), *Isostasy and Flexure of the Lithosphere*, 458 pp., Cambridge University Press.
- Weertman, J. (1971), Theory of water-filled crevasses in glaciers applied to vertical magma transport beneath oceanic ridges, *Journal of Geophysical Research*, 76(5), 1171-1183.
- White, J. D. L., and B. F. Houghton (2006), Primary volcanoclastic rocks, *Geology*, 34(8), 677-680.
- Wilshire, H. G., and S. H. Kirby (1989), Dikes, joints, and faults in the upper mantle, *Tectonophysics*, 161(1-2), 23-31.
- Wilson, J. T. (1963), A possible origin of the Hawaiian Islands, *Canadian Journal of Physics*, 41(6), 863-870.
- Wood, D. A., J. L. Joron, M. Treuil, M. Norry, and J. Tarney (1979), Elemental and Sr isotope variations in basic lavas from Iceland and the surrounding ocean floor, *Contributions to Mineralogy and Petrology*, 70(3), 319-339.
- Wright, T. L., and F. W. Klein (2006), Deep magma transport at Kilauea volcano, Hawaii, *Lithos*, 87(1-2), 50-79.
- Wyllie, P. J., K. G. Cox, and G. M. Biggar (1962), The habit of apatite in synthetic systems and igneous rocks, *Journal of Petrology*, 3(2), 238-243.
- Ye, S., J. P. Canales, R. Rihm, J. J. Dañobeitia, and J. Gallart (1999), A crustal transect through the northern and northeastern part of the volcanic edifice of Gran Canaria, Canary Islands, *Journal of Geodynamics*, 28(1), 3-26.
- Zienkiewicz, O. C. (1989), *The Finite Element Method*, 1<sup>st</sup> ed., McGraw-Hill, London.

## **APPENDIX A:**

Adapted version of:

Longpré, M.-A., R. del Potro, V. R. Troll, and G. R. Nicoll (2008), Engineering geology and future stability of the El Risco landslide, NW-Gran Canaria, Spain, *Bulletin of Engineering Geology and the Environment*, 67(2), 165-172.

This work is the product of collaborative research conducted while the main author was on the Ph.D. register at the University of Dublin, Trinity College. The author carried out field work at the El Risco landslide, in Gran Canaria, in April 2005, with the assistance of G. R. Nicoll. The numerical models and stability analysis are the work of R. del Potro, and the author could not reproduce this part of the work on his own. The present author was responsible for writing and editing the article and received help from R. del Potro, V. R. Troll and G. R. Nicoll.

## A.1 Abstract

A 200-m-long segment of the only main road in NW-Gran Canaria is built on landslide deposits near the village of El Risco. Structural mapping and topography analysis reveal that the N-S striking landslide head scarp is the upper part of a sub-circular failure surface. The southern side of the landslide is delimited by a much older E-W strike-slip fault. Prior to pavement resurfacing in 2006, cracks in the road tarmac at the northern and southern sides of the landslide suggested ongoing creep movement. Slope stability analyses suggest that peak ground acceleration (PGA) was the most likely trigger for initial failure. Regional seismicity may pose a risk of a further sudden movement in the foreseeable future.

## A.2 Introduction

Coastal regions of volcanic ocean islands are often characterised by steep and unstable slopes, which pose considerable challenges for road engineering. Transportation infrastructure needs to accommodate heavier traffic loads due to the dense and increasing population; there are 610 inhabitants per km<sup>2</sup> in Mauritius; 520 in Gran Canaria; 420 in Tenerife and 315 in La Réunion [United Nations, 2004; Instituto Nacional de Estadística, 2006]. Careful planning by engineers is required to minimise road construction costs and optimise road endurance with minimum maintenance. Complex measures and designs, such as long tunnels excavated to bypass steep topography, are efficient but very cost intensive. Where traffic flows are smaller and budgets for infra-structure low, the construction of winding and often narrow roads are a cost-effective alternative.

In Gran Canaria where the population of 807,000 is increased by some 3 million tourists per year [Instituto Nacional de Estadística, 2006], only one direct route (road GC-200) links the villages of the west, such as San Nicolás de Tolentino and Mogán, to the urban centres of Las Palmas and Maspalomas in the north and the south of the island (Figure A.1). Other roads through the mountainous centre of the island, such as GC-210, are extremely winding and narrow with some segments only single-track. Located on the edge of the cliff-dominated western coastline, the GC-200 is slightly less winding and narrow, but is heavily used by both local and commercial traffic as well as by tourists wanting to appreciate the spectacular scenery. A 200-m-long section of this road, located 2 km north of the village of El Risco crosses the El Risco landslide (Figures A.2, A.3). A power line and a dirt track that descend to the coast also partly cross the landslide.

Based on a combination of fieldwork, examination of vertical and oblique aerial photographs and slope stability analyses, the paper presents a detailed study of the El Risco landslide. Generalised parameters are used to consider the mechanisms and causes of the failure and to evaluate the present-day stability and the risk of future instability.

### A.3 Background Geology

In north-west Gran Canaria, the Miocene shield-building basalts, the oldest sub-aerial rocks of the island ( $\geq 14$  Ma), dominate the landscape [McDougall and Schmincke, 1976; van den Bogaard and Schmincke, 1998]. These lava flows, which dip slightly to the east, are moderately altered, with many feldspar phenocrysts replaced by zeolite and clay minerals. Moreover, abundant calcite, zeolites and gypsum occur in cracks, vesicles and voids whilst part of the ferromagnesian minerals and the matrix is replaced by alteration minerals such as serpentine and epidote.

A 19-km-wide coastal re-entrant, cutting into the basalts of north-west Gran Canaria, represents the trace of a Miocene giant landslide, with the deposits extending some 20 km off-shore [Funck and Schmincke, 1998]. Erosion and smaller slope failures within this coastal embayment, including the study site, maintain the cliff-dominated shore, characterised by slopes of  $45^\circ$  and steeper. Several faults are reported from the region, either concentric or radial to the Miocene central Tejeda caldera [Schmincke, 1967; Troll et al., 2002].

Dykes of variable composition, mostly radial to the Tejeda caldera, are frequently encountered in the region [Schmincke, 1976]. Five distinct dykes that can be traced over several hundred metres crop out in the vicinity of the El Risco landslide (Figures A.2, A.3) although not identified within the landslide deposits. Two dykes (P1 and P2) of phonolitic composition are the most prominent intrusive features. Both are sub-vertical, have a broad north-west trend, a width of about 1.5 m and a distinctive pinkish colour. A narrower phonolitic dyke (P3), trending broadly west, is encountered at the coast and is cut by P1. Two basaltic dykes (B1 and B2) are observed. B1 is a massive  $\sim 0.5$  m wide dyke and trends broadly north; it is cut by both P1 and P2. B2 is altered and displays an olivine-rich core; it generally trends north but is irregular with several offshoots. It is cut by P2, but its relationship with P1 cannot be determined on the basis of present exposure.

A horizontal offset of  $\sim 55$  m is observed for three dykes (P2, B1, B2, see Figure A.2) whilst no offset of P1 is obvious although a 200-m-long segment of this dyke is

missing and probably was removed or covered by the landslide. The observed displacement is due to an E-W strike-slip (sinistral) fault located at the southern boundary of the study site and characterised by a well-developed and solidified fault breccia. The attitude of the fault plane, exposed in three main areas, is 085/65 N. In one site below the road, a fault plane section (2-m-high, ~30-m-long) contains intense calcite and zeolite mineralisation. Slickensides found in two locations (Figure A.2) plunge 2-4° to 264° (S84°W), indicating strike-slip movement. The fault extends beyond the landslide area inland for at least 200 m, with small vertical displacements estimated to be up to 15-20 m down-dip to the north. These observations suggest that this fault is older than the landslide and probably related to Miocene cyclic activity of the Tejada magmatic system [cf. *Troll et al.*, 2002].

#### **A.4 The El Risco Landslide**

The El Risco landslide is some 45,000 m<sup>2</sup>, extending between 75 and 275 m above sea level. Field observations and cross sections show it to be abruptly delimited to the east by a 65-80° head scarp with a weakly arcuate N-S trend (Figures A.2, A.3, A.4). The head scarp is considered to represent the exposed prolongation of a sub-circular failure surface underlying the displaced rock mass. The surface of the head scarp is irregular and rough and neither fault breccia nor slickensides were observed. No trace of the failure surface is exposed below the road to the north. To the south, however, the head scarp terminates at right angles to the older strike-slip fault (Figure A.2). Whilst the older strike-slip fault did not act as a primary failure surface, it appears to have provided a constraint to the southern extent of the landslide.

The upper part of the failed mass is composed of detached blocks that kept their relative stratigraphic position but were rotated backwards (Figure A.3f). In contrast to the regional basaltic lavas dipping <15°E, the displaced flows have dips of 20-25°E towards the landslide head which steepen to 45°E in the middle part, just below the road, before shallowing to 10°E towards the toe. Following *Varnes* [1978], the El Risco landslide would be described as a rotational slump. However, the two lobes of landslide deposits forming the landslide toe consist of disaggregated blocks which were probably emplaced at higher velocities as a small-scale debris avalanche.

Although the toe of the rotational plane is obscured by the landslide material, field observations and analysis of topographic profiles suggest that the lower part of the sub-circular failure surface is located slightly above 125-135 m above sea level (Figure A.4b).

Pre-failure topography was inferred by comparing topographic patterns encountered inside and outside the landslide area. This suggests that a significant volume of deposits from the northern arm of the slide may have been transported to the beach where it was probably rapidly eroded by wave action (Figure A.4c). From the assumed pre-failure topography, the inferred position of the failure surface and the landslide area, a volume of around one million cubic metres may have been displaced.

During the spring 2005 fieldwork, cracks in the road tarmac were observed along the northern and southern edges of the slide (Figure A.3d), suggesting ongoing creep. The GC-200 road was subsequently resurfaced in 2006.

## A.5 Slope Stability Analyses

Back-analysis based on 2D homogeneous limit equilibrium models (LEM) was undertaken following Bishop's modified method [Bishop, 1955]. The non-circular *Spencer* [1967] and *Janbu* [1957] methods were also tested. All three methodologies produced very similar stability and geometrical values for the El Risco landslide; therefore, Bishop's modified method was retained for simplicity. It was assumed that prior to failure the site could be considered as a well-defined block delimited by the strike-slip fault to the south and a fluvial valley to the north; potential regional/local vertical discontinuities were not considered in the models. The main source of uncertainty in such slope stability models arises in the values of the parameters characterising the slope conditions at the time of failure, essentially the rock-mass strength parameters, the water table conditions, the original topography and failure geometry. A combination of parameter sensitivity analyses and slope instability back-analyses were used to assess the values.

### A.5.1 Rock-Mass Strength

The rock mass involved in the El Risco landslide is entirely composed of hydrothermally altered, partly scoriaceous basaltic lava flows of Miocene age. The rock mass strength parameter values used in the study are shown in Table A.1. According to the Geotechnical Strength Index (GSI) proposed by *Hoek et al.* [1995], the rock mass is BLOCKY and the condition of the joints is FAIR, giving a minimum GSI of 45. Using *Watters and Delahaut* [1995]'s scale (0-4, i.e. no alteration - completely altered to clay) the degree of alteration corresponds to a value of 2. In the first model (i),  $\phi'$  values ranging from 20 to 40° and  $c'$  values of 0 to 300 kPa were used based on other studies [*Watters et al.*, 2000; *Concha-Dimas*, 2004; *Thomas et al.*, 2004; *Zimbelman et al.*, 2004; *Apuani et al.*, 2005] and field

observations. Based on preliminary results from the first model, a friction angle of  $30^\circ$  was assumed for the second model (ii) and a cohesion value of zero was taken to represent residual strength conditions. Unit weight ( $\gamma$ ) values of 19 to 28 kN/ m<sup>3</sup>, spanning most volcanic materials, were used to assess the effect of material density on slope stability for model (i) and, given its negligible effect on the stability analyses, a representative value of 24 kN/ m<sup>3</sup> was taken for (ii).

#### A.5.2 Water Table Conditions

Little is known of the ground water conditions at El Risco, due to the lack of data on rock permeability and precipitation and the absence of wells in the area. However, the observed basaltic lava flows are generally fractured with their top and bottom breccias apparently forming horizons of increased permeability [Cabrera and Custodio, 2004]. In the absence of clay-rich units, perched water tables are unlikely to develop in the area. The proximity of the slope to the sea, the elevation of the failure surface above sea level and the existence of lower land behind the scarp indicate generally dry conditions are likely to have pertained on the upper sector of the slope, where the failure developed. Nevertheless, different ground water table elevations were considered, from 0 to 100% in 10% increments. Following Dupuit–Forchheimer theory [Bear, 1972], the water table model was simplified to an ellipse with the major and minor axis lengths equal to the modelled slope width and maximum water table height (Figure A.5a).

#### A.5.3 Peak Ground Accelerations (PGA)

Ground accelerations resulting from seismic events are a very common trigger for rock slope instabilities [Keefer, 2002]. Most significant to the present study is seismic activity related to an off-shore strike-slip fault oriented NNE-SSW and located between the islands of Gran Canaria and Tenerife, 30 km from the El Risco site. This system has been active historically, with recorded magnitudes of up to 5.2 [Mezcua et al., 1992] whilst palaeoearthquake investigations indicate maximum values of  $M=6.8$  [González de Vallejo et al., 2003]. In addition, lower magnitude earthquakes (generally  $M<3$ ) have been repeatedly reported for all the Canary Islands [Instituto Geográfico Nacional, data 1993-2004]. From this, two seismic scenarios were modelled: a deep (15-50 km)  $\sim M7$  earthquake at a distance of  $\sim 30$  km and a shallow ( $< 20$  km)  $\sim M3$  earthquake at a distance of  $\sim 10$  km. Following a number of empirical solutions which relate peak ground acceleration (PGA) to event magnitude and distance from source [Okamoto, 1984; Joyner



and Boore, 1993; Campbell and Bozorgnia, 1994], PGA values of up to 0.35 g were chosen (Figure A.5b). This is consistent with other studies [e.g. Voight *et al.*, 1983; Hürlimann *et al.*, 2000].

#### A.5.4 Results

##### (i) Pre-Failure Conditions

The parameter sensitivity tests indicate that small variations in rock mass strength parameters significantly affect the factor of safety (Figure A.6a).

The depth and geometry of a circular failure plane is mainly controlled by the cohesion of the material ( $c'$ ). The results of the analysis of the inferred pre-failure and present-day slopes, following the work of Wesley and Leelaratnam [2001], show that a cohesion value of ~200 kPa and an angle of internal friction of ~30° best reproduce the observed/inferred failure surface (Figure A.6b). Using these values, under dry conditions an initial, static factor of safety of 1.349 was obtained.

The modelling indicated that the initial factor of safety is not affected by water table heights of up to 60% of the total maximum height (Figures A.5a, A.6b). Water table heights between 60% and 100% of the total maximum height result in a gradually reduced factor of safety, to below 1 for values above ~90%.

Peak ground accelerations have a more significant effect on the factor of safety; a PGA value of ~0.22 g being sufficient to decrease the factor of safety to a value of 1 (Figure A.6c).

##### (ii) Current Stability of the Failed Mass

Using the residual cohesion value of 0 kPa and an angle of internal friction of 30°, the model showed a factor of safety of 1.252 for the present-day slope under dry conditions (Figure A.7a). As with model (i), the factor of safety remains constant with water table heights up to 50% of the total maximum height. A sharp decrease in the factor of safety is observed with higher values, with a value of ~65 % resulting in a factor of safety of 1 (Figure A.7b). The relationship between the factor of safety and peak ground acceleration established in model (i) also pertains for model (ii) although the factor of safety is reduced to 1 with a peak ground acceleration of ~0.1 g (Figure A.7b).

---

## A.6 Discussion and Conclusion

The El Risco landslide, located within the trace of a giant Miocene landslide in north-western Gran Canaria, is a  $\sim 10^6 \text{ m}^3$  rotational slump and covers an area of  $\sim 45,000 \text{ m}^2$ . The failed mass consists of moderately altered, partly scoriaceous basaltic lava flows. Before failure, the mass was bounded by a strike-slip fault to the south and an eroded valley to the north, in a region where north-south and east-west trending fractures are common and thought to be related to the influence of Miocene volcanic edifices. The failure, possibly recent although older than the road, occurred along a sub-circular, N-S striking failure surface, aided and constrained by the pre-existing E-W strike-slip fault.

Slope stability analyses were undertaken, based on the following assumptions:

- 1) the failed block was semi-detached before failure; and
- 2) the only three potential factors to have influenced slope failure were
  - a) low shear-strength of the material,
  - b) an increase of pore water pressures during peak precipitation events and
  - c) peak ground accelerations caused by seismicity.

The modelling suggests that high pore water pressures alone were unlikely to have caused initial failure while peak ground accelerations equal to or greater than 0.22 g may have been sufficient. Using empirical equations [Okamoto, 1984; Joyner and Boore, 1993; Campbell and Bozorgnia, 1994], it was found that such peak ground accelerations could have been generated by a seismic event  $\geq M7$  along the sub-marine strike-slip fault, located 30 km off-shore, which could have taken place in the geological past [González de Vallejo et al., 2003]. With an earthquake epicentre within a 10 km radius, a  $\geq M6$  event would have been required, suggesting that the smaller and more common  $\sim M3$  seismic shocks are unlikely to have triggered the initial failure.

Modelling the current slope stability conditions suggests a factor of safety = 1.252. This is consistent with the ongoing creep of the landslide mass indicated by cracking of the road tarmac at the northern and southern extremities. The calculations show that a water table height of 65% of the total maximum height would create pore pressures high enough to destabilise the slope. With a 10% safety margin, a failure could be triggered if the water table rises to some 165 m above sea level at a location directly beneath the landslide head.

This situation is difficult to envisage at the El Risco site, unless the permeability of horizons between individual lava flows has been overestimated.

It was calculated that a seismic event generating a peak ground acceleration of only 0.1 g at the El Risco site would cause further failure of the landslide mass under dry conditions. Applying a 10% safety buffer indicate a threshold PGA value of 0.09 g, equivalent to a  $\geq M5$  earthquake along the NNE-SSW sub-marine fault 30 km west of El Risco or a  $\geq M4.5$  earthquake located within a 10 km radius. Considering that at least two  $\geq M5$  seismic events occurred historically at the sub-marine fault between Gran Canaria and Tenerife and a M3-4 earthquake occurred in the vicinity of the El Risco site as recently as 1999 [*Instituto Geográfico Nacional*, data 1993-2004], both of these scenarios are likely to occur again in the foreseeable future.

Other secondary factors that could contribute to future failure of the El Risco landslide include:

- a) further alteration of the material by weathering and erosion of the landslide toe
- b) anthropogenic activity, such as the removal of landslide material during road construction and the vibrations caused by traffic.

It should also be remembered that Gran Canaria is a volcanic island and therefore may be affected by future volcanic activity and accompanying seismicity. Such activity would most likely take place in the north-east of the island and, although there is no indication that it is imminent in the near future, it could potentially contribute to accelerated slope movement at El Risco.

Notably, other sections of the GC-200 road along Gran Canaria's north-western coastline share the same characteristics as those of the El Risco landslide site, hence nearby slopes might respond in a similar way to an external triggering event.

It is recommended that monitoring is undertaken, including regular observation as well as the installation of monitoring instruments (inclinometres and piezometres) to determine the precise displacement rates and hydrological conditions in the area. In addition, in view of the hazards presented by re-activation of the El Risco landslide, the costs of periodical road stabilisation should be estimated and compared to that of the construction of a new road section bypassing it.

## A.7 References

- Population Division of the Department of Economic and Social Affairs of the United Nations Secretariat (2004), *World Population Prospects: The 2004 Revision and World Urbanization Prospects: The 2003 Revision*, Retrieved on 15 January 2007 from:  
<http://esa.un.org/unpp>.
- Apuani, T., C. Corazzato, A. Cancelli, and A. Tibaldi (2005), Physical and mechanical properties of rock masses at Stromboli: a dataset for volcano instability evaluation, *Bulletin of Engineering Geology and the Environment*, 64(4), 419-431.
- Bear, J. (1972), Dynamics of fluids in porous media, *Environmental Science Series American Elsevier, New York*. 764 pp.
- Bishop, A. W. (1955), The use of slip circles in the stability analysis of slopes, *Geotechnique*, 5, 7-17.
- Cabrera, M. C., and E. Custodio (2004), Groundwater flow in a volcanic-sedimentary coastal aquifer: Telde area, Gran Canaria, Canary Islands, Spain, *Hydrogeology Journal*, 12(3), 305-320.
- Campbell, K. W., and Y. Bozorgnia (1994), Near-source attenuation of peak horizontal acceleration from worldwide accelerograms recorded from 1957 to 1993., paper presented at 5th U.S. National Conference on Earthquake Engineering, Berkeley, California.
- Concha-Dimas, A. (2004), Numerical Modeling in understanding catastrophic collapse at Pico de Orizaba, Mexico, Ph.D. thesis, University of Nevada, Reno.
- Funck, T., and H.-U. Schmincke (1998), Growth and destruction of Gran Canaria deduced from seismic reflection and bathymetric data, *Journal of Geophysical Research*, 103(B7), 15393-15408.
- González de Vallejo, L. I., R. Capote, L. Cabrera, J. M. Insua, and J. Acosta (2003), Paleoearthquake evidence in Tenerife (Canary Islands) and possible seismotectonic sources, *Marine Geophysical Researches*, 24(1-2), 149-160.
- Hoek, E., P. K. Kaiser, and W. F. Bawden (1995), *Support of underground excavations in hard rock*, Balkema, Rotterdam.
- Hürlimann, M., J. Marti, and A. Ledesma (2000), Mechanical relationship between catastrophic volcanic landslides and caldera collapses, *Geophysical Research Letters*, 27(16), 2393-2396.
- Instituto Geográfico Nacional, Ministerio de Fomento, Servicio de información sísmica, *Información sísmica, boletines definitivos de sismos próximos (1993-2004)* (2007). Retrieved on 15 January 2007 from:  
[http://www.fomento.es/MFOM/LANG\\_CASTELLANO/DIRECCIONES\\_GENERALES/INSTITUTO\\_GEOGRAFICO/Geofisica/sismologia/informacionsis/default.htm](http://www.fomento.es/MFOM/LANG_CASTELLANO/DIRECCIONES_GENERALES/INSTITUTO_GEOGRAFICO/Geofisica/sismologia/informacionsis/default.htm)
- Instituto Nacional de Estadística, *Poblaciones referidas al 1 de enero de 2006 por Islas y sexo* (2006). Retrieved on 15 January 2007 from:  
[http://www.ine.es/inebase/cgi/axi?AXIS\\_PATH=/inebase/temas/t20/e260/a2006/10/&FILE\\_AXIS=is01.px&CGI\\_DEFAULT=/inebase/temas/cgi.opt&COMANDO=SELECCION&CGI\\_URL=/inebase/cgi/](http://www.ine.es/inebase/cgi/axi?AXIS_PATH=/inebase/temas/t20/e260/a2006/10/&FILE_AXIS=is01.px&CGI_DEFAULT=/inebase/temas/cgi.opt&COMANDO=SELECCION&CGI_URL=/inebase/cgi/)
- Janbu, N. (1957), Earth pressure and bearing capacity calculations by generalized procedure of slices, *Proceedings of the 4th Conference of the International Society for Soil Mechanics and Foundation Engineering (ISSMFE), London*, 2, 207-212.
- Joyner, W. B., and D. M. Boore (1993), Methods for regression analysis of strong-motion data, *Bulletin of the Seismological Society of America*, 83(2), 469-487.
- Keefer, D. K. (2002), Investigating landslides caused by earthquakes - A historical review, *Surveys in Geophysics*, 23(6), 473-510.
- McDougall, I., and H.-U. Schmincke (1976), Geochronology of Gran Canaria, Canary Islands: Age of shield building volcanism and other magmatic phases, *Bulletin of Volcanology*, 40(1), 57-77.
- Mezcua, J., E. Burforn, A. Udías, and J. Rueda (1992), Seismotectonic of the Canary Islands., *Tectonophysics*, 208, 447-452.
- Okamoto, S. (1984), Introduction to earthquake engineering, *University of Tokyo Press*, 629 pp.
- Schmincke, H.-U. (1967), Cone sheet swarm, resurgence of Tejedra caldera, and the early geologic history of Gran Canaria, *Bulletin of Volcanology*, 31(1), 153-162.

- Schmincke, H.-U. (1976), The geology of the Canary Islands, in *Biogeography and Ecology in the Canary Islands*, edited by G. Kunkel, pp. 67-184, W. Junk, The Hague.
- Spencer, E. (1967), Method of analysis of the stability of embankments assuming parallel interslices forces, *Géotechnique*, 17(1), 11-26.
- Thomas, M. E., N. Petford, and E. N. Bromhead (2004), Volcanic rock-mass properties from Snowdonia and Tenerife: implications for volcano edifice strength, *Journal of the Geological Society*, 161, 939-946.
- Troll, V. R., T. R. Walter, and H.-U. Schmincke (2002), Cyclic caldera collapse: Piston or piecemeal subsidence? Field and experimental evidence, *Geology*, 30(2), 135-138.
- van den Bogaard, P., and H.-U. Schmincke (1998), Chronostratigraphy of Gran Canaria, in *Proceedings of the Ocean Drilling Program, scientific results*, edited by P. P. E. Weaver, H.-U. Schmincke, J. V. Firth and W. Duffield, pp. 127-140, Ocean Drilling Program, College Station, Texas.
- Varnes, D. J. (1978), Slope movements types and processes. Landslides analysis and control transportation research board, *National Academy of Sciences, Special Report*, 176(Chapter 2), 11-33.
- Voight, B., R. J. Janda, H. Glicken, and P. M. Douglass (1983), Nature and Mechanics of the Mount St-Helens Rockslide-Avalanche of 18 May 1980, *Geotechnique*, 33(3), 243-273.
- Watters, R. J., and W. D. Delahaut (1995), Effect of argillic alteration on rock mass stability, in *Clay and Shale Slope Instability*, edited by W. C. Haneberg and S. A. Anderson, pp. 139-150, Reviews in Engineering Geology. Geological Society of America, Boulder, CO.
- Watters, R. J., D. R. Zimbelman, S. D. Bowman, and J. K. Crowley (2000), Rock mass strength assessment and significance to edifice stability, Mount Rainier and Mount Hood, Cascade Range volcanoes, *Pure and Applied Geophysics*, 157(6-8), 957-976.
- Wesley, L. D., and V. Leelaratanam (2001), Shear strength parameters from back-analysis of single slips, *Geotechnique*, 51(4), 373-374.
- Zimbelman, D. R., R. J. Watters, I. R. Firth, G. N. Breit, and G. Carrasco-Nunez (2004), Stratovolcano stability assessment methods and results from Citlaltepetl, Mexico, *Bulletin of Volcanology*, 66(1), 66-79.

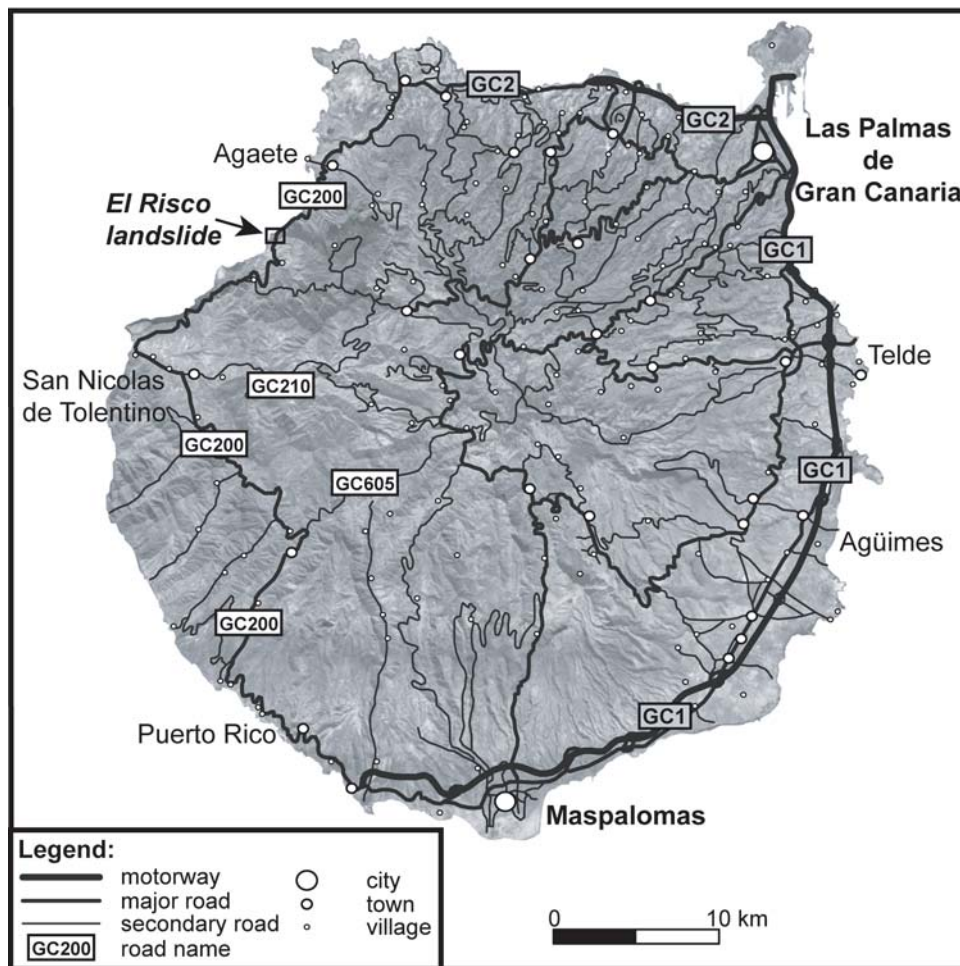


**Figure A.1** Satellite image of Gran Canaria showing the location of roads, cities and villages. The black rectangle (enlarged in Figure A.2) corresponds to the location of the El Risco landslide.

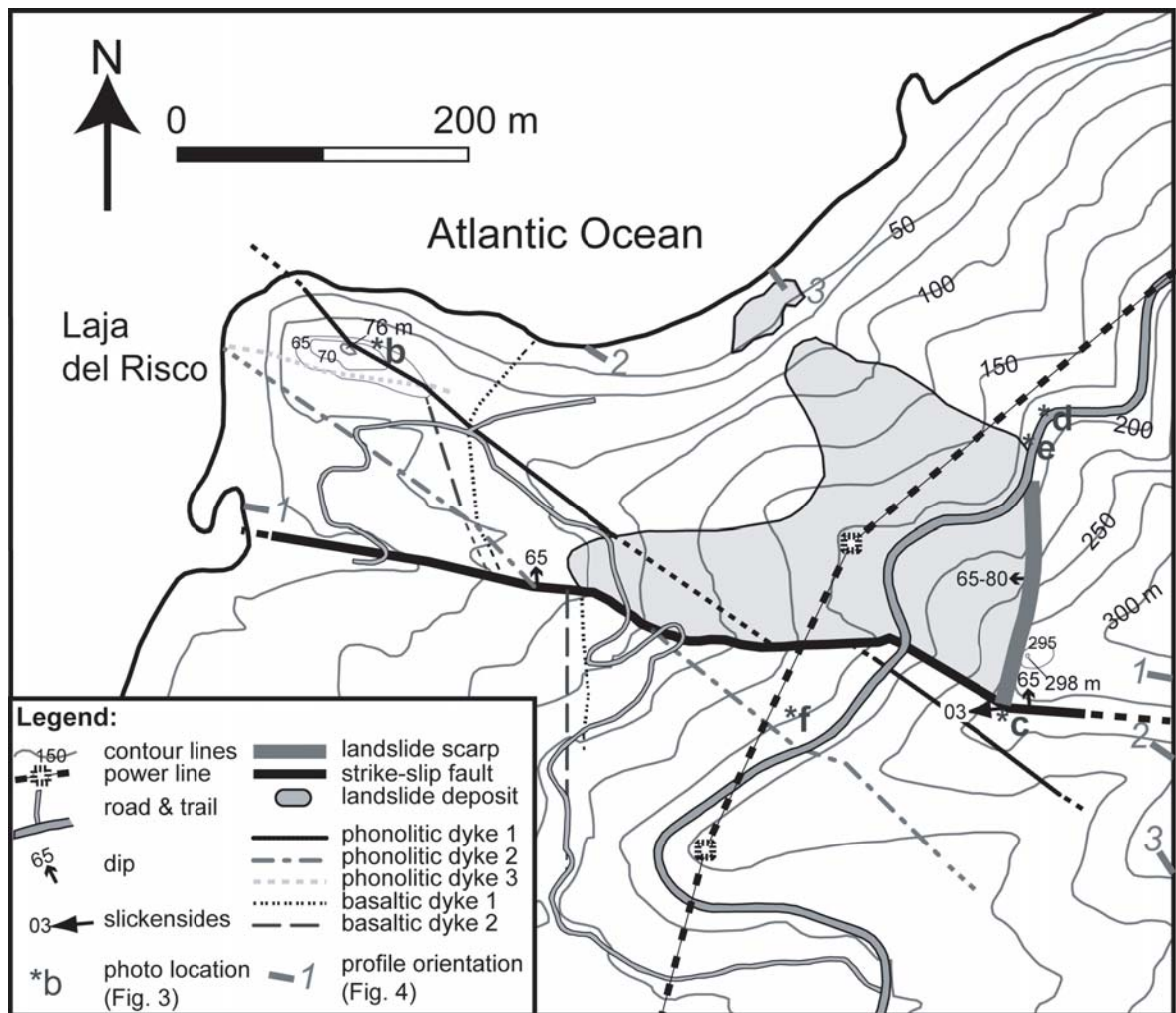


**Figure A.2** Topographic map of the El Risco landslide and surroundings. Locations of photographs (Figure A.3) and topographic profiles (Figure A.4) are indicated.



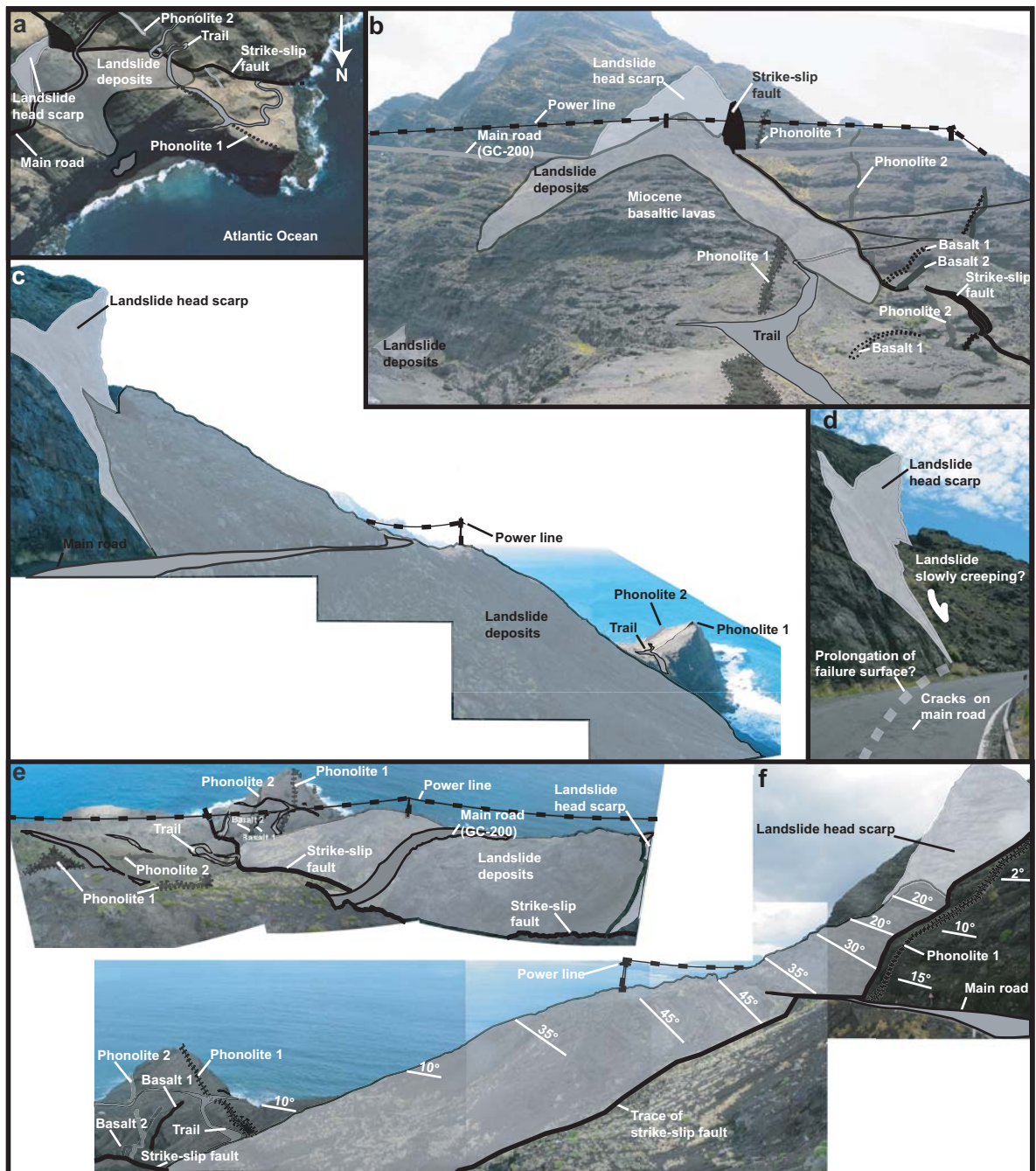


**Figure A.3** Images of the El Risco landslide with the affected infra-structures and the major geological features labelled. **a** Satellite image of the El Risco landslide, courtesy of GRAFCAN. **b** Panorama of the landslide as seen from the west, and **c** from the north. **d** Photo (taken in April 2005) of cracks in road GC-200 coincident with the northern landslide edge. **e** View from the east. **f** Photo mosaic taken from the south showing rotation of landslide blocks.



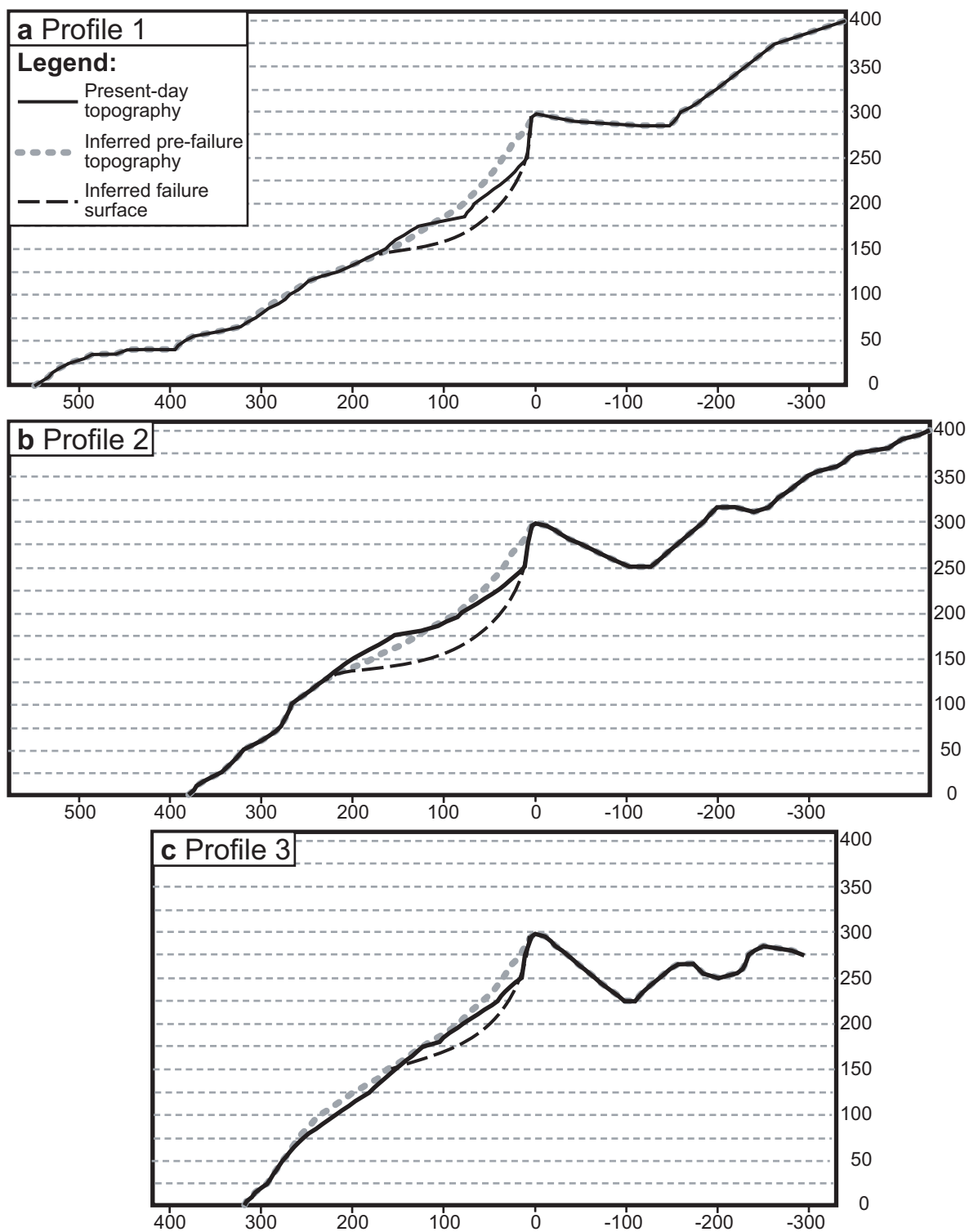


**Figure A.4** Current topography, inferred pre-failure topography and inferred failure surface geometry for **a** profile 1, **b** profile 2 and **c** profile 3 of Figure A.2.

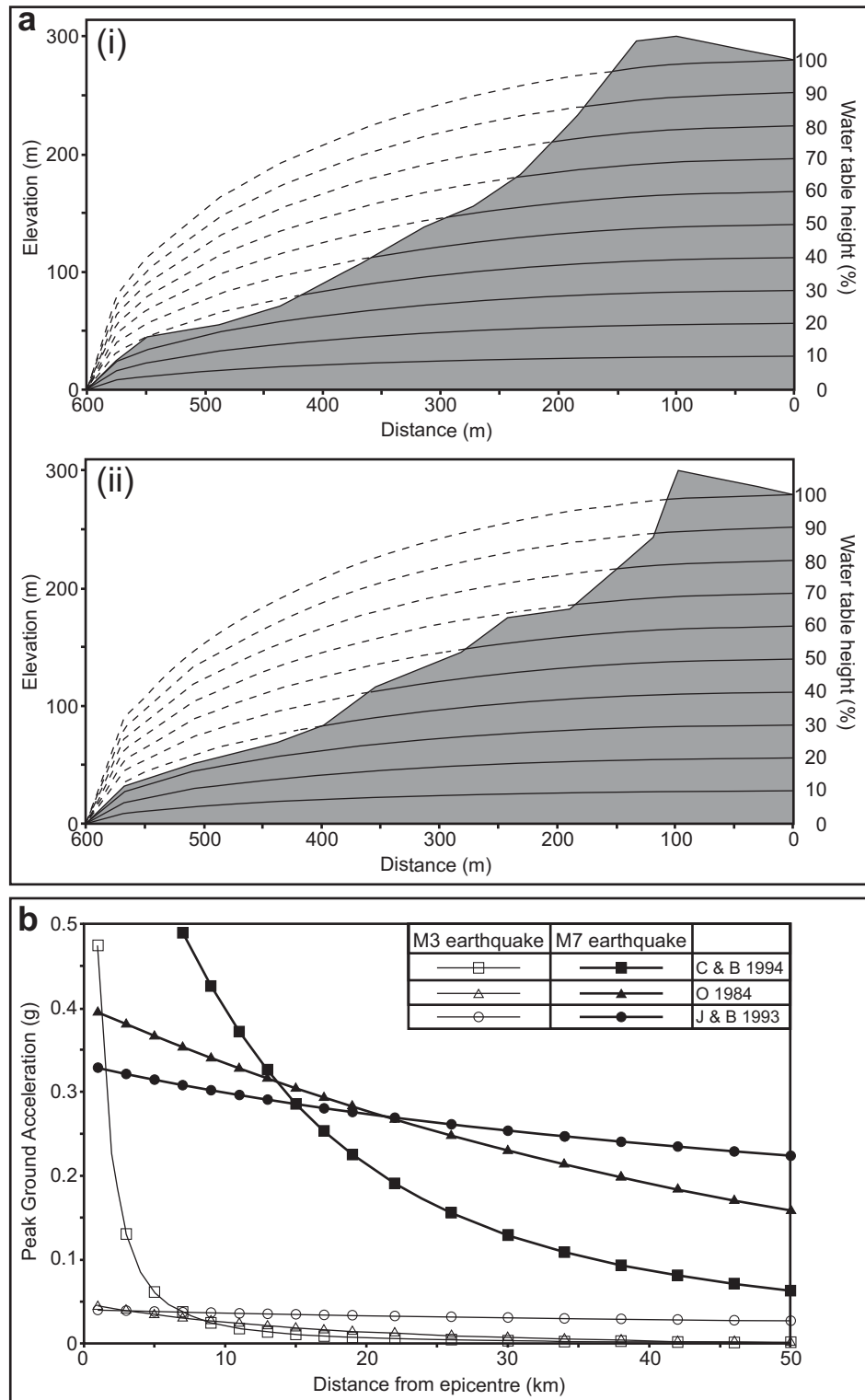


**Figure A.5** **a** (i) Pre- and (ii) post-failure water table geometries used in the stability models, following the Dupuit–Forchheimer theory. **b** Peak ground acceleration as a function of earthquake magnitude and distance to the epicentre using the empirical equations of *Campbell and Bozorgnia* [1994], *Joyner and Boore* [1993] and *Okamoto* [1984].

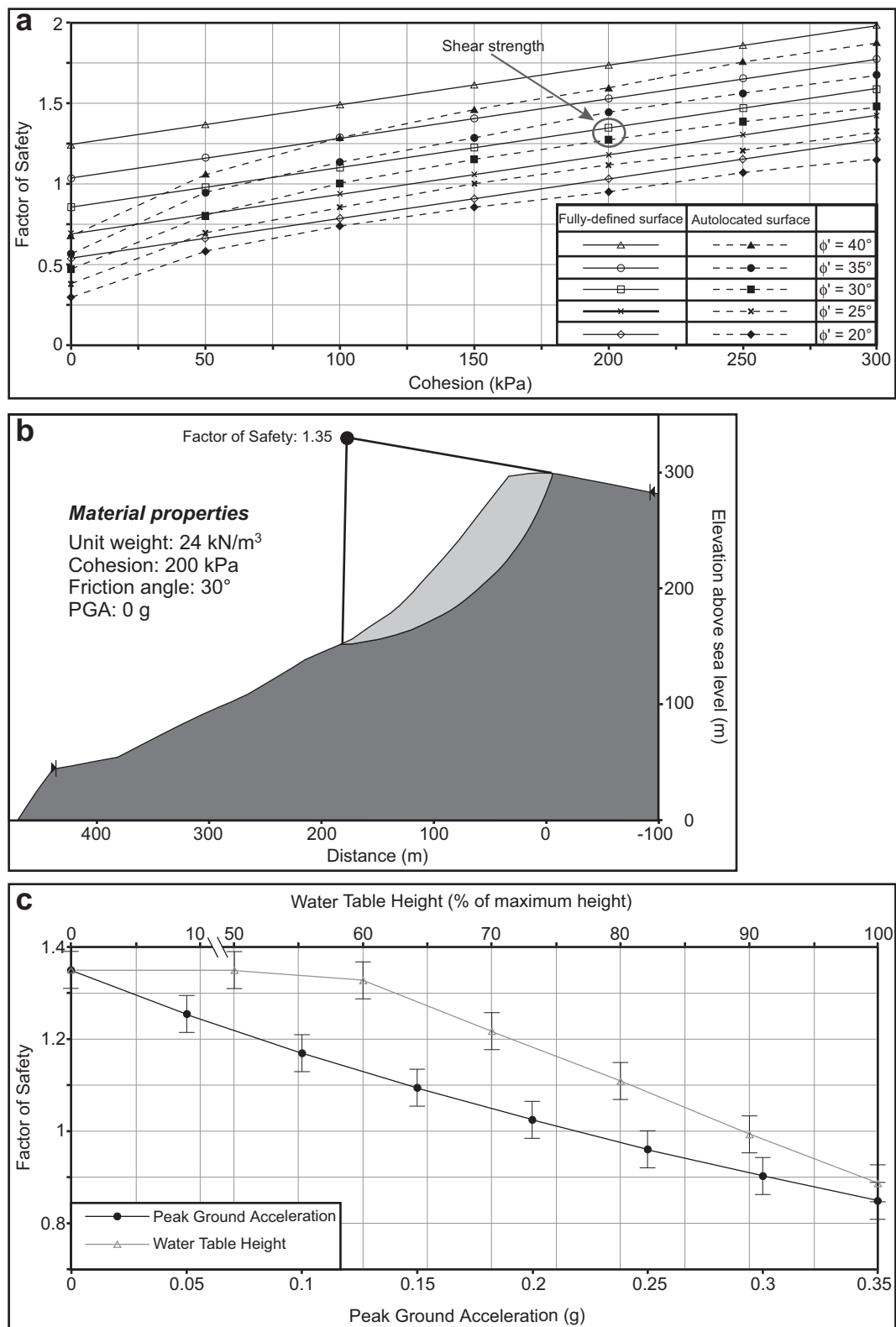


**Figure A.6** Results for models (i) **a** Factor of safety as a function of material cohesion for different angles of internal friction, for models with a user-specified failure surface (fully-defined) and models with a non-specified failure surface (autolocated), following the methodology proposed by Wesley and Leelaratanam [2001]. **b** Calculated initial failure surface. **c** Comparison of the decrease in the factor of safety induced by peak ground accelerations and increasing water table heights. The error bars represent the variation given by the range of material unit weights used in the calculations.

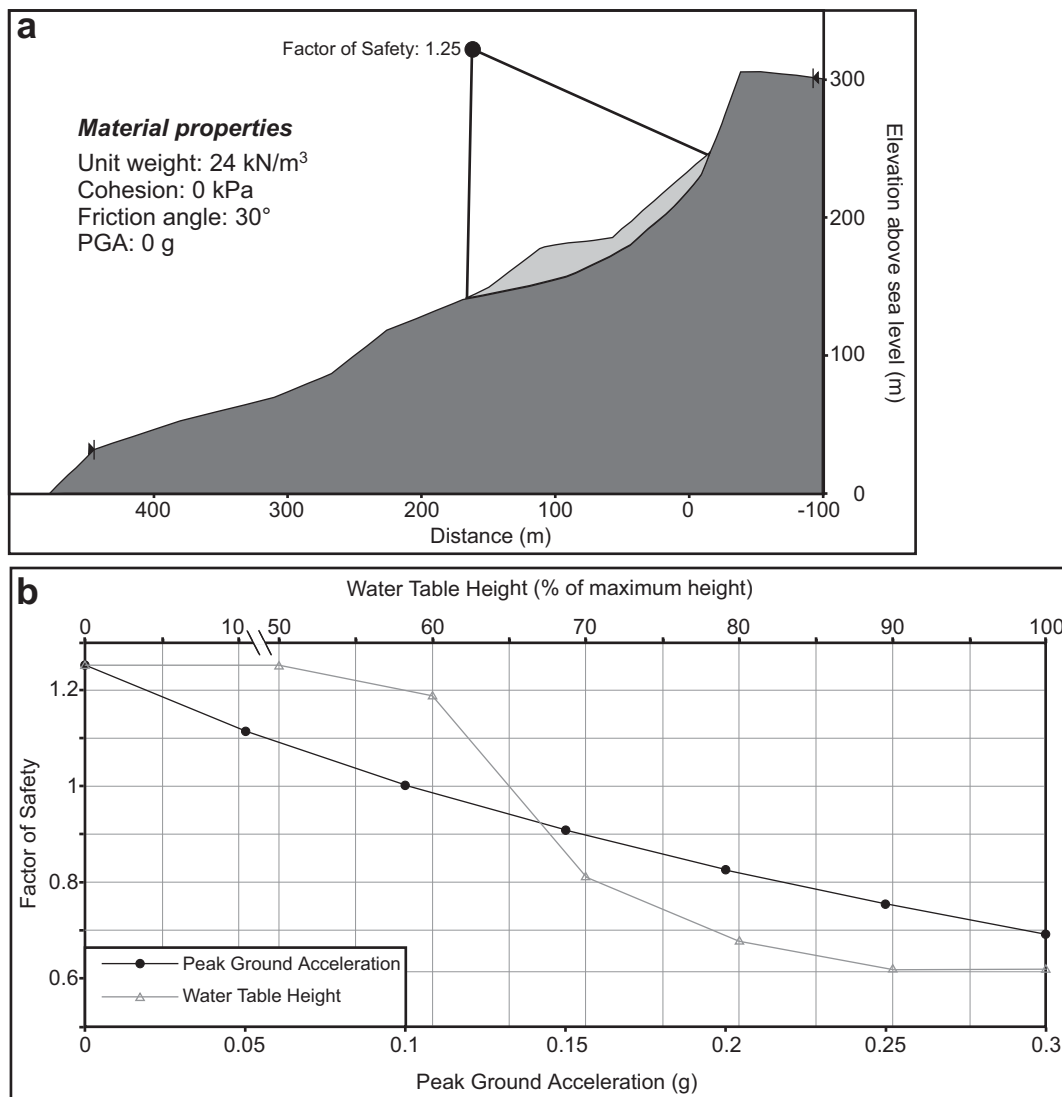


**Figure A.7** Results for models (ii) **a** Calculated failed mass geometry. **b** Comparison of the decrease in the factor of safety induced by peak ground accelerations and increasing water table heights for the present state of the slope.

**Table A.1** Values of the parameters used in the stability models.

Model	Unit weight ( $\gamma$ , kN/m <sup>3</sup> )	Friction angle ( $\phi'$ , °)	Cohesion ( $c'$ , kPa)	Peak ground acceleration (g)	Water table height (%)
(i)	19 - 28	20 - 40	0 - 300	0 - 0.35	0 - 100
(ii)	24	30	0	0 - 0.3	0 - 100

## **APPENDIX B: ADDITIONAL STRATIGRAPHIC CONSTRAINTS (CHAPTER 3)**

Here, we discuss further the stratigraphy of Teno by (1) giving additional details on the location of the Masca and Carrizales unconformities and by (2) reviewing radiometric dates and palaeomagnetic readings in the light of the unconformity-bounded formations. A discussion of the possible geographic extent of Los Gigantes Formation is also included. Radiometric dating was performed by *Abdel-Monem et al.* [1972], *Ancochea et al.* [1990], *Thirlwall et al.* [2000] and *Guillou et al.* [2004]. *Leonhardt and Soffel* [2006], in their magnetostratigraphy-based approach, assigned the different K-Ar and Ar-Ar ages of previous workers to each of Teno's stratigraphic unit. For each formation, a representative 'average age' was then calculated and correlated to the geomagnetic polarity time-scale (GPTS) of *Cande and Kent* [1995].

## B.1 Location of Unconformities

The Masca Unconformity, which truncates the lowermost and steeply seaward dipping Masca lavas, does not crop out along the main road, but can be traced in at least five cliff faces northwest of Masca village (Figure 3.1, 3.2, 3.3). It is well exposed in the barranco to the west of Masca village at [319280, 3132600] and, on strike with this, above the road at [319680, 3132400], implying that it must be hidden behind walls supporting the steep slopes along the road. As mapped by *Walter and Schmincke* [2002], the exposure above the road east of the village is the easternmost exposure of the Masca Unconformity, which must necessarily be crosscut by the Carrizales Unconformity in this vicinity (Figure 3.2).

The Carrizales Unconformity, in contrast to the Masca Unconformity, is not readily visible from a distance in the cliff faces. However, since it follows and crosses the main road (TF-436, Figure 3.2) serving the Teno massif, several good quality outcrops reveal its nature, notably along the road section passing by the peak of El Roque between Cruz de Gilda and the entrance of the small road descending towards Los Carrizales village. Along this road segment, which is basically parallel to the Carrizales Unconformity, stratigraphic level is constantly near the top of the Carrizales Formation, where plagioclase-phyric lavas crop out. Two localities ([318650, 3133640] and [318390, 3133770]), in particular, show details of the deformation of the Carrizales Formation at the approach of the Carrizales Unconformity. To the south, plagioclase-phyric lavas of the Carrizales Formation are cut by faults and shear planes. This is overlain by a zone of highly deformed lavas and sills, where several discrete small shear zones can be observed [see *Walter and Schmincke*, 2002 for details]. Beyond a few hundred meters east of Masca village, only the Carrizales Unconformity divides the Masca and El Palmar formations.

The unconformities are apparently not exposed beyond Roques del Carrizal ridge to the west and may be concealed by peripheral lava flows overflowing the embayments. However, the palaeo-embayments that they define must have extended to the north or northwest. Inspection of the northwestern coast along the road towards Punto de Teno reveals the absence of major unconformities in this region [cf. *Walter and Schmincke*, 2002]. In the west, we infer the prolongation of the unconformities to the north based on (1) the relatively old ages obtained by *Abdel-Monem et al.* [1972] and *Ancochea et al.* [1990] that suggest that the northwestern part of Teno is old and has not been affected by a ~6.1-Ma-old landslide, (2) the consistent orientation of dyke swarms that may have

wrapped around the region affected by flank instability [Walter and Schmincke, 2002; cf. Walter *et al.*, 2005], (3) the occurrence of erosional canyons that may be due to the presence of concealed palaeo-landslide scarps and (4) the expected U-shape morphology of the palaeo-embayments, characteristic of well-exposed and more recent giant landslide scars around the world (Figure 3.1).

Near the Cherfe outcrop at its easternmost exposure, the Carrizales Unconformity clearly swings from an east-southeast to a northeast trend (Figure 3.1). The extrapolation of this trend was inferred by Walter and Schmincke [2002] to be the most reasonable assumption for the eastern prolongation of the Carrizales Unconformity. Moreover, K-Ar dating by Guillou *et al.* [2004], giving an age of 5.7 Ma at the base of the northeastern part of Teno may indicate that this part of the massif post-dates the giant landslides and belongs to the El Palmar Formation, assuming that the El Palmar lavas are contained within the palaeo-landslide embayment. UTM coordinates given for these authors' sample TN-8 are inconsistent with the locality plotted on Figure 3 of Guillou *et al.* [2004]. This discrepancy is resolved in Figure 3.1 of this work by re-plotting the old UTM coordinates [H. Guillou and J. C. Carracedo, personal communication 2007].

## B.2 Masca Formation

For the Masca Formation, Leonhardt and Soffel [2006] averaged ages of 6.42, 6.02 [Thirlwall *et al.*, 2000], 6.11 and 5.99 Ma [Guillou *et al.*, 2004] for their correlation to the GPTS. Based on our detailed mapping and the precise sample localities plotted on Google Earth [Guillou *et al.*, 2004; M. Thirlwall, personal communication 2007], however, lavas dated at 6.02 and 5.99 Ma belong to the Carrizales Formation whilst the sample dated at 6.11 Ma on the dirt track towards Cumbre Bolicos is part of the El Palmar Formation [Guillou *et al.*, 2004]. Therefore, possibly only one reliable age is available for the Masca Formation, that is 6.42 Ma of Thirlwall *et al.* [2000]. Three older K-Ar dates that are potentially unreliable [cf. Thirlwall *et al.*, 2000] may be attributed to this formation and give ages of 6.3, 6.7 and 6.7 Ma [Abdel-Monem *et al.*, 1972; Ancochea *et al.*, 1990] (Figures 3.1, 3.2, Table 3.1).

All Barranco de Masca sites investigated by Leonhardt and Soffel [2006] indicated reverse polarity, but samples taken in the Barranco del Carrizal (BC-1 and BC-2), which are clearly stratigraphically below the Masca Unconformity, gave normal and intermediate polarity (Figures 3.1, 3.2, Table 3.1). Two samples of Abdel-Monem *et al.* [1972], taken in



lower northwest Teno, showed normal polarity. *Leonhardt and Soffel* [2006]’s sample UM-3 with normal polarity was taken near Cherfe outcrop, but apparently stratigraphically below the Carrizales Unconformity (Figure 3.2, Table 3.1). This sample is therefore from near the top of the Masca Formation and indicates that the last emissions of this group may have been extruded at the very beginning of the C3An.1n chron.

Assuming that all Masca rocks were reversely magnetised, *Leonhardt and Soffel* [2006] inferred that this formation was extruded between 6.269 and 6.137 Ma (chron C3An.1r). In the light of the clarifications provided here, however, it is evident that the palaeo-magnetic record of these volcanics is more complicated than stated by these authors. The Masca Formation may have been extruded over a longer time period, probably starting in the normal chron C3An.2n, continuing in the reverse chron C3An.1r and ending in the normal chron C3An.1n (Table 3.1). Although unlikely, it may be even older, starting in the reverse chron C3An.2r between 6.567-6.935 Ma and extending into the normal chron C3An.2n between 6.567 and 6.269 Ma.

### B.3 Carrizales Formation

For the Carrizales Formation, *Thirlwall et al.* [2000]’s sample TE6 (6.02 Ma), *Guillou et al.* [2004]’s TN-6 (5.99 Ma, reverse polarity) and *Leonhardt and Soffel* [2006]’s UM-1 (normal polarity) were taken at nearly the same locality, that is close the roundabout ~200 m north of Masca village [M. Thirlwall, personal communication 2007, see also geographical coordinates of *Guillou et al.* [2004] and *Leonhardt and Soffel* [2006]] (Figure 3.2, Table 3.1). Two additional samples (C-1 and TA-1) of *Leonhardt and Soffel* [2006] belong to the Carrizales Formation and have normal polarity. As suggested by these authors, the onset of the Carrizales Formation extrusion appears to have taken place close to the transition between the C3An.1r and C3An.1n chrons, near 6.137 Ma ago. This constrains the Masca Collapse to have such an age.

### B.4 El Palmar Formation

Regarding the El Palmar Formation, ages of 6.1 Ma (*Thirlwall et al.* [2000]’s TE12) and 6.1, 5.9, 5.7 and 5.5 Ma (*Guillou et al.* [2004]’s TN-4, TN-7, TN-8 and TN-5, respectively) have been obtained, as well as potentially unreliable ages of 5.6, 5.5 and 5.0 Ma [*Abdel-Monem et al.*, 1972; *Ancochea et al.*, 1990] (Figures 3.1, 3.2, Table 3.1). All investigated samples but TN-4 (low inclination) and TN-5 (reverse polarity) yielded normal polarity readings. Since *Guillou et al.* [2004]’s localities for these samples near Cumbre Bolicos

correspond to the upper El Palmar Formation (according to our mapping, these are stratigraphically above the Carrizales Unconformity), the extrusion of these volcanic must have extended into the reverse polarity chron C3n.4r between 5.894 and 5.230 Ma. It is unclear, however, to what extent El Palmar volcanism continued into this period. The region of Cumbre Bolicos is the highest part of the Teno massif; yet, it may have suffered severe erosion since the last Miocene emissions. According to *Paris* [2002] and *Paris et al.* [2005] erosion rates may be on the order of 60-160 m per million years during the long term volcanic hiatus of typical Canarian volcanoes. Therefore, it is likely that a significant thickness of the El Palmar Formation may have been removed in the last 5 Ma. Thus, we cannot exclude that the extrusion of these lavas may have significantly extended into the C3n.4r chron [cf. *Leonhardt and Soffel*, 2006].

An apparent age discrepancy exists for *Guillou et al.* [2004]’s sample TN-4, which appears anomalously old for its stratigraphic position. Although apparently from conformable units only ~100 m apart in elevation (note that the elevation of 1030 m for TN-4 given by *Guillou et al.* [2004] does not fit the corresponding coordinates, which are consistent with an elevation of ~1250 m) samples TN-4 and TN-5 would have an age difference of 0.6 Ma. This seems unreasonable and a younger age for TN-4 is likely, assuming that its locality is correct [*Guillou et al.*, 2004].

## B.5 Los Gigantes Formation

In contrast to the other stratigraphic formations, the Los Gigantes Formation is not delimited by the angular unconformities (Figures 3.1, 3.2) and its geographic extent may be tentatively explained in two ways: (1) Assuming a central volcano with a summit near Cumbre Bolicos, Los Gigantes lavas may have been formed as the Carrizales Collapse embayment had been completely filled by El Palmar lavas. With the topographic barrier overcome, i.e. at altitudes at least exceeding 1100 m near Cherfe outcrop in eastern Teno, lavas were once more free to flow to the south, or south-west. In this context, the Los Gigantes Formation may be equivalent to the uppermost El Palmar Formation, or to its now eroded portion. (2) Los Gigantes and El Palmar lavas represent distinct phases of the evolution of Teno. Eruptive centres at the origin of these two groups may have been decoupled; the Los Gigantes Formation may have been erupted from peripheral vents, with products mostly preserved in the south. In any case, the transition between the Masca and Los Gigantes formations proposed by *Guillou et al.* [2004] is approximated (see “Upper Teno” in their Figure 3) and, therefore, we have re-mapped it based on the geometrical

## APPENDIX B: ADDITIONAL STRATIGRAPHIC CONSTRAINTS (CHAPTER 3)

---

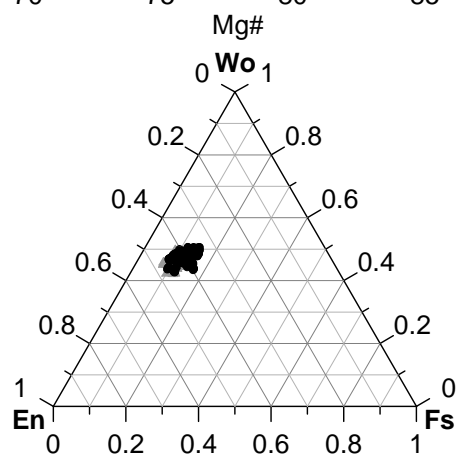
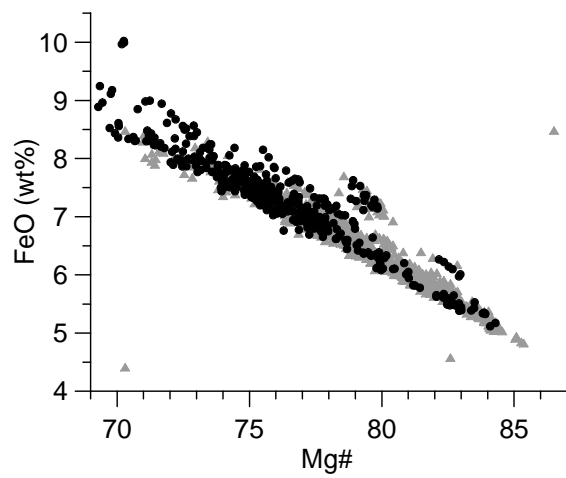
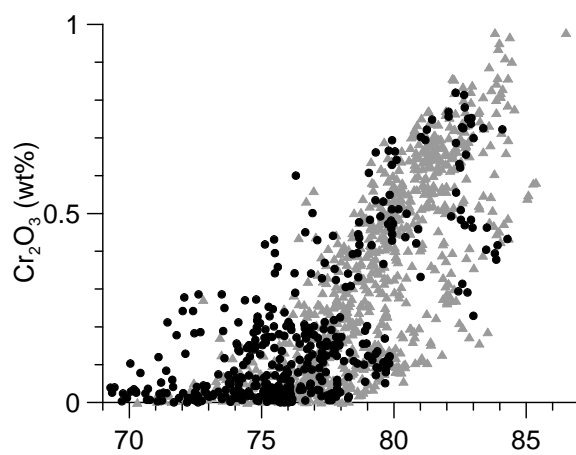
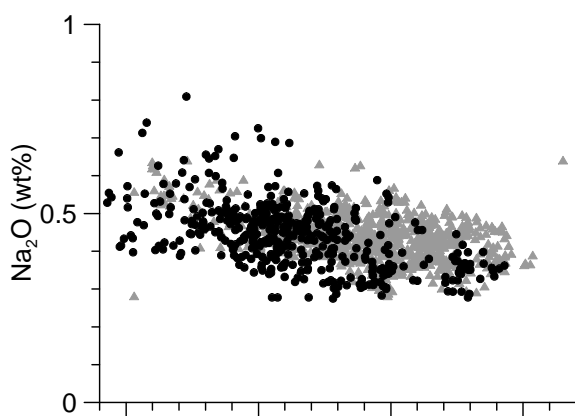
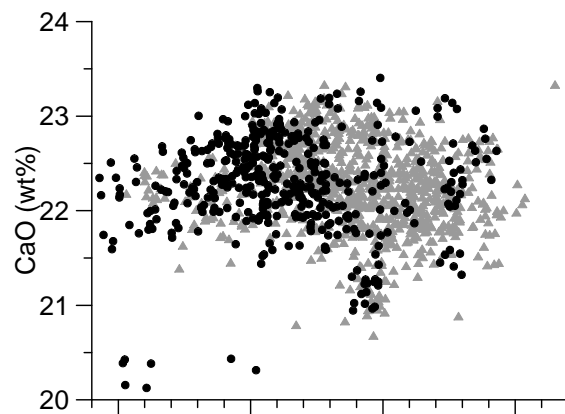
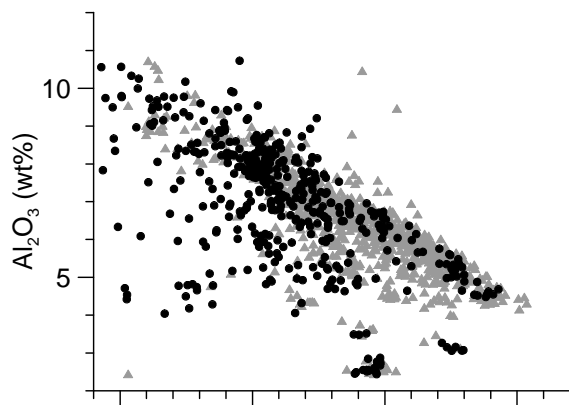
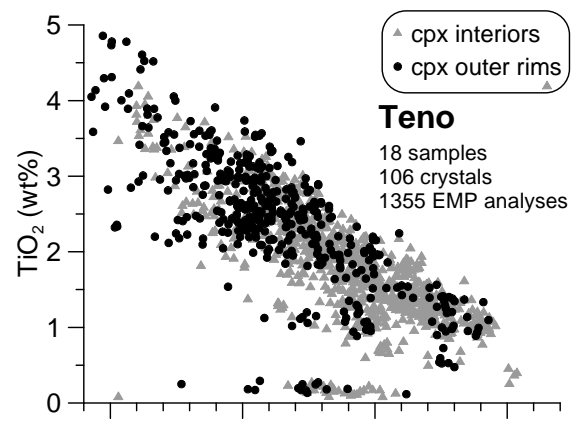
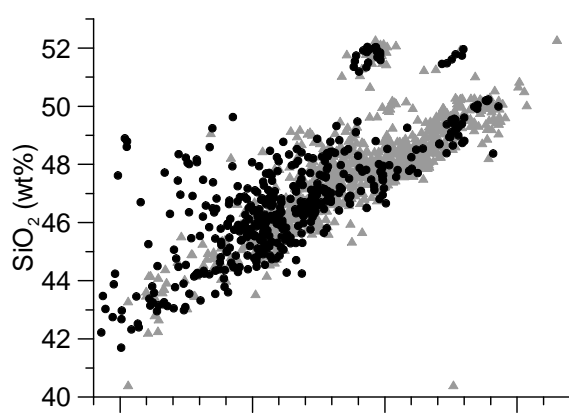
constraints provided by typical dips ( $\sim 15^\circ$ ) of Los Gigantes lavas at their type locality and the occurrence of the Carrizales Unconformity at altitudes of  $\sim 1100$  m at the Cherfe outcrop (Figures 3.1, 3.2). The Carrizales Unconformity is inferred to have extended to such altitudes in most part of the massif prior to erosion.

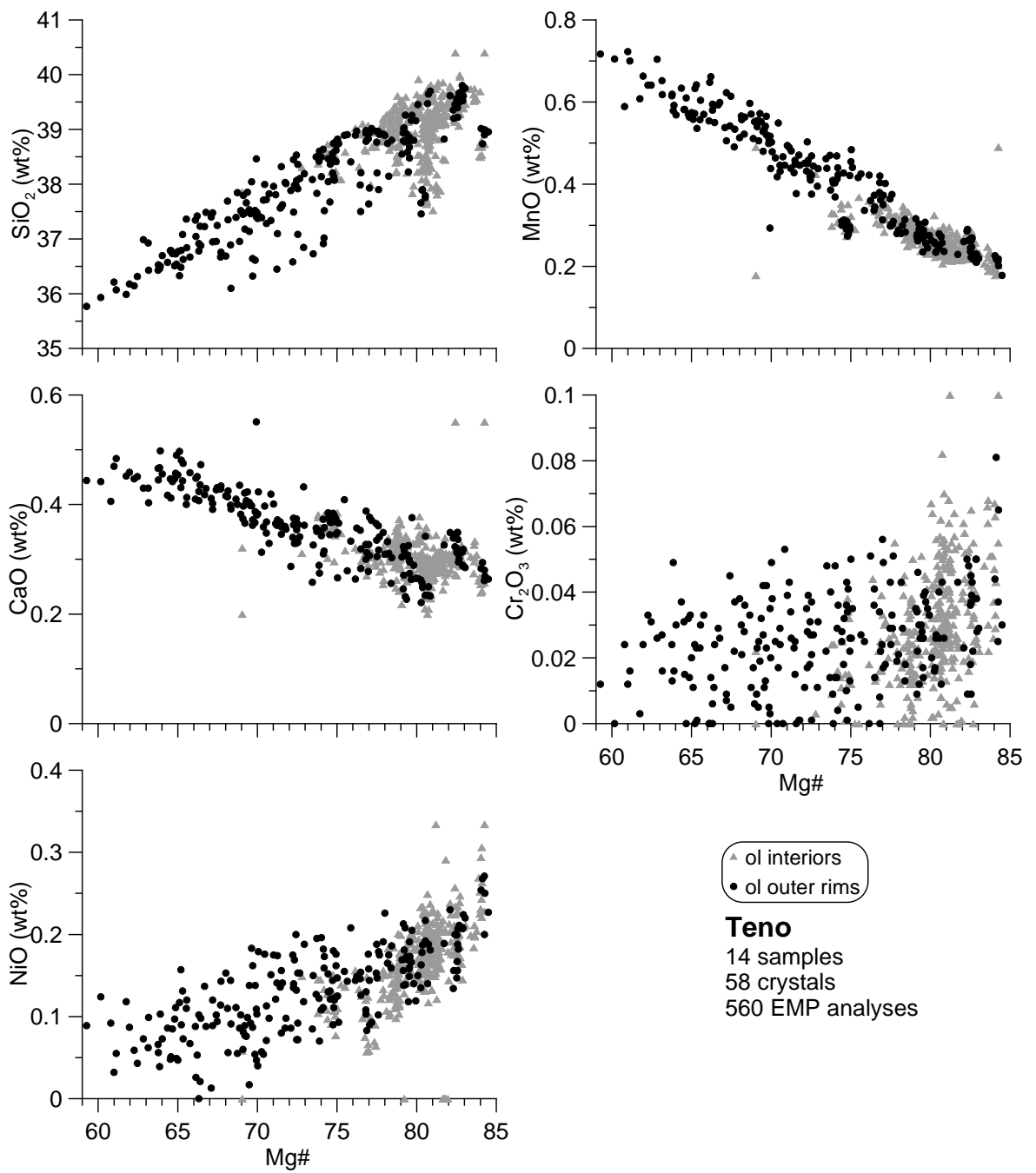
Exposures at the Los Gigantes type-locality suggest that lavas of this formation add up to significant thicknesses near the coast. Inland, however, the Los Gigantes Formation may not necessarily be very thick even though it is found over a wide altitude range (0-1100 m). It may actually form a thin layer of gently dipping volcanics, mostly capping the Masca Formation without clear discordance in the outermost parts of the massif. Possibly, however, the Masca and Los Gigantes formation may be told apart in their erosion pattern. It appears plausible that, due to their older age and more complex post-emplacement volcano-tectonic history, the Masca Formation may be weaker and more easily eroded. In the cliffs surrounding Barranco de Masca, a clear break in erosion pattern can be observed and we could not confidently observed the Masca Unconformity crosscutting this transition. This could potentially be a candidate for the division between the Masca and Los Gigantes formations, at least in this part of the massif.

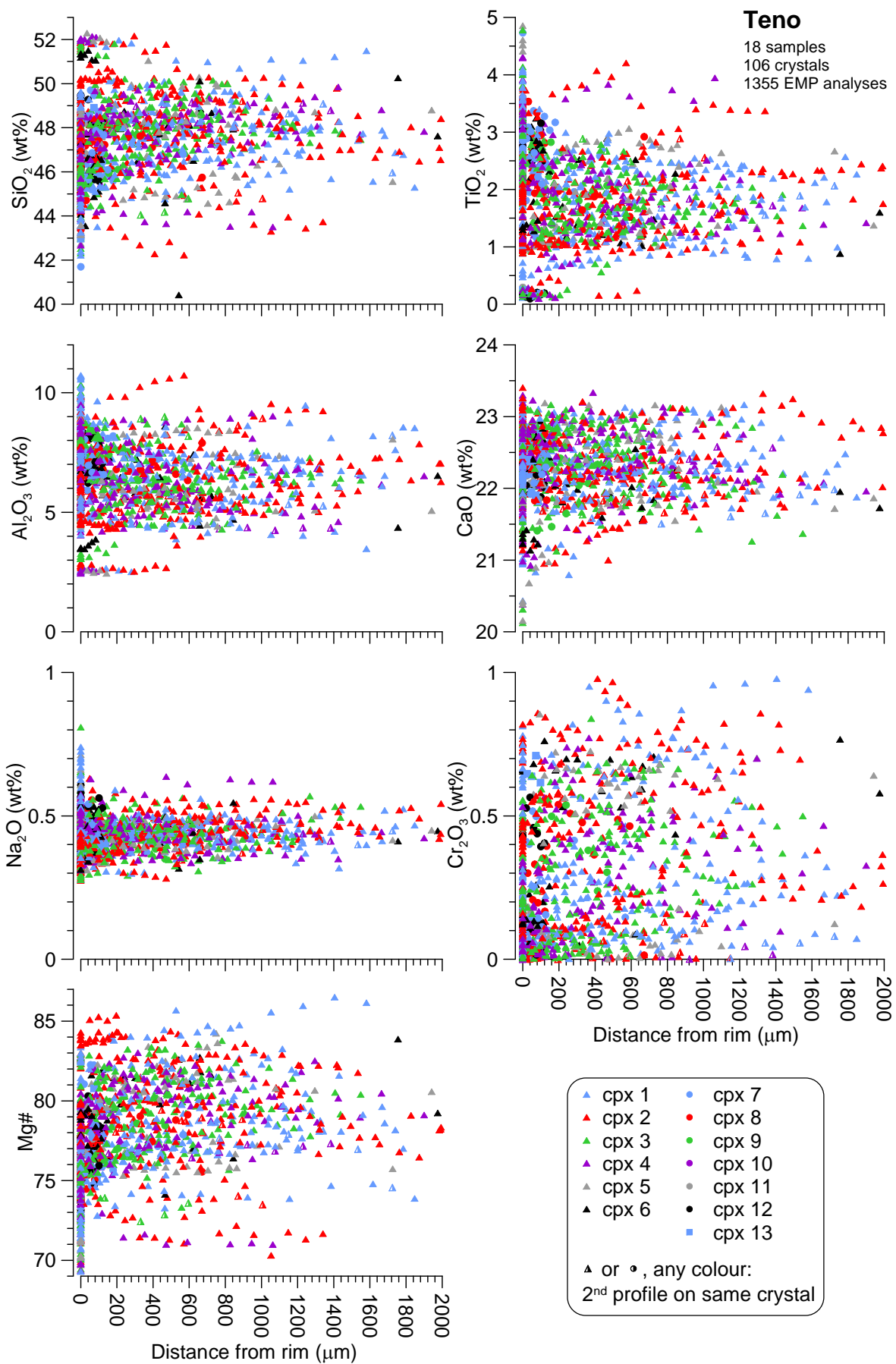
*Guillou et al.* [2004] obtained ages of 5.2, 5.3 and 5.5 Ma for Los Gigantes samples, all characterised by normal polarity. In addition, two potentially unreliable ages of 5.3 and 4.5 Ma may be attributed to this formation [*Ancochea et al.*, 1990]. This supports the view of *Leonhardt and Soffel* [2006] that these volcanics were probably mostly extruded within the normal polarity chron C3n.4n between 5.230 and 4.980 Ma. However, *Leonhardt and Soffel* [2006]'s (TA-2) is most probably from the Los Gigantes Formation equivalent in northwest Teno and shows reverse polarity, perhaps in correlation with Cumbre Bolicos lavas (Figure 3.1, Table 3.1)[*Leonhardt and Soffel*, 2006]. Although a volcanic hiatus of up to  $\sim 0.5$  Ma between the El Palmar and Los Gigantes Formation is consistent with magnetostratigraphy [*Leonhardt and Soffel*, 2006], the available data may not be sufficient to resolve this issue, due to potential erosion and relatively poor agreement of K-Ar ages in the upper El Palmar Formation (i.e. TN-4 and TN-5 of *Guillou et al.* [2004]).

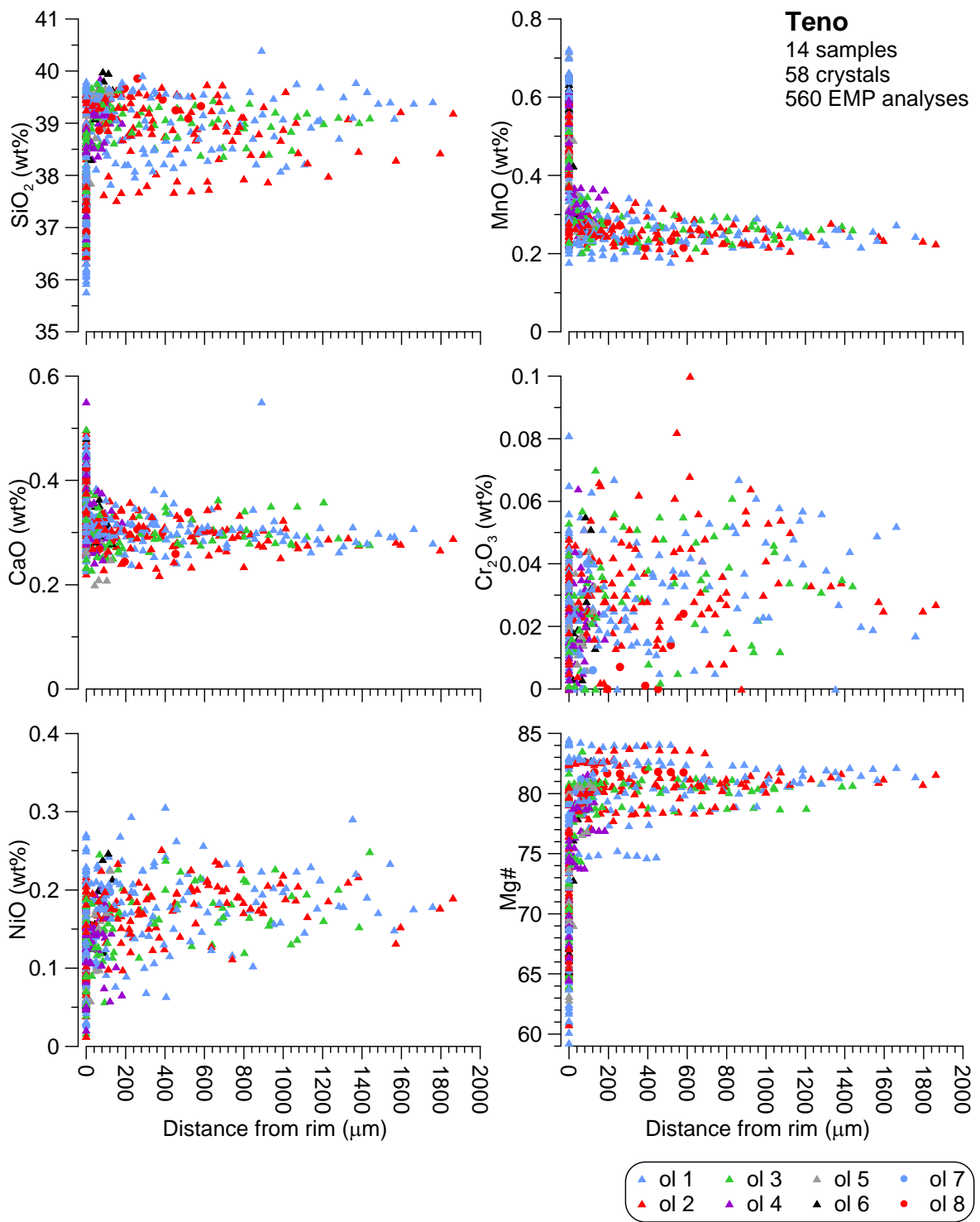
## **APPENDIX C: MINERAL CHEMISTRY PLOTS (TENO MASSIF)**

This appendix contains plots of mineral chemistry data for the Teno massif. The composition of clinopyroxene and olivine crystals in major element oxides is first shown as a function of Mg#, then as a function of distance from the crystal rim, for the whole dataset. Data for single samples (sample number indicated in top-right corner) are then plotted against distance from the crystal rim. Colour codes refer to different crystals, as explained in the key. Some clinopyroxene crystals have been analysed on more than one profile; these generally correspond to sector-zoned crystals.



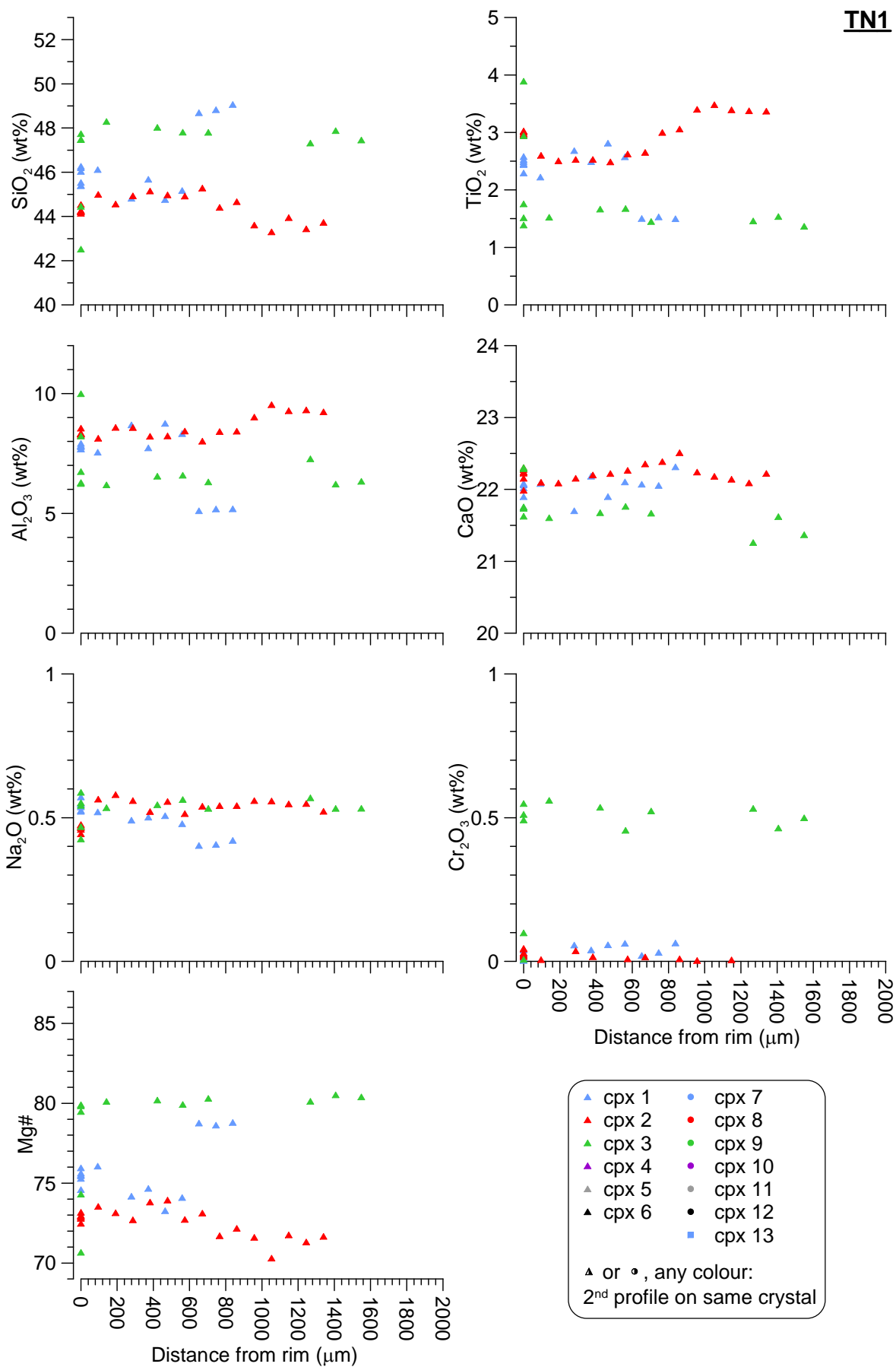


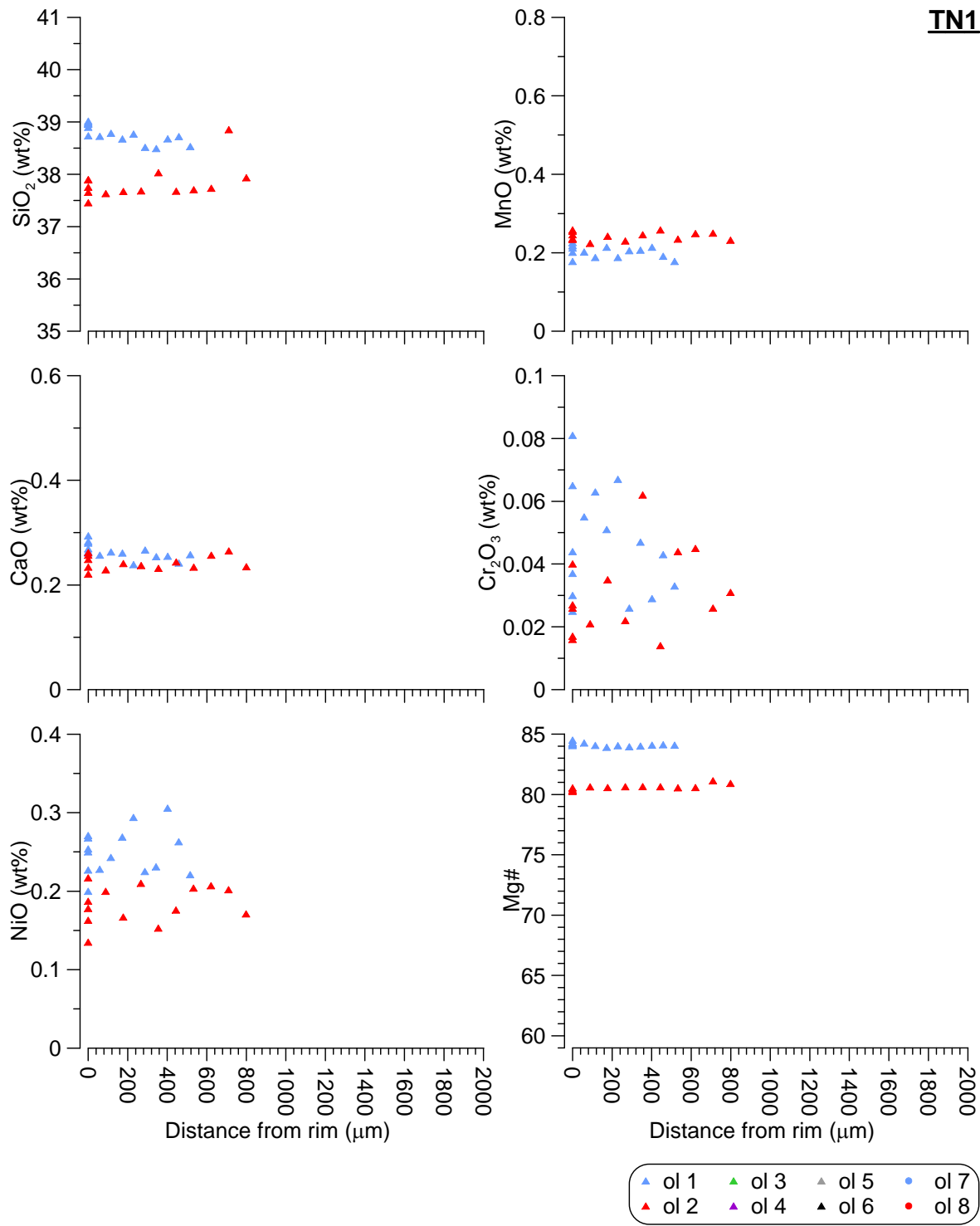


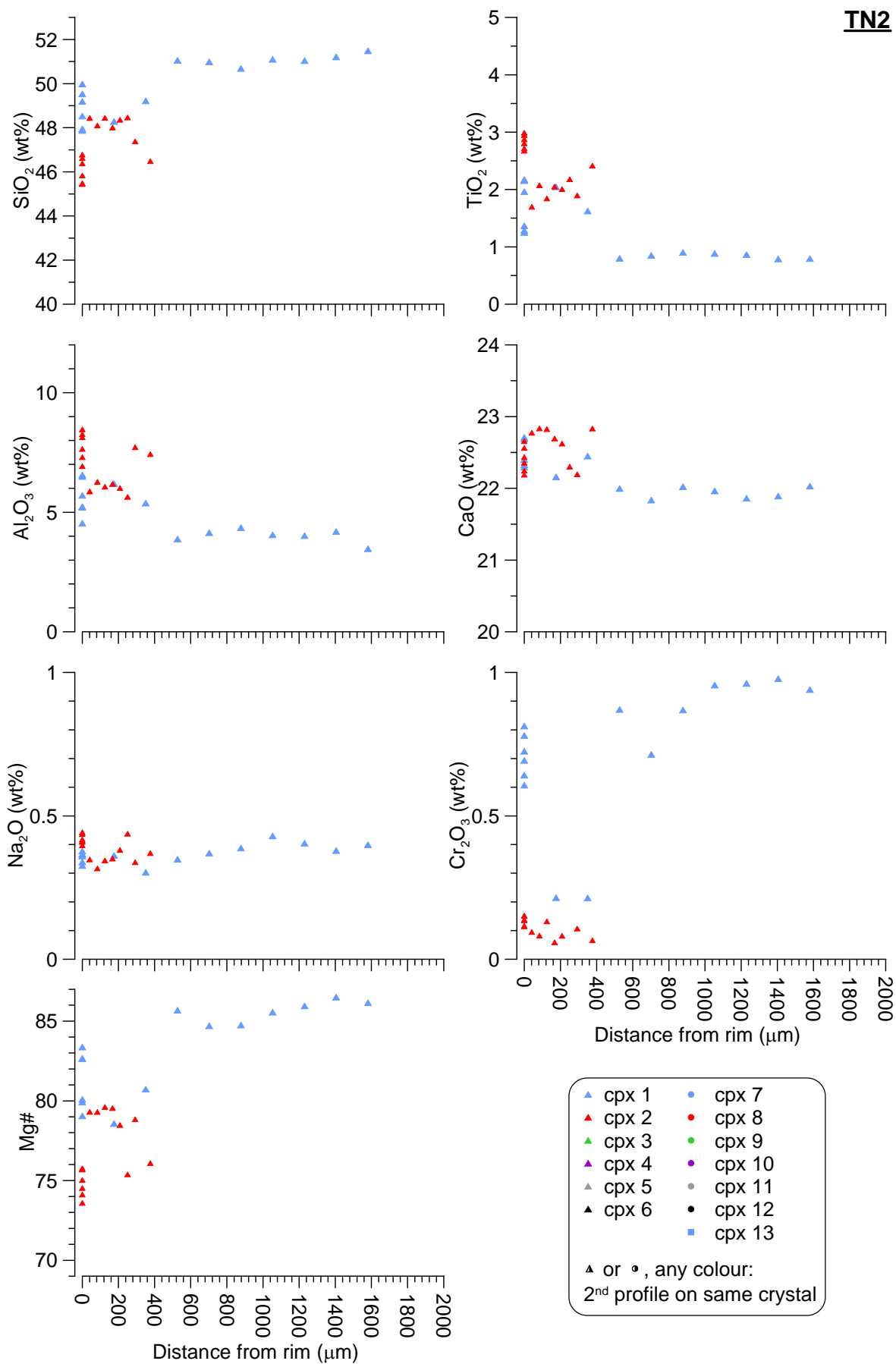


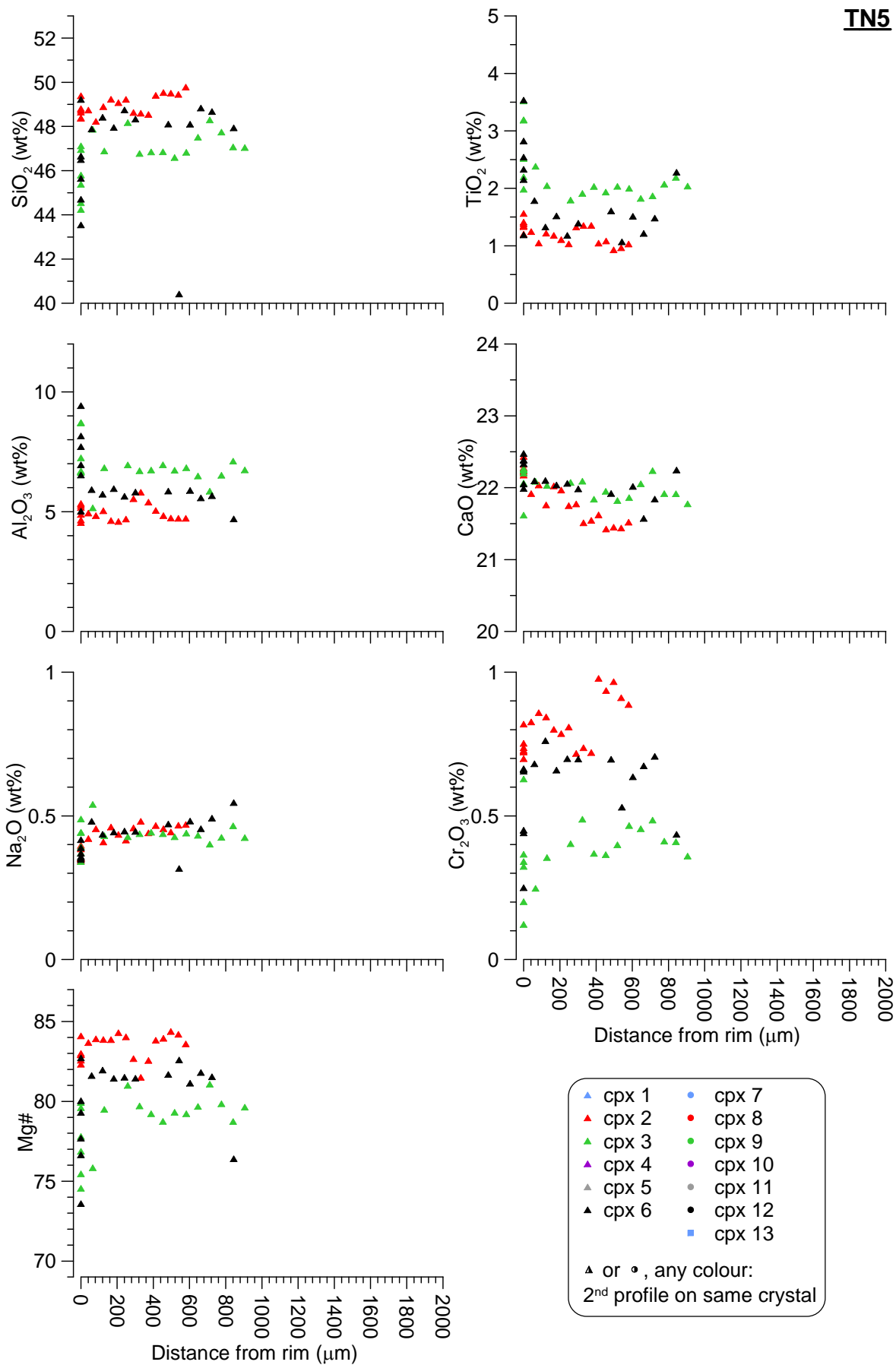


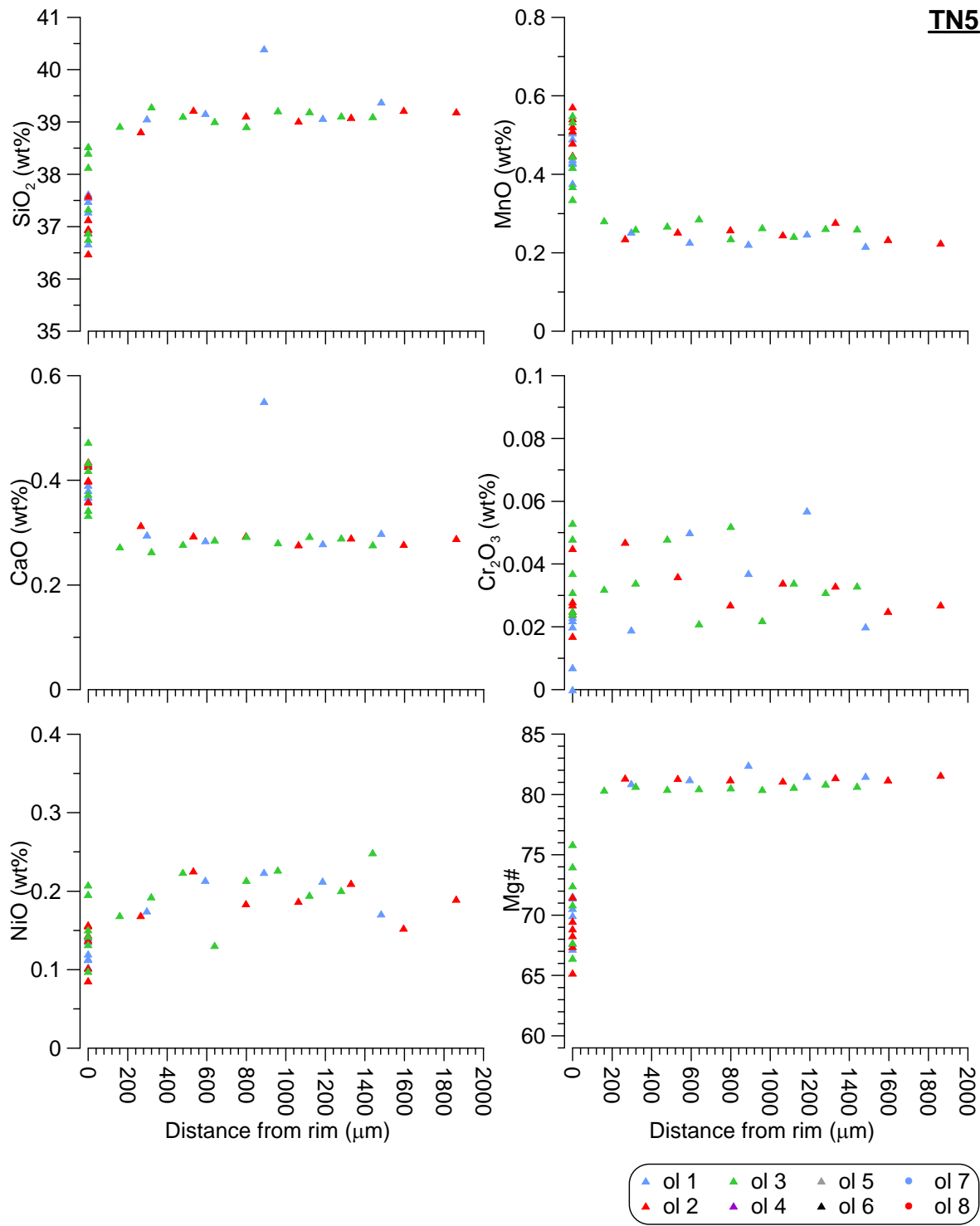
**TN1**



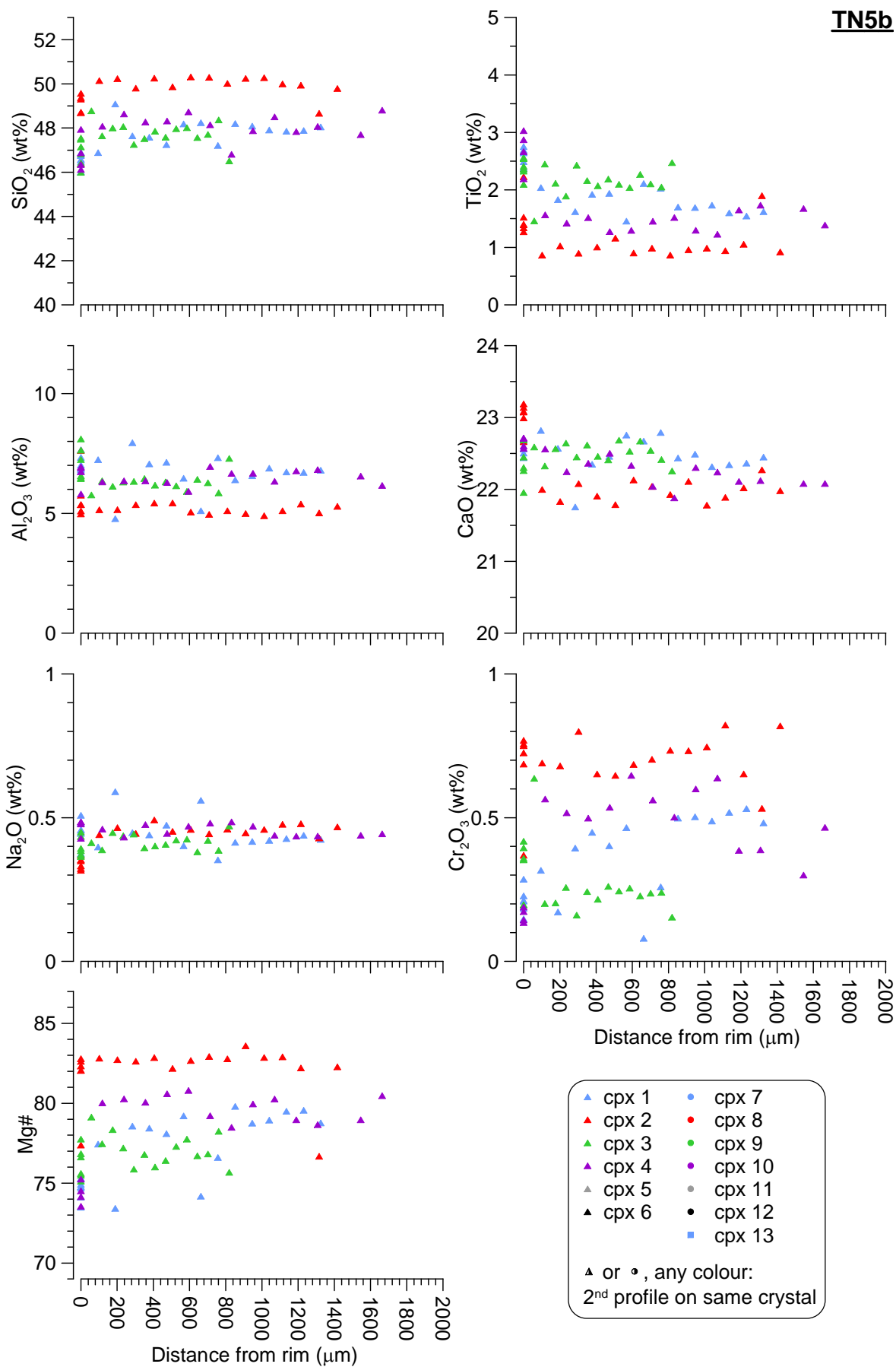




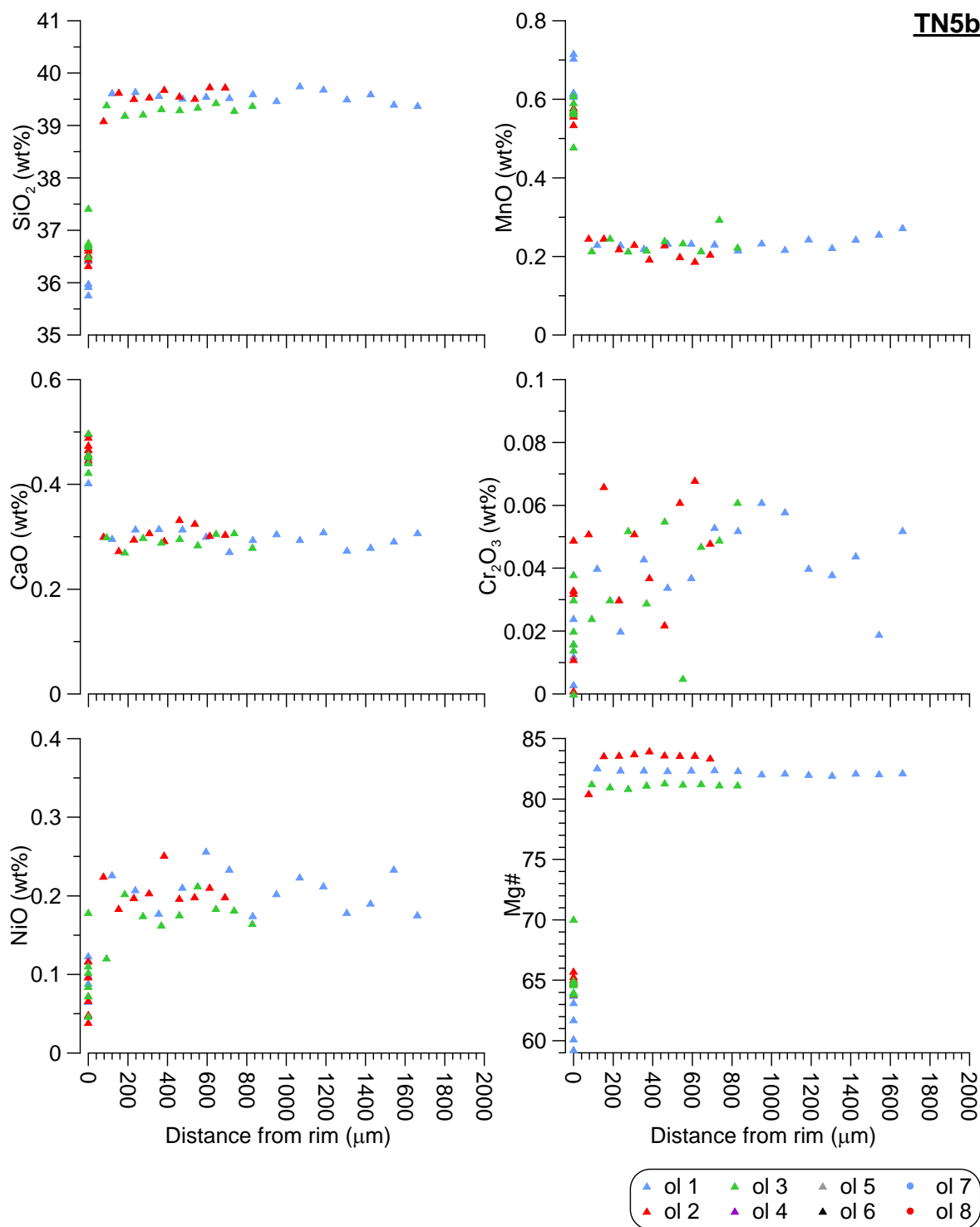


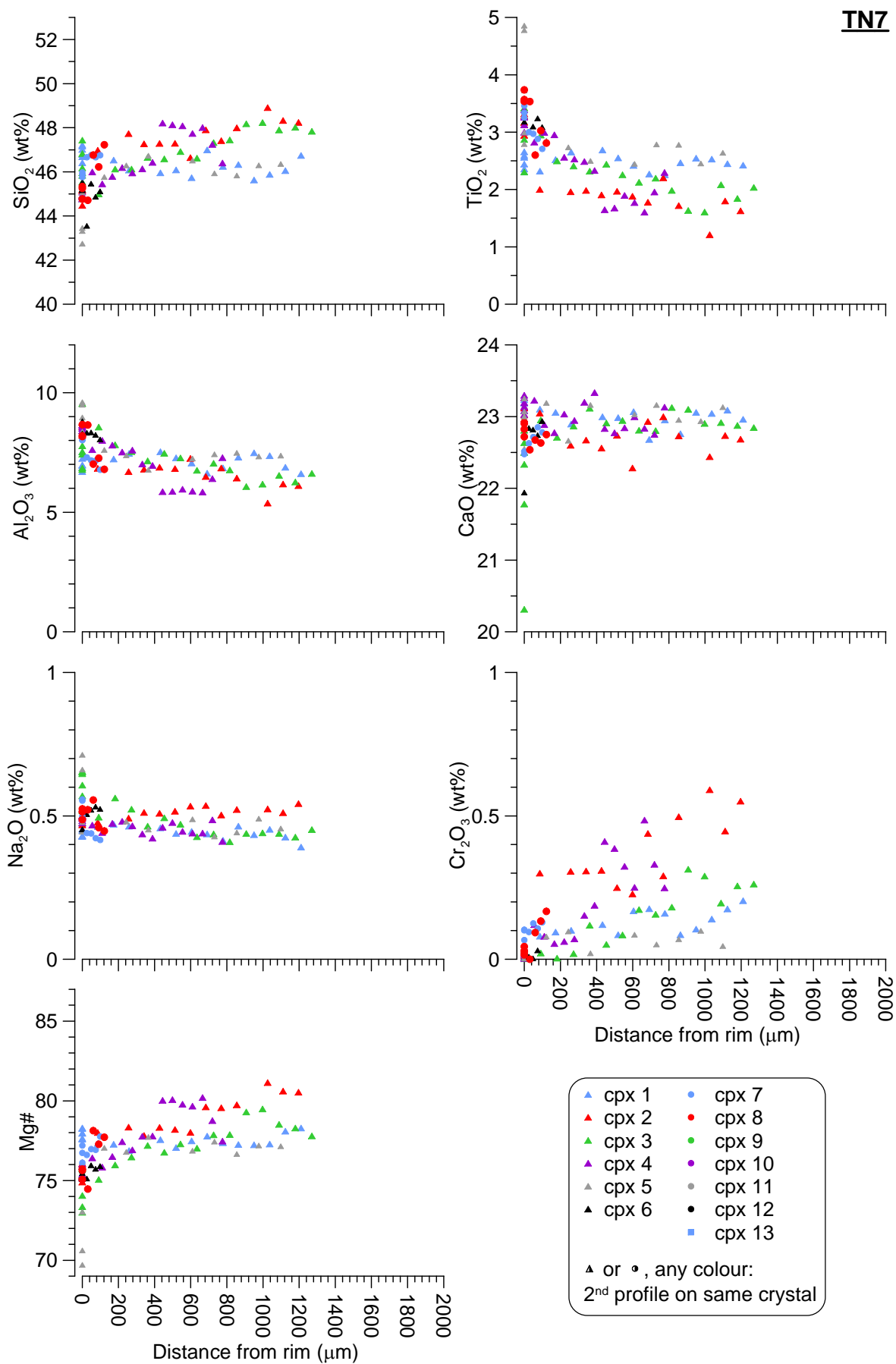


**TN5b**



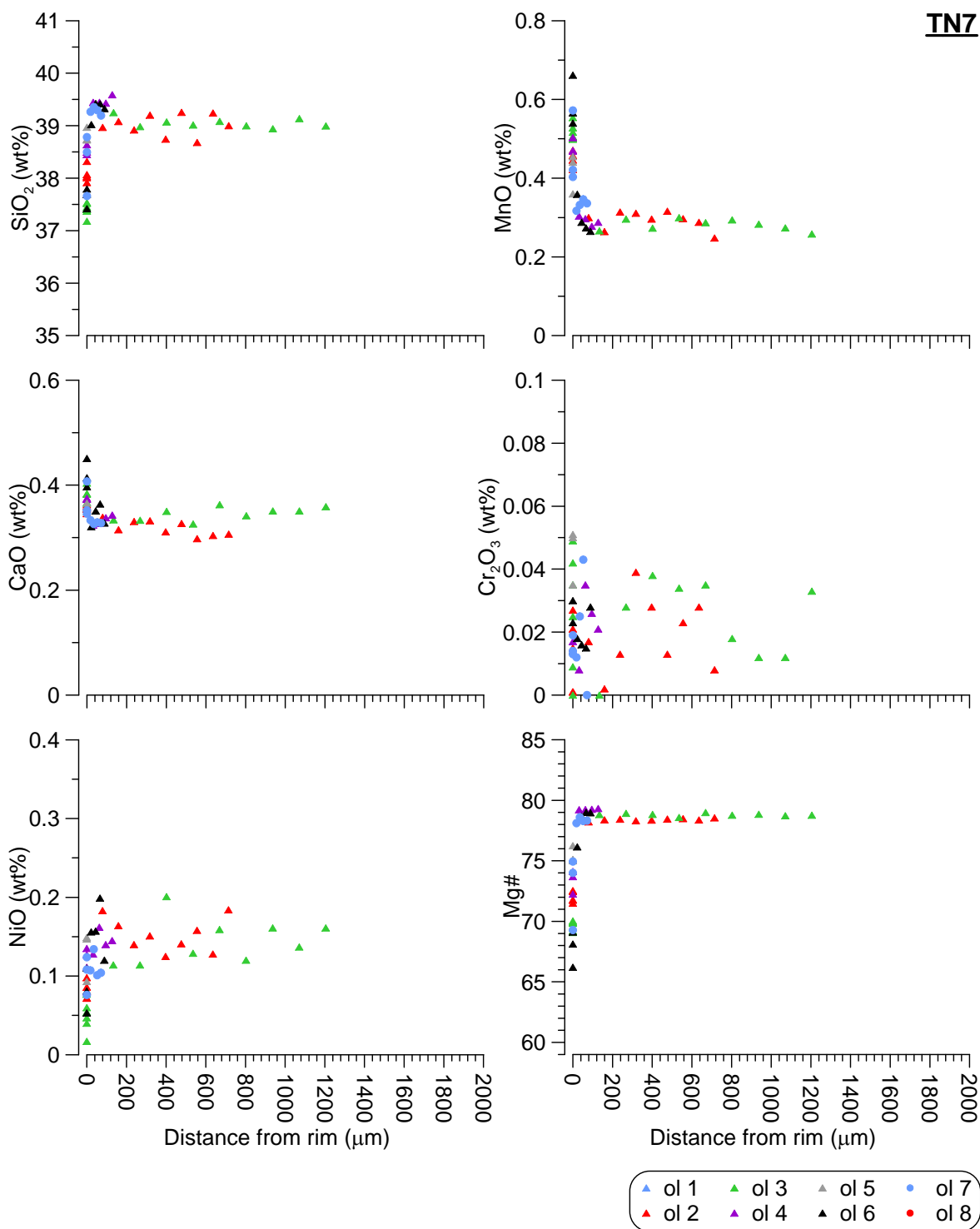
**TN5b**



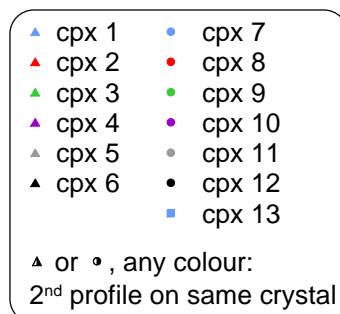
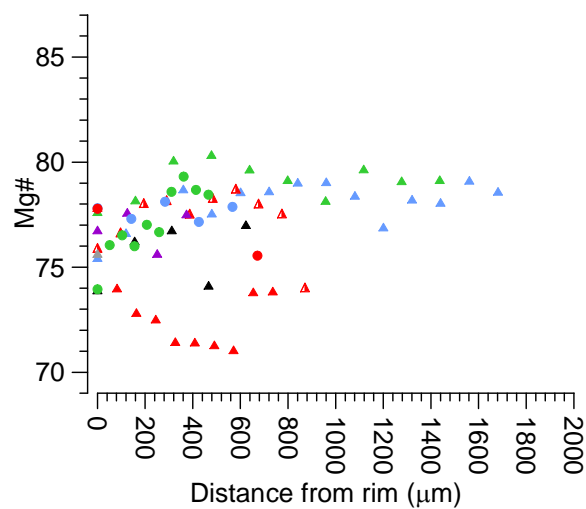
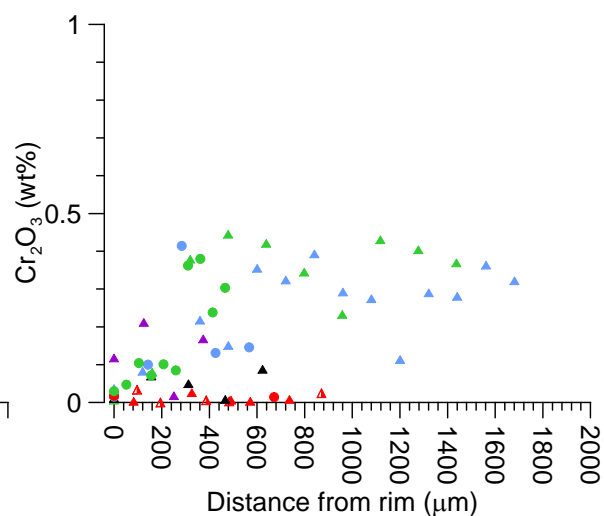
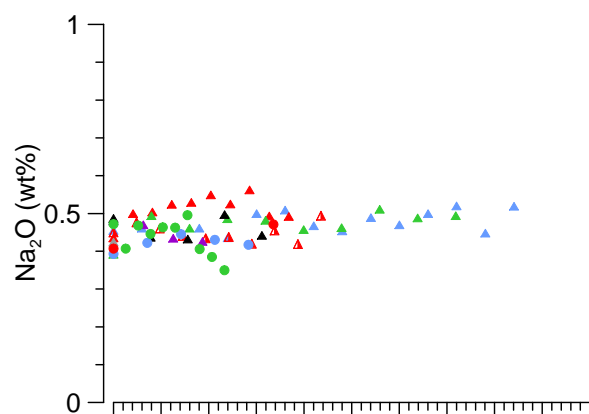
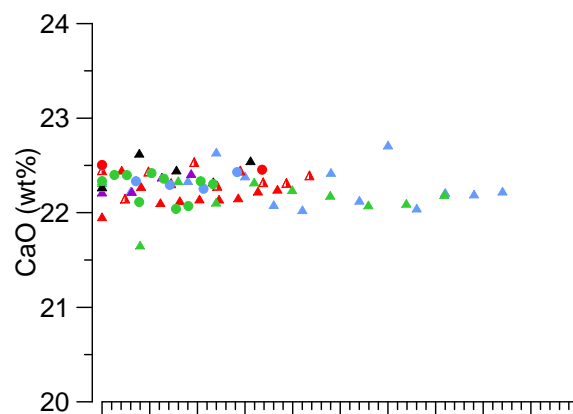
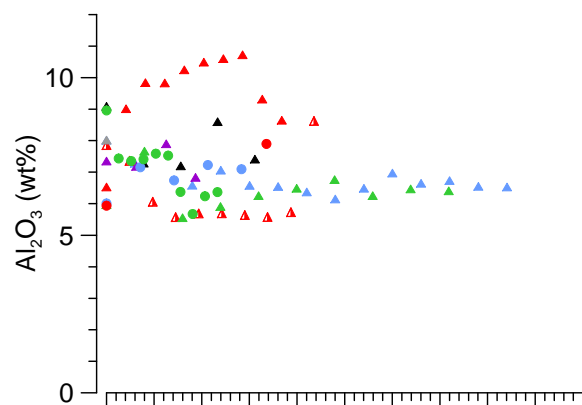
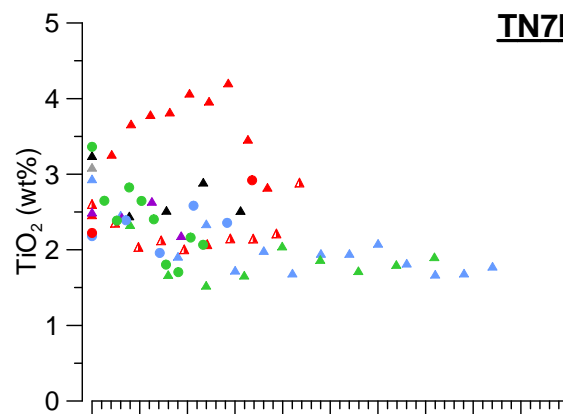
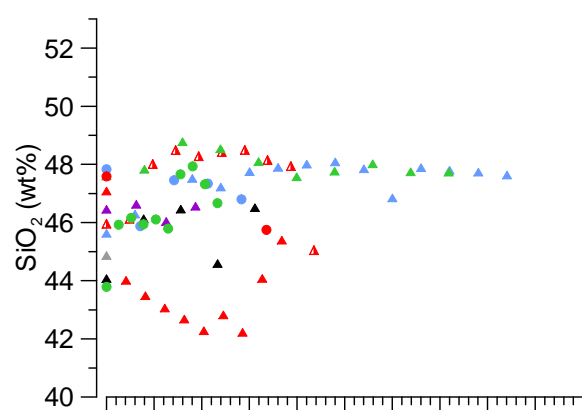




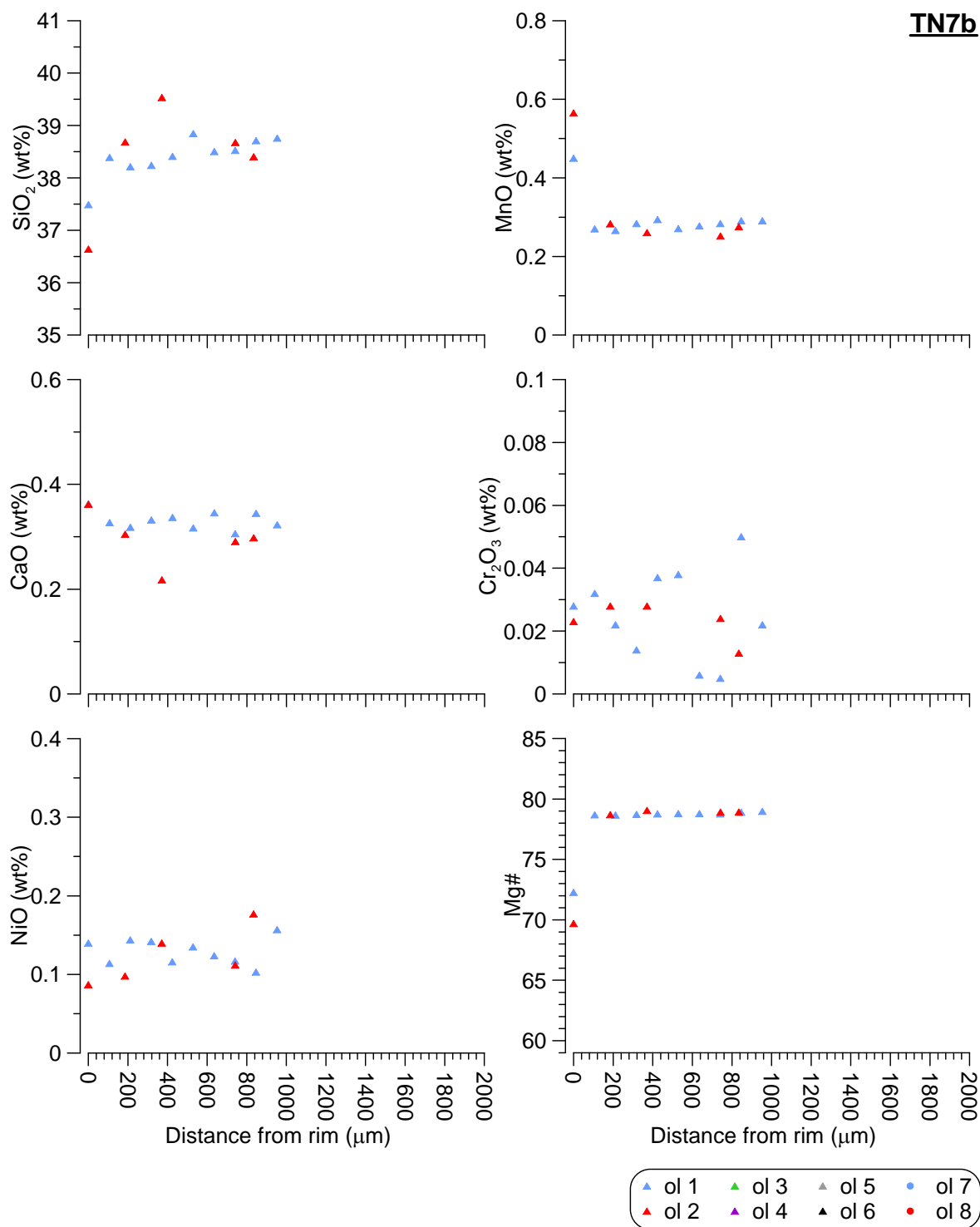
**TN7**



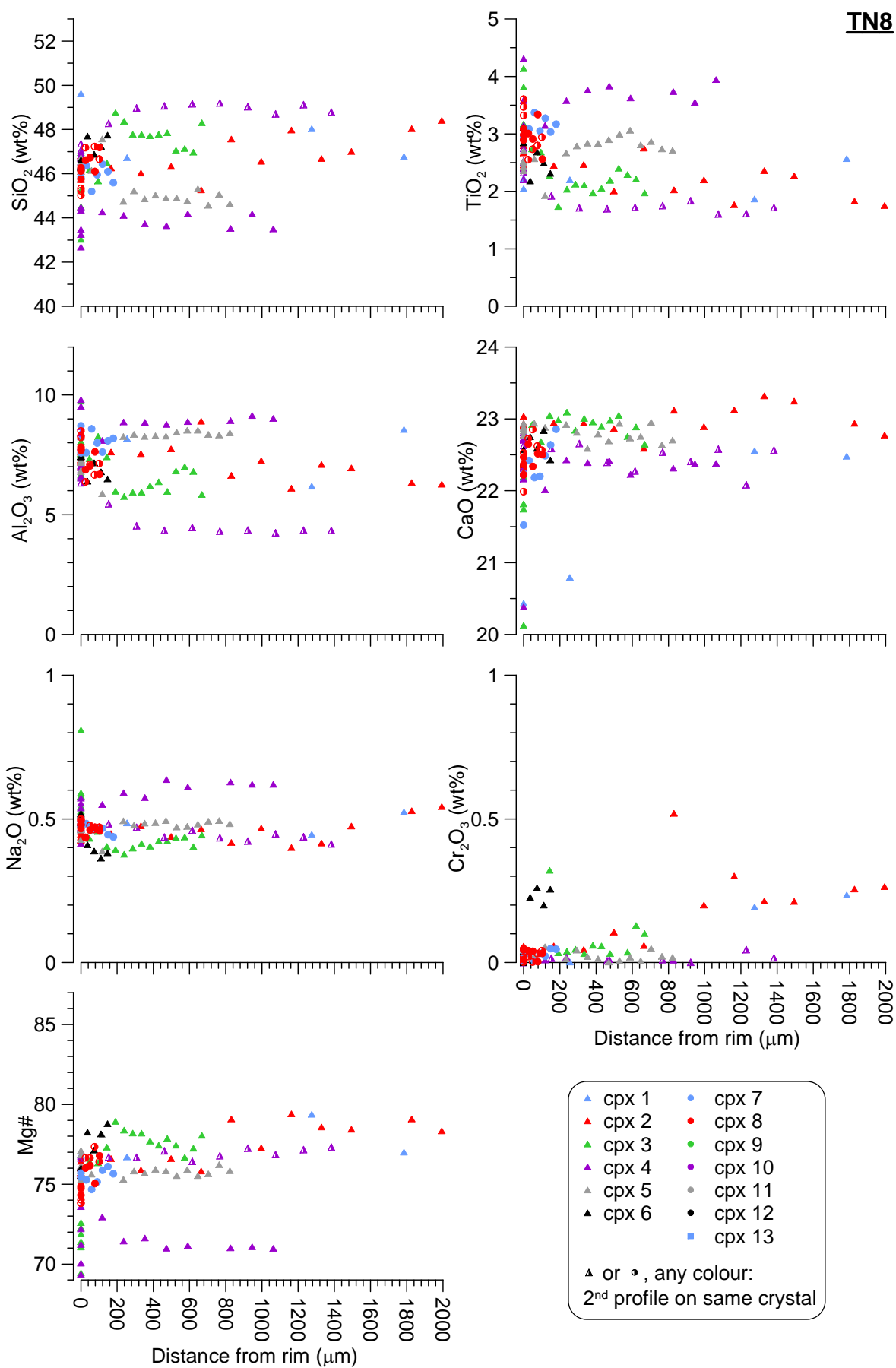
**TN7b**



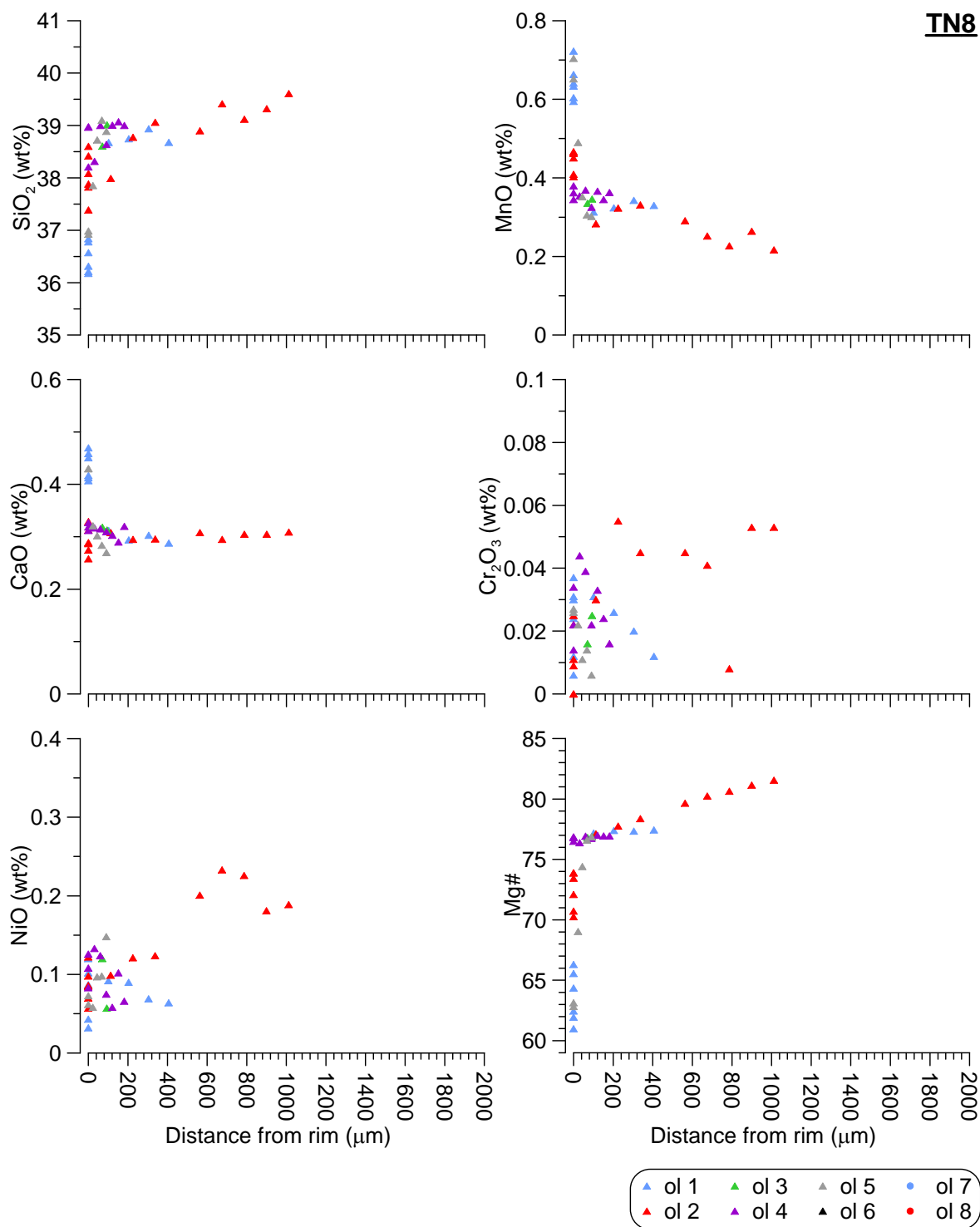
**TN7b**

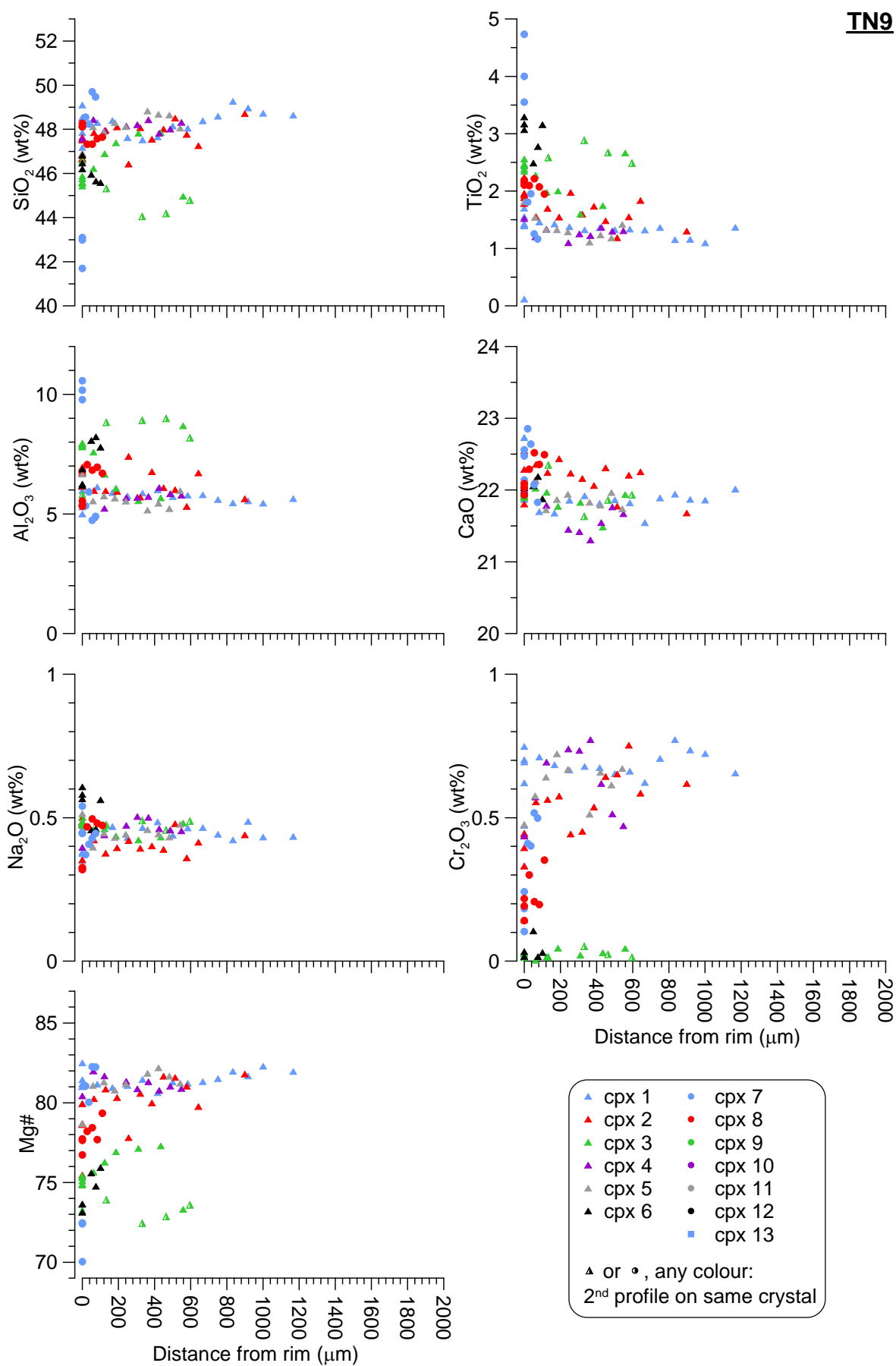


**TN8**

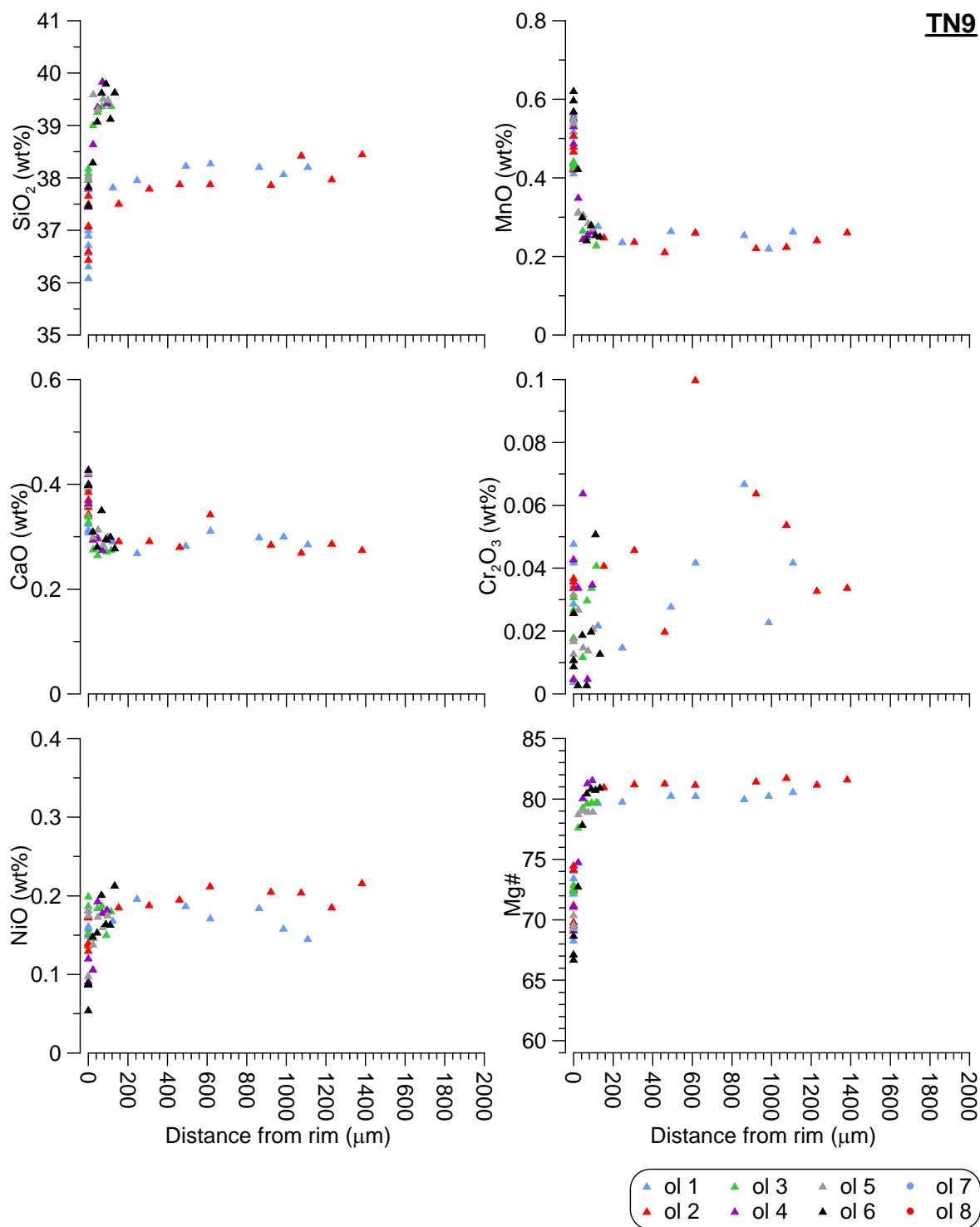


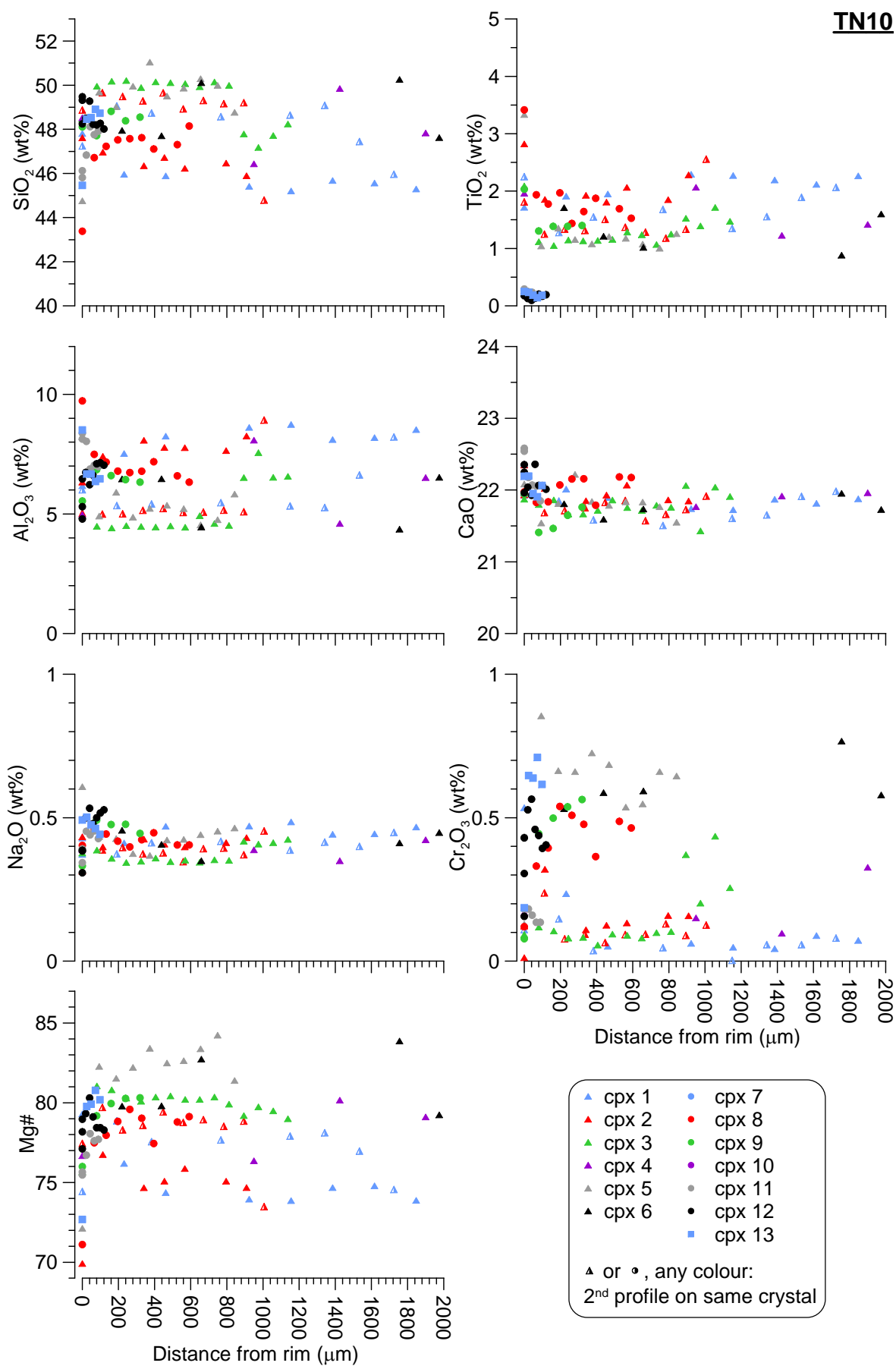
**TN8**





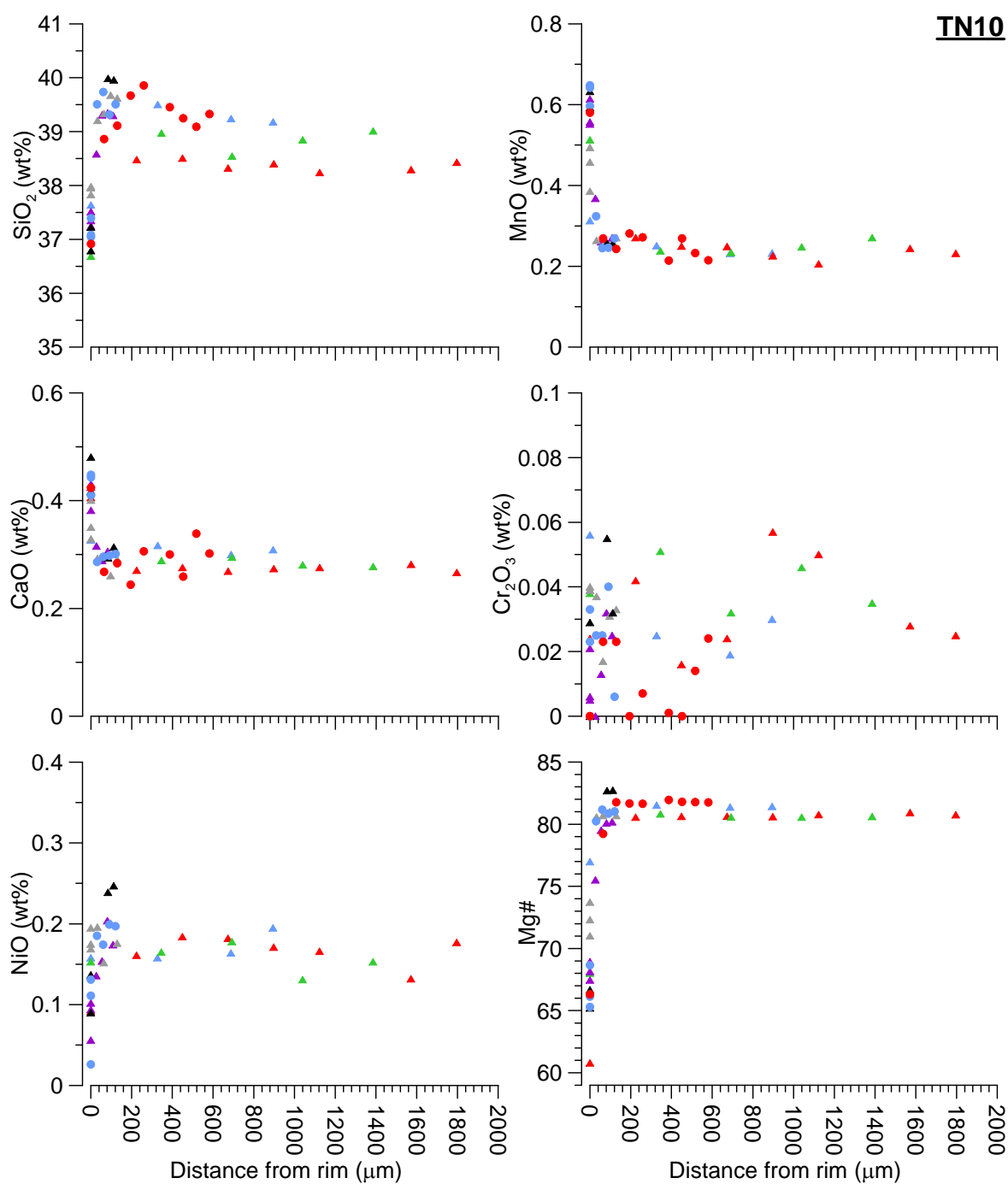
**TN9**

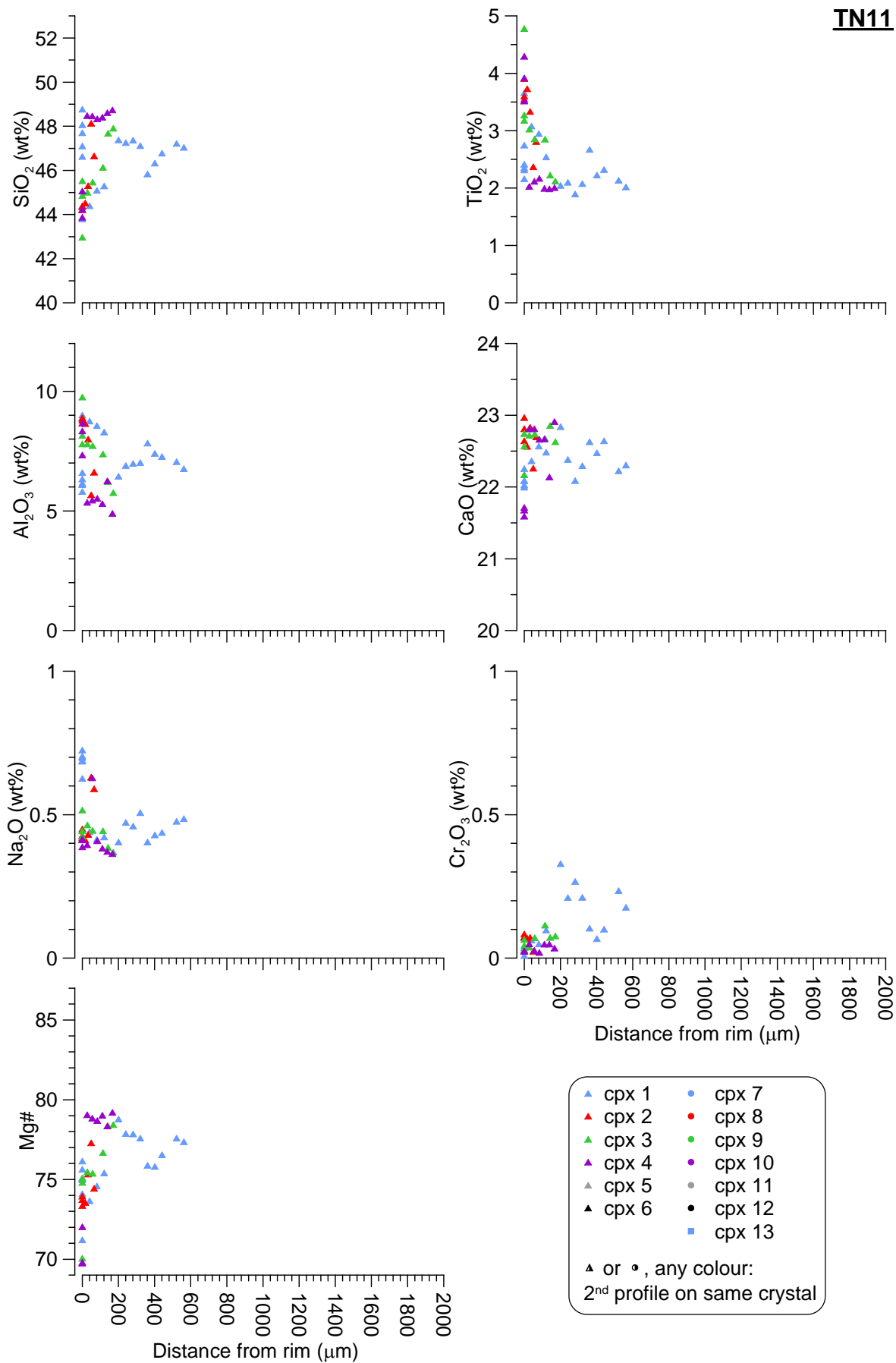


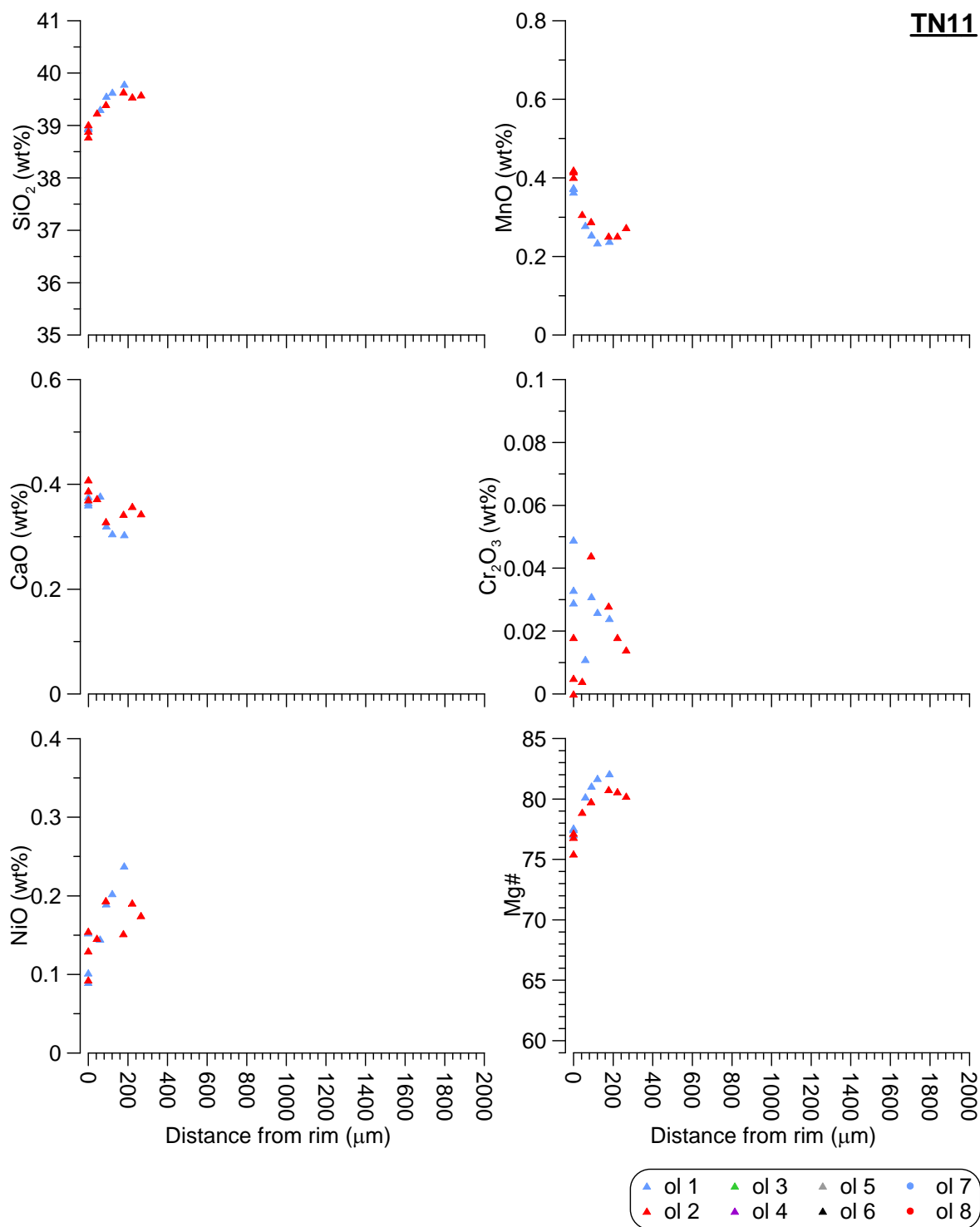


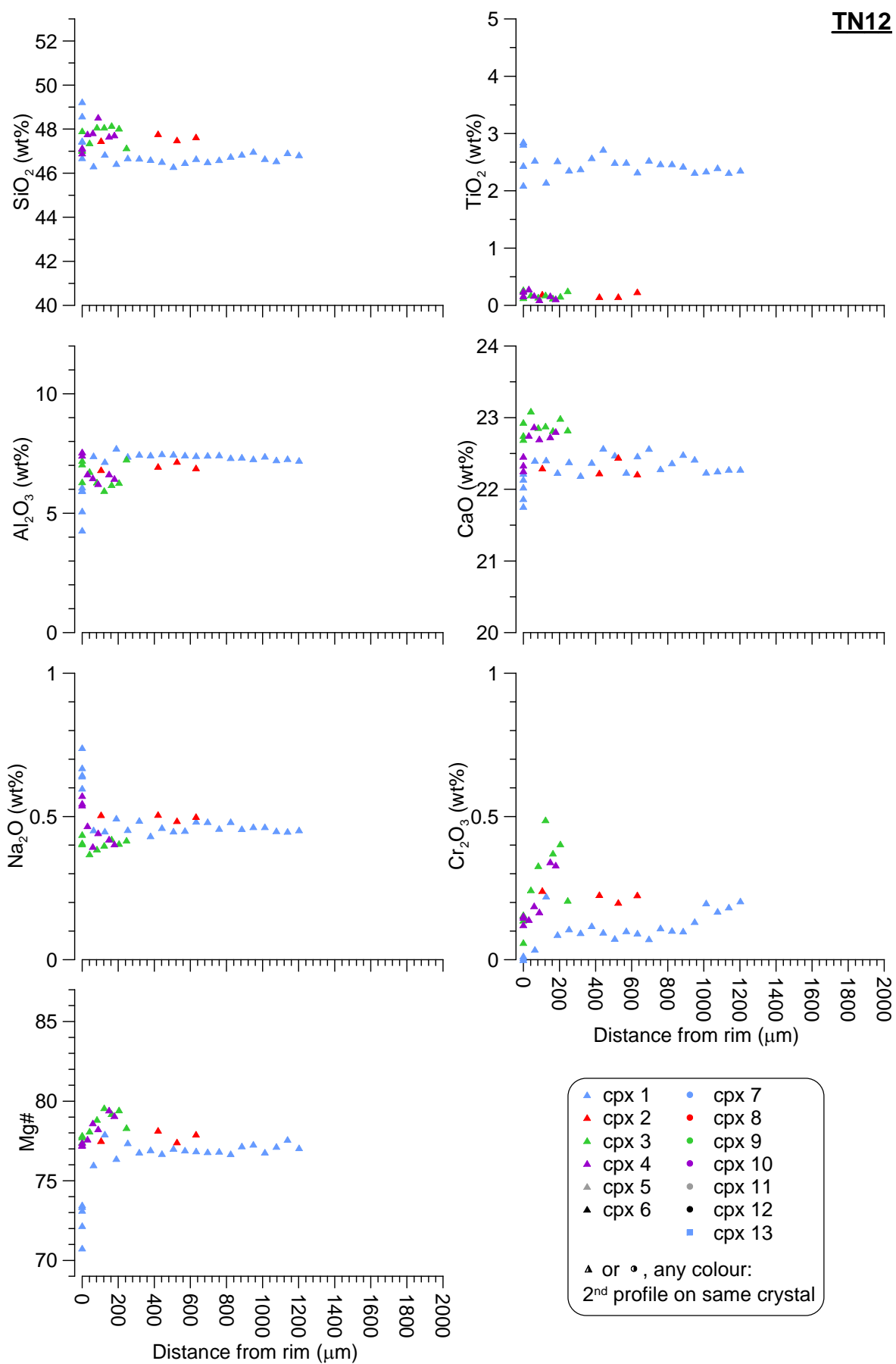


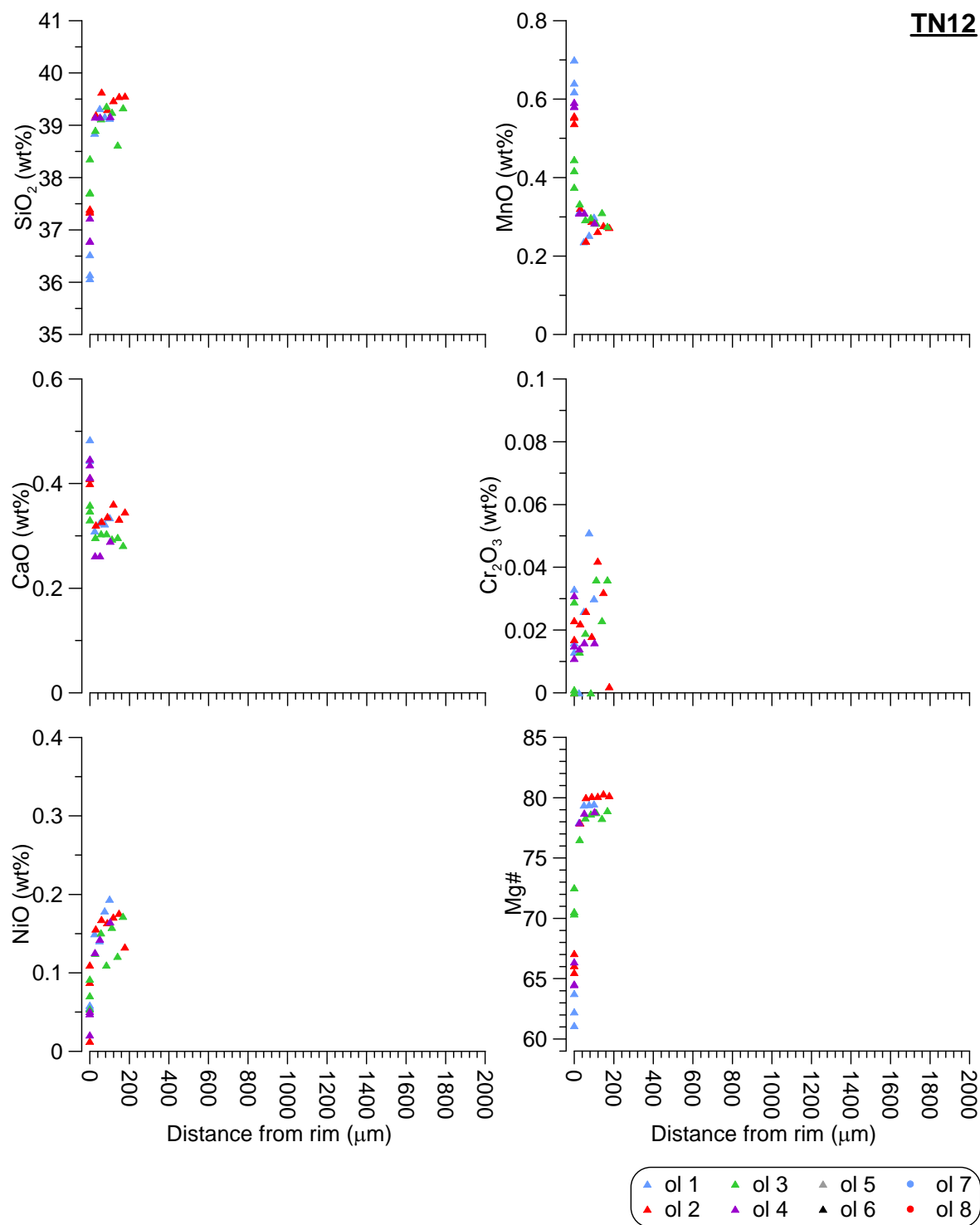
**TN10**

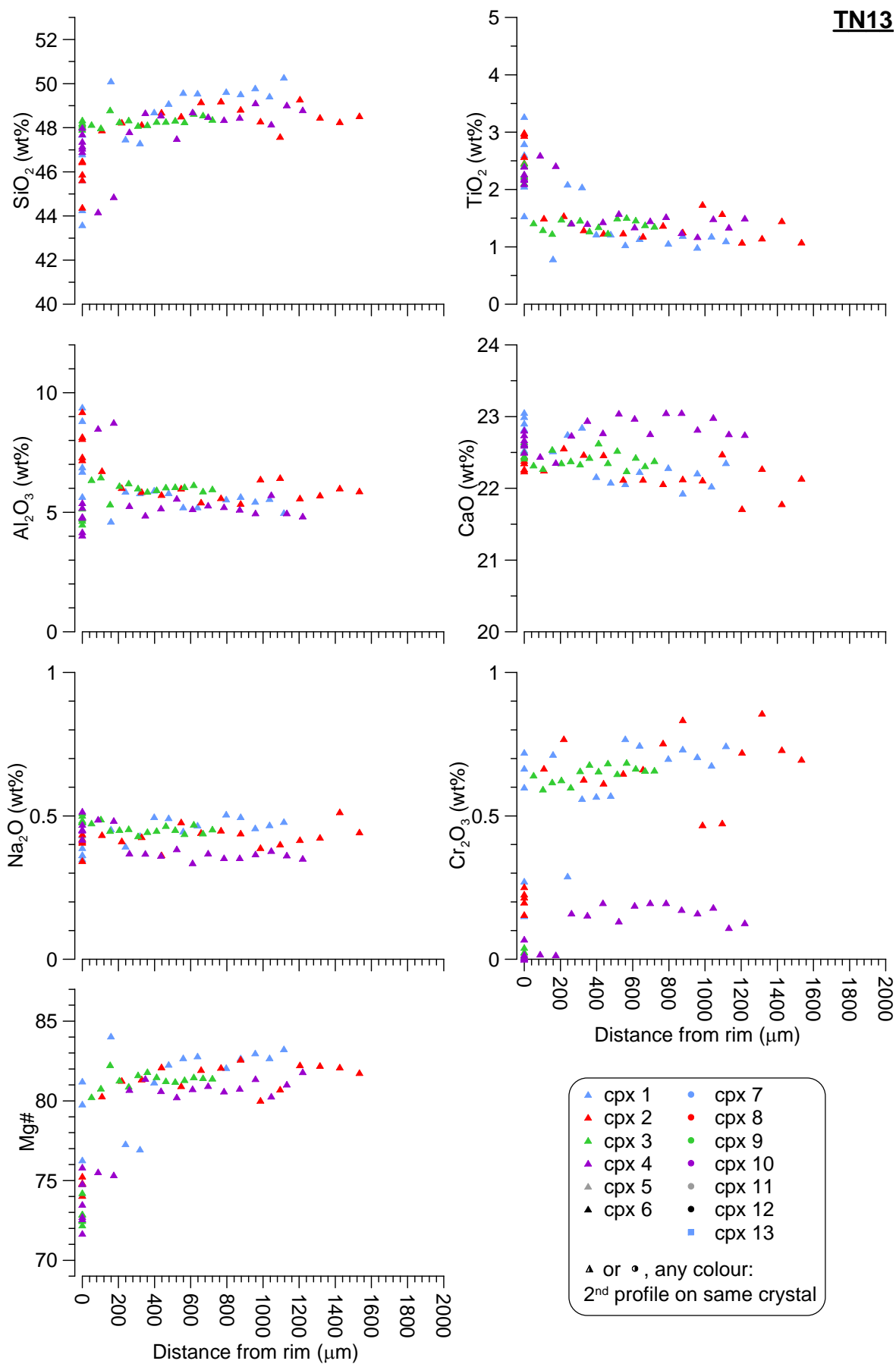




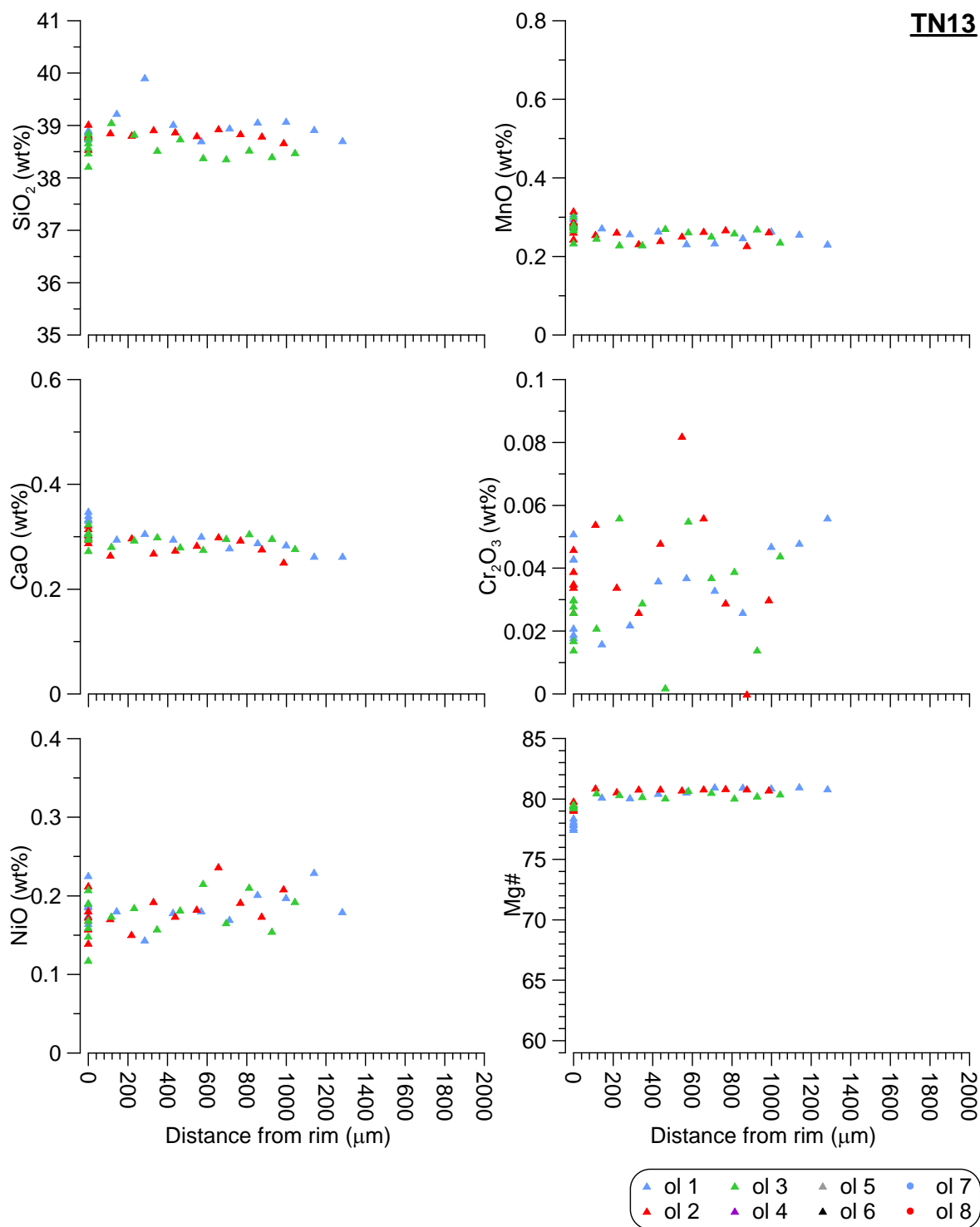






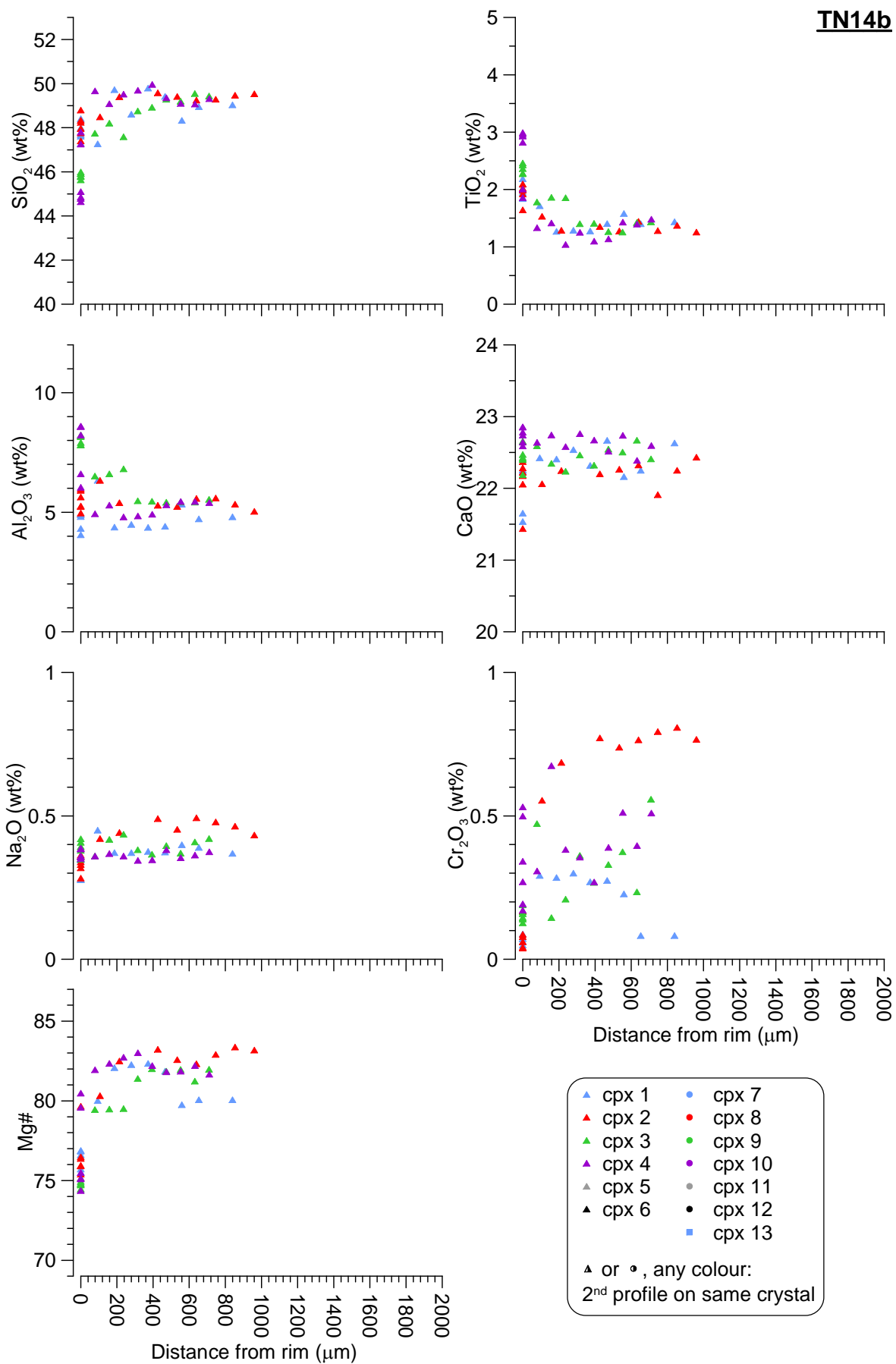


**TN13**



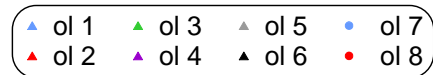
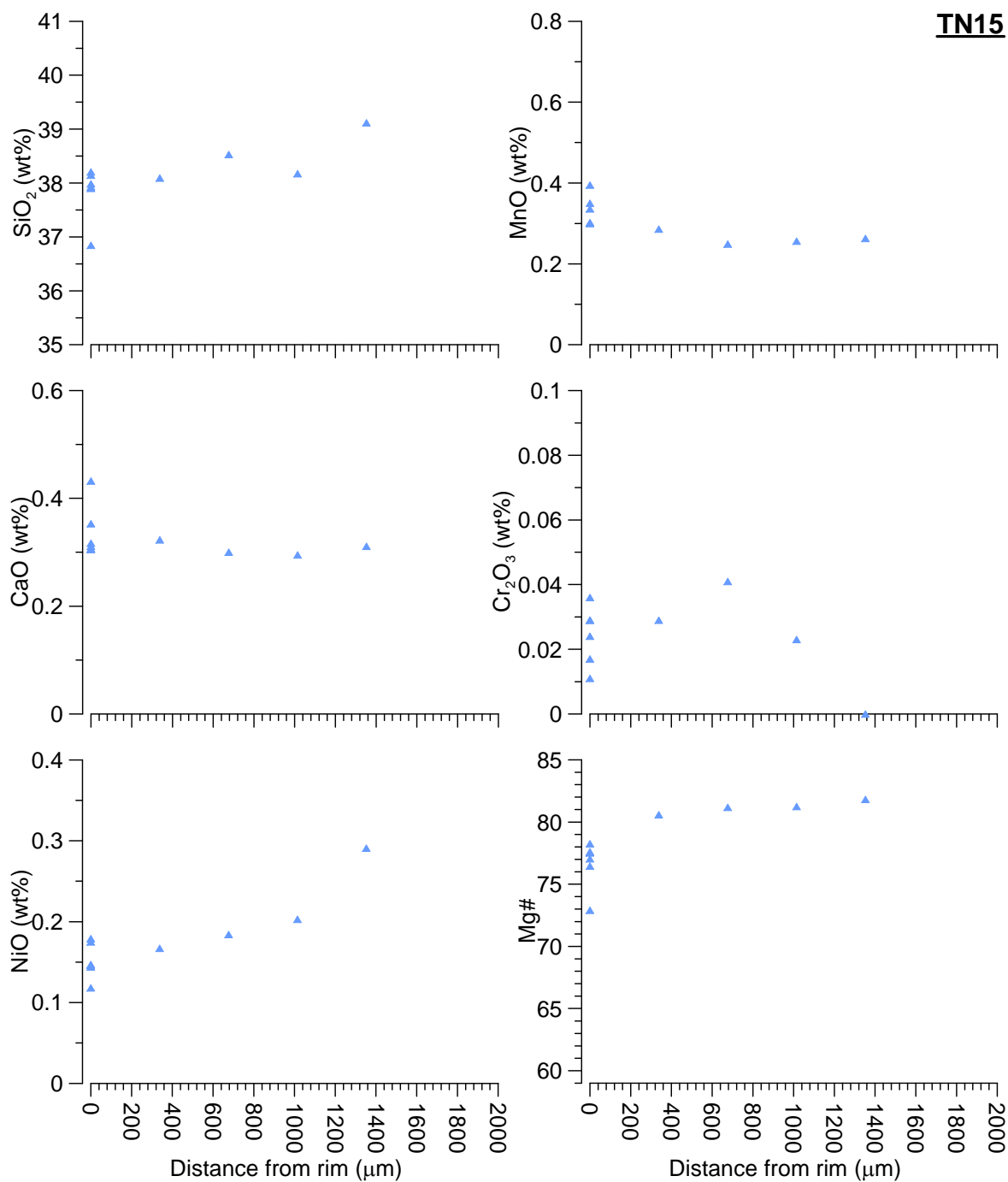


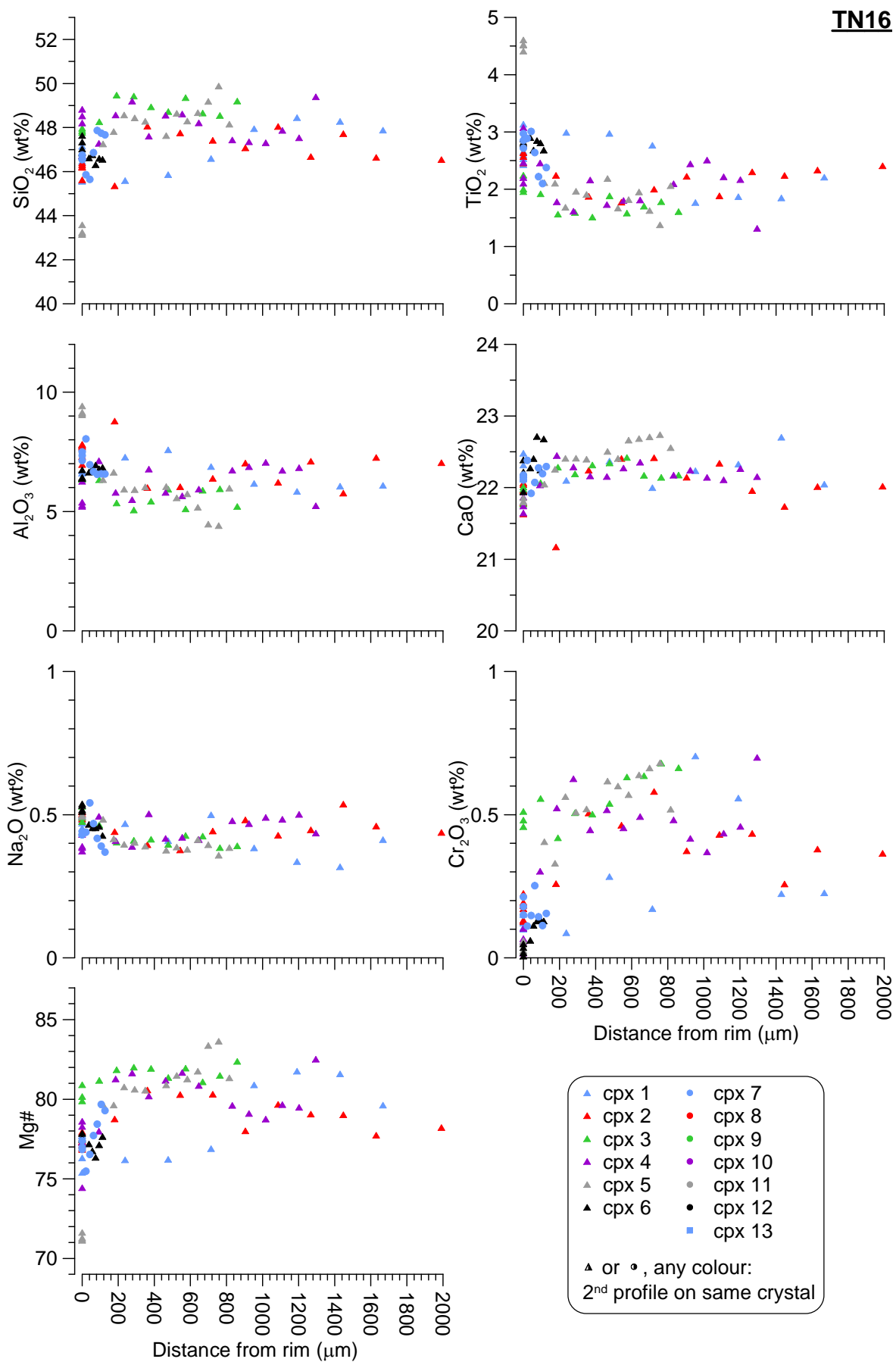




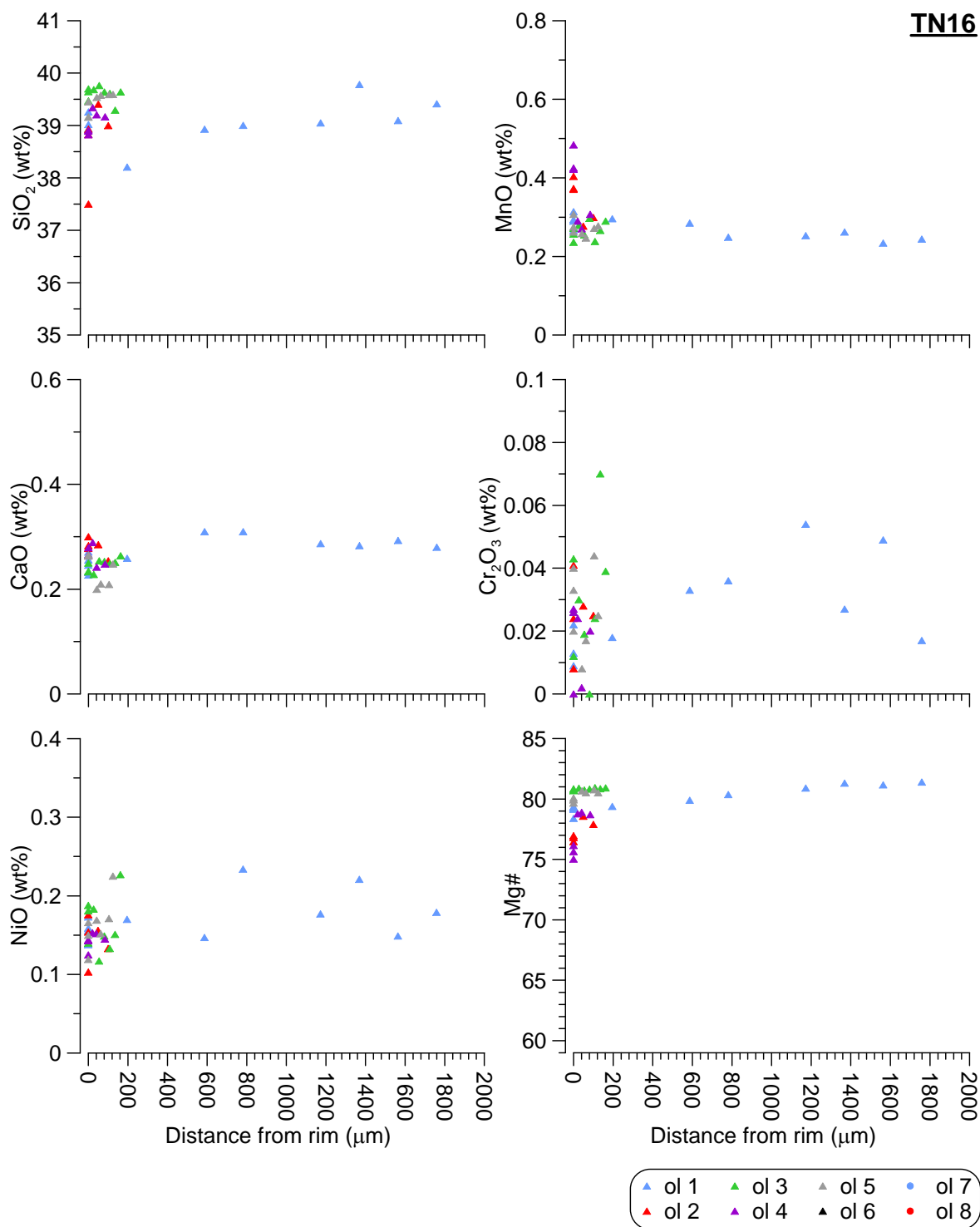


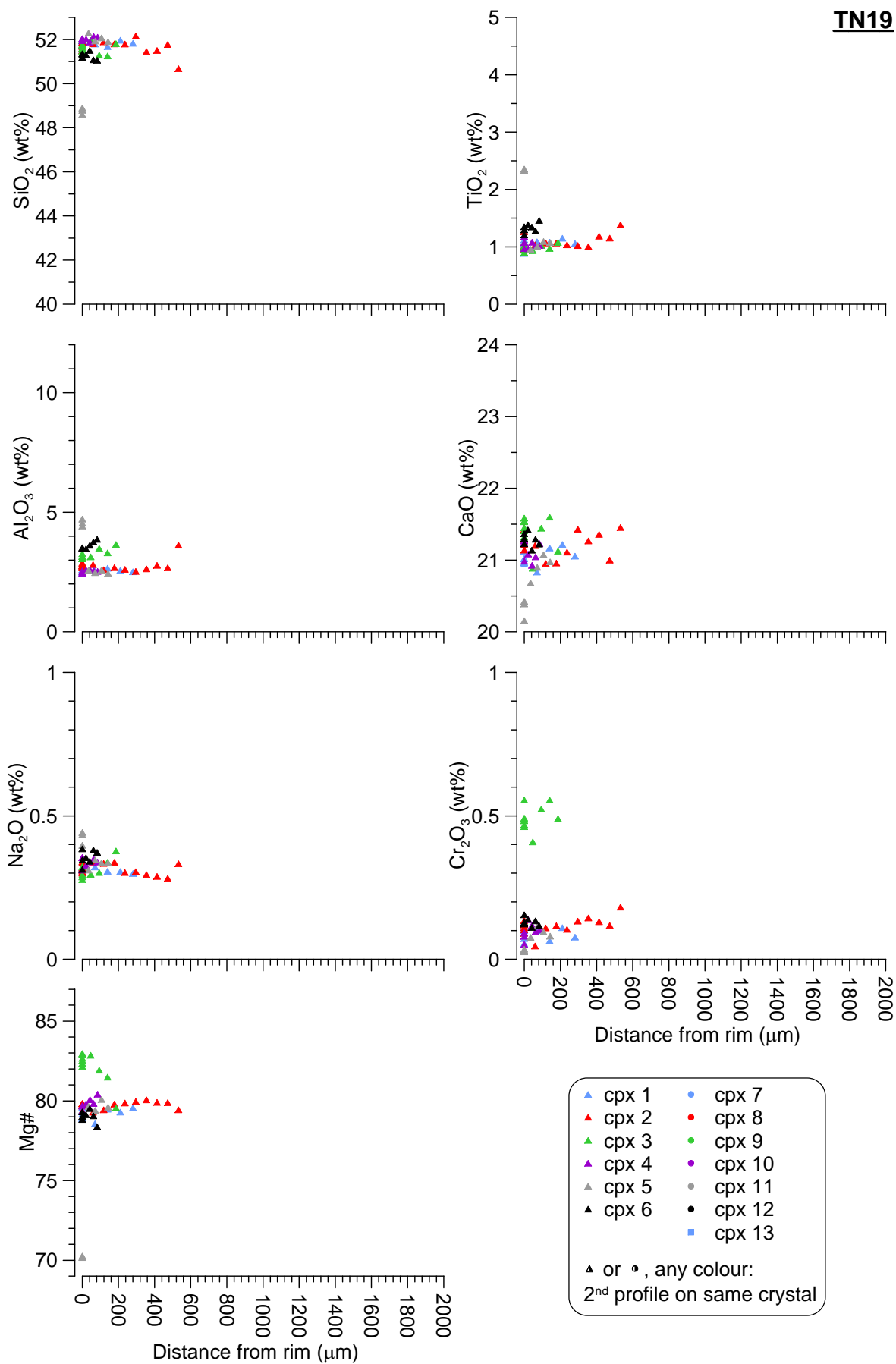
**TN15**

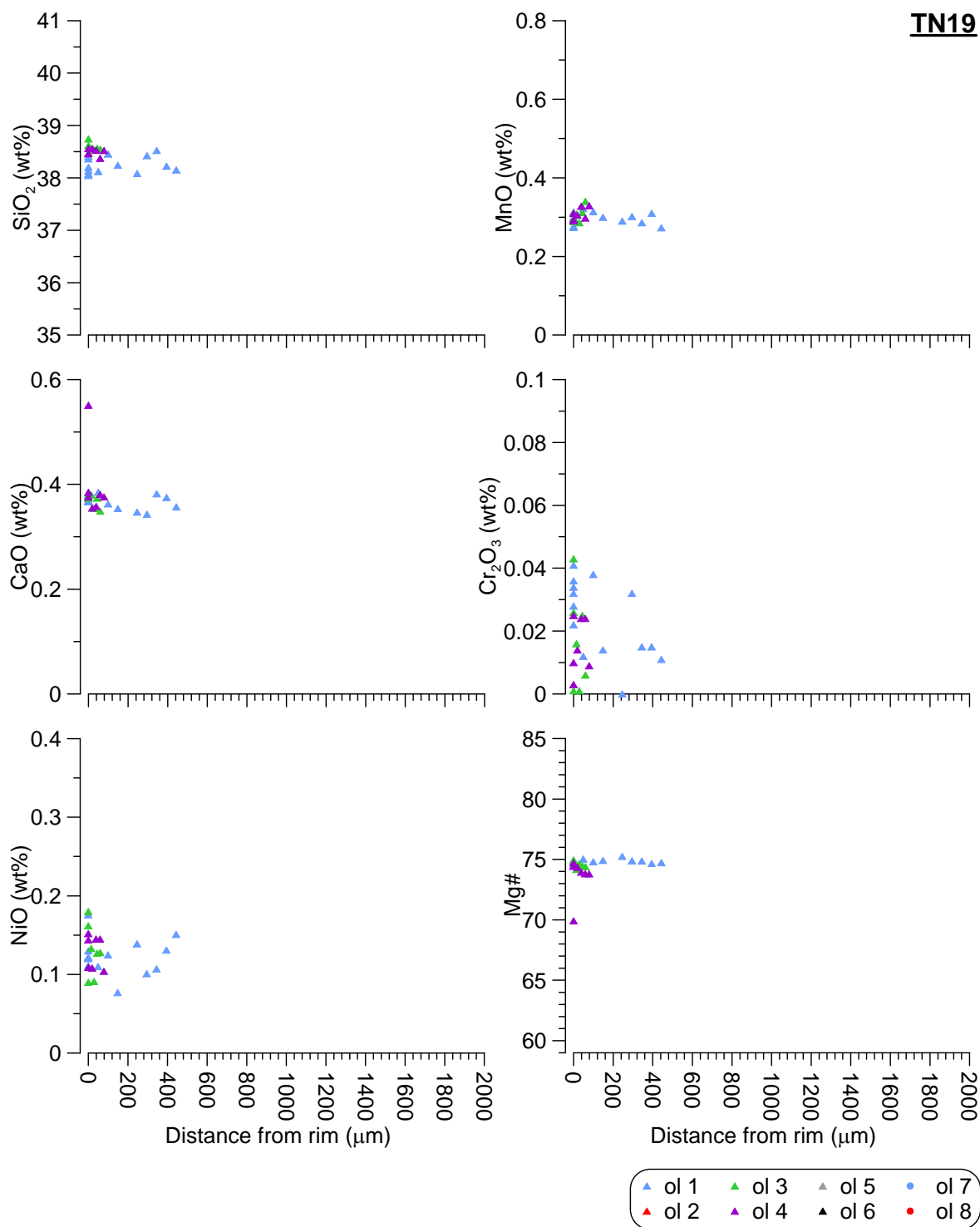


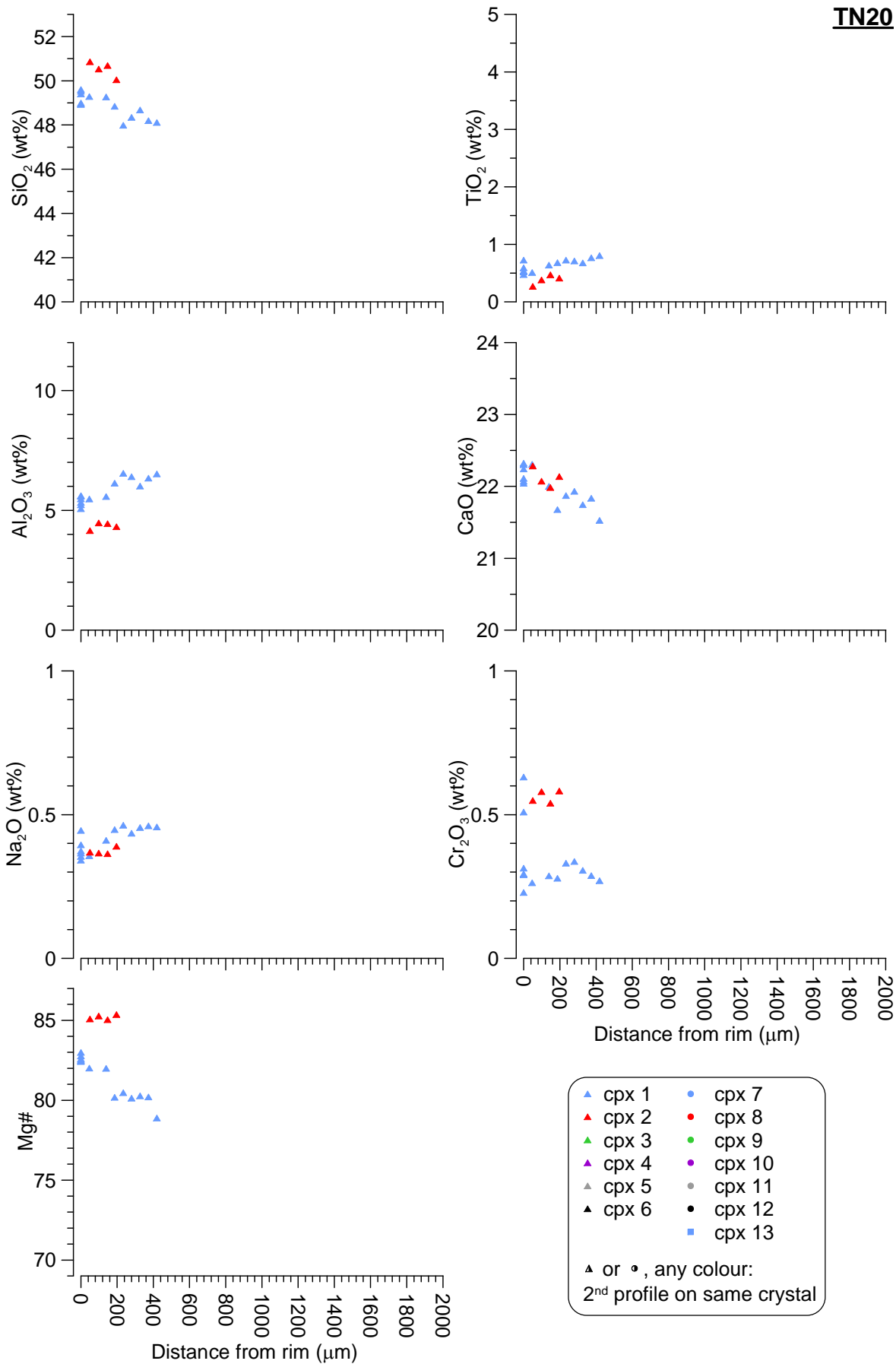


**TN16**

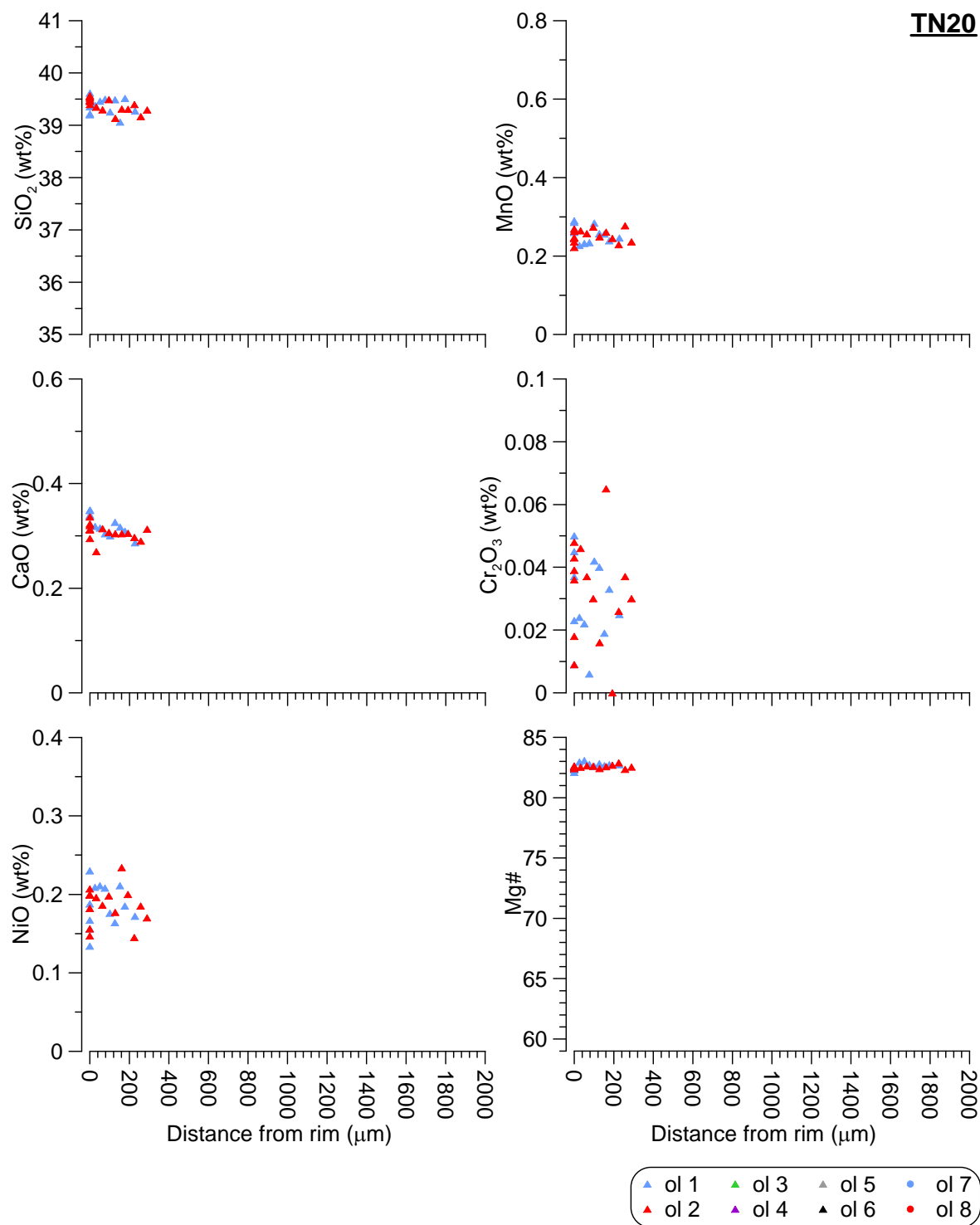




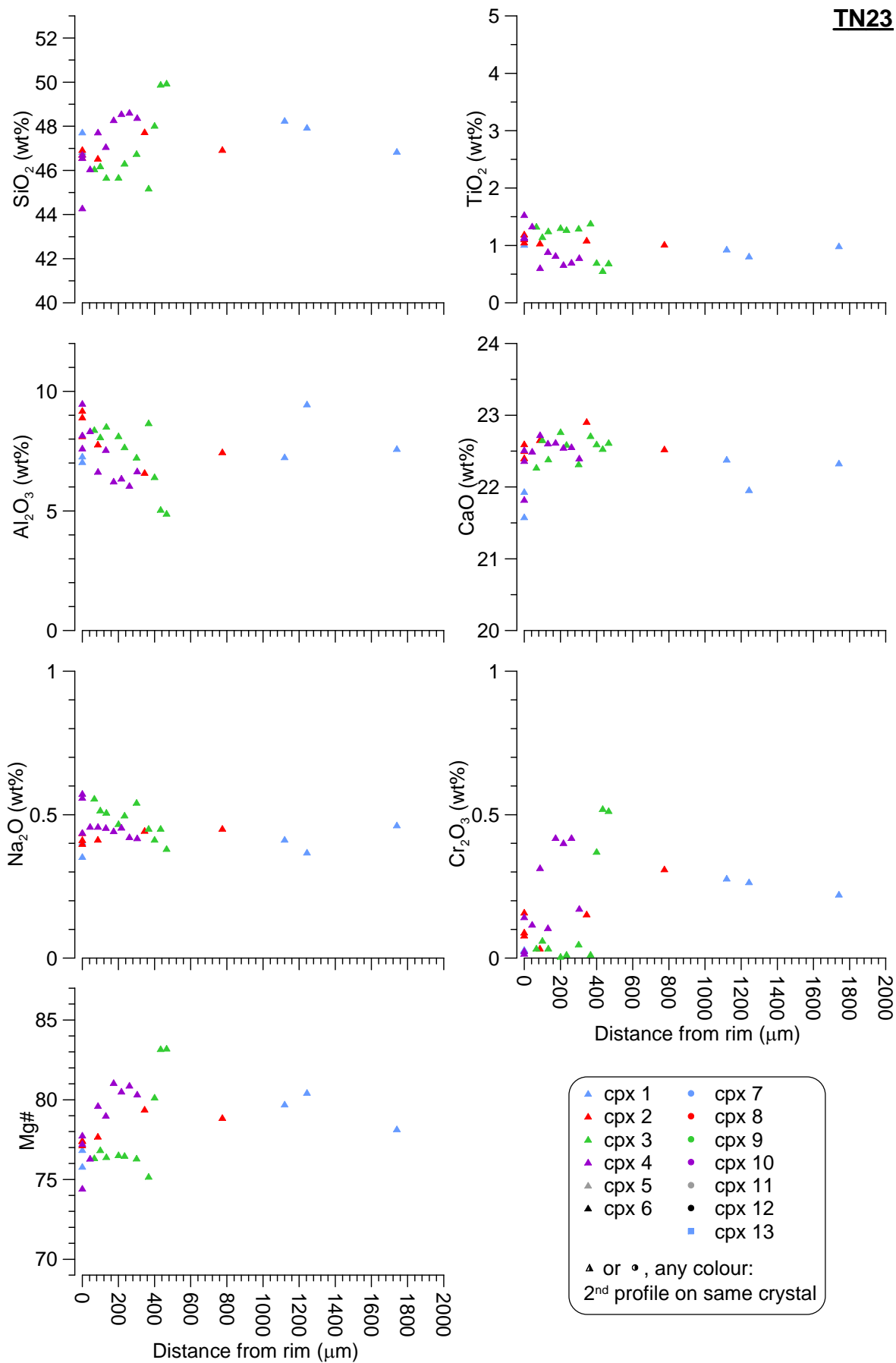


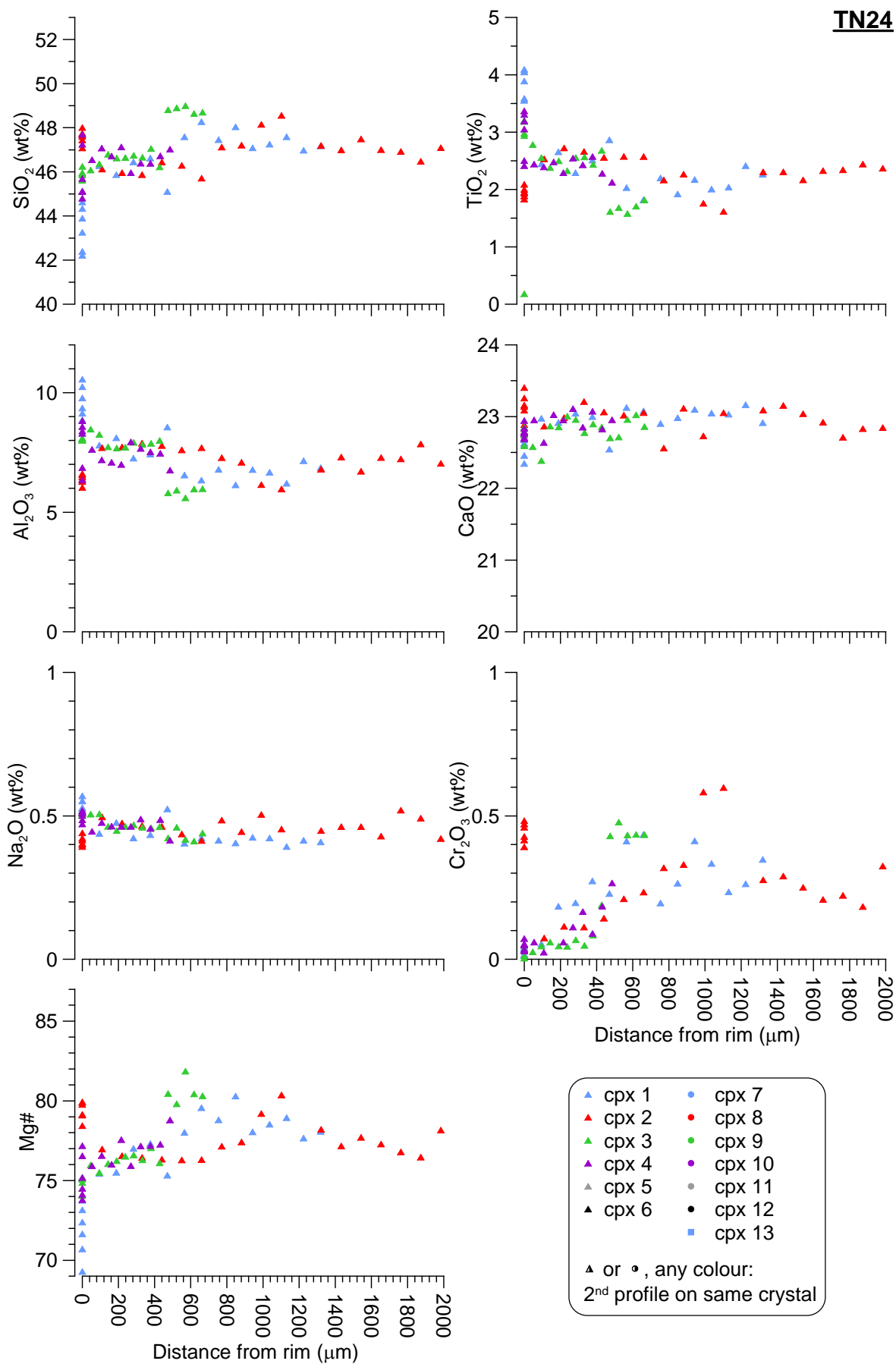


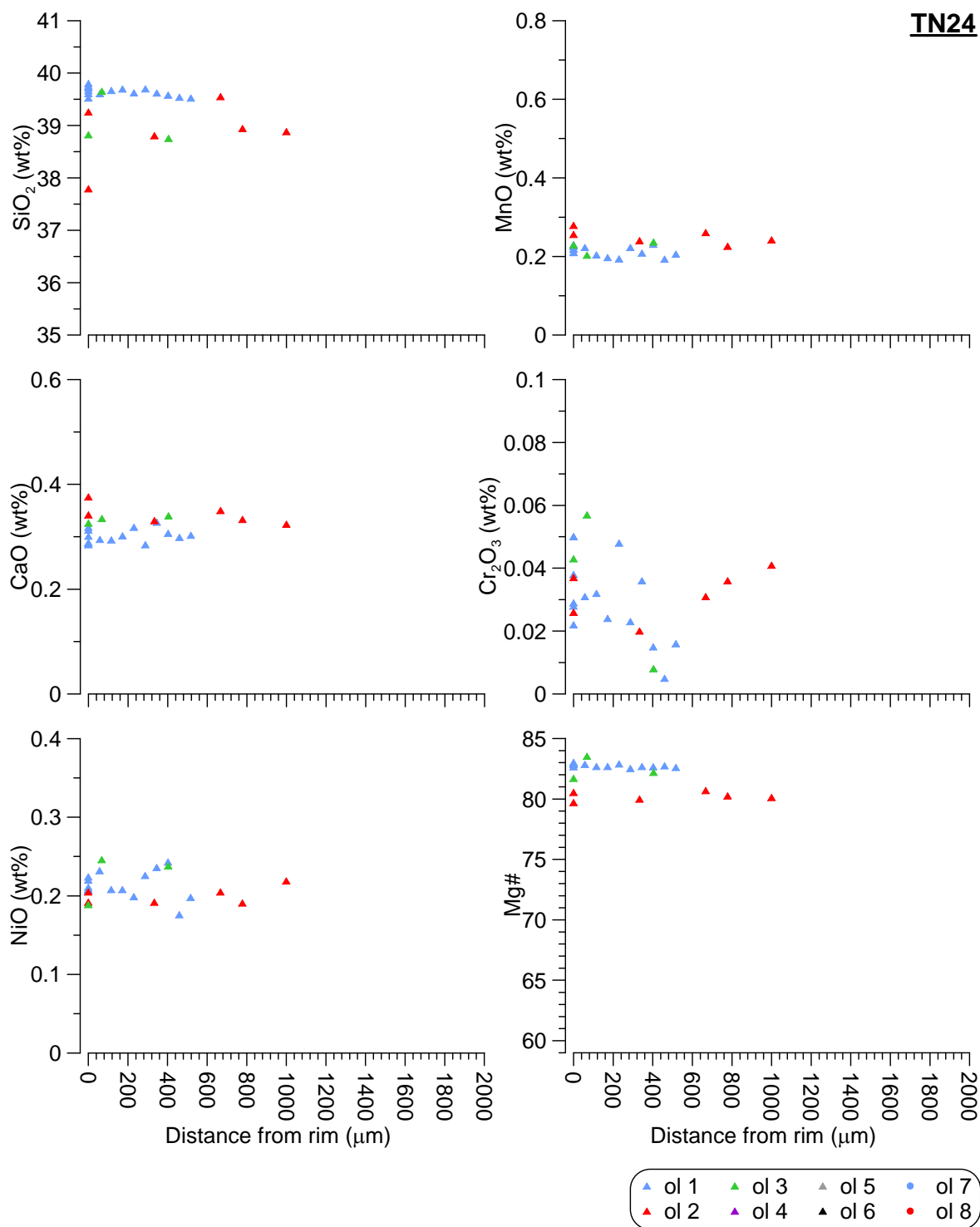






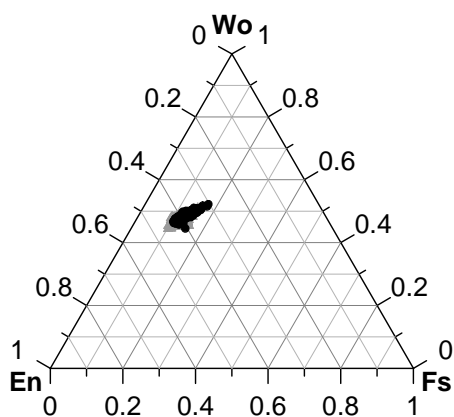
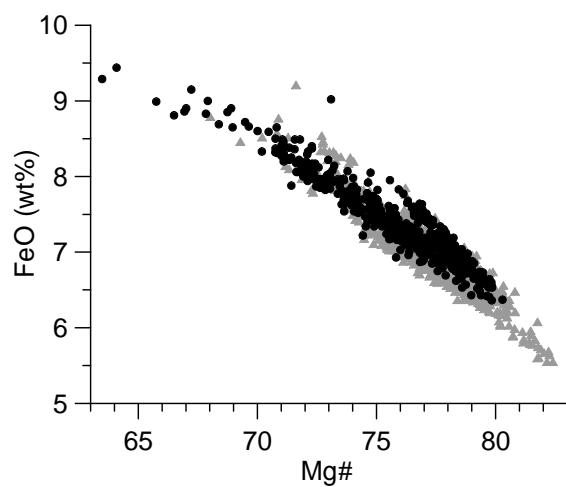
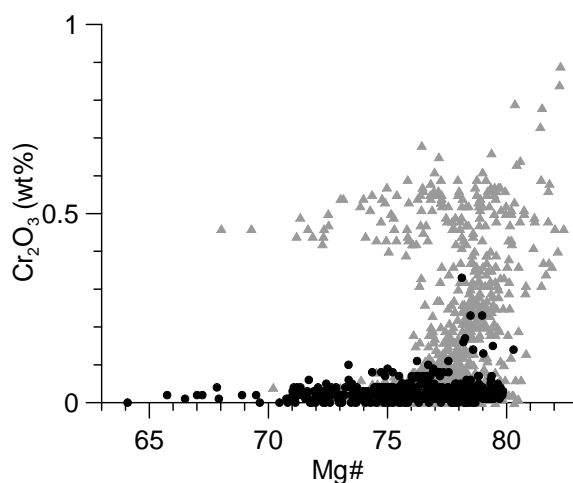
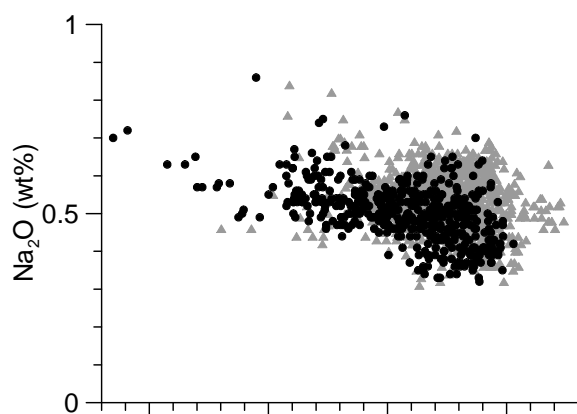
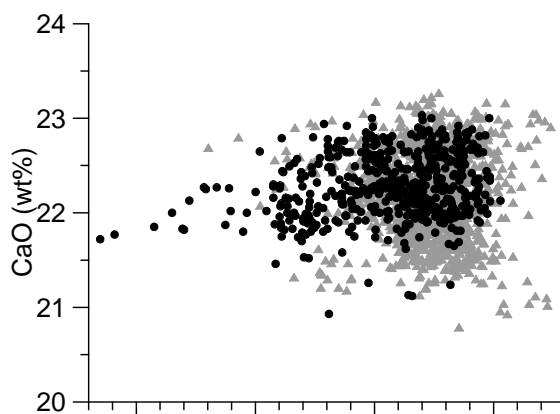
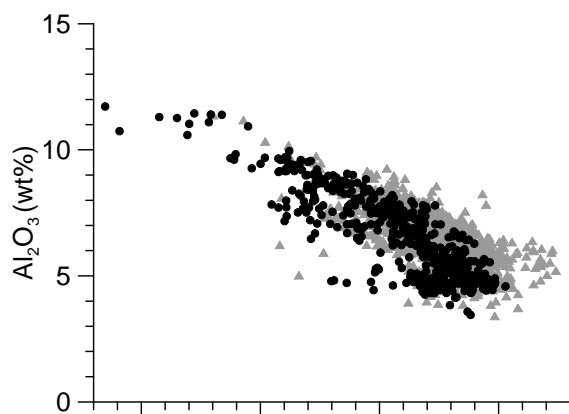
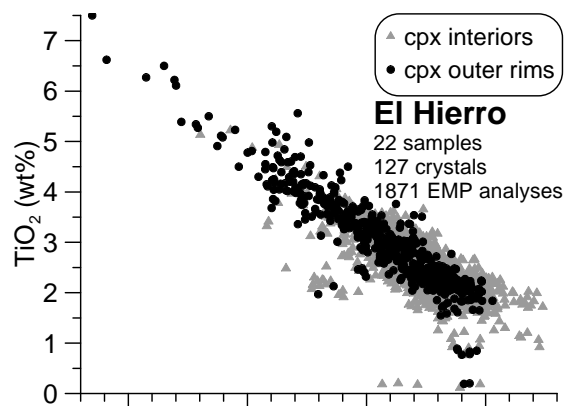
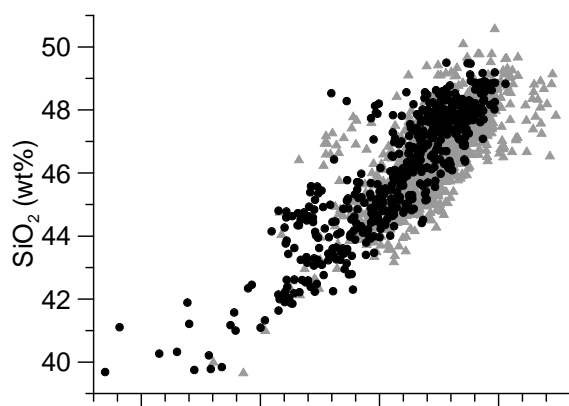


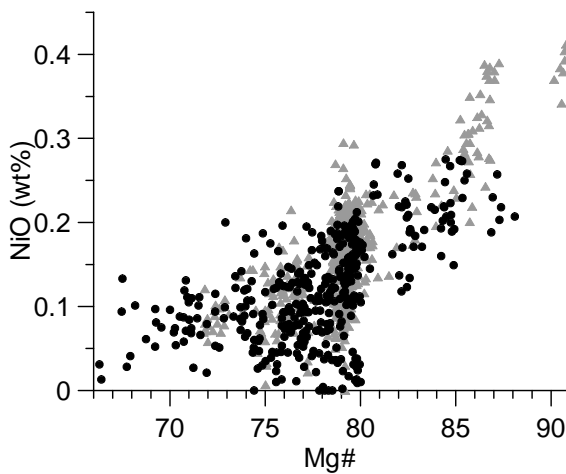
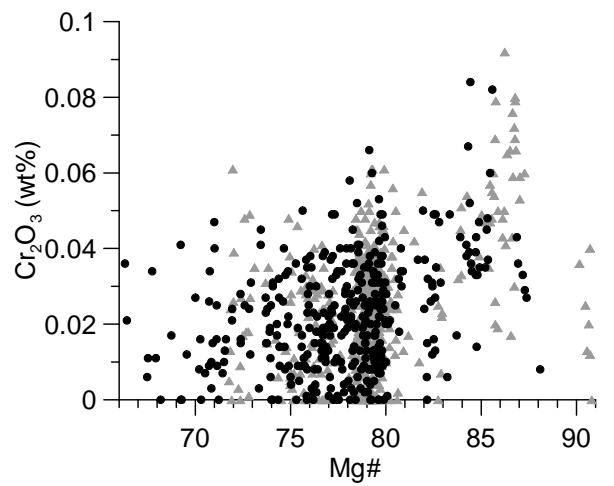
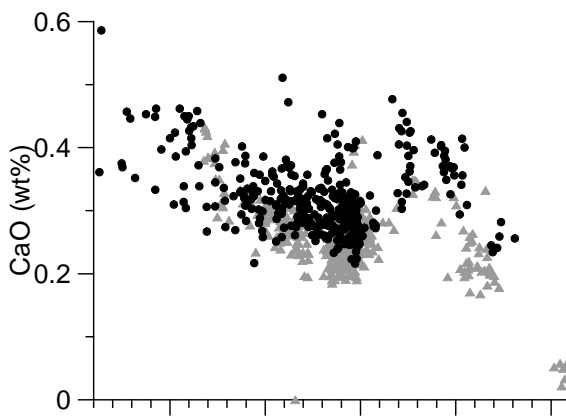
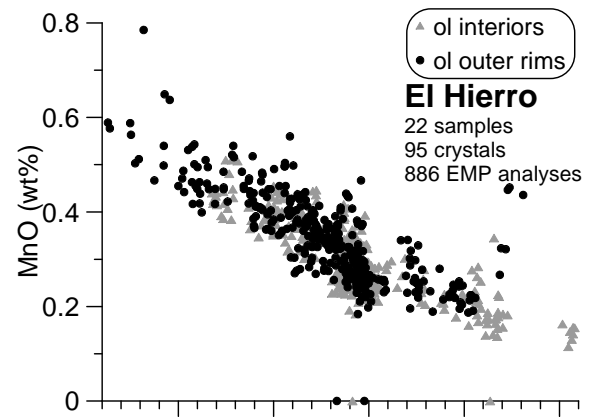
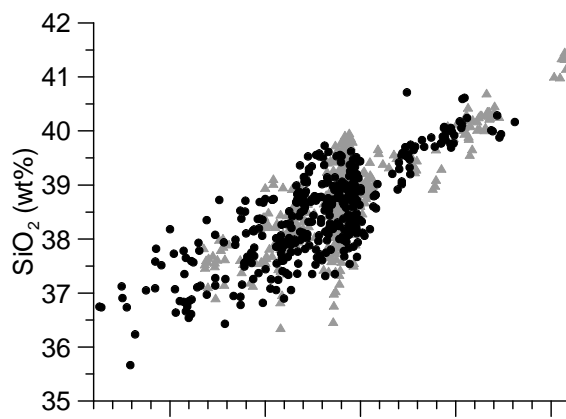




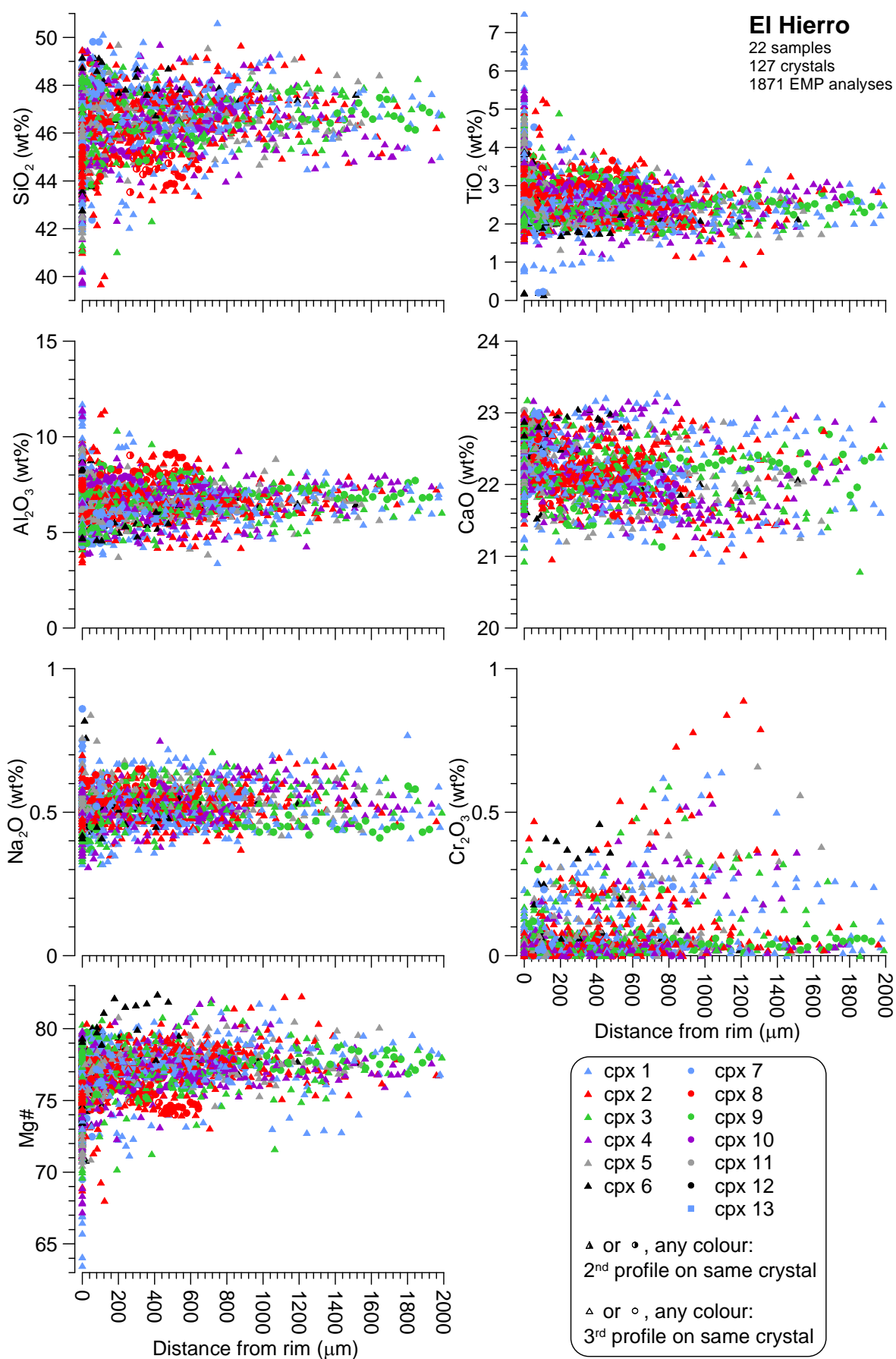
## **APPENDIX D: MINERAL CHEMISTRY PLOTS (EL HIERRO)**

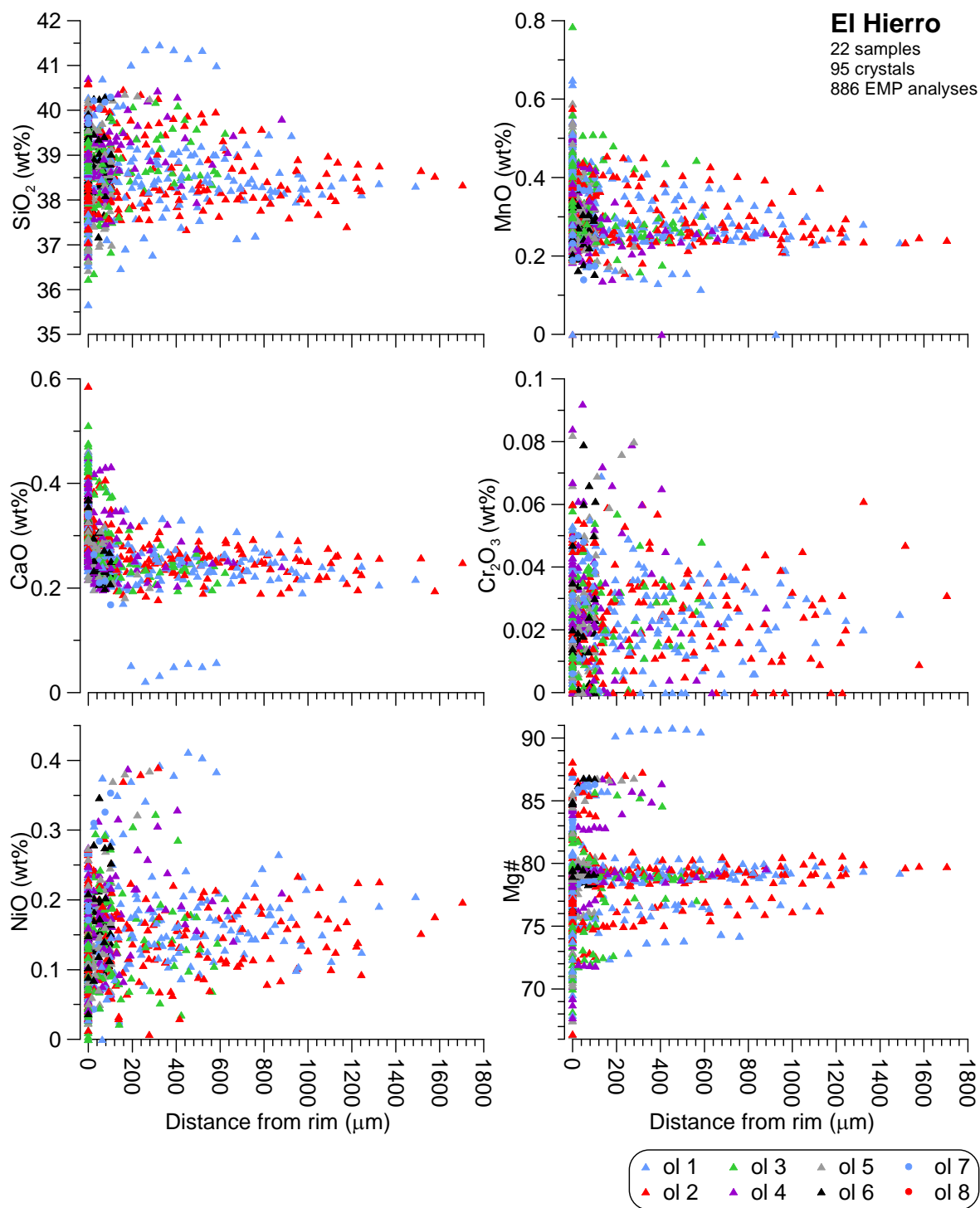
This appendix contains plots of mineral chemistry data for El Hierro Island. The composition of clinopyroxene and olivine crystals in major element oxides is first shown as a function of Mg#, then as a function of distance from the crystal rim, for the whole dataset. Data for single samples (sample number indicated in top-right corner) are then plotted against distance from the crystal rim. Colour codes refer to different crystals, as explained in the key. Some clinopyroxene crystals have been analysed on more than one profile; these generally correspond to sector-zoned crystals.



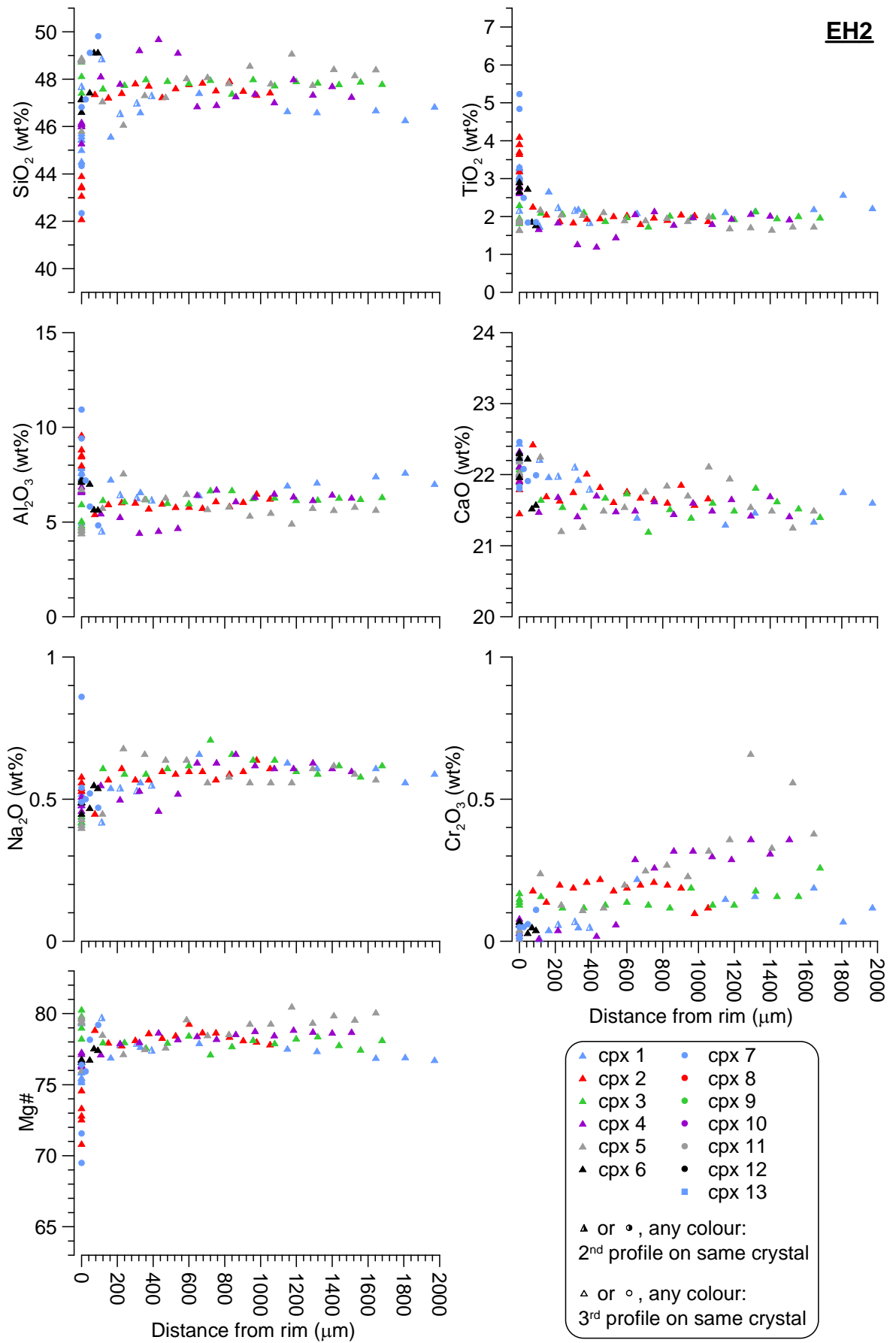




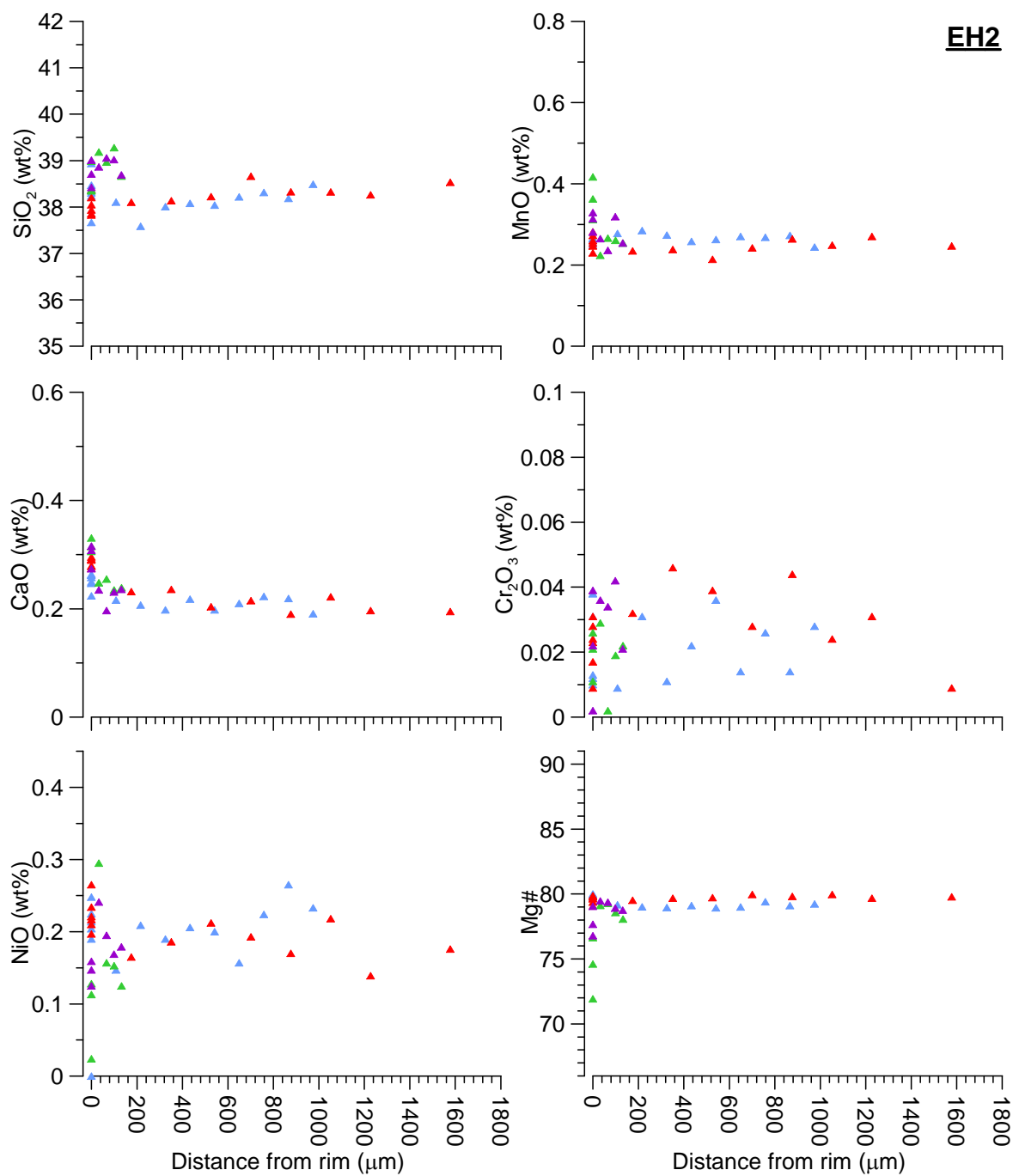




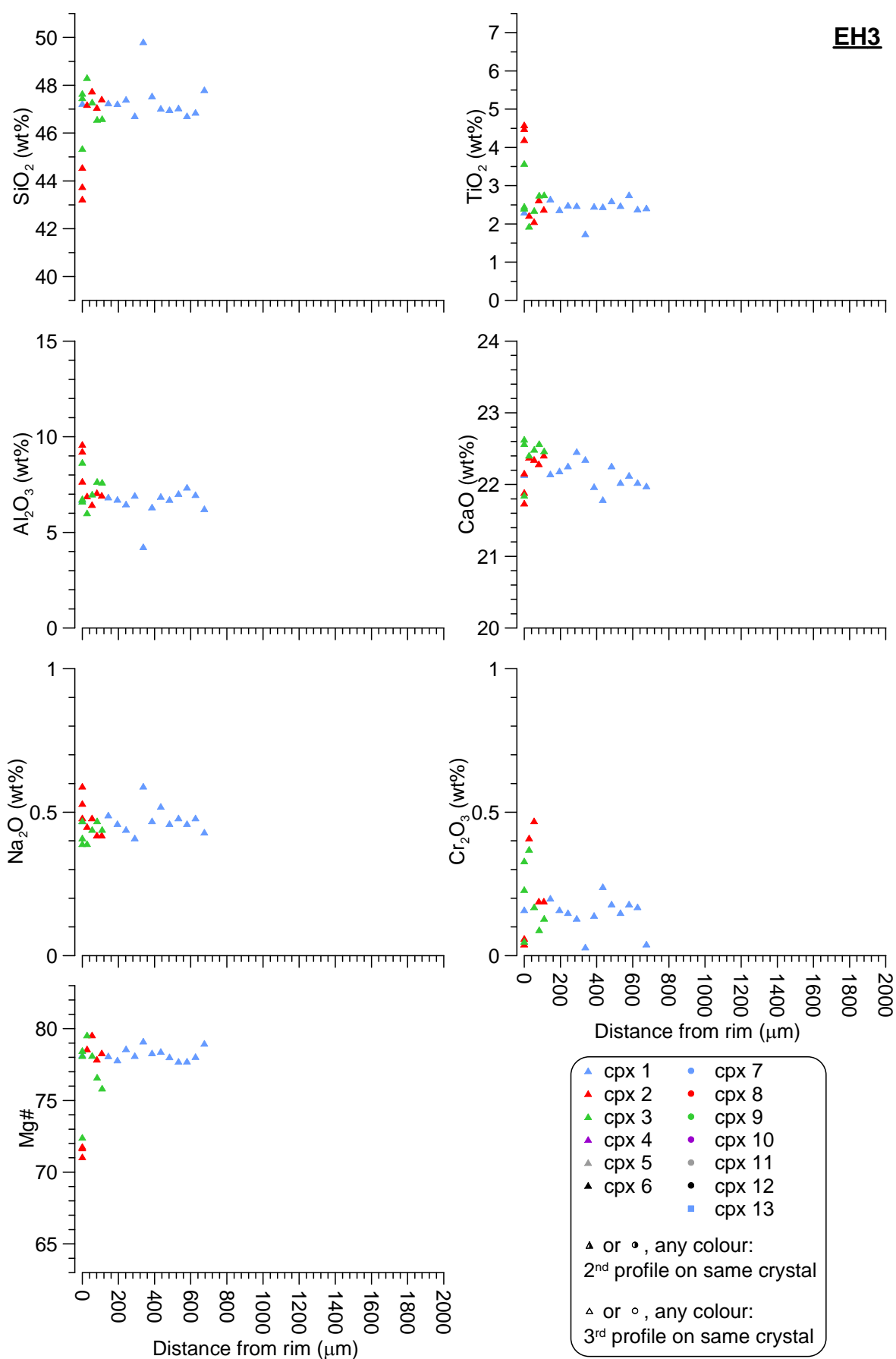
**EH2**



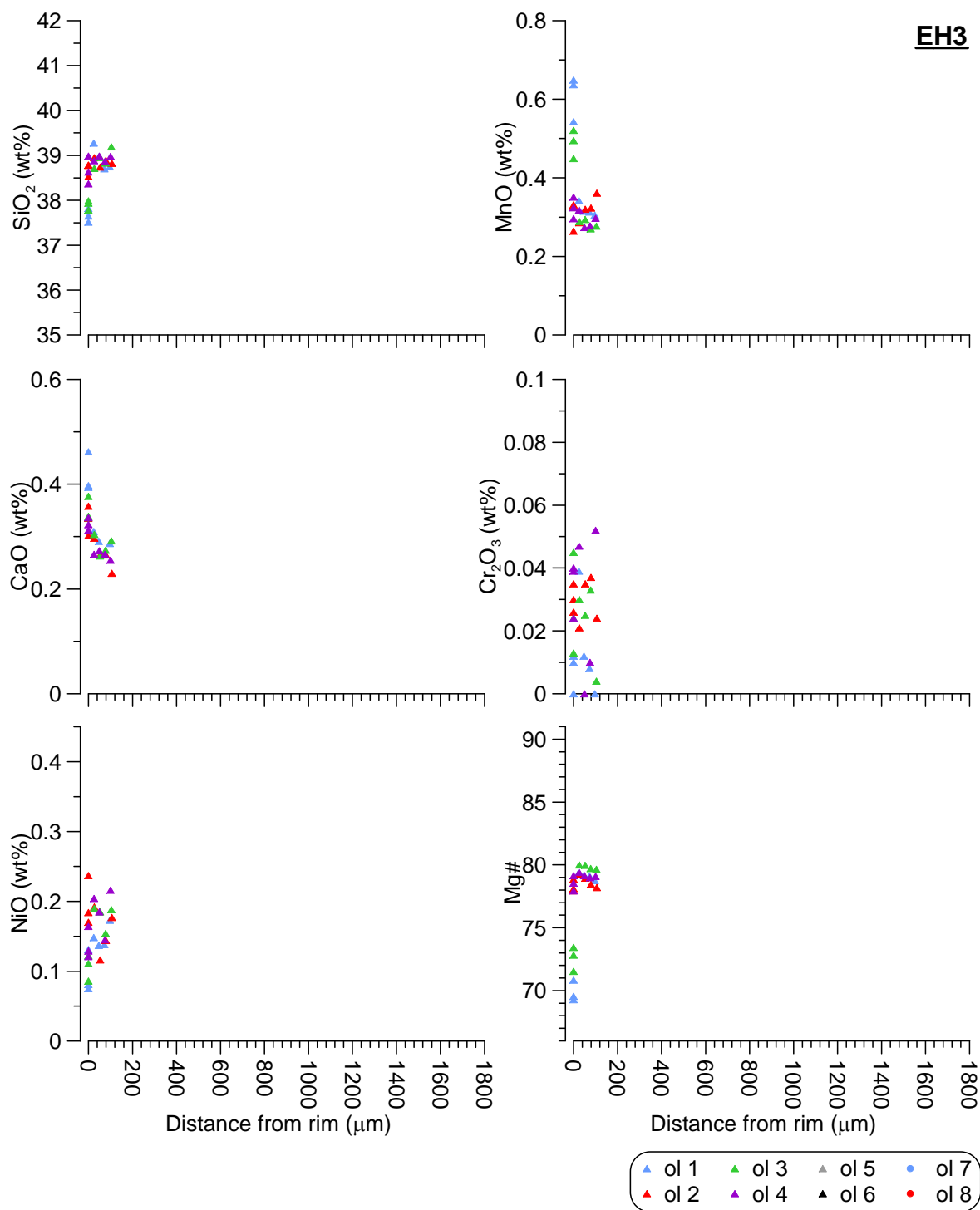
**EH2**



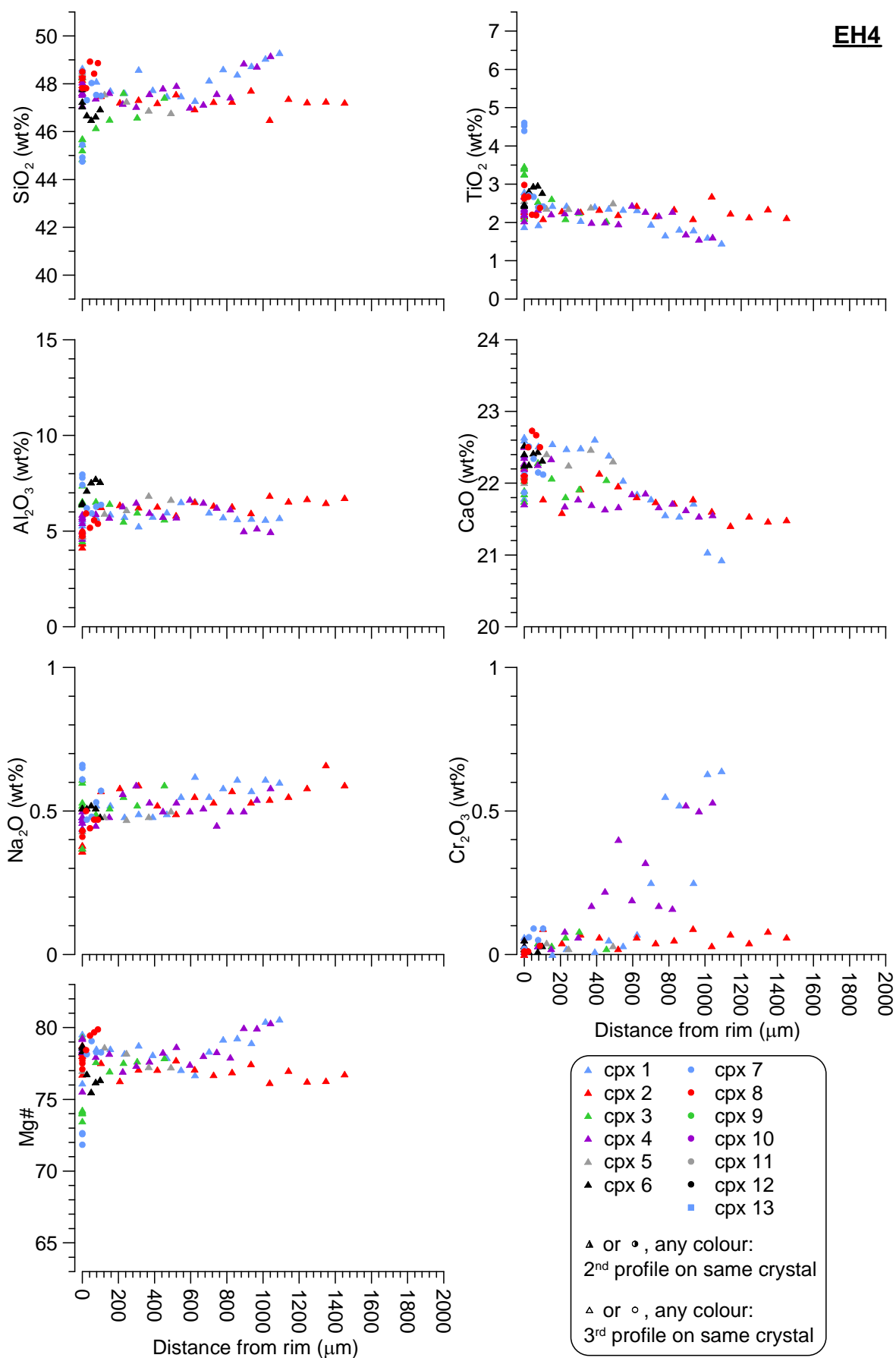
**EH3**



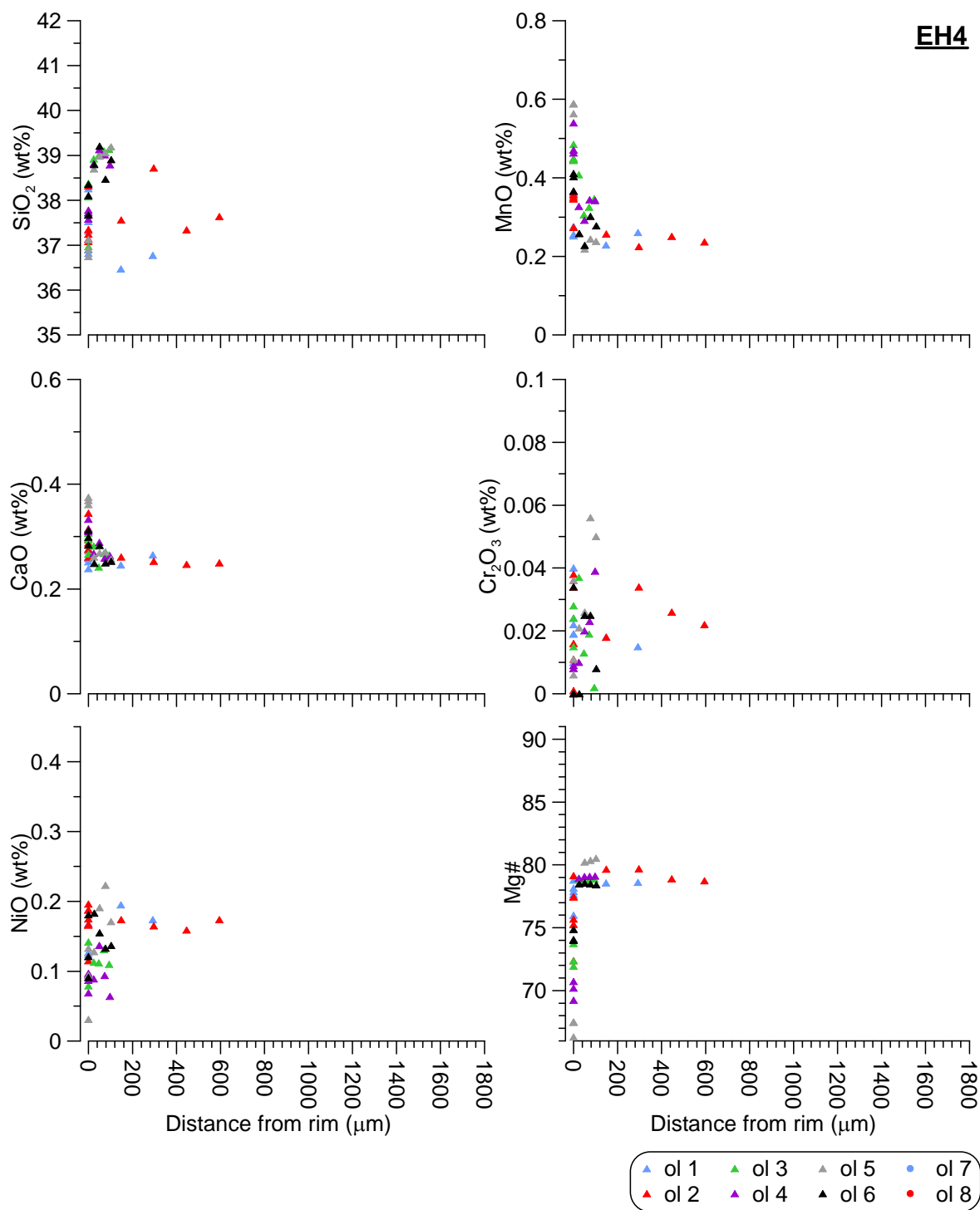
**EH3**



**EH4**

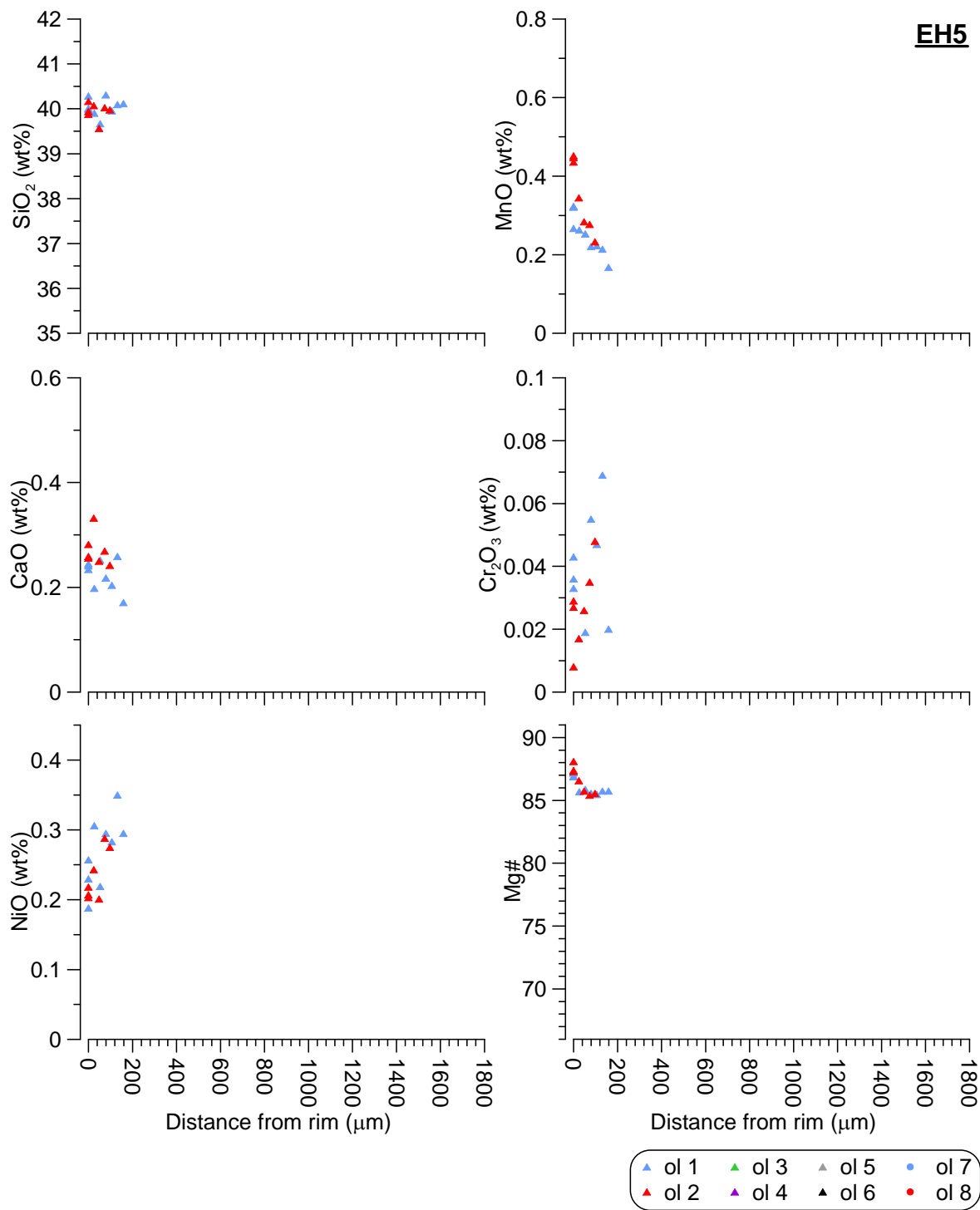


**EH4**

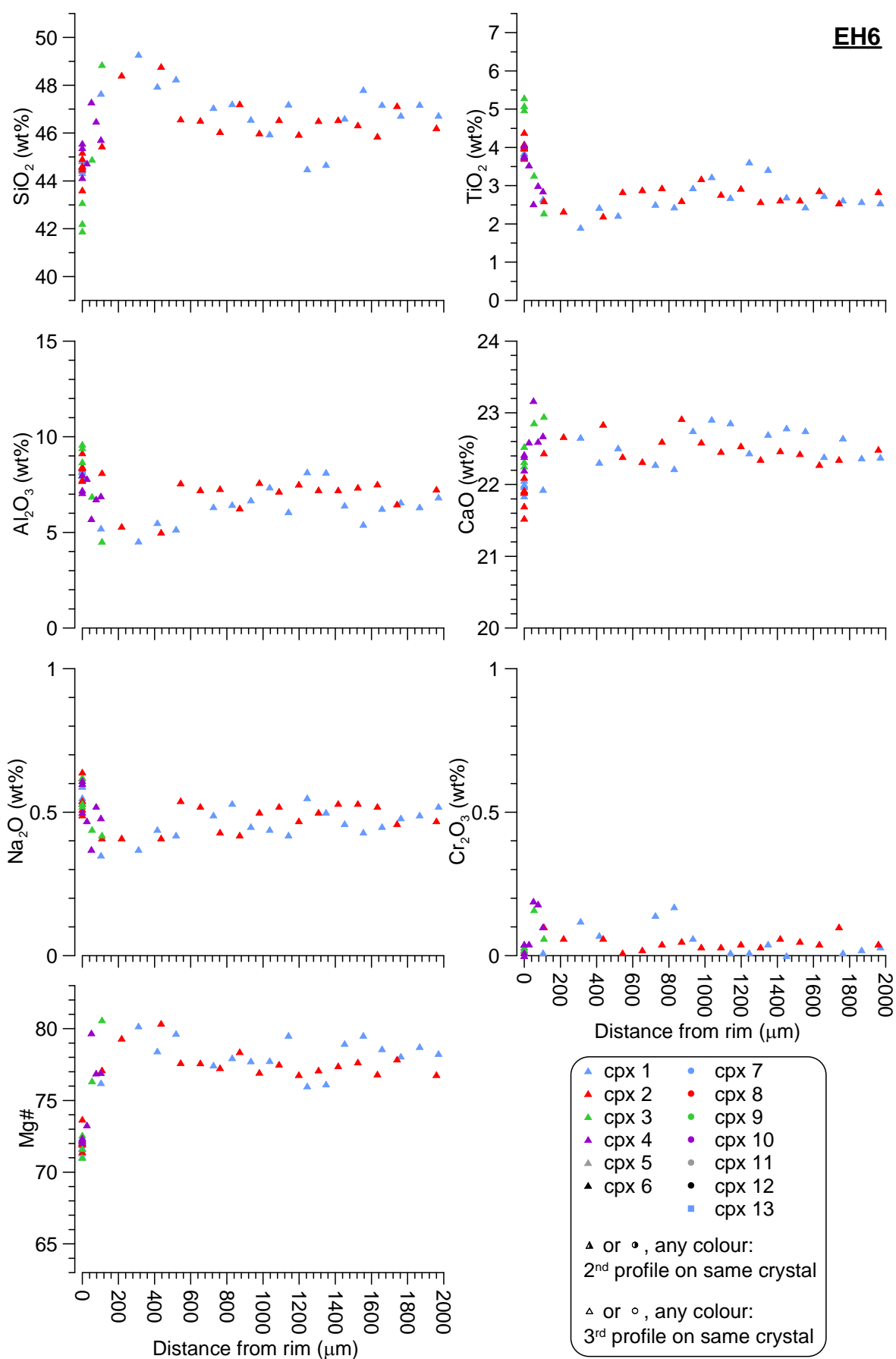




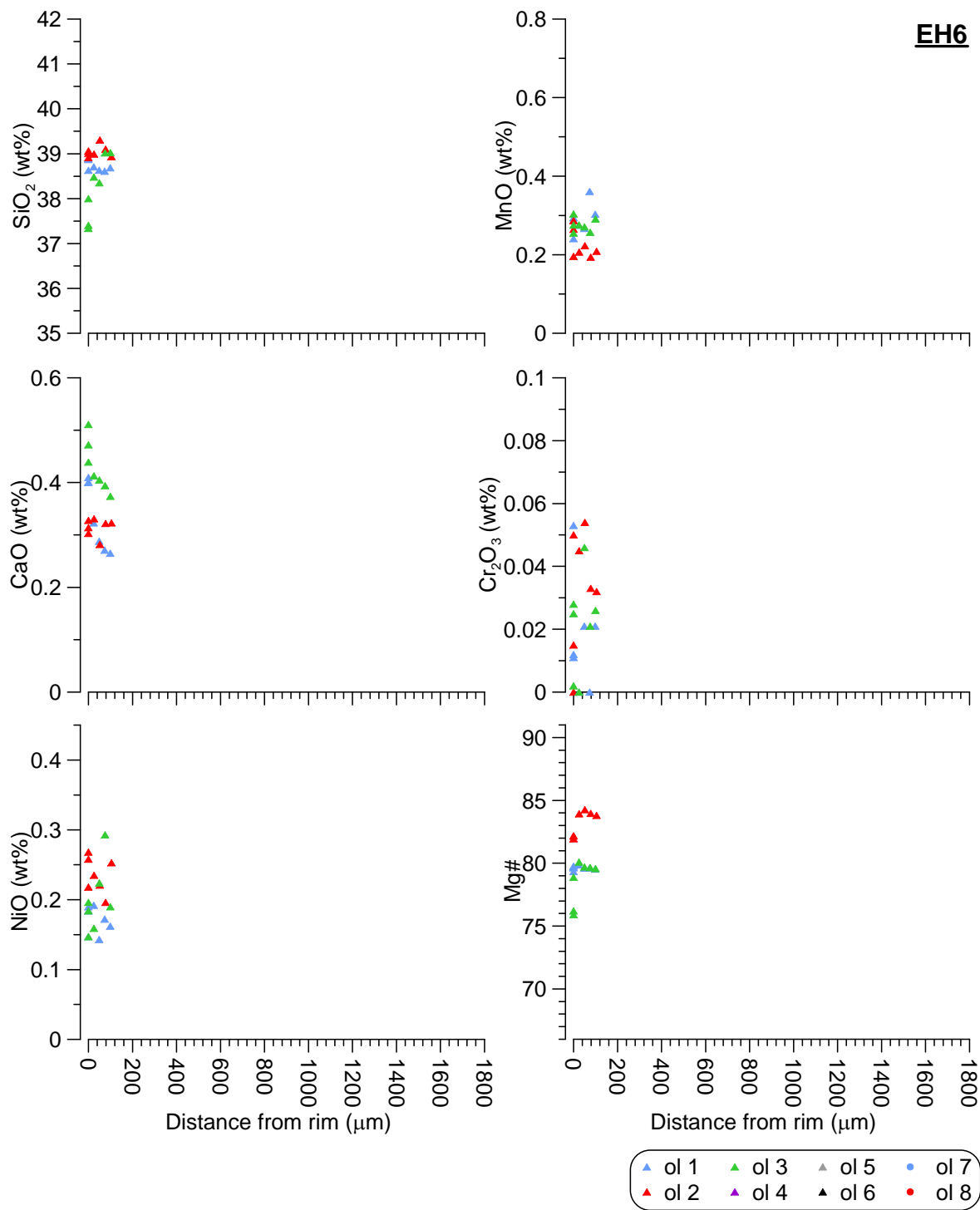
**EH5**



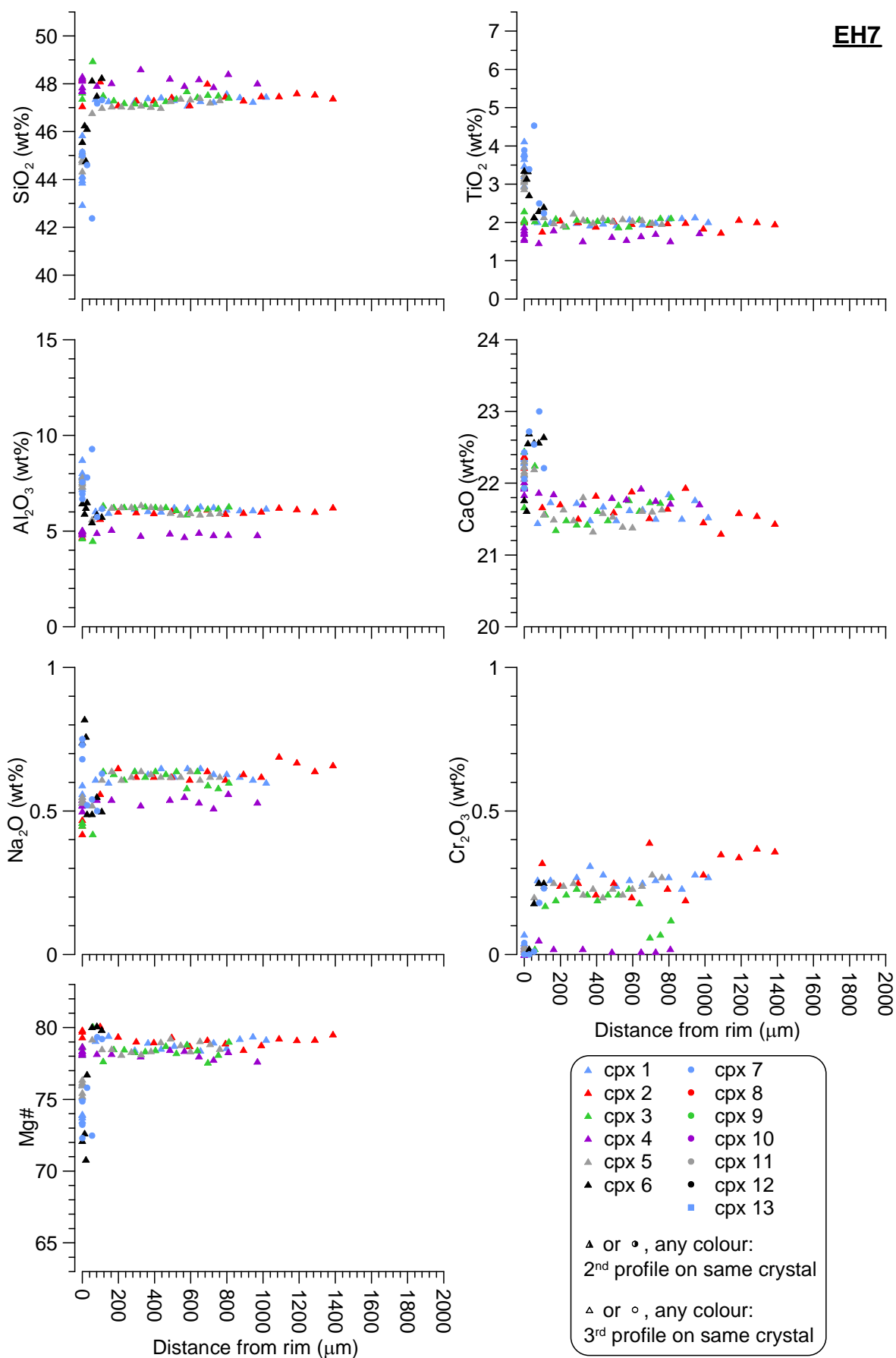
**EH6**



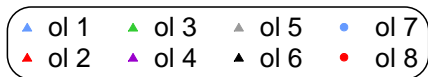
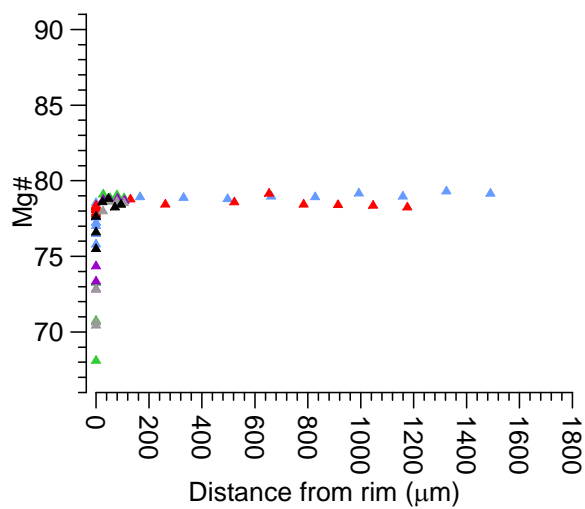
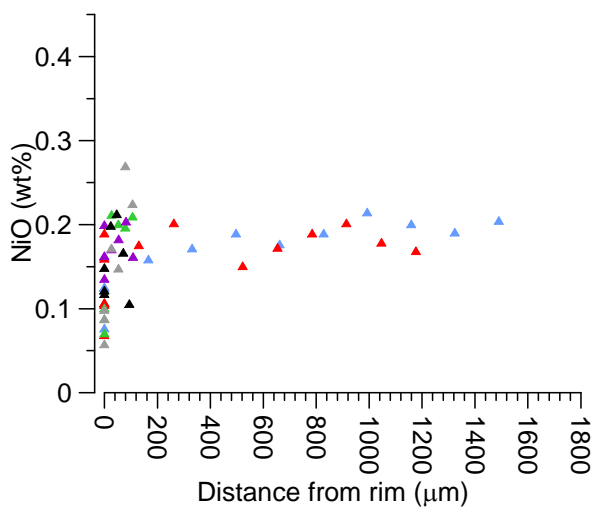
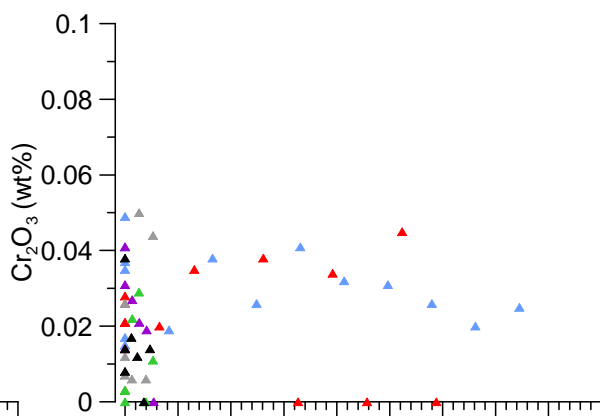
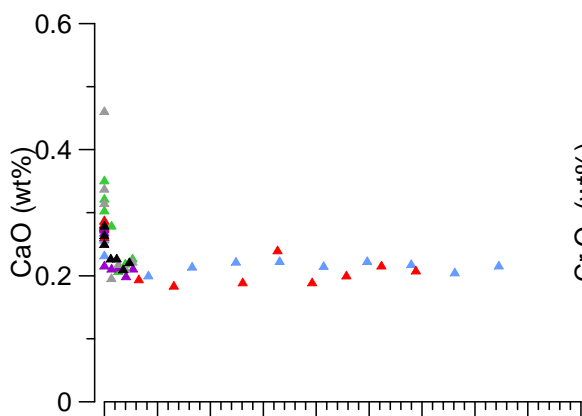
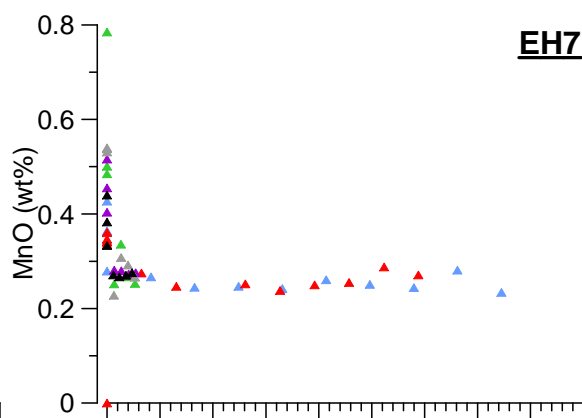
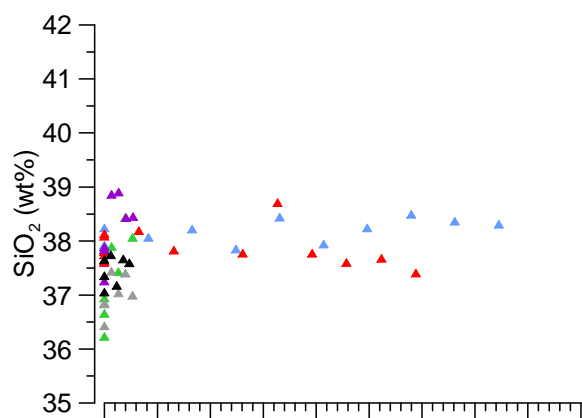
**EH6**



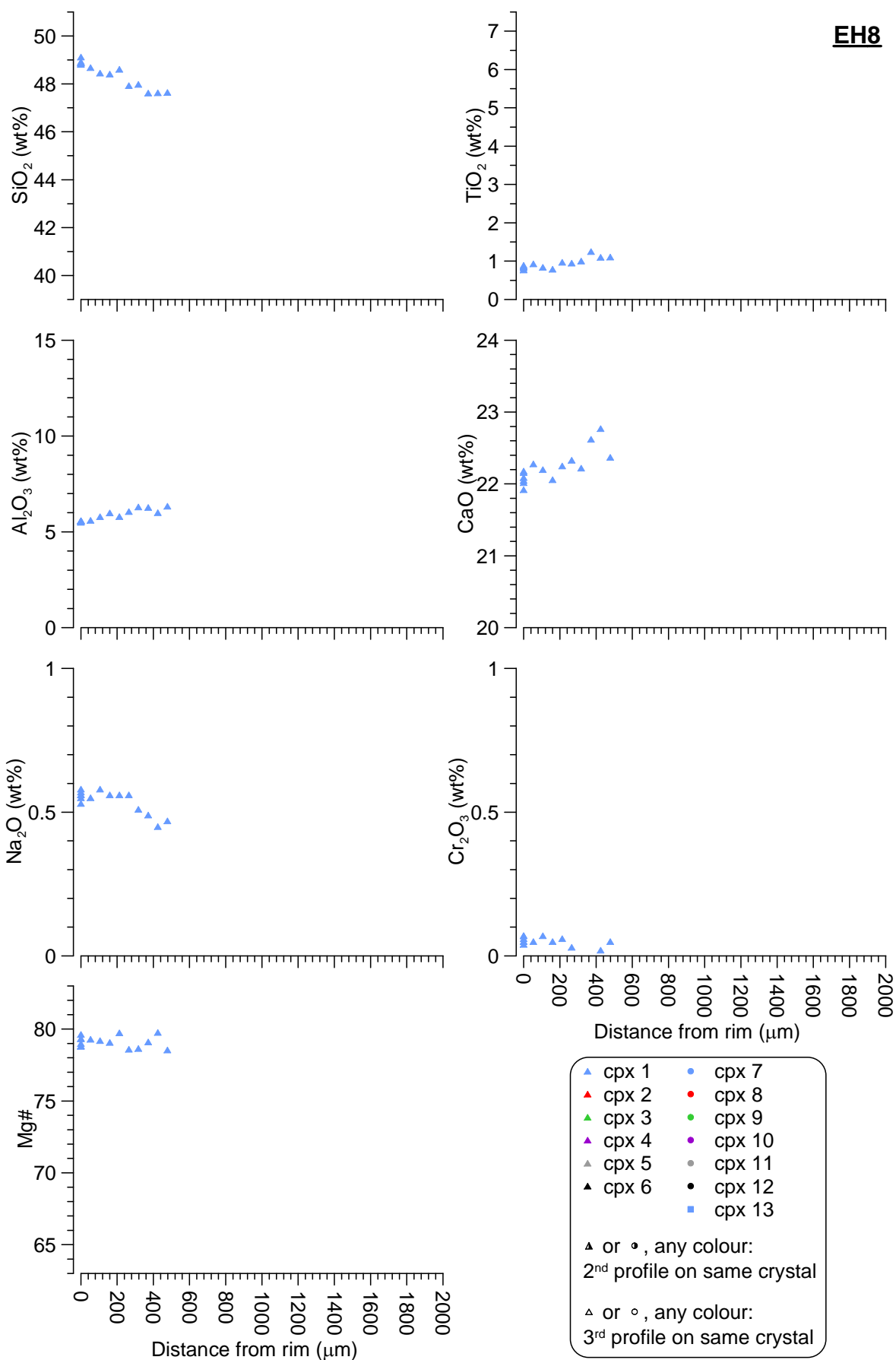
**EH7**



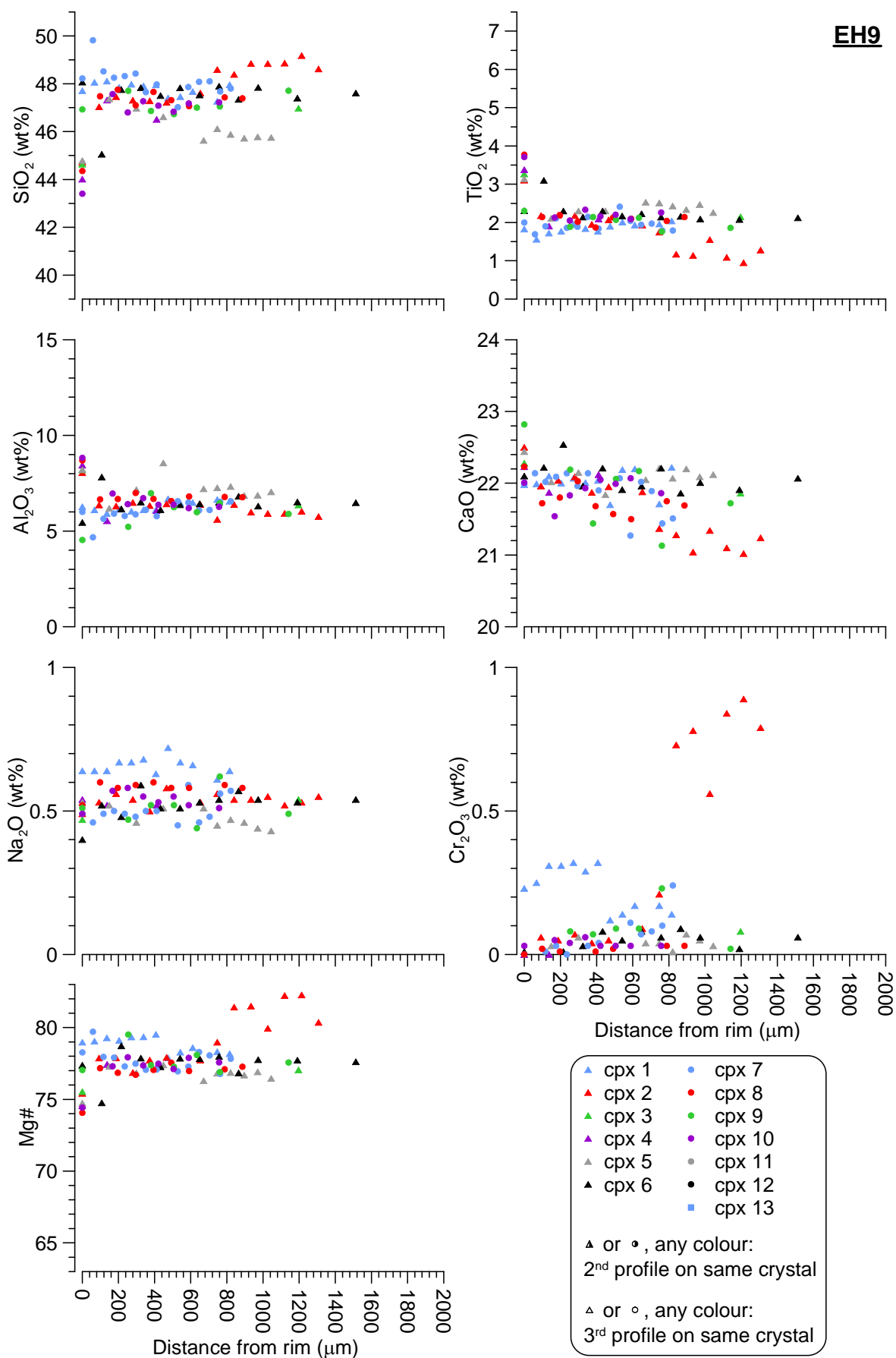
**EH7**



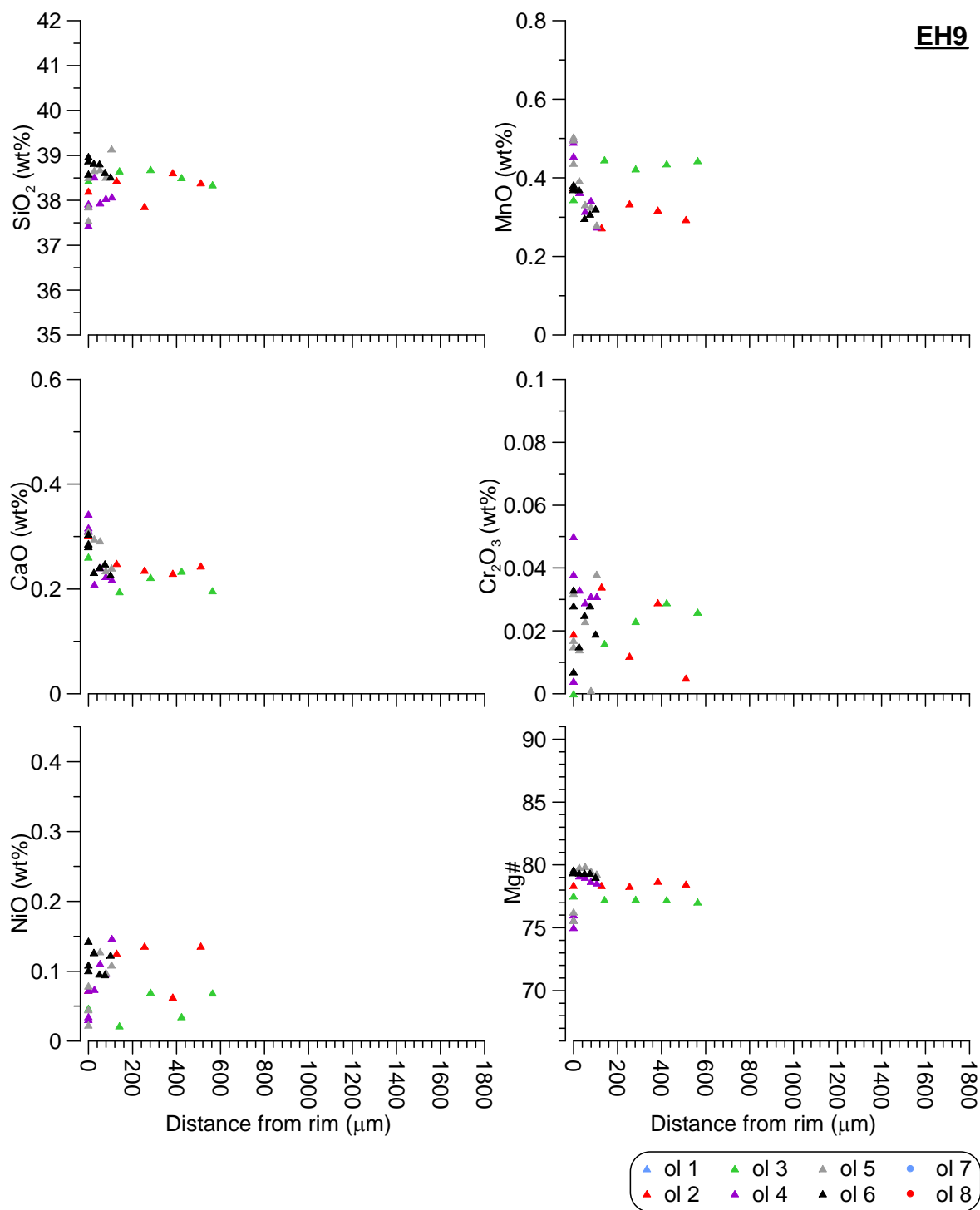
**EH8**



**EH9**

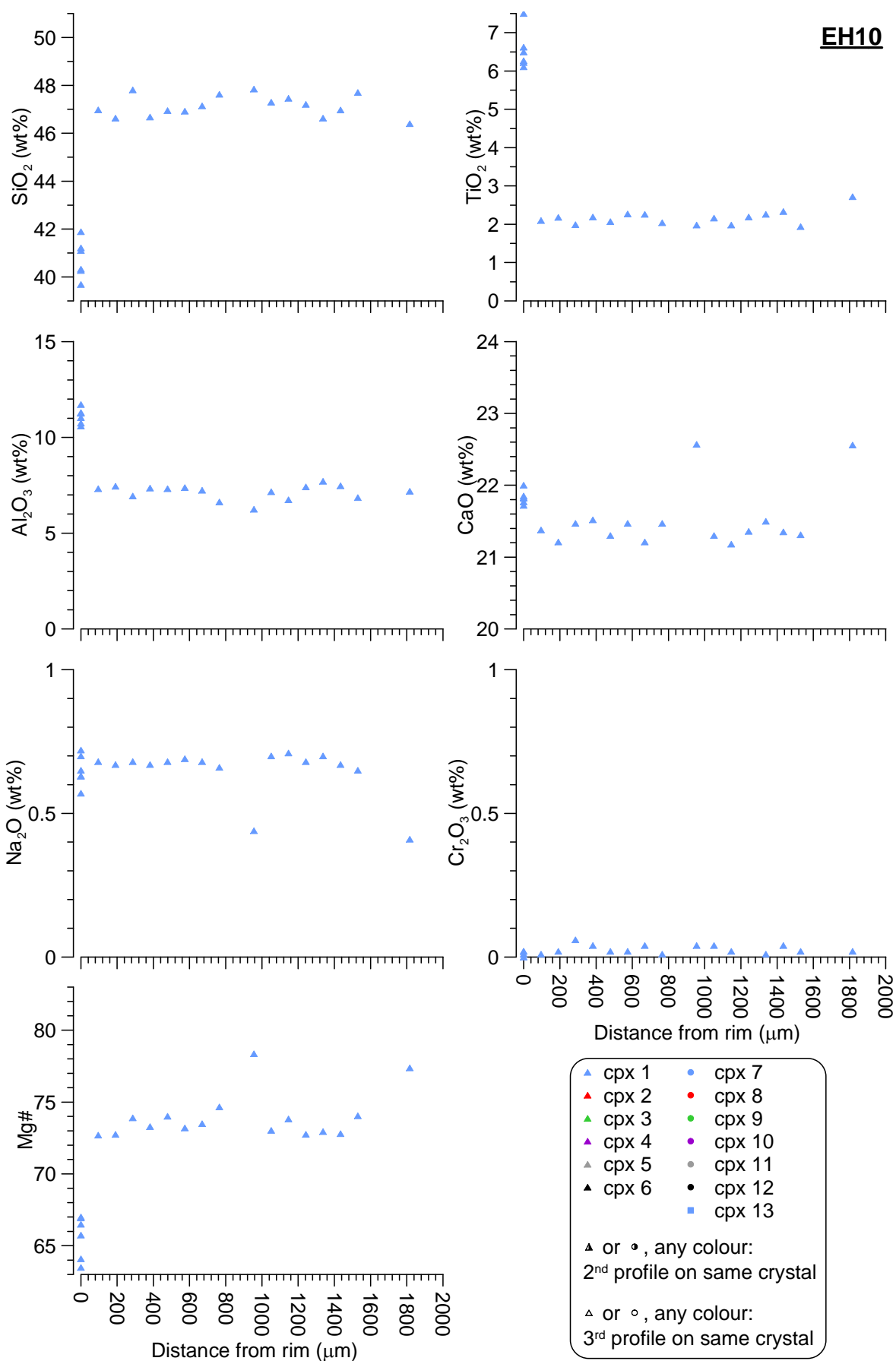


**EH9**

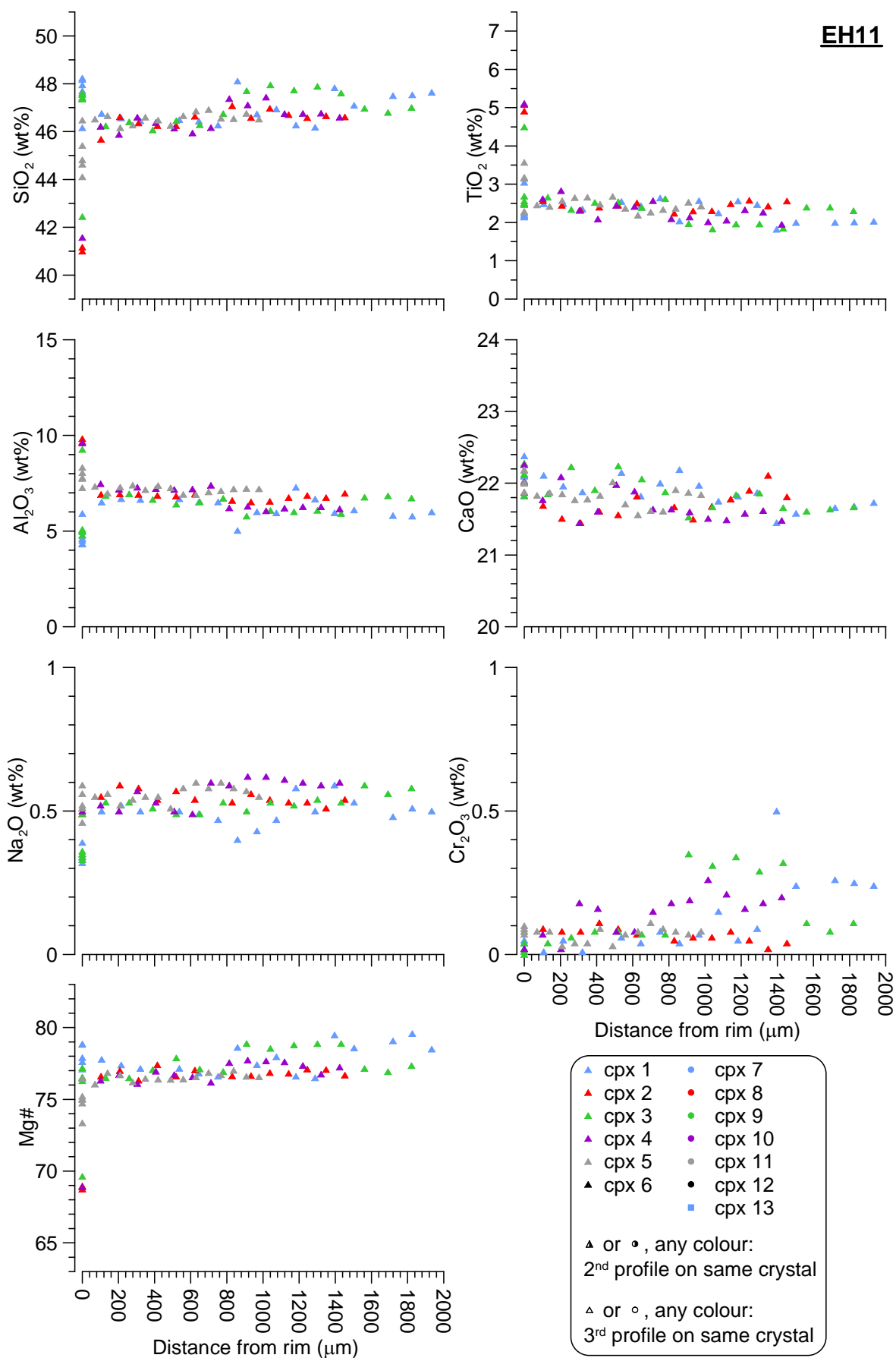




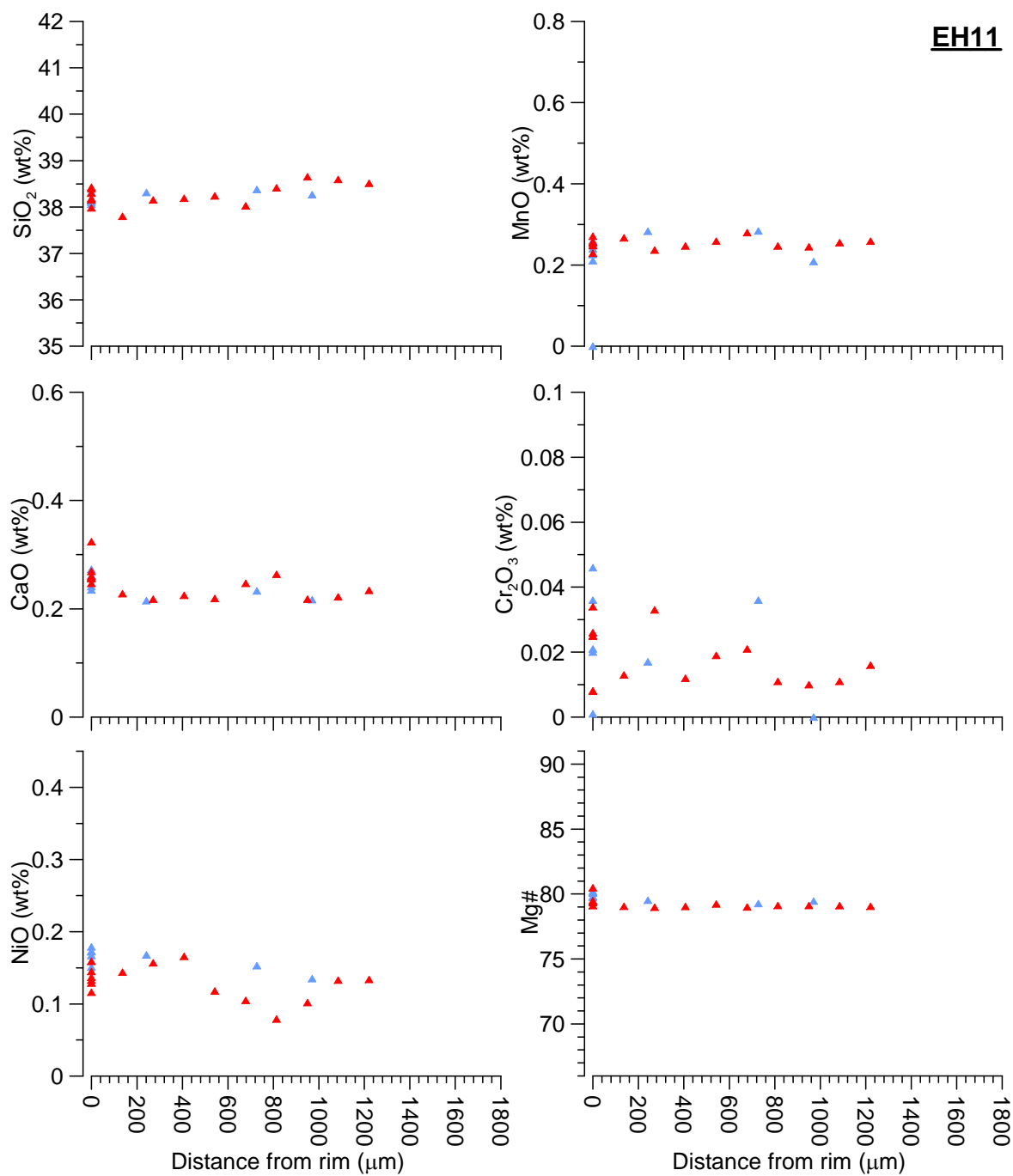
**EH10**

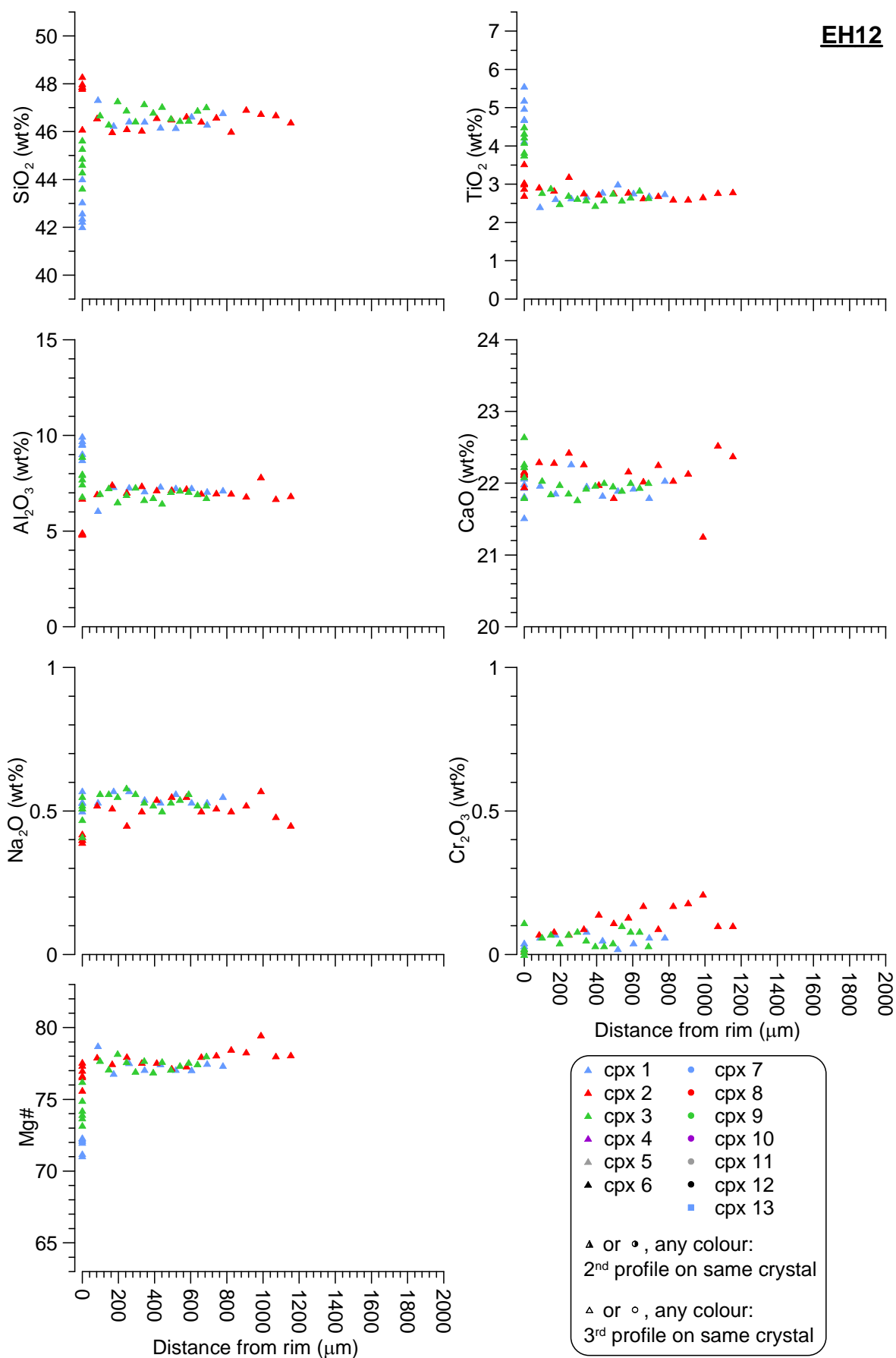


**EH11**

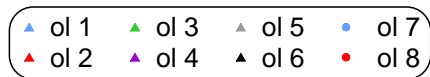
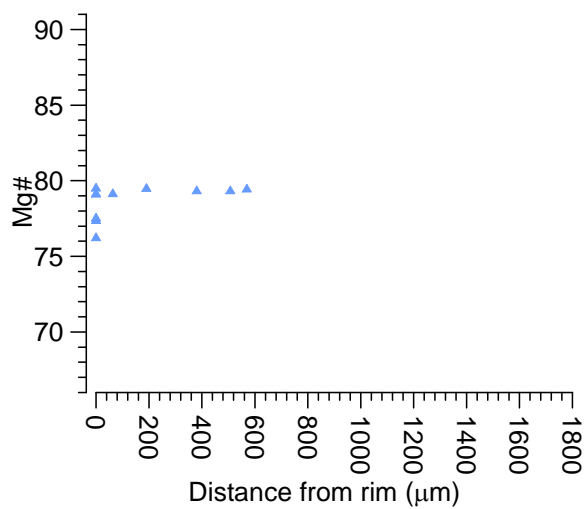
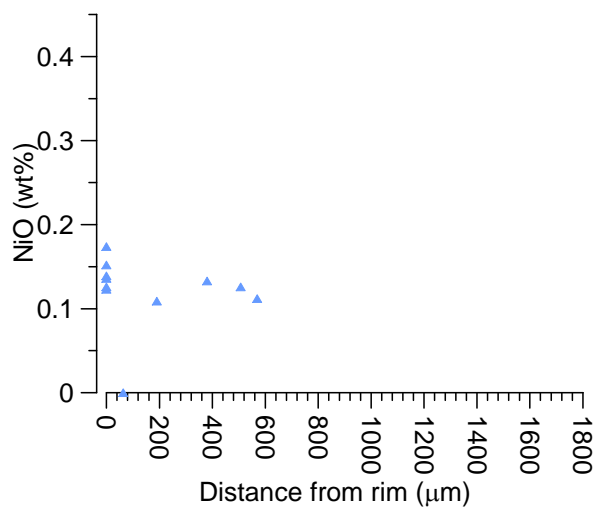
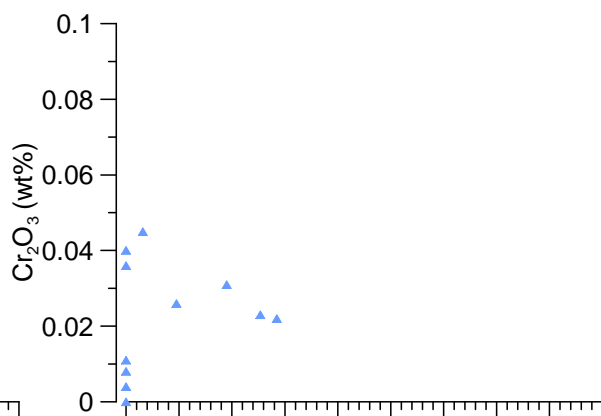
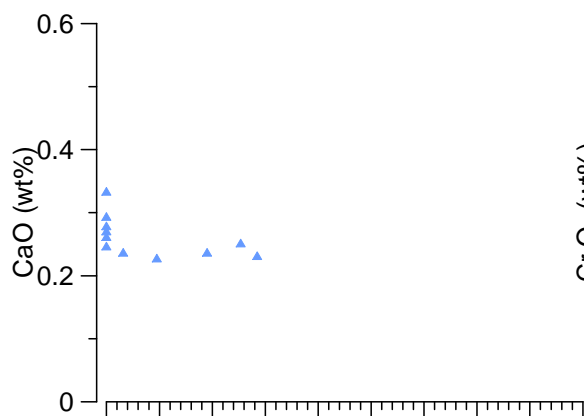
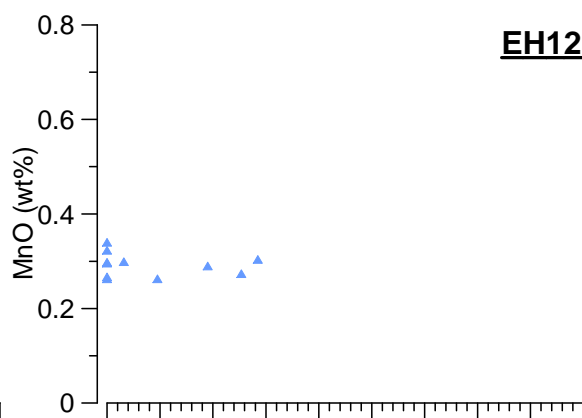
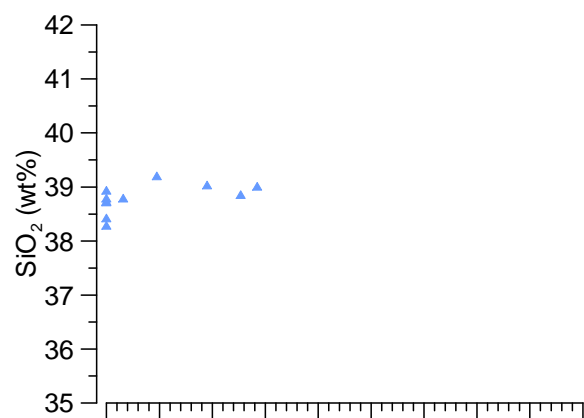


**EH11**

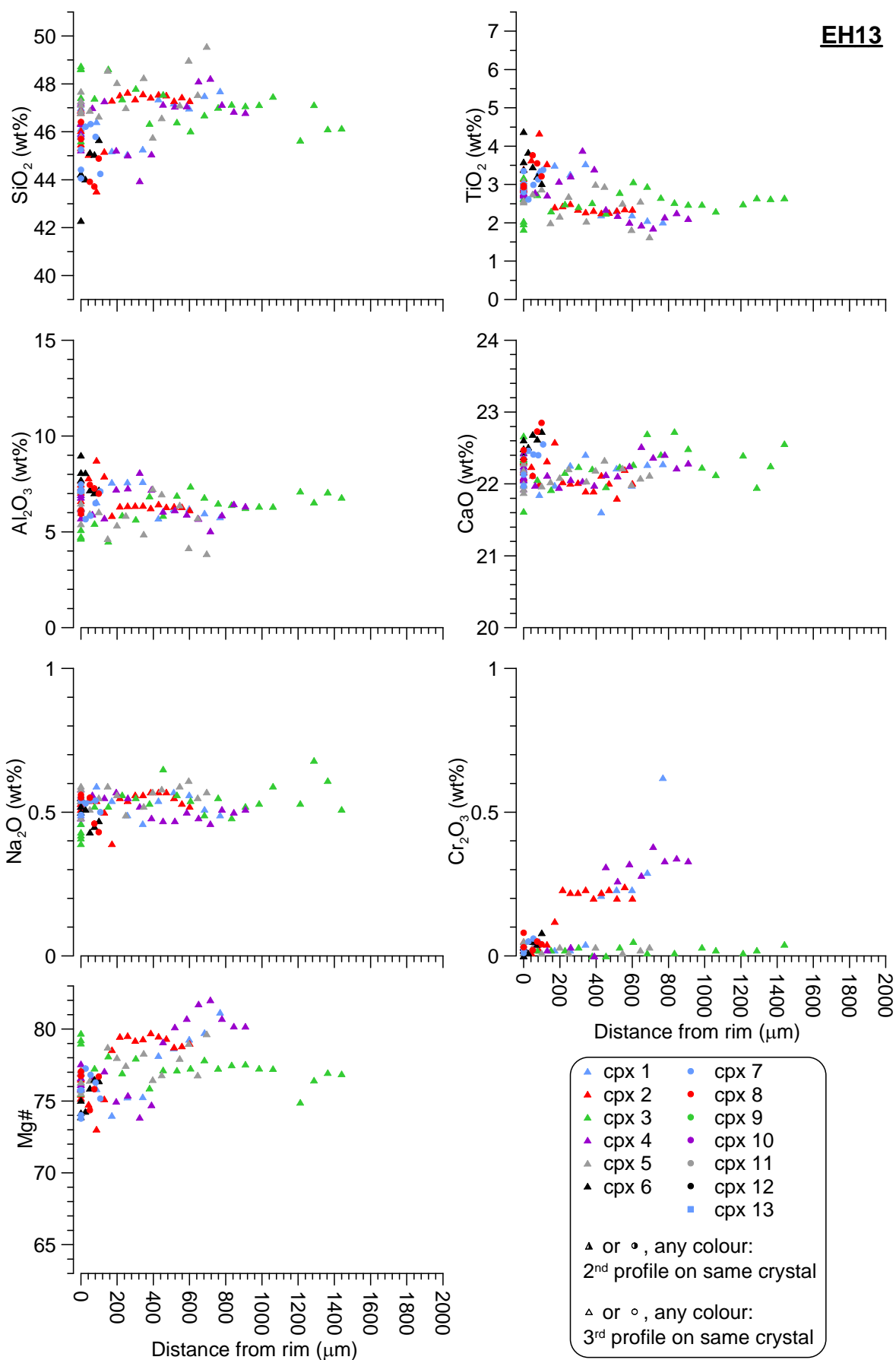


**EH12**

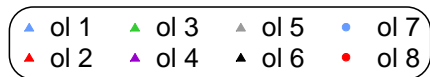
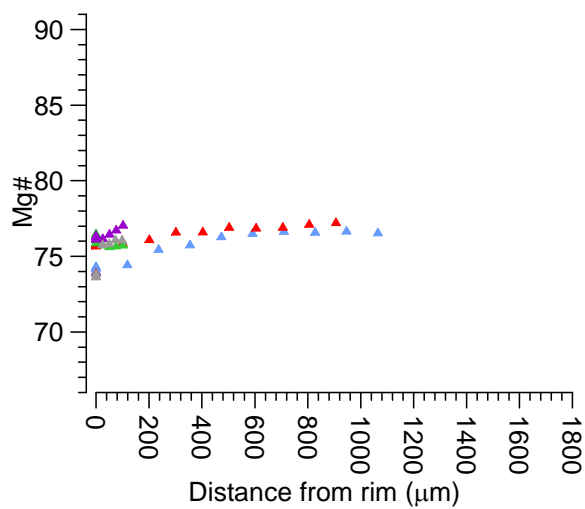
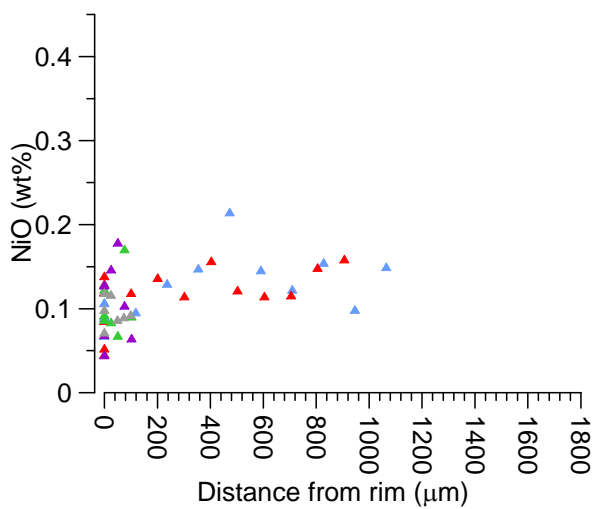
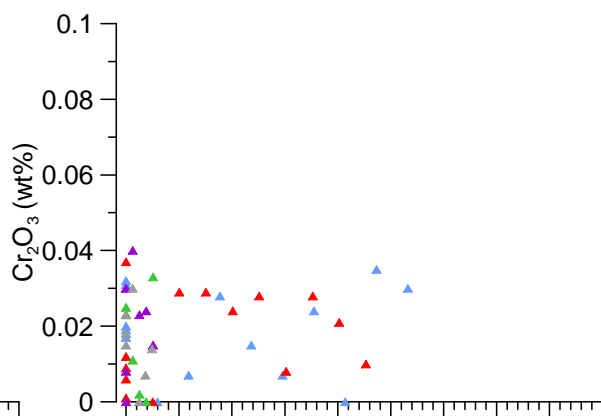
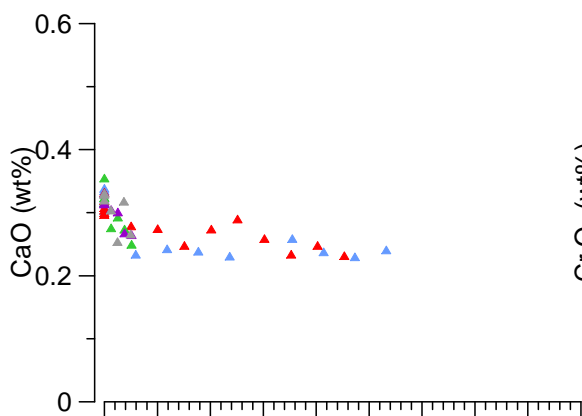
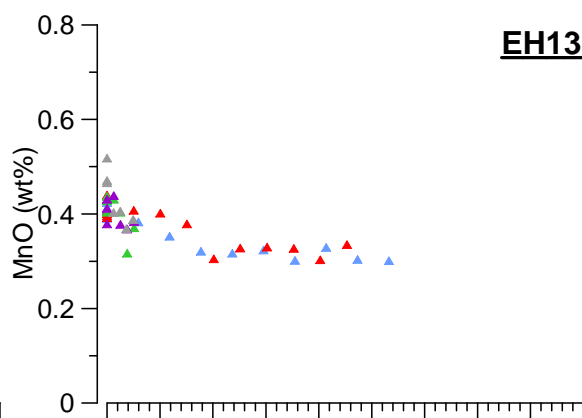
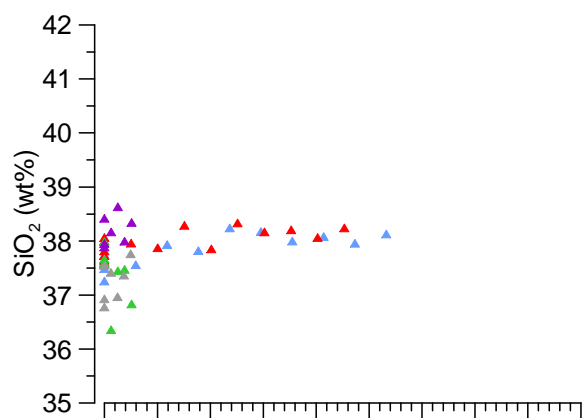
**EH12**



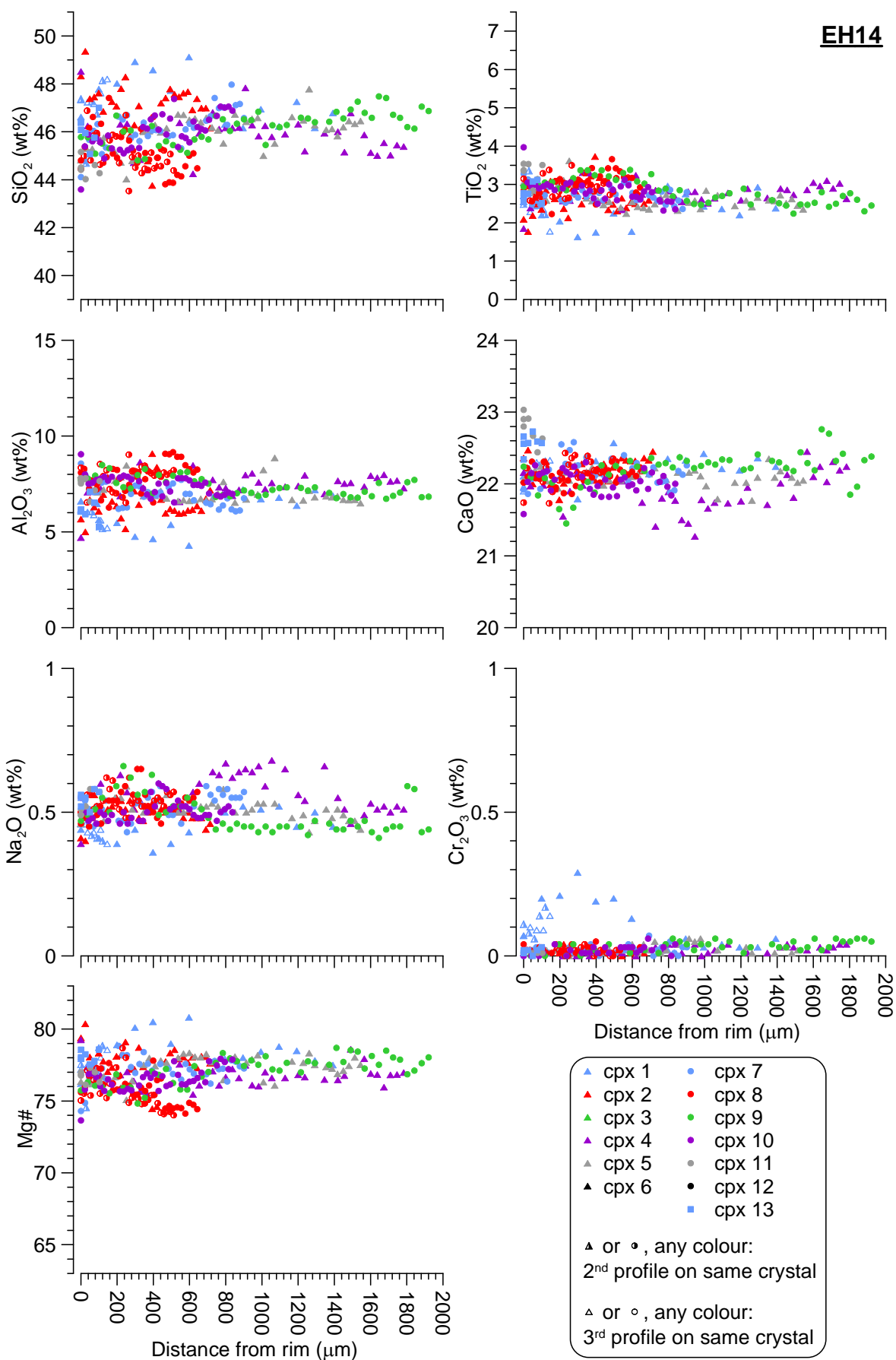
**EH13**



**EH13**

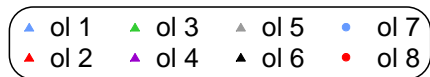
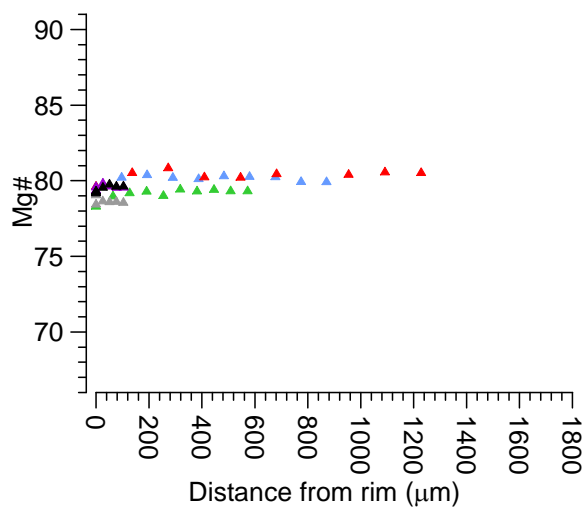
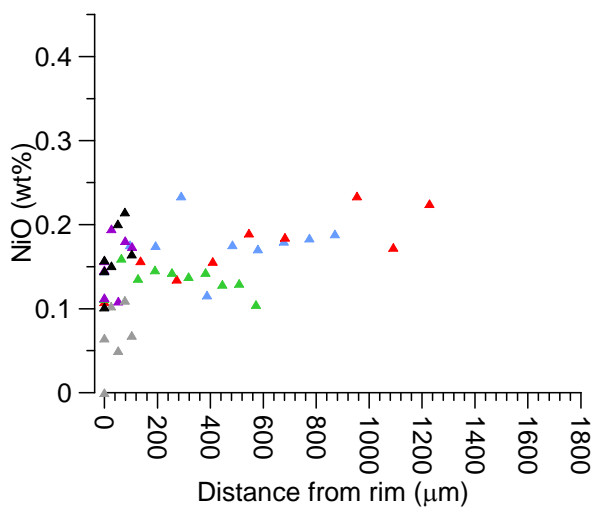
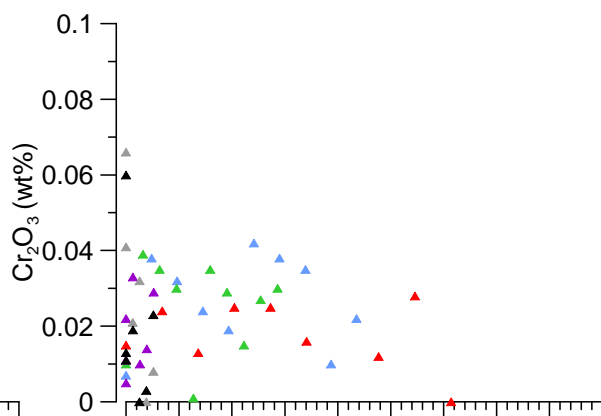
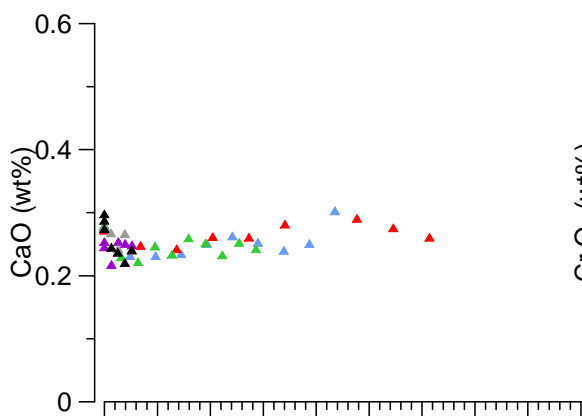
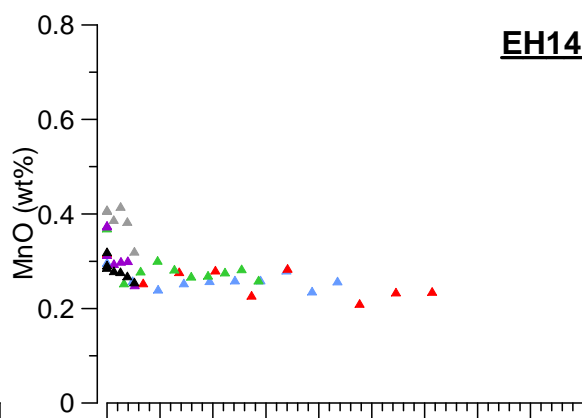
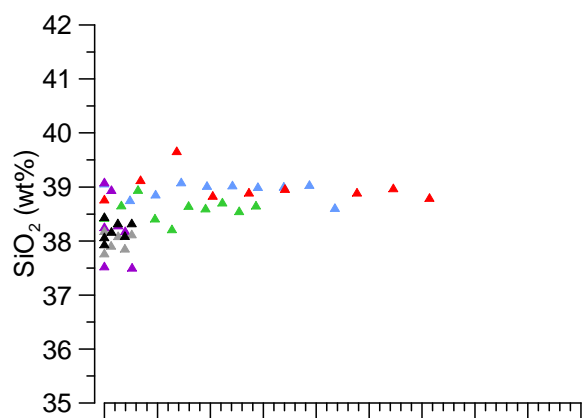


**EH14**

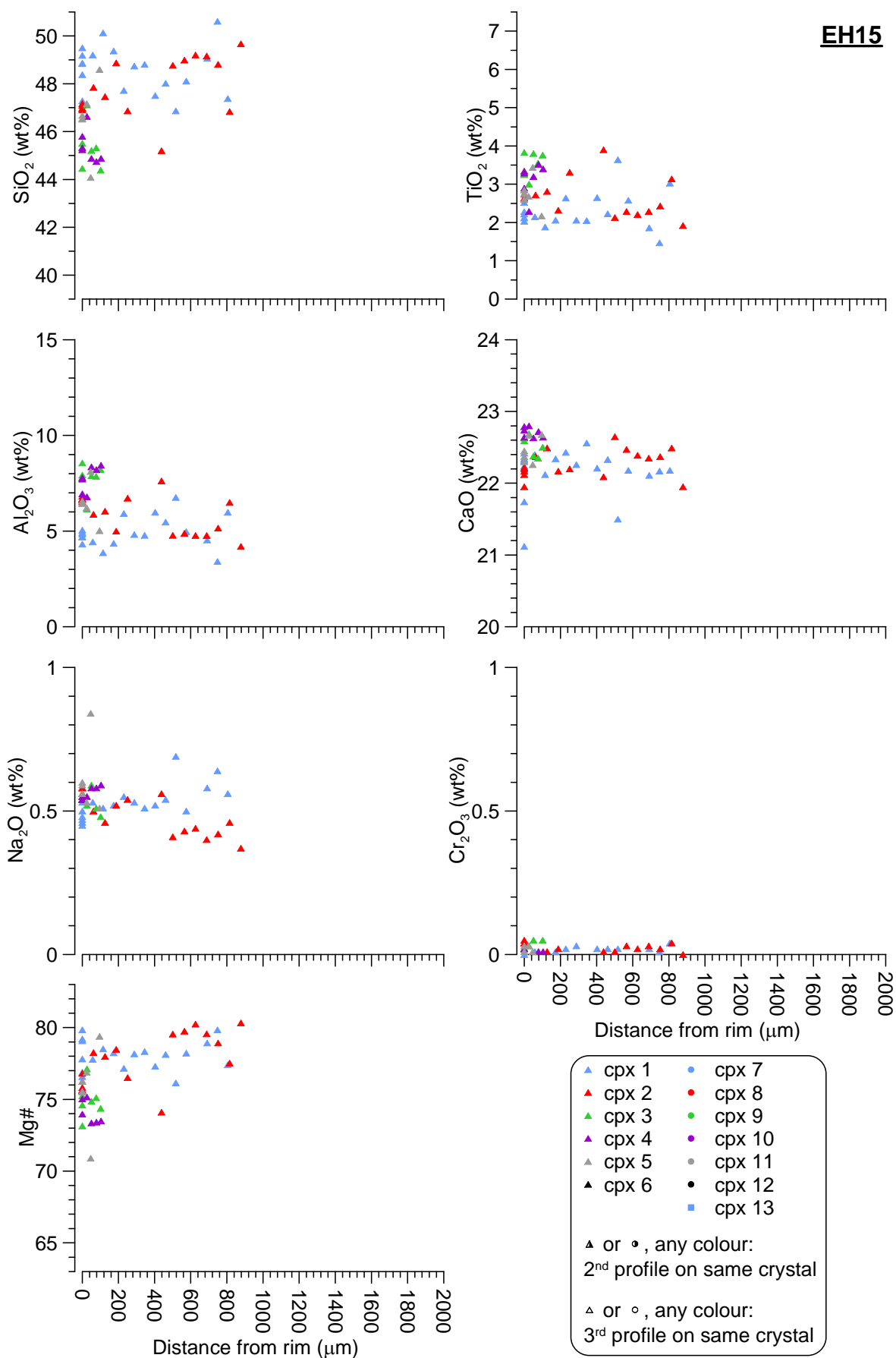




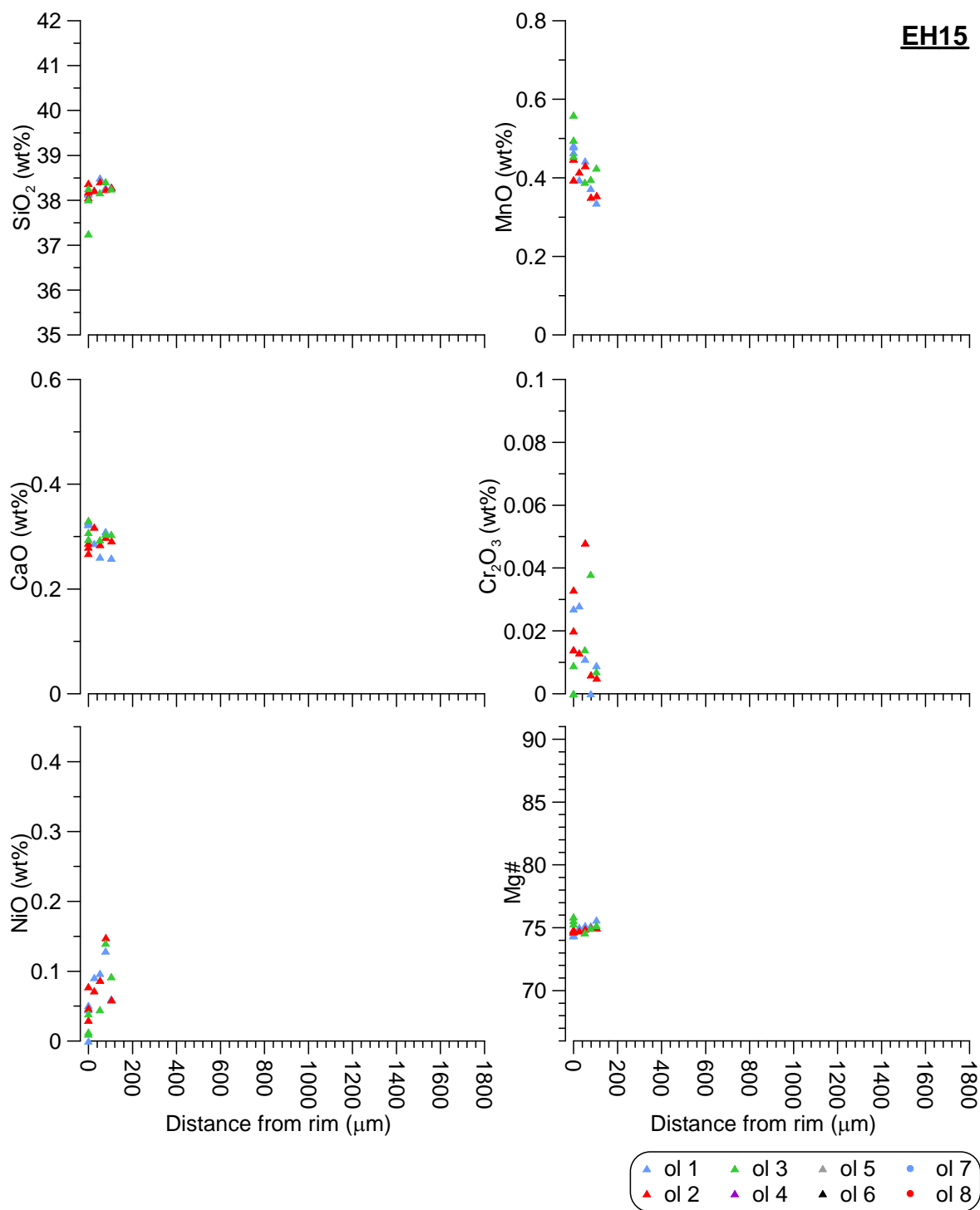
**EH14**



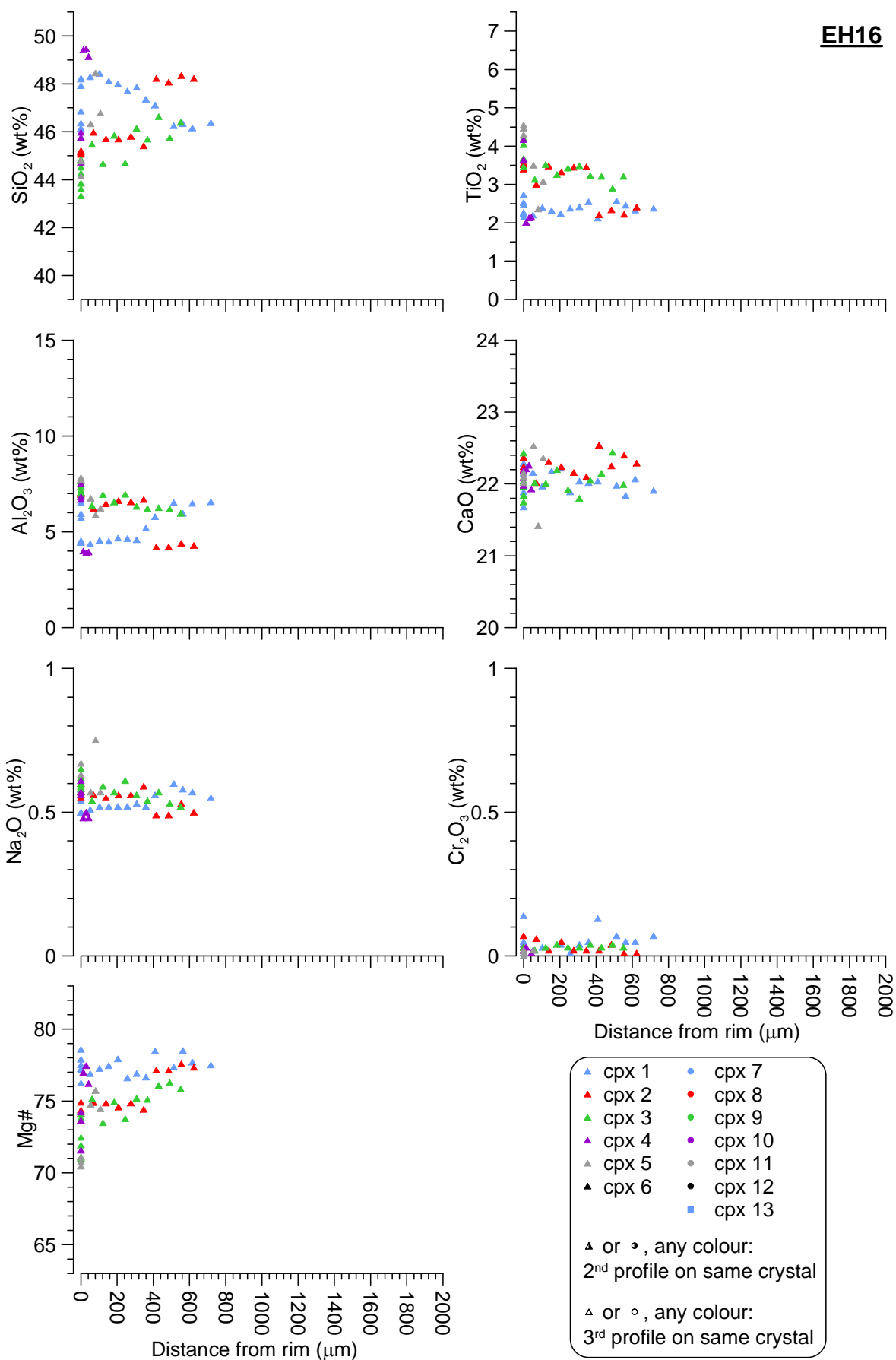
## EH15



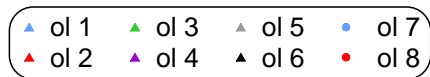
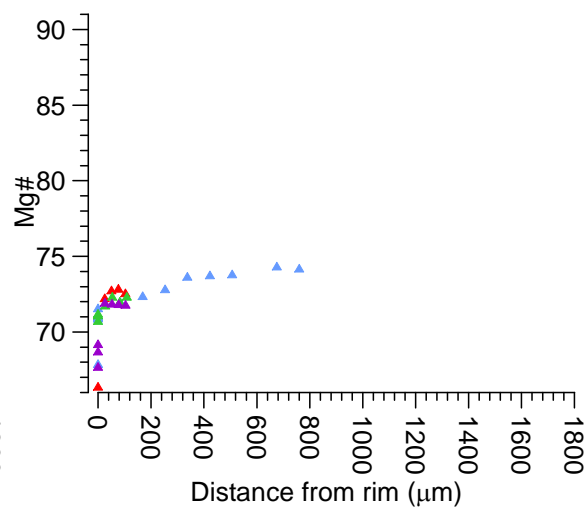
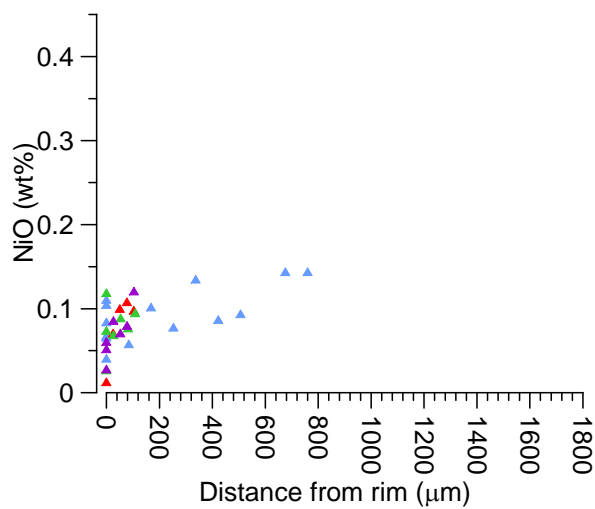
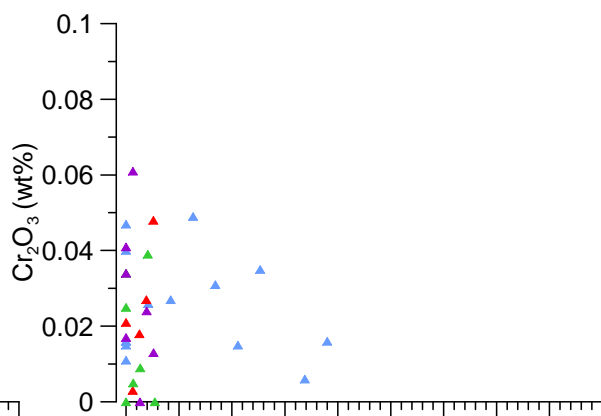
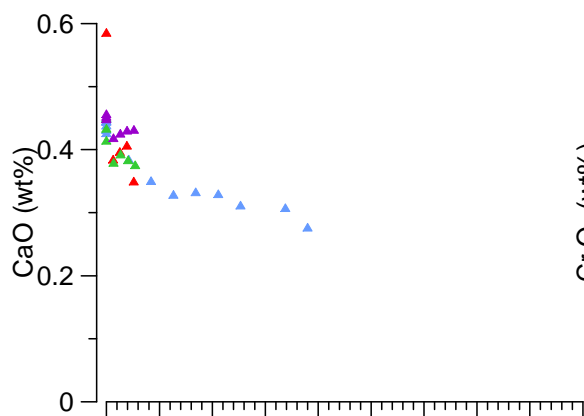
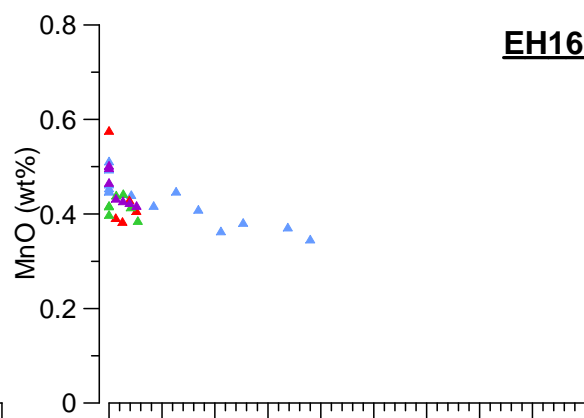
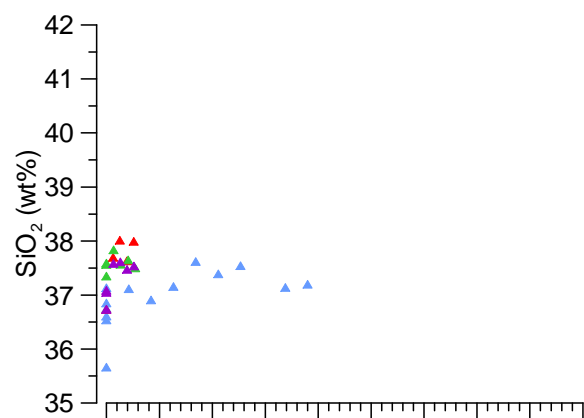
**EH15**



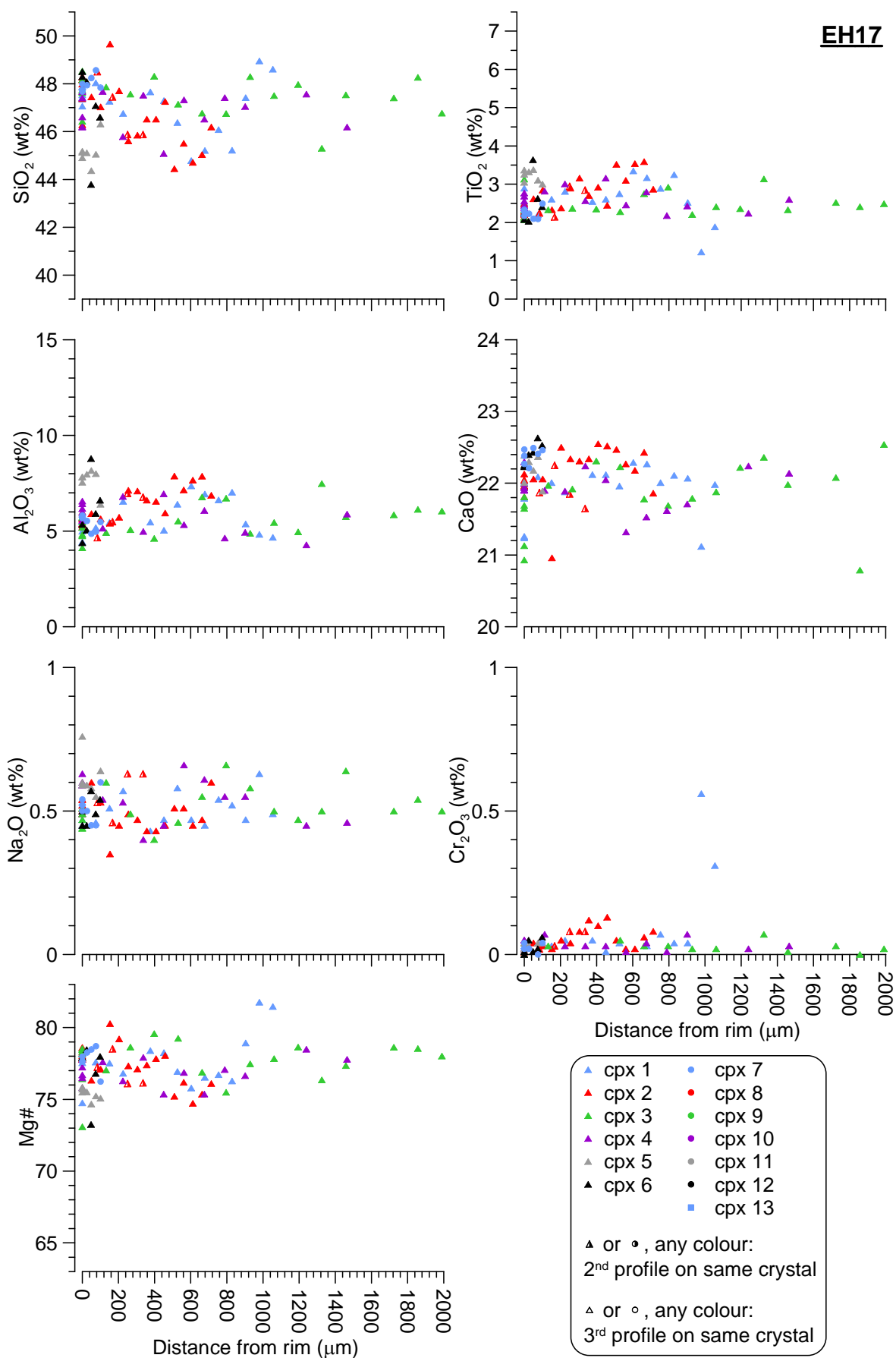
**EH16**



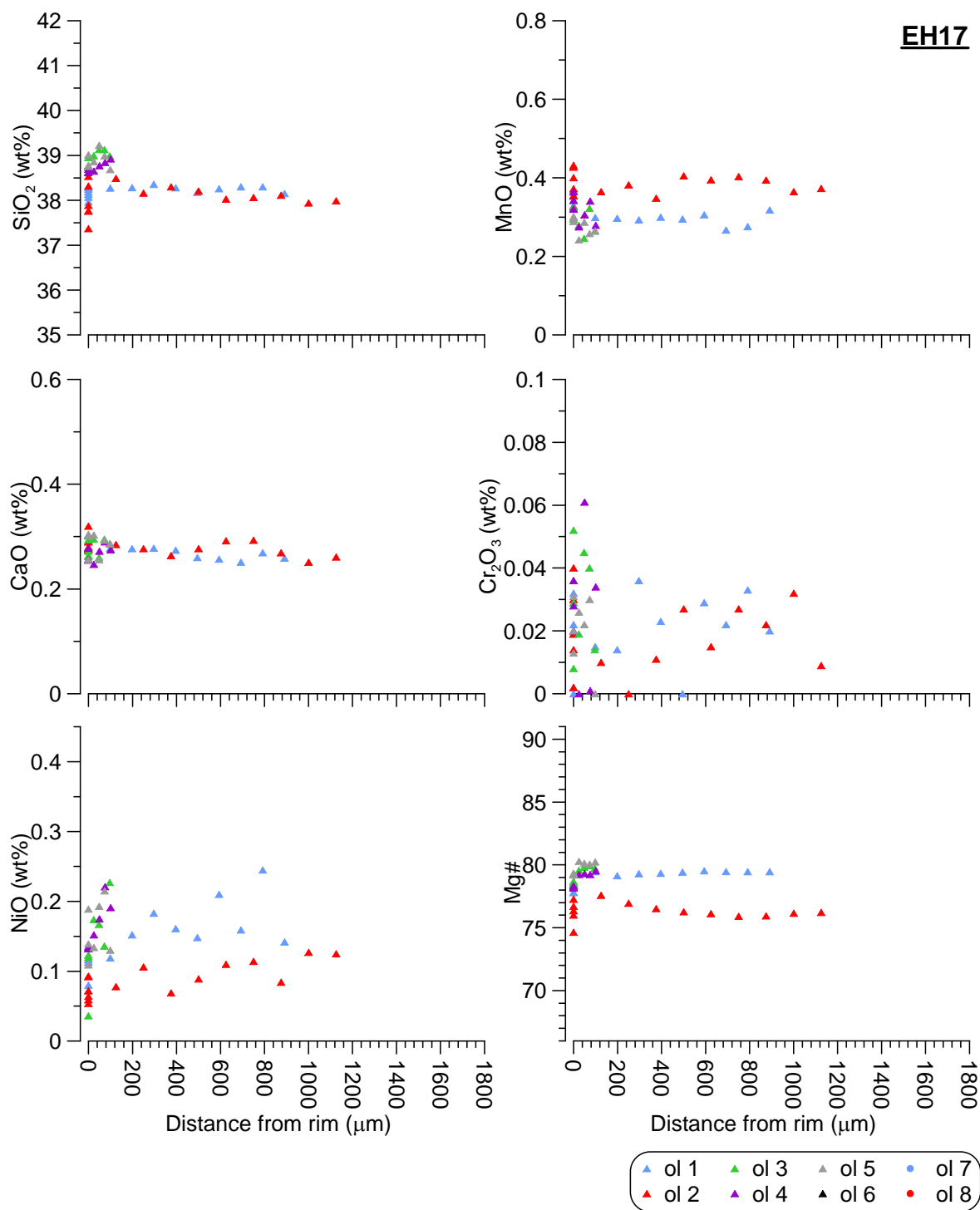
**EH16**



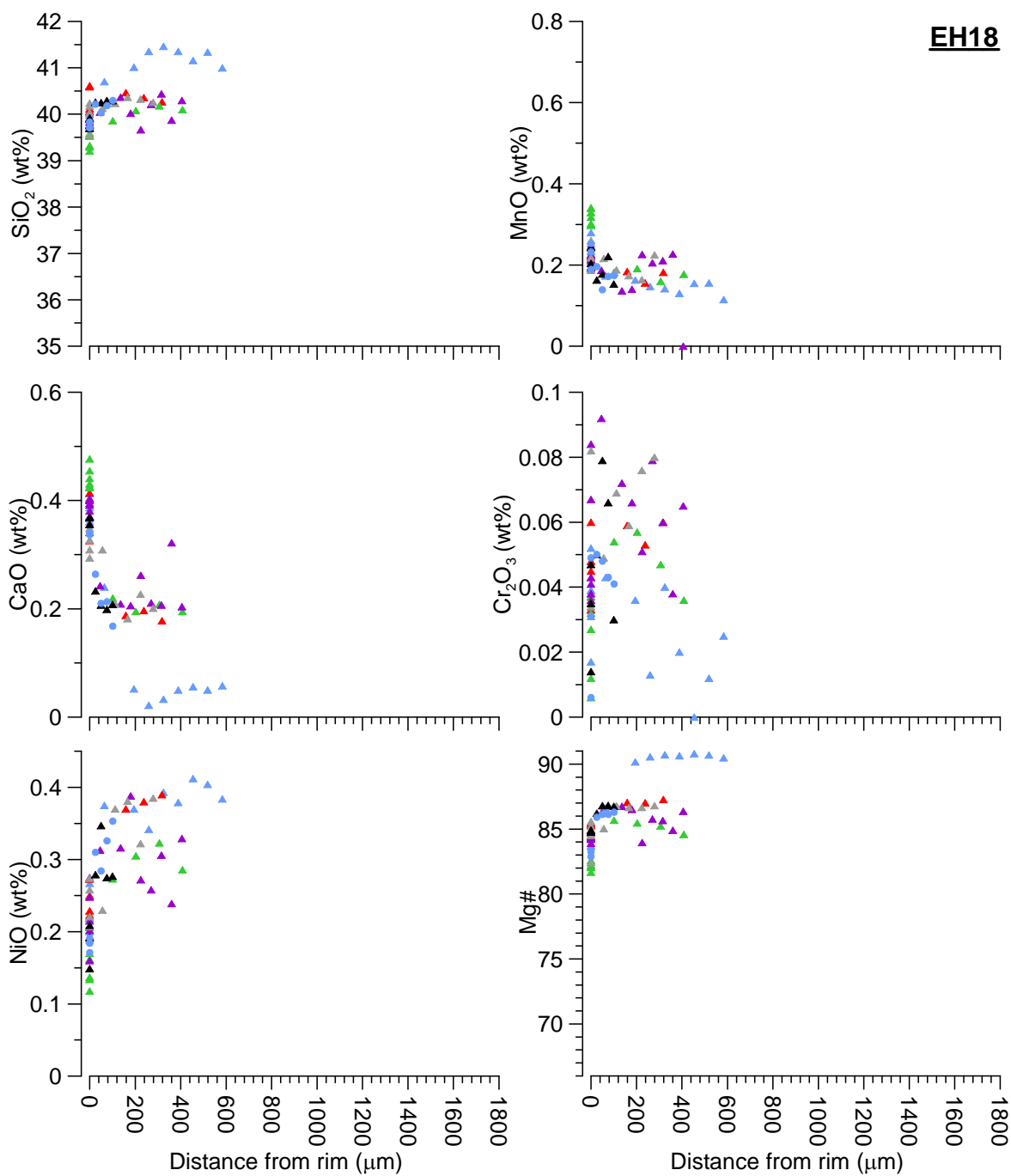
**EH17**



**EH17**

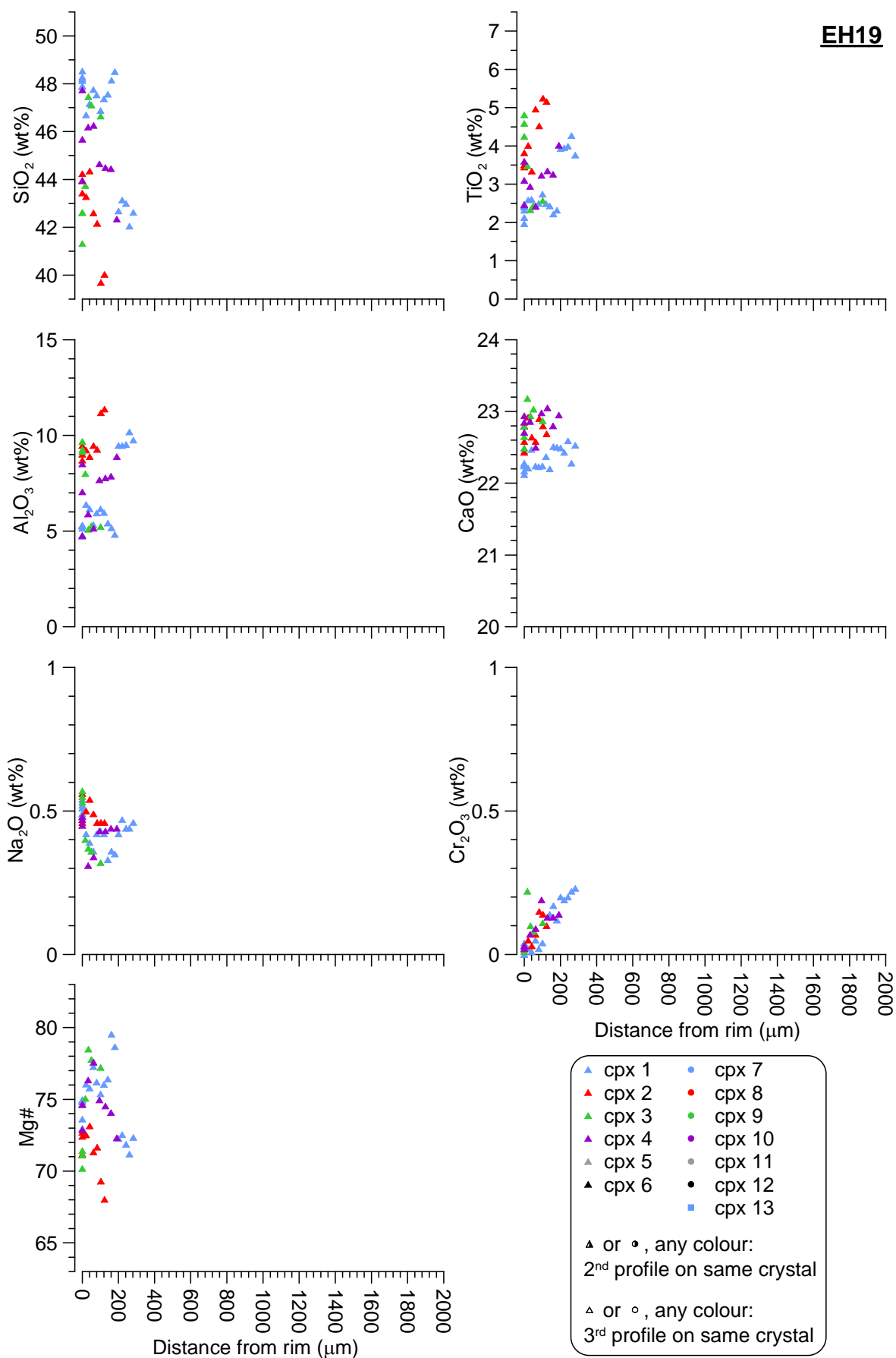


**EH18**

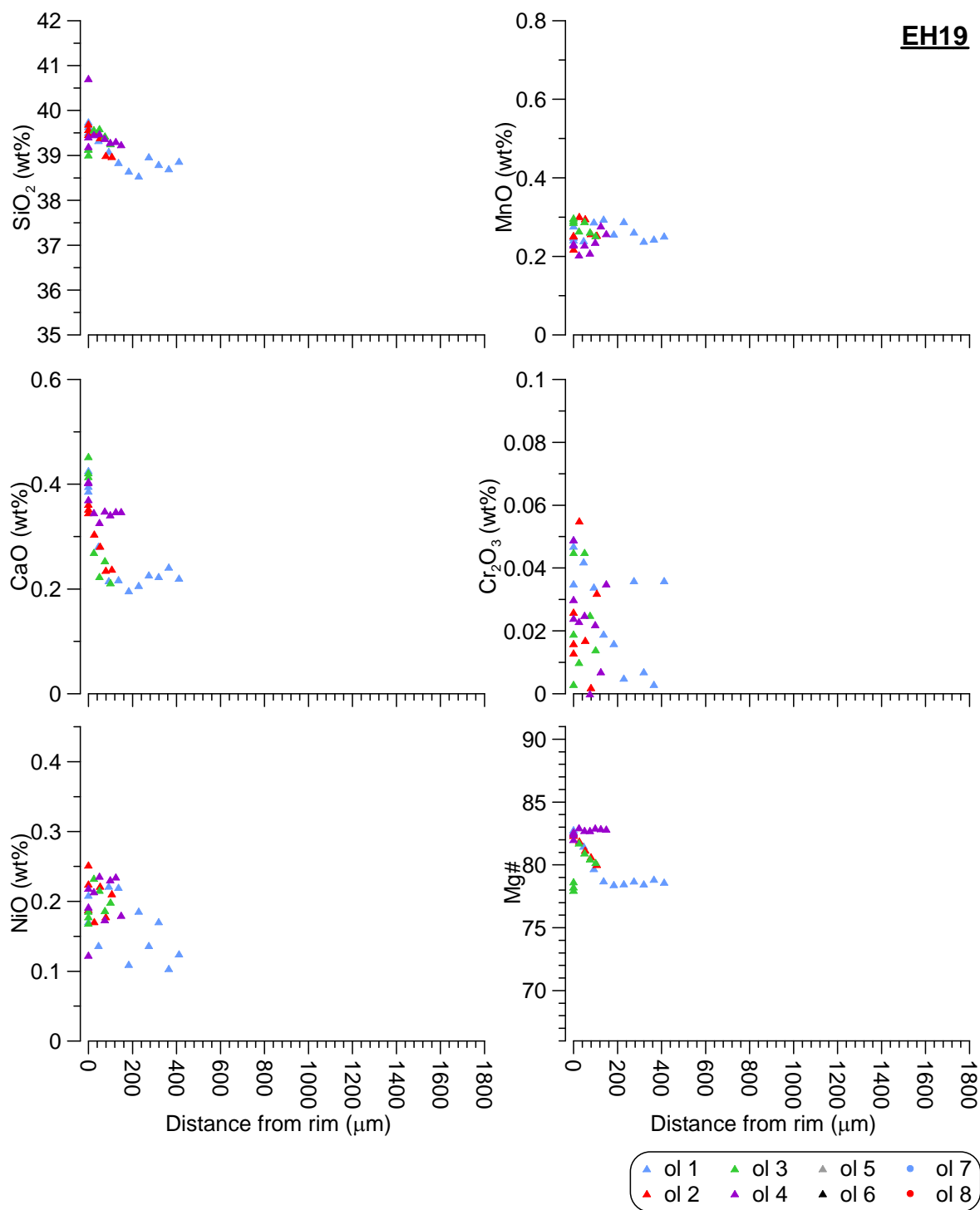


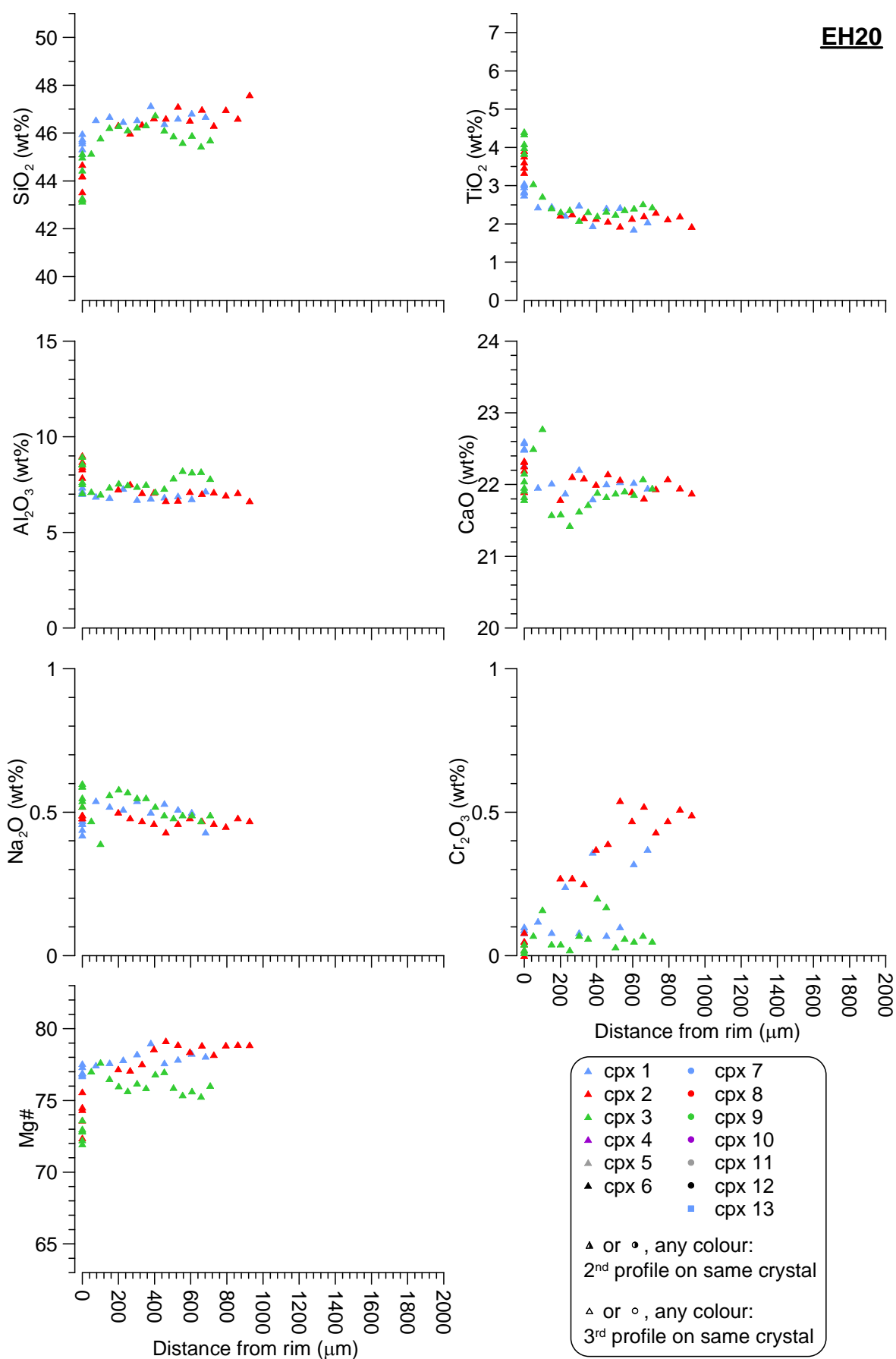


## EH19

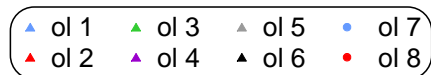
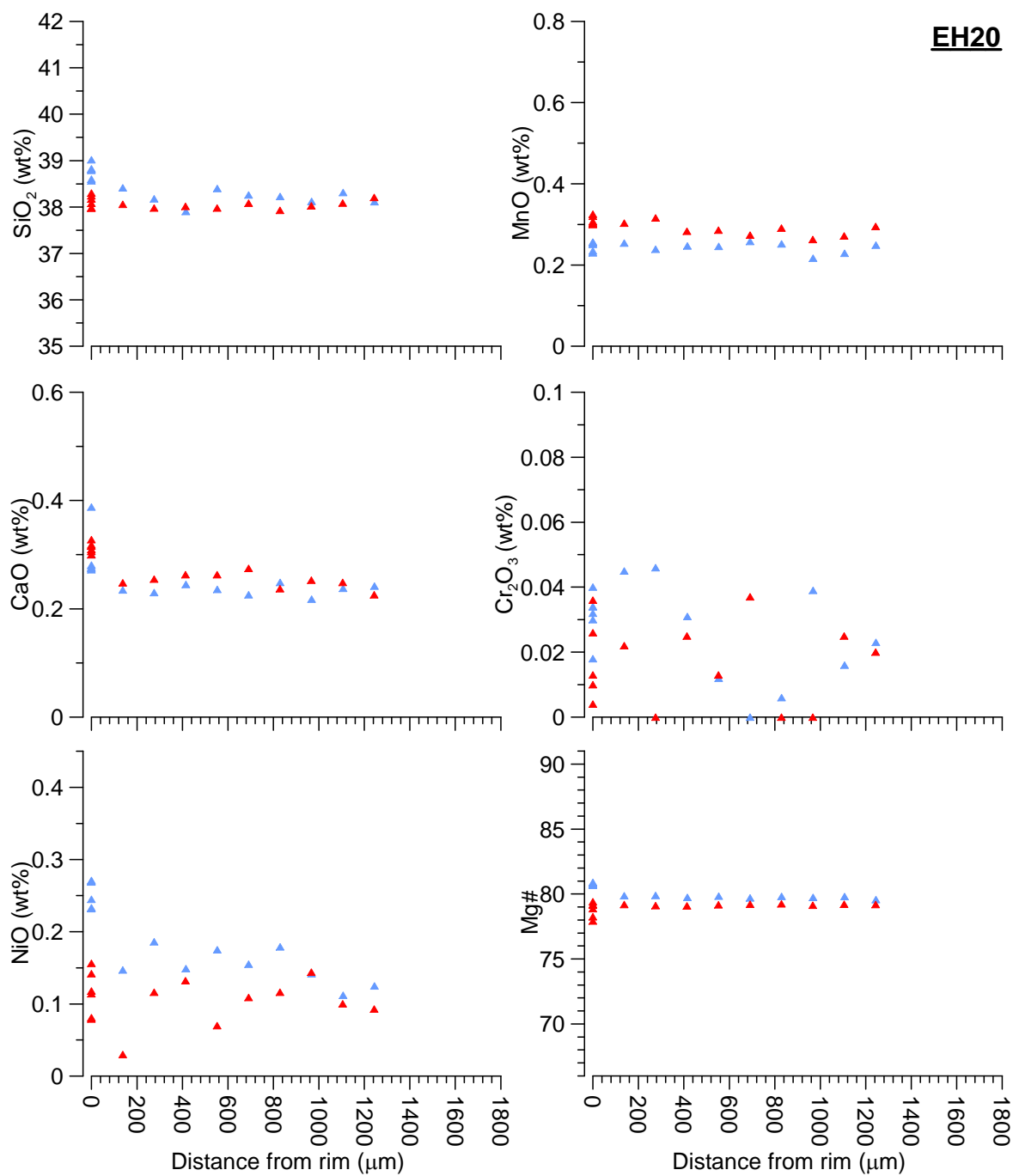


**EH19**

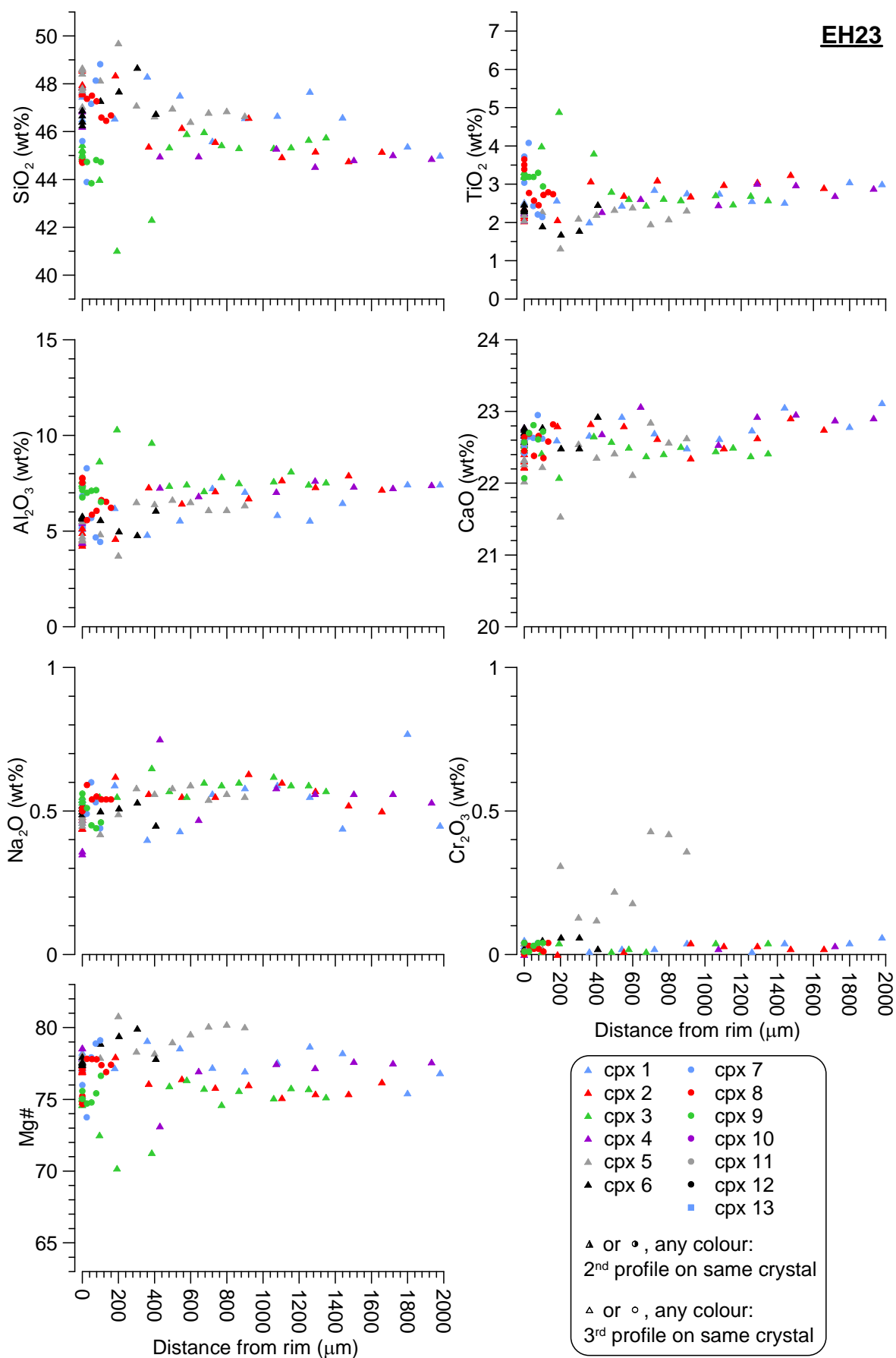




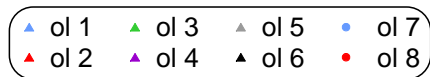
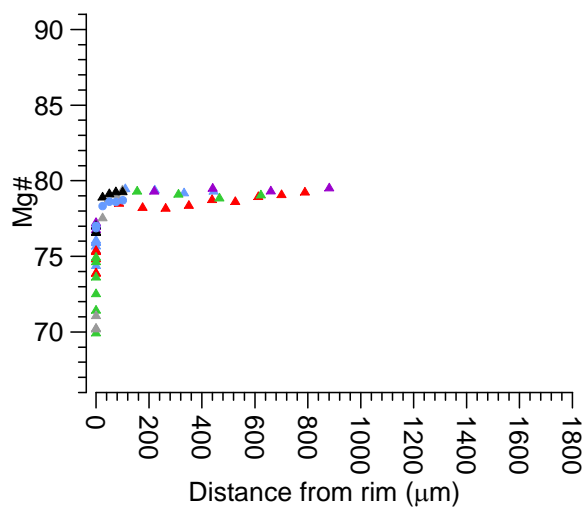
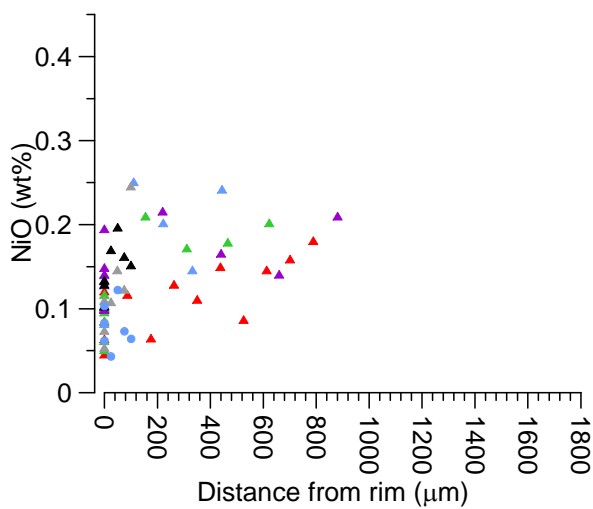
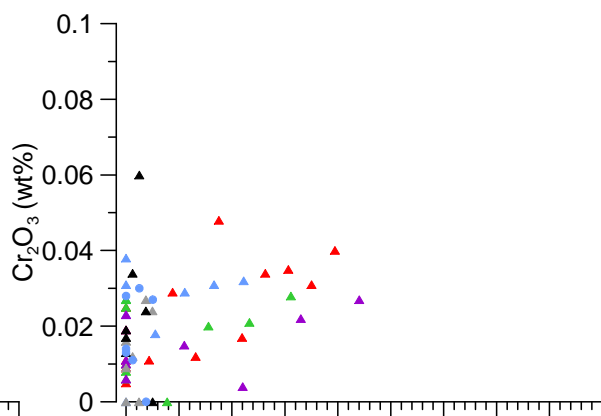
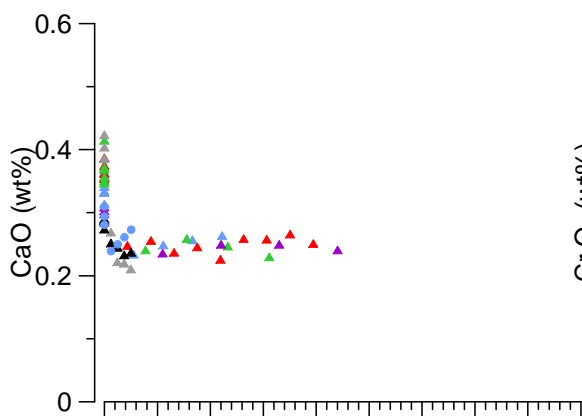
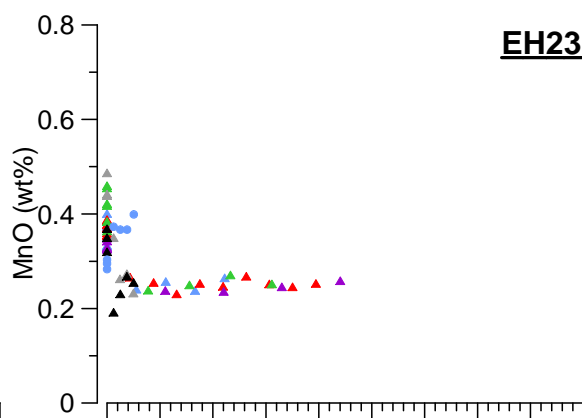
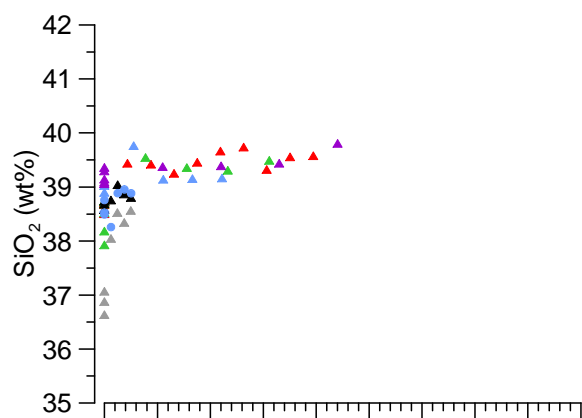
**EH20**



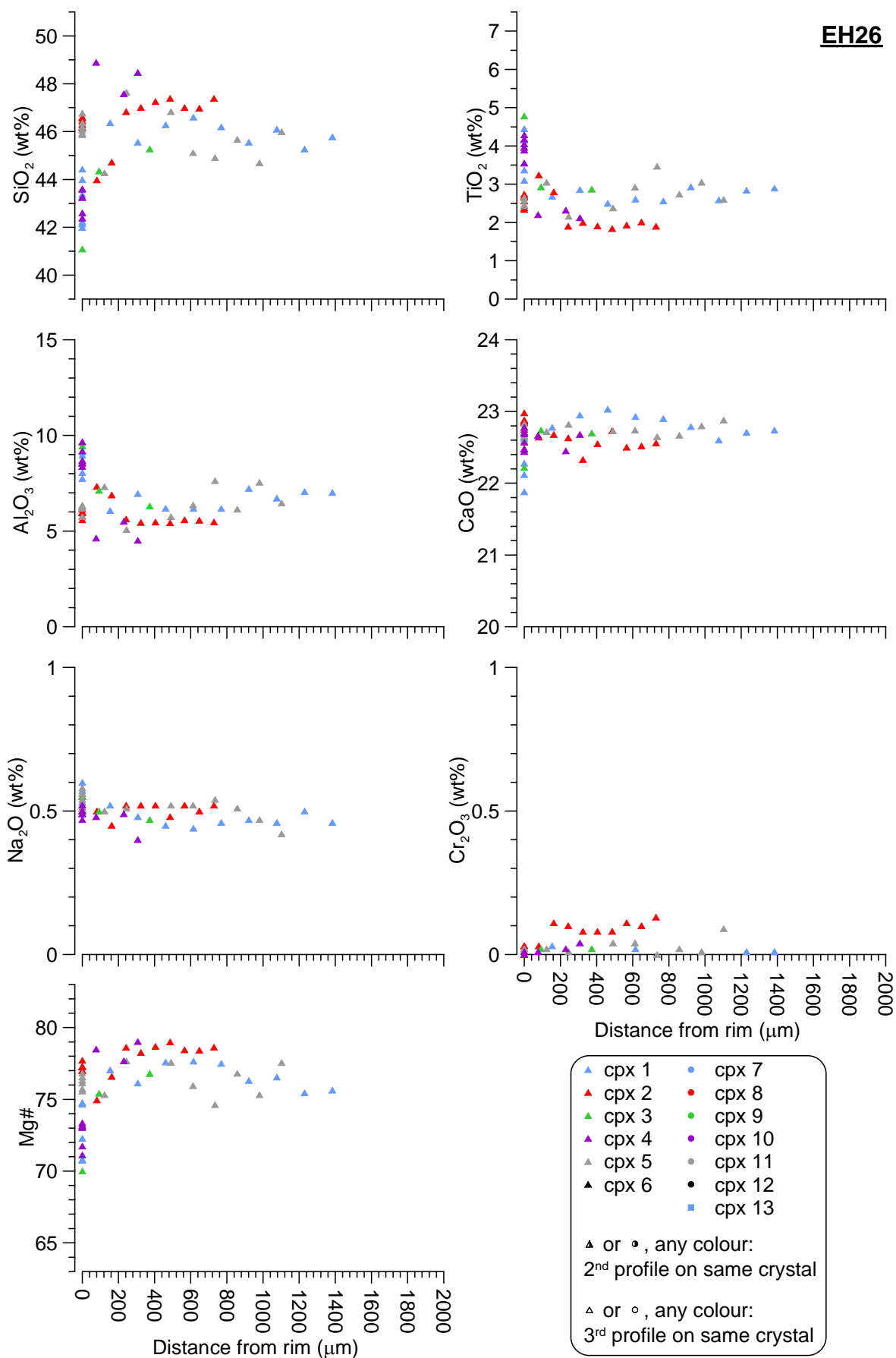
**EH23**



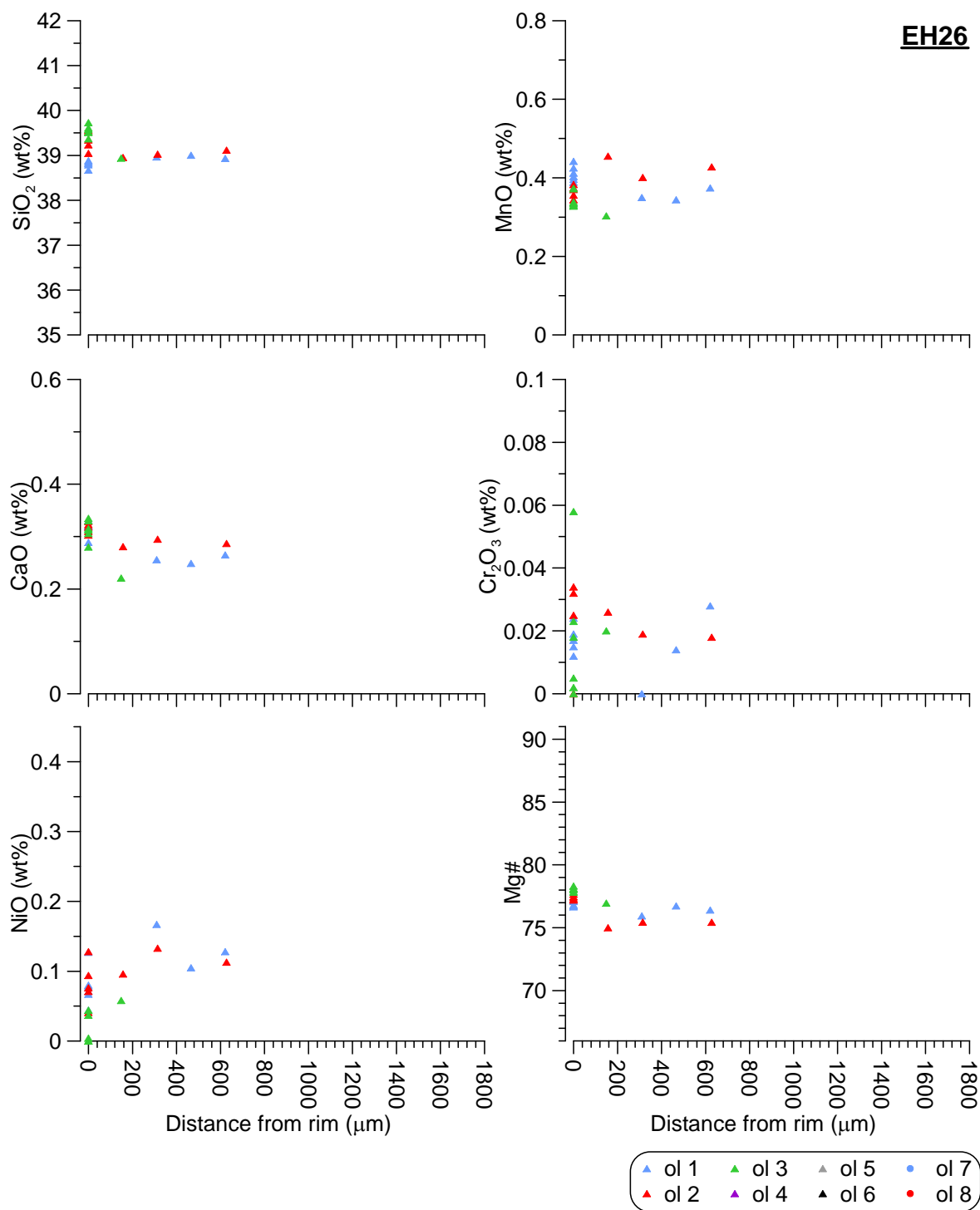
**EH23**



# EH26

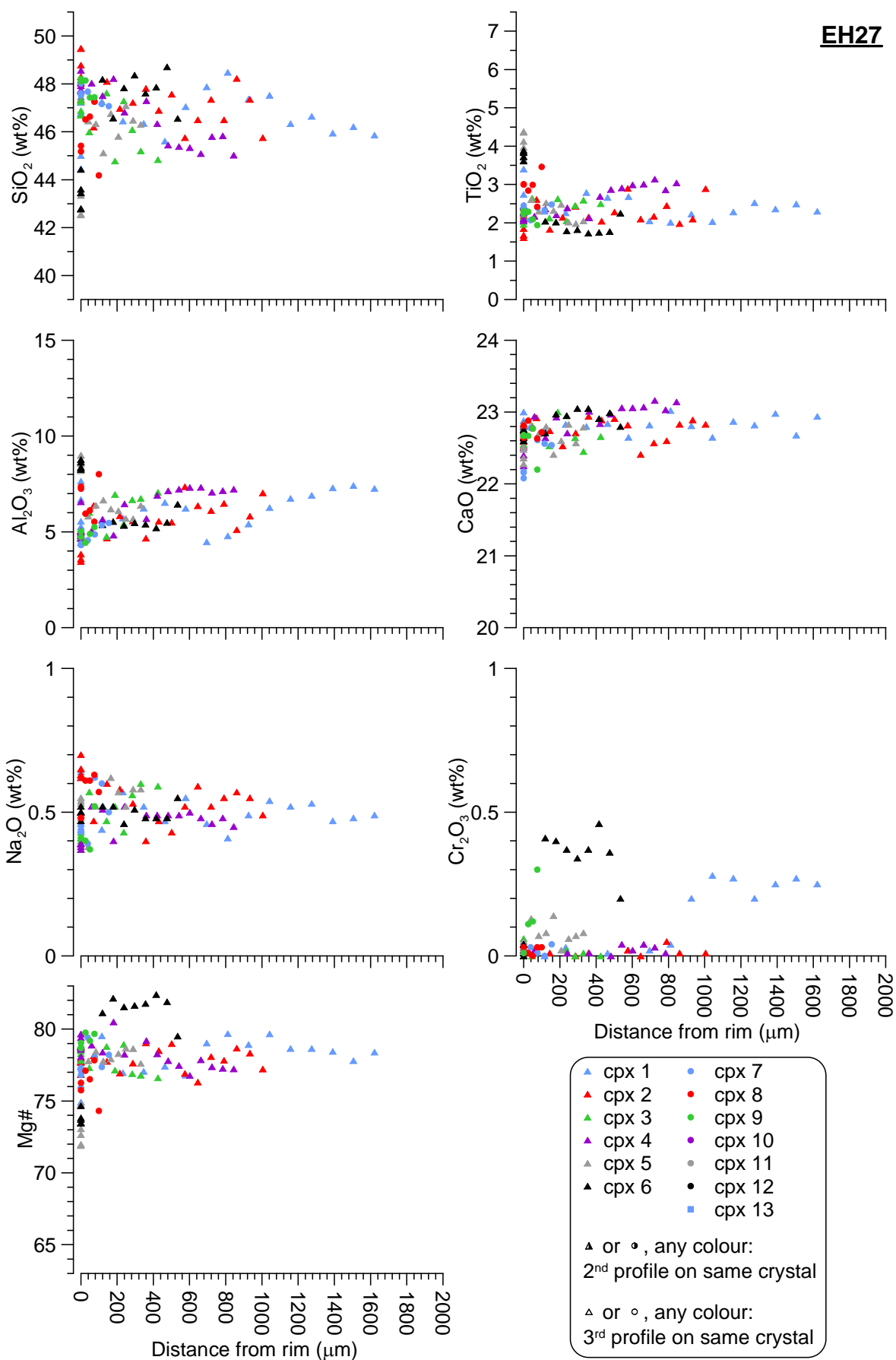


**EH26**

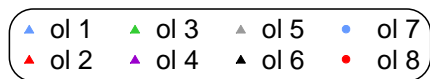
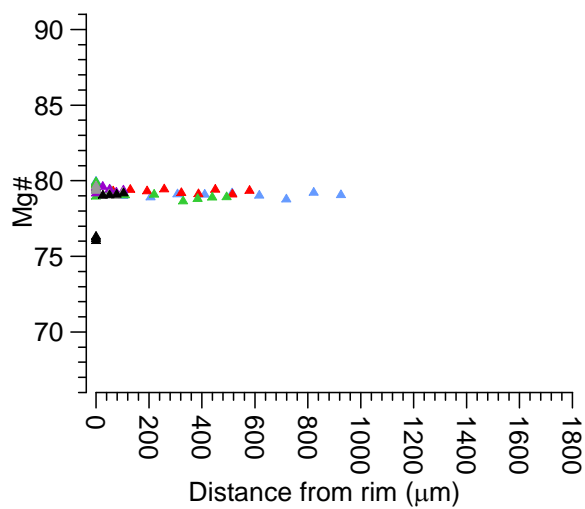
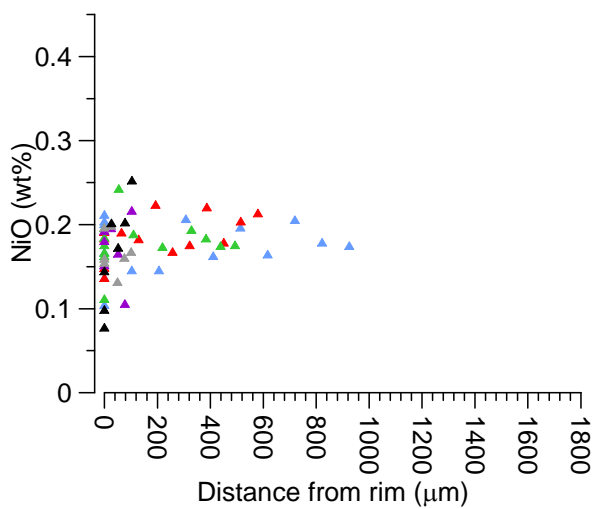
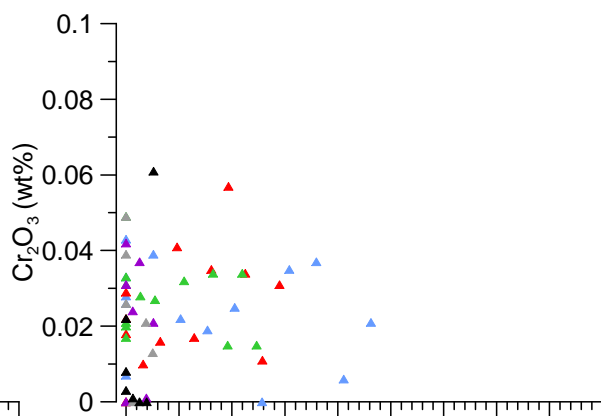
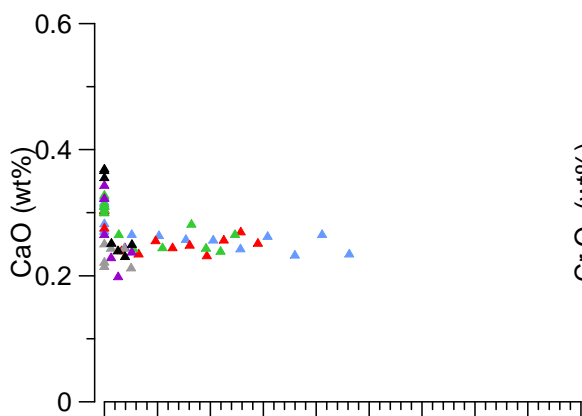
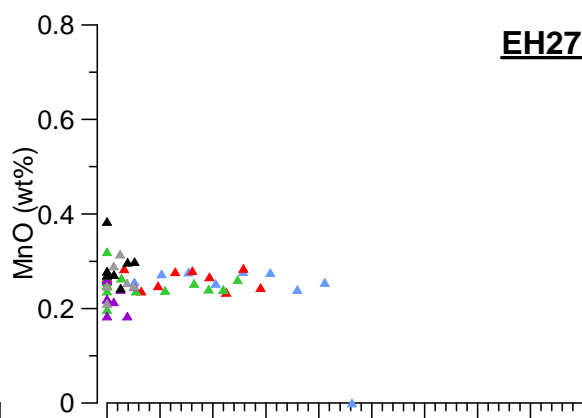
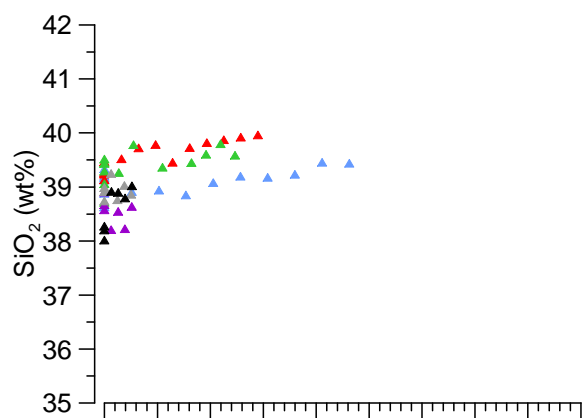


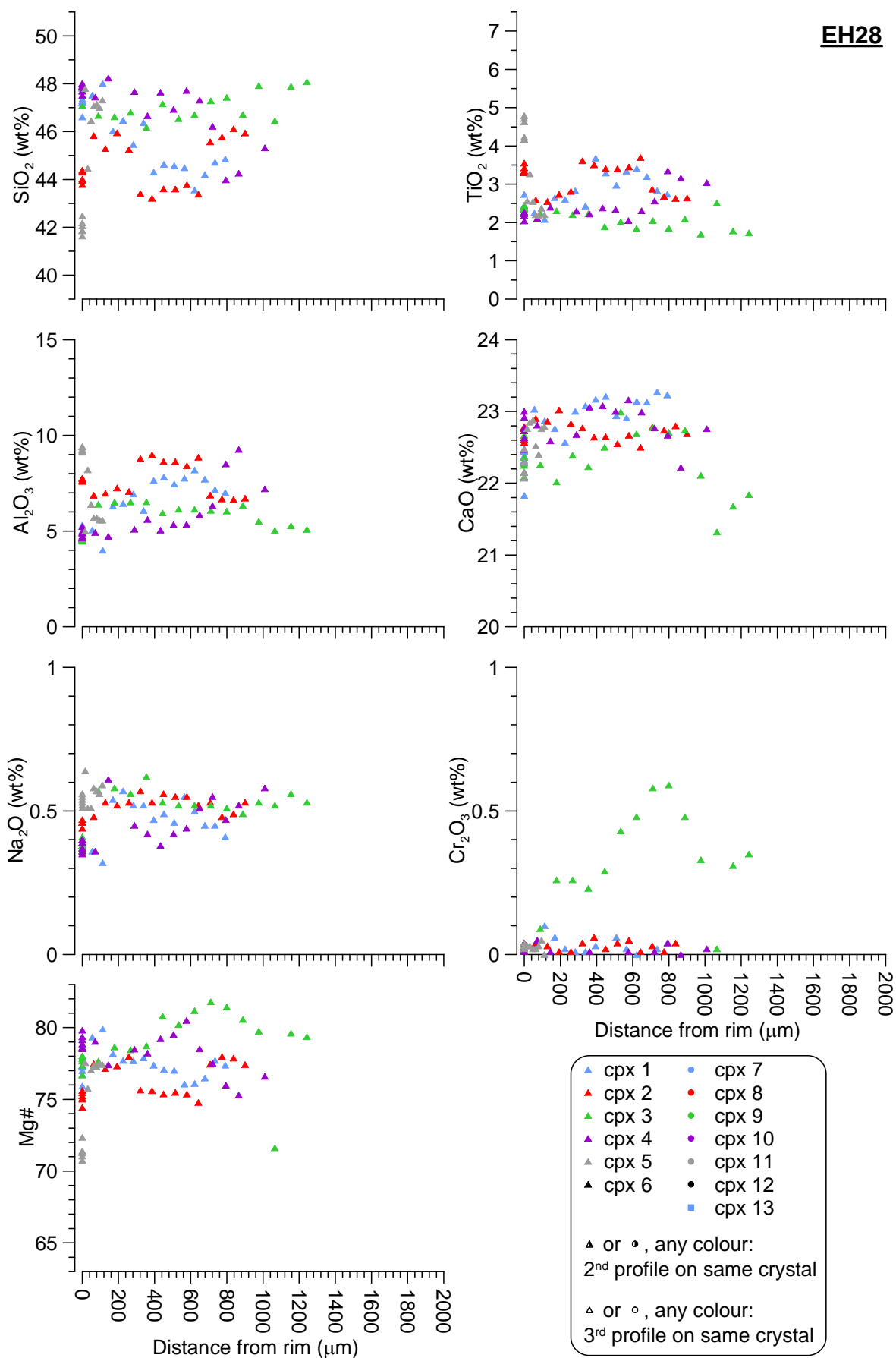


**EH27**

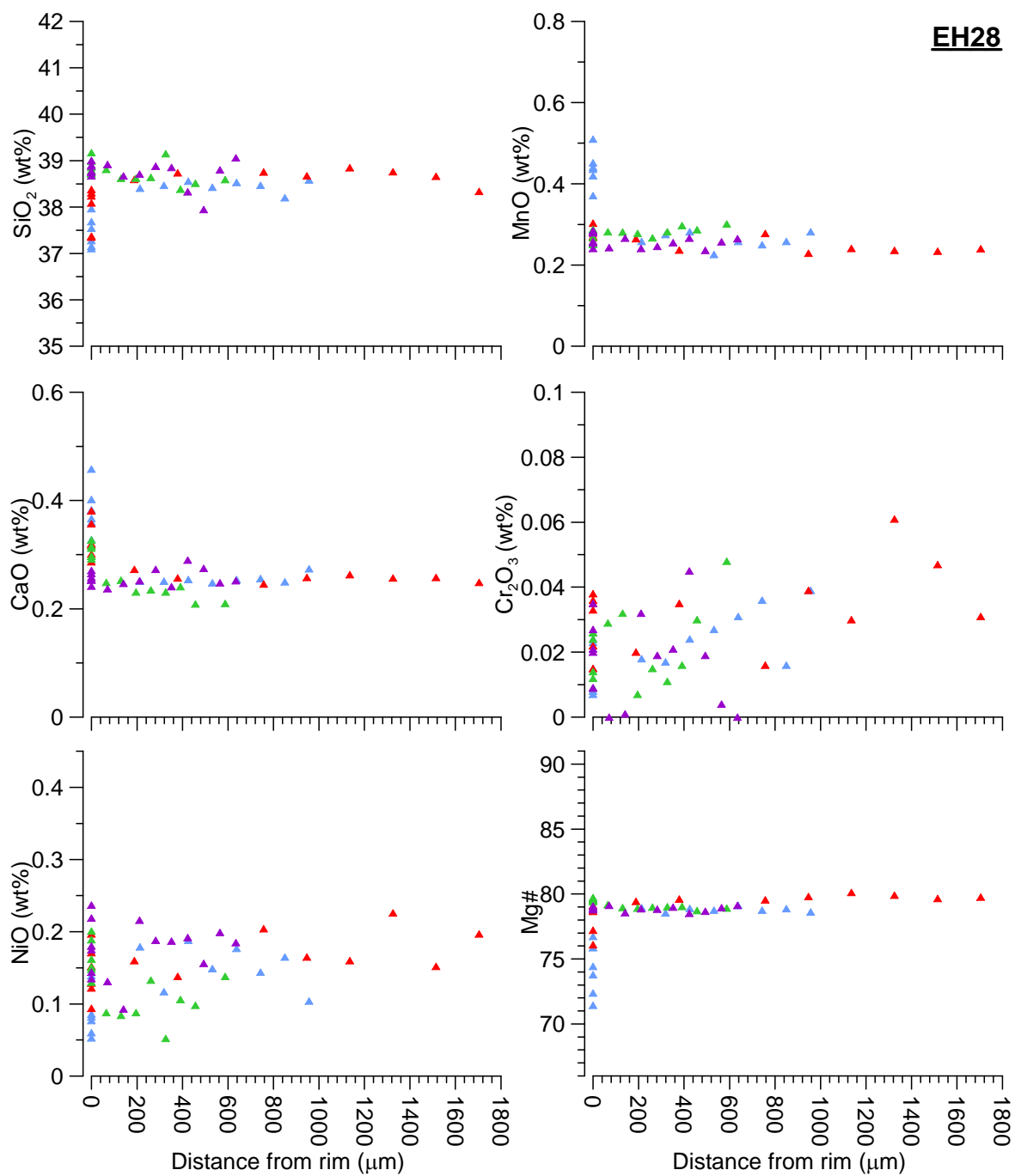


**EH27**





**EH28**



▲ or ●, any colour:  
2<sup>nd</sup> profile on same crystal

▲ or ●, any colour:  
3<sup>rd</sup> profile on same crystal

**EH29**

